Final report for the ”Melt-Vessel Interactions” Project

B.R. Sehgal, T.N. Dinh, R.R. Nourgaliev, V.A. Bui, J. Green, G. Kolb, A. Karbojian, S.A. Theerthan, A. Gubaidulline

Division of Nuclear Power Safety
Royal Institute of Technology
SE-10044 Stockholm, Sweden

Maria Helle, Olli Kymäläinen, H. Tuomisto
IVO Power Engineering Ltd.
Rajatorpantie 8, Vantaa
FIN-01019
Finland

J.M. Bonnet, S. Rougé, M. Narcoux, A. Liégeois
CEA - Grenoble
17 rue des Martyrs
38054 GRENOBLE CEDEX 9
France

B.D. Turland and G.P. Dobson
AEA Technology plc
A32 Winfrith, Dorchester
Dorset DT2 8DH
UK

A. Siccama
ECN Nuclear Research
NRG Petten
Westerduinweg 3, P.O.Box 25
The Netherlands

K. Ikonen
VTT Energy
P.O.Box 1604, FIN-02044 VTT
Finland

F. Parozzi
ENEL - SRI/PAM/GRA
Via Reggio Emilia, 39-20090
Segrate MI Italy

N. Kolev
SIEMENS
Germany

M. Caira
Univ. of Roma
Italy

European Union R&TD Program • 4th Framework
MVI Project Final Research Report, 479 p.
April 15, 1999

Abstract

The **M**elt **V**essel **I**nteraction (**MVI**) project is concerned with the consequences of the interactions that a core melt, generated during a postulated severe accident in a light water reactor, may have with the pressure vessel. In particular, the issues concerned with the failure of the vessel bottom head are the focus of the research. The specific objectives of the project are to obtain data and develop validated models, which could be applied to prototypic plants, and accident conditions, for resolution of issues related to the melt vessel interactions.

The project work has been performed by nine partners having varied responsibility. The work included a large number of experiments, with simulant materials, whose observations and results are employed, respectively, to understand the physical mechanisms and to develop validated models. Applications to the prototypic geometry and conditions have been also performed.

This report is volume 1 of the Final Report for the Project, in which a summary of the progress achieved in the experimental program is provided. We have, however, included some aspects of the modeling activities. Volume 2 of the Final report describes the progress achieved in the modeling program.

The progress achieved in the experimental and modeling parts of the Project has led to the resolution of some of the issues of melt vessel interaction. Considerable progress was also achieved towards resolution of the remaining issues.

Contents

Chapter 1

Introduction and Background

During last 40 years, nuclear power has proved to be a reliable and economically competitive source of energy. However, like any other Hi-tech large-scale energy technology, it is associated with risks to life and health.

1.1 Severe accident safety research

The light water reactor (LWR) systems engineered and constructed in the western countries followed a definite design philosophy for ensuring a very low level of risk to the public. Briefly, the plant systems are designed with the defense in depth concept. The systems are designed to withstand, with a single failure, and prevent a severe accident in which core damage could occur. The design goals for core damage frequency range from 10^{-4} to 10^{-6}/reactor·year. The plant systems are also designed to withstand the loadings due to the design-basis accidents and incidents, and specified external events, e.g., earthquakes, fires, tornados, floods etc. In addition, with characteristic foresight, the designers provided a strong containment system to contain any fission product radioactivity produced even in the beyond-the-design-basis accidents.

The containment structures are designed to withstand pressures much beyond those imposed by the energy release during the design basis accidents. Mitigation measures are provided in the containment buildings, e.g., the suppression pool in the boiling water reactors (BWRs) and the sprays, fan coolers and ice condensers in pressurized water reactors (PWRs) for long term heat removal from the containment buildings. The objectives of these containment safety systems is to keep the pressure low and protect the integrity of the containment in the beyond-the-design-basis accidents. In terms of public safety, it is perhaps self-evident that if containment integrity is not violated, public safety is not compromised.

The severe accident, even if it progresses to the core melt on the floor, will not

be a life-threatening event from the point of view of public safety, if the containment remains intact and leak-tight. Adequate performance of the containment in the aftermath of a postulated severe accident, thus, is of vital concern. In particular, it has been determined that maintaining the integrity of the containment for the first few hours, after any fission product releases in the severe accident, can reduce the containment airborne radioactivity by orders of magnitude. This is a direct consequence of the time constant for aerosol deposition on the containment walls and floors.

Early containment failure, thus, has to be obviated by design or by accident management. Late failure of the containment has also been questioned recently. Perhaps, the public anathema to evacuation and to even a minor land and water contamination is forcing a re-examination of the regulatory attitudes and safety philosophy. Consideration of the requirement of 24 hours as the time for containment leaktightness for the new plants in USA and the moves in Germany towards the design of the containment, which will not fail under extreme loadings, are indicative of these new attitudes and philosophy. These containment performance goals, laudable as they are, for the new plants, will be difficult to achieve if the old evaluation philosophy of using conservatism at each step is employed. Thus, it is imperative, that the new containment performance goals are accompanied by rational evaluation methodologies.

1.2 Severe accident phenomena and safety issue

The radioactive elements remain in the reactor fuel, where they are produced. In order to release significant amount of radioactivity, the fuel elements must be damaged. This can happen only when the fuel temperature excursion is occurred, and the fuel melts or disintegrates. *The basic aim of the reactor safety is to prevent fuel overheating*. This is achieved by designing and operating the nuclear power plant so that the power is always controlled and the core is well cooled. If the safety systems do not operate effectively, the fuel can overheat and, in severe instances, melt partially or completely.

The last decade (80s) is characterized by considerable investment from utilities and regulatory bodies into research of different phenomena associated with core melt progression inside the reactor pressure vessel (RPV) and the containment. Knowledge of basic phenomena and mechanisms, related to the core meltdown process, has increased year by year. Different analytical models have been developed and verified by experiments. These models are implemented into integral and separate-effect computer codes, which describe thermohydraulics and structural response of the reactor vessel and containment, starting from an assumed initiating event.

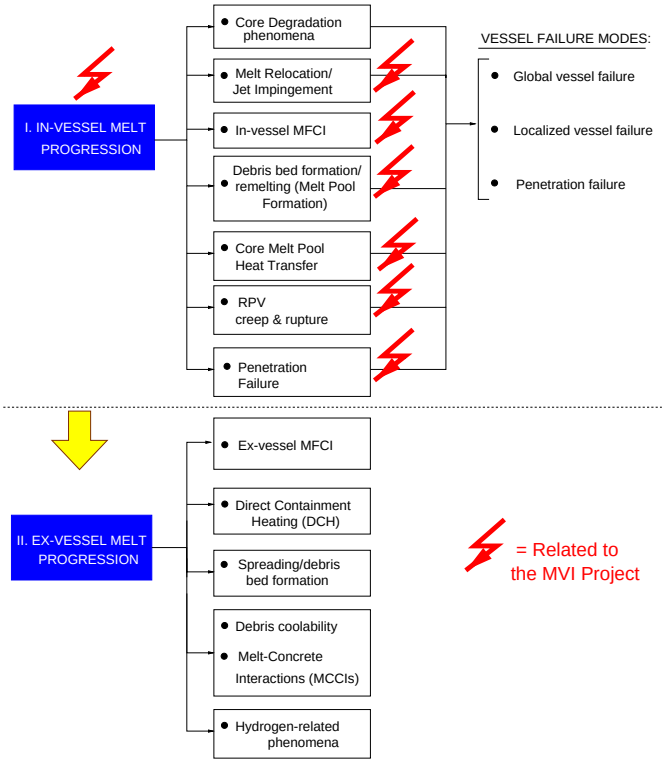

Fig. 1.1: *Summary of major severe accident phenomena and relevance of the present study.*

In general, severe accident progression can be divided into the in-vessel and ex-vessel stages, fig.1.1. A great number of challenging phenomena, beginning from those involved in core degradation, and finishing with molten corium-concrete interactions (fig.1.1), are within the research interest of nuclear engineering community. Importance of each phenomenon is dependent on the accident scenarios and severe accident management scheme implemented in a particular reactor[1].

[1] *E.g., ex-vessel FCIs* (and, precursor to them, reactor vessel penetration failure and hole ablation) are of importance for Swedish BWRs, since melt jet fragmentation and subsequent debris bed coolability is the major severe accident management concept for BWRs of ABB design. *In-vessel melt retention* (IVMR), by flooding the reactor vessel, is the management scheme for a severe accident in the Loviisa VVER-440 (Finland) and in the AP-600 (USA) reactors. *Jet impingement* and *melt pool natural convection* heat transfer are the phenomena of importance for determining the feasibility of the IVMR concept.

1.3 In-vessel melt progression

Major stages of the IVMP, together with modes of the vessel failure, are outlined in fig.1.2. The scheme sketches the simplified sequences of phenomena and possible interactions, which are typical for most LWRs.

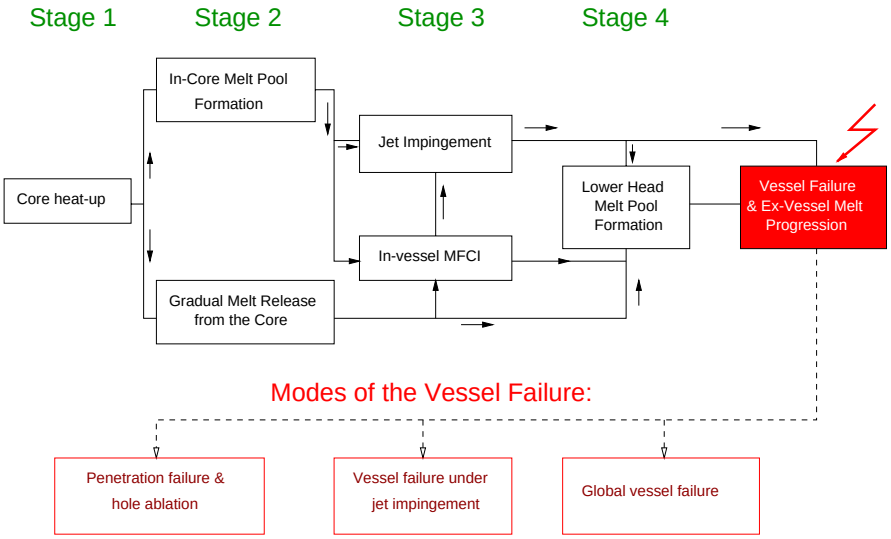

Fig. 1.2: *Outline of the In-Vessel Melt Progression (IVMP) stage of a severe accident.*

1.3.1 Core heat-up and degradation

IVMP starts from core heat-up (stage 1). Once the water level in the reactor vessel drops, such that the core becomes uncovered, the fuel clad temperature will rise rapidly due to the decay heat in the fuel. At about 900°C, zirconium (in the fuel cladding) and steam begin to produce hydrogen and generate more heat. The heat-up of the fuel is accelerated, when the temperature exceeds about 1200°C. At this level of temperature, the $Zr - H_2O$ reaction will be violent and the rate of heat generation may be much much greater than that of the decay heat.

Once the temperature of the clad material reaches the melting point, the molten material starts to relocate downwards. Being in contact with colder solid structures, the melt may solidify again, forming a barrier for the molten material coming later (”candling” and ”blockage” processes).

There is a number of integral and separate-effect codes, developed for modeling of transient core heatup and melting, such as the well-known integral codes SCDAP/RELAP5 [5], MAAP [19], APRIL [18] and MELPROG [6]. These codes

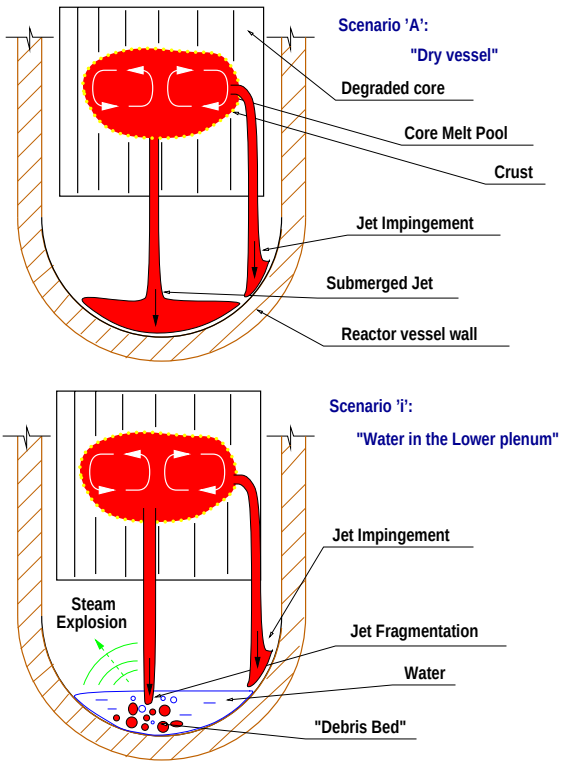

Fig. 1.3: *Schematic of in-vessel melt relocation/jet impingement and MFCI phenomenology.*

contain core degradation mechanistic models, with different levels of sophistication. Several separate-effect codes, such as DEBRIS [7], [8], ICARE2 [9] and MESOCO-2D [2] have been developed for simulation of the late-phase melt progression in the reactor core, by using a two-dimensional quasi-continuum approach in a multifluid formulation.

1.3.2 Jet impingement

If the heat transfer rate is sufficiently high during the core heat-up and degradation stages of a severe accident, considerable amount of the molten core materials might be trapped in the reactor core, forming the in-core melt pool (ICMP), fig.1.3. Eventually, the crust of the ICMP fails, and molten materials relocate to the lower head of the RPV in form of oxidic or metallic jet. In such a scenario, it has been recognized (Rempe et al., 1993 [22], and Theofanous et al., 1995 [27]) that vessel wall ablation (melting) due to jet impingement heat transfer could be a vessel failure mode, which has to be evaluated for assessment of the resulting containment loadings.

1.3.3 Molten Fuel - Coolant Interactions (MFCIs)

In case of scenarios, involving the presence of water pool in the lower plenum of the RPV during the early stage of a severe accident, extremely hot melt ($\sim 3000K$) may be in contact with coolant. MFCI[2] is very important and, probably, the least understood issue of a severe accident. It starts with *premixing stage*[3], during which extremely complex physics of multiphase steam-water-melt mixture takes place. Once the multiphase liquid/liquid/vapor/(solid) state is established, the mixture could support a thermal detonation wave (*steam explosion stage*), assuming all the necessary conditions for explosive vapor formation are met, Henry (1995) [10].

In-vessel MFCIs are of great importance from two major points of view. First, the destructive energetic in-vessel steam explosions (so-called '$\alpha-$mode') may present a potential threat for vessel and containment ('missile effect') integrity, Theofanous (1995) [26]. Second, fragmentation of the core melt jet determines the porosity of the debris bed formed in the RPV lower plenum. Additionally, if the molten corium jet is fragmented during its passage through the water pool, there is no direct attack of the jet upon the vessel wall, and, hence, a potential danger for localized vessel failure by jet impingement is reduced[4].

1.3.4 In-vessel melt retention (IVMR)

The idea of this severe accident management concept is to ensure the vessel integrity by submerging the reactor vessel into the water pool. Technical feasibility of the IVMR strategy was first demonstrated for Loviisa (Finland) nuclear power plant, incorporating a Russian VVER-440 reactors (Theofanous, 1989 [24]). Related research program has been going on for the past several years (Kymäläinen et al., 1992 [16], 1993 [17]). Later, similar strategy was proposed for the AP-600 reactor, and its feasibility has been examined by Theofanous and co-workers (1995) [27]. Independently, the idea of the in-vessel melt retention has been pursued also by Henry and co-workers (Henry et al., 1991 [11], 1993 [12]) and by Hodge (1991) [14].

[2]FCI is another frequently used abbreviation for (Molten) Fuel - Coolant Interactions.

[3]In some references ([10]), this stage is termed as coarse mixing, or coarse pre-fragmentation.

[4]From severe accident management strategy point of view, this may have a *positive* and *negative effects*. *E.g.*, the earlier vessel failure for Swedish BWRs prevents the possibility of massive melt release due to a global vessel rupture. In contrast, the aims of the in-vessel melt retention (IVMR) concept for the Loviisa VVER-440 and AP-600 reactors are to retain the vessel integrity during the course of a severe accident.

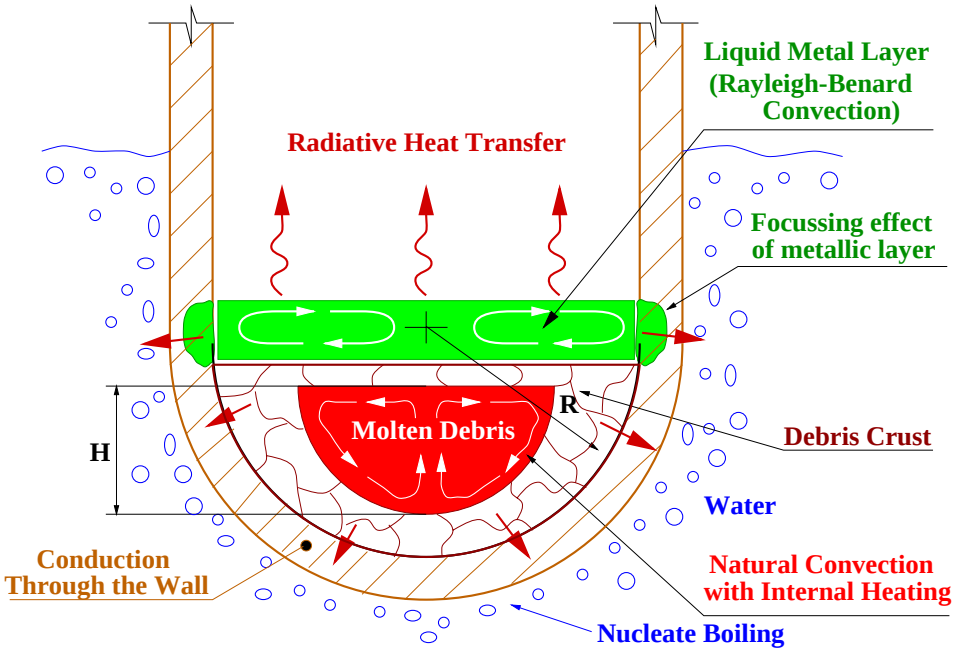

Fig. 1.4: *Schematic of In-Vessel Melt Retention (IVMR) phenomenology.*

Melt pool natural convection heat transfer is of fundamental significance in assessing the feasibility of the IVMR. Fig.1.4 describes *phenomenology* of the late phase of the IVMR. The decay-heat from the molten corium pool is extracted by nucleate boiling on the outside surface of the RPV. Due to the large difference in the melting point between the vessel wall and oxidic melt pool, a thin oxidic crust layer exists on the vessel inside wall, which serves as a thermal insulation, preventing the vessel wall from melting. Because of the density difference between the oxidic and metallic melts, the metallic-rich component might separate into the overlaying layer, fig.1.4. Natural convection in this layer is driven by *a)* heat addition from the (downward) oxidic decay-heated melt pool and *b)* heat removal upwards (mainly by radiation heat transfer) and horizontally (from the cooled vertical vessel wall). In this case, natural convection flow pattern is a combination of the Rayleigh-Bénard convection and vertical wall boundary layer flow.

Metallic layer focussing effect. The metallic melt layer might be significantly superheated (especially in case of thin metal layers). In addition, the freezing temperatures of the metallic melt (composed of Fe + Zr mainly) and the vessel wall (carbon steel) are close to each other. Thus, the driving temperature difference for sidewall heat removal is large, and there is a potential risk for

vessel wall meltthrough. Thermal loadings on the AP-600 RPV have been recently evaluated by Theofanous et al. (1995) [27]. The assessment of metallic layer natural convection heat transfer was based on the experimental integral heat transfer characteristics, available for Rayleigh-Bénard and vertical boundary layer natural convection flows. The analysis was supported by a confirmatory "mixed natural convection" simulant experiment (MELAD). Sufficient safety margin was demonstrated for thick metal layers (about 1 m in height). For high-power reactors, though, the feasibility of IVMR has not been proven yet. There is a concern with respect to the enhancement of the heat flux, imposed on the vessel side wall, due to the focussing effect of the metallic layer [4].

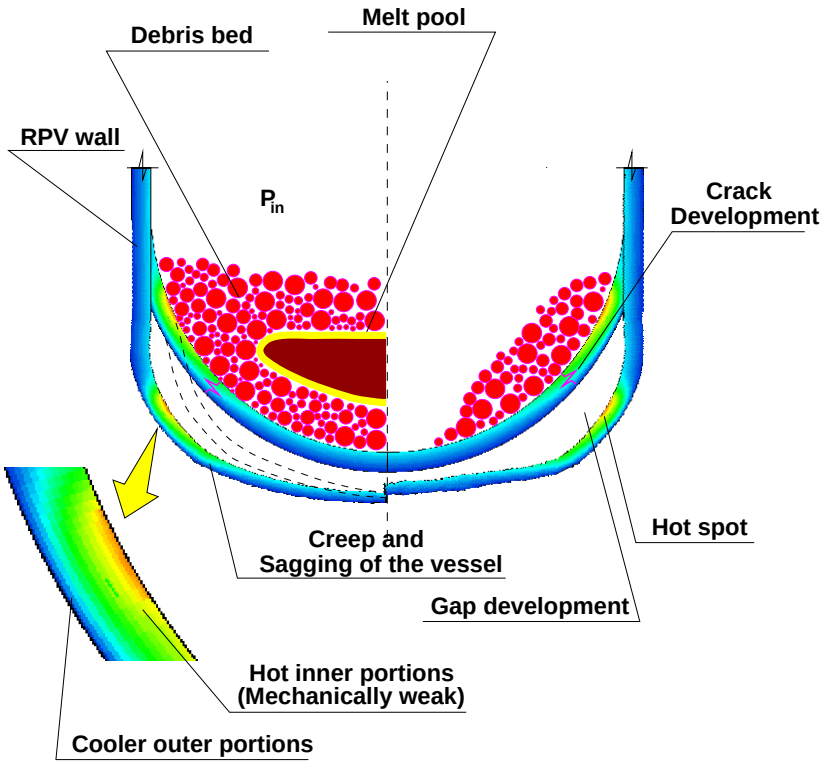

Fig. 1.5: *Phenomenology of global and local creep rupture.*

Vessel creep and rupture. Depending on accident scenarios, reactor design and accident management procedures, the in-vessel debris configuration may be different, fig.1.5. In general, the heat, transferred from the debris to the vessel, will cause the vessel heat-up and reduction of mechanical strength of the vessel material. As a consequence, the lower head wall can be subjected to significant thermal and pressure loadings, and the lower head could fail due to creep rupture

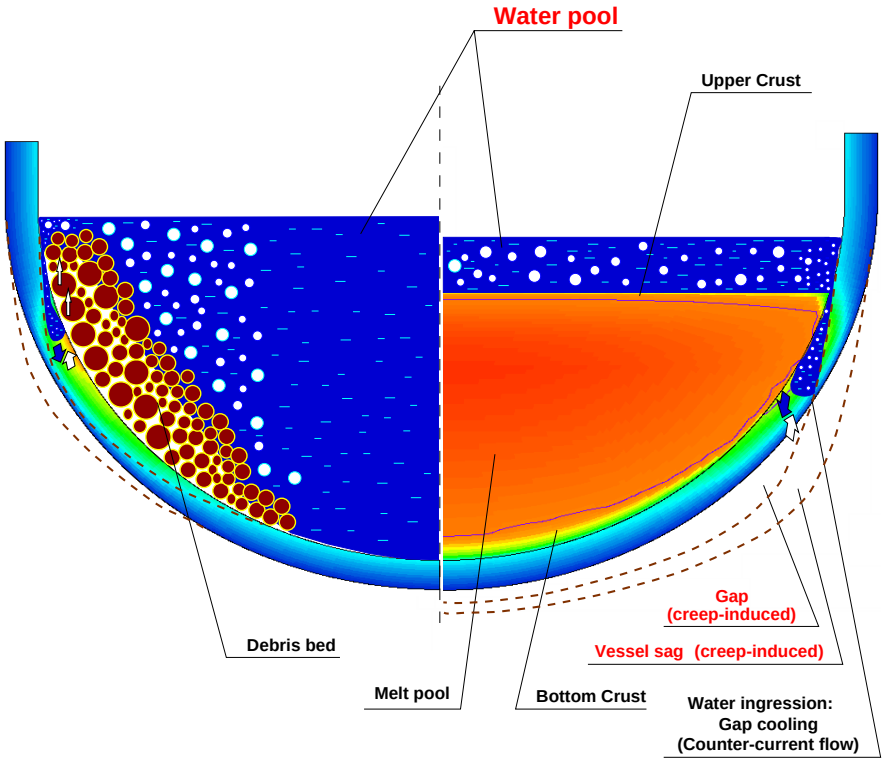

Fig. 1.6: *Phenomenology of water ingression and gap cooling.*

(fig.1.5).

Most studies of the vessel creep and rupture involve application of finite-element method, shell theory or simplified analytical techniques to investigate the vessel creep deformation in a thermo-elastic-(plastic) regime (an extensive review can be found in Rempe et al., 1993 [22]). Only a limited number of experiments are currently available. Uniaxial tensile tests have been performed for different reactor vessel steels in the USA, Russia, Germany and France. So far, only a few multiaxial experiments, investigating creep rupture of the reactor carbon steel at high-temperature, have been accomplished. In the RUPTHER experimental program (CEA, France, Sainte and Cotoni, 1997 [23]), a simple thin shell tube is subjected to internal pressure and axial thermal gradient loading (temperature up to 1000°C). The data obtained in this experiment can be used for validation of different structural mechanics models. Recently, LHF (Lower Head Failure) experiments have been performed at SNL, investigating creep failure of relatively large vessels (1/5th-scale), held at pressures of about 100 and 50 bars, while the vessel bottom head is heated to temperatures of about 1000K (Chu et al., 1997 [3]).

Gap cooling. It was recently proposed, that addition of water into the reactor lower plenum may prevent the vessel creep failure. The success of this accident management scheme largely depends on whether the water can penetrate into the gap, which may have developed between the debris and the creeping vessel. Since the core melt relocation and debris bed formation are highly three-dimensional processes, it is difficult to predict a pattern of water channeling in-between the vessel and the debris. Another important question is whether the gap thermal hydraulics allows water ingression to sufficient depth, to cool the lowermost region of the vessel, and thereby prevent its creep failure.

Several experimental programs are currently underway. Experiments in FAI, USA (Henry and Hammersley, 1996, [13]), KAERI, Korea (LAVA facility, Kim and Kim, 1997, [15]) and JAERI, Japan (Maruyama et al., 1996, [20]) involve high-temperature iron thermite (Fe+Al_2O_3 or Al_2O_3 only) as a corium simulant. No sustained heating is provided. Russian (Asmolov et al., 1997, [1]), German (Zeisberger et al., 1997, [29]) and Korean (CHFG facility, Kim and Kim, 1997, [15]) experiments are aimed at investigation of heat transfer in gaps, preset to a specified thickness, using low-temperature simulant coolants. All these tests are currently underway, and, perhaps, their data will be available in near future.

1.4 Problem and project formulation

Much research has been performed in the last 15 years on the phenomenology of the progression of severe accidents in LWRs. Much has been learned and some of the severe accident issues, related to containment performance, have been resolved. These include for example, PWR containment failure due to an in-vessel steam explosion [28], PWR containment failure due to direct containment heating resulting from the high pressure ejection of the core melt into the containment [21] and the BWR MARK-I containment failure due to liner melt attack [25]. Resolution of these issues was based on probabilistic arguments, supported by realistic descriptions of the phenomena, which were validated, to various extents, by experimental data.

1.4.1 The key issues

There are areas of severe accident phenomenology, which have received attention, but the state of the art has not advanced enough to resolve some of the key issues. Such an area is the late phase of in-vessel melt progression, when the core melt interacts with the contents of the lower head and may fail it. The key issues (questions) are:

1. can the lower head fail immediately, in spite of the presence of water, due to the attack of a melt jet released from the core,

2. what is the fraction of the melt jet that fragments in water,

3. what is the frequency of a steam explosion and what are its effects,

4. can the melt (debris) be cooled by the water in the lower head to preclude vessel failure,

5. if water cannot be supplied, can the melt be retained within the lower head by cooling the vessel external surface with water,

6. in the absence of water, inside and/or outside the lower head, how long will it take to fail the lower head by the melting and creep processes, and finally,

7. what is the rate of enlargement of the hole at the vessel failure site caused by the discharge of core melt through it?

Issues nos.2 and 3 are being addressed, respectively, by the experiments in the Molten Fuel-Coolant Interaction (MFCI) Project. The remaining issues (questions) listed above, are addressed by the research conducted in the current MVI Project.

1.4.2 Project objectives

The general objectives of the research work in the MVI Project are to obtain data and develop validated models for the resolution of issues nos. 1, 4, 5, 6, and 7 listed in section 1.4.1.

The experiments are performed with simulant materials. Specifically, the objectives are to perform experiments:

a) at RIT, on the vessel wall ablation due to the impingement of a melt (oxidic and metallic) jet; relates to issue no. 1,

b) at RIT, on the melt coolability process inside the vessel, in the presence of water, in particular, on the efficacy of the postulated gap cooling; relates to issue no.4,

c) at the COPO and BALI facilities, at IVO International and CEA Grenoble respectively, on in-vessel melt retention in the presence of a crust and external cooling; relates to issue no.5,

d) at the SULTAN facility at CEA, Grenoble on the critical heat flux during external cooling; relates to issue no.5,

e) at RIT on the lower head failure due to the melting and the creep processes; relates to issue no.6,

f) at RIT on the vessel hole ablation process; relates to issue no.7.

g) at RIT on the melt pool natural convection and melt stratification (SIMECO facility); relates to issue no.5.

The melt simulant materials employed are electrically-heated for experiments in b), c), f) and g). A supplementary objective is to experimentally determine the influence of the melt thermophysical properties on MVI process.

Phenomenological models are developed by the partners on each of the MVI processes investigated through experiments. The models were validated against the data obtained in the experiments conducted in the MVI Project, and against other pertinent data available.

1.5 Methodology and technical approach

The approach of the experimental work is to employ simulant materials, coupled with scaling analyses to demonstrate the applicability of the data obtained to prototypical accident geometries and conditions. The experiments are performed at more than one scale, and with more than one melt and vessel simulants. The controlling parameters for each interaction studied are varied systematically. The extent of parameter variation needed is determined through the scaling analyses.

Various temperature melt simulant materials were employed in the RIT experiments. These included water (16°C to 100°C), molten metal alloys (70°C to 250°C), molten salt (180°C to 450°C) and molten oxide mixtures (900°C to 1350°C). The physical property variations of the molten salt and oxide mixtures, with temperature, were chosen to represent those of the UO_2+ZrO_2 mixture melt. For example, the ΔT between the liquidus and solidus temperatures of the salt and oxide melt mixtures were kept approximately the same, as for the UO_2+ZrO_2 melt mixture. Attempts were made to have similar viscosities.

The COPO and the BALI experiments employed, primarily, water mixed with salt ($ZnSO_4$) to simulate the melt in, respectively, half and full scale slice experiments. These experiments employed direct electric heating to generate the heat in the salt water.

In the SIMECO facility, internal heating in the pool is provided by thin wire heaters uniformly distributed in the semicircular section. They can supply up to

4 kW of power in the pool. Stratification of water and salt water (with different concentrations), parafin oil and water, are employed, respectively, as simulant for miscible and immiscible fluids.

The FOREVER/C1 facility employed 1/10-scaled 15Mo3-(German)-steel vessel of 400mm diameter, 15mm thick and 750mm high. The high-temperature (up to 1300$^{\circ}C$) oxide melt is prepared in a SiC-crucible placed in a 50kW induction furnace and is, then, poured into the test section. A $MoSi_2$ 50kW electric heater is employed in the melt pool to heat and keep its temperature in the range up to 1200$^{\circ}C$.

1.6 Project partner work program

The work program at RIT icluded the following experiments on:

- melt jet impingement,
- in-vessel melt coolability,
- lower head failure, and
- vessel hole ablation.
- melt pool natural circulation.

These experiments were performed with different melt and vessel simulant materials.

The in-vessel melt retention thermal loading experiments have been performed at the COPO and the BALI facilities. The number of experiments were about 12 at the COPO facility and a similar number at the BALI facility. The tests employed constant temperature boundary conditions. The COPO and BALI facilities employed liquid nitrogen and an organic, respectively, to freeze the salt water simulant for the melt. The modified Rayleigh number Ra' in these tests was as high as 10^{17}, which is the value estimated for the prototypic geometry and accident conditions.

The SULTAN facility at CEA obtained CHF data on a large heated plate, which can be held at different inclinations to the horizontal. Data is obtained for different mass flow velocities of cooling water available at different pressures. This data is pertinent to the external cooling of the bottom head, for the scenario of in-vessel melt retention.

The RIT's SIMECO experimental facility was designed to investigate the heat transfer at the boundaries of an internally-heated stratified pool during mixing and separation process. The objectives are to determine the effect of, the miscibility

or immiscibility of the layers, the density difference between the layers, the layer thickness and the melt generation in one or all layers, on heat transfer.

The FOREVER experimental facility at RIT was built to obtain data and develop validated models on (i) the melt coolability process inside the vessel, in the presence of water, and, in particular, on the efficacy of the postulated gap cooling to preclude vessel failure; and (ii) the lower head failure due to melting and the creep processes in the absence of water inside and/or outside the lower head.

The experiments at RIT are supported by model development for the melt jet impingement, in-vessel melt coolability, lower head failure and the vessel hole ablation processes of the MVI. In addition, RIT performed computational fluid dynamics (CFD) analysis of the melt natural circulation at high Ra numbers.

The model development on the MVI processes is pursued by other partners. Specifically, AEA Technology developed relatively simple models in the LOWHED code (previously developed at AEA Technology) for the MVI processes and validated them against the data obtained at RIT, IVO, CEA and other experimental facilities. AEA Technology also worked on the compatibility of models developed by different partners. VTT developed models for the structural and creep behavior of the vessel, subject to the thermal and pressure loads, as calculated by the validated models developed at RIT and at AEA Technology. The ECN work was to analyze the natural circulation data obtained at the BALI facility. The University of Rome's work was to develop a CHF model based on the data measured at the SULTAN facility at CEA Grenoble. The ENEL work was devoted to further development of the CORIUM-2D code and the SIEMENS work was specifically oriented on the analysis of a metal layer on top of the oxidic pool, in order to determine if there is a "focusing effect", which increases the local thermal loading on the vessel wall next to the metal layer. Again, this work is related to determining the feasibility of the in-vessel melt retention with ex-vessel cooling.

Bibliography

[1] Asmolov, V., Kobzar, L., Nikulshin, V., and Strizhov, V., 1997, Experimental Investigation of Critical Heat Flux in Gaps, presented at the *1997 CSARP Meeting*, May 5-8, Bethesda, Maryland.

[2] Bürger, M., Buck, M., Mayr, P., and Schatz, A., 1995, Modeling of In-Vessel Late-Phase Melt Progression Within the KESS Code, *ANS Proceedings of the 1995 National Heat Transfer Conference*, pp.322-331, 1995.

[3] Chu, T.Y., Pilch, M.M., and Bentz, J.H., An Assessment of the Effects of Heat Flux Distribution and Penetration on the Creep Rupture of a Reactor Vessel Lower Head, *Twelfth Proceedings of Nuclear Thermal Hydraulics*, 1997 ANS Winter Meeting, November 16-20, 1997, Albuquerque, NM, pp.135-144.

[4] Conclusions and Recommendations of the OECD/CSNI/NEA Workshop on Large Molten Pool Heat Transfer, *Proceedings of the OECD/CSNI/NEA Workshop on Large Molten Pool Heat Transfer*, Grenoble, France, March 9-11, 1994, pp.3-6.

[5] Davis, K.L. et al., 1995, SCDAP/RELAP5/MOD 3.1 Code Manual, *NUREG/CR-6150 EGG-2720*, June 1995.

[6] Dosanjh, S.S. et al., 1989, MELPROG-PWR/MOD1: A two-Dimensional, Mechanistic Code for Analysis of Reactor Core Melt Progression and Vessel Attack Under Severe Accident Conditions, Sandia National Laboratories, NUREG/CR-5193 SAND88-1824 R3, May 1989.

[7] Dosanjh, S.S., 1989, Melt Propagation and Oxidation in Core Debris Beds, *AIChe Symposium Series*, 85(269):36-41, 1989.

[8] Dosanjh, S.S., 1990, Melt Progression, Oxidation and Natural Convection in a Severely Damaged Reactor Core, *Technical Report*, NUREG/CR-5316, February 1990.

[9] Gonzales, R., et al., 1993, Recent Developments in the ICARE2 Code, In *Workshop on Severe Accident Research in Japan*, SARJ, Tokyo, Japan, November 1-2, 1993.

[10] Henry, R.E., 1995, Externally Triggered Steam Explosion Experiments: Amplification or Propagation?, *Nuclear Engineering and Design*, v.155, pp.37-44.

[11] Henry, R.E., Burelback, J.P., Hammersley, R.J., Henry, C.E., and Klopp, G.T., 1991, Cooling of Core Debris Within the Reactor Pressure Vessel Lower Head, *ANS Summer Meeting*, Orlando, Florida.

[12] Henry, R.E., and Fauske, H.K., 1993, External Cooling of a Reactor Vessel Under Severe Accident Conditions, *Nuclear Engineering and Design*, v.139, p.31.

[13] Henry, R.E., Hammersley, R.J., 1996, Quenching of Mellow Surfaces in a Narrow Annular Gap, presented at the *5th Int. Conf. Simulation Methods in Nuclear Engineering*, Montreal, Canada, September 1996.

[14] Hodge, S.A., 1991, Identification and Assessment of BWR In-Vessel Accident Management Strategies, *ANS Trans.*, v.64, p.367.

[15] Kim, S.B, and Kim, H.D., 1997, Recent Severe Accident Research Activities at KAERI, presented at the *1997 CSARP Meeting*, May 5-8, Bethesda, Maryland.

[16] Kymäläinen, O., Hongisto, O., Antman, J., Tuomisto, H., and Theofanous, T.G., 1992, COPO: Experiments for Heat Flux Distribution from a Volumetrically Heated Corium Pool, *Proceedings of the 20-th Water Reactor Safety Information Meeting*, Bethesda, Maryland, October 21-23, 1992.

[17] Kymäläinen, O., Tuomisto, H., Hongisto, O., and Theofanous, T.G., Heat Flux Distribution from a Volumetrically Heated Pool with High Rayleigh Number, *Proceedings of the 6th Int. Topical Meeting on Nuclear Reactor Thermal Hydraulics, NURETH-6*, Grenoble, France, October 1993, pp.47-53.

[18] Lahey, T.Jr., and Podowski, M.Z., 1990, Degraded BWR Core Modeling APRIL.MOD3 Severe Accident Code, Final Report ESEERCO Project EP 84-04, July 1990.

[19] ”MAAP Development for Severe Accident Management Applications”, 1989, *SAIC Proposal No.1-284-71-900-07*, v.1, Technical, 15 June 1989.

[20] Maruyama et al., 1996, Studies in In-Vessel Debris Coolability in ALPHA Program, *Proc. 24th Water Reactor Safety Information Mtg.*, Bethesda, Maryland, October 21-23, 1996, NUREG-CP/0157, v.2, p.161, U.S. Nuclear Regulatory Commission (1997).

[21] Pilch, M.M., Yan, H., and Theofanous, T.G., 1994, The Probability of Containment Failure by Direct Containment Heating in Zion, NUREG/CR-6075, December 1994.

[22] Rempe, J.L. et al., 1993, Light Water Reactor Lower Head Failure Analysis, *Technical Report*, NUREG/CR-5642 EGG-2618, October 1993.

[23] Sainte Catherine C., and Cotoni, V., 1997, Specification of the 1st REVISA Pre-Test Calculations based on RUPTHER Creep Test at 1000°C with variable pressure, DRN/DMT/SEMT/RDMS, EU FI4S-CT96-0024, September 1997.

[24] Theofanous, T.G., 1989, Some Considerations on Severe Accidents in Loviisa, Theofanous & Co., Inc. January 1989, IVO Proprietary Report.

[25] Theofanous, T.G., et al., 1993, The Probability of MArk-I Containment Failure by Melt Attack of the Liner, NUREG/CR-6025, November 1993.

[26] Theofanous, T.G., 1995, The Study of Steam Explosions in Nuclear Systems, *Nuclear Engineering and Design*, v.155, pp.1-26.

[27] Theofanous, T.G., et al., 1995, In-Vessel Coolability and Retention of a Core Melt, *DOE/ID-10460*, v.2 (July 1995).

[28] Theofanous, T.G., and Yuen, W.W., 1995, The Probability of Alpha-Mode Contaiment Failure Updated, *Nuclear Engineering and Design*, v.155, pp.459-473.

[29] Zeisberger, A., Horner, P., and Mayinger, F., 1997, Cooling Mechanisms at the Bottom of Relocated Porous Debris, *Transactions of American Nuclear Society*, 1997 ANS Winter Meeting, November 16-20, 1997, Albuquerque, NM, v.77, pp.270-271.

Chapter 2

Melt jet attack on the RPV wall

2.1 Background

Heat transfer under jet impingement conditions was studied experimentally by a number of authors in the last decade, due to its' numerous industrial applications, in which liquid jets are employed to remove the heat from high heat-flux surfaces. Only a few of these studies were devoted to the investigation of jet impingement heat transfer, with phase change of the jet fluid material (solidification) and of the plate material (melting). Such a situation may occur (e.g., in metal, chemical and nuclear industry) when a relatively high temperature melt jet, at T_j, interacts with the colder surface of a plate (at T_w), which has melting temperature $T_{w,mp}$ less than the solidification temperature of the jet material $T_{j,sol}$, i.e. ($T_w < T_{w,mp} \leq T_{j,sol} < T_j$). Specifically, a postulated severe (core melt-down) accident in a light water reactor (LWR) may involve a scenario of high-temperature (2000-3500K) jet of molten core materials impinging upon the reactor pressure vessel (RPV) lower head wall. This is the application motivating this study. Particularly, the solidification temperature of melt corium jet $T_{j,sol}$ may range from 1700K (for metal jets) to 3000K (for oxidic jets). The melting point of the impingement surface (i.e. reactor vessel steel) is about 1700K. In such a scenario, it has been recognized [1]-[2] that vessel wall ablation (melting) due to the jet impingement heat transfer could be a vessel failure mode, which has to be evaluated for (a) efficacy of accident management scheme, and (b) resulting containment loadings.

Thus, the physical situation of present interest features a downward melt corium jet impinging upon a meltable solid wall (vessel steel) (Fig.2.1). Therefore, studies related to jet impingement heat transfer without phase change will not be reviewed here (see e.g., [3] for a review). We should note here that much of the stagnation zone heat transfer data from single phase jet impingement experiments have been generalized in correlation form $Nu = A \cdot Re^m Pr^n$, with parameters

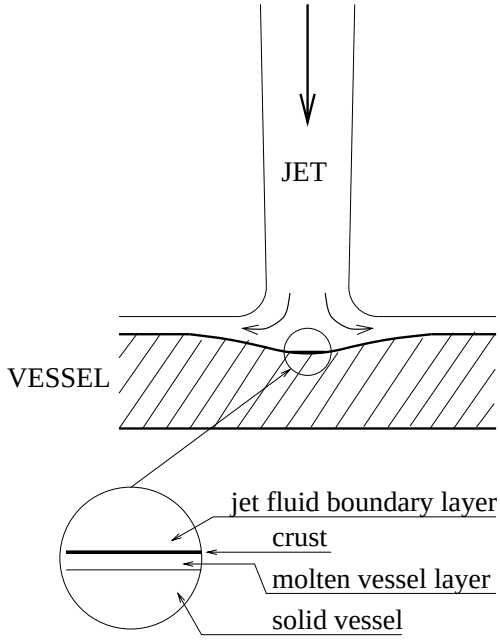

Fig. 2.1: Jet impingement upon a meltable plate.

"m" and "n" vary in the range [0.45-0.55] and [0.33-0.4], respectively. For example, experimental data and results of numerical simulation of jet impingement heat transfer (without phase change) were found to fit reasonably well with correlation (2.1), which was derived from classical stagnation flow modeling.

$$Nu_o = 0.55 \cdot \sqrt{2} \cdot Re^{0.5} \cdot Pr^{0.35} \tag{2.1}$$

A very limited number of correlations are available for jet impingement heat transfer with phase change (that occurs when $T_{mp,p} < T_j$ and/or $T_{mp,p} < T_{mp,j} < T_j$). Yen and Zehnder (1973) [4] performed water-ice experiments and correlated their integral heat transfer data as $Nu = 0.88 \cdot Re^{0.94} Pr$. Swedish et al. (1979) [5] and Epstein et al. (1980) [6] performed water-ice, water-octane, water-oil, and water-mercury experiments. However, all these experiments employed an *upward* water jet against meltable surfaces [4] [5] [6]. The situation of interest in the present work is associated with solid substrate ablation due to heat transfer from a downward liquid (melt) jet, impinging vertically upon the solid surface. More recently, Saito et al. (1990) [7] performed high-temperature jet impingement experiments and proposed the correlation (2.2).

$$Nu_o = 0.0033 \cdot Re \cdot Pr \tag{2.2}$$

The data base supporting this correlation is, however, rather limited. Most of the tests were conducted with molten salt jet impingement on tin plates, in the Re

range [$7{\cdot}10^4$-$3.5{\cdot}10^5$], and with Pr numbers about 1. Two additional tests with thermite jets impinging upon steel plate, having Re numbers about 1900 and Pr = 5.46 were conducted.

As can be seen, the latter correlation (2.2) significantly differs from earlier correlations (2.1) of jet impingement heat transfer in stagnation zone *without phase change*. Furthermore, the significant difference between correlations used in studies by Swedish, Epstein et al. [5] [6] and that by Saito [7] causes large uncertainty in reactor safety assessments, when extrapolating this kind of correlations to higher Reynolds numbers (10^6-3.10^6) and lower Prandtl numbers (0.1-0.6). More importantly, no good explanations for the difference are available, which may help to resolve the uncertainty in the assessment of the jet impingement heat transfer.

Jet impingement experiments were performed at Ispra facility BLOKKER-I, in which around 100kg of UO_2 impinged onto preheated stainless steel plates. It is noteworthy that a crust at the interface was found for all cases, with the thinnest crust occurring for the 5-degree inclined plate and thicker for 45 and 90-degrees plates [8].

Experiments on metal jet impingement were performed by several groups, for a review see e.g., [9]-[10]. A correlation $Nu = 0.0152 \cdot Re^{0.92} \cdot Pr^{0.8}$ was obtained and proposed for molten metal jets. Such a jet fluid has Prandtl numbers significantly lower than 1 (say, 0.005 to 0.05).

The present study aims to develop an understanding of the physical mechanisms, which determine heat transfer characteristics of jet impingement with phase change boundary conditions, thereby, providing an insight into the applicability ranges of different jet impingement heat transfer correlations.

2.2 RIT/NPS Experimental Program

An experimental program on jet impingement heat transfer, involving phase change, was pursued at the Royal Institute of Technology (RIT/NPS, Stockholm).

2.2.1 Simulant Materials

First, low-temperature simulant experiments were performed, employing water (with T_j in the range 3^{o}C to 99^{o}C) as melt simulant, and ice and salt ice (with T_w in the range from -50^oC to -15^oC) as impingement plates. Description of the experimental facility, experimental technique were first presented in [11]. Experimental data obtained from the water-ice tests were found to agree well with Saito's correlation (2.2). A subsequent paper [12] reported briefly about experiments to examine the effects of jet fluid properties and of impingement configuration (presence of liquid layer above the impingement surface, inclined angle of

impingement). Different pairs of jet fluid and plate material:

- [water]-[ice],

- [water]-[salt ice],

- [Cerrobend]-[Cerrobend],

- [Tin]-[Cerrobend],

- [Hitec]-[Cerrobend],

- [molten binary salt mixture $NaNO_3 - KNO_3$]-[Cerrobend],

- [molten binary salt mixture $NaCl - KCl$]-[Al],

- [$CaO - B_2O_3$]-[Al]

were employed, providing a large variations in the jet Reynolds number (up to 3.10^5) and jet fluid Prandtl number (from 0.02 to 100).

2.2.2 Experimental Arrangement and Measurements

The low-temperature set of impingement tests were conducted in the NPS laboratory using the experimental arrangement shown in Figure 2.2. Water jets of four different diameters and ranging in temperature from 3 to 99^{o}C were directed onto both pure and salted (20 w/o $NaCl$) ice plates. The melting point of the ice plate was lowered to -16.5^{o}C via the $NaCl$ addition, and this in turn allows the possibility of a crust layer formation between the melt and the substrate solid.

The test facility was an elevated 60 liter tank, which could be heated or cooled, connected to a long tube section in order to ensure a fully developed jet flow profile. Jet velocities were obtained from timing of the volumetric discharge, along with static head pressure differences. The variation in the jet Reynolds number, Re_{jet}, was obtained as a result of the significant variation in water properties with temperature, coupled with different jet diameters employed. The ratio of the distance from the jet pipe exit to the upper plate surface, H_f to jet diameter D_j, was maintained between 2 and 8.

The experimental conditions and data for both water-ice and water-salt-ice jet impingement tests are presented in Appendix of the present report. The range of experimental conditions can be seen as $\approx$4,400 $< \mathrm{Re}_{jet} <$ $\approx$290,000 for water with $\approx$2 $<$ Pr $<$ $\approx$12. The experimentally measured thermocouple traces allow for the determination of the ablation front speed, and, thus, the ablation heat fluxes. The obstruction of flow due to the presence of the thermocouple probes located in the stagnation zone is considered to be negligible.

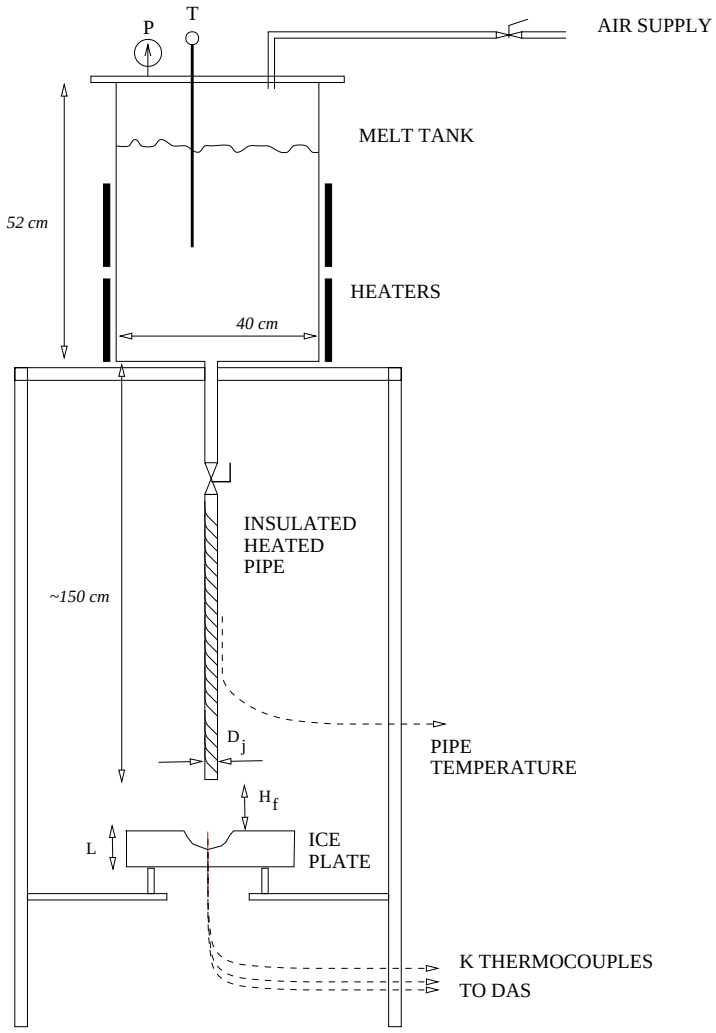

Fig. 2.2: Jet Impingement Experimental Arrangement

A large number of tests utilized a jet which impinged normally to the flat surface. Subsequent testing was conducted, which varied the impact angle of the jet to the plate, and also some tests were conducted in which an overlying pool of water was established, just prior to the start of the impingement.

The ice plates were formed inside a low temperature freezer with capability to -60^{o}C. Several, small (0.5mm OD), K-type thermocouples were installed into the ice plates at known separation distances in order to ascertain the erosion rates. The distance of separation between thermocouples was made to be closer at the upper surface, and was as little as 2mm in most cases. Thermocouples, lower in the test plates, were separated by greater distances. The data was recorded on a Hewlett-Packard data acquisition system, typically using a high-speed millivolt

reading with subsequent RTD correction and polynomial conversion. Scanning of the thermocouples could be accomplished with typical speeds of 3-4 Hz. In addition to the thermocouples directly under the stagnation zone, other thermocouple groupings were installed at radial distances greater than the jet radius, to examine heat transfer outside the stagnation zone. In general, the heat transfer from these measurements was not significantly different from that measured directly in the impingement region, since these thermocouple groupings were, typically, not outside the cavity which was formed by the jet impingement flow. In addition to the tests conducted with water and ice/salt-ice, a smaller test section, similar in function to that shown in Figure 1, was employed for conducting salt-metal, salt-salt, and metal-metal jet impingement with phase change. The liquid volume employed was reduced to a maximum of 10 liters inside a 16cm diameter and 50cm high cylinder which was electrically heated. The volume was pressurized with air, up to 3 bar, in order to obtain higher jet velocities. Tube diameters of 6.3, 15, and 25mm were employed and thermocouples were used, as before, to obtain ablation front velocities. Cerrobend alloy (T_{mp}=70^{o}C) and Sn (T_{mp}=232^{o}C) were used as melt simulants.

For the liquid metal tests a circular plate of typically 25-40mm thickness was formed, with embedded 0.5mm diameter thermocouples in the center. The metal in the test section was melted using electrical heaters and the jet tube was heated to the same temperature, as the melt, with electrical heaters. Some oxidation of the Cerrobend metal was evident which, in turn, produced a slight elevation in the melting point to ≈73-80^{o}C. In this set of tests it was desired to maintain the melt temperature relatively constant, between tests, due to the fact that little information is available about the Cerrobend viscosity dependence with temperature. For this reason, the majority of tests were conducted at 110^{o}C. The Pr number for Cerrobend at this temperature is roughly 0.03. Two complementary tests employing a Sn jet onto a Cerrobend plate were also performed.

Description of test facility and experimental arrangement for high temperature tests is given in Appendixes of the present report.

2.2.3 Data Processing

The method for calculating jet impingement heat fluxes and subsequent Nu numbers is presented below.

The ablation front speed can be determined from the known distance of separation between individual thermocouples positioned below the impinging jet;

$$V_{ablation} = \frac{R_{TC(i)} - R_{TC(i+1)}}{t_{TC(i)} - t_{TC(i+1}} \tag{2.3}$$

The reference temperature difference is that between the melt jet and its corresponding melting point ($\Delta T_{ref} = T_j - T_{mp}$). Since the progression of the melt front is rapid, conduction in the plate material can be assumed to be small and the sensible heat of the plate is incorporated into the heat of fusion;

$$H^*_{fusion} = H_{fusion,p} + C_{p,p}(T_{mp,p} - T_\infty) \tag{2.4}$$

One can then determine the heat flux as;

$$q_{abl} = V_{abl}\rho_p H^*_{fusion,p} \tag{2.5}$$

For these single-component tests, it was shown by Swedish [5] and Furutani [13], that the convective heat flux can be accounted for as;

$$q^*_{imp} = q_{abl}\frac{B}{ln(1+B)} \tag{2.6}$$

where

$$B = \frac{C_{p,j}(T_j - T_{mp}))}{H^*_{fusion,p}} \tag{2.7}$$

Finally, the Nusselt number is determined as

$$Nu_o = \frac{q^*_{imp}}{\Delta T_{ref}}\frac{D_j}{\kappa_j} \tag{2.8}$$

$$q_{cond} = \rho_p C_{p,p}(T_{mp,p} - T_{\infty,p})V_{abl} \tag{2.9}$$

2.3 Analysis of experiments

2.3.1 Oxide Melt Jet Attack of the Reactor Vessel Wall: Phenomena and Prediction Method

2.3.1.1 Experimental Findings from Non-Metal Melt Jet Impingement Tests

In this section, we describe major experimental findings which provide the background for establishing a phenomenological understanding of heat transfer mechanisms involved in the jet impingement, with phase change, process.

The measured temperature histories were translated into jet impingement heat fluxes and Nu numbers. Comparisons to Eq.(2.1) and Eq.(2.2) are provided in Figures 2.3-2.4for all the data collected for the normally-impinging water-ice and water-salt-ice tests. The results clearly show that the laminar stagnation zone

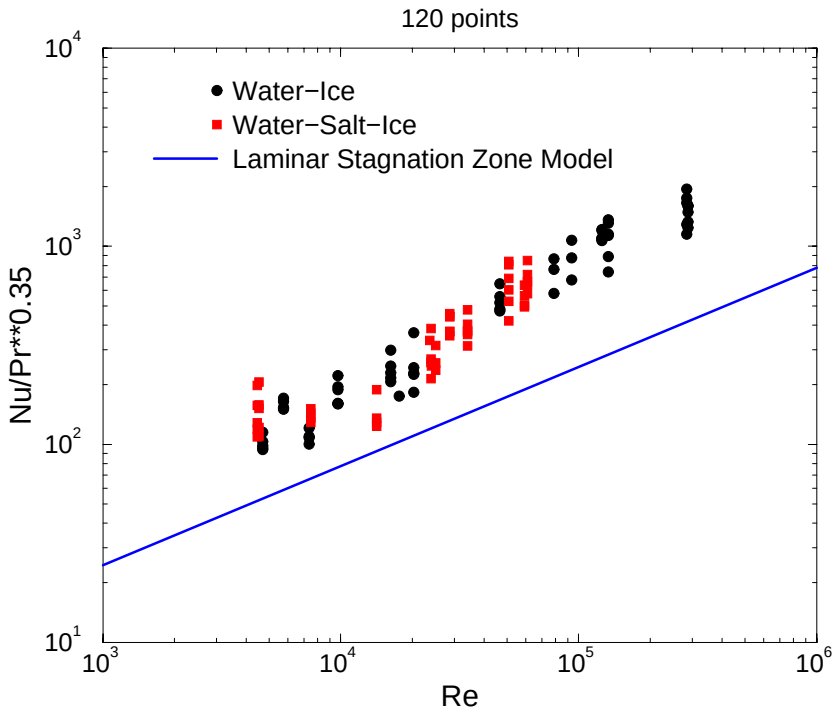

Fig. 2.3: Comparison of Experimental Data to Laminar-Stagnation-Zone Model

model underpredicts the measured data, whereas the Saito correlation agrees quite well with the data. The good agreement between the current results obtained with water jet and those with the salt and alumina jets used by Saito [7] justifies the use of such simulant materials for investigating phase change impingement.

It was found from analyses of RIT jet impingement experiments that a crust boundary condition is effective during the entire jet impingement duration. This is in a good agreement with findings from the BLOKKER-I core melt experiments [8] about the crust formation and stability (at least as a thermal boundary condition).

In general, analysis of the experimental results obtained for regimes, where *significant surface ablation* occurred, showed that the functional form of the heat transfer correlation $Nu = f(Re, Pr)$ is quite different from the conventional one [e.g., Eq.(2.1)], developed previously for jet impingement heat transfer on a flat smooth solid surface, without any change in the surface configuration due to a phase change. Our analyses concluded that for the currently existing data bank in the range $2 \cdot 10^4 < Re < 3.5 \cdot 10^5$, the correlation by Saito and co-workers, i.e. Eq.(2.2) is a better approximation than the correlation of laminar stagnation flow

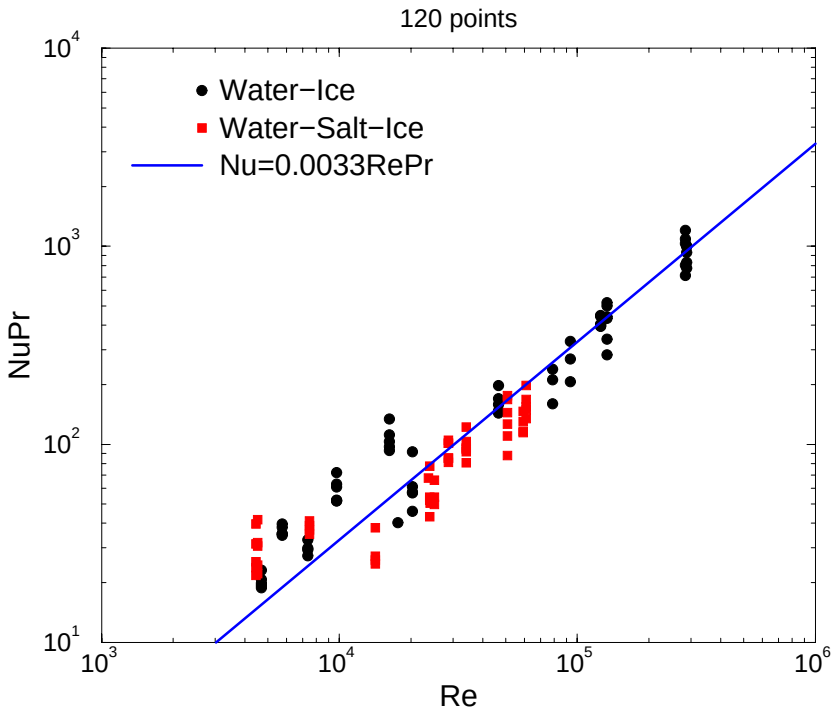

Fig. 2.4: Comparison of Experimental Data to Saito's Turbulent Correlation

model i.e. Eq.(2.1).

It is a reproducible experimental fact that jet impingement heat transfer data can be well described by the laminar stagnation flow model Eq.(2.1), provided that no ablation of the slab upper surface was evident. Thus, the laminar stagnation flow model, derived, for cases without phase change, was found to be applicable for phase change conditions until significant ablation has occurred. Since the heat transfer rate was derived from phase change front propagation, it can be concluded that both phase change and isothermal boundary conditions are not the direct cause of heat transfer augmentation in the later phase of impingement upon the meltable slab.

Also, it was established that the impingement heat transfer can be characterized by laminar regime in an initial phase, transition-to-turbulence in a transition phase, and turbulent regime in a subsequent later phase [11]. Some experimental data of heat transfer during the initial period of jet impingement and surface ablation are shown in Fig.2.5, which includes both cases with and without crust formation. The Reynolds number range of the tests shown in Fig.2.5 is from $2{\cdot}10^4$ to $5{\cdot}10^4$. Notably, low initial temperature ($\simeq -50^o$C) of the ice slab was employed

in these tests.

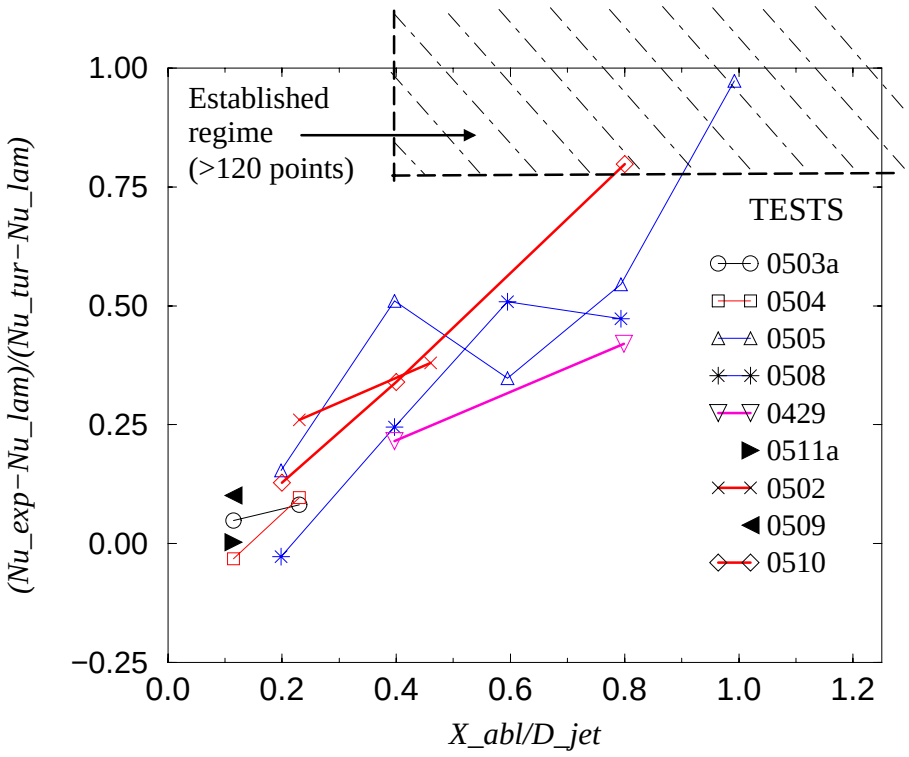

Fig. 2.5: Jet impingement heat transfer during the initial ablation period [water-ice and water-salt ice experiments; Nu_{lam} from Eq.(1), Nu_{tur} from Eq.(2)].

Special tests were then performed in order to address the question of whether heat transfer augmentation is caused by macroscopic changes in the impingement zone geometry (phase-change-induced cavity formation) or is it associated with microscopic phenomena of the impingement surface (e.g., phase-change-induced surface roughness). It was found that a pre-formed large-scale (larger than the jet diameter) cavity (with smooth impingement surface) does not affect the heat transfer behavior observed earlier. Thus, it appears that some micro-surface characteristics are responsible for heat transfer augmentation when the impingement slab is significantly ablated. The validity of such an assumption was examined in a test series, in which a few pits were artificially generated on the initial surface of a meltable slab. The diameter and depth of the pith were much smaller than the jet diameter. It was observed that laminar regime essentially did not exist and the transition to turbulent regime in such tests occurred much earlier in time than in the case with an initial smooth slab surface.

Wall roughness effects on stagnation-point heat transfer beneath an impinging liquid jet were recently investigated, experimentally, by Gabour and Lienhard (1994) [15]. The experiments were performed on surfaces with well-controlled roughness and without phase change. Height of the roughness elements was in the range 5 μm to 28 μm. It was found that the surface roughness causes an increase of heat transfer. The higher the surface roughness, the steeper the curve-fits, $Nu = f(Re)$ of the experimental data obtained. Effect of the jet fluid Prandtl number, however, was not examined in [15]. No heat transfer law (dependent on the roughness element height) was established in Ref.[15].

Finally, two other aspects were examined in this test program concerning the effect of inclination angle and the presence of an overlying melt pool layer above the solid plate through which the jet must pass. Some past work involving inclined jets is provided by Furutani (1989) [13] and McMurray [17], Pessanha (1989) [18] yet none of these provides a conclusive influence of inclination on jet impingement with phase change process. Although only a few tests were conducted under these conditions, they revealed that the inclination angle effect is very small. This is likely due to the fact that after a short period of ablation, other factors are of much greater importance. Qualitatively, it was seen that the inclination led to slightly faster regime transition timeframes.

The effect of an overlying pool was found to be some laminarization of the jet, prior to its impingement on the plate surface. This, in turn, slows the transition from the laminar to the turbulent heat transfer regime.

2.3.1.2 Phenomena of Jet Impingement Heat Transfer under Phase Change Boundary Conditions

2.3.1.2.1 Driving physical mechanism

Based on experimental evidence, it is proposed that turbulence is the major physical mechanism which governs the physics of fluid flow and heat transfer in the impingement area under phase change conditions.

Theoretically, the stagnation zone is characterized by a flow deceleration from the initial jet velocity (in the vertical direction) to an essentially zero flow velocity. All turbulence, if present in the jet mainstream, should disappear in the stagnation zone since the velocity fluctuations in the normal-to-surface direction are damped. Therefore, the laminar stagnation flow model, coupled with a potential flow model for the horizontal direction spreading liquid film, is able to describe flow characteristics and heat transfer data under jet impingement conditions. This holds as far as the assumption of a smooth impingement surface is valid.

Under jet impingement conditions with phase change of, both, the jet and plate materials, , molten mass of the original meltable slab and/or the floating

crust of the jet fluid are radially removed from the impingement area by the shear force of the jet flow. Such crust formation and plate erosion processes will certainly involve inhomogenieties. Once, the plate surface has ablated to a certain extent, the microscopic morphology of the boundary (crust or plate) surface can no longer be considered as smooth. Qualitatively, jet is impinging upon a *rough surface*, and the flow structure in the impingement zone may deviate from the laminar-stagnation one. We believe that the surface roughness k is able to generate vortexes in the boundary layer δ and to provide a non-zero flow velocity field in the impingement zone. Consequently, an augmented flow provides significantly higher turbulent rates of heat exchange between the boundary surface and the mainstream jet flow.

2.3.1.2.2 Basic theoretical concept

In order to, theoretically, support our hypothesis about the surface-roughness-induced turbulent heat transfer in the impingement zone, we employ the Reynolds analogy between heat transfer and skin friction for boundary-layer flows. In the case of stagnation-point (laminar) flow, we have (see e.g., [14]) that

$$Nu \sim \sqrt{Re \cdot Pr} \qquad [Pr \to 0]$$

$$Nu \sim \sqrt{Re} Pr^{1/3} \qquad [Pr \to \infty \quad (Pr > 0.6)]$$

or

$$Nu = \frac{1}{2} C_f' \cdot Re \cdot F(Pr)$$

where C_f' is the skin-friction coefficient. In general, the above relationships agree well with heat transfer correlations for jet impingement (non phase change) for liquids with different fluid Prandtl numbers (see [3]).

It is important, however, to note that, for the laminar stagnation flow regime, the heat transfer coefficient decreases with the increase of the jet diameter [Eq.(2.1; $h \sim D_j^{-1/2}$]. This because the jet diameter determines the length scale (depth) of the stagnation zone, which is a resistance layer between the surface and the mainstream flow. Another dependence of interest is $h \sim \nu^{-1/6} \sim \delta_\nu^{-1/6}$, i.e. the thicker the viscous boundary layer δ_ν, the lower the heat transfer rate.

In contrast, the heat transfer coefficient in Saito's correlation Eq.(2.2) does not depend on (i) the jet diameter D_j and (ii) the jet fluid viscosity ν.

First, this means that heat transfer regime in the impingement zone centerline (described by Saito's correlation) is self-similar, i.e. does not depend on the jet

length scale. In other words, the "stagnation" heat transfer is governed by local flow characteristics (flow velocity) rather than by the macro flow characteristics in the whole impingement and spreading area.

Second, since

$$Re \cdot Pr = \frac{U_j \cdot D_j}{\nu_j}\frac{\nu_j}{\alpha_j} = \frac{U_j \cdot D_j}{\alpha_j} = Pe$$

one can re-write Eq.(2.2) as

$$Nu_o = 0.0033 \cdot Re \cdot Pr = 0.0033 \cdot Pe \tag{2.10}$$

Thus, the Peclet number Pe is the only governing dimensionless group for heat transfer in the augmented "stagnation" flow (in contrast to the two independent dimensionless groups Re and Pr for the laminar stagnation flow heat transfer). This finding simplifies the scaling rationale for jet impingement heat transfer, with phase change boundary conditions. More importantly, the heat transfer is found to be independent of the jet fluid viscosity, i.e. the viscous boundary layer δ_ν has no influence on the physical mechanism which governs the jet impingement heat transfer. Thus, the above analysis appears to indicate that for the phase-change conditions the length scale of surface roughness may be larger than the thickness of the viscous boundary layer.

Indeed, the skin-friction coefficient C'_f for a rough surface is independent of Reynolds number for relatively high Reynolds-number flows [1]. However, C'_f depends strongly on the roughness parameter. Assuming that the phase-change-induced surface roughness is somewhat similar to the roughness of a slab made of concrete or rivetted steel, C'_f may range from 0.005 to 0.007 [14]. Employing the Reynolds analogy in a simplified form (without accounting for turbulent Prandtl number), we have

$$h = \frac{1}{2} \cdot U_\infty \cdot \rho \cdot C_p \cdot C'_f \tag{2.11}$$

[1]Note that Moxon attempted to discuss the Saito correlation in terms of the Reynolds analogy and the friction factor [9]. He, however, did not augment the skin factor for surface roughness. Therefore, the skin factor as a function of $\mathrm{Re}^{-0.2}$ led him to an equation, which still strongly depends on viscosity and jet diameter. He validated his model on molten metal jet impingement data. It is well known that the behavior of thermal *vs* hydrodynamic boundary layers in liquid-metal fluids differs significantly from that in liquids which have Prandtl numbers of order of unity and does not conform to the Reynolds analogy assumed for the equation derivation.

or

$$Nu = \frac{1}{2} \cdot Re \cdot Pr \cdot C'_f = \frac{1}{2} C'_f \cdot Pe \tag{2.12}$$

Using the above chosen range of C'_f, Eq.(2.12) becomes

$$Nu = (0.0025 \div 0.0035) \cdot Pe \tag{2.13}$$

It can be seen that Eq.(2.13) is almost identical to Eq.(2.2) or Eq.(2.10). Thus, all the above analyses appear to confirm the preposition that the augmented heat transfer regime [described by Saito's correlation or Eq.(2.12)] is associated with phase-change-induced surface roughness [2].

Fig.2.6 depicts Eqs.(2.13) and the existing experimental data base. The data base includes results of the earlier tests by Saito and co-workers [7] and recent RIT tests performed by the authors of this study. Several simulant fluids were employed, such as molten salt mixture $NaCl$ and thermite melt Al_2O_3 [7], as well as water (in the temperature range from 3^{o}C to 99^{o}C) [11]. The fluid Prandtl number ranges from 0.75 to 11.8 . It is instructive to note that the data set taken from the Saito's study may include some points which are not fully turbulent. Also, there exist some uncertainties associated with measurements of the ablation front propagation velocity in very fast transient tests (at higher range of the jet Reynolds numbers). Nevertheless, one can see that Eqs.(2.13) can describe, reasonably well, the general trend of heat transfer law in a wide range of the Peclet numbers $10^4 < Pe < 1.5 \cdot 10^6$.

Discussion. Since, the physical process in question is governed by microscopic mechanisms and factors such as phase change and surface roughness, the scattering of heat transfer data quite natural (factor of 3). Even though the general tendency of $Nu = F(Re, Pr)$ in the fully augmented regime is well established, there exist large uncertainties in determining the *transition law* from the laminar stagnation flow regime to the fully augmented flow regime (see Fig.2.5).

[2]Interestingly, the experimental data from [15] for relatively high surface roughness (28.2 μm) tend to indicate the dependence $Nu \sim Re$. Furthermore, the curve-fits (Fig.5c of [15]) seem to become parallel, while increasing the surface roughness parameter k^*, which confirms that $Nu \sim Re$ is a limiting relationship. Using $Pr \simeq 8.4$, one can show that the upper-limit Nu data could be described by $Nu = 0.5 \cdot C'_f \cdot Pe$, with C'_f = 0.003. In fact, the skin factor may depend not only on the surface roughness k, but also on Re and Pr for cases $\delta_\nu \geq k$. The self-similarity of the skin factor (C'_f = constant) may be reached for the jet Reynolds numbers larger than its critical value $Re > Re_*$, where $\delta_\nu << k$. It should be noted that, in most cases of our interest, the jet Reynolds number is more than Re_*, particularly, owing the large surface roughness induced by phase change processes.

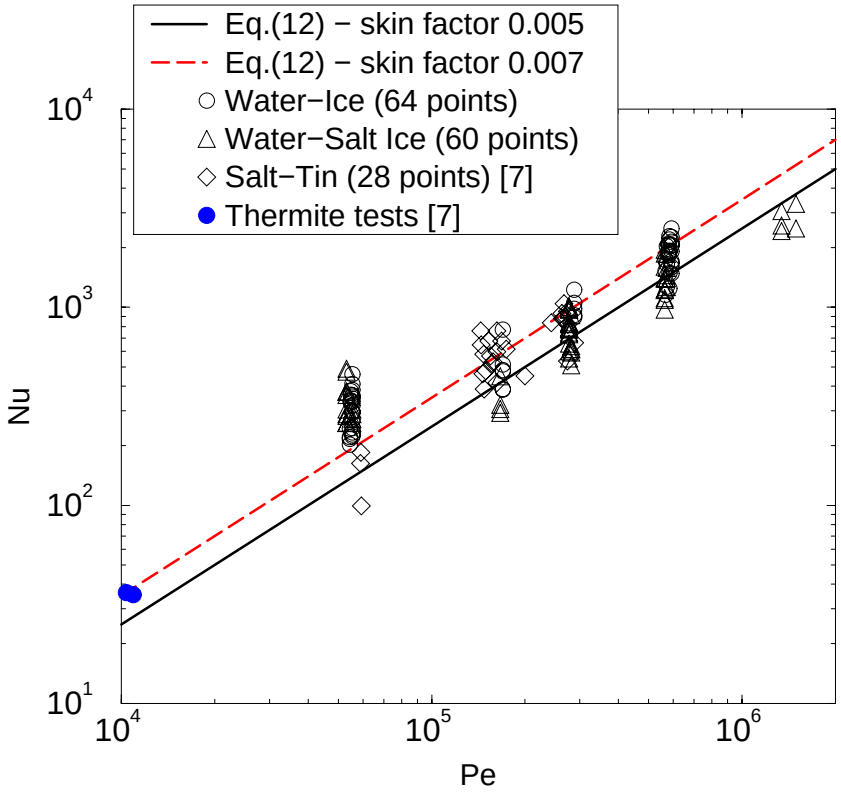

Fig. 2.6: Existing experimental data base vs. Eq.(12) (unsubmerged perpendicular liquid jets).

A deviation of water-ice and water-salt ice data from Eq.(2.13) at low Peclet numbers may be due to the fact that the skin friction factor (surface roughness) may also depend on material and mechanical properties of the substrates, which undergo ablation upon jet impingement. However, for high Reynolds (and Peclet) number conditions, i.e. close to prototypical conditions, this effect may well be overwhelmed, since the viscous boundary layer becomes very thin for those conditions.

Potentially, another important characteristic is the jet fluid Prandtl number. Even though for the fully turbulent (augmented) flow regime, the fluid Prandtl number alone is not a governing scaling group, it may have a significant effect on the transition behavior. It is related to the fact that the transition law depends on the relationship between the thickness of the viscous boundary layer δ_ν and the characteristic size of the surface roughness k. Since no direct measurements of surface roughness created during a phase-change moving interface can be performed, it is very difficult to generalize the transition behavior, observed in specific simulant tests, to prototypic reactor conditions. Therefore, the transition law

must be examined for different pairs of jet fluid and plate materials, for which one or another aspect of prototypic conditions may be represented. This is the subject of continued study at RIT/NPS.

2.3.1.2.3 Related phenomena

The effect of jet-plate inclination was experimentally found to be not sufficiently significant, both in the laminar regime and for the phase-change conditions [12]. A reduction in heat transfer for inclined jet impingement [in comparison to the normal (90^o) jet impingement] was found to be about 20-30% for inclination angles up to 45^o, for the laminar flow regime [18]. In contrast, the inclination may lead to an earlier transition to turbulent heat transfer regime. It was also found that after the impingement cavity formed in the solid plate, the inclination between the jet and the plate has no effect on the impingement heat transfer; Fig.2.7.

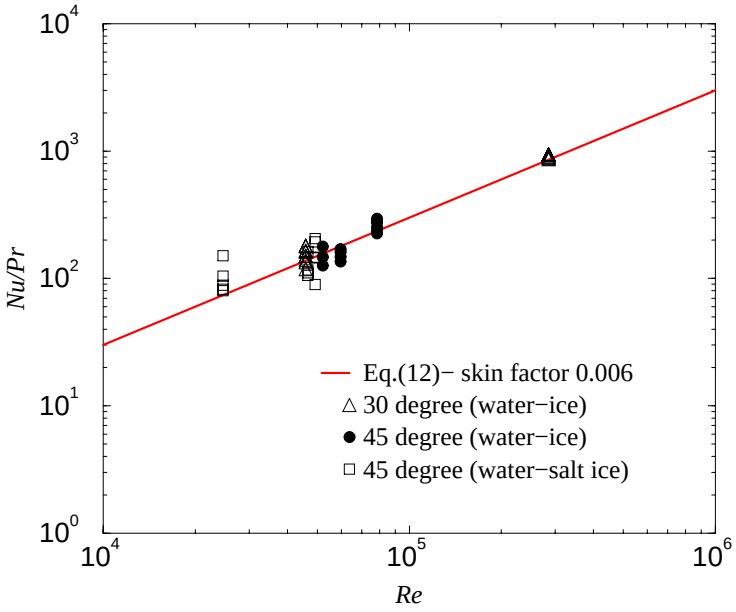

Fig. 2.7: Inclined liquid jet impingement heat transfer (RIT simulant experiments).

Jet impingement experiments, with pre-installed liquid layers (initial depth L_o), were performed at RIT to examine the effect of the jet liquid accumulation. It was found that the presence of liquid layer L_o has a laminarizing effect on the jet flow, and hence, provides some delay to the transition-to-turbulence. In

fact, the shear between the jet and the liquid layer may cause jet erosion and/or deceleration of the jet. This means that the actual Reynolds number of the jet is lower than its value, determined from the diameter and velocity of the initial jet, entering the (deep) liquid layer. It can be seen from Fig.2.8 that most of measured Nu numbers, obtained with $\frac{L_o}{D_j} > 2$, are 25-50% lower than those, obtained for $\frac{L_o}{D_j}$ in the range from 0 (no liquid layer) to 1.5 (shallow layer).

In the prototypic pool there may exist an initial layer of water, which tends to soften the impact of the impingement of a core melt jet on the reactor vessel wall. However, the effect of the water layer on the jet behavior depends on a number of parameters and phenomena. Particularly, hydrodynamics of the core melt jet in the water pool is affected by ratio of the jet liquid and water densities, as well as by boiling mechanisms, induced by the high-temperature core melt.

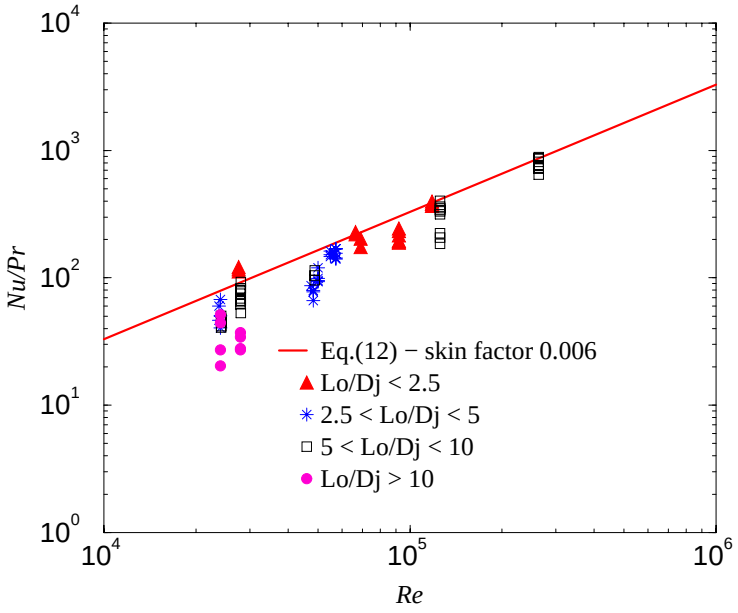

Fig. 2.8: Submerged liquid jet impingement heat transfer (RIT simulant experiments).

In the present study, crust is found to be effective, and thus the temperature driving force is that between the jet temperature and its own solidification point. This condition (of crust existence) was examined by Epstein et al. [6], Saito et al. [7] and Sehgal et al. [12]. Under high heat flux conditions the crust is very thin. The thickness of the molten layer of plate material (beneath the crust) should also be very small as a result of the impingement (stagnation) pressure of the high ve-

locity jet flow. Therefore, time scales for heat conduction through the crust layer and the molten plate layer are small in comparison with similar conduction (and phase change) time scales for the original solid plate (vessel), and in comparison with the time period of impingement. In such a case, the impingement heat flux determined on the crust-fluid interface can be used as the thermal boundary condition for evaluating heat conduction and phase change in the remaining solid part of the original plate (vessel wall).

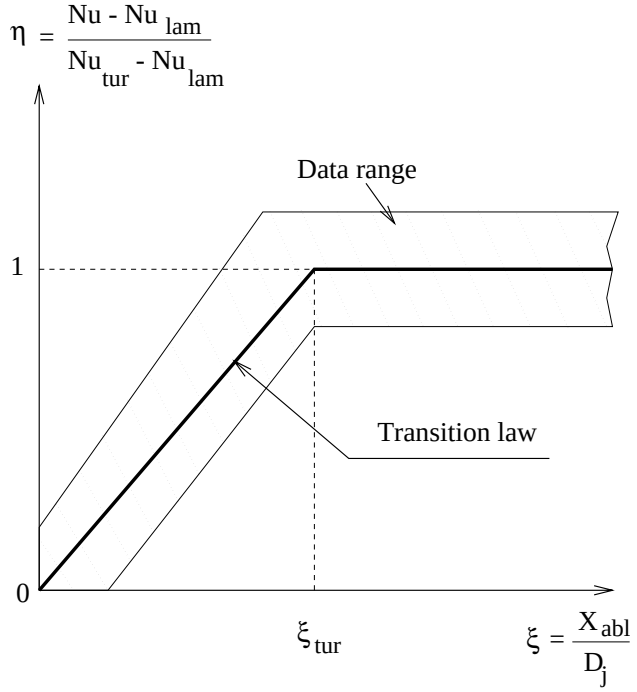

Fig. 2.9: Concept and parameters of jet impingement heat transfer.

2.3.1.3 Prediction Method

2.3.1.3.1 Impingement heat transfer modeling

In order to calculate the ablation rate of the solid plate, heat fluxes during the impingement period must be provided. For reactor applications of interest, the inclination of the impingement surface with respect to the jet and the accumulation of the jet fluid above the impingement surface (in the reactor vessel) may affect the impingement heat transfer rates. However, the effects of these two phenomena are not accounted for in the present model. As a result, the model will provide conservative assessments of the vessel ablation rates.

Two distinct (limiting) regimes of heat transfer can be modeled in a straightforward manner. Namely, heat transfer in the initial impingement period is determined from the laminar stagnation flow model [correlation (2.1)]. The turbulent heat transfer correlation (2.2) by Saito and co-workers is applied to calculate the impingement heat flux under augmented flow conditions.

Since the phase-change-induced surface roughness k and its relationship with the boundary layer thickness can not be modeled in the present macroscopic approach, the ablation depth is proposed as the physical parameter which governs the transition law between the two limiting heat transfer regimes. So far, heat transfer data from water-ice and water-salt ice experiments indicate that heat transfer in the transition period features the linear relationship between $\eta = \frac{Nu - Nu_{lam}}{Nu_{tur} - Nu_{lam}}$ and $\xi = \frac{X_{abl}}{D_j}$, where X_{abl} is the impingement-induced ablation depth of the solid plate. This transition behavior and its parameters are described in Fig.2.9. Here, Nu_{lam} is determined by Eq.(2.1), and Nu_{tur} by Eq.(2.2).

The critical ablation depth ξ_{tur}, over which a fully turbulent (augmented) flow and heat transfer regime is established is not certain. From RIT experimental results ξ_{tur} is in the range from 0.6 to 1. However, ξ_{tur} may approach zero if an initially rough surface is present inside the vessel where the jet impinges.

2.3.1.3.2 Features of ablation calculations

A method of calculating heat conduction the solid plate (vessel), with a moving phase change boundary, was developed in [16]. This method is employed here to simulate the jet-impingement-induced vessel ablation process. The moving rate of phase-change boundary is defined through the difference between the heat flux imposed on the interface, q_{imp}, and that taken away by heat conduction, q_{cond}, as follows

$$U_{abl}(z,t) = \frac{q_{imp} - q_{cond}}{\rho_w H_{fusion,w}} \tag{2.14}$$

q_{cond} is determined from the solution of the heat conduction equation in the solid-phase domain. Calculated values of U_{abl} are then used to track the phase-change interface. Simulation of the conduction-controlled crust growth in the initial contact phase was also included [16].

In most cases, *one-dimensional analyses* (in the jet direction) may be sufficient to evaluate the maximum ablation of the vessel. As observed in the RIT jet impingement experiments with meltable plates, the centerline of the impingement zone is subjected to maximum heat flux. Calculations performed for the laminar stagnation flow condition indicate that impingement heat flux is rather

uniform in the impingement area (within 20%) [3]. For turbulent profile of jet velocity, the maximum heat flux is at the centerline of the impingement area. With phase change induced roughened surface in the impingement zone, the heat transfer should become even more uniform owing to the self-similarity of the physics of fluid flow and heat transfer. Thus, one dimensional analyses [3] will be employed for the assessment in the next section.

2.3.1.5 Summary

New experimental and analyses results foster understanding of physical mechanisms which govern the jet impingement heat transfer under phase change conditions. It was found that a crust boundary condition is effective during the jet impingement duration. The heat transfer is enhanced due to the turbulence generated by the surface roughness associated with phase change. As a result, the scaling law, based on the Peclet number, was proposed.

A new model of jet impingement heat transfer under phase change conditions was developed and applied to analyze reactor vessel ablation due to impingement of a core melt jet during the scenario of core melt relocation to the lower plenum.

With fixed melt volume and relatively smaller diameter jets, the pouring period is long and most of the vessel ablation will occur under turbulent flow conditions. In such cases, Saito's correlation is applicable. Meltthrough is possible for core melt jets of diameters less than 5cm (mass of relocated melt is 20 tonnes).

In general, it was found that the use of Saito's correlation (in previous reactor safety studies) provides a conservative assessment. The use of Epstein's laminar stagnation flow model provides underestimates of the reactor vessel wall ablation.

2.3.2 Molten-Metal Jet Impingement: Insights from Experiments and Analyses

The focus of this section is molten-metal jet impingement upon a metal substrate using the low melting point alloy Cerrobend and common tin (Sn) as simulant materials. The range of experimental conditions covers jet Reynolds numbers from 44,000 to 210,000 with melt Pr number of approximately 0.005-0.03. It was found that the experimentally measured heat transfer lies below that of the earlier Liu and Epstein models but above that of the extrapolated Saito correlation which includes phase change.

It is found that the RIT/NPS data are in a reasonable agreement with Sato' correlation: $Nu = 0.0152 \cdot Re^{0.92}.Pr^{0.8}$ obtained from metal-jet impingement

[3]For the inclined jet cases (inclination angle ϕ), the actual vessel thickness to be employed in the ablation calculations is $L_w^{\phi} = L_w/cos(\phi)$ (see also section III.3).

tests.

Explanation and analysis of the experimental phenomena and some bounding analysis with respect to prototypical situations are presented. These experiments constitute a needed addition to the relatively scarce data concerning liquid metal jet impingement with phase change.

2.3.2.1 Related Heat Transfer Correlations

The analytical derivation obtained by Liu et al. [19] for laminar jet impingement heat transfer is one of the only known works applicable to low Pr number fluids. It does not consider phase change of the substrate material and can be written as

$$Nu_j = \frac{\sqrt{1.83} \cdot \sqrt{2Pr/\pi}}{1 + 0.804552 \cdot \sqrt{2Pr/\pi}} Re_j^{1/2} \tag{2.15}$$

for $Pr < 0.15$, but can be simplified to the following for $Pr < 0.06$

$$Nu = 0.96 \cdot \sqrt{Re \cdot Pr} \tag{2.16}$$

Of particular importance is the experimental work conducted by Saito and co-workers [7] in which molten $NaCl$ and Al_2O_3 was directed onto Sn and iron plates respectively. The parameter range covered by Saito's correlation, Eq.(2.2) was approximately 7x10^4 $\leq Re \leq$ 3.5x10^5 and 0.75 $\leq Pr \leq$ 1.2 . (The two alumina onto steel plate experiments had Re = ≈2000 and Pr = 5.5.) A quite similar Re number dependency was observed in water-ice impingement tests done by Yen and Zehnder [4] ($Nu^* \sim Re^{0.94}.Pr$).

Comparison of the Liu and Saito correlations is instructive in this instance. Extrapolation of the Saito correlation to the conditions of low Pr numbers, typical of molten metal jets, must be done with great caution, since these are far outside the range of experimental data from which it was derived. This is necessary however since the Saito correlation provides some of the only known jet impingement heat transfer data which includes substrate phase change. Comparison is made using material properties for molten zirconium (Pr = 0.057) and for Cerrobend alloy (used in this investigation with Pr = 0.03). The predicted jet-based Nu numbers are provided in Figure 2.10. As is evident in this figure, the difference in predicted heat transfer (Nu number) becomes greater at low Re number with Pr numbers typical of liquid metals. The fact that the turbulent Saito correlation underpredicts that of the laminar Liu (and also Epstein and other) models further emphasizes the fact that application of this model outside its experimental data range poses difficulties. The experiments conducted for this paper directly address jet impingement heat transfer, including phase change, for $Re \cdot Pr$ (Pe)

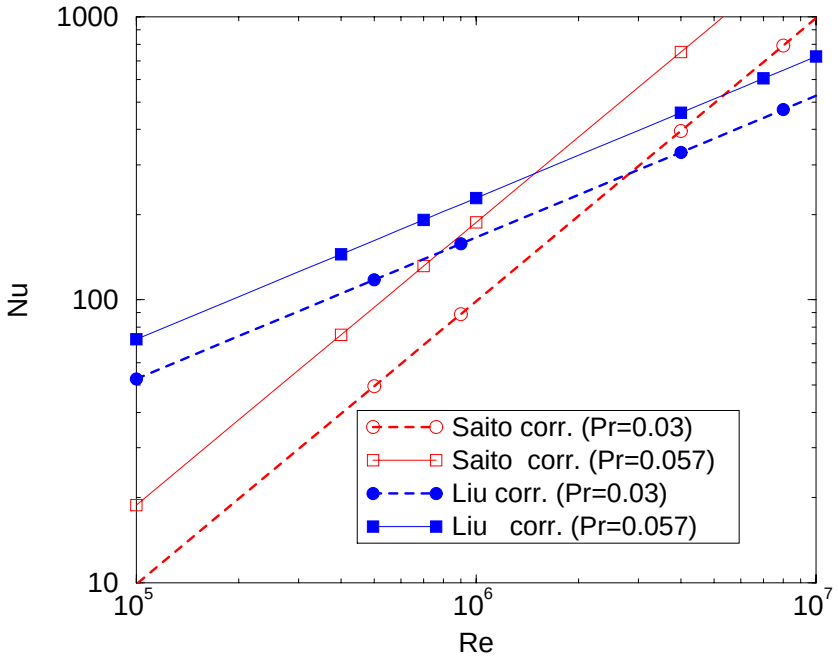

Fig. 2.10: Jet Heat Transfer Predicted by Liu and Saito Correlations.

combinations not previously studied but of importance to severe accident metallic melt relocation.

There does exist some experimental information for prototypical oxidic and stainless steel melt jets impinging upon steel plates as shown in the work by Powers [20]. The resulting correlation is unfortunately not amenable to predicting jet impingement heat transfer for cases other than that from which it was obtained. Moxon [9] considers these and a similar test conducted at KfK to conclude that once the initial crust layer has been removed (the mechanism for which was indeterminate) that it did not re-establish. Experiments conducted by Sienicki and Spencer [21] using prototypical melts revealed little or no substrate erosion due to the impinging jet, which is perhaps due to the low superheat of the melt.

As it was mentioned (Section 2) a study of molten-metal jet impingement heat transfer was performed by Sato and co-worker (1991) [10]. The data base is, however, scarce and needs to be improved. Based on a limited number of tests, Sato et al. proposed the following correlation for molten metal jets.

$$Nu = 0.0152 \cdot Re^{0.92} \cdot Pr^{0.8} \tag{2.17}$$

As it can be seen later, correlation can describe experimental data obtained in

the present study with uncertainty factor of 2x.

2.3.2.2 RIT/NPS Experimental Investigation

The test facility was comprised of a heated tank with a maximum melt capacity of 10 liters connected to a long heated pipe section of variable diameter and of sufficient length to ensure a fully developed flow profile prior to exiting. Although the tank has the capability to be pressurized with air, in this series of experiments pressurization was not performed. The impingement plates were made in circular molds into which pre-measured volumes of molten Cerrobend alloy was poured and allowed to solidify and cool. In the center of these plates several small diameter (0.5mm) K-type thermocouples were installed at precise separation distances from one another. The first thermocouple corresponded to the upper surface of the plate when removed from the mold. For the majority of other tests the thermocouple ends were placed at depths of 2, 4, 6, 9, 12, 15, 19, 23, and 27mm from the upper surface. Additional thermocouple groupings were placed 10 mm from the center stagnation zone thermocouples in order to compare heat transfer results. The ablation rates, and thus heat transfer, obtained from these probes was consistent with that obtained from the centrally aligned thermocouples. When soldered together, the center grouping of thermocouples was $\approx$3mm in diameter and thus is not considered to have substantially influenced the impingement flow field. Plate thicknesses varied from 20 to 40 mm.

The response of the embedded thermocouples is measured using a high speed Hewlett-Packard data acquisition system connected to a 486 PC. Typical scanning rates of 3-4 Hz were obtained with good noise rejection. Direct millivolt measurements were performed with subsequent RTD and polynomial conversion to degrees centigrade.

During the impingement period of a typical test there was considerable splattering of the melt jet which was contained inside the test facility housing. In all cases the melt jet volume was sufficient to fully penetrate the plate thickness. Final plate shapes revealed a slightly elliptical (larger opening at the upper surface) cavity formed by the jet with substantially rough surface characteristics.

Nine tests using the Cerrobend alloy and 2 using pure tin were conducted. Cerrobend, also known by its trade name MCP-70, is a mixture of 50% Bi, 26.7% Pb, 13.3% Sn and 10% Cd which exhibits a melting point of 70^oC. Thermal properties for the two melt simulants used are listed in Table 2.1. These values have been obtained from both standard reference compendiums as well as through special laboratory measurements conducted in support of this test program. Due to the fact that information concerning the Cerrobend alloy viscosity, as a function of temperature, is not readily available, all of the experiments using it as melt were conducted at a constant temperature of 110^oC.

For the two tests which employed Sn as melt, the jet diameter was maintained constant at 25mm but the melt temperature was changed from close to the freezing point in one test to ≈80 K superheated in the second test.

Table 2.1: Simulant Material Property Data

Property	Cerrobend	Tin
ρ (kg/m^3)	9670	7280
$T_{mp,metal}$ (K)	343	505
Δh_{fus} (kJ/kg)	46	61
$C_{p,liq}$ (J/kgK)	177	227
$C_{p,sol}$ (J/kgK)	164	–
κ (W/mK)	18	67
μ (Pa-s)	0.0018-0.0037	0.0013-0.0017
Pr	≈0.03	≈0.005

Variation in jet Re number was accomplished by varying the diameter of the heated exit pipe from the tank. The discharge pipe was maintained heated and insulated to ensure no temperature change of the melt fluid from that established in the tank. A standard ball valve was used to start the discharge flow. Once the valve was opened, the decrease in tank level was timed in order to determine the jet velocity. A more accurate method of melt-level decrease was obtained by placing thermocouples into the tank at known levels from the tank bottom surface. A listing of the experiments conducted and the relevant test conditions is given in Table 2.2.

A representative trace of the thermocouple readings obtained during a test using Cerrobend as both melt and plate is shown in Figure 4. The depths in mm from the upper impingement surface are shown next to each temperature trace. It is evident that for those thermocouples located at greater depths from the surface that conduction heat transfer prior to phase change plays a role. This effect has been taken into consideration and included in the ablation rate energy balance. The final column in Table 2.2 presents the number of valid Nu number data points obtained from each test.

2.3.2.3 Analysis of Results

The temperature response of the thermocouples in the jet stagnation zone were analyzed for each of the experiments. A database of the experimental Nu numbers was compiled along with their corresponding Re and Pr numbers. This data is presented in Figure 2.12 as a function of the jet Pe number. Nusselt numbers pre-

Table 2.2: Molten Metal Jet Impingement Data

Test	Melt Material	Plate Material	D_{jet} (mm)	T_{melt} (^{o})	U_{jet} (m/s)	Re (-)	δ_w (mm)	# Points (-)
0619B	Cerro	Cerro	15	112	3.0	145,050	30	8
0624	Cerro	Cerro	15	110	2.9	140,215	20	2
0626	Cerro	Cerro	15	110	2.8	135,380	20	4
0715	Cerro	Cerro	25	110	2.6	209,516	22	3
0723	Cerro	Cerro	6.3	110	2.2	44,675	20	7
0724	Cerro	Cerro	15	110	3.1	149,900	20	7
1020	Cerro	Cerro	25	110	1.8	145,080	29	7
1218	Cerro	Cerro	15	110	1.9	91,870	40	3
1220	Cerro	Cerro	15	110	2.0	102,970	40	9
1128	Tin	Cerro	25	315	1.3	154,330	40	9
1202	Tin	Cerro	25	250	0.9	92,125	40	9

dicted by Eq.(2.2) (Saito) and Eq.(2.16) (Liu) are included for comparison along with the experimental data from SNL and KfK tests as taken from the work of Moxon (1990) [9]. Although not explicitly stated in the form of a Nu number, the plate thicknesses and melt-through times given in [20], [9] can be employed to extract average ablation, and thus heat transfer, rates for these steel-onto-steel experiments. There remains some uncertainty associated with the Nu numbers determined from the SNL/KfK tests and this is primarily attributable to the choice of thermal properties (C_p, κ, Δh_{fus}) for the molten steels/iron employed. The sensitivity of the predicted heat transfer rates to the chosen property values can be high (see for example [22] for representative thermal properties).

The choice of Pe number as the independent variable is based on the suggestion that the jet impingement process with phase change (as well as hole ablation due to higher temperature melt flow) is strongly influenced by the surface roughness of the melting interface. When the surface roughness becomes greater than the thickness of the viscous boundary layer the heat transfer is enhanced. The surface roughness thus diminishes the impact of viscosity, and, as such, the heat transfer can be determined by the viscosity-independent Pe number.

It is clear that the data falls between that predicted by the Liu and Saito correlations. This is not wholly unexpected since the conditions of low Pr number fluid, accompanied by substrate melting, were not considered in these earlier investigations. Notably, the Liu equation [Eq. (2.16)] was obtained from a laminar boundary layer solution of the mass, momentum and energy equations. Applying that same procedure but with the use of an effective viscosity ($\nu_{eff} = \nu + \nu_t$) and

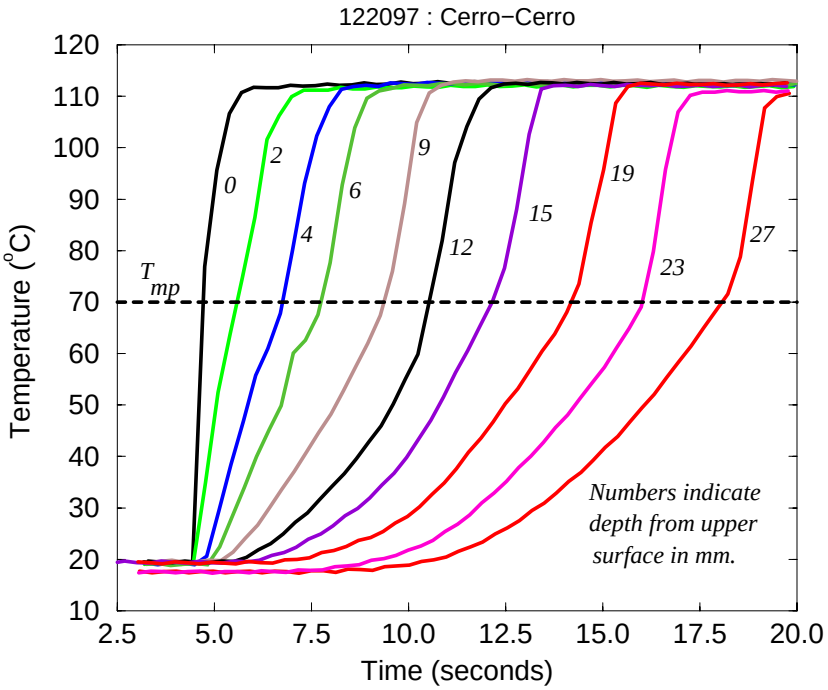

Fig. 2.11: Temperature traces in the stagnation zone for Cerrobend jet onto Cerrobend plate (#1220).

thermal diffusivity ($\alpha_{eff} = \alpha + \alpha_t$) in the momentum and energy equations, one can obtain a similar correlation;

$$Nu = 0.96\sqrt{Re^*} \cdot \sqrt{Pr^*} \tag{2.18}$$

where Re^* = $U_{jet}D_{jet}/\nu_{eff}$ and Pr^*=ν_{eff}/α_{eff}. Thus

$$Nu = 0.96\sqrt{\frac{U_{jet}D_{jet}}{\alpha_{eff}}} = 0.96\sqrt{Pe} \cdot \sqrt{\frac{\alpha}{\alpha_{eff}}} \tag{2.19}$$

Since $\alpha < \alpha_{eff}$, the resulting Nu number in the case of phase change, and thus an increased level of turbulence due to surface roughness, should be smaller than that obtained without phase change. In fact, the ratio α_{eff}/α may vary in a wide range depending upon the surface-roughness-induced turbulence characteristics. From the measured data, it is seen that this ratio is in the range from 2 - 10.

The data from Figure 2.12 was statistically analyzed using the SAS software and can be represented in the following form;

$$Nu = 0.47 \cdot Pe^{0.5} \tag{2.20}$$

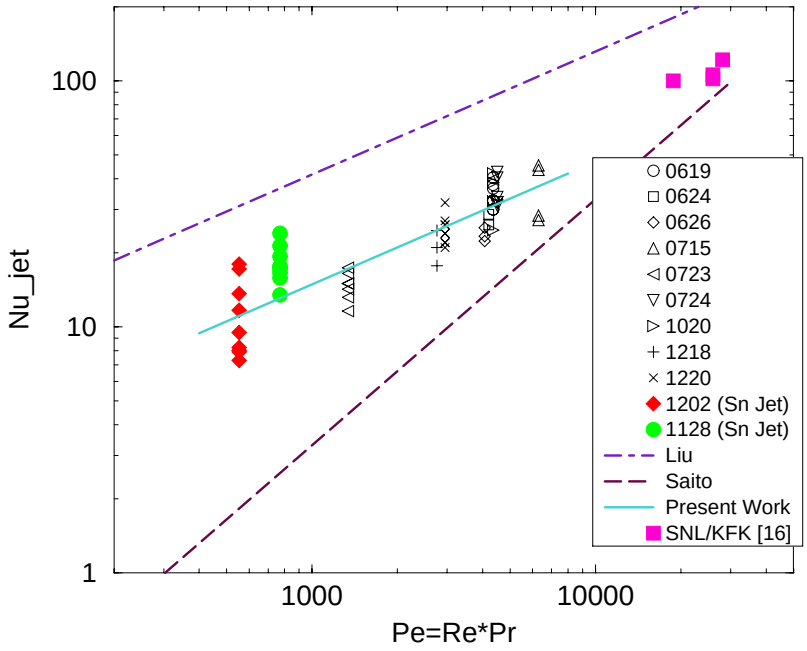

Fig. 2.12: Liquid Metal Jet Impingement

The regression calculation reveals an r^2 coefficient of 0.8 which is indicative of a significant degree of correlation for the 68 data points available.

The heat transfer data was also analyzed as a function of the ablation depth under the stagnation zone. Presentation in this fashion is useful in determining whether transitions between heat transfer regimes, or formation of the eroded cavity, is significantly influencing the measured heat transfer. Such results are presented for two Cerrobend and two Sn melt tests in Figure 2.13. Generally, there is no discernable pattern as the melt front progresses into the plate material and the measured Nu numbers are seen to fall within a reasonable band of data scatter during the impingement period.

Finally, it should be noted that Eq.(2.17) by Sato et al. [10] predicts, with uncertainty factor of 2x, the experimental data obtained in the present study (Figure 2.14). Although it does not feature similar power for Re and Pr, the powers in Sato's correlation are quite close (0.92 and 0.8, respectively).

Figure 2.15 shows the performance of Sato's correlation, Eq.(2.17), in comparison with Liu and Saito correlations. It is interesting to note that for high Reynolds numbers Sato's correlation, Eq.(2.17), provides higher Nusselt number than

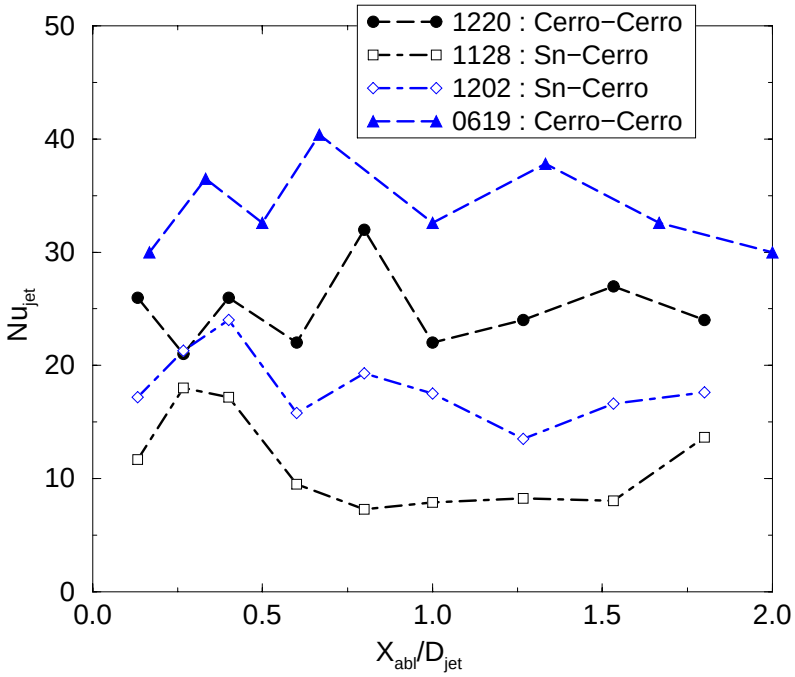

Fig. 2.13: Variation in heat transfer as impingement front progresses.

Eq.(2.20). In general, taking into account experimental uncertainties in heat transfer data, it appears that experimental correlation of Sato et al. can be recommended for calculation of molten-metal jet impingement heat transfer as to provide conservative assessments of the vessel failure due to molten-metal jet impingement.

2.4 Concluding Remarks

There are several areas of severe accident phenomenology, which have received attention, but the state of the art has not advanced enough to resolve some of the key issues.Such an area is the late phase of in-vessel melt progression, when the core melt interacts with the contents of the lower head and may fail it. In particular, the scenario of interest is the one in which the accumulated melt in the original core boundary is released to the lower head as a jet, either from the side of the core boundary, as happened in the TMI-2 accident, or from the bottom of the core plate. The jet attack on the vessel lower head wall may produce sufficient vessel ablation to fail the vessel immediately.

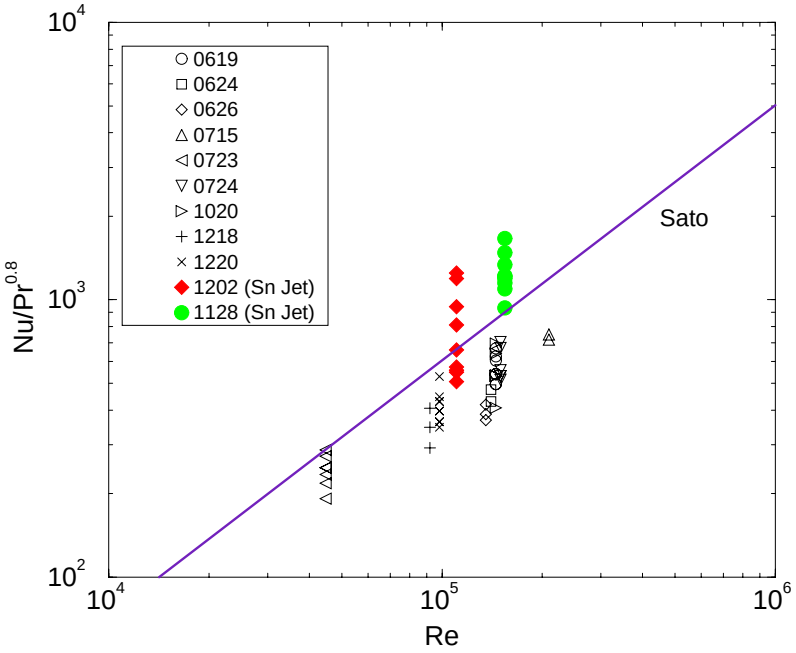

Fig. 2.14: Comparison of RIT/NPS data with Sato experimental correlation.

A simple test apparatus was constructed in which experiments were performed using:

1) water at different temperatures representing the melt and the ice or salt-ice plates representing the vessel wall,
2) molten salt, as melt and tin and cerrobend plates as vessel wall, and
3) molten oxide mixture as melt and Al plate as vessel wall. The following outstanding results are obtained.

Data were obtained with thermocouples embedded in the stagnation zone. In most tests a hole was created in the plates. Configurations in which jets impinge at an angle on the plates, and in which they traverse through a pool before impinging the substrate of the plate, were also tested. The data obtained are plotted in Fig. 1 as functions of the jet Re and Pr numbers. The earlier data obtained by Saito is also plotted on the same graph. The following outstanding results are obtained.

a) The crust formed by the melt is effective during the jet impingement process. Thus, the driving temperature for the heat transfer to the substrate is the melt

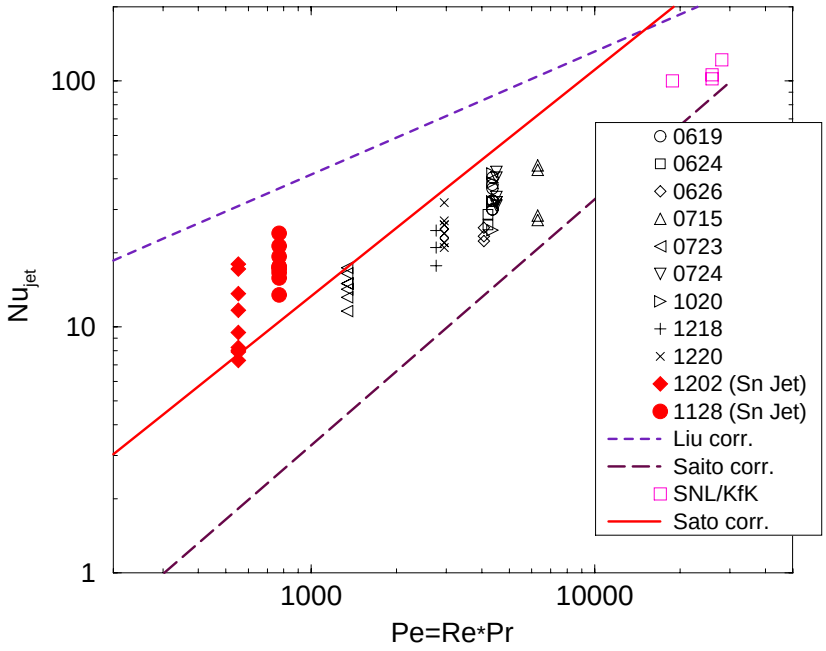

Fig. 2.15: Comparison of RIT/NPS data with Sato experimental correlation.

superheat i.e. Tmelt-Tliq.

b) The surface temperature roughness created by the phase change process (crust formation, substrate melting) causes rapid transition to turbulent heat transfer, and to a heat transfer correlation which does not depend on melt viscosity.

c) For the oxide melt jets, the heat transfer correlation is: Nu = (0.0025 - 0.0030)·Pe, where $Pe = Re.Pr$ is the Peclet number, which is independent of melt viscosity.

Similar experiments were performed with various molten metal jets impinging on different substrates14. Good agreement was obtained with Sato's15 correlation: $Nu = 0.0152 \cdot Re^{0.92}.Pr^{0.8}$.

It is believed that sufficient understanding of the jet impingement issue has been achieved. The above correlations can be employed to assess the consequences of jet impingement for prototypic conditions.

Some estimates on the potential for vessel failure were made. It was found that for a given melt volume, thin jets are of greater concern for vessel failure, since

they impinge for a longer time than thick jets. For a twenty tonne melt volume, a jet of 10 cm diameter at a superheat of 100K will not fail the prototypic vessel wall (150mm). Failure may occur if the jet diameter remains at 5 cm. In this case, however, the jet is likely to break up and not be of concern for sustained ablation. In general, it is believed that jet impingement may be of some concern; however, with water present in the lower head, the probability of vessel failure is very small.

Bibliography

[1] J.L. Rempe et al. ”Light Water Reactor Lower Head Failure Analysis”. NUREG/CR-5642. EGG-2618 (October 1993).

[2] T.G. Theofanous et.al., ”In-Vessel Coolability and Retention of a Core Melt”, DOE/ID-10460 (July 1995).

[3] R.R. Nourgaliev and T.N. Dinh, ”Numerical Simulation and Analysis of Axisymmetric Free-Surface Liquid Jet Impingement on Horizontal Plate: Friction and Heat Transfer in the Stagnation Zone”, RIT/NPS Report MVI.JI.M01 (May 27, 1996), Royal Institute of Technology, Stockholm, 18p.

[4] Y. Yen and A. Zehnder, ”Melting Heat Transfer with Water Jet”, Int.J. Heat Mass Transfer, 16 (1973), p.219.

[5] M.J. Swedish et al., ”Surface Ablation in the Impingement Region of a Liquid Jet”, AIChE J., 25 (4) (1979), p .630.

[6] M. Epstein et al., ”Simultaneous Melting and Freezing in the Impingement Region of a Liquid Jet”, AIChE J., 26 (5) (1980), p .743.

[7] M. Saito et al., ”Melting Attack of Solid Plates by a High Temperature Liquid Jet - Effect of Crust Formation”, J. Nuclear Engineering and Design, 121 (1990), pp.11-23.

[8] D. Magalon, R. Zeyer and H. Hohmann, ”100 kg-Scale Molten UO_2 Out-of-pile Interactions with LMFBR Structures: Plate Erosion and Fuel Freezing in Channels”, presented at the International Conference on Fast Reactor Core and Fuel Structural Behaviour, Inverness, G.B., 1990 (quoted from Ref.[1]).

[9] D. Moxon, ”Ablation by a Liquid Jet”, Proceedings of the Conference on Fast Reactor Safety, pp.619-633, 1990, Snowbird, Utah, USA.

[10] K. Sato, A. Furutani, M. Saito, M. Isozaki, K. Suganuma, and S. Imahori, ”Melting Attack of Solid Plates by a High Temperature Liquid Jet. (ii) Erosion

Behavior by a Molten Metal Jet", ANS Proceeding of the 27th National Heat Transfer Conference, Vol.5, pp.311-322, 1991, Minneapolis, MN, USA.

[11] J. A. Green, W. Dong, T.N. Dinh, and B.R. Sehgal, "Experiments on Melt Jet Impingement and Vessel Hole Ablation", Proceedings of the International Topical Meeting on Probablistic Safety Assessment PSA-4, September 29 - October 3, 1996, Park City, Utah, 1996.

[12] B.R. Sehgal, W.G. Dong, J.G. Green, and T.N. Dinh, "Experiments and Analyses of Melt Jet Impingment during Severe Accidents", Proceedings of the Fifth International Topical Meeting on Nuclear Thermal Hydraulics, Operations, and Safety (NuTHOS-5), Beijing, China, April 1997.

[13] A. Furutani et al., "Erosion Behavior of Solid Plate by a Liquid Jet - Effect of Molten Layer", ANS Proc. 1989 National Heat Transfer Conf., Philidelphia, PA (August 1989), pp.263-271.

[14] H. Schlichting, Boundary Layer Theory, Sixth Edition, McGraw-Hill Book Company, 1968.

[15] L.A. Gabour and J.H. Lienhard V, "Wall Roughness Effects on Stagnation-Point Heat Transfer Beneath an Impinging Liquid Jet", J. Heat Transfer, Vol.116, pp.81-87 (1994)

[16] T.N. Dinh, V.A. Bui, R.R. Nourgaliev, T. Okkonen, and B.R. Sehgal, "Modeling of Heat and Mass Transfer Processes During Core Melt Discharge From A Reactor Pressure Vessel", Nuclear Engineering and Design, Vol. 163, pp.191-206 (1996).

[17] McMurray, D. C., P. S. Myers, and O. A. Uyehara, "Influence of Impinging Jet Variables on Local Heat Transfer Coefficient Along a Flat Surface with Constant Heat Flux," Proceedings of Third International Heat Transfer Conference, Vol. II, (1966), pp. 292-299.

[18] J.A. Pessanha and M.Z. Podowski, "Ablation of Solid Walls Subjected to Impinging Inclined Jets", ANS Proceedings of the 1989 National Heat Transfer Conference, Philadelphia, PA, August 1989.

[19] Liu, X., L.A. Gabour, and J.H. Lienhard V, "Stagnation-Point Heat Transfer During Impingement of Laminar Liquid Jets: Analysis Including Surface Tension," Transactions of the ASME - Journal of Heat Transfer, **Vol. 115**, (1993), pp. 99-105.

[20] Powers, D.A., ”Erosion of Steel Structure by High-Temperature Melts,” Nuclear Science and Engineering, Vol. 88, (1984), pp.357-366.

[21] Sienicki, J.J. and B.W. Spencer, ”Analysis of Reactor Material Experiments Investigating Corium Crust Stability and Heat Transfer in Jet Impingement Flow,” ANS Proceedings of 1985 National Heat Transfer Conference, Denver, CO, August, 1985.

Chapter 3

In-vessel melt retention by external cooling

3.1 Introduction and Background

A hypothetical core melt accident in a light water reactor (LWR) may result in accumulation of core debris in the lower head of the reactor pressure vessel (RPV). The core debris, if unquenched, may heat up and commence natural circulation. The core melt pool formed likely will consist of a decay-heated oxidic region at the bottom and a metal layer on the top. The thermal loadings exerted on the vessel wall by the naturally circulating pool have been a subject of study for the last several years. The primary interest has been the determination of the feasibility of the accident management scheme of retaining the melt within the lower head by cooling the vessel outside wall with water.

Much has been learned since the focused studies began. An evaluation of the in-vessel melt retention management scheme for the AP-600 was performed by Theofanous et al. (1995), who found sufficient margin for the critical heat flux for heat removal at the vessel outer wall, over the thermal loading imposed by the circulating melt inside the lower head. The metal layer resident on top of the oxidic pool was found to focus the heat added to it from the oxidic pool towards the vessel wall. However, for the AP-600 geometry and scenario, it was found that the metal layer would be quite thick and the focused heat flux at the vessel wall was lower than the critical heat flux at the vessel outer wall.

The AP-600 evaluation was based on data obtained from the COPO (Kymäläinen et al., 1994), UCLA (Asfia and Dhir, 1994) and the mini-ACOPO (Theofanous et al., 1995) experiments, employing water, freon and water, respectively as melt simulants. The mini-ACOPO experiments also employed the heat capacity of the melt simulant in a transient cool-down mode to obtain the heat transfer data. A

reasonable equivalence between the volumetric heating and the transient cool-down has been demonstrated through CFD analyses (Nourgaliev et al., 1996).

Experiments and analyses have been continuing since the evaluation performed for the AP-600. The mini-ACOPO experiments have been transformed into ACOPO experiments, employing a one-half scale 3-D representation of the lower head; again employing water and the transient cool-down technique. The COPO facility has employed top and side wall cooling to create a crust (ice), i.e. a truly isothermal boundary. The BALI experiments, conducted in Grenoble, have employed a full scale 110^o slice facility, with water as melt simulant, also cooled at top and side wall to create an ice crust boundary.

The RASPLAV Program (Asmolov, 1997), conducted in Russia, employs prototypic (UO_2-ZrO_2) melt materials in a 200 kg slice facility, in which the thermal loadings imposed by the prototypic melt on a cooled vessel wall are measured. Two tests have been conducted so far, for which data is being analyzed. In addition, the RASPLAV Program has also employed a salt test facility in which experiments with eutectic and non-eutectic salt have been conducted. The data in some of the tests have been analyzed, while others need further analysis.

A separate-effect experiment (Bonnet, 1997) on the focusing effect of the metallic layer has been performed at the BALI facility. This experiment employed water as the metal-layer simulant. A focusing effect of $\simeq$ 2.0 was found, which increased to $\simeq$ 6.0 for very thin layers (aspect ratio of $\simeq$ 1/40).

We believe the recent changes in the situation with respect to the prediction of the thermal loadings on the vessel wall, and with respect to the feasibility of the in-vessel melt retention may be described as follows:

- The RASPLAV experiments, conducted at $Ra' \leq 10^{11} - 10^{12}$, have shown corium melt stratification for prototypic compositions and temperatures. The interpretation of the data obtained with respect to stratification has not been completed so far. If the stratification is found to be stable, and prototypic, for the accident composition and temperatures, it may affect the natural circulation flow fields. The magnitude of the effects of stratification at the prototypic Ra' numbers (when the flows would have greater turbulence than for those in the RASPLAV tests) has not been determined.

- The measured values of the Nu_{up}, Nu_{dn} and Nu_{sd}, obtained from the recent isothermal-boundary COPO and BALI experiments, appear to be larger than those obtained from the ACOPO facility, which did not have crusts at the boundaries. These measured values are also larger than those derived from the Steinberner and Reineke correlation. The Ra' number scaling, however, holds. These differences may be due to the changes in the boundary layer heat transfer at the crust boundary, or due to the change in the

thermal expansion of water at +4°C. Resolution of these differences has not been achieved so far.

- The salt experiments performed in the RASPLAV Program have also shown some differences in the heat transfer at the boundaries of a naturally convecting pool with or without crust boundaries.

- The metal layer resident on top of a heat generating oxidic material pool was found to focus the heat, received by it, towards the cooled side wall of the vessel; thereby indicating that the vessel corner may be the most failure-prone location. This has been confirmed by separate-effect tests.

  However, evaluations employing integral two-dimensional analyses of the oxidic pool, metal layer and vessel have indicated a significant amelioration of the peaking of heat flux at the vessel location next to a thin metal layer.

We believe that the recent changes have introduced uncertainties, which may not allow a straight-forward evaluation of the feasibility of in-vessel melt retention for a severe accident in reactors, with high power densities, in which thin metal layer could be formed and oxidic melt stratification could occur. Currently there are no integral experiments, employing either prototypic or simulant materials, modeling the prototypic integral situation of an oxidic pool and a metal layer, which can support such evaluation.

3.2 EU MVI Experimental programs on melt pool heat transfer

3.2.1 IVO Experiments on the COPO facility

The objective of the COPO II experiments is to measure heat flux distributions from a two-dimensional, large scale (1:2), volumetrically heated pool. The molten corium is simulated by water-zincsulfate solution. The modified Rayleigh number corresponds to the one in a prototypic corium pool ($\sim 5 \cdot 10^{15}$). As distinctive feature of COPO II, the pool boundaries are cooled by liquid nitrogen in order to create frozen boundary conditions. Two versions of the facility exist, one simulating an elliptically shaped lower head (VVER) and another one with semicircular shape (western PWR). Specific questions addressed in the COPO II experiments are the detailed heat flux distribution on the upper boundary, effect of bottom geometry, effect of non-constant fluid properties, effect of crust boundary, and heat transfer phenomena in stratified pools.

Facility and test matrix

Two versions of the facility exist, one simulating an elliptically shaped lower head (VVER) and another one a semicircularly shaped lower head (western PWR). A schematic of the COPO II facilities is shown in Figures 3.1-3.2.

Specific questions addressed in the COPO II experiments are the detailed heat flux distribution on the upper boundary, effect of bottom geometry, effect of non-constant fluid properties, effect of crust boundary, and heat transfer phenomena in stratified pools. Altogether 21 experiments (out of which 17 within the MVI-project) have been carried out using different temperature levels, boundary conditions and pool configurations, as shown in Table 3.1.

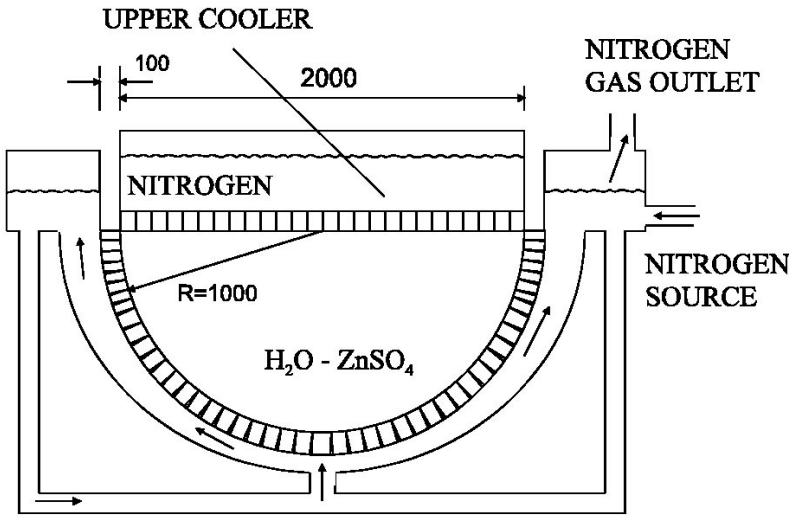

Fig. 3.1: Schematic of the COPO II-AP, homogeneous pool test setup.

Tests with homogeneous pool

The average heat transfer coefficients measured in the COPO II tests seem to deviate somewhat from what might have been expected based on earlier experiments. Particularly, the measured average upward heat transfer coefficients were higher than predicted by the widely used correlation by Steinberner and Reineke, and also higher than measured in the three-dimensional ACOPO facility [12]. On the

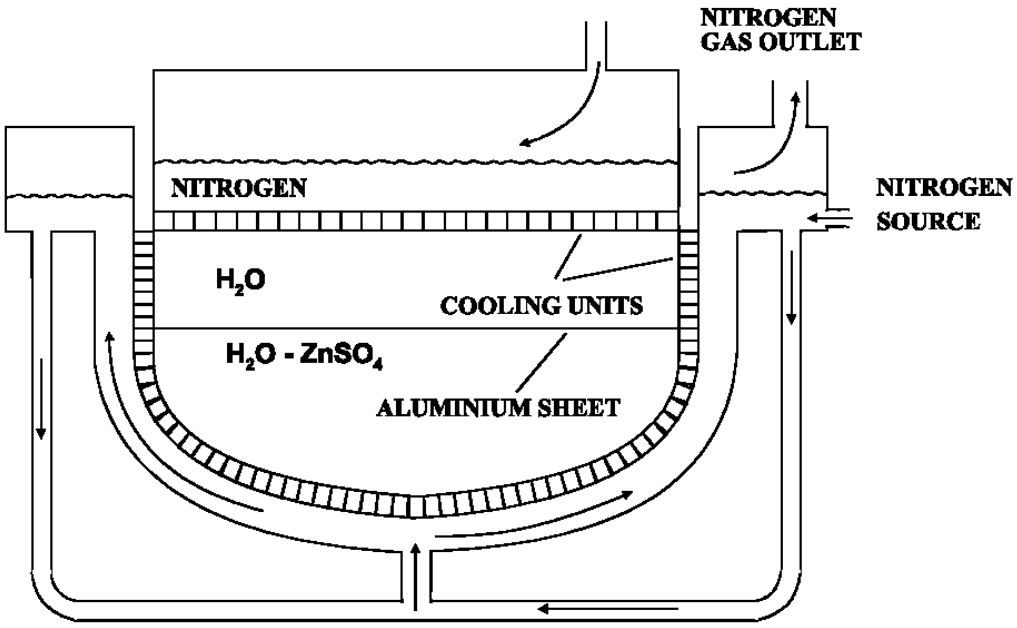

Fig. 3.2: Schematic of the COPO II-Lo, stratified pool test setup.

other hand, the results are in good agreement with the results from the French BALI facility [14]. Similarly to COPO II, pool boundaries are frozen in the BALI experiments. The reason for the discrepancy between the results from different facilities has been studied cooling only the upper surface of the test section. The results indicate that the presence of ice enhances the heat transfer at the upper boundary (Figure 3.3).

At the side and bottom boundaries the measured heat transfer coefficients in COPO II-Lo were clearly higher than measured in COPO I and predicted by the Steinberner and Reineke correlation. At the curved boundary the measured heat transfer coefficients in COPO II-AP were slightly lower than in BALI experiments.

The measured heat flux profile at the upper boundary is relatively flat. The deviation from the average value is about 10%. When the upper boundary is cooled, the peaking of the sideward heat flux just below the upper surface of the pool is rather small, if any.

Table 3.1: Test matrix of COPO II experiments

Objective	Facility	Number of Runs	Schedule
Shape effect, scale effect (homogenous pool)	COPO II-AP	2 (4 power levels)	completed before MVI project (12/95)
Base case test (homogenous pool)	COPO II-Lo	2	completed before MVI project (7/95) completed before MVI project (7/95)
Base case cont'd, shape effect (homogenous pool)	COPO II-Lo	5	part of MVI-project completed 9/97
Adiabatic upper surface (homogenous pool)	COPO II-Lo	1	part of MVI-project completed 9/97
Stratified pool	COPO II-Lo	2 (3 power levels)	part of MVI-project completed 11/96
Shape effect, scale effect (homogenous pool)	COPO II-AP	1	part of MVI-project completed 2/98
Stratified pool	COPO II-AP	2	part of MVI-project completed 5/98
Crust effect (homogenous pool only upper boundary cooled)	COPO II-AP	6 (13 power levels)	part of MVI-project completed 10/98

Tests with stratified pool

In the stratified pool tests, in which the upper, non-heat-generating layer was simulated by a layer of distilled water separated from the bottom layer by a thin aluminum sheet, the upward heat transfer coefficients from the non heated layer are well predicted by the correlation by Globe and Dropkin (Figure 3.4).

The sideward heat transfer coefficients from a thick non-heat-generating layer are well predicted by the Churchill and Chu correlation when the side wall is vertical (Figure 3.5). For small aspect ratios or inclined walls, the Churchill and Chu correlation seems to slightly overestimate the sideward heat transfer. A small dependency on the distance from the top of the pool may be seen in the local Nusselt numbers at the level of thick non-heat-generating layer. For thinner layers or inclined walls, the profile is more flat.

3.2.2 CEA BALI experimental program

Objective

The objective of the BALI experiments is to obtain data on the thermal hydraulic behaviour of a naturally convecting corium pool in the lower head of the vessel. The corium melt is represented by salt water and the lower head by a slice at scale 1:1 of constant thickness (15 cm). These dimensions provide values of internal Rayleigh number Ra_i of 10^{16} to 10^{17}, matching those in the prototypic situation. The pool is cooled from the bottom and top and heated electrically from the sides by Joule effect. The coolant is an organic liquid which may be used with a temperature ranging from 0°C to - 80°C, thus an ice crust forms on the pool top

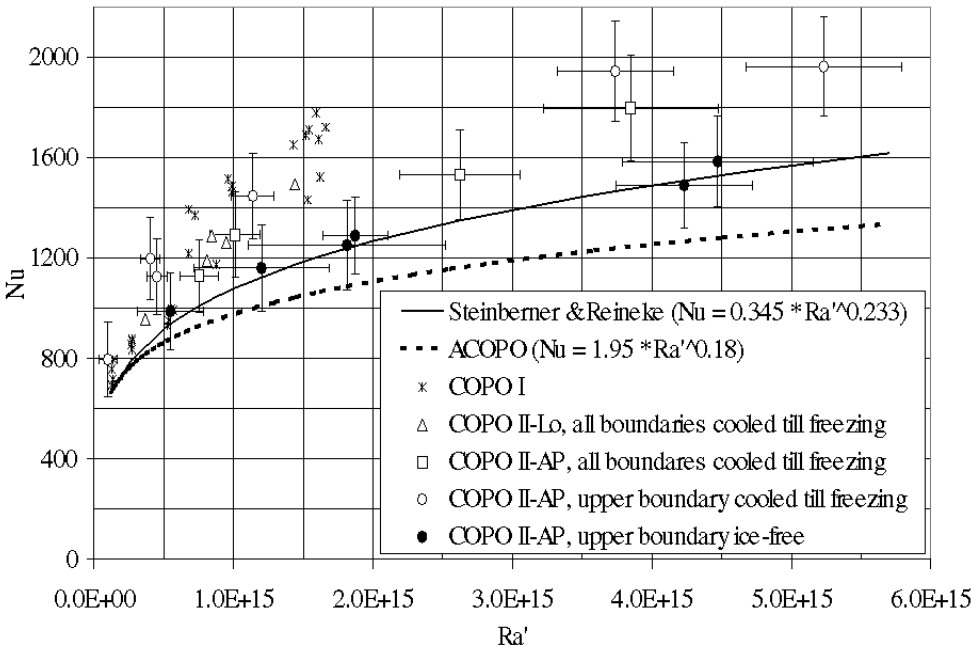

Fig. 3.3: *COPO: Average upward Nusselt Numbers*

and bottom surfaces to provide constant temperature boundary conditions. The measurements consist of heat flux distributions over the pool boundaries and the axial temperature distributions in the pool. Void fractions and velocity fields are also measured. The test matrix will vary the water height, power density, water viscosity, pool porosity, cooling conditions and the superficial gas velocity.

Test matrix

The following tests have been performed:

- 1st test campaign about the effect of internal Rayleigh number : $10^{15} < Ra < 10^{17}$ H=1.0m, 1.5m and 2.0m with and without top cooling (10 tests);
- 2nd test campaign about the effect of Prandtl number : Pr $\simeq$5, 100 and 1000; H=1.5m with top cooling (4 tests);
- 3rd test campaign about the effect of pool porosity (simulation of oxidic debris in metallic pool): spherical glass balls dia. 1 cm, H=1.0m and 1.5m with and without top cooling (3 tests);

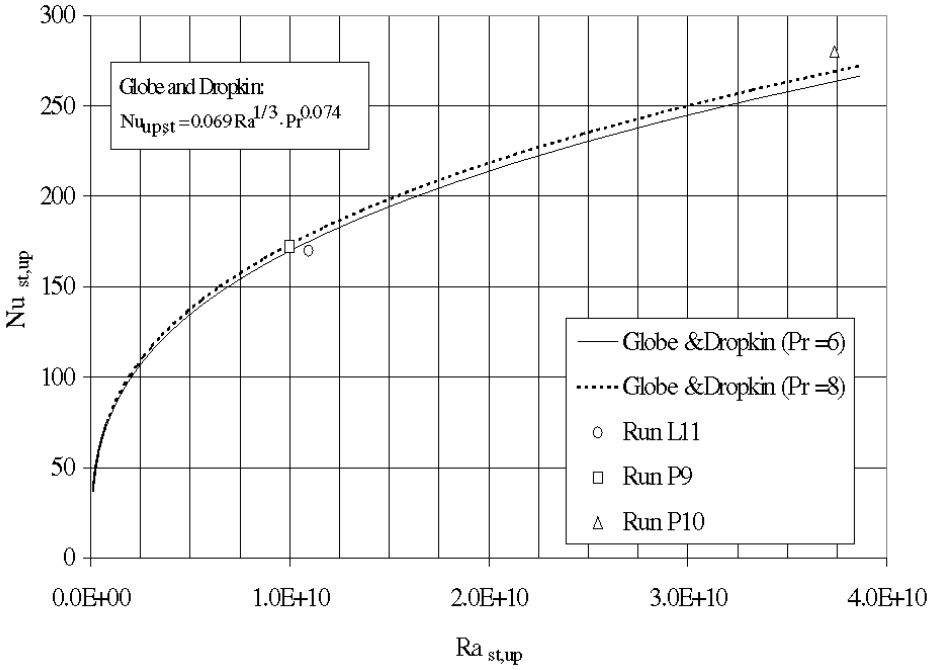

Fig. 3.4: *COPO: Average Nusselt number through the non-heat-generating layer.*

- Specific test about the effect of gas injection (simulation of partial steel vaporisation): $V_{gas} \sim 0.5 - 1$cm/s H=1.5m uniform cooling;

Facility and experimental measurements

The facility is described in the report [15]. This document has been sent with the 8 first draft test reports in June 97. In December 98, the project of final BALI test reports [16], including a synthesis of the results and the 18 individual test reports has been transmitted to the MVI members.

For all tests, thermal balances, temperature and heat flux profiles are given for steady state. The 0.1 Hz transient record are available on CDROM on request. For some tests, 100 Hz record of temperature fluctuations in upper unstable area, P.I.V. measurements for velocity fields and video record of flow motion are also available on request. Unfortunately local void fraction measurements for the specific test with gas injection were impossible.

Experimental results

The first test campaign was started in September 1996. Seven tests have been run with 1.5 meter high hemi-cylindrical geometry, for different power densities and

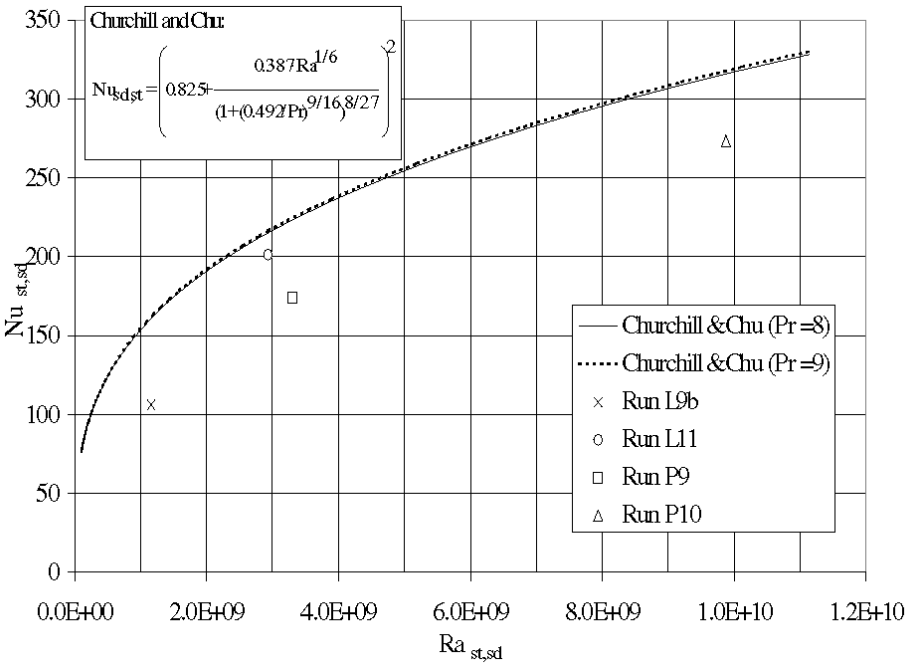

Fig. 3.5: *COPO: Average sideward Nusselt number at the non-heat-generating layer. Run P9 and P10 were carried out with COPO-II-AP facility, in which the vertical wall at the level of non-heat generating layer was inclined.*

for one of them without top cooling. After appropriate test section modifications, six other 2.0 meter height tests were run from January to March 97.

The basic analysis of the first test campaign for the upward heat flux, showed that the BALI data were in line with the values extrapolated from the latest COPO results. BALI results are, however, 20for downward heat transfer. The aspect ratio has no effect on the average upward heat transfer; the results obtained for 2.0 meter high pool follow the same trend as those for the 1.5 m high test.

From this experimental program, the data base on heat transfer in corium pool has been enlarged. For the first time, prototypic values of internal Rayleigh number have been obtained ($Ra_i \simeq 10^{16} - 10^{17}$) for French PWR reactor. A good agreement is observed with the COPO-II results. The comparison with 3D ACOPO experiment shows some difference for absolute heat exchange coefficients, but the power split is the same : 44% of the residual power extracted from the top of an homogeneous corium pool (H/R=1). From experimental results and simplified transposition model, 3D correlations are derived for reactor applications. As a complement for global heat transfer correlations, simplified shapes of temperature and heat flux profiles can be used. From viscous test results, we

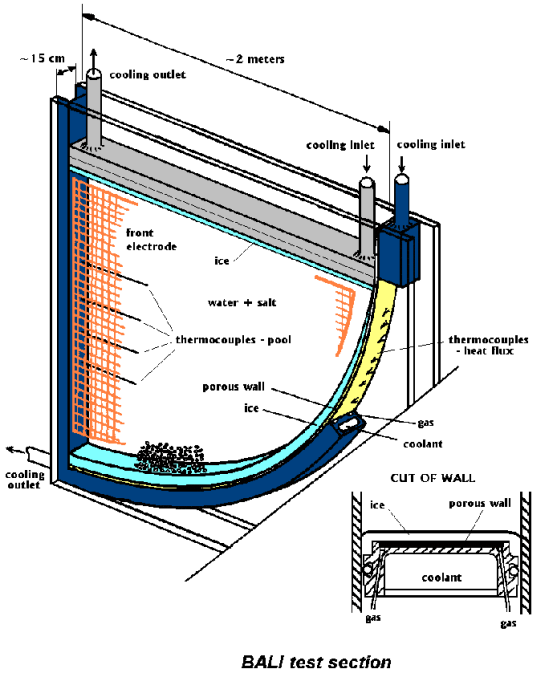

Fig. 3.6: *BALI: In-vessel test section.*

can conclude that the effect of viscosity on upward heat transfer is small. For downward heat transfer, a change in the flow regime is observed : the turbulent boundary layer flow becomes laminar with an heat flux peak at the top of the pool. From porous test results, in our range of Rayleigh number and for 10mm diameter glass balls, we observe that the upward heat transfer is not affected whereas downward heat transfer is reduced and the heat flux profile shape becomes similar to profile observed for laminar boundary layer flow.

Outlook

Up to now, the tests performed in BALI facility has been mainly devoted to homogeneous pool configurations. The analysis of severe accident scenario, taking also into account the physico-chemistry effect, shows that stratified configurations have to be consider. The BALI facility can be used to enhance the experimental data base on heat transfer phenomena for stratified pool configurations in simulant fluids but at full scale :

- Metallic layer on top of oxidic pool (layers separated by oxidic crust);
- Stratification due to the miscibility gap (effect observed in RASPLAV ex-

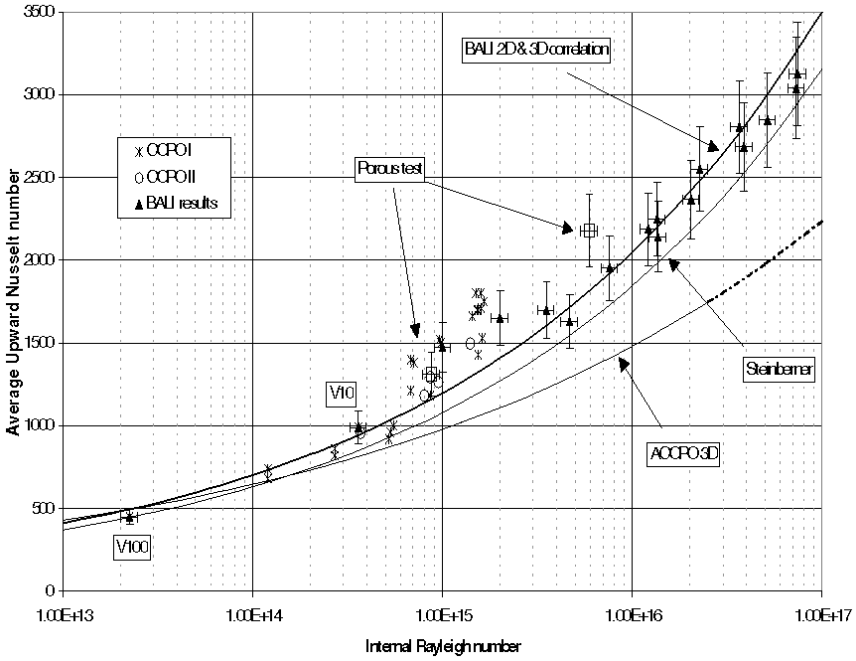

Fig. 3.7: *BALI: Average Nusselt numbers at the upper boundary.*

periment) → layer with high Zr concentration on top or at bottom of an oxidic pool depending on the density ratio (which is not well known at present).

3.2.3 RIT SIMECO experimental program

The **SIMECO** (Simulation of In-vessel MElt COolability) experimental facility (Fig. 3.9) was developed in order to investigate the effects of (i) boundary crust and mushy layer on natural convection heat transfer; (ii) melt stratification on natural circulation; (iii) turbulent flow on the possible amelioration of melt stratification; (iv) integral and multidimensional heat transfer between and in, the melt pool, the top metallic layer and the vessel; (v) to determine the effect of, the miscibility or immiscibility of the layers; (vi) the density difference between the layers; (vii) the layers thickness and the heat generation in one or all layers, on heat transfer.

Experiment facility and test matrix

The experiment facility consist of a slice-type geometry including a semicircular section and a vertical section (Fig. 3.9). Brass is used for the slice walls, except

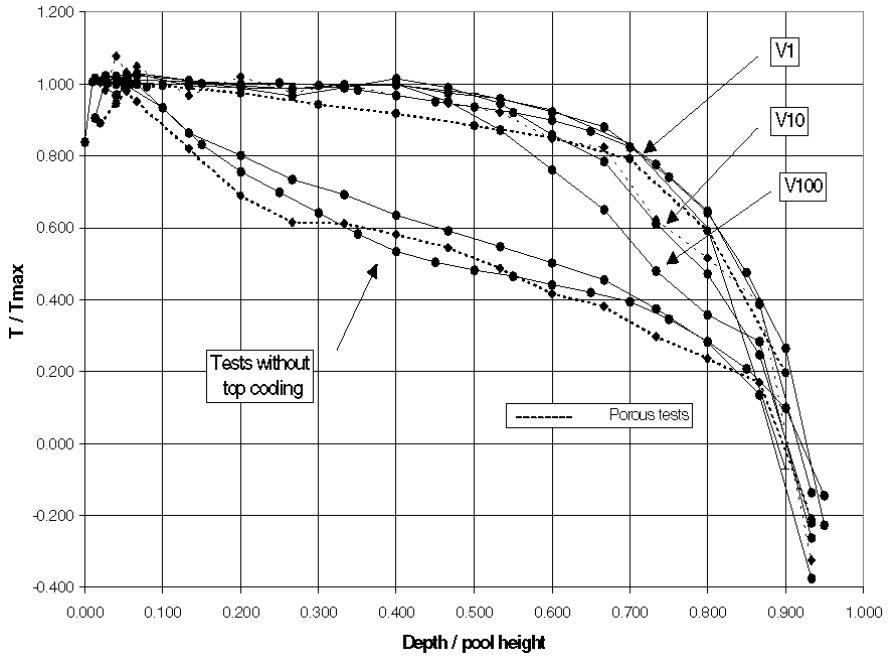

Fig. 3.8: *BALI: Temperature distribution in the pool.*

for the front wall which is made of special glass allowing visualisation of the entire test section. The vessel wall is made from a 23 mm thick brass plate and is cooled by controlled flow rate water loops (Fig. 3.10). On the top of the pool a controlled flow rate water heat exchanger is used to provide the boundary cooling conditions.

Internal heating in the pool is provided by thin wire heaters uniformly distributed in the semicircular section. They can supply up to 4 kW of heating to the pool. Water and binary salt mixtures are employed as melt pool simulant. Both eutectic mixture (50%-50%) and non-eutectic mixture (20%-80%) of $NaNO_3$-KNO_3 are used in the SIMECO experiments. Stratification of, water and salt water (with different salt concentrations), parafin oil and water, are employed, respectively, as simulant for miscible and immiscible fluids.

Water temperature measurments are used to obtain the average heat flux on the side walls and on the top of the pool. A total of 36 K-type thermocouples are kept inside the brass vessel wall at different angular locations in order to derive local heat fluxes as a function of angle. Inside the pool, 34 K-type thermocouples are installed to measure the local temperature variation with emphasis on the near wall region and the interface between the two layers. Video recording of the interface is used in order to track interface behavior and mixing process.

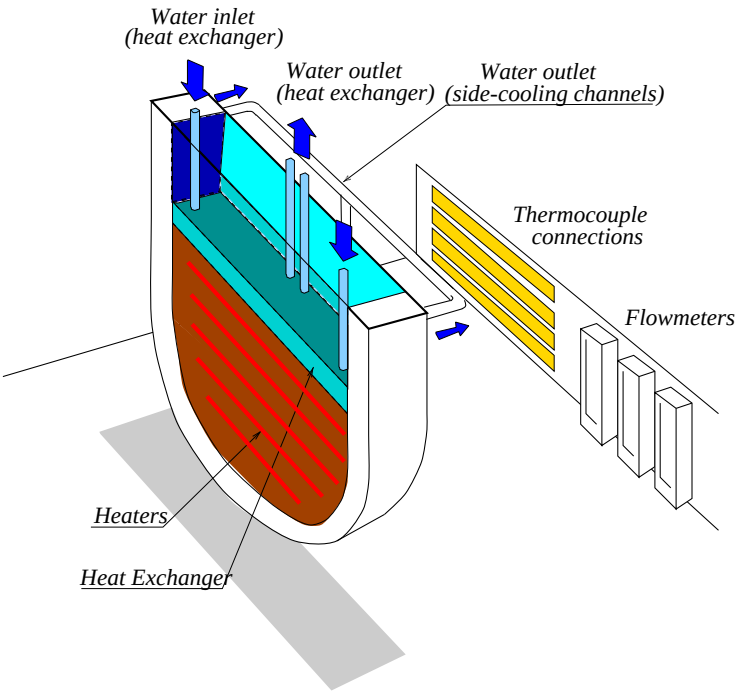

Fig. 3.9: Simeco experimental facility - Overview.

The SIMECO test matrix is designed to cover different heat generation rates, different top and sidewall cooling conditions, and different simulants. A brief description of the main paramameters of all experiments realized so far is summarized in Tables 3.2-3.5.

Results of water experiments

The SIMECO water test series was conducted in order to test the facility performance after each modification. In this case, truly isothermal boundary conditions were not provided on the pool boundaries as the vessel wall adapted itself to the heat fluxes.

Figures 3.11-3.12 present the dimensionless centerline temperatures and heat fluxes for differents water tests. The centerline temperature is nondimensionalized by the the ”bulk” temperature, which is the volume average pool temperature, the elevation from the bottom of the pool is non dimensionalized by the pool height. A stratification of the temperature is observed in the lower part of the pool and a quite uniform distribution in the upper regions is achieved due to the convection mixing (Fig. 3.11). The heat fluxes display the familiar peaking at the pool corner (Fig. 3.12).

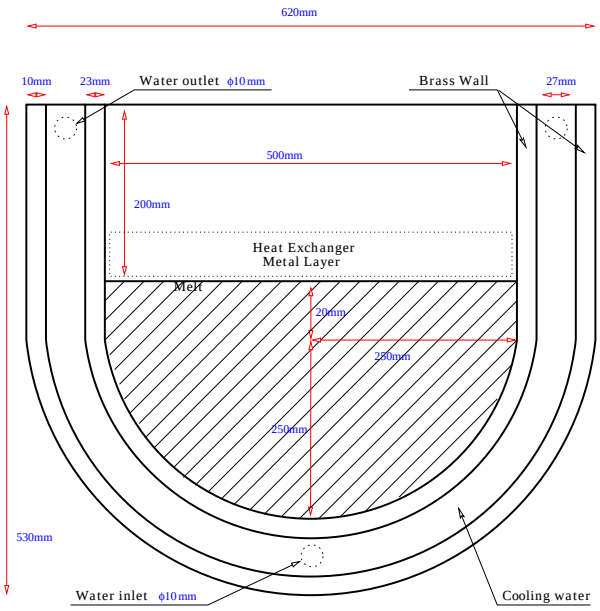

Fig. 3.10: SIMECO experimental facility - Main dimensions.

Results of salt experiments

The salt tests were 4h to 7h long, but in all cases the steady state regime was reached no later than 2.5 hours after the beginning of the experimental procedure. All the salt data presented in Figs. 3.13 and 3.14 were acquired in the steady state regime.

The centerline temperature and heat fluxes obtained during several salt tests are presented respectively on figures 3.13-3.14. High temperature are reached relatively rapidly from the bottom of the pool, and only stratified temperature can be observed (Fig. 3.13). Highest heat fluxes were measured in the pool corner from 80^o to 90^o (Fig. 3.14).

Results of experiments with stratified pools

Two kind of interface behavior have been identified. Unstable interface is characterized by blurred boundaries and for low density differences ($<5\%$), while stable interface is defined by distinct boundaries and higher density differences ($>5\%$). Images of the interface evolution between the two layers are recorded by a video camera. Movement of the upper layer is extracted from the processing of these images . Figures 3.15&3.17 present the thickness upper layer evolution for unsta-

Table 3.2: List of SIMECO experiments with water as simulant

Experiment	Remarks
SW-1	No heat exchanger, full power.
SW-2	No heat exchanger, full power, medium cooling flow.
SW-3	No heat exchanger, full power.
SW-4	With heat exchanger, full power.
SW-5	Full power, high cooling flow.
SW-6	Full power, high cooling flow, hot water for cooling (55^{o}C).
SW-7	Full power, high cooling flow.
SW-8	Half power, high cooling flow.
SW-9	Full power, high cooling flow.
SW-10	Full power, high cooling flow, addition of a pipe on back wall.
SW-11	Full power, high cooling flow, modification of back wall.
SW-12	Full power, high cooling flow.

Table 3.3: List of SIMECO experiments with $NaNO_3$-KNO_3 (50%-50%) as simulant

Experiment	Remarks
SSEu-1	Transient cool down.
SSEu-2	Full power, transient heat up and cool down.
SSEu-3	Full power, steady state pool.
SSEu-4	Full power, steady state pool, addition of a pipe on back wall.
SSEu-5	Full power, steady state pool.
SSEu-6	Full power, steady state pool.
SSEu-7	Full power, steady state pool, modification of the back wall.
SSEu-8	Full power, steady state pool.
SSEu-9	Full power, steady state pool, hot water for cooling (55^{o}C).
SSEu-10	Full power, steady state pool, hot water for cooling (55^{o}C).
SSEu-11	Full power, steady state pool, without heat exchanger on top.

ble and stable interfaces. The upward/downward heat flux splitting is presented for unstable and stable interfaces on figures 3.16&3.18.

For unstable interface the mixing process is faster than that for stable interface. A sudden disappearance of the interface is observed for all unstable interfaces (Fig. 3.15) corresponding to the complete mixing of the upper layer with the downward pool. As the mixing is complete, the upward/downward heat flux splitting rise to a steady state value of 1.5 step by step (Fig. 3.16). During the mixing process of the upper layer with stable interface, the heat flux split is constant around a value of 0.5 (Fig. 3.16). As soon as the mixing is complete it increase steadily to a steady state value of 1.6 (Fig. 3.16).

In summary, the upward/downward splitting heat flux is affected by the stratification, more heat is transfered downwards when stratification is present. Miscibility of the two layers has to be taken ino account. Immiscibility of the two layers makes more heat to flow downward compared to miscibles fluids. For a

Table 3.4: List of SIMECO experiments with miscible fluids stratification (Water/Salt water)

Experiment	Remarks
SE-W-1	With heat exchanger, full power, 10.48% density difference.
SE-W-2	No heat exchanger, full power, 10.48% density difference.
SE-W-3	No heat exchanger, full power, 10.48% density difference.
SE-W-4	With heat exchanger, full power, 10.48% density difference.
SE-W-5	No heat exchanger, full power, 20.96% density difference.
SE-W-6	With heat exchanger, full power, 20.96% density difference.
SE-W-9	Full power, 30.13% density difference.
SE-W-10	With heat exchanger, full power, 2.12% density difference.
SE-W-11	With heat exchanger, full power, 5.22% density difference.
SE-W-12	Uniform water pool, full power.
SE-W-13	Uniform salt water pool (5.22%), full power.
SE-W-14	Uniform salt water pool (20.96%), full power.
SE-W-15	Uniform salt water pool (10.48%), full power.
SE-W-16	Uniform salt water pool (30.13%), full power.
SE-W-17	Both layers heated, full power, 30.13% density difference.
SE-W-25	Low power, 30.13% density difference.
SE-W-26	Both layers heated, low power, 30.13% density difference.
SE-W-27	same as SE-W-17, upper layer thickness : 8 cm.
SE-W-28	Both layers heated, high power, 5.22% density difference.
SE-W-29	same as SE-W-28, upper layer thickness : 8 cm.
SE-W-30	Low power, 5.22% density difference.
SE-W-31	same as SE-W-28, upper layer thickness : 12 cm.
SE-W-32	Both layers heated, low power, 5.22% density difference.

larger density difference ($>5\%$) between the two layers, the interface is sharper and imposes a greater resistance for the upward heat transport. The upward heat transport increases when both layers have heat generation. The steady state results for the splitting heat flux, (that is after mixing of the two layers), are unaffected by the amount of the initial stratification.

3.3 RIT studies on modeling and analysis of melt pool heat transfer

In this section, results of series of studies, on natural convection heat transfer in decay-heated core melt pools which form in a reactor lower plenum during the progression of a core melt-down accident, are described. The emphasis is on the modeling and prediction of turbulent heat transfer characteristics of natural convection in a liquid pool with an internal energy source. Methods of computational fluid dynamics (CFD), including direct numerical simulation, were applied for investigation.

Table 3.5: List of SIMECO experiments with immiscible fluids stratification (Parafin oil/Water)

Experiment	Remarks
SE-W-7	With heat exchanger, full power, 13.53% density difference.
SE-W-8	No heat exchanger, full power, 13.53% density difference.
SE-W-18	Both layers heated, full power.
SE-W-19	Full power, upper layer thickness : 1 cm.
SE-W-20	Full power, upper layer thickness : 6 cm.
SE-W-21	Both layers heated, low power, upper layer thickness : 8 cm.
SE-W-22	Both layers heated, low power, upper layer thickness : 12 cm.
SE-W-23	Both layers heated, full power.
SE-W-24	Low power.

3.3.1 Introduction

The key distinguishing feature of the large self-heated core melt pool, resident in the lower head of the vessel of a LWR, is natural circulation at very high Rayleigh number ($10^{14} - 10^{16}$). The flow is turbulent and the imposed heat flux on the vessel wall varies greatly over the azimuthal angle. The COPO data [18], measured at Rayleigh numbers of $10^{14} - 10^{15}$, have shown that the heat flux is very low at the bottom part of the head and rises to substantial values in the upper elevations of the head; and along the vertical wall of the vessel. This measured behavior is very fortunate, since the heat removal capability, due to the boiling process on the outside surface of the head, has also been found to vary in the same fashion. Thus, the feasibility of in-vessel melt retention becomes possible, if it can be demonstrated that the heat removal capability is substantially larger than the thermal loading everywhere along the circumference of the lower head. Prediction of the heat fluxes, in prototypical situations, have relied on representation of the turbulence in the high-Rayleigh-number melt pool, through the standard ($k - \epsilon$) models. Analysis of the COPO and the UCLA experiments, performed with these models, have not been successful, since the discrepancies between the measured and the calculated results have been very large. It has been found that advanced turbulence models would be needed to correctly predict the flow field and the heat transfer characteristics of a high-Rayleigh-number melt pool. The work [34], which formed the basis of this statement, was reported in Grenoble.

Natural convection flow and heat transfer in fluids with internal energy sources are also of interest for geophysical and astrophysical systems. Fluid dynamics and heat transfer in such systems (e.g., earth mantle, stars, and decay-heated nuclear reactor core melt) are driven by natural convection, induced by the volumetric heat generation. Dimensionless groups for the description of the natural convection process are the Rayleigh number ($Ra = \frac{q_v H^5}{\alpha\kappa\nu} g\beta$) and Prandtl number

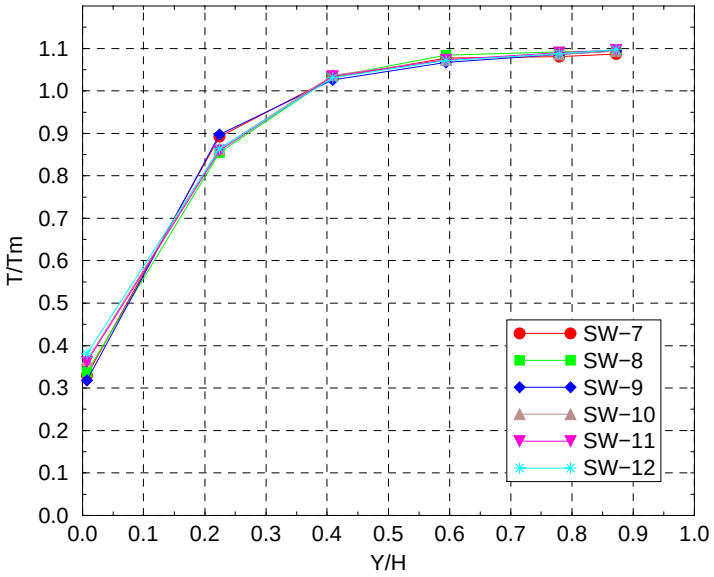

Fig. 3.11: Centerline temperature in the liquid pool (Water as simulant).

($Pr = \nu/\alpha$). The Prandtl number is a liquid property, however, the Rayleigh number strongly depends on the characteristic size (height) of the liquid pool (H) and the rate of internal heat generation (q_v), as well as the physical properties of fluid. Thus, the Rayleigh number is high ($\simeq 10^{16}$) in a large system, and in systems with high heat generation density. Since, a significant fraction of the heat generated in the pool has to be removed through its upper isothermally-cooled boundary, the flow field consists of countercurrent ascending hot-plumes and falling cooled-blobs. The flow field is inherently unsteady and unstably-stratified. It may be turbulent, even, at relatively low Rayleigh number ($\simeq 10^6$). Analytic description and prediction of the flow field has been hampered by our knowledge of the character of turbulence in such flow fields.

Turbulence modeling for such flow fields has been a subject of study at KTH. In a previous study [34], we showed that the widely-accepted engineering approach, employing a low-Reynolds-number $k - \epsilon$ model, failed to describe both energy splitting (upward *vs.* downward heat transfer) and local heat flux distribution for the high-Rayleigh-number conditions of interest. In order to provide a basis for developing the appropriate description and prediction methods, data on turbulence structure and characteristics are needed. There is only one measurement of the temperature fluctuations in an internally-heated fluid layer [35]. No systematic experimental studies to obtain the turbulence data in such flow fields

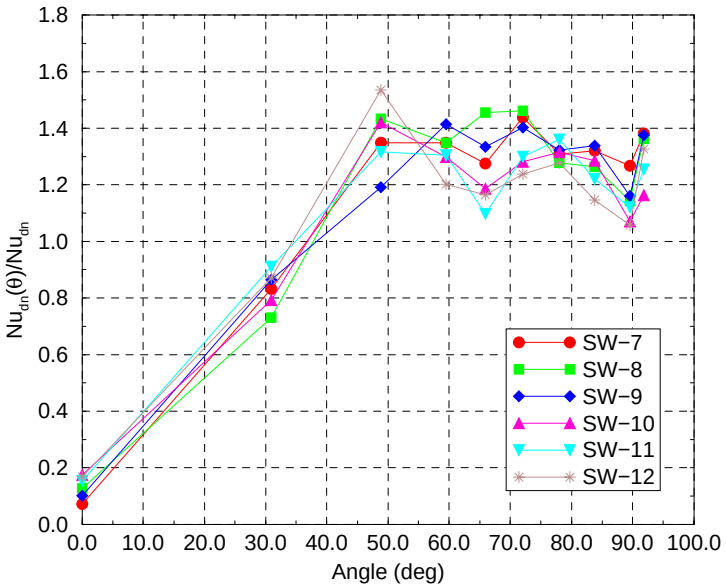

Fig. 3.12: Heat flux distribution (Water as simulant).

have been performed.

In order to produce a turbulence data base, direct numerical simulation (DNS) can be employed. In this method, the full three-dimensional time-dependent conservation equations of mass, momentum, and energy are solved on grids which resolve the largest and the smallest scales of turbulence. The calculated time-dependent flow and temperature fields can, then, be analyzed for the fluctuations induced by turbulence. In general, such a calculation has to be performed with a very fine grid structure to adequately represent the small scale turbulence in the flow fields of interest. In the past, DNS has been used (in FZK, Germany) for analyzing natural convection heat transfer in fluid layers with internal heat generation with low values of Ra numbers ($3{\cdot}10^4 \div 4 \cdot 10^6$) [36].

Since, the in-vessel melt retention may become an important safety objective in the design of the future and, perhaps, in the accident management of current plants, care has to be taken in studying the various phenomena which are related to the issue resolution. The basic objective is to predict the relevant phenomena for the prototypical accident conditions. Thus, the applicability of the measured data, or the correlations derived from the measured data, has to be established and the uncertainties determined. In this context, most uncertainties are introduced by the non-prototypicalities in the experiments. Examples of those for the melt pool experiments are (i) use of simulant fluids, (ii) differences in the boundary conditions

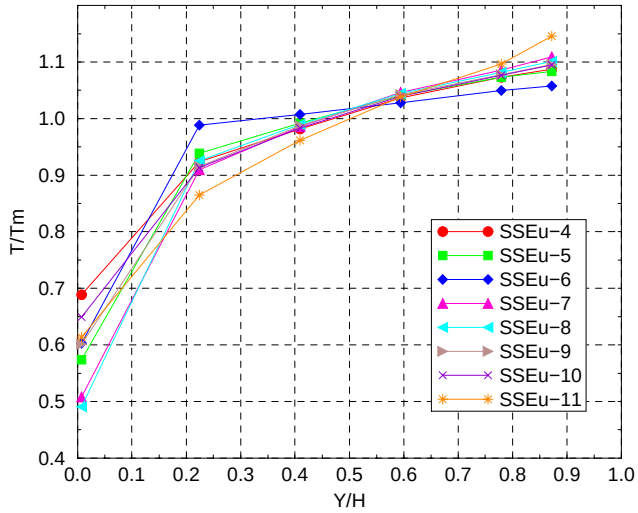

Fig. 3.13: Centerline temperature in the liquid pool ($NaNO_3$-KNO_3 (50%-50%).

from those at prototypic conditions, (iii) differences in the mode of heat generation and/or in heating uniformities. The uncertainties in the application of the data base, or correlations, can be evaluated, through detailed calculations which have been validated as much as possible. That is the focus of the studies, summarized in the following pages, and published recently in proceedings of various meetings and in the archival literature.

3.3.2 Approach

Methods of computational fluid dynamics are employed for analysis purposes. The methodology employed in our studies is to extensively validate computational models against available experimental data, and, then, apply the models as research vehicle for predictions and comparative analyses.

A commercially available, general-purpose computer code CFX (FLOW3D) [37] is employed for calculations. Analyses are performed to evaluate grid resolution and time step requirements for the DNS calculations. The time-average of top wall heat fluxes, the temperature fields and the Reynolds stresses are determined. Performance of different assumptions used in $k-\epsilon$, and Reynolds stress, modeling are examined against turbulence ”data” obtained from DNS.

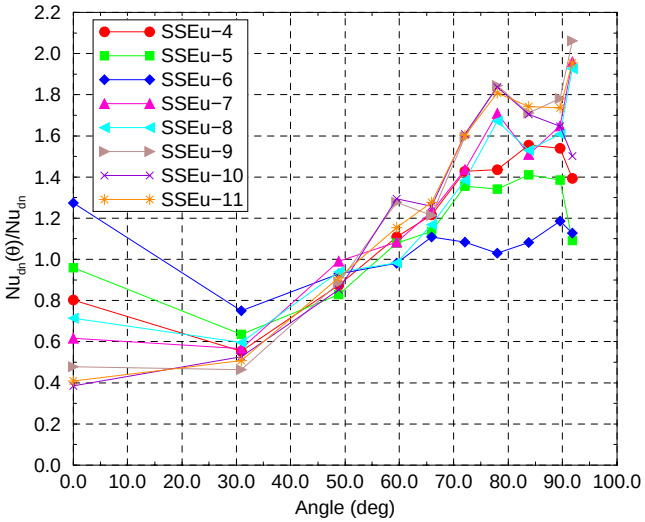

Fig. 3.14: Heat flux distribution ($NaNO_3$-KNO_3 (50%-50%) as simulant).

3.3.3 A selected list of papers published

[1] T.N. Dinh and R.R. Nourgaliev, "On Turbulence Modeling in Large Volumetrically Heated Liquid Pools", *Intern. J. Nuclear Engineering and Design*, 1997, v.169, pp.131-150.

[2] R.R. Nourgaliev and T.N. Dinh, "An Investigation of Turbulence Characteristics in an Internally Heated Unstably Stratified Fluid Layers", Proceedings of the *1996 National Heat Transfer Conference*, in the session "Scaling and Simulation", Houston, Texas, August 3-6, 1996. Also, accepted to *Intern. J. Nuclear Engineering and Design*, 1997.

[3] T.N. Dinh, R.R. Nourgaliev, and B.R. Sehgal, "On Heat Transfer Characteristics of Real and Simulant Melt Pool Experiments", *Proceedings of the Seventh International Topical Meeting on Nuclear Reactor Thermal Hydraulics NURETH-7*, Albany, N.Y., USA, NUREG/CP-0142, Vol.2, pp.827-845, 1995. Also *Intern. J. Nuclear Engineering and Design*, 1997, v.169, pp.151-164.

[4] R.R. Nourgaliev, T.N. Dinh, and B.R. Sehgal, "Natural Convection in Volumetrically Heated and Sidewall Heated Melt Pools: Three-Dimensional Effects", *Proceedings of the IMACS-COST Conference on* Computational Fluid Dynamics "3D Complex Flows", Lausanne, Switzerland, 1995. **Notes on Numerical Fluid Mechanics**, Vol.53, pp.202-209, (ed. M. Deville, S. Gavrilakis and I.L. Ryhming) Viewed, Braunschweig 1996.

[5] R.R. Nourgaliev, T.N. Dinh, and B.R. Sehgal, "Simulation and Analysis of

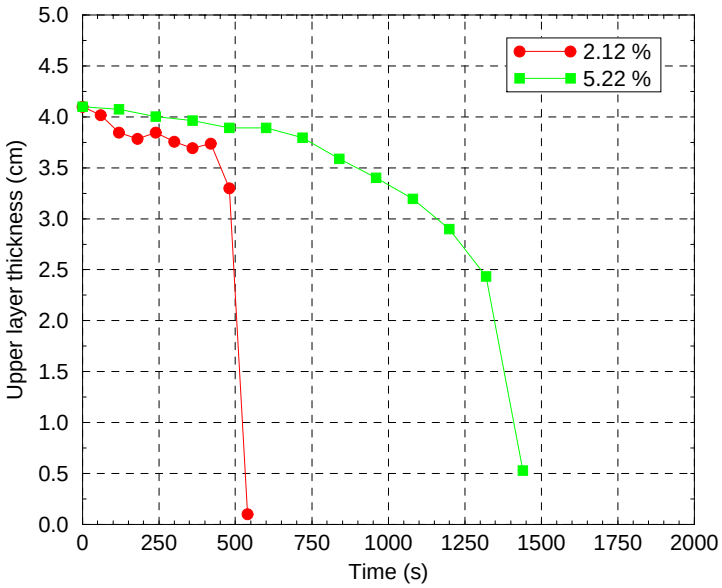

Fig. 3.15: Upward layer thickness for unstable interface.

Transient Cooldown Natural Convection Experiments", Proceedings of the *1996 National Heat Transfer Conference*, in the session "Fundamental Phenomena in Severe Accidents", Houston, Texas, August 3-6, 1996. Also, *Intern. J. Nuclear Engineering and Design*, 1997, v.178, pp.13-27.

[6] R.R. Nourgaliev, T.N. Dinh, and B.R. Sehgal, "Effect of Fluid Prandtl Number on Heat Transfer Characteristics in Internally Heated Liquid Pools with Rayleigh Numbers up to 10^{12}", *Intern. J. Nuclear Engineering and Design*, 1997, v.169, pp.165-184.

3.3.4 Summary of research results

The research work performed at RIT, within EU MVI project, can be divided into three parts, namely, 1) investigation of turbulent natural convection heat transfer characteristics, and examination of the capability of turbulence models, 2) examination of experimental methods and experimental heat transfer data base with respect to their applicability for reactor prototypic conditions, 3) prediction of potential effect of Prandtl number of core melt.

In the first part, development, validation, and application of numerical methods and models were performed to analyze turbulent heat transfer characteristics in a liquid pool with an internal energy source, with particular emphasis on physics

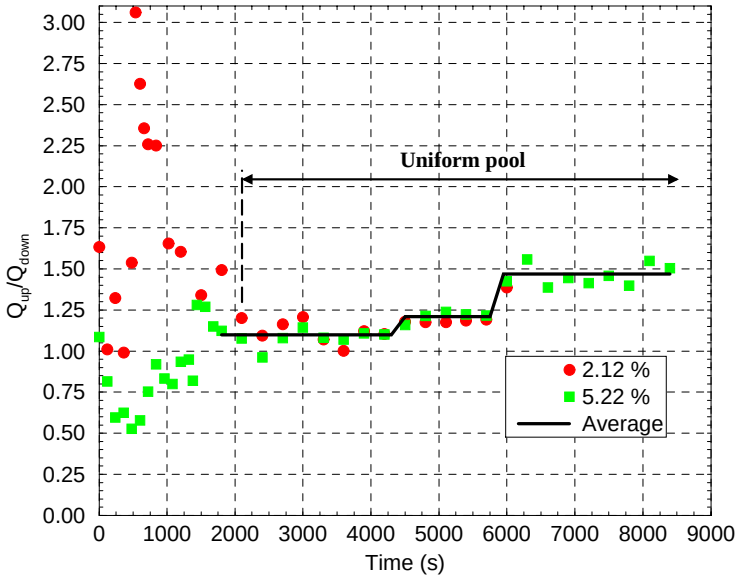

Fig. 3.16: Upward/downward heat flux splitting for unstable interface.

of the unstable stratification region.

In the second part current understanding of experimental data base was advanced by comparative analyses, and by simulations of experiments performed in the past.

In the third part systematic examination of potential effect of core melt Prandtl number on surface-average and local heat transfer characteristics was performed through a computational fluid dynamics (CFD) code,

Turbulence modeling and turbulent heat transfer characteristics

Turbulence modeling. Natural convection heat transfer in a volumetrically heated liquid pool under high-Rayleigh-number (up to 10^{15}) conditions is investigated. The available turbulence modeling techniques are first reviewed, with a particular emphasis on selecting models capable of treating the mechanisms of turbulence relevant to high-Rayleigh-number natural convection. As a practical exercise, numerical analyses are performed for experiments simulating a molten corium pool in the lower head of an externally cooled VVER-440 reactor pressure vessel (COPO) and Steinberner-Reineke experiments in a square cavity. It is shown that standard forms of the low-Reynolds-number $k-\epsilon$ model fail to describe turbulent natural convection heat transfer regimes prevailing in these ex-

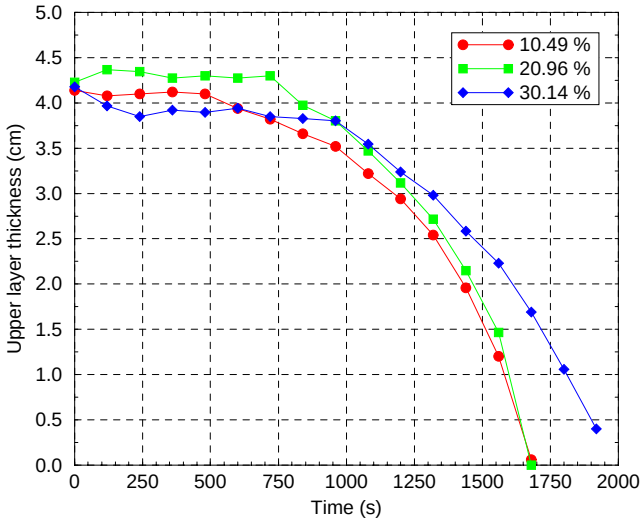

Fig. 3.17: Upward layer thickness for stable interface.

periments.

Natural convection in a volumetrically heated corium pool at high Ra numbers is, then, analyzed with a new low-Reynolds-number $k-\epsilon$ model to describe the stratification-induced non-isotropy of turbulence with the eddy-diffusivity approach. The buoyancy-induced turbulence anisotropy is modeled by means of the local Richardson number. *Phenomenological corrections* are proposed for the turbulent Prandtl number and the near-wall viscosity, accounting for the effects of density/temperature stratification on turbulence.

These corrections were employed in the $k-\epsilon$ model to produce excellent agreement with the experimental data obtained in the Finnish COPO experiments [38], [18] and Steinberner-Reineke tests [39]. Most importantly, local heat fluxes on vertical and curved pool boundaries are correctly predicted by the model. Nevertheless, we should note that these modifications of the low-Reynolds-number $k-\epsilon$ model are experiment-specific: they cannot compensate for the fundamental deficiencies of the two-equation turbulence model. For reactor cases, the proposed corrections should be validated, and this requires greater experimental data base at high-Rayleigh-number conditions. Local temperature and velocity measurements, and data on turbulent intensity distribution in different regions of density/temperature stratification, are essential for development of more general models to describe the turbulence characteristics.

The analytical estimates of turbulent heat fluxes have shown that the buoyancy-induced stratification in the vicinity of the upper horizontal cooling surface in-

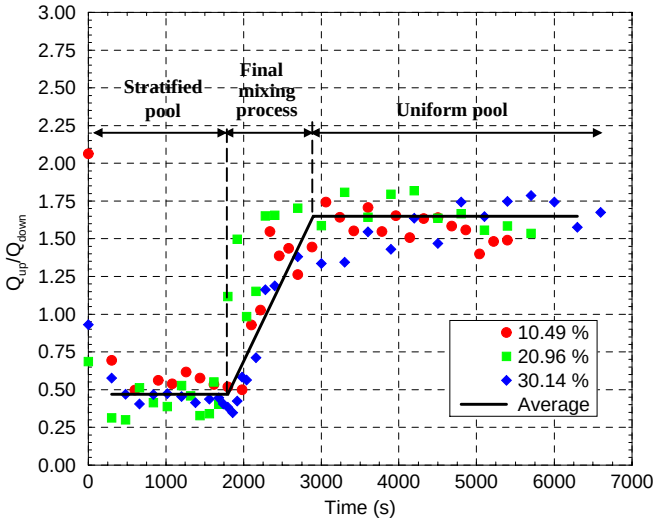

Fig. 3.18: Upward/downward heat flux splitting for stable interface.

duces very complicated effects on turbulence, and creates difficulties in accounting for these mechanisms in the k-ϵ framework. By making certain assumptions about relative values of turbulent stresses and turbulent heat fluxes, in corresponding regions of liquid pools, *theoretical correlations* for turbulent Prandtl number and turbulent viscosity can be obtained for the turbulence field. These results can then be employed in a k-ϵ model to reduce the phenomenological inadequacy and empiricism of this model.

In general, description of turbulent buoyant flows will, eventually, require application of an advanced Reynolds-stress model. However, there are significant uncertainties in the formulation of the higher-order models; and difficulties in implementing these models into a general Navier-Stokes code. The aim of any additional development in turbulence modeling should be is to find the level of modeling, which can provide acceptable agreement with experimental data, but still remain simple enough to be employed for the solution of complex three-dimensional flows with irregular boundaries. In fact, most computer programs developed for reactor applications are based on the two-equation turbulence models. It is believed that the approach developed in this study can contribute to further development of efficient computational methods for estimating heat transfer in large volumetrically-heated liquid pools. After further checking and validation, these methods could be fruitful in analyzing prototypic melt pool behavior, and, in particular, the sensitivity of heat flux distributions to variations in the geometry of the vessel lower head and of the properties of the prototypic core melt material.

Direct numerical simulation. Direct numerical simulation (DNS) of naturally-convecting flow in internally-heated fluid layers, with a constant temperature boundary condition on the upper surface and an adiabatic boundary condition on the bottom surface, was performed using a finite-difference method. This approach enabled the determination of the top wall heat fluxes, the mean temperature fields, the distributions of Reynolds stresses and turbulent heat fluxes. Good agreement with heat transfer data was achieved for Ra numbers up to $5 \cdot 10^{12}$, but reliable turbulence data were obtained only for several Rayleigh numbers in the range $5{\cdot}10^6 \div 5{\cdot}10^8$. In particular, the calculated Nusselt number, temperature distributions within the fluid layer and temperature fluctuations are in good agreement with the experimental data of Kulacki et al. [35], [40]. Also, the calculated turbulent heat fluxes agree well with those predicted by the analytical model of Cheung [41].

The turbulence data obtained are important for developing Reynolds-stress type correlations and finding reliable methods for describing turbulent natural convection heat transfer to the isothermally cooled upper surface in an internally-heated liquid pool.

The calculated turbulent characteristics (Reynolds stresses and turbulent heat fluxes) indicate significant anisotropy of turbulent transport properties. So, the isotropic eddy diffusion approach cannot be used to describe turbulent natural convection heat transfer under unstable- stratification conditions.

Analysis of the thermal-variance-balance showed an important role of diffusive transport of $\overline{T'^2}$, and remarkable non-equilibrium of thermal-variance E_T. Turbulence constants, needed for modeling of turbulent diffusion, and of dissipation of thermal-variance, are shown to be strong functions of Rayleigh and Prandtl numbers, and are non-uniformly distributed in the fluid layer. Thus, developing a higher order turbulence model for this type of flow, is not straightforward.

Fluids with two different Prandtl numbers ($Pr = 7$ and $Pr = 0.6$) were investigated. Similar thermal fields were obtained for different Pr numbers, however, remarkably different hydro-field results were calculated. As a consequence, important turbulence parameters and constants are shown to be strongly dependent upon the fluid Prandtl number.

Finally, it is worth mentioning that the numerical method and simulation approach, utilized in the present work, are sufficiently robust and general. The technique can, therefore, be used for studies of turbulent natural convection flows in complex geometries.

Applicability of experimental heat transfer data base

Quantification of non-prototypic conditions: a scoping study. As the in-vessel melt retention is becoming an important accident management measure for

some existing plants and for some advanced, medium-power light water reactor designs, some care has to be taken in studying various phenomenological aspects relevant to issue resolution. The basic objectives of the past, and current, experiments and analyses, related to large core melt pools in the reactor vessel lower plenum, are (a) obtain insight into the physics of the heat transfer process and (b) determine the thermal loading imposed on the lower head under *prototypical conditions* of interest.

Experimental investigations of heat transfer under conditions of interest might be classified into two main groups: (i) large scale *simulant experiments* and (ii) *small-scale real material tests*. In present study, it was found that that careful scaling and other design considerations are crucial for planning and analysis of the core melt tests, and to assure the applicability of data from the simulant experiments to prototypical situations. In general, one should consider four different experimental scaling and design issues, which are caused by (1) *physical properties of the simulant fluids*, (2) *geometrical configuration of melt in the tests, pools*, (3) *boundary conditions*, and (4) *heating methods*.

The common approach to melt pool simulant material experiments is to express the measured heat flux data in the form of correlations, $Nu = f(Ra)$. The relatively small-scale experiments using reactor materials, as a rule, involve problems to demonstrate their relevance to prototypic conditions e.g., due to applied heating methods, slice geometry of melt pools, low values of the Rayleigh number, and other measurement and test performance problems. Analytical modeling has not, so far, proved reliable to describe turbulent natural convection flows and heat transfer at Raleigh numbers of 10^{16} that would exist in the large core melt pools in the lower head. Moreover, the set of identified, important physical phenomena may require separate-effects investigations by experiments and/or modeling. Certainly, the highest priority has to be given to the phenomena, that could have the largest effect on heat fluxes imposed on melt pool boundaries.

In the present study, an overview is provided for the scaling and other design-effects of internally-heated natural convection heat transfer experiments. The most reliable calculations performed have modeled relatively low-Rayleigh-number regimes (Ra up to 10^{12}). These are adequate to predict thermal hydraulics in small-scale corium-melt experiments, and to assess sensitivity of heat fluxes to selected separate effects. However, for $Ra > 10^{12}$ there are several phenomena whose significance can only be assessed reasonably. We have performed original computations for liquid pools with internal energy sources to quantify the general trends of the effects of various parameters.

First, calculations performed for $Ra < 10^{12}$ in square and semicircular cavities show that descending boundary flows are able to penetrate into the bottom part of liquid pools with small fluid Prandtl numbers (Pr = 0.6-1.2), rendering thus conditions for destabilization of the lower fluid layers and, therefore, enhancing

heat transfer to the lowermost part of cooled pool walls.

Second, it was shown that effects of temperature dependence of physical properties have to be taken into account when melt superheat over the melt solidus point is low which could be the case in small-scale corium melt experiments, since corium properties chang significantly near the solidus temperature for the particular corium mixture.

Third, slice thickness-to-height ratios, $\Delta x/H$, should be more than 0.25 for slice experiments, in order to eliminate wall effects of face and back surfaces.

Fourth, the side-wall heating method would be useful for experiments with prototypical core melts, should related design effects be accounted for in experiment analysis and interpretation.

Finally, it was shown that the magnitude of of the Lorentz force are proportional to, both, the electrical conductivities and their temperature variations. In order to achieve conditions where influence of electromagnetic forces on natural convection flow and heat transfer is minor, the height-to-power and oxide-to-metal ratios should be chosen through test of design calculations. For this purpose, an appropriate analysis method was developed in this paper.

Three-dimensional effects and side-wall heating. Computational modeling has been carried out in order to explore the heat transfer characteristics of naturally convecting volumetrically and side-wall heated melt pools in order to delineate the differences between the two methods of heating to represent the prototypic conditions. Rather high Ra numbers ($\sim 10^{12}$) were selected for the numerical analysis. For such Ra numbers, uncertainties in turbulence modeling do not overwhelm other uncertainties in modeling. Even if the flow field at $Ra = 10^{12}$ may be quite similar to that for higher values of Ra number; extrapolation of the summary given below to Ra numbers higher than 10^{12} should be made with caution.

3D computations of natural convection flow field provide higher heat transfer rates to the cooled upper pool surface than the 2D simulations. Therefore, 3D modeling is recommended for the analysis of slice geometry experiments.

The 3D modeling results confirm the significant effect of fluid Pr number on heat transfer rate distribution in the lowermost part of the hemispherical pool. It was found that the descending boundary flows penetrate the stagnant fluid layer at the bottom part and increase the heat transfer. This is significant for the convergent geometry of the spherically bottomed lower head.

The numerical analyses performed, have provided a more solid basis for obtaining insight into the physics of side-wall heated natural convection flows and heat transfer. The calculational results indicate significant 3D effects in the side-wall heated melt pools when slice thicknesses is varied. These effects are quite minor for the internal heating case. In general, the side-wall heated experiments

would not simulate the prototypic decay-heated melt pool in the lower head. However, for certain slice thickness-to-pool-depth ratio the heat transfer characteristics at the downward surface are similar in the side-wall and internal heating cases. The upward heat flux magnitudes are, however, significantly different.

Transient cooldown technique. A recently developed experimental approach to determine natural circulation heat transfer characteristics of a volumetrically-heated liquid pool, namely, transient cooldown [42], was examined numerically. The finite-difference method was employed to obtain the heat fluxes in the fluid layers and in a hemispherical cavity under transient cooldown conditions, which were compared to those obtained with the internal heating experimental method. The pseudosteady-state experimental technique was also examined and the results obtained were compared with those of transient cooldown and internal heating cases. The results of analysis may be summarized as follows:

The transient cooldown method provides an excellent representation of the internal heating in the unstably stratified regions of the pool, since it provides equivalent mixing level and turbulent motion length scale;

The stably-stratified regions near the pool bottom, whose volume may depend upon the Ra number, may not be as well represented. The heat flux from those regions to the pool wall is determined primarily by conduction and not by the boundary layer flows, as in the unstably stratified regions. The absence of the volumetric heat source in the transient cooldown case, and the low level of fluid motion may result in storage of cold fluid on the cooled bottom, resulting in lower heat flux measurements. These remarks are derived from the results calculated for $Ra = 10^{12}$ to 10^{14}. It is possible that for $Ra = 10^{16}$, prevalent in the prototypic accident conditions, the extent of the stably stratified region may be smaller than that found in this study, i.e. $0 \leq \phi \leq 15^{\circ}$.

The large effect of the Pr number, below $Pr = 1$, on the calculated heat flux from the stably-stratified region of the pool, found earlier for the internal-heating simulation, may not be well represented by the transient cooldown method. However, the pseudo-steady-state natural convection calculation agreed much better with the internal heating calculation.

We believe that the numerical method developed here provides good estimates and trends for the characteristics of the liquid pool natural convection heat transfer. An analysis of various experimental options can be performed. The simulations described here, however, do not extend to the conditions of $Ra = 10^{16}$, where the turbulence effects are large, and whose general representation in the 3D numerical calculation has not been achieved so far.

We recommend that comparison of the internal heating (IH), transient cooldown (TCD) and pseudo-steady-state natural convection (PSSNC) methods, e.g. in the

COPO test facility with $Ra \simeq 10^{16}$, be performed. The heat fluxes in the pool bottom region, where stably-stratified liquid layers may develop and accumulate, should be examined experimentally, to delineate any difference between the three methods.

Prandtl number effect. The work is devoted to a systematic analysis of the physics of natural convection in internally-heated fluid pools with different Pr numbers, in isothermally-bounded, two-dimensional closed square, semicircular and elliptical cavities, three-dimensional semicircular slice and hemispherical enclosures.

The results of the calculations showed that the fluid Pr number has relatively a small effect on the averaged Nu numbers in the convection-dominated regions. The decrease of Pr number may cause the decrease of averaged Nu numbers on the top and side walls of cavities, up to 30% for the Pr number range considered ($Pr \sim 0.2 \div 7$). In the conduction-dominated regions (stably-stratified bottom part of enclosures) the influence of fluid Pr number on heat transfer is more significant and it grows with increasing Ra number. Fluids with lower Pr number have relatively low viscosity and high thermal conductivity in comparison to those for fluids with higher Pr number. The low viscosity (*ν-phenomenon*) causes weak resistance of the stratified layers to the penetration-attack of the descending flows from the convection-dominated side wall region; and from falling thermals from the unstably-stratified top wall region. So some parts of the bottom layers for low Pr number fluids may cease to be stably-stratified. In such cases, flow convection may lead to higher Nu numbers. The other effect is from the relatively higher thermal diffusivity- *α-phenomenon* in fluids with low Pr number. This leads to the higher heat conduction rates in the stably-stratified regions. The size of stably-stratified regions, and, therefore, the extent to which the two ν or α phenomena dominate, depend on the cavity geometry (curvature of the bottom wall) and on the Ra number.

The Nusselt number around the bottom surface of the square cavity is, thus, affected by the fluid Pr number. Both the averaged Nu number and its local distribution on the bottom wall are higher for lower Pr number fluids. The curved downward wall of the semicircular cavity can be divided into the convection-dominated part and the stably-stratified part. The Nusselt number is lower in the convection-dominated part and higher in the conduction-dominated part, as the fluid Pr number decreases. These effects, however, compensate each other on the average and the overall bottom wall Nu number is not significantly affected by the fluid Pr number. Similar behavior of the bottom Nu number was observed in cases with elliptical cavity.

Three-dimensional computations for semicircular and hemispherical cavities

confirmed the fluid Prandtl number effects discovered by two-dimensional computations. The geometrical 'convergence' of the curved bottom wall in hemispherical enclosures leads to stronger Pr number effects than those in a semicircular cavity.

We recommend that simulant experiments using low-Prandtl-number fluids and pool configurations of interest, such as semicircular, elliptical or hemispherical cavities be performed. The objective will be to validate the local Nu number effects found in this paper, and to account for them in correlations for the local Nusselt numbers along the cavity wall. Computational analysis similar to that presented in the paper has yet to be performed for high Ra numbers ($10^{13} \div 10^{17}$), since a reliable turbulence model, verified by an experimental data base has not yet been developed.

3.3.5 Concluding remarks

We believe that the situation with respect to prediction of thermal loadings on the vessel wall due to the natural circulation heat fluxes can be summarized as follows:

- The decay-heated corium melt natural circulation flow fields for the prototypic conditions, during the postulated severe accident, are highly turbulent.
- The Rayleigh number (Ra) serves as a reliable correlation and scaling parameter for the average heat fluxes, imposed on the boundaries, by the melt pool. The correlations, derived from the data obtained in the scaled experiments with simulant materials, may, even, be extended to higher values of Ra numbers, and, thus, apply to the prototypic conditions.
- The experiments, however, are not always perfect, i.e., they may have non-prototypicalities in heating and heating-uniformity, in boundary conditions, use of simulant fluids instead of corium, etc. The effects of such non- prototypicalities on the measured thermal loadings can be determined, either through further separate-effect and integral experiments, or, through detailed calculations,
- It has been demonstrated, through analysis of the many experiments performed with naturally-circulating pools, that detailed mechanistic CFD calculations can predict the average and local heat fluxes measured in many of the experiments. Thus, the CFD calculations can, also, predict the thermal loadings exerted by the naturally-circulating melt pools.
- The above conclusion about the reliability of CFD predictions, however, applies to low-turbulence pools, where the laminar flow approximation is

sufficiently accurate. For description of the prototypic highly turbulent melt pools, a general turbulence model, which would represent the highly unusual turbulence field in the unstably-stratified flows, found in the prototypic accident situation, has not been developed, yet.

- Measurements of turbulence flow field parameters have been performed, only, in small scale, and in simple, natural circulation experiments. Turbulence flow field characteristics can also be derived from very detailed, and time-consuming, direct numerical simulation (DNS) calculations, as has been achieved in this report. The derived characteristics may provide sufficient information to construct an accurate turbulence model which, could, then, be used to determine thermal loadings for prototypic conditions reliably.

- The calculations, at present, however, can be used to great advantage for determining the effects of non-prototypicalities in the experiments, from which the correlations on thermal loadings are derived. This obviates the need for countless separate-effect and integral effect experiments to assess the effects of those non-prototypicalities. The calculations may not be able to obtain "exact" estimates, since the turbulence flow fields are not "exactly" modeled. However, the importance of specific non- prototypicalities can be assessed, and good estimates on trends of their effects on the correlations, derived from the experiments, could be obtained.

- The calculations can also be used to design experiments and to assess the fidelity and accuracy of measurement techniques. Thus, innovative techniques e.g., using melt heat capacity, rather than heating, as the source for natural circulation, can be (and has been in these studies) investigated for generality of application.

- There are very few experiments on natural circulation with prototypical materials ($UO_2 - ZrO_2 - Zr$) melts (the only large-scale tests are in the RASPLAV facility). They are also not at prototypic scale ($Ra \leq 10^{11} - 10^{12}$). CFD analyses of these experiments with the laminar flow approximation is valid and accurate. Thus, any differences observed between the prototypic and the simulant material experiments, can be successfully rationalized
through CFD analyses.

- The simulant material experiments performed so far have not modeled the presence of a crust at the boundaries, as it would be in a prototypic corium pool. While, it appears that the Ra number scaling would apply to a pool

enclosed in crusted boundaries, an experimental confirmation of this has not been obtained so far. Projected COPO experiments and the salt and corium experiments in the RASPLAV Project may provide the data base needed.

- The CFD analysis of the various experiments in which crusts are formed will provide information on the effects of a crust on the thermal loadings. In particular, analysis may be used, intelligently, to merge the conclusions derived from the high Ra number watery experiments of COPO and from the salt experiments of RASPLAV Project, together with those derived from the analysis of the corium experiments in RASPLAV and of the uncrusted pool experiments in spherical geometry of the ACOPO facility. In this manner, the results of such diverse experiments could be applied to the prototypic melt pools that could undergo natural circulation in the lower head.

From the above summary, it is clear that the analyses efforts described in the report and in the attached published papers are appropriately focussed and need to be continued. We have, also, recently performed preliminary analyses on the effects on the effects of crust on natural convection and on thermal loadings. These are reported in references [43]-[44].

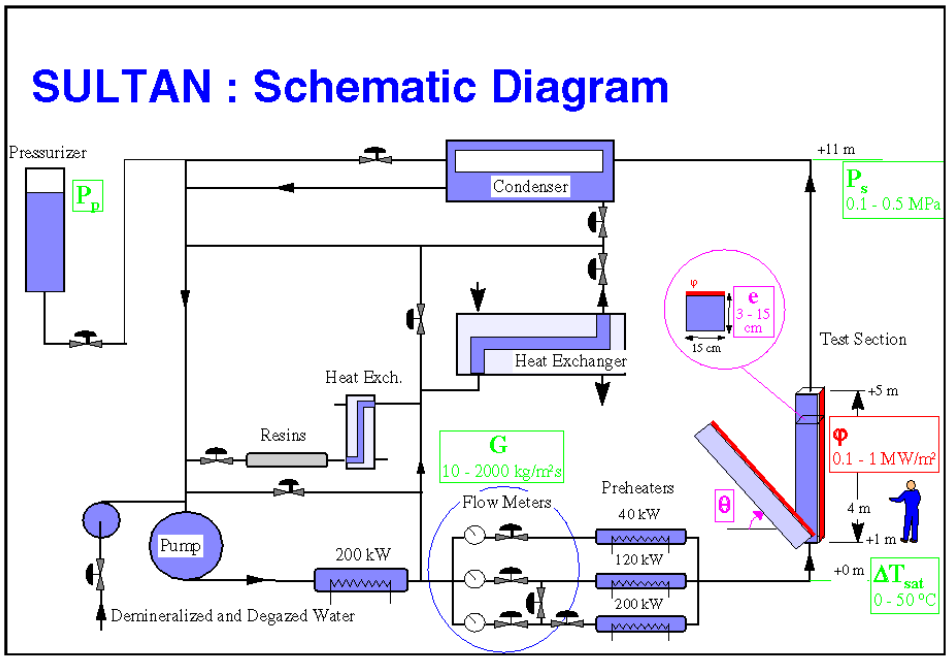

Fig. 3.19: SULTAN: Schematic Diagram.

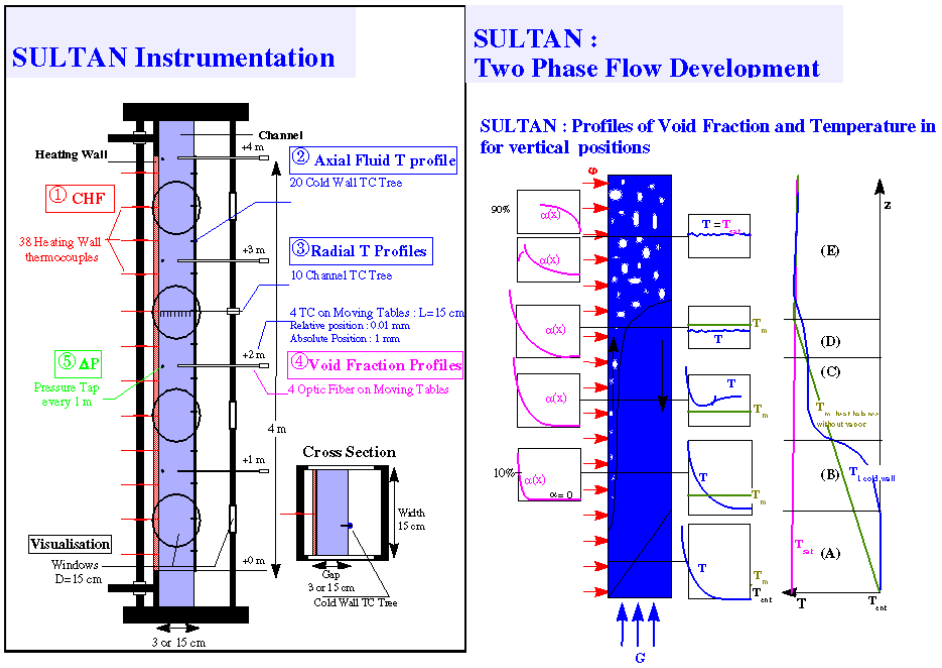

Fig. 3.20: SULTAN: Instrumentation and schematic of two-phase flow development.

3.4 Experimental program on external cooling (SULTAN)

In case of severe accident, a molten pool may form at the bottom of the lower head, and some pessimistic scenarios estimate that heat fluxes up to 1.5 MW/m^2 should be transferred through the vessel wall. An efficient, though completely passive, removal of heat flux during a long time is necessary to prevent total wall ablation, and a possible solution is to flood the cavity with water and establish boiling in natural convection. High heat exchanges are expected, especially if the system design (deflector along the vessel, riser etc.) emphasize water natural circulation, but are unfortunately limited by the critical heat flux phenomena(CHF).

CHF Data are very scarce in the adequate range of hydraulic and geometric parameters and are clearly dependent of the system effect in natural convection. The system effect can both modify flow velocity and two phase flow regimes, counter-current phenomena and flow static or dynamic instabilities.

The objective of the SULTAN experiment is to determine the Critical Heat Flux for the configuration of a flooded reactor vessel or a core catcher under natural or forced circulation.

3.4.1 Test facility

SULTAN Program is supported by CEA, EdF and FRAMATOME. The SULTAN facility (Fig.3.19) was designed as a full scale analytical forced convection experiment, on a wide range of parameters covering most of the situations involved in a slow transitory situation after a severe accident (mass velocity : 10-5000 kg/s/m^2, pressure : 0.1-0.5 MPa, inlet subcooling : 50-0°C, heat flux : 0.1-1 MW/m^2 (with some data up to 2 MW/m^2)). Fluid is demineralized and degassed water.

The Test section itself (Fig.3.20) is simplified regarding reality, the purpose being to validate codes and calculate as many different realistic situations as desired. It is a flat plate, 1.5 mm thick, 4 m long and 15 cm wide, uniformly electrically heated, in a rectangular channel. Channel width (gap) can be enlarged from 3 to 15 cm, and the test section can be inclined from vertical to horizontal position. It is highly instrumented: mass velocity, electric power, absolute and differential pressures, wall temperatures, fluid temperatures, local void fraction, large windows for video films and high speed films. Precision of measurement is between 1 and 3 % of the measures.

3.4.2 Campaigns

Five campaigns of tests are included in the MVI project :

1. Campaign 1: Inclination 90°, gap 3 cm
2. Campaign 2: Inclination 10°, gap 15 cm
3. Campaign 3: Inclination 90° : gap 15 cm
4. Campaign 4: Inclination 45°, gap 15 cm
5. Campaign 5: Inclination 45°, gap 3 cm (only one pressure 0.1 MPa)

These campaigns are performed on a wide range of parameters :

- Outlet pressure : 0.1 to 0.5 MPa
- Inlet subcooling : 50°C to 0°C
- Mass flow velocity : 20 to 2000 kg/s/m^2
- Heat flux : 100 to 1000 kW/m^2

3.4.3 Experimental results

Two phase flow in SULTAN channel was thoroughly observed and measured, in order to better predict and calculate the behavior of a complete natural convecting system, with an emphasis on the evaluation of the recirculating mass flow rate and the static stability of the system based on the Internal and External Characteristics method [13].

Flow behavior

A general description of the flow in the test section will first try to sum up all the information provided by local measurements and films (Fig.3.20).

First, a thermal layer develops near the heated plate, but never reaches the opposite side in large gaps or inclined positions of the test section. Thermal stratification is observed for inclined positions. Due to the low inlet flow velocities, mixed convection regimes are common in the test section, inducing internal recirculation cells which tend to homogenize temperatures, profiles of temperature become flatter, a secondary maximum can be observed on the cold wall opposite to the heated wall.

A two phase layer starts to develop in subcooled conditions. Subcooling is dependent of heat flux, flow velocity and test section inclination and can be up to 50°C. Bubbles are first separate, with a oblong shape, about 3 or 4 cm long and 1 cm thick, which coalesce when they become numerous.

Generation of vapor is poorly predicted by correlations like Saha-Zubers [3], it is probably partly due to the fact that this correlation was established for smaller and uniformally heated channels A new correlation will be optimized but is not yet available.

The two phase layer thickens in a more or less wavy manner, its development is highly non linear and increases much faster when saturation is imminent. In subcooled conditions, it never invades the whole channel and the maximum void fraction, up to 40% is always located on the heated plate.

When saturation is reached , the vapor invades the whole channel, even for large gaps and low inclinations. Stratification is important : for inclined positions of test section, the maximum of void fraction remains on or very near the heated plate whereas, for vertical positions, it moves toward the center of the channel, and can reach 90%.

Two different regimes may be observed : the first one corresponds to a rather steady two phase flow, with the particularity of heterogeneous vapor inclusions in size, from a few mm to about 1 m.

The second regime is pulsated flow with a period of 1 to 3 seconds, big pockets of vapor develop and are washed away periodically, count current water follows.

CHF is avoided by a persisting thin film of liquid on the heated plate. Such a regime was described by Theofanous [4] and Chu [5] on the bottom of their hemispherical test sections. It was observed on SULTAN facility for inclinations of 10°, up to 1MW/m^2 for gap 3 cm, but only up to 500 kW/m^2 for gap 15 cm. Though its erratic aspect, this regime does not modify the average pressure drops in the test section, nor the limits of CHF.

A phenomena of reversal flow , with water flowing back from the pipe between the end of the test section and the condenser, was observed when outlet mean velocity was low enough, that is to say for any configurations at low heat fluxes, but only for vertical position, gap 15 cm and pressure 0.5 MPa at 1 MW/m^2. This phenomena improves considerably the limit of CHF, but is not easily predicted by the existing correlations of flow reversal, like Wallis or Puskina and Solokin [6].

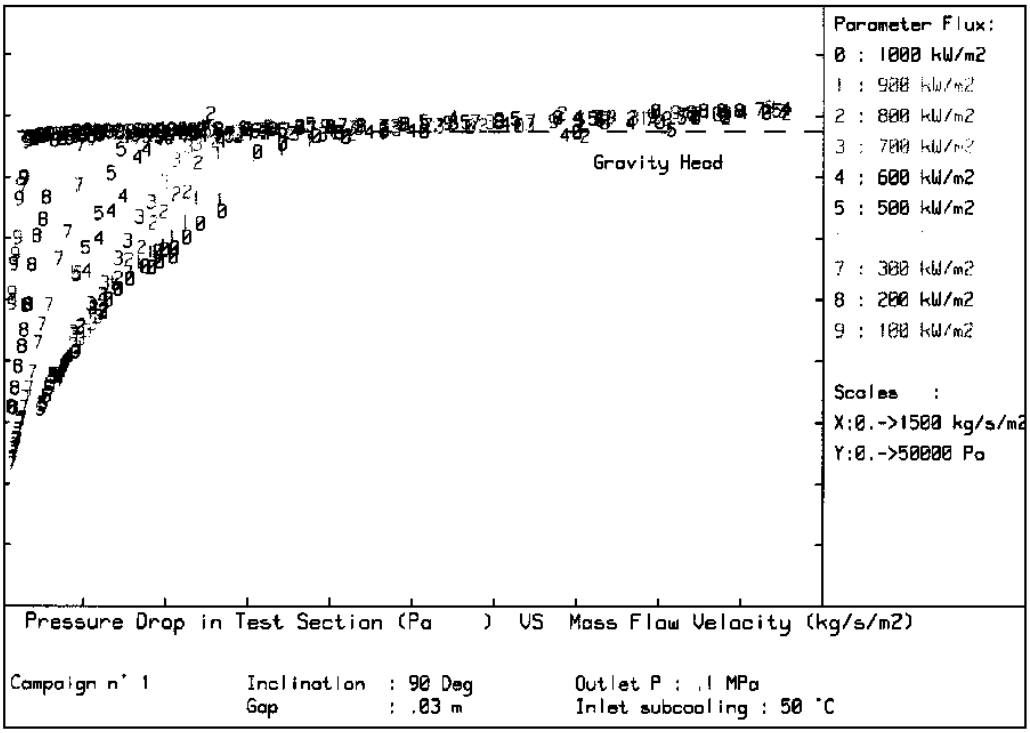

Fig. 3.21: *SULTAN: Pressure drop in test section vs. mass flow velocity (campaign 1).*

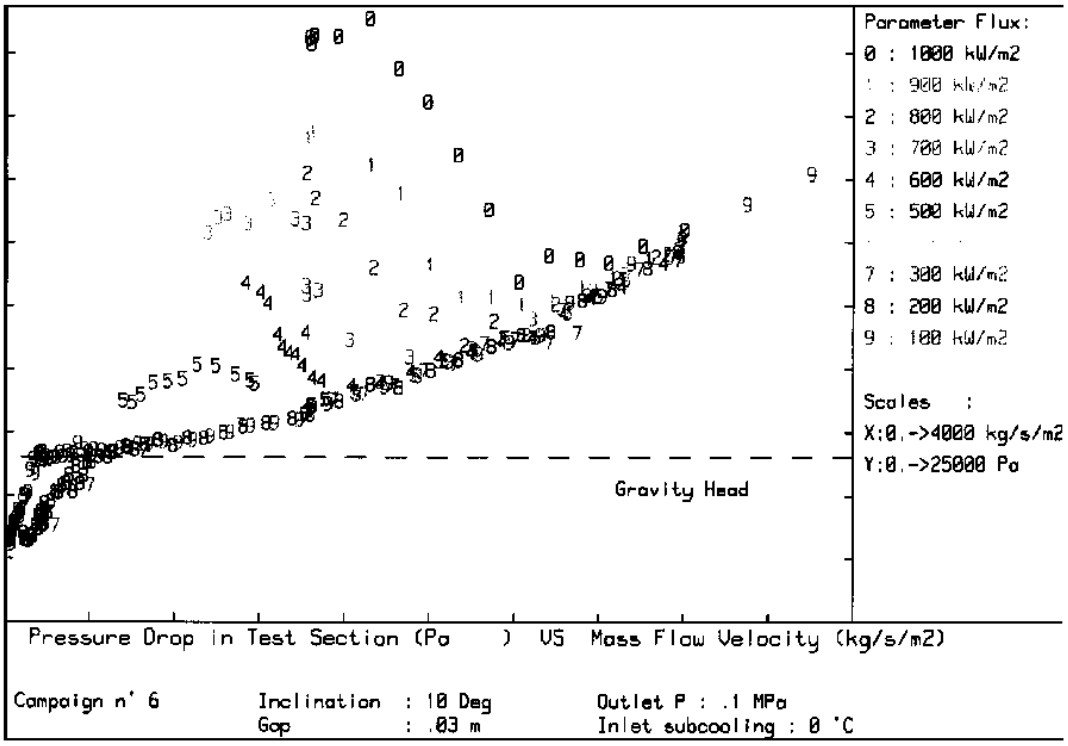

Fig. 3.22: *SULTAN: Pressure drop in test section vs. mass flow velocity (campaign 6).*

Pressure drops

The Internal Characteristics (IC) of the test section, i.e. the variation of pressure drop versus the mass velocity for constant thermohydraulic conditions of pressure, heat flux and inlet subcooling, were systematically investigated.

For vertical position (Fig.3.21), the IC shape is the same for any gap, pressure, inlet subcooling and heat flux: the slope of the IC is quite flat at high mass flow velocity and tend to gravity head value, then becomes steeper after average saturation is reached. CHF always occurs rather low on the steep slope, for saturation conditions.

For that kind of IC curves, natural circulation should be efficient up to 1 MW/m^2 and even more, provided that the rest of the circuit is designed for little friction pressure drops. A two phase adiabatic riser above the heated length could improve significantly the performance of the circuit. No static instabilities are expected as the IC curve is strictly monotonous. Dynamic instabilities should be of small amplitude thanks to the steeples of the slope.

For inclined position of 10°, the behavior is more complex and of three kind : at low heat fluxes (< 400 kW/m^2), there is no difference with the vertical position. For large gap of 15 cm and high heat fluxes, CHF occur on the flat part of the IC, before average saturation is reached, there is no opportunity that steady natural convection should be established. For small gaps (Fig.3.22) of 3 and 6 cm and high heat fluxes, boiling start at high mass velocity and the IC curves tend to the S shape measured in small channels. Static instability is there expected in natural convection, with a rapid reduction of flow rate and destruction of the heated plate.

CHF Limits

191 CHF Data have been obtained on SULTAN facility. Dry patches are generally rather small (2-6 cm^2) and cannot expend much due to the thinness of the heated plate. Though CHF location is expected at the end of a uniformly heated test section, many dry patches have occurred at lower elevation, within the last meter and even the last two meters for inclined positions. In term of local quality, it still represent little difference, but was taken into account in the SULTAN CHF Correlation giving Heat Flux (F) in MW/m^2, in term of Cover Pressure (P) in MPa, mass velocity (G) in kg/s/m^2, local thermodynamic quality (X), gap (E) in m and inclination ($Q = sin(I)$, I inclination above horizontal):

$$F = A_0(E,P,G) + A_1(E,G)\cdot X + A_2(E)\cdot X_2 + A_3(E,P,G,X)\cdot Q + A_4(E,P,G,X)\cdot Q_2 \tag{3.1}$$

Standard deviation: 9.7%; with

$$\begin{aligned} G &= ln(G) \\ A_0 &= b_0 + b-1\cdot E\cdot G + b_2/P^2 + b_3\cdot G + b_4\cdot E/P + b_5\cdot E/P^2 \\ &\quad + b_6\cdot P\cdot G^2 \\ A_1 &= b_7\cdot G_2 + b_8\cdot E\cdot G \\ A_2 &= b_9\cdot E \\ A_3 &= b_{10}\cdot G2 + b_{11}\cdot E\cdot P + b_{12}\cdot X\cdot G \\ A_4 &= b_{13}\cdot P + b_{14}\cdot G + b_{15}\cdot X + b_{16}\cdot E \end{aligned} \tag{3.2}$$

$$\begin{aligned} b_0 &= .65444 & b_4 &= 1.36899 & b_8 &= -4.49425 & b_{12} &= .855759 & b_{16} &= 2.2636 \\ b_1 &= -1.2018 & b_5 &= -.077415 & b_9 &= 9.28489 & b_{13} &= -1.74177 & & \\ b_2 &= -.008388 & b_6 &= .024967 & b_{10} &= -.0066169 & b_{14} &= .182895 & & \\ b_3 &= .000179 & b_7 &= -.086511 & b_{11} &= 11.62546 & b_{15} &= -1.8898 & & \end{aligned} \tag{3.3}$$

The term $A_0 + A_1 \cdot X$ represents the general behavior of CHF phenomena, extensively studied for PWR conditions [7],[8] [9]: heat flux decreases almost linearly with X, with a positive influence of G at low quality and a negative one at high quality.

The term $A_2 \cdot X_2$ expresses the fact that, for high quality, the curves F versus X tend toward an asymptotic flat line: due to flooding phenomena, the heated plate is wetted by counter current water and boiling crisis is suppressed. In that particular case, boiling crisis does not depend any more of the conditions at the outlet of the test section, but of the amount of water stored above it and of the delay before uncovering. Flooding phenomena is correlated to low outlet velocities, it was then more or less observed on SULTAN for all campaigns at low heat fluxes, but only restricted to vertical position, gap 15 cm and pressure 0.5 MPa for heat fluxes up to 1 MW/m^2 (campaign 3) and even 2 MW/m^2 (campaign 8). This configuration was then maintained for more than 2 hours, until uncovering.

The influence of inclination is expressed through the terms $A_3 \cdot Q + A_4 \cdot Q_2$. As expected [10] [11] heat flux decreases when inclination increases. The expression is very similar to the correlation obtained on the ULPU experiment, though it is difficult to compare as ULPU correlation does not take into account the effect of gap, pressure, velocity and local subcooling or quality, this last parameter being predominant.

The other parameters have a limited influence: F increases slightly when the pressure P increases. Gap seems to have no effect when CHF is reached for saturated conditions (generally in vertical position) and a limited positive effect in subcooled conditions (corresponding to inclined positions of test section).

Bibliography

[1] Asfia, F.J. and V.K. Dhir, "Natural Convection Heat Transfer in Volumetrically Heated Spherical Pools", *Proceedings of the OECD/CSNI/NEA Workshop on Large Molten Pool Heat Transfer*, Grenoble, France, March 9-11, 1994.

[2] Asmolov, V.V., Personal communications, 1997.

[3] P.N. Saha, N. Zuber, Point of net vapor generation void fraction in subcooled boiling, *Proc. 5th Int. Heat Transfer Conf.*, Volume IV, pp. 175-179, 1974.

[4] S. Angelini, T.G. Theofanous, The mechanism and prediction of a critical heat flux in inverted geometrics, Department of Chemical and Mechanical Engineering Center for Risk Studies and Safety, University of California, Santa Barbara, CA 93106.

[5] T.Y. Chu, S.E.E. Slezaci, J.H. Bentz, W.F. Padedag, Large scale boiling experiments of the flooded concept for In-Vessel retention, *OECD/CSNI/NEA Workshop on Large Molten Pool Heat Transfer*, Nuclear Center Grenoble, France, March 9-11, 1994.

[6] J.M. Delhaye, M. Giot, M.L. Riethmuller, Thermohydraulics of Two-Phase Systems for Industrial Design and Nuclear Engineering, Hemisphere Publishing Corporation, McGraw-Hill Book Company, chapter 4, pp. 61-68, 1981.

[7] R.W. Bowring, A simple but accurate round tube uniform heat flux, dryout correlation over the pressure range 0.7 - 17 MN/m^2 (100 - 2500 psia), AEEW-R-789, 1972.

[8] G.F. Hewitt, J.M. Delhaye, N. Zuber, Multiphase Science and Technology, Hemisphere Publishing Corporation, vol.2, chapter 4, 1986.

[9] D.C. Groeneveld, A general CHF prediction for water suitable for reactor accident analysis, Rapport interne CEA, 1982.

[10] T.G. Theofanous, S. Syri, The coolability limit of a pressure vessel lower head, NUREG/CP-0142, Volume I, pp. 627-647, , NURETH-7, Saratoga Springs, NY, September 10-15, 1995.

[11] F.B. Cheung, K.H. Haddadn Y.C. Liu, Critical Heat Flux (CHF) phenomenon on a downward facing curve surface, NUREG/CR-6507, PSU-ME-97-7321, June 1997.

[12] T.G.Theofanous, M.Maguire, S.Angelini and T.Salmassi, "The first results from the ACOPO Experiments," Nuclear Engineering and Design, 169, pp. 49-57, 1997.

[13] S. Rouge, SULTAN Test Facility for Large-Scale Vessel Coolability in Natural Convection at Low Pressure, *Nuclear Engineering and Design*, 1996.

[14] L. Bernaz, J.-M. Bonnet, B. Spindler, C. Villermaux, Thermalhydraulic Phenomena in Corium Pools: Numerical Simulation with TOLBIAC and Experimental Validation with BALI, *Proceedings ot the OECD/CSNI Workshop on 'In-Vessel Core Debris Retention and Coolability'*, pp. 185-193, Garching, Germany, 3-6 March, 1998.

[15] J.M.Bonnet, BALI project - Description of the facility, SETEX/LTEM/97-21, CEA, Grenoble, 17 rue des Martyrs, 38054 GRENOBLE CEDEX 9 - France.

[16] J.M.Bonnet, BALI test reports for in-vessel configurations, SETEX/LTEM/98-114, CEA, Grenoble, 17 rue des Martyrs, 38054 GRENOBLE CEDEX 9 - France.

[17] T.G. Theofanous et. al., Experience from The First Two Integrated Approaches to In-Vessel Retention Through External Cooling, presented at the OECD/CSNI/NEA Workshop on Large Molten Pool Heat Transfer, Grenoble, France, March 9-11, 1994.

[18] O. Kymäläinen, H. Tuomisto, O. Hongisto and T.G. Theofanous, Heat Flux Distribution from a Volumetrically Heated Pool with High Rayleigh Number, Proceedings of the 6th Int. Topical Meeting on Nuclear Reactor Thermal Hydraulics, NURETH-6, Grenoble, France, October 1993, pp.47-53.

[19] H. Tuomisto and T.G. Theofanous, A Consistent Approach to Severe Accident Management, Proc. of the Specialist Meeting on Severe Accident Management Programme Development, OECD/CSNI/SESAM, September 23-25, 1991, Rome, Italy.

[20] H. Tuomisto and T.G. Theofanous, A Consistent Approach to Severe Accident Management, *Nuclear Engineering and Design* (in press)

[21] T.G. Theofanous et. al., Critical Heat Flux Through Curved, Downward Facing, Thick Walls, presented at the OECD/CSNI/NEA Workshop on Large Molten Pool Heat Transfer, Grenoble, France, March 9-11, 1994.

[22] O.H. Kymäläinen, H. Tuomisto and T.G. Theofanous, Critical Heat Flux on Thick Walls of Large, Naturally Convecting Loops, ANS Proc. 1992 National Heat Transfer Conference, San Diego, CA, August 9-12, 1992, HTD Vol 6, 44-50.

[23] B. Frantz and V.K. Dhir, Experimental Investigations of Natural Convection in Spherical Segments of Volumetrically Heated Pools, ASME Proc. 1992 National Heat Transfer Conference, San Diego, CA, August 9-12, 1992, HTD Vol 192, 69-76.

[24] F.J. Asfia and V.K. Dhir, Natural Convection Heat Transfer in Volumetrically Heated Spherical Pools, presented at the OECD/CSNI/NEA Workshop on Large Molten Pool Heat Transfer, Grenoble, France, March 9-11, 1994.

[25] G.L. Hawkes and J.E. O'Brien, ARSAP AP600 In-Vessel Coolability Thermal Analysis, Final Report, DOE/ID-10369.

[26] R.J. Hammersley, R.E. Henry, D.R. Sharp and V. Srinavas, In-Vessel Retention for the AP600 Design During Severe Accidents, presented at the Second Intern. Conference on Nuclear Engineering (ICONE-2), San Fransisco, CA, March 21-24, 1993.

[27] R.E. Henry and H.K. Fauske, External Cooling of a Reactor Vessel Under Severe Accident Conditions, *Nuclear Engineering and Design*, Vol 139, 31-43. (1993)

[28] R.E. Henry et. al., Cooling of Core Debris Within the Reactor Vessel Lower Head, *Nuclear Technology*, Vol 101, 385-399 (1993)

[29] R.J. Hammersley et. al., Cooling of Core Debris Within a Reactor Vessel Lower Head with Integral Support Skirt, presented at the 1993 ANS Winter Meeting, San Fransisco, CA, November 14-18, 1993.

[30] S.A. Hodge, Identification and Assessment of BWR In-Vessel Accident Management Strategies, Invited paper for the Ray DiSalvo Memorial Accident Management Session, *Transactions of the ANS*, Vol 64, 367-368.

[31] J.M. Bonnet, S. Rouge and J.M. Seiler, Large Scale Experiments for Core Melt Retention, presented at the OECD/CSNI/NEA Workshop on Large Molten Pool Heat Transfer, Grenoble, France, March 9-11, 1994.

[32] T.Y. Chu, S.E. Slezak, J.H. Bentz and W.F. Pasedag, Large-scale Boiling Experiments of the Flooded Cavity Concept for In-Vessel Core Retention, presented at the OECD/CSNI/NEA Workshop on Large Molten Pool Heat Transfer, Grenoble, France, March 9-11, 1994.

[33] T. Okkonen, In-Vessel Core Debris Cooling Through External Flooding of the Reactor Pressure Vessel. Situation Report by a Group of Experts. OECD/NEA/CSNI. February 1994. NEA/CSNI/R(94)6.

[34] T.N. Dinh and R.R. Nourgaliev, "Numerical Analysis of Two-dimensional Natural Convection under High Rayleigh Number Condition in Volumetrically Heated Corium Pool", *Proceedings of the OECD/CSNI/NEA Workshop on* Large Molten Pool Heat Transfer, Grenoble, France, pp.269-319, 1994.

[35] F.A. Kulacki and M.Z. Nagle, "Natural Convection in a Horizontal Fluid Layer with Volumetric Energy Sources", *ASME J. Heat Transfer*, Vol.97, pp.204-211, 1975

[36] G. Grötzbach, Direct Numerical and Large Eddy Simulation of Turbulent Channel Flows. In: *Encyclopedia of Fluid Mechanics*. Vol.6, pp.1337-1391, Ed.: N.P. Cheremisinoff, Gulf Publ. Houston, 1987.

[37] CFX-F3D. Version 4.1 User Manual. AEAT, England, October 1995.

[38] O. Kymäläinen, O. Hongisto, J. Antman, H. Tuomisto and T.G. Theofanous, COPO: Experiments for Heat Flux Distribution from a Volumetrically Heated Corium Pool, Proceedings of the 20-th Water Reactor Safety Information Meeting, Bethesda, Maryland, October 21-23, 1992

[39] U. Steinberner and H.H. Reineke, Turbulent Buoyancy Convection Heat Transfer with Internal Heat Sources, Proceedings of the 6th Int. Heat Transfer Conference, Toronto, Canada (1978), Vol.2, pp.305-310.

[40] F.A. Kulacki and A.A. Emara, Steady and Transient Thermal Convection in a Fluid Layer with Uniform Volumetric Energy Sources, *Journal of Fluid Mechanics*, Vol.83, part 2, pp.375-395 (1977).

[41] F.B. Cheung, Natural Convection in a Volumetrically Heated Fluid Layer at High Rayleigh Numbers, *Int.J. Heat Mass Transfer*, Vol.20, pp.499-506 (1977).

[42] Theofanous T.G., et.al., *In-Vessel Coolability and Retention of a Core Melt*, DOE/ID-10460, v.2 (July 1995).

[43] T.N. Dinh, V.A. Bui, R.R. Nourgaliev, and B.R. Sehgal, "Crust Dynamics under PWR In-Vessel Melt Retention Conditions", ANS Proc. of 1996 National Heat Transfer Conference, Texas, 1996, HTC-Vol.9, pp.368-375.

[44] V.A. Bui, T.N. Dinh, and B.R. Sehgal, "In-Vessel Core Melt Pool Formation during Severe Accidents", ANS Proc. of 1996 National Heat Transfer Conference, Texas, 1996, HTC-Vol.9, pp.86-94.

Chapter 4

Mechanisms, mode and timing of reactor vessel failure

4.1 Introduction and Background

During the course of a hypothetical severe accident in a light water reactor (LWR), large amounts of molten core materials may be relocated to the reactor pressure vessel (RPV) lower plenum. Depending on accident scenarios, reactor design and accident management procedures, the in-vessel debris configuration may be different, fig.1.5. In general, the heat, transferred from the debris to the vessel, will cause the vessel heat-up and weaken the vessel strength. The lower head wall may be subjected to significant thermal and pressure loads, and is liable to failure due to melting or creep rupture (fig.1.6). For assessment of severe core meltdown accident progression, the mode, timing and size of vessel failure is of paramount importance.

It was proposed recently, that the presence of water in the reactor lower plenum prevented the TMI-2 vessel failure. The vessel gap cooling is proposed as an efficient mechanism of keeping the vessel wall cool and preventing vessel failure. The success of this mechanism largely depends on *a)* whether a gap is formed and maintained between the corium melt crust and the creeping vessel and *b)* whether water can penetrate into the gap to cool the vessel. Since the core melt relocation, debris bed formation, crust formation and vessel creep are highly three-dimensional process, it is difficult to apriori predict the existence of the gap and of the pattern of water channeling in-between the vessel wall and the debris. Another important question is whether gap thermal hydraulics allows water ingression to sufficient depth to cool the lowermost regions of the vessel, and prevent its creep failure.

4.1.1 Creep modeling

Tables 4.1 and 4.2 summarize previous numerical studies of thermo-mechanical loadings on the lower plenum of the RPV during a severe accident. In general, most studies involve application of finite-element method, shell theory or simplified analytical techniques to invesigate the vessel creep deformation in a thermo-elastic-(plastic) regime. There are many uncertainties associated with creep modeling:

- The existing methods are based on fits obtained by standard uniaxial creep tests. It is not clear, whether these approaches are accurate enough to predict multiaxial creep processes.

- Another, more fundamental drawback of widely-used creep models is that they are based on the equation of state approach, which assumes the response of the material to be dependent explicitly on the present state. It has been argued that the only valid representation of creep is the one that incorporates the memory of past events. The equation of state theory, which is adopted in most methods, on practical grounds, does not possess this feature [Kraus, 1980].

- There are many uncertainties associated with mechanical properties of prototypical carbon steel (elastic modulus, stress-strain relationships, thermal expansion coefficient, etc.) at high-temperatures.

4.1.2 Creep rupture criteria

Overwhelming majority of previous creep rupture analyses employed Larson-Miller Parameter (LMP) approach [Larson and Miller, 1952] to estimate time-to-rupture of the vessel shell. An advanced approach involves the damage concept, which allows to take into account the transient temperature and pressure loading histories ([Kraus, 1980]). Experience has shown that both LMP method and LMP with incremental damage procedure may significantly underestimate the rupture strain (1995 [Theofanous et al., 1995]). Different strain-based failure criteria would avoid this problem ([Theofanous et al., 1995] [Duijvestijn, 1997]).

4.1.3 Experiments

The above-presented overview of analytical studies of creep rupture clearly indicates that the currently-existing numerical and analytical methods are prone to a large number of uncertainties when assessing both the creep deformation and the time to rupture for prototypical geometry and thermo-mechanical loadings. Only

data from a limited number of experiments are currently available. Table 4.3 reviews experiments on creep deformations and rupture at high-temperature conditions. Uniaxial tensile tests have been performed for different reactor vessel steels in the USA, Russia, Germany and France. So far, only a few multiaxial experiments investigating creep rupture of the reactor carbon steel at high-temperature conditions have been accomplished. In the RUPTHER experimental program, *e.g.*, a simple thin shell tube was subjected to internal pressure and axial-gradient thermal loading (temperature up to 1000°C). The data obtained in this experiment may be used for validation of different structural mechanics models. Recently, the LHF (Lower Head Failure) experiments have been performed at SNL, investigating creep failure of relatively large vessels (1/5th-scale), held at a pressure of about 100 bars, while the vessel bottom head is heated to temperatures of about 1000K ([Chu et al., 1997]). The energy transfer to the reactor vessel from the core debris is simulated using a hemispherical resistance heater. Effects of peaking in the local distribution of heat transfer, and the impact of penetrations on the vessel failure time were the major focus of the LHF-1,2,3,4 experimental tests.

4.2 FOREVER experimental program

The current FOREVER program includes three major test series [Sehgal et al., 1998] [Sehgal et al., 1998] [Sehgal et al., 1999]. In the first series, we investigate the vessel deformation and creep behavior under thermal attack by naturally-convecting oxidic-melt pool (FOREVER/C serie). The focus is placed on physical mechanisms which may govern the debris-vessel gap formation. In addition, data is obtained on the creep rate at several locations on the lower head, which could be employed for validation of creep models and codes. In contrast to the SNL LHF experiments [Chu et al., 1997] (which simulate the TMI-2 scenario with 10 MPa pressure loading), the depressurized scenarios are the focus of the FOREVER tests.

The second series FOREVER/G will be devoted to the gap cooling. Water will be supplied to the top of the melt pool after the vessel wall creep has occurred to a certain extent. Water ingression into the gap between the melt pool crust and the creeping vessel will be detected by thermocouples, mounted on the inner surface of the vessel wall.

In the third series FOREVER/P, effects of penetrations on the vessel deformation and creep processes will be investigated.

4.2.1 Scaling rationale for FOREVER/C serie

Table 4.4 summarizes scaling ratios for the values of the most important geometrical, thermal and mechanical loading parameters for a prototypic reactor case and for the FOREVER/C test. Since the vessel creep deformation and gap opening are the focus in the FOREVER/C test series, the current scaling considerations are limited to the effective stresses, their components and distributions, as well as the vessel strain and gap formation. The scaling methodology of the gap cooling and the penetration failure have yet to be developed for the future test series, FOREVER/G and FOREVER/P.

From Table 4.4 it can be seen that, with the vessel geometry and test conditions chosen, membrane stresses are modeled exactly, while the thermal stresses are not. More importantly, however, in the FOREVER/C test the stress distribution is dominated by the thermal stresses, having a maximum value in the region of 45-60^o, as in the prototypic reactor accident. This is the major difference between the FOREVER and Sandia LHF experiments (Chu et al., 1997). The internal pressure-induced membrane stresses dominate the creep and rupture processes in the LHF experiments, while thermal stresses dominate these processes in the FOREVER/C experiments.

4.2.2 Experimental facility and procedure

The facility employs 1/10th-scale carbon-steel vessels 400mm diameter, 15mm thick and $\simeq$600mm high. The auxiliary systems are designed to provide an overpressurization up to 4 MPa in the test vessel. Thus, severe accident scenarios with RCS depressurization are modeled. Up to 20 liters of binary-oxidic melts with 100-300 K superheat are employed, as simulant for the prototypic corium melt. The temperature difference between the melt liquidus and solidus is about 50K and the liquidus temperature ranges from 1300K to 1400K.

The high-temperature (up to 1700K) oxide melt is prepared in the Si-C-crucible of a 50kW induction furnace and is, then, poured into the test section. The pressure vessel is heated to about 600°C, prior to the melt delivery. Specified overpressurization is then supplied with an inert gas supply. A $MoSi_2$ 50kW electric heater is employed in the melt pool to heat and maintain its temperature in the range desired to obtain the specified wall temperatures, Fig.4.2. In order to assure personnel safety all the test equipment are installed inside a concrete containment with 40 cm thick walls; Fig.4.3.

A number of K-type thermocouples are used to measure the temperature of the melt (debris) at different locations in the hemispherical pool and to determine the thermal response of the vessel wall, fig. 4.4. The vessel deformation and creep are measured by position transducers. Up to 20 linear displacement transducers

(LDT) are mounted at five latitude locations of the hemispherical lower head and used to measure the creep rate of the three-dimensional vessel.

Appendix I presents additional information on experimental design and measurement technique.

Table 4.1: *Review of prior analytical research (RPV creep deformation and rupture).*

	Institution/Organization Year/Ref.	*Method of study*	*+ Purposes. - Major results of the study.*
1	(EPRI, US), [Anderson et al., 1983].	+2D FEM Analysis (MARC code). +Thermo-elastic creep.	+Global creep rupture. -Approximate solution for calculating time to rupture is developed.
2	(SNL, US), [Chambers, 1987].	+2D FEM Analysis (COYOTE and JAC codes). +Thermo-elastic analysis. +(no creep effects included).	+Global creep rupture. +Importance of thermal strains. -No significant effects of thermal strains on vessel failure are found.
3	(SNL, US), [Dosanjh and Pilch, 1991].	+1D model of thermal and mechanical response of the vessel lower head. +LMP approach for creep rupture.	+Global creep rupture. -Pressure and BC have the greatest effect on failure times.
4	(INEL, US), [Thinnes, 1988]. (INEL, US), [Thinnes and Moore, 1989]. (INEL, US), [Shah, 1986].	+2D FEM Analysis (COUPLE/FLUID and ABAQUS codes). +Thermo-elastic-plastic creep. +LMP approach for creep rupture.	+Global creep rupture. +TMI-2 accident analysis. +Crack growth analysis.
5	(GRS, Germany), [Gruner and Schulz, 1989].	+2D FEM Analysis (ADINA) code. +Thermo-elastic-plastic creep. +LMP approach for creep rupture with life fraction rule.	+Global creep rupture.
6	(ORNL, US), [Hodge and Ott, 1989]. (ORNL, US), [Hodge et al., 1991].	+LMP approach for creep rupture.	+Global creep rupture for BWRs. -The vessel penetrations are predicted to fail long before global vessel failure.
7	(INEL, US), [Rempe et al., 1993].	+Simplified approach for global creep rupture. +Theory of shells for local creep rupture.	+Global creep rupture. +Crack growth analysis. +Local creep rupture. +Review of literature.

Table 4.2: *Review of prior analytical research (RPV creep deformation and rupture, cont.).*

	Institution/Organization Year/Ref.	*Method of study*	*+ Purposes. - Major results of the study.*
8	(INEL, NRC US), [Rempe and Walker, 1994].		+Review.
9	(INEL, US), [Chavez and Rempe, 1994]	+2D FEM Analysis (ABAQUS code). +Thermo-elastic-plastic creep. +LMP approach for creep rupture with life fraction rule.	+Global creep rupture for BWR vessel.
10	(Univ. of Wisconsin, US), [Witt, 1994].	+Shell theory. +Thermo-elastic-plastic creep. +LMP approach for creep rupture with life fraction rule.	+Local creep rupture. +Analysis of TMI-2 accident in support of the OECD TMI-2 IP project.
11	(DOE, US), [Theofanous et al., 1995].	+3D FEM Analysis (ABAQUS code). +Thermo-elastic-plastic creep. +LMP approach for creep rupture with life fraction rule.	+Global creep rupture. for AP600. +Ductile tearing.
12	(PSI, Switzerland), [Duijvestijn, 1997]	+3D FEM Analysis (ADINA code). +Thermo-elastic-plastic creep. +Ultimate strain criterium for creep rupture.	+Global creep rupture. +Local creep rupture.
13	(Seoul Natl Univ, Korea), [Kwang, 1997]	+2D FEM Analysis (ABAQUS5.5 code). +Thermo-elastic-plastic creep.	+Global creep rupture. +Analysis of LHF-1 experiment.
14	EU-funded Projects (REVISA, RPVA), [Schulz, 1995]. Participants: AEA Technology (UK). ANPA/DISP, ENEA-DRI, University of Pisa, ENEA-VDN (Italy). CEA-IPSN, CEA-DRN (France). GRS/MPA, KFA, KFK, Siemens-KWU (Germany). VTT (Finland)	+2D/3D FEM Analysis (CASTEM 2000, MARC, ADINAT, PASULA codes) +Experiments on material properties	+Global creep rupture. +Local creep rupture.

Table 4.3: *Review of prior experimental research (RPV creep deformation and rupture).*

	Institution/Organization Year/Ref.	*Method of study*	*+ Purposes. - Major results of the study.*
15	(KfK, Germany), [Müller and Kuhn, 1991].	+uniaxial tensile tests.	+High-temperature creep and tensile data for German RPV steel (20MnMoNi55).
16	(INEL, NRC, US), [Thinnes et al., 1994].	+uniaxial tensile tests.	+High-temperature creep and tensile data for US RPV steels (SA533B1 and SA508-CL2).
17	(CEA, France), [Sainte, 1995].	+uniaxial tensile tests.	+High-temperature creep and tensile data for French RPV steel (16MND5).
18	RUPTHER experimental program (France).	+Pressurized thin shell carbon steel cylinders. +Temp. up to 1000° C.	+Multiaxial creep rupture data for high-temperature. conditions.
19	(Kurchatov Inst., Russia), [Degaltsev et al., 1997]	+uniaxial tensile tests.	+High-temperature creep and tensile data for Russian RPV steel (15X2HMFA).
20	LHF experimental program, (SNL, US), [Chu et al., 1997]	+1/5th-scale carbon steel pressure vessel. +P=10MPa, T up to 1000 K. +Resistance heaters for thermal loading.	+Global creep rupture. +Effect of penetrations. +Effect of heat flux peaking.

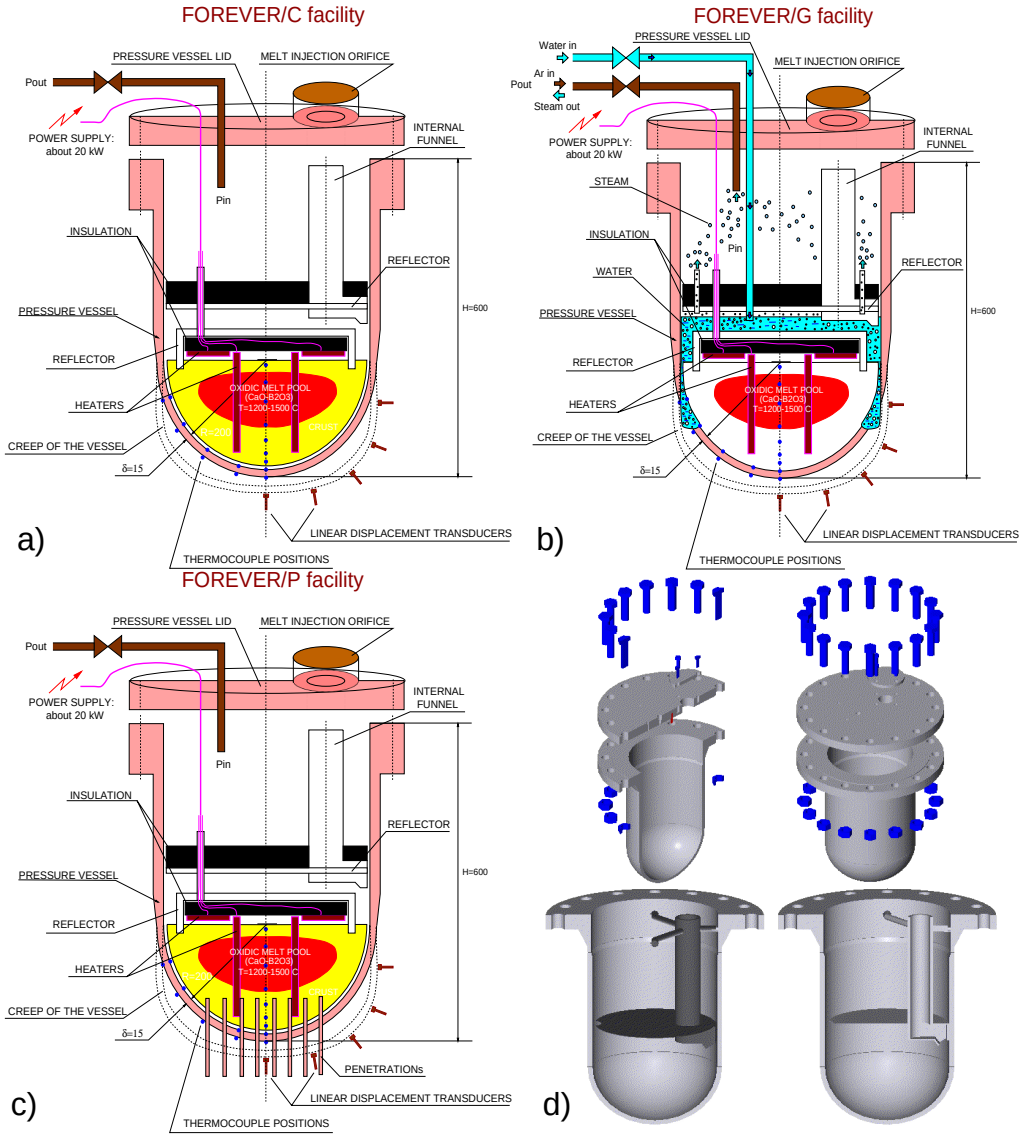

Fig. 4.1: *Schematic of the FOREVER/C (a), FOREVER/G (b) and FOREVER/P (c) tests. Design of the pressure vessel (d).*

Table 4.4: *Scaling consideration of the FOREVER/C tests*

%	*Scaling Parameter*	*FOREVER/C Exp.*	*Reactor case*	*Ratio*
	Geometry			
1	Shape	Hemispherical lower head + Cylindrical part		
2	Inner diameter, m	$\simeq$ 0.4	$\simeq$ 4	1:10
3	Wall thickness, m	0.015	$\simeq$ 0.15	1:10
4	Volume of the lower head, l	$\simeq$ 17	$\simeq 1.7 \cdot 10^4$	1:1000
	Thermal loading			
5	Vessel wall temperature, K	1000 ... 1250	1000 ... 1700	-
6	Heat flux, MW/m^2	0.03 ... 0.1	0.03 ... 0.1	1:1
7	Vessel wall temp. drop, K	15 ... 50	150 ... 500	1:10
	Mechanical loading			
8	Internal pressure, MPa	2	2	1:1
9	Deadweight pressure, MPa	negligible		
10	Membrane stresses σ_p, MPa	$\simeq$ 13	$\simeq$ 13	1:1
11	Effective thermal stresses (max) σ_t^{max}, MPa	30 ... 100	300 ... 1000	1:10
12	Stress ratio: σ_p/σ_t^{max}	1:2 ... 1:10	1:20 ... 1:100	10:1
	Vessel deformation and creep			
13	Maximum strain (rupture), %	16 ... 20	16 ... 27	$\simeq$ 1:1
14	Maximum displacement, mm	0 ... 15(rupture)	0 ... 150(rupture)	1:10
15	Angle of maximum strain, ^{o}	45 ... 60	45 ... 60	1:1

Fig. 4.2: *Internal heater: out-of-vessel test.*

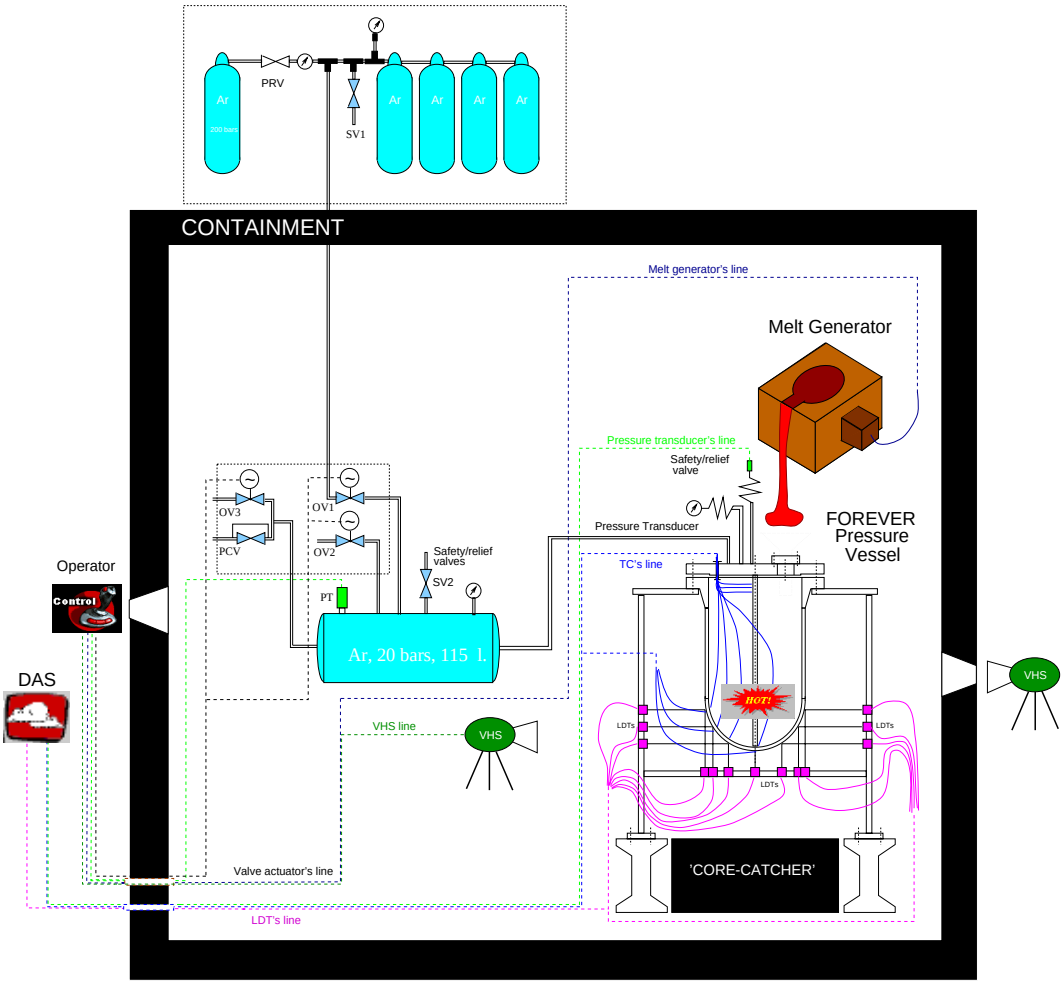

Fig. 4.3: *Schematic of the FOREVER/C experimental set-up.*

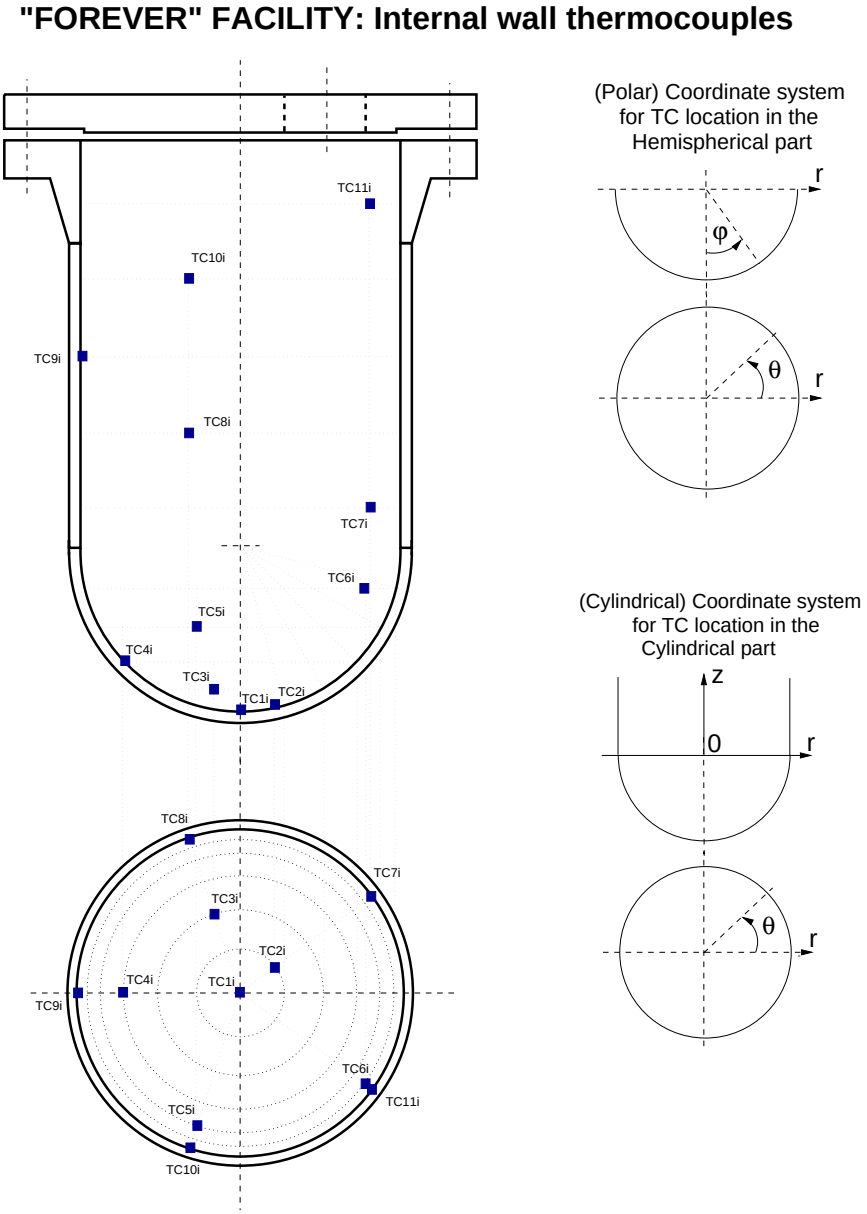

Fig. 4.4: *Location of internal wall thermocouples.*

Table 4.5: *Experimental conditions and parameters of the FOREVER/C1 test.*

%	*Parameter*	*Value*
1	Average pressure at the steady-state, MPa	2.5
2	Average power at the steady-state, kVA	22
3	Maximum temperature of the external surface of the vessel measured at the steady-state, $^{\circ}C$	800
4	Position of the maximum temperature, $^{\circ}$	$60-90^{\circ}$
5	Maximum temperature of the melt measured at the steady-state, $^{\circ}C$	1100
6	Maximum total displacement of the vessel wall measured, mm	10
7	Maximum creep displacement of the vessel wall measured, mm	6
8	Angular Position of the maximum displacement measured, $^{\circ}$	45°
9	Estimate of the maximum total strain, calculated as $\varepsilon_{\theta}^{max} = \frac{\Delta r^{max}}{R}$, %	5
10	Estimate of the average creep strain rate, calculated as $\overline{\dot{\varepsilon}} \sim \frac{\Delta r^{max,creep}}{R \cdot t_{exp}}$, %/hr	0.125
11	Total duration of the experiment, hrs	28
12	Duration of the thermal steady-state, hrs	21
13	Duration of the pressurization, hrs	24

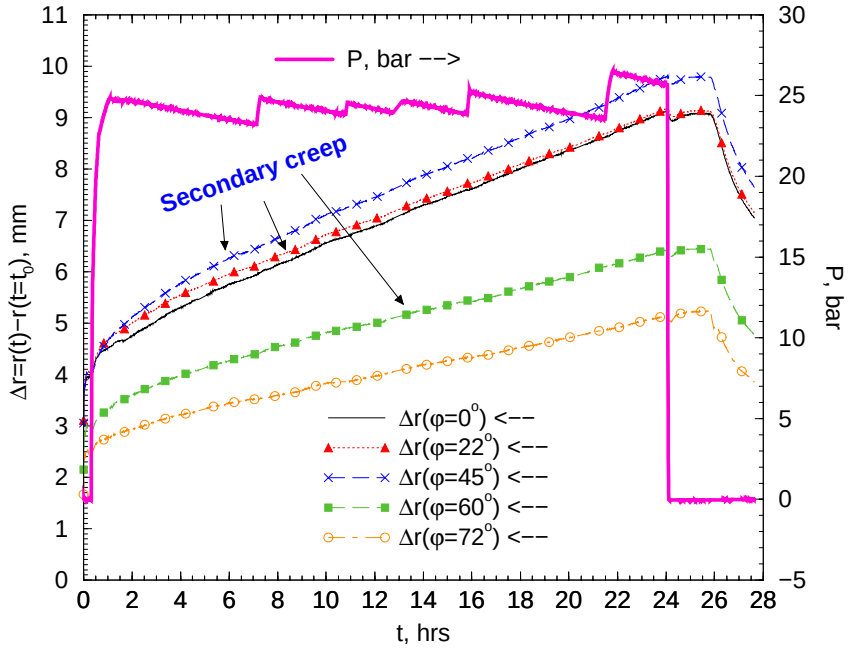

Fig. 4.5: *History of the vessel wall displacements and internal pressure.*

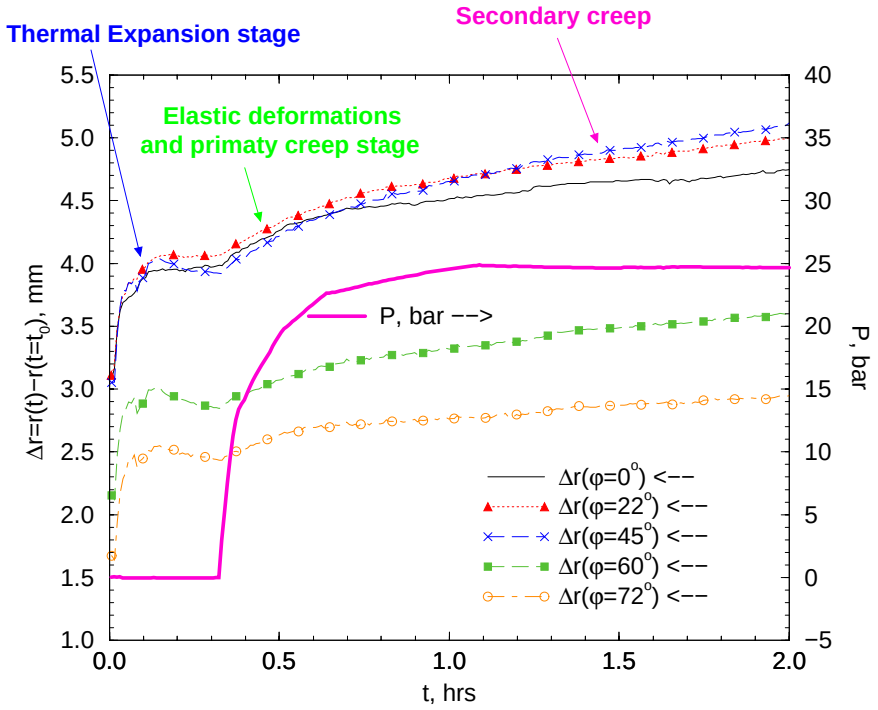

Fig. 4.6: *History of the vessel wall displacements and internal pressure, in the beginning of the test, (t from 0 to 2 hrs).*

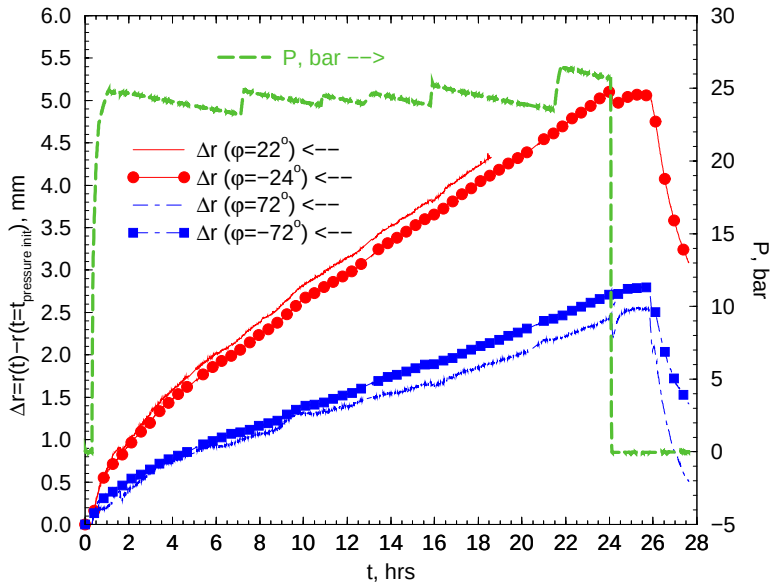

Fig. 4.7: *Creep displacement at the position ($\phi \simeq \pm 24^\circ$) and ($\phi = \pm 72^\circ$) of the vessel, and internal pressure as a function of time.*

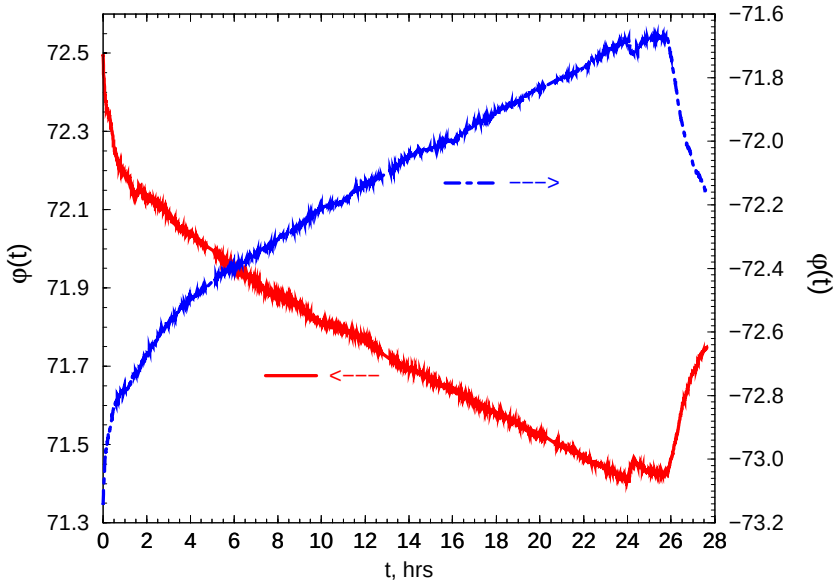

Fig. 4.8: *History of the angular displacement, measured at the angular position $\phi \simeq \pm 72$.*

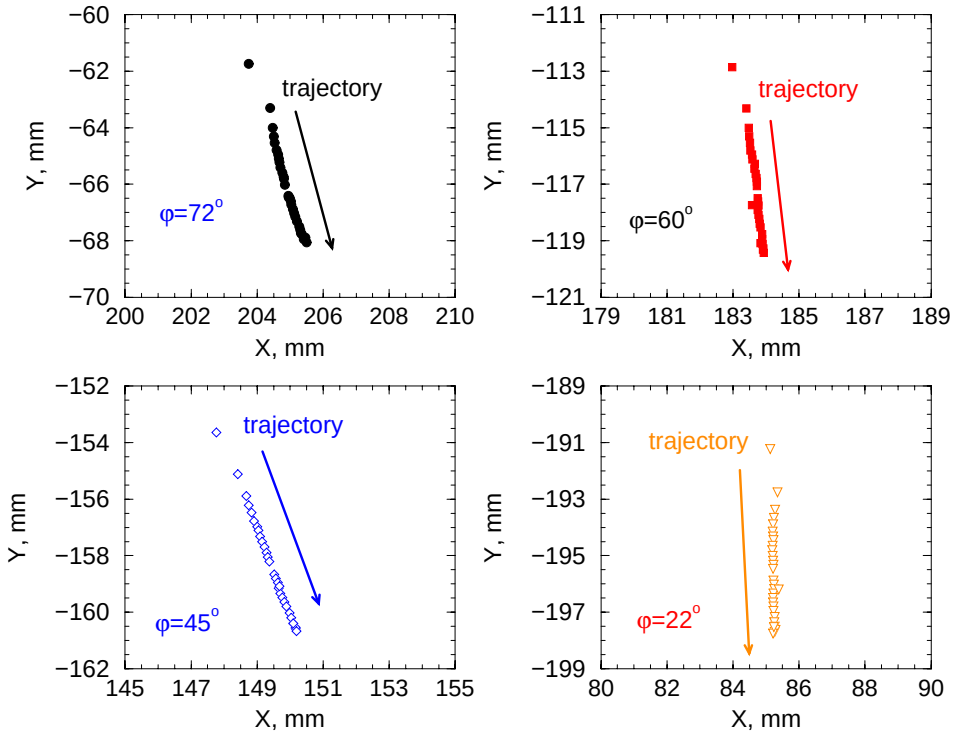

Fig. 4.9: *Displacements of the LDT measurement points in cartesian coordinates.*

4.2.3 Experimental results and discussion

Chronology of the test

The experiment started with melt delivery to the pressure vessel. After the vessel temperature had become steady, 20 min after the melt delivery, the pressurization system was activated. The internal pressure $P_{int} \simeq 25$ bar was kept for 24 hrs, until the maximum creep strain reached 5%. Experimental conditions and parameters of the FOREVER/C1 test are summarized in Table 4.5.

History of displacements

Figs.4.5-4.6 present the measured total vessel wall displacements, as functions of time, for five different measurement points. As seen, during the first 20 minutes of the test, the vessel wall radially expanded in the range from 2.5 to 4 mm, depending on the angular position. After pressurization, which was activated about 20 minutes after the melt delivery, the measurable creep deformation started, fig.4.6. Notably, the creep strain rate was nearly constant, $\overline{\dot{\varepsilon}} \simeq 0.125$ %/hr, fig.4.5.

The creep deformation of the vessel was observed to be quite symmetrical, which can be deduced from the radial and angular displacement data, presented in figs.4.7 and 4.8.

The measured radial creep deformations vary from 1mm (at $\phi \simeq \pm 75^{\circ}$) to 5mm (at $-45^{\circ} < \phi < +45^{\circ}$). At the same time, the maximum of angular displacement is located in the region of $\phi \simeq 80^{\circ}$. From the experimental data on the vessel creep deformation, it was found, that the vessel displacement was directed downwards, rather than radially, Fig.4.9.

In fact, the vessel wall temperature in the lowest region of the lower head was relatively low (see fig.4.10) and could hardly cause significant creep deformations. Thus, it is believed that creep process was taking place only in the corner regions, where the maximum temperature was located. Because the deformation was directed downwards, it caused equivalent displacement of the bottom part. Therefore, the vessel wall thinning should have occurred in the corner, while the bottom part must be mostly intact.

Figs.4.11 and 4.12 show the view of the vessel in the very beginning of the test and after the test. It can be seen, that due to high-temperature-conditions, significant vessel wall oxidation took place. Creep displacement of the outer surface of the lower head was also evident, when viewed along with cylindrical part of the vessel.

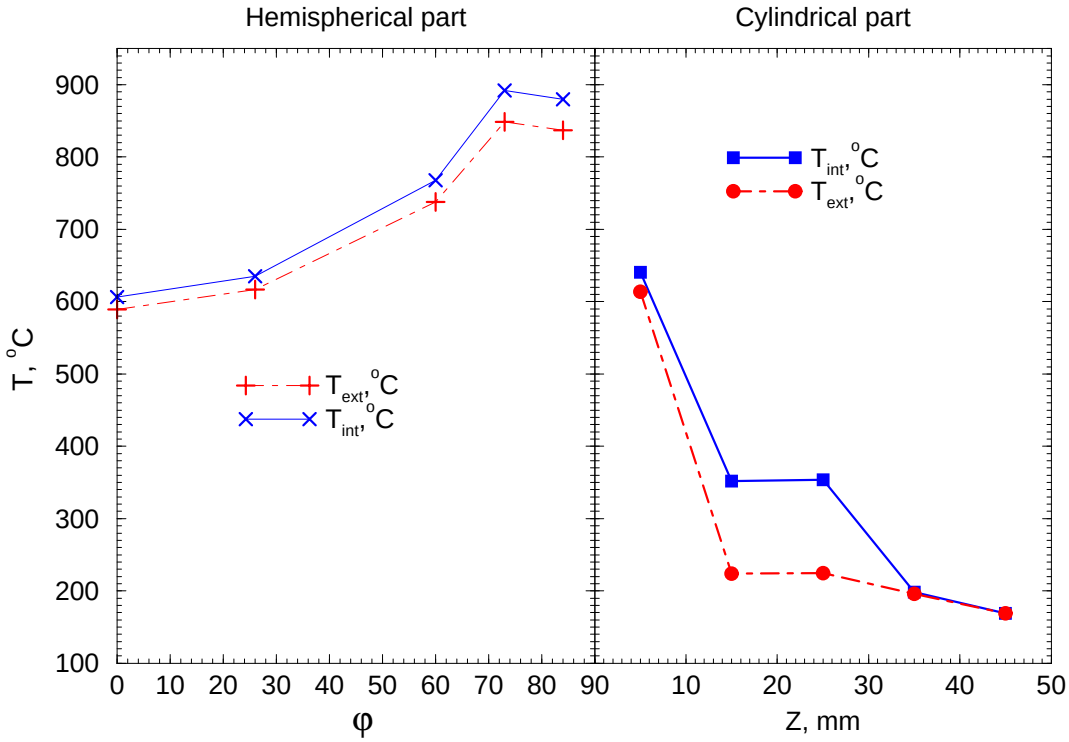

Fig. 4.10: *Local temperature distribution on the inner and outer surface of the vessel wall, at the steady-state stage of experiment (t=8 hrs.).*

Thermal loadings and natural convection in the melt pool

Fig.4.13 presents the history of power in the melt internal heaters. During the first hour of the experiment, the power supply of heaters was raised up to about 22kW and maintained near this level during the whole experiment, until the power shut down at 26^{th} hour of the test.

Temperatures in the melt pool were measured by three centerline thermocouples, fig.4.13. As can be seen, the temperature inside the liquid melt pool achieved nearly steady-state in 0.5 hr, and stayed at the level of 1050-1100°C until the depressurization. This corresponds to the melt superheat above the liquidus point of $\simeq 50$°C. The lowest thermocouple was located 3 cm above the vessel wall, in the crust. Due to the crust growth during the first 3-4 hrs (see pre-test calculations by the MVITA code, fig.4.14), this thermocouple registered slow temperature drop from about 850°C in the begining of the test to about 700°C at the steady-state stage, fig.4.13.

Temperatures of the vessel wall were registered by 21 internal and external thermocouples, see fig.4.4. Steady-state conditions for upper ($\phi > 60°$) lower

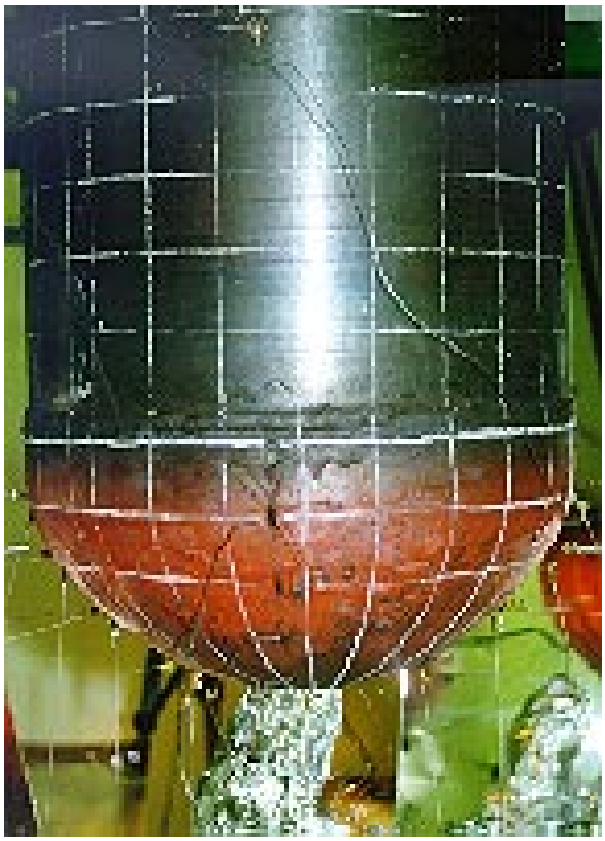

Fig. 4.11: *View of the hot pressure vessel in the begining of the test.*

head thermocouples were achieved in 1 hr after the beginning of the test. The lower thermocouples ($\phi < 60°$) reached nearly steady-state conditions after 3-4 hrs of the test, when the bottom crust was fully established and achieved steady-state thickness.

In fig.4.10, the local distribution of temperature is presented for hemispherical and cylindrical part of the vessel. From the wall temperatures, the heat flux at the wall is calculated as

$$q_w = q_{rad} + q_{conv} = \varepsilon\sigma\left(T_w^4 - T_{cont}^4\right) + h_{conv}\left(T_w - T_{cont}\right) \tag{4.1}$$

The vessel wall emmissivity is taken as $\varepsilon = 0.9$, the temperature in the containment is $T = 320K$ (measured during the test), and the convective heat transfer coefficient is estimated as $h_{conv} = 10$ W/(m^{2}K). The evaluated heat flux distribution is plotted as a function of angle (in the hemispherical part) and axial coordinate (in the cylindrical part) in fig.4.15. The maximum wall heat flux is located in the hemispherical part, $\phi \simeq 75°$, where the maximum wall temperature is registered. The local distribution is typical for natural convection in the hemispherical melt pool, with minimum heat flux at the very bottom.

Fig. 4.12: *View of the cold pressure vessel after the test.*

Fig.4.16 presents the evaluated total heat removal, integrated begining from the very bottom of the hemispherical part, and finishing at the top of the cylidrical part. It can be seen, the the heat balance is within 90%[1].

Table 4.6 presents the comparison of the evaluated natural convection heat transfer characteristics with available experimental correlations. Ra number is calculated as

$$Ra = \frac{g\beta q_v R_h^5}{\kappa\alpha\nu} \tag{4.2}$$

where $R_h = 0.16$m is the height of internal heaters. Power splitting $\frac{Q_{up}}{Q_{dn}}$ is compared with the experimental correlations by [Theofanous et al., 1995]:

$$\begin{array}{lll} Nu_{up} = 0.345 Ra^{0.233} & Ra = 10^{12} - 10^{15} & \text{Transient cooldown in the hemispherical pool} \\ Nu_{dn} = 0.048 Ra^{0.27} & Ra = 10^{12} - 10^{13} & \text{Transient cooldown in the hemispherical pool} \end{array} \tag{4.3}$$

[1]The rest 10% are due to the uncertainties in the evaluation of the wall temperature, wall heat flux, and, in addition, can be attributted to the heat losses through the lid and by convection of the Ar.

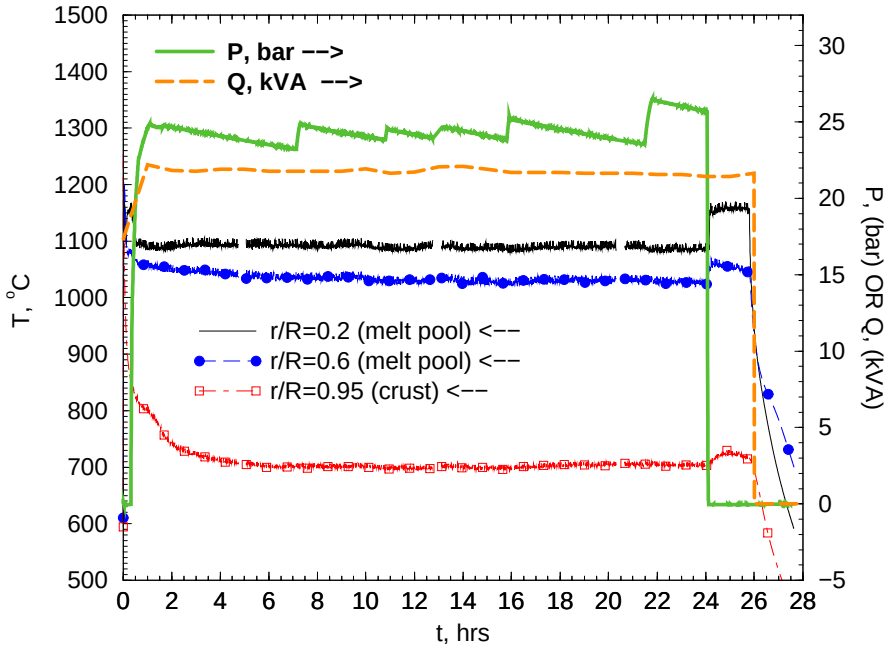

Fig. 4.13: *Temperature of the melt as a function of time, measured at the centerline, at different radial locations. History of the pressure and power supply.*

and Mayinger et al. (cited from [Nourgaliev et al., 1997]):

$$
\begin{aligned}
Nu_{up} &= 0.36 Ra^{0.23} \quad Ra = 10^7 - 5 \cdot 10^{10} && \text{Internal heating in the semicircular pool} \\
Nu_{dn} &= 0.54 Ra^{0.18} \quad Ra = 10^7 - 5 \cdot 10^{10} && \text{Internal heating in the semicircular pool}
\end{aligned}
\tag{4.4}
$$

It can be seen, that the fraction of heat removed through the bottom surface is higher in the FOREVER/C1 experiment, than that predicted by the experimental correlations (4.3) and (4.4). This indicates, the upper crust was not effective, and the upper boundary condition is different from the isothermal. In the FOREVER experiment, thick insulation is provided in the vessel on top of the melt pool, which may not promote formation of crust.

After the test, the vessel was cut and the melt-vessel interface was examined, fig.4.17. It was found that no measurable gap was created in the FOREVER/C1 test. This indicates that the crust adhered to the wall and crept together with the vessel. Similar phenomenon might occur in the prototypic reactor situation, however, this test did not employ any water in the vessel before the melt was

Table 4.6: *Natural convection heat transfer characteristics*

%	*Parameter*	*Value*	*Dimension*
	Steady-State at about 8 hrs.:		
1	Ra #	$3.6 \cdot 10^9$	-
2	q_v	2.56	MW/m^3
3	$\overline{q}_{w,dn}$	44	kW/m^2
4	$\overline{q}_{w,up}$	88	kW/m^2
5	$\frac{Q_{up}}{Q_{dn}}$, exp.	$\simeq 1$	-
6	$\frac{Q_{up}}{Q_{dn}}$, correlation (4.3)	$\simeq 1.59$	-
7	$\frac{Q_{up}}{Q_{dn}}$, correlation (4.4)	$\simeq 1.28$	-

poured. This preliminary observation will be subjected to confirmation in the future FOREVER tests.

More complete data from the FOREVER/C1 test is given in Appendix I.

4.3 Conclusions

The FOREVER/C1 test is the first integral experiment, in which a decay-heated oxidic melt pool was maintained in long-term contact with the hemispherical lower head of a pressurized, creeping, steel vessel. The experiment was successful. A sizeable database was obtained on melt pool temperatures, melt pool energy transfer, heat transfer rates, heat flux distribution on the melt (crust)-vessel contact surface, vessel temperatures, and time-dependent multiaxial vessel wall creep deformation.

The multiaxial three-dimensional creep deformation data obtained for prototypic reactor vessel steels at high-temperature conditions, could be employed for validation of models for creep deformation, in structural mechanics codes.

We believe that the FOREVER test has provided crucial data and knowledge base to advance the current understanding of the in-vessel melt pool convection and the vessel creep behavior. Further FOREVER experiments are expected to provide the needed data for the potential of in-vessel gap coolability and for the influence of penetrations on the mode of failure during the vessel creep scenario.

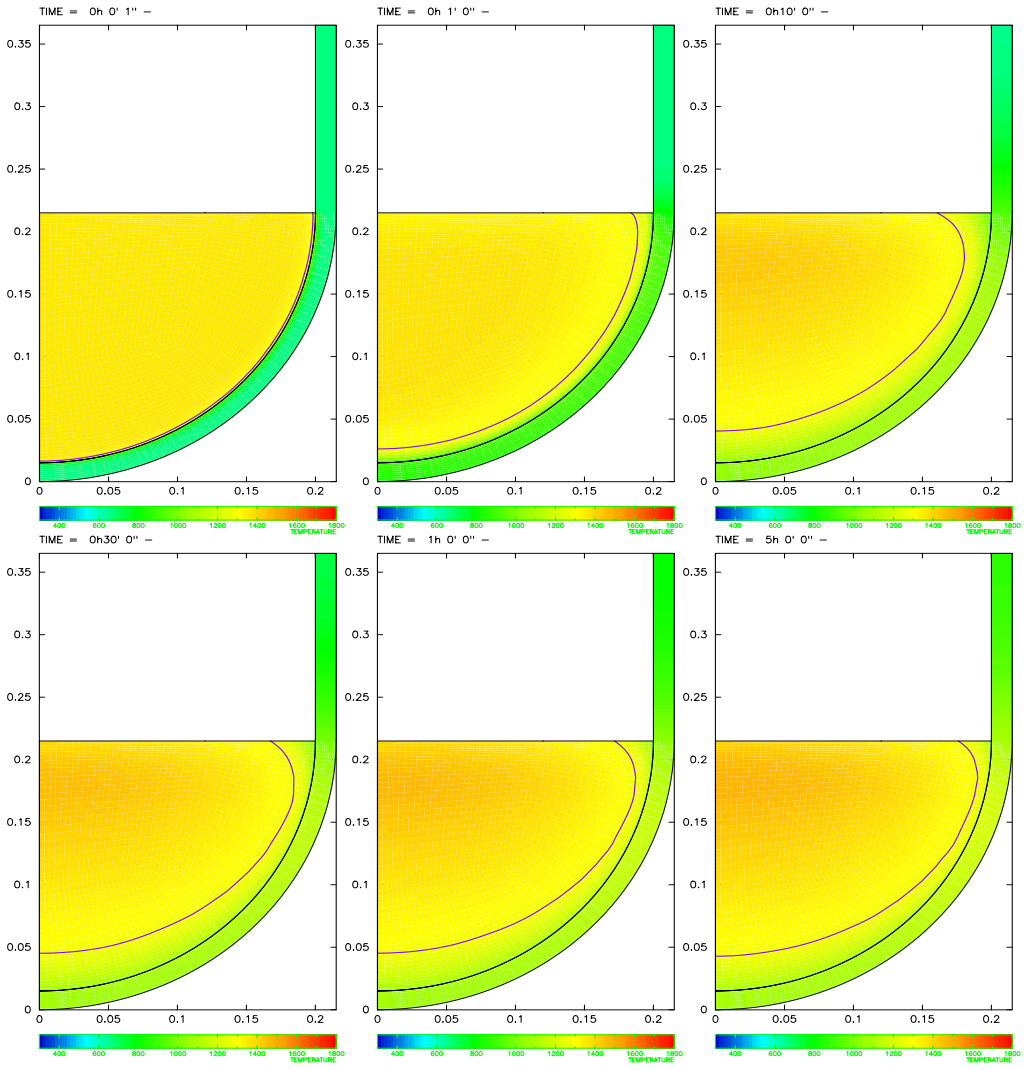

Fig. 4.14: *Evolution of crust formation and melt pool temperature. Pre-test calculation by the MVITA code.*

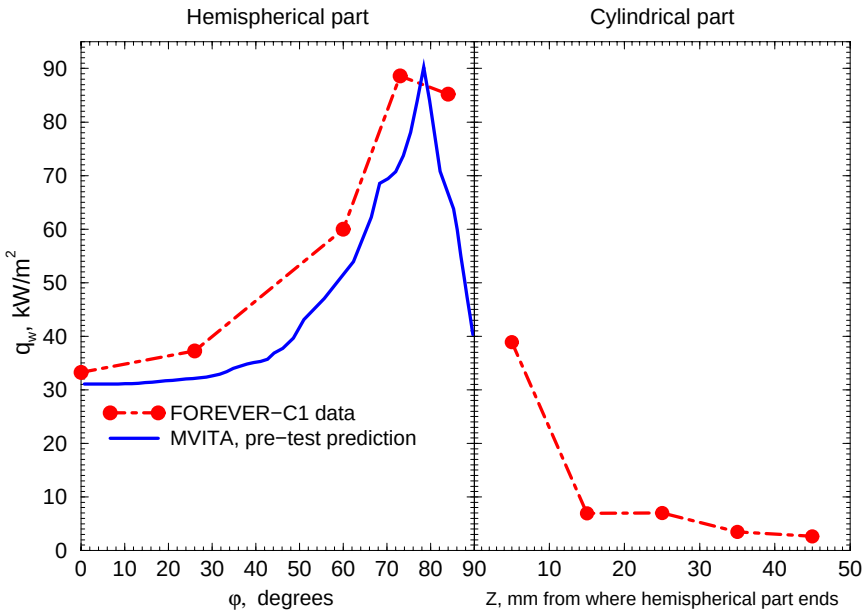

Fig. 4.15: *Evaluation of the local heat flux distribution on the vessel wall, the steady-state stage of the experiment (t=8 hrs.).*

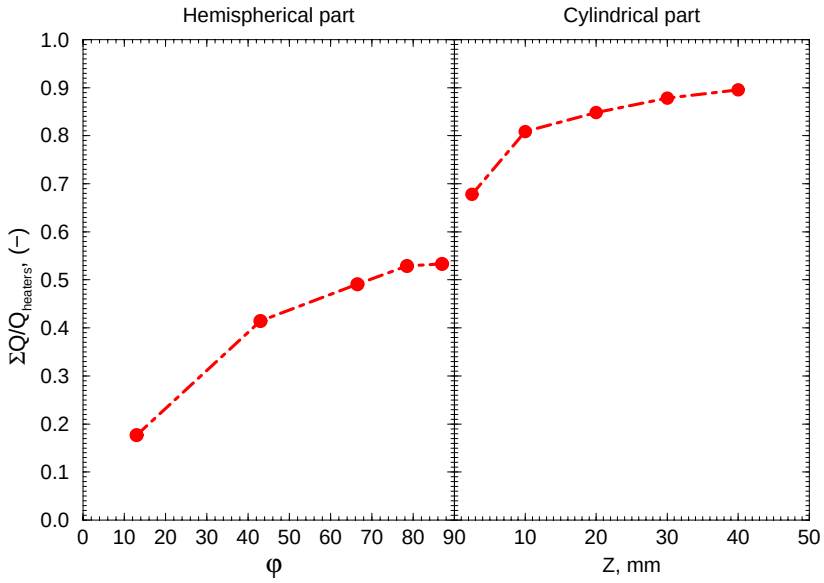

Fig. 4.16: *Evaluation of the local distribution of the heat losses through the wall, at the steady-state stage of experiment (t=8 hrs).*

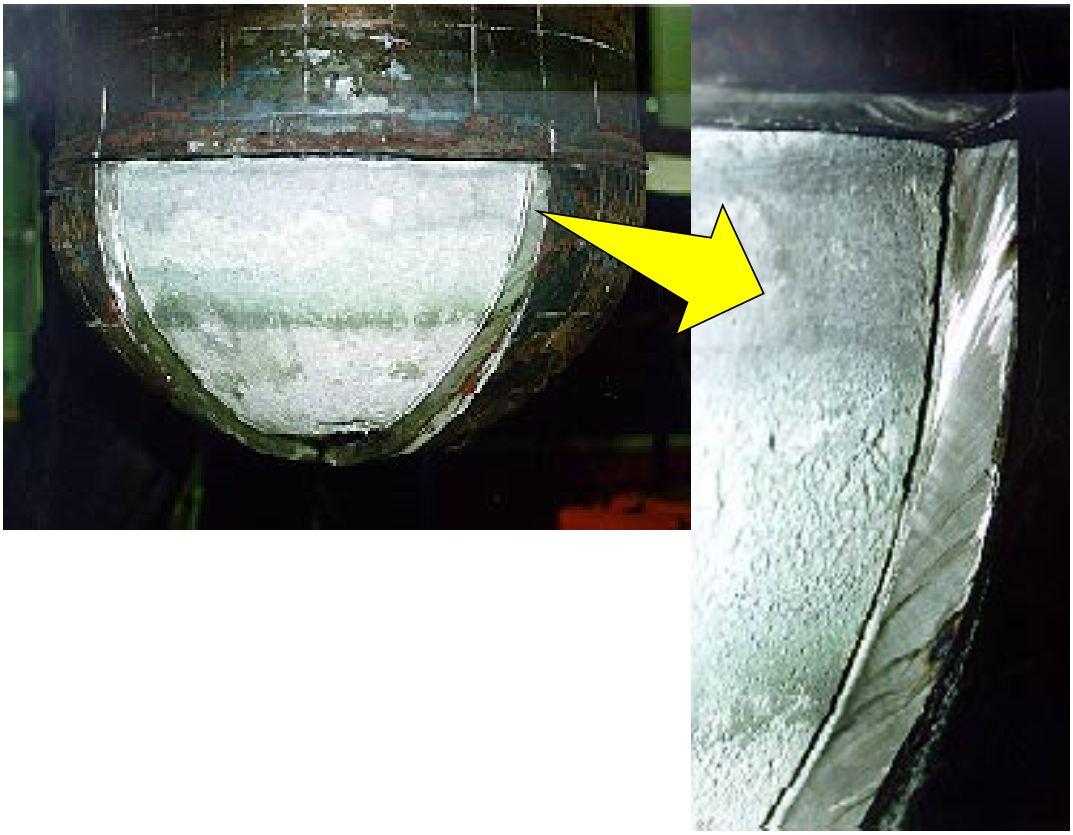

Fig. 4.17: *View of the solidified melt after the test.*

Bibliography

[Anderson et al., 1983] Anderson, L. E., et al., Effects of a Hypothetical Core Melt Accident on a PWR Vessel with Top-Entry Instrument, *EPRI IDCOR Program Technical Report 15.2A*, June 1983.

[Chambers, 1987] Chambers, R. S., A Finite Element Analysis of a Pressurized Containment Vessel during Core Melt Down, *SAND87-2183*, 1987.

[Chavez and Rempe, 1994] Chavez, S. A., and Rempe, J. L., 1994, Finite Element Analyses of a BWR Vessel and Penetration under Severe Accident Conditions, *Nuclear Engineering and Design*, **148**, 413-435.

[Chu et al., 1997] Chu, T. Y., Pilch, M. M., and Bentz, J. H., An Assessment of the Effects of Heat Flux Distribution and Penetration on the Creep Rupture of a Reactor Vessel Lower Head, *Twelfth Proceedings of Nuclear Thermal Hydraulics*, 1997 ANS Winter Meeting, November 16-20, 1997, Albuquerque, NM, 135-144.

[Degaltsev et al., 1997] Degaltsev, Yu., Karlov, O., Vasiliev, B., and Ostapov, E., Investigation of High-Temperature Strength of 15X2HMFA Vessel Steel in Temperature Range of 1000-1300$^{\circ}C$, *Rep. RP-TR-29*, Russian Research Center "Kurchatov Institute", OECD RASPLAV Project, June 1997.

[Dosanjh and Pilch, 1991] Dosanjh, S. S., and Pilch, M. M., Lower Head Creep-Rupture Sensitivity Studies, *Nuclear Science and Engineering*, **108**, 172-183.

[Duijvestijn, 1997] Duijvestijn, G., Birchley, J., and Reichlin, K., Prediction of Thermoplastic Failure of a Reactor Pressure Vessel under a Postulated Core Melt Accident, *Computers & Structures*, **64** (5/6), 1239-1249.

[Gruner and Schulz, 1989] Gruner, P., and Schulz, H., Investigations of the Primary Pressure Boundary within Risk Analyses of German PWRs, *SMIRT-10/M*, 1989.

[Hodge and Ott, 1989] Hodge, S. A., and Ott, L. J., Failure Modes of the BWR Reactor Vessel Bottom Head, *Boiling Water Reactor Severe Accident Technology Program, ORNL/M-1019*, May 10, 1989.

[Hodge et al., 1991] Hodge, S. A., et al., External Flooding of a BWR Reactor Vessel as a Late Accident Mitigation Strategy, *ORNL/NRC/LTR-91-9, Oak Ridge National Laboratory*, August 27, 1991.

[Kraus, 1980] Kraus, H., Creep Analysis, *John Wiley & Sons*, New York-Chichester-Brisbane-Toronto, 1980.

[Kwang, 1997] Kwang Jin Jeong, Dong Cheol Lim, Il Soon Hwang, Creep Rupture Behaviour of a PWR Lower Head in a Core-Melt Accident, *Transactions of American Nuclear Society*, 1997 ANS Winter Meeting, November 16-20, 1997, Albuquerque, NM, **77**, 273-274.

[Larson and Miller, 1952] Larson, F.R., and Miller, J., A Time Temperature Relationship for Rupture and Creep Stresses, *Trans. A.S.M.E.*, **174**.

[Müller and Kuhn, 1991] Müller, S., and Kuhn, W., Ermittlung von Festigkeits- und Verformungskennwerten des Stahls 20MnMoNi55 von Raumtemperatur bis 900$^{\circ}C$, *Forschungsvorhaben 1 500 806*, KfK-Auftrags-Nr.180601 P08A, Karlsruhe, 1991.

[Nourgaliev et al., 1997] Nourgaliev, R. R., Dinh, T. N., and Sehgal, B. R., Effect of Fluid Prandtl Number on Heat Transfer Characteristics in Internally Heated Liquid Pools with Rayleigh Numbers up to 10^{12}, *J. Nuclear Engineering and Design*, **169**, 165-184.

[Rempe and Walker, 1994] Rempe, J. L., and Walker, T. J., Overview of NRC Sponsored LWR Lower Head Failure Research Program, *Nuclear Engineering and Design*, **148**, 327-341.

[Rempe et al., 1993] Rempe, J. L. et al., Light Water Reactor Lower Head Failure Analysis, *Technical Report*, NUREG/CR-5642 EGG-2618, October 1993.

[Sainte, 1995] Sainte, C. C., Tensile Tests Characterization of Pressure Vessel Steel at High Temperatures (20 up to 950$^{\circ}C$), *Rapport DMT/95-236*, CEA Saclay, 1995.

[Schulz, 1995] Schulz, H., Progress Made in the Area of Reactor Pressure Vessel Behaviour, Proceedings of the *FISA 95 symposium on EU research on severe accidents*, held in Luxemburg from 20 to 22 November 1995, 187-200.

[Sehgal et al., 1998] Sehgal, B. R., Nourgaliev, R. R., Dinh, T. N., Bui, V. A., Green, J. A. and Karbojian, A., FOREVER Experiment on Thermal and Mechanical Behavior of a Reactor Vessel during a Severe Accident, *Proceedings ot the OECD/CSNI Workshop on 'In-Vessel Core Debris Retention and Coolability'*, Garching, Germany, 3-6 March, 1998.

[Sehgal et al., 1998] Sehgal, B. R., Nourgaliev, R. R., Dinh, and Karbojian, A., Integral Experiments on In-Vessel Coolability and Vessel Creep: Results and Analysis of the FOREVER-C1 test, *Proceedings ot the SARJ-98, Workshop on Severe Accident Research held in Japan*, Tokyo, Japan, 4-6 November, 1998.

[Sehgal et al., 1999] Sehgal, B. R., Nourgaliev, R. R., Dinh, and Karbojian, A., FOREVER Experimental Program on Reactor Pressure Vessel Creep Behavior and Core Debris Retention, *Proceedings ot the SMiRT-15, 15^th International Conference on Structural Mechanics in Reactor Technology*, Seoul, Korea, 15-20 August, 1999.

[Shah, 1986] Shah, V., Creep Rupture Failure of Reactor Pressure Vessel Lower Head During Severe Accidents, *International ANS/ENS Topical Meeting on Operability of Nuclear Power Systems in Normal and Adverse Environments*, Albuquerque, NM, September 29, 1986.

[Theofanous et al., 1995] Theofanous T. G. et al., *In-Vessel Coolability and Retention of a Core Melt*, DOE/ID-10460, v.2 (July 1995).

[Thinnes et al., 1994] Thinnes, G. L., Korth, G. E., Chavez, S. A, and Walker, T. J., High-Temperature Creep and Tensile Data for Pressure Vessel Steels SA533B1 and SA508-CL2, *Nuclear Engineering and Design*, **148**, 343-350.

[Thinnes, 1988] Thinnes, G. L., TMI-2 Lower Head Creep Rupture Analysis, *EGG-TMI-8133*, August 1988.

[Thinnes and Moore, 1989] Thinnes, G. L., and Moore, R. L., Comparison of Thermal and Mechanical Responses of the Three Mile Island Unit 2 Reactor Vessel, *Nuclear Technology*, **87**(4).

[Witt, 1994] Witt, R. J., Local Creep Rupture Failure Modes on a Corium-Loaded Lower Head, *Nuclear Engineering and Design*, **148**, 385-411.

Chapter 5

Vessel hole ablation and melt discharge

5.1 Introduction and Background

In the highly unlikely event of a severe reactor accident in a light water reactor (LWR), a potential exists for the formation of a particulate debris bed in the hemispherical lower head volume. With insufficient cooling, this debris bed could re-melt due to fission product decay heat, and a melt pool could be formed. The size, composition and temperature of this melt pool is highly dependent upon the severe accident scenario by which it is formed. Regardless of its formation however, the melt pool can attack the lower melting point vessel steel wall, and in the absence of either internal or external cooling, a failure location can develop. Recall that an 80-20% binary mixture of UO_2-ZrO_2 (corium) exhibits liquidus and solidus temperatures of approximately 2900 and 2825K, respectively, while the vessel steel will have a melting temperature of $\approx$ 1700K. Failure sites could develop as the result of melt attack at a penetration (control rod or instrument tube) [9], [10] [1] or, possibly, from partial erosion of the steel shell due to jet impingement [5], [19], as the melt relocates from the original core region. In addition, vessel creep, due to extended times at high temperatures, could potentially develop into a breach of the lower pressure vessel steel wall [20]. It should be noted here that as soon as a creep-induced failure site appears, the melt flow through the failure site will primarily determine the rate of the increase of the vessel failure area, at that site, since the pressure loading will be relieved.

As the melt discharges through the failure site, the ablation rate of the RPV steel will depend upon many factors. One of the most important of these will be the stability and the persistence of the crust layer, which forms between flowing melt material and the ablating pressure vessel. The crust presents a resistance to

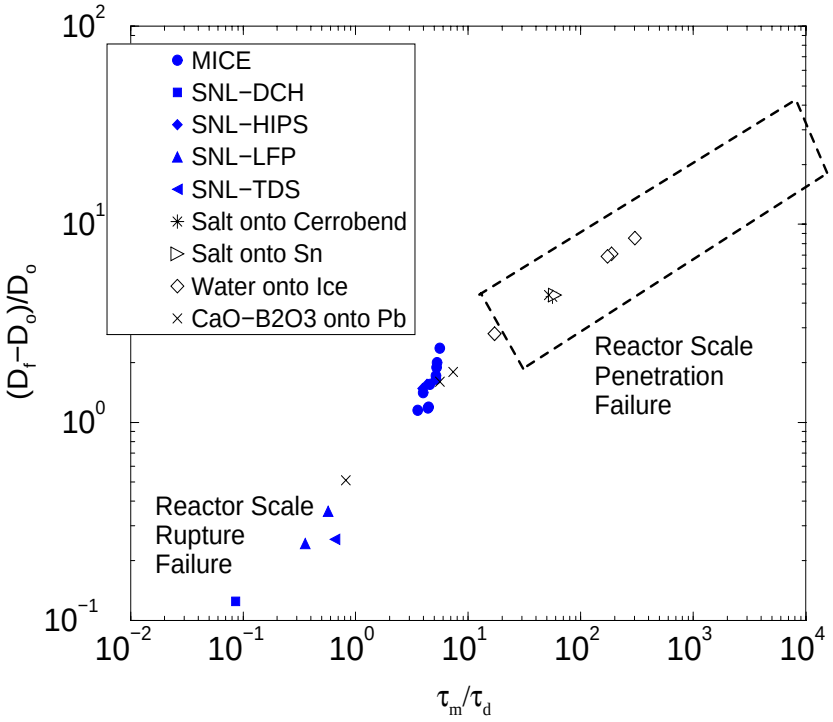

Fig. 5.1: Hole Ablation Scaling

heat transfer from the melt, thereby reducing the ablation rate. Crust formation depends strongly upon the initial melt superheat and the initial structure temperature. The mechanical stability of crust layers in this situation is highly uncertain, since the crust may be swept out along with the molten vessel wall material by the flow of the corium melt through the failure site.

Currently, there does not exist a substantial database of fluid and heat transfer process related to phase-change-hole-ablation dynamics. A review of related experiments can be found in the references by Pilch [7]. Many of these experiments were conducted at SNL in support of the DCH issue resolution [8], however, as shown in Fig.5.1 the limited hole enlargement in these experiments did not bring these data into the scale-range needed for the scenario of penetration failures in prototypical accident. The scaling methodology developed by Pilch was tested only against the thermite data obtained at SNL [7] . Past studies [8]-[21] employed the temperature difference between melt temperature and vessel melting point (Δ T = T_{melt}-$T_{mp,w}$) rather than that between the melt temperature and solidus temperature when a crust is formed (Δ T = T_{melt}-$T_{sol,m}$). That choice ensures conservatism, however, it is not clear how much conservation has been

added. More recently, Chu et al. [17] employed Δ T = T_{melt}-$T_{sol,m}$ for assessments of vessel hole ablation, in the THIRMAL code.

The experimental research program at RIT/NPS has been focused on reducing the uncertainties, associated with failure site ablation, from, both, an integral and a dynamic point of view; and to obtain data in the scale range needed for penetration failure. Employing the scaling methodology of Pilch [7], Figure 5.1 shows the data obtained at SNL and, the data obtained at RIT/NPS with various simulant melt and vessel wall materials. The data is plotted for Pilch's scaling parameter: ratio of hole enlargement/initial hole size on the y axis and the ratio of characteristic time for melt discharge through the original hole size/characteristic time for doubling of the hole size, due to the ablation process. Also shown by, a dotted rectangle, is the range of the x- and y-scale values needed for the reactor-scale penetration failures. It is seen that the RIT/NPS data falls in the scale range needed. As noted above, a variety of simulant materials were employed, in order to better understand the parameters of primary importance. Great care must be exercised when extrapolating the results from smaller, and thus often laminar flow, scaled experiments to the anticipated turbulent behavior for hole flow in the prototypical situation. A more detailed look at the scaling rationale and initial experiments can be found in the references of Sehgal et al. [13]-[14] as well as by Dinh et al. [3]. The earlier tests were conducted with the simulant materials PbO-B_2O_3 for melt, and Pb plates for vessel wall. Corrosion and health concerns prompted the switch to alternate melt simulants. The melt simulant CaO-B_2O_3 has been employed at both 4 and 20 liter volumes ($\approx$ 10 and 60 kg respectively). Additionally, a test program, using water as melt simulant, and salted ice plates as simulant for RPV wall, was conducted to obtain data at high Reynolds numbers for the melt flow. Some limited tests using binary salt mixtures onto low- melting-point-alloys and metals were also conducted. In addition, a two-dimensional transient, mechanistic model named "Hole Ablation Modeling In Severe Accidents" (HAMISA) was developed to describe the hole ablation process and determine the rate of melt discharge from the vessel to the containment as a function of time. This report will present the results of these experiments and the comparison of the experimental observations with the predictions obtained from the HAMISA model [3].

5.2 Experimental program (RIT)

5.2.1 Oxidic Melt Simulant

Since, the oxidic simulant CaO-B_2O_3 is non-magnetic, it is heated inside a steel crucible, using a 50kW/25kHz induction generator. The first set of experiments was conducted using a crucible and coil capable of 5 liter capacity, while sub-

Table 5.1: Thermo-Physical Properties of Simulant Materials.

Material	T_{liq}	T_{sol}	Δh_{fus}	k_l	k_s	ρ	$c_{p,l}$	$c_{p,s}$	σ	μ
	(K)		(kJ/kg)	(W/m.K)		(kg/m^3)	(J/kg.K)		(N/m)	(mPa·s)
Melt										
CaO-B_2O_3	1300	1250	460	3.0	2.0	2500	2200	1530	0.15	100-300
$NaNO_3$-KNO_3	553	493	255	0.45	0.6	1830	1560	1340	0.11	1.5-2
Water	273	273	33.3	0.6	2.45	960-990	4180	1800	0.06	1.7-0.31
Plates										
Lead	600	600	23.3	16	32	11344	129	129	0.44	1.4
Cerrobend	343	343	39.8	18	18	9670	184	146	0.35	3.3
Steel	1793	1793	247	27	35	7700	835	750	0.3	5.4

sequent experiments have employed a larger, 25 liter, arrangement. Oxidation at high temperatures is minimized with argon gas flow. Once the melt has been generated and the desired superheat obtained, the crucible is remotely tipped and melt poured into the test section, which is schematically depicted in Fig.5.2. Pour times from the furnace to test section are 10 seconds or less. This pour time must be kept small in order to minimize melting of the upper surface of the test plate. The test section walls are heated to minimize heat loss, while a distributor plate precludes any direct impingement of the melt onto the lower instrumented plate, representing the vessel wall.

A mechanical plug mechanism is inserted into the initial failure site (D_o) and is removed, once all of the melt has been delivered from the furnace. Initial hole diameters of both 10 and 20 mm were used. For the 16cm ID test section, a 5 liter melt provides roughly 25cm of melt pool height. Both lead and aluminum plates have been employed as plate materials. Standard 1mm OD K-type thermocouples were embedded within the plates at known radial and axial locations, in order to observe the progression of the melt front and to deduce ablation velocities. The plate size was 0.25x0.25m square, and tests with plate thicknesses of 30 and 40mm were performed for Pb, while thicknesses of 10 and 20 mm were employed when using Al.

The melt was formed from powdered CaO and H_3BO_3, with the water content of the acid evaporated during heating. Chemical analysis of post-test samples revealed reasonably good ($\pm$2%) control of the mixture composition and thus the liquidus, solidus temperatures and the in-between mushy-zone. Some iron (Fe_2O_3) impurity from the induction crucible has been observed, however its mass percentage has been found to be less than 5%. The presence of the iron compounds serves to slightly lessen the solidus and liquidus temperatures from their reference values. The corrosion characteristics of the melt-crucible are good, allowing for repeated use of the same crucible over several tests. The melt temperature is nominally 1423-1473K which corresponds to a melt superheat in

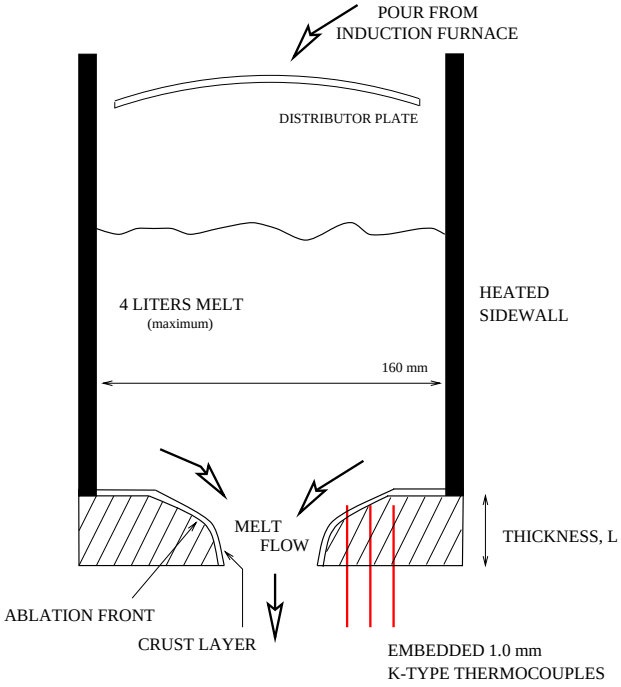

Fig. 5.2: Experimental Arrangement

the range of 125-175K. Thermophysical properties, for the melt and the vessel simulant materials employed in the current test program, are provided in Table 5.1.

Results from the experiments using CaO-B_2O_3 indicated a strong multi-dimensional behavior of the ablation front. Representative tests performed with a 40mm thick Pb plate provided some insight into the failure site enlargement characteristics. Temperature traces from several of the thermocouples at equivalent radial locations are given in Figure 5.3 at specific depths from the upper surface. The final shapes of the ablated Pb plates were pressed into epoxy for measurement and assessment. In one test, the 10mm diameter initial hole size was enlarged to a roughly circular 50mm hole at the bottom surface. Midway through the same 40mm thick plate, the final hole was $\sim$60mm in diameter while the uppermost surface was pitted and nonuniform due to the time period of melt-substrate contact prior to flow in the hole. That is to say, in this test, the upper surface was not entirely representative of ablation dynamics, since it suffered some melting prior to removal of the mechanical plug. A second similar test resulted in nonuniform melt discharge and a final elliptical shape hole of dimensions $\sim$50x60mm diameter. In this experiment, only a slight melt flow was observed for the first 30 seconds, however this was followed by an abrupt and rapid discharge period.

Several important aspects are evident from the temperature traces. First, the

ablation front speed can indeed be obtained from the data and secondly, there is clear evidence of the crust existence during the course of the tests. Ablation front velocities are in the range of 5mm/s at the upper surfaces and decrease to roughly 1mm/s near the bottom of the plate. Crust behavior is seen in the temperature traces as a momentary ”leveling off” in the temperature rise followed by a second rapid rise up to the melt temperature. That is to say, as melt discharge continues, the thermocouples indicate the passing of a crust layer past their location.

Several tests were conducted using the oxidic melt discharge through aluminum plates. However, due to the high thermal conductivity of Al, these tests did not result in ablation but rather a simple discharge of the melt through the hole, coupled with creep of the plate due to the high temperatures and melt mass loading. Pre-heating and insulation of the Al plates did not serve to alter this behavior.

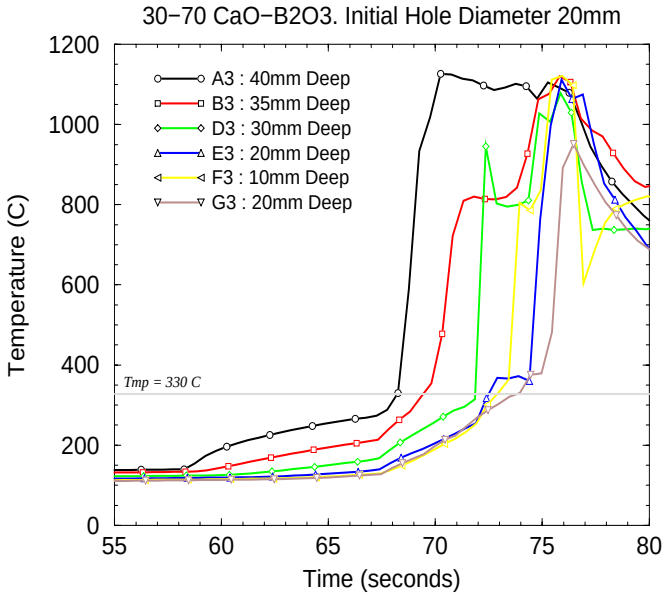

Fig. 5.3: Temperatures - Test 0409

5.2.2 Water as Melt Simulant

A second series of experiments were conducted using water as the melt simulant and salted ice as the simulant vessel wall material. The salt, used in a 10 w/o concentration, allows for a lower temperature melting point (-9^{o}C) and also provides the added benefit of stabilizing the ice block during freezing.

The salt-ice plates were formed in a low temperature (as low as -60^{o}C) freezer and for many of the tests K-type thermocouples were embedded at known distances from the pre-formed cylindrical hole. A test section of 80 liter capacity was used, which employed a slide gate below the melt volume. In this fashion, the water in the test section could be separated from the instrumented ice plate prior to the start of the test. Additionally, the melt simulant volume could be heated or cooled using a separate tank system. Upon opening of the slide gate, the melt (water) comes into contact with the lower plate and begins to ablate the hole as flow is discharged through it. The tank water level was measured, versus time, to provide an indication of the melt discharge rate. A representative trace of temperatures from the embedded thermocouples in the ice plate is shown in Figure 5.4. These thermocouples were separated by a distance of 5mm at a depth of 25mm from the top surface. The ablation front speeds measured in this case range between 3.5-4.0$\cdot 10^{-3}$ m/s. For illustration, accounting for the sensible and fusion heat of the ice plate reveals that an ablation speed of this magnitude corresponds to a heat flux of roughly 0.25 MW/m^2. In addition, the melt discharged from the ablated hole was collected and its mass measured versus time.

Table 5.2 provides a listing of all tests conducted using water and ice as simulant materials. The last column in Table 5.2 shows the measured final hole size immediately after the melt volume has exited. The designation ”B” refers to the bottom of the salt-ice plate while ”T” refers to the top. Note that the dimensions provided for the final hole size are averaged values since the final hole geometry is not perfectly symmetrical. As can be seen, the tests encompassed variations upon the initial hole size, the melt temperature and the plate thickness. The variability in the initial salt-ice plate temperature is due to the time required to install the plate into the test section, upon removal from the low temperature freezer.

The general observation from these tests was that the final hole geometry was mainly cylindrical, that is to say, there was no significant difference between the diameter at the top or bottom of the salt-ice plates. This differs from that for the earlier oxidic melt experiments where the final plate shapes were multidimensional, exhibiting a much wider entrance diameter (see for example the plate geometry when using PbO-B_2O_3 as melt in Sehgal et al. [14]). This aspect points to the melt viscosity as playing a significant role in the ablation dynamics.

Some of the water-salt-ice tests employed very low melt temperatures, which resulted in a clean ice crust to form on the upper plate surface and within the ablation hole. This crust layer was measured (post-experiment) to range from 2-5mm in thickness. Obviously, the ablation rates were significantly less for these cases due to the crust formation.

Table 5.2: Water-Salt-ice Hole Ablation Tests

Test	w/o Salt	D_o (mm)	δ_{plate} (mm)	T_{melt} (^oC)	$T_{o,plate}$ (^oC)	V_{melt} (liters)	Discharge Time (s)	D_{final} (mm)
0917A	10	20	50	23	-30	78	16	72 B / 72 T
0917B	10	20	50	41	-28	78	12	65 B / 72 T
0918	10	10	60	48	-20	78	14	87 B / 94 T
0919	10	10	60	46	-33	78	15	86 B / 90 T
0923	10	10	60	80	-40	76	12	96 B / 90 T
0925	10	20	60	3	-30	76	77	25 B / 28 T
1002	10	10	38	11	-41	78	27	60 B / 64 T
1015	0	10	80	44	-24	78	14	94 B / 100 T
1016	10	20	79	91	-31	78	10	105 B / 103 T

5.2.3 Other Simulants

To examine the influence of melt viscosity, a pair of similar experiments were conducted using paraffin oil as the melt simulant, in conjunction with the 10 w/o salt-ice plate, whose particulars are shown in Table 5.3. Even with heating of the paraffin oil melt, and, thus, decreasing the melt viscosity and increasing the Reynolds number, the ablation of the initial 20mm hole was not much increased. The final shape of the hole was much different from that observed with the water-salt-ice tests in that the upper region of the hole exhibited a curved or sloped geometry while the bottom of the hole was cylindrical. This points to the fact that because of the very long discharge time, and thus contact time between melt and plate, that multidimensional ablation on the upper surface becomes significant. That is to say, conduction from the melt to the upper plate surface plays a greater role. Also, the higher melt viscosity and Pr number create a thicker dynamic boundary layer and, thus, diminish the role of surface roughness in augmenting heat transfer. This in turn implies a higher entrance-region heat transfer and can also account for the higher ablation rates seen at the upper region of the hole.

Table 5.3: Paraffin Oil-Salt-ice Hole Ablation Tests

Test	w/o Salt	D_o (mm)	δ_{plate} (mm)	T_{melt} (^oC)	$T_{o,plate}$ (^oC)	V_{melt} (m^3)	t_d (s)	D_{final} (mm)
1023	10	20	60	29	-37	73.8	128.8	22 B / 30 T
1024	10	20	63	45	-38	69.3	79.7	28 B / 42 T

Another test series employed the binary salt mixture of $NaNO_3$-KNO_3. Both eutectic as well as mushy zone regions of the binary salt mixture phase diagram were employed by varying the composition. In these tests the melt is formed inductively in a 25 liter steel crucible. Similarly to the oxide tests, the melt is poured into the heated test section and the plug mechanism removed from the plate. The

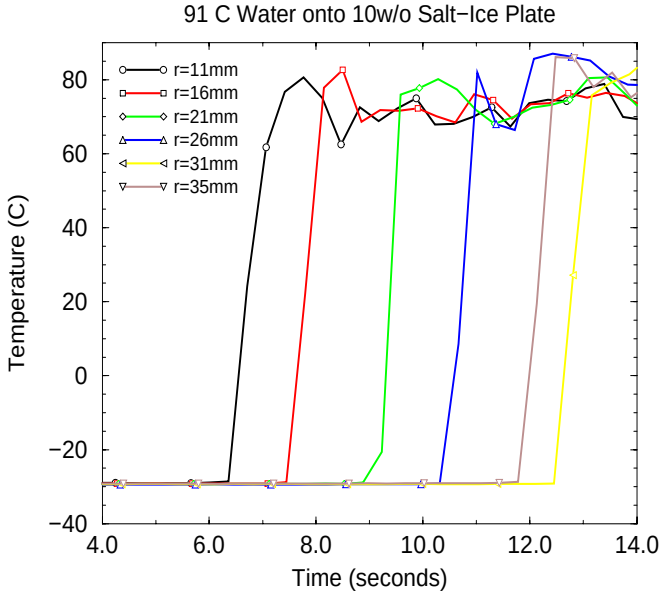

Fig. 5.4: Temperatures - Test 1016

most recent results from these tests can be found in Table 5.4. Comparison of test 1205 with that of 1211 indicates little, if any effect, which can be attributed to the fact that the former test employed a $\approx 60^o$C "mushy-region".

More details about binary salt-metal hole ablation tests are provided in Appendix E of the present report.

Table 5.4: $NaNO_3$-KNO_3 Salt-Metallic Hole Ablation Experiments

Test	Melt Compos.	Plate Material	D_o (mm)	δ_{plate} (mm)	T_{melt} (^{o}C)	$T_{o,plate}$ (^{o}C)	V_{melt} (m^3)	t_d (s)	D_{final} (mm)
1129	20%-80%	Cerrobend	10	50	450	25	25	12	65 B / 63 T
1205	20-80	Tin	10	50	420	25	25	11	56 B / 54 T
1211	50-50	Tin	10	50	440	50	23	11	60 B / 68 T

5.3 HAMISA code development and validation

This section summarizes the findings from research conducted at the Royal Institute of Technology - Division of Nuclear Power Safety (RIT/NPS) concerning reactor pressure vessel hole ablation during a hypothetical light water reactor (LWR)

severe accident. The major physical mechanisms which govern the vessel hole enlargement during core melt discharge from the reactor vessel lower plenum were identified and analyzed. Substantial insight into these processes has been gained. The understanding achieved has been incorporated into the mechanistic HAMISA model with excellent comparisons to experimental data. The remaining uncertainties in prototypical reactor assessments are primarily attributable to the melt conditions and geometrical aspects at the time of vessel failure.

5.3.1 Introduction

The configuration of the in-vessel melt debris/pool at the time of lower head failure will be highly dependent upon the accident progression scenario variables up to the point in time of vessel failure. The extent of core-melt relocation, and the possibility of melt quenching due to the presence of coolant in the lower plenum regions, are two examples of such variables. The melt ejection out of the vessel would be governed by the driving forces (vessel over-pressure, hydraulic head of the melt pool) as well as the melt flow and heat transfer-induced ablation of the lower head wall around the initial failure site. The lower head failure location may affect the discharge flow, although eventually, most heat-generating material could be ejected. The melt discharge rate and other characteristics (composition, superheat) are important for determining the consequences of the ex-vessel fuel-coolant interactions (FCIs). Thus, an improved understanding of lower head ablation during melt discharge through a local failure site, is a necessary step towards defining the progression of the ex-vessel FCI process [6].

We consider the vessel ablation process, which increases the size of a hole, or a local failure, in the wall of the reactor pressure vessel (RPV) lower head, as the core melt is discharged into the containment (see Fig.5.5). Depressurization of the reactor coolant system is assumed to occur prior to vessel failure. This is a wholly justifiable assumption for the Nordic BWRs since primary system depressurization is a required accident management procedure under the circumstances considered. Global vessel failure (i.e. a nearly complete breach of the reactor pressure vessel) is not considered here, since failure of penetration tubes (control rod or instrumentation tubes), or local vessel creep failure, are much more likely failure mechanisms [11].

Previous work & experimental background A review of experiments conducted in the past, mainly at Sandia National Laboratory (SNL), can be found in the paper by Pilch [8]. Pilch also proposed a scaling methodology, which indicated that the SNL experiments did not fall in the prototypic-condition parameter range for penetration failures. A review of concepts employed in relevant reactor

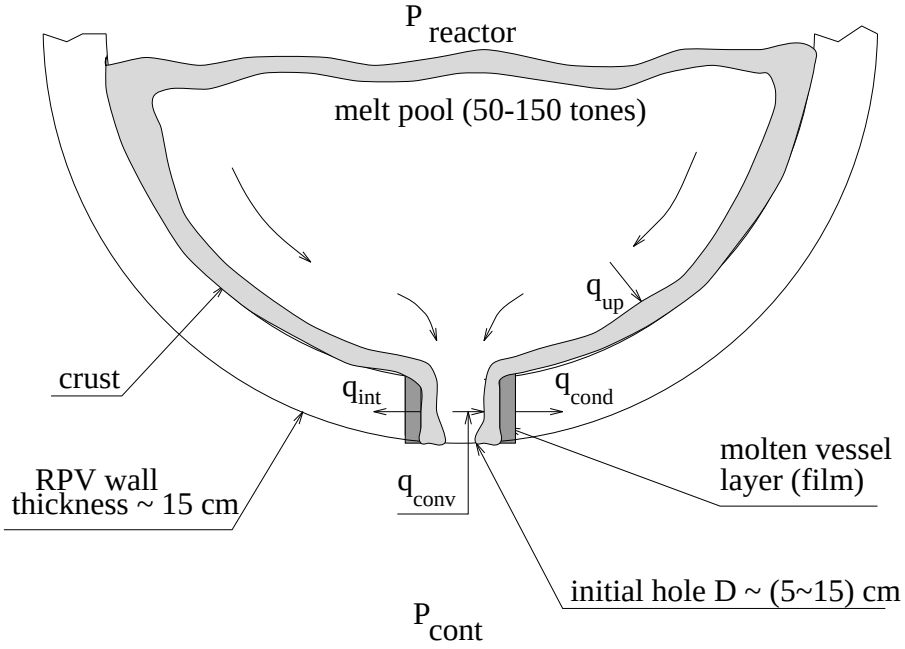

Fig. 5.5: Physical picture of hole ablation phenomenology.

safety assessments can be found in [3] and will not be repeated here.

Model development and experiments have been pursued at RIT/NPS in order to gain an improved understanding of the complicated melt-vessel interaction processes which occur during vessel failure and melt discharge. Several aspects which govern the hole ablation process such as vessel heat conduction and phase change, melt thermal-hydraulics in the lower plenum, prior to, and during, the discharge process, melt discharge flow characteristics and gas blowthrough, and crust formation and its stability, were addressed in [3] [15]. The continued enlargement of the initial failure site in the RPV lower head is determined by these processes. It was found that not only integral scaling parameters (timing and final hole opening) matter, but also the scaling groups for separate component processes may be able to change the physical picture under consideration. Furthermore, it was found that experiments are needed to resolve phenomenological uncertainties associated with in-hole convective heat transfer, crust formation and stability, and discharge flow rates.

In earlier RIT/NPS experiments, molten binary oxidic materials ($PbO - B_2O_3$ and $CaO - B_2O_3$) were employed as working fluids. Recent experiments have employed more prototypic ranges of the integral scaling parameters by using several pairs of simulant materials for melt and plate, namely [molten binary salt mixtures-Cerrobend], [water - salt-water ice], [paraffin oil - salt-water ice] [16]. Also, large variations in fluid Prandtl number and discharge flow Reynolds num-

ber were covered. These experiments provide a necessary database for advancing the level of knowledge concerning the governing mass and energy transfer mechanisms and for validating the predictive capability of the various empirical correlations which must be employed for such a problem.

Objectives. Analyses are performed for cases in which a core melt pool was formed inside the RPV lower head, prior to the melt discharge. The primary objectives of this section are to identify and to analyze physical mechanisms which may limit the dynamics of the vessel hole enlargement, and hence to provide bounding assessments of melt discharge flow rates used in quantification of the consequences of ex-vessel fuel-coolant interactions [6].

Method and work performed. First, limiting mechanisms of vessel hole enlargement will be identified, with particular emphasis on scenario- and reactor design-dependent aspects. Second, the experimental observations and data are employed to assess the major phenomenological uncertainties. Next, the HAMISA model [3] and computer code, which has been developed at RIT/NPS, is used to perform simulations. The new information and experimental data obtained was used to validate the performance of the HAMISA model under high-Reynolds-number conditions. In particular, the influence of phase change on convective heat transfer, and the effect of a finite vessel wall thickness on the discharge coefficient were introduced into the HAMISA model.

Reactor predictions of the vessel hole ablation and core melt discharge processes, and discussion of their implications, while accounting for limiting mechanisms, are presented in the following sections.

5.3.2 Phenomenology of Hole Ablation and Limiting Mechanisms

The phenomenology of hole ablation and related processes can be decomposed based as follows:

- **(i)** convective heat transfer in the discharge hole and in the lower head melt pool during the discharge process;
- **(ii)** vessel heat conduction and phase change;
- **(iii)** discharge flow characteristics.

In the paper by Dinh et al. [3], several important phenomena were examined, namely crust existence, entrance and property effects on laminar and turbulent convective heat transfer in the discharge hole, gas blowthrough and multidimensional heat conduction and phase change in the vessel wall.

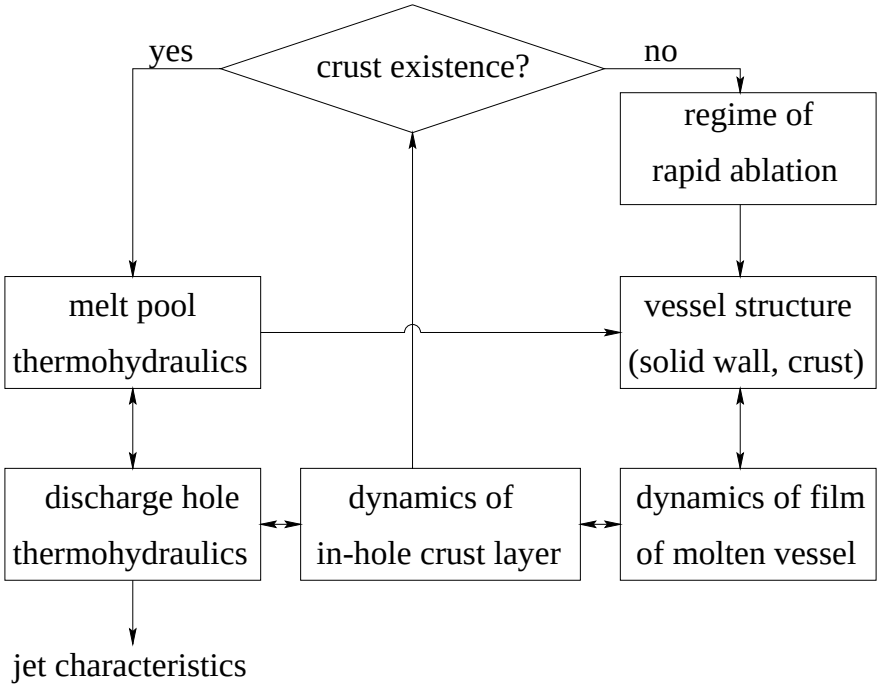

Fig. 5.6: Hole ablation phenomenological scheme.

However, there remained phenomenological uncertainties related to **(a)** crust behavior under high-Reynolds number flow conditions, **(b)** convective heat transfer with phase change (freezing/melting) boundary conditions, and **(c)** discharge flow rate (or discharge coefficient) through a hole of finite length. Resolution of these phenomenological uncertainties is discussed in the next section, while in this section we focus on uncertainties associated with scenarios of accident progression and specific design features applicable to the reactor lower plenum.

In-hole crust growth and stability. Initial calculations which employed an earlier version of the HAMISA model (version HAMISA.0) indicate that the hole ablation rate depends strongly on whether a crust layer exists as a thermal boundary resistance to the in-hole melt flow. In reactor cases, discharge of some $9m^3$ of core melt may lead to final hole sizes up to 0.6m for the case without crust and 0.3-0.4m when a crust layer is present. More importantly, hole enlargement dynamics are completely different for the two cases, such that the characteristic time of the

melt discharge process for the case without crust is on the order of 1 second or less, while that in the case with crust can extend to several tens of seconds. Therefore, the limiting mechanisms of hole ablation are based on phenomena which ensure crust growth and stability.

Initial debris crust layer in the lower plenum. In previous reactor safety assessments (including the modeling effort of ref. [3]) the presence of an initial debris crust layer (IDCL) in the reactor pressure vessel lower plenum was ignored. Simulations of debris heating and melt pool formation in the RPV lower head, performed using the MVITA code of RIT/NPS [2], revealed that a thick crust layer exists at the lowermost region of the reactor lower plenum. This crust layer may be as much as 0.2m thick at the moment of melt pool formation and persists at a thickness of 0.05m, until circumferential vessel rupture is predicted. It should be mentioned that neither the failure of the lower head penetrations (instrument nozzles or control rod drive mechanisms) nor any external heat sink was simulated using the MVITA code.

Hole ablation dynamics are affected by the IDCL through a number of heat and mass transfer mechanisms, as described below.

- The IDCL is a heat capacitor and as an oxidic material it will exhibit a relatively large heat of fusion. Opening of the intial hole (in both the IDCL and the vessel wall) requires melting of both the wall and the debris crust which lies above the vessel.

- For the section of the hole which is in the IDCL, the question of ”crust existence” plays no role. Subsequently, the melt-to-hole heat fluxes, and thereby the ablation rates, in this portion of the hole will be limited primarily by the melt superheat.

- Ablation of the hole section in the IDCL supplies a mass of remelted crust into the melt flow boundary layer before it enters the hole section in the vessel wall. In addition, heat transfer from the melt flow to its crust lowers the melt flow boundary layer temperature. According to estimates of conduction-controlled phase change behavior at the contact between melt and steel vessel ([3]) the lower melt flow boundary layer temperature will significantly reduce the characteristic time necessary for crust formation. Under such conditions, it was found that crust growth dominates crust remelting even at the entry region of the vessel-hole section.

- Entrance effects on the melt flow heat transfer, for the case of a phase change boundary, will be substantially reduced or eliminated when an IDCL is present.

- Given all of the above mechanisms, particularly the addition of the "cool" melt to the boundary layer and the reduced entrance effect, it is evident that vessel wall heat fluxes will decrease with increasing IDCL thicknesses.

- Also, the low velocity of melt flow in the lower head pool and the relatively low superheat of melt located next to the IDCL will result in little if any re-melting and erosion of the IDCL by the pool flow. Furthermore, the IDCL is a thermal resistance to energy transfer from melt pool to the vessel wall, particularly during the discharge period. Consequently, it limits multi-dimensional pre-heating of the vessel prior to ablation.

The arguments made above clearly demonstrate the important role of an initial debris crust layer in limiting the dynamics of the vessel hole enlargement during the melt discharge process.

5.3.3 Validation

The HAMISA model is validated against low and intermediate-temperature experiments. The HAMISA model includes zero- and one-dimensional models of transient heat transfer in the experimental melt pool prior to and during melt discharge. Options included in the HAMISA model account for specific effects of experimentation, such as melt pouring into the vessel and growth of the melt crust prior to melt discharge, heat removal from the melt pool to upper and side structure of the vessel, for example. One-dimensional modeling of convective heat transfer in the discharge hole and a two-dimensional model of heat conduction and phase change in the initial debris crust layer and vessel wall are implemented in the present version [3]. Three component models, namely (i) discharge coefficient, (ii) convective heat transfer with phase change boundary condition in the discharge hole and (iii) pool-crust interface heat transfer, were significantly improved, based on insight obtained from relevant experiments (see Fig.5.7).

Discharge flow rate calculations

Standard hydraulic pressure losses will necessarily be associated with the discharge of the melt volume through the vessel failure hole. Earlier considerations, such as that found by Pilch in [8], accounted for the in-hole melt flow pressure loss by the use of common discharge coefficients, C_d. In [8] a value of 0.6 is recommended for the discharge coefficient based upon flow through a sharp-edged orifice coupled with the fact that it provided good agreement to vessel rupture failure tests. However, for penetration-type failures the melt must flow through a hole of at least a thickness equivalent to the RPV and in the case of an IDCL,

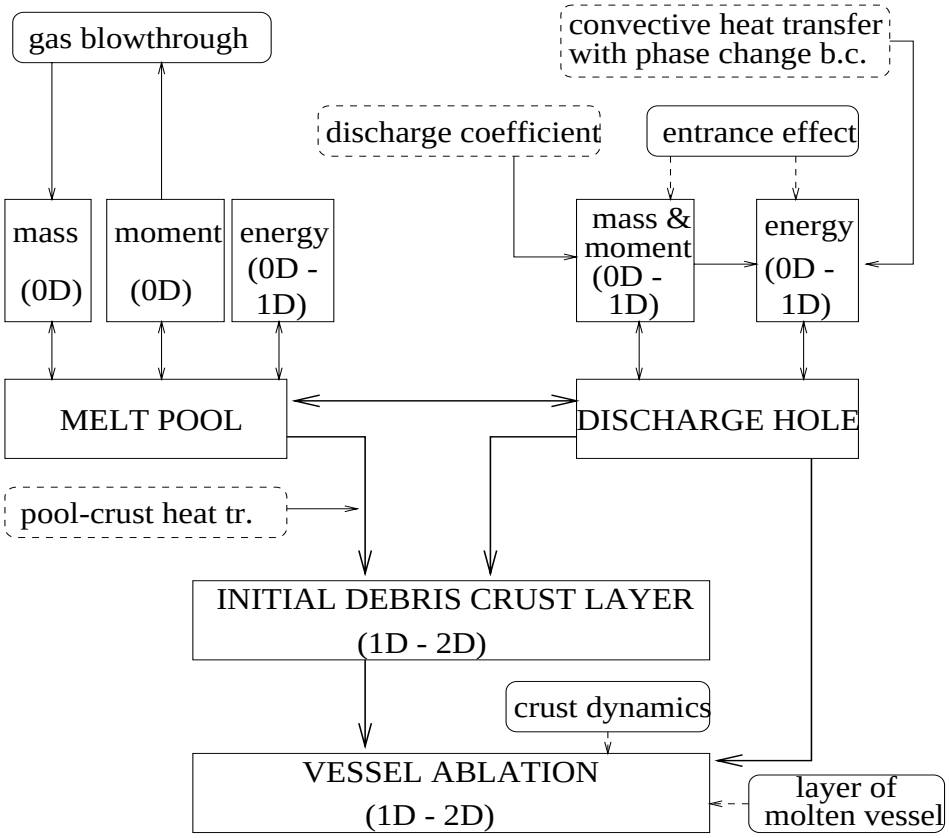

Fig. 5.7: Component models of the HAMISA model.

over a longer distance. This is not characteristic of flow through an orifice and the longer in-hole flow distance will present both entrance and exit losses along with the frictional pressure losses for the in-hole section of flow.

A series of separate effects tests were conducted in order to better examine the role of frictional pressure losses for conditions applicable to hole ablation dynamics. A 90 liter tank was assembled with a bottom plate thickness of δ_w in which a central hole of diameter, D, was drilled. Both the thickness and hole diameter of the plate were varied during these tests to cover a range of δ_w/D from 0.08 to 4 using 15 and 25mm diameter holes. Such an aspect ratio for melt flow is representative of the ranges envisioned in reactor scale penetration failures. The working fluid was water which ranged in temperature from 3 to 70^{o}C. Fluid discharge through the plate hole was initiated by removal of a plug mechanism and the drop in water level was measured to determine the discharge velocity in time (in some tests the mass discharged was collected and measured in time with a scale connected to a PC data acquisition system). Since there was no tank overpressure, the experimental discharge coefficient could be calculated in time

as;

$$C_d = \frac{U_{exp}}{\sqrt{2 \cdot g \cdot H}} \tag{5.1}$$

Variation in the tank water temperature allowed for a Pr number variation from 2 to 12 and the measured discharge velocities yielded a Re number range from 16,000 to 250,000. Excellent repeatability was observed throughout the test series thereby providing confident statistical measures.

Results from over 50 experimental runs are summarized in Fig.5.8 where the discharge coefficient is plotted against the measured discharge velocity. Each point represents an average of all tests conducted with identical water temperature and δ_w/D. It is evident from these results that the use of 0.6 for the discharge coefficient will underpredict the melt ejection velocity. Only for the conditions of very thin plate thicknesses, thus approaching similarity to an orifice, were values of 0.6-0.7 realized. Considering the dimensions of RPV penetrations and wall thickness (see for example Fig.5.5) the discharge coefficient can be as much as 70% (and more) greater in comparison to that predicted for an orifice.

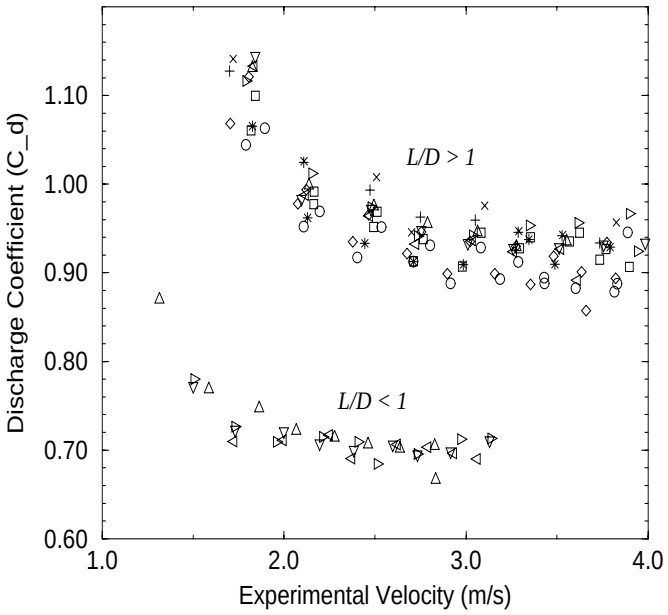

Fig. 5.8: Experimental discharge coefficient as a function of discharge velocity in RIT tests.

In light of these experimental observations an improved model for the in-hole pressure drops was incorporated into the HAMISA program. The discharge flow

rate is determined from the following equation for flow through a hole of finite length.

$$U = C_d\sqrt{\frac{\Delta P}{\rho}} = \frac{1}{F\rho}[\sqrt{2(P_{RPV} - P_{cont} + \rho g H)}] \tag{5.2}$$

where F is the overall form loss coefficient and the driving pressure difference is that between the primary system and containment. The total form loss is a summation of the contraction (F_{cont} ~0.45), in-hole ($F_{in-hole} = f(Re)$) and expansion losses (F_{exit} ~1.0) with values taken from classical fluid dynamics. Friction for the in-hole flow is considered flow-regime dependent and several correlations have been provided for depending upon the value of the flow Re number.

The discharge experiments reported here certainly do not cover all aspects which may be applicable to reactor vessel failures. Other factors such as the melt viscosity and surface tension as well as the possibility for a rounded (smoothed) entrance geometry may reveal further insight which can then be incorporated into predictive tools such as the HAMISA model.

It may be argued that the sensitivity of the hole ablation process to the failure location melt flow pressure drop is not large. That is to say, that accounting for the hole entrance, in-hole and exit losses does not significantly influence the final vessel hole size. This arises as a result of two competing ablation mechanisms. In the first, an increased value of the discharge coefficient will produce increased melt ejection velocities for equivalent hydraulic driving forces. This in turn reduces the *time* of melt flow ablation for a given melt volume. In the second mechanism, the increased melt velocity will result in enhanced convective heat transfer from the flow to the ablating wall (increased Re) thereby increasing the *rate* of vessel ablation. Combined, these two mechanisms may indeed only slightly influence the final predicted hole size but the vessel melt source rates for ex-vessel FCIs may be significantly affected. Therefore, a more mechanistic model which captures both effects, such as the one proposed and incorporated in the HAMISA code, is preferable, especially when consideration of an IDCL is made.

Convective heat transfer in the discharge hole

As a result of recent RIT experiments involving both hole ablation and jet impingement with phase change [16], [5] a new model for heat transfer from the flowing melt to the solid interface has been proposed. Dinh and co-workers [4] have shown that the surface roughness associated with the phase change process enhances energy transfer from the melt to the ablating structure. In a series of water-ice and water-salt ice jet impingement experiments it was recognized that the surface roughness, resulting from the phase change of the melting plate material was a controlling factor in the transition from laminar to turbulent heat transfer

regimes in the jet stagnation zone. Experimental observations from the jet impingement research may then be extended to the vessel ablation conditions, considered here, due to the underlying similarities in the heat transfer mechanisms between the two processes.

The change of phase of an ablating wall material will produce a roughened surface, regardless of whether or not the conditions for crust layer existence are met. This, in turn, influences the hydrodynamic and thermal boundary layers which must develop and flow past the surface. When the surface roughness becomes thicker than the hydrodynamic sublayer the convective heat transfer will be enhanced, and more importantly, the dependence upon length scales may be reduced or eliminated altogether. Determination of the convective heat transfer from the melt flow to the crust interface will, from classical considerations, depend upon the in-hole skin factor (C'_f), and the Re and Pr numbers for the flow. Under the rough surface conditions associated with phase change, the viscous sublayer is believed to be thin and the skin factor of the surface will become independent of Reynolds number as is the case for common pipe flow. It is clear that the impact of the surface roughness will be significantly influenced by values of the melt fluid Pr number since this number reflects the relationship between the inertial and thermal boundary layers.

For turbulent flow conditions, which is the case in the prototypical situation, the energy transfer can be determined using the Reynolds analogy [12]

$$h = \frac{1}{2} U_\infty \cdot \rho \cdot C_p \cdot C'_f \tag{5.3}$$

For rough surfaces the value of C'_f may range from 0.005 to 0.007. Eq.5.3 can be easily rearranged as

$$Nu = \frac{1}{2} \cdot Re \cdot Pr \cdot C'_f = \frac{1}{2} C'_f \cdot Pe \tag{5.4}$$

Notice that the combination of the Re and Pr numbers removes any influence of the fluid viscosity, and the governing dimensionless group then becomes the Peclet number.

Consideration of the aforementioned surface roughness effects for the case of RPV ablation dynamics, reveals for the turbulent, high Re number, conditions anticipated that the convective energy transfer from the flowing melt to the stable crust layer will be enhanced depending upon the magnitude of the surface roughness, that it will become independent of the Re number and finally that entrance effects for the flow will be minimized. Concerning this latter item, the implication is that the growth of the failure site will be approximately cylindrical as the result of a much more uniform heat flux along the flowpath for melt.

The above models for melt-flow pressure drop and convective heat transfer in the discharge hole were incorporated into the HAMISA code. Validation of the models was obtained by comparison to hole ablation experiments using corium simulant materials conducted at the RIT/NPS laboratory.

Comparison to experimental ablation rates

Descriptions of the hole ablation experiments conducted at RIT can be found in the references by Green et al. [5] and Sehgal et al. [16] and thus will not be repeated in detail here. Briefly, certain volumes of melts from simulant materials were generated and placed in contact with a plate in which thermocouples were embedded and in which an initial hole of known diameter had been placed. Rates of plate ablation, and thus heat transfer, were derived from the embedded thermocouple response, along with the more important integral parameters i.e., the final hole size, timing of melt discharge and the shape of the ablated region. The relevant melt-plate simulant combinations involved water-salt ice, $NaNO_3$+KNO_3-cerrobend alloy, $NaNO_3$+KNO_3-Sn, and paraffin oil-salt ice. Table 5.5 provides a listing of the relevant parameters for several of the RIT/NPS hole ablation experiments.

Table 5.5: RIT Hole Ablation Experiments

Test	Melt Fluid	Plate Material	D_o (mm)	δ_w (mm)	T_{melt} (^{o}C)	$T_{o,plate}$ (^{o}C)	V_{melt} (m^3)
0917A	Water	Salt-Ice	20	50	23	-30	78
0917B	Water	Salt-Ice	20	50	41	-28	78
0918	Water	Salt-Ice	10	60	48	-20	78
0919	Water	Salt-Ice	10	60	46	-33	78
0923	Water	Salt-Ice	10	60	80	-40	76
0925	Water	Salt-Ice	20	60	3	-30	76
1002	Water	Salt-Ice	10	38	11	-41	78
1015	Water	Salt-Ice	10	80	44	-24	78
1016	Water	Salt-Ice	20	79	91	-31	78
1023	Paraffin Oil	Salt-Ice	20	60	29	-37	74
1024	Paraffin Oil	Salt-Ice	20	63	45	-38	69
1129	20-80 (Na,K)NO_3	Cerrobend	10	50	450	25	25
1205	20-80 (Na,K)NO_3	Tin	10	50	420	25	25
1211	50-50 (Na,K)NO_3	Tin	10	50	440	50	23

In these experiments it was clear that the crust layer played a controlling role in the ablation process. The reduction of the melt liquid temperature (see e.g. 0925 in Table 5.5) yielded extended discharge times due to the only slight ablation. Crust layers of varying thickness were found on the in-hole and upper surface of the plates. Visual observation of the final ablated hole conditions revealed that the

final surface was indeed substantially roughened and, that for all but the paraffin-oil tests, the final hole geometry was reasonably cylindrical, indicating a uniform ablation heat transfer.

The relevant experimental conditions and thermodynamic properties were then supplied as input for the HAMISA model. In these simulations the aforementioned entrance and exit form loss coefficients were supplied along with an average skin factor of 0.0055. The experimental plate was nodalized in two dimensions. Results are presented in Table 5.6 from which it is clear that the agreement between HAMISA and the experiments is very good and that both the final hole diameters as well as the melt discharge times are properly predicted.

Table 5.6: HAMISA Validation on RIT/NPS Hole-Ablation Experiments

Test	Experiment		HAMISA	Experiment	HAMISA	$\Delta D/D_o$	τ_m/τ_D
	$D_f{}^T$	$D_f{}^B$	D_f (mm)	t_d (s)	t_d (s)	(-)	(-)
0917A	72	72	70	16	18	2.5	13
0917B	72	65	76	12	15	2.8	23
0918	94	87	87	14	13	7.7	233
0919	90	86	85	15	13	7.5	219
0923	90	96	96	12	11	8.6	309
0925	28	25	24	77	78	0.2	0.5
1002	64	60	59	27	32	4.9	45
1015	100	94	88	14	12	7.8	228
1016	103	105	107	10	8	4.4	56
1205	54	56	50	11	12	4.3	56
1211	68	60	50	11	12	4.9	59

The data obtained from the RIT/NPS hole ablation tests also provides important information regarding the relevant scaling parameters for prototypic penetration-type failures. This is seen in Fig.5.9 where the RIT data is presented according to the scaling parameters of Pilch [8] which are shown in the last columns of Table 5.6. The boxed region represents postulated severe accident conditions for a corium melt pool of volumes 1.3 to 19 m^3, at system pressures of 2 to 10 bar, and for different initial failure sizes as presented in the paper by Sehgal and co-workers [15]. As can be seen in the figure, the recent simulant hole ablation tests extend the available experimental database. In addition, the Reynolds number of the in-hole flow was sufficiently high ($3{\cdot}10^5$). More importantly, in all the experiments, the crust was found to be effective and, hence, limited the hole enlargement.

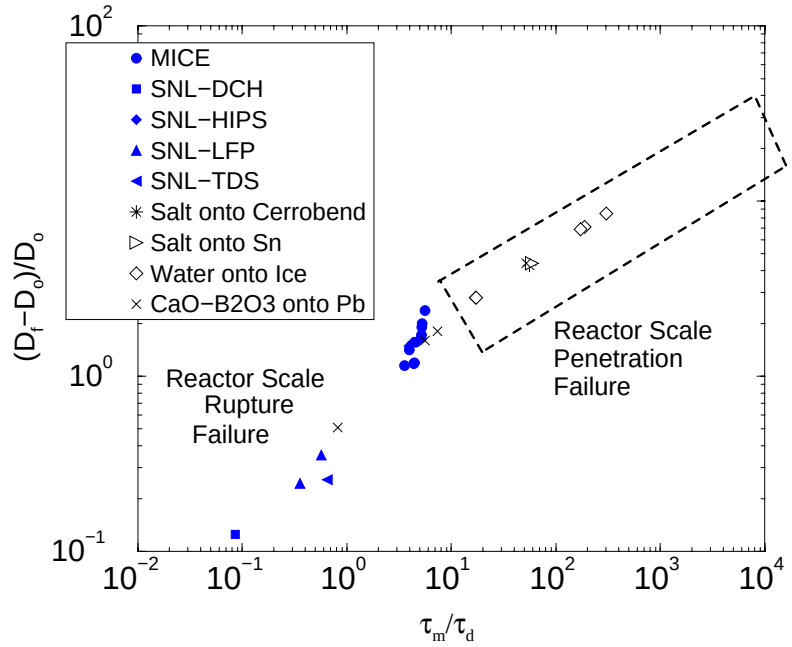

Fig. 5.9: Hole ablation scaling.

5.3.4 Related Aspects

Scenario- and design-dependent aspects

Two major parameters can be used to categorize boundary and initial conditions for the hole ablation process: location of (initial) failure site and configuration of the in-vessel debris at the moment of vessel failure. Both of these parameters depend on the accident scenario progression and specific design features of the reactor lower plenum.

It is obvious that if only a small amount of molten material is present in the lower plenum at the time of vessel failure then no significant vessel-hole ablation will occur. More importantly, in such a case, the melt jet which is ejected will remain close to the original small diameter. Such a jet may even fragment in air, and if not, most probably as it passes through the coolant (liquid) pool. Subsequently the flow rate of core melt discharged from the RPV will be determined by the heat-up and remelting of the debris, which will take substantial time. Thus, in this scenario the containment failure by steam explosion, or through base-mat melt through may not be credible.

Corium melt-phase properties

Oxidic melt pools, such as corium, present unique challanges to phase change related processes in light of their *mushy* zone behavior. The melt pool thermodynamics will be further complicated by the fact that unoxidized metals such as Zr, as well as other melted core structural materials, will also be present in the pool. There remain significant uncertainties not only in determining accurate corium physical properties but also for the melt phase diagram itself. From this arises the question: what temperature gradient is appropriate for use in determining fluid-to-structure energy transfer rates: (T_{melt}-T_{sol}) or (T_{melt}-T_{liq})? The answer, obtained from the analysis of the RIT binary-salt experiments, is (T_{melt}-T_{liq}). Nevertheless, this question must be further investigated as better information on the core melt phase diagram and properties and observations from reactor-material experiments are made available.

As can be seen from Table 5.6, in most experimental runs, the final hole is quite cylindrical, so that it can be concluded that two-dimensional heat conduction in the experimental plates as well as entrance effects on convective heat transfer are negligibly small. For experiments, employing paraffin oil as working fluid, the hole is two-dimensional, reflecting both 2D heat transfer during the long period of melt (oil) discharge and possible entrance effects for the highly viscous oil. Similarly, in a prototypic situation, two-dimensional ablation of the reactor vessel and overlying fuel crust (IDCL) can occur in case of small melt superheat, i.e. dominance of mushy-phase highly-viscous melt.

5.3.5 Concluding Remarks

Phenomena and factors of potential importance to dynamics of vessel hole enlargement during core melt discharge from the reactor pressure vessel were identified and analyzed. Phenomenologically, the major findings are as follows;

- It appears that the in-hole crust is stable (or at least exists as a boundary condition) even under high Reynolds number and high heat flux conditions. Corium, as a binary oxidic melt, may even help to hasten the crust formation. Some other factors (addition of cooler mass from melting crust into the melt boundary layer, long hole, reduced entrance effect) tend to stabilize the crust.

- The presence of a corium crust layer above the vessel wall reduces the heat up of the vessel wall during the core melt discharge process. This crust layer significantly limits the vessel ablation due to the heat capacity (sensible heat and heat of phase change) of the oxidic material. It also increases the length

of the discharge hole and hence affects the in-hole frictional losses, the hole entrance and exit loss coefficients, and the heat flux distribution.

- Accounting for the non-orifice form of the discharge hole leads to a shorter discharge period for a given melt volume.
- For low Prandtl number fluids (such as corium), phase change may significantly affect the convective heat transfer, since phase-change-induced surface roughness may be thicker than the viscous sublayer for high Reynolds number flows. This phenomenon may provide augmentation of the heat transfer coefficient and lead to nearly uniform hole growth.

5.4 Summary and conclusions

An experimental program at RIT/NPS has been conducted, which aims to reduce the uncertainty level associated with ablation dynamics of a failure site in the RPV lower head. There is very little scaleable experimental information available regarding failure site growth dynamics resulting from the flow of a fluid at temperatures greater than the melting point of structure. An important aspect is the impact of a mushy-region crust layer, which can form, and reduce the ablation rate and the final area of the failure site. Clearly, this issue is important since the melt discharge rate from the failure site location will determine the major containment loading during a severe accident.

Various melt and vessel wall simulants were employed in the test program, in order to, better, examine the influence of material properties upon the ablation phenomena. It was realized that the melt viscosity plays an important role in hole ablation. That is because the crust layer of melt which can form upon the ablating hole will undoubtedly exhibit a significant surface roughness. In lower viscosity melts the thickness of the boundary layer is small enough that the surface roughness governs the heat transfer, thereby minimizing any entrance effects, and producing a much more uniform (one-dimensional) ablation. In the experimental program, it was found that for the higher viscosity melts (binary oxide and paraffin oil) the final hole shape was very much two-dimensional, with a significantly wider ”mouth”, or upper surface, than the exit. Conversely, with the water and salt melt simulants the ablation profile may be characterized as one-dimensional. In all of the experiments, it was clear that the crust boundary condition prevails all the time, i.e., the temperature difference driving the ablation is the melt temperature and the melt liquidus temperature (i.e. $\Delta T = T_{melt} - T_{liq}$). Thus, even though the crust may be swept out by the melt flow, it re-establishes itself i.e., and the time required for crust formation appears to be much less than the rate of crust sweep-out.

The experimental program on hole ablation demonstrated:

i) the discharge coefficients of vessel hole ablation is closer to 1.0 than to 0.6;

ii) the crust boundary condition persists through the whole scenario, reducing the heat transfer to the vessel wall and its ablation. It is believed that melt superheat i.e. $\Delta T = T_{melt} - T_{liq}$ should be used for determining the heat transfer;

iii) the ablation process appears to create a rough surface, which promotes a high heat transfer coefficient from melt to interface;

iv) for low Prandtl number fluids (corium), the thermal boundary layer thickness may be less than the roughness height. Thus, the heat transfer may be represented as a function of the viscosity-independent Peclet number ($Pe = Re.Pr$).

It is believed that the HAMISA model could be employed, with confidence, to predict the hole ablation dynamics process during the prototypic accident scenarios.

It is believed that the hole ablation phenomenology is quite well understood.

Bibliography

[1] Chavez, S.A. and J.L. Rempe, ”Finite Element Analyses of a BWR Vessel and Penetration under Severe Accident Conditions,” Nuclear Engineering & Design, Vol. 148, (1994), pp. 413-435.

[2] V.A. Bui, T.N. Dinh, and B.R. Sehgal, ”In-Vessel Core Melt Pool Formation during Severe Accidents”, Proceedings of the 1996 National Heat Transfer Conference, in the session ”Fundamental Phenomena in Severe Accidents”, Houston, Texas, August 3-6, 1996, HTC-Vol.9, pp.86-94.

[3] Dinh, T. N., V.A. Bui, R.R. Nourgaliev, T. Okkonen and B.R. Sehgal, ”Modeling of Heat and Mass Transfer Processes During Core Melt Discharge from a Reactor Pressure Vessel,” Nuclear Engineering and Design, Vol. 163, pp. 191-206, (1996).

[4] Dinh, T.N., W.G. Dong, J.A. Green, R.R. Nourgaliev, and B.R. Sehgal, ”Melt Jet Attack of the Reactor Vessel Wall: Phenomena and Prediction Method,” Proceedings of NURETH-8, Tokai-mura, Japan, October, 1997.

[5] Green, J. A., T. N. Dinh, W. Dong, and B. R. Sehgal, ”Experiments on Melt Jet Impingement and Vessel Hole Ablation Phenomena”, PSA’96 - International Topical Meeting on Probabilistic Safety Assessment, Park City, Utah, (1996).

[6] T.J. Okkonen, T.N. Dinh, V.A. Bui, and B.R. Sehgal, ”Quantification of the Ex-Vessel Severe Accident Risks for the Swedish Boiling Water Reactors”. A scoping study performed for the APRI project. July 1995. *SKI Report No.95:76*. Swedish Nuclear Power Inspectorate (SKI), 195p (1996).

[7] M.M. Pilch, ”Continued Enlargement of the Initial Failure Site in the Reactor Pressure Vessel”, Nuclear Engineering & Design, Vol. 164, (1996), pp. 137-146.

[8] Pilch, M. M., Y. Yan and T. G. Theofanous, ”The Probability of Containment Failure by Direct Containment Heating in Zion”, NUREG/CR-6075 and SAND93-1535, (June, 1993).

[9] Rempe, J. L., G. L. Thinnes, S. A. Chavez, "A Simpler Approach for Predicting LWR Vessel Failure During Severe Accident Conditions," Nuclear Engineering and Design, Vol.148, pp 365-383, (1994).

[10] Rempe, J. L. and T. J. Walker, "Overview of NRC Sponsored LWR Lower Head Failure Research Program," Nuclear Engineering and Design, Vol.148, pp. 327-341, (1994).

[11] J.L. Rempe et al. "Light Water Reactor Lower Head Failure Analysis". NUREG/CR-5642. EGG-2618 (October 1993).

[12] Schlichting, H., Boundary Layer Theory, 6^{th} Edition, McGraw-Hill Book Company, New York, 1968.

[13] Sehgal B.R., J. Andersson, T.N. Dinh and T. Okkonen, "Scoping Experiments on Vessel Hole Ablation During Severe Accidents", Proceedings of the Workshop on Severe Accident Research in Japan, SARJ-4, Japan, Oct.-Nov., 1994, pp.230-236.

[14] Sehgal, B. R., V.A. Bui, T.N. Dinh, J. Andersson and T. Okkonen, "Experiments on Vessel Hole Ablation During Severe Accidents", Proceedings of the International Seminar on Heat and Mass Transfer in Severe Reactor Accidents, Izmir, Turkey, 1995.

[15] B.R. Sehgal, J. Andersson, V.A. Bui, T.N. Dinh, and T. Okkonen, "Experiments on Vessel Hole Ablation During Severe Accidents", Proceeding of the International Seminar on "Heat and Mass Transfer in Severe Reactor Accidents", Izmir, Turkey, 1995; Begel House Publ. Inc., 1996.

[16] B.R. Sehgal, J.A. Green and T.N. Dinh, "Experimental and Analytical Investigations of Vessel-Hole Ablation during Severe Accidents", Proceedings of the Fifth International Topical Meeting on Nuclear Thermal Hydraulics, Operations, and Safety (NuTHOS-5), Beijing, China, April 1997.

[17] Sienicki J.J. , C.C. Chu, B.W. Spencer, W. Frid, and G. Löwenhielm, "Ex-Vessel Melt-Coolant Interactions in Deep Water Pool: Studies and Accident Management for Swedish BWRs", Proceedings of the CSNI Specialist Meeting on Fuel-Coolant Interactions, Santa Barbara, January 5-8, 1993, NUREG/CP-0127, NEA/CSNI/R(93)8.

[18] Sienicki, J.J. and B.W Spencer, "Superheat Effects on Localized Vessel Breach Enlargement During Corium Ejection", Trans. ANS, Vol. 52 (1986), pp.522-524.

[19] Theofanous, T. G., C. Liu, S. Addition, S. Angelini, O. Kymäläinen, and T. Salmassi, ”In-Vessel Coolability and Retention of a Core Melt,” DOE/ID-10460, Vol. 2, (July, 1995).

[20] Witt, R.J., ”Local Creep Rupture Failure Modes on a Corium-Loaded Lower Head,” Nuclear Engineering & Design, Vol. 148, (1994), pp.385-411.

[21] Zion Probabilistic Safety Study, Commonwealth Edison Co., Chicago, IL. 1981.

Chapter 6

Application of data and models to prototypic accident situations

6.1 Jet impingement

6.1.1 Oxidic melt jet impingement

In this section, calculations are performed for selected scenarios of core melt relocation to the RPV lower plenum (with steel wall thickness L_w = 15 cm). The purpose of these calculations is to apply the methodology developed for assessments of the jet impingement vessel failure mode. These assessments are compared to the previous evaluations [1].

6.1.1.1 Scenarios of in-vessel core melt progression

It is assumed that the total melt mass available at the moment of melt relocation to the RPV lower plenum is approximately 20 tonnes or V_m = 2.5 m^3 [1]. More probably, the melt is released from the pool corner (scenario "a"), although the failure at the pool bottom (scenario "b") cannot be ruled out. Thus, the impingement is inclined in the former scenario and normal in the later one. In both cases, the free melt path may be sufficiently long to provide high impingement velocities ($V_j = \sqrt{2 \cdot gH} \simeq$ 7-9 m/s). It is believed that it is more probable for the in-core melt pool to form in the upper part of the reactor core, since a large portion of energy from the decay-heated melt pool, should it form, is removed through the upper pool surface.

In scenario "b" the melt discharge from the in-core melt pool is driven by the hydraulic head of the full height of the melt pool, and, therefore, the discharge velocity is high and the initial hole in the core plate will be significantly enlarged during the melt relocation duration. Thus, an initial jet diameter of 5 cm may end

up as 20 cm in this scenario. Another feature of this scenario is melt accumulation in the lowermost bottom of the vessel. Experiments [3] however revealed that the jet impingement heat transfer is not significantly affected by the presence of an accumulated melt layer until its depth is over 5 jet diameters. Since, during the melt relocation the jet diameter increases, the effect of melt accumulation is not considered in the present analysis and as such, the assessment below should be conservative.

In scenario "a" the melt release is driven by a relatively small hydraulic head and can be limited by the ablation of the pool's corner crust. Thus, long pouring of a small diameter jet may be typical for this scenario. Eventually, the initial hole in the pool's side crust will enlarge in both vertical and horizontal directions, rendering conditions for melt release as a planar jet. However, only axisymmetric jets are considered in the present analysis, which may be shown to be the most conservative jet impingement loading of the RPV wall lower head.

Other important scenario-dependent aspects are the initial and boundary conditions of the vessel wall. While the external vessel cooling condition appears to have only a minor effect on the impingement-induced ablation process, the initial vessel wall temperature T_w^o may significantly affect the ablation rate U_{abl}.

6.1.1.2 Parametric study and major results

Calculations were performed for a number of cases. Material properties of core melt and vessel steel are as proposed in Ref.[1]. The jet impingement velocity is chosen U_j = 7.5m/s which is a reasonable (average) value.

It should be noted that the transition-to-turbulence parameter ξ_{tur} may significantly affect the vessel melting attack by a large diameter melt jet. Analysis results show that the impingement process is almost laminar with 15cm-diameter jets. This factor, together with the much shorter impingement period, τ, for a large diameter jet ($\tau \sim D_j^{-2}$ for a fixed volume melt), produce small wall ablation depths. However, the wall ablation process, for a small diameter jet ($D_j << L_w$) and for relatively long impingement period is dominated by the turbulent flow regime. The use of Saito's correlation provides a conservative assessment of the reactor vessel ablation (Chapter 8, [1]). The use of the laminar stagnation flow model (or Epstein's correlation [2], Appendix H [1]) would significantly underestimate the vessel ablation depth during the jet impingement process.

For conservative assessment of the reactor vessel ablation, it is assumed that ξ_{tur} equals 0 in all the calculations whose results are presented hereafter. The ablation rate is then independent of the jet diameter, but the cumulative ablation depth depends linearly on the impingement duration τ_{imp} ($\tau_{imp} = \frac{V_m}{U_j \cdot \pi D_j^2/4}$).

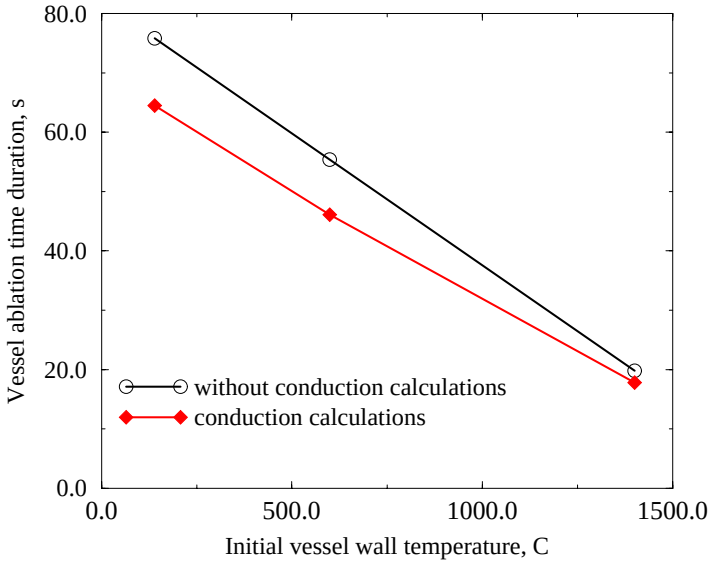

Fig. 6.1: Calculated ablation time periods τ_{abl} for different initial vessel wall temperatures T_w^o (melt superheat 175K).

Wet or dry lower plenum. The initial temperature profile in the steel vessel wall T_w^o is determined by the presence, or absence, of water in the lower plenum at the moment of oxidic core melt relocation to it. If the coolant is absent in the lower plenum, T_w^o may vary around the vessel bottom due to the radiative heat transfer from the core melt and hot core plate above. It can be seen from Fig.6.1 that the time periods τ_{abl} needed to ablate the vessel wall, through and through, decrease with the increase of the initial vessel wall temperature T_w^o.

Heat conduction in the vessel. It was found from the analysis of the ablation dynamics results that heat conduction in the vessel tends to slow down the ablation front propagation in the early phase (1-2 s) of impingement when $q_{cond} \simeq q_{imp}$. Depending on the initial vessel temperature, crust layers of different thicknesses may form. However, very soon, the heat conduction leads to pre-heating of the solid vessel, due to the high conductivity of steel. Then, the heat conduction flux q_{cond} is overwhelmed by the impingement heat flux q_{imp}, to start the vessel ablation. In the latter ablation phase, the ablation rate even increases slightly.

Fig.6.1 also shows the calculated results obtained by a simple energy-balance

assessment, in which the ablation rate is determined as

$$U_{abl}(z,t) = \frac{q_{imp}}{\rho_w H^*_{fusion,w}} \tag{6.1}$$

with $H^*_{fusion,w} = H_{fusion,w} + C_p \cdot (T_{w,mp} - T^o_w)$. In such a case, the ablation rate is a linear function of time, since the time-dependent effect of the heat conduction in the vessel is not accounted for. As seen, such a simplification causes slight underprediction of the vessel ablation rate.

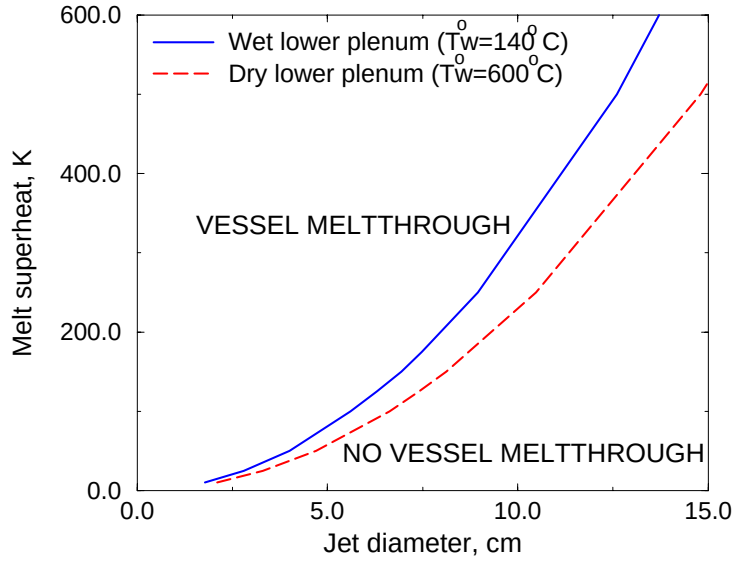

Fig. 6.2: Vessel ablation map (U_j = 7.5 m/s, $V_m = 2.5m^3$).

Vessel ablation map. Calculation results can be presented in the form of a vessel ablation map, in which a so-called "vessel-meltthrough" line is used to separate the chart into two sections: in the upper part of the chart, the vessel is likely to be melted through, while in the lower part, the cumulative erosion depth is less than the thickness of the RPV wall. The two parameters of the vessel ablation map are the melt superheat $\Delta T_j = T_j - T_{liq}$ and the melt jet diameter D_j. In this calculation, the jet diameter is assumed to be constant during the jet impingement process. The liquidus temperature of the oxidic core melt is nearly 3000K, while the mushy-zone temperature range is 50K. As seen, small-diameter jets ($D_j < 5$ cm) with melt superheat of less than 100K can threaten the vessel integrity during the melt relocation period.

This map was established for the chosen melt mass, melt jet velocity, vessel thickness and materials (core melt, steel) properties [1], among which melt mass is the most sensitive parameter for the ablation results. In practice, the ablation depth is proportional to the melt mass available for relocation, and therefore, "vessel meltthrough" line in the ablation map will be lower for higher melt masses.

6.1.2 Molten metal jet impingement

6.1.2.1 Reactor Accident Scenarios

In a hypothetical severe accident in a Light Water Reactor (LWR) the inability to provide long term decay heat removal is assumed with the resulting likelihood of melting of the reactor core internal structures. Since the majority of the reactor core is comprised of nuclear fuel ($UO2$), metallic cladding (Zircaloy), and structural materials (including control rod drives), the lower melting point materials will be melted first with resulting candling down and accumulation upon the various core structures. At extended times into the severe accident a molten corium ($UO_2 - ZrO_2$) pool may form within the core boundaries which can include a sizeable fraction of molten metals (Zr, steels). Separation of the lighter metallic components from the heavier oxidic corium melt may occur during the core melt-down scenario.

Two scenarios are proposed which involve the direct melt-attack of the RPV lower head by a relocating metallic jet. In the first scenario it is assumed that the molten metal materials have been separated from the oxidic melt in the in-core melt pool and that they are substantially superheated above their melting point ($T_{mp,metal}$). Relocation of this melt mass layer could be in the form of a coherent jet impinging directly upon the RPV head when dry conditions in the lower plenum region are assumed. In addition, the jet may pass through a coolant or shallow melt layer prior to contact with the vessel steel. A second scenario can be envisioned where relocated metal components, which had earlier frozen in place upon lower core structures such as the lower core plate and flow distributor, are remelted as the decay-heated oxidic materials gradually penetrate into the core lower regions.

The potential therefore exists for direct molten metal attack of the RPV lower head during melt pool relocation events which could threaten vessel integrity. A phenomenological look at jet impingement processes described is provided in schematic form in Figure 6.3. It should be emphasized that these postulated scenarios do not take into account any melt-coolant interactions which might drastically alter the jet behavior. That is to say that no provision has been made to account for an existing coolant volume in the lower plenum through which the jet must pass. If such a pool were present then the fragmentation and breakup of the

jet as well as the potential for an in-vessel steam explosion must be considered. Here, it is assumed that the jet is coherent and of constant diameter, composition and temperature.

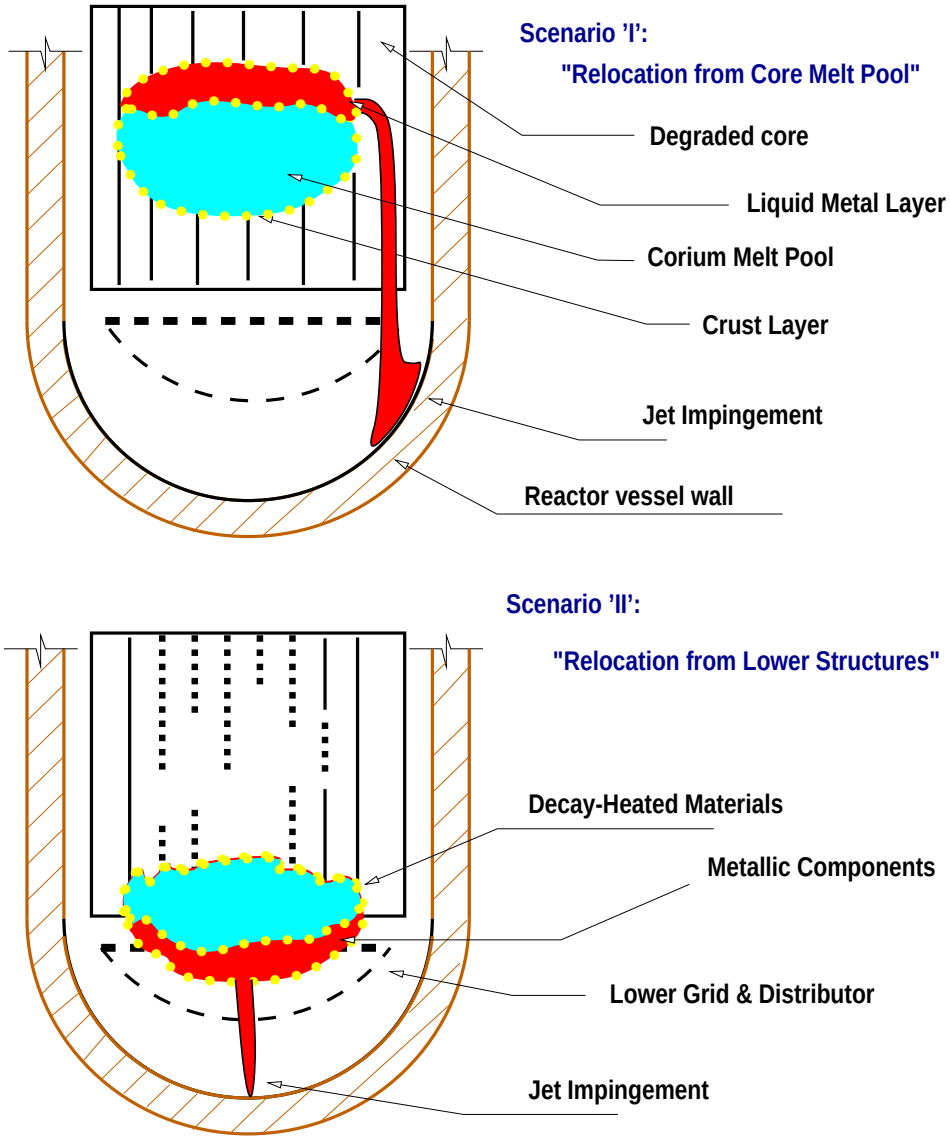

Fig. 6.3: Jet Impingement Scenarios

6.1.2.2 Reactor-Scale Considerations

Depending upon the reactor design and core damage scenario up to the point of molten-metal relocation, the volume and temperature of metallic melt available

can vary widely. A maximum value of $2m^3$, which is essentially the entire clad volume, provides a rough upper limit for scoping considerations. Interaction of the Zr cladding with high temperature steam will result in a significant fraction of the metal being oxidized and in addition, it is extremely unlikely that the entire clad volume would relocate at one time given the core geometry (i.e. all the metallic materials could not possibly segregate into a single volume available for relocation). An assumption of approximately $0.5m^3$ of metallic melt volume provides a reasonable assessment to be used in simple scoping calculations. The metallic layer superheat can however be as much as 1000 K since the melting point of the metals is much lower than that of the oxidic core materials. Determination of the localized thermal loading upon the RPV lower head should not be significantly affected by the formation of a crust layer of Zr upon the ablating surface since the temperature driving difference will remain essentially constant throughout the process. Recall that the RPV steel has slightly lower melting point ($T_{mp,Fe}$=1808^{o}C) than that of the molten Zr cladding material ($T_{mp,Zr}$=2123^{o}C).

Two final parameters necessary for assessing prototypical scale melt jet impingement are the jet velocity and diameter. The jet velocity, U_j, will depend upon the jet acceleration pathlength. For the two scenarios considered previously (Figure 1), use of appropriate jet fall lengths provide velocities of 9 and 4.5 m/s respectively. The jet diameter can also exhibit a range of values and this parameter is likely to increase during a relocation event due to convective ablation of the melt-containing structure (hole ablation). Melt jet diameters of 5 to 20 cm are pre-supposed.

Given these parameter values and ranges, it is clear that for the assumed metallic melt volume the larger diameter jet and velocity will correspond to shorter interaction periods and hence vessel ablation depths. The dimensionless jet Re can vary from $0.3 \cdot 10^6$ to $2.6 \cdot 10^6$ with impingement periods of 3-7 s for large jets and 56-110 s for the smaller jet diameters. Employing the aforementioned $0.5m^3$ of metallic volume with 1000 K of melt superheat results in quite high heat transfer coefficients, in the range of 50,000 to 130,000 W/m^{2}K. The convective jet energy obtained in this manner can then be equated to that necessary to heat and melt the pressure vessel steel ($\rho_{Fe}[\Delta h_{fusion} + C_{p,Fe}(T_{jet} - T_o)]$) and to determine effective ablation depths. For the large diameter jets the resulting ablation depths range from 16 to 23 mm when both Liu and Saito correlations are employed. This is clearly much less than the typical 150 mm vessel wall and vessel integrity, ignoring mechanical loadings, is not threatened. For the longer duration events associated with the smaller jet diameters, the ablation depths increase significantly to values in excess of the RPV wall thickness, with the higher heat transfer predicted by the Liu correlation yielding the more limiting cases. Reduction of the melt superheat to only 500K still predicts vessel attack of greater depth than the wall thickness. Such small diameters as used here (0.05m) may indeed be unre-

alistic over the entire pour period given the complex geometry and the fact that ablation of the containing-structure, whether it be a crust layer or a part of the reactor itself, will ablate and thus increase the area for jet flow. However, this analysis does reveal the need for a more extensive database for jet impingement heat transfer, under phase change conditions, especially when considering low Pr number (metallic) materials.

More detailed considerations of this process could provide a probability distribution for the key parameters driving this process, such as the molten metal mass, the diameter of coherent jet discharge and the melt superheat.

6.2 In-vessel melt retention by external cooling

The state of knowledge with respect to PWR in-vessel core-melt progression has not changed substantially from the picture conveyed by the TMI-2. It is believed that a melt pool will be formed in the original core volume and will drain along the side of the core, into the lower plenum, to commence the thermal loading on the lower head. The new information is on the effects of accident-management actions, e.g., water addition to a hot core. This increases the damage and hydrogen generation, due to the increase in Zircaloy oxidation by the steam produced. This could increase the volume and mass of the in-core melt pool, if quenching does not occur. The initial attack of the melt on the lower head is in the form of a jet, whose composition may well be fully-oxidic. There is uncertainty as to presence of a Zirconium metal layer which could drain earlier into the water pool and lead to steam explosion. We, however, consider the occurrence of a pure metal layer as unlikely.

6.2.1 MVITA model

In this section, analysis of the melt pool formation and vessel heat-up in late phase of in-vessel core melt progression is performed for Westinghouse PWR. A computer code named MVITA is utilized. The MVITA model and code have been developed by at RIT/NPS (Bui and Dinh, 1996, Bui et al., 1997, Dinh et al., 1997, Sehgal et al., 1998).

The MVITA model is based on effective conductivity-convectivity modeling (ECCM) of the natural convection heat transfer in an internally-heated pool. Two-dimensional energy conservation equation is solved in a general-coordinate system to enable simulation of heat transfer in a complex geometry pool. The effective conductivity is based on an Eckert-type boundary layer heat transfer correlation, and the effective velocity is the turbulent fluctuation velocity in natural convection flows. The method is found to work well in rectangular, semicircular

and hemispherical cavities with different heating and boundary conditions. The ECCM approach has been extensively validated against related experimental data on melt pool and metallic layer natural convection heat transfer which has been described in publications listed in the above paragraph.

A temperature-based enthalpy formulation is employed to model the phase change in a multi-component mixture. Remelting of the debris, and melting of the vessel, as well as multidimensional heat transfer between the crust, vessel and metal layer have been modeled. The method is numerically robust and features good prediction capability.

6.2.2 Assessments of the vessel thermal loading in selected severe accident scenarios

In this section, results of the MVITA code calculations for prototypic reactor situations will be discussed. A large quantity of core materials is assumed to present in the lower plenum of the AP-600 reactor vessel. Geometrical characteristics of the RPV and physical properties of oxidic and metallic phases were taken from [27]. External vessel cooling is employed as the accident management strategy, so that an isothermal boundary condition is set for the external vessel surface ($T \simeq$ 390K).

This study aims to assess the thermal margin of the in-vessel melt retention scheme for three configurations, namely "**A**" without metallic layer; "**B**" with a thin layer (H = 0.1 m) and "**C**" with a thick layer (H = 0.8 m) of molten metals above the oxidic debris. Fig.6.4 shows the computational mesh as a multi-block domain [1].

Initial conditions of 2000K for the oxidic debris and 1550K for the metallic layer were employed in the calculations whose results are presented here. It is worth noting that the initial conditions influence the time periods of the debris heating up and remelting, but they are of minor importance to the assessments of the in-vessel melt retention. It is because the thermal load to the RPV lower head is maximized when the debris pool has reached a steady thermal state (see also [27]).

More importantly, the effect of radiative heat transfer from the upper surface of the debris (or the metallic layer) was investigated. In the report by Theofanous et al. [27] it was assumed that the energy radiated from the surrounding cavity to the layer is negligible. This assumption holds for the situations when the surface temperature of the surrounding structure T_∞ is lower than the surface temperature

[1] See refs.[44] [4] for more discussion on numerical aspects of phase change modeling and solution of the energy equation in a complex domain including the conjugated regions of the oxidic pool, crust, molten steel and solid vessel.

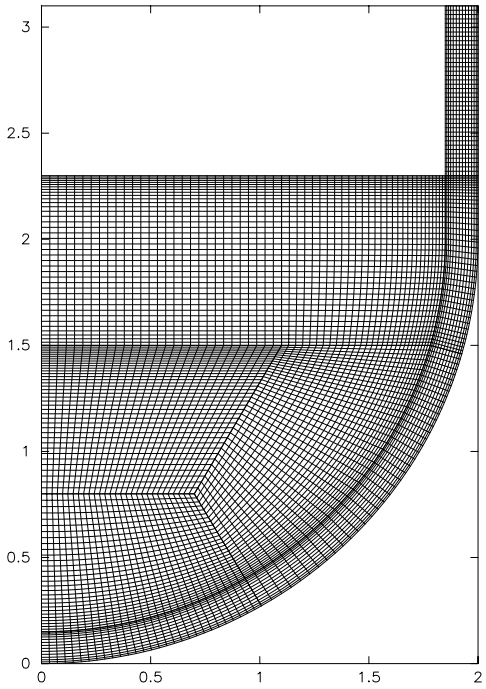

Fig. 6.4: Computational mesh. Case C (thick metallic layer).

of the metallic layer T_{up} (then $T_{up}^4 >> T_\infty^4$). However, as it was found from the calculation results for case "C", temperature of the upper surface of the metallic layer is only slightly higher than the melting point of the metallic phase. At the same time, the surface of the surrounding structure, which is exposed to the metallic layer, is also at the steel melting-point temperature. In such a case ($T_{up} \simeq T_\infty$), the resulting radiative heat removal from the upper surface is limited, so that the vessel thermal loading increases.

Previous assessments of the impact of the metallic layer, e.g. [27], indicated that the thin metallic layer may threaten the vessel thermal margins against critical heat fluxes. However, it was determined from the MVITA calculations that the sideward heat fluxes from the metallic layer to the vessel wall are well below the maximum heat fluxes occurring at the molten oxidic pool corner. Firstly, it is because the thick oxidic crust at the pool corner provides a high thermal resistance to the direct heat flux from the pool to the metallic layer. As a result, heating of the metallic layer (from below) is non-uniform, and the Rayleigh number Ra_{RB} decreases towards the near-wall region. Secondly, the thick, highly-conductive, steel vessel acts as a heat distributor, so that the multi-dimensional heat diffusion significantly reduces the effect of any local hot spot occurring on the inner side of the vessel, such as the heat fluxes peaking in the thick metallic layers or the high heat fluxes imposed by the thin metallic layers.

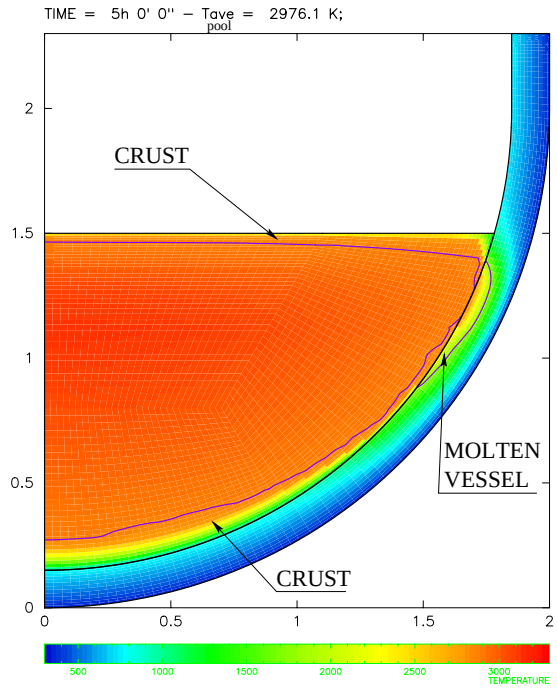

Fig. 6.5: Steady state configuration of in-vessel melt retention (Case "A", without upper metallic layer).

Figs.6.5-6.7 depict the calculated temperature fields in the three chosen cases. The metal melting point is assigned for T_∞ (T_∞ = 1600K) in order to be conservative. It can be seen that the vessel melting occurs at the corner region of the debris pool. For case "B" the thin metallic layer is fully liquid, while for case "C" the solid crust exists in the peripheral region of the thick metallic layer (Fig.6.7). Essentially, no significant melting of the steel vessel was predicted in the region where the metallic layers touch the vessel.

In the case of thick metallic layer, although the heat is mainly removed through the side wall, large contact surface with the vessel wall can keep the resultant heat flux low. Moreover, the metallic side crust helps to prevent the vessel from melting. In the case of thin metallic layer, the metallic layer is highly superheated ($\sim$ 500K). This is in contrast to the case with thick metallic layer, when the metallic layer was found to be only slightly superheated. Thus, for the case of thin metallic layer, the upward heat removal becomes significant, and only a part of the heat transferred from the decay-heating oxidic debris is removed through the side boundary of the metallic layer. However, the thermal loading from the thin metallic layer is concentrated in a small surface area. In such a case, heat diffusion in the steel vessel helps to minimize any possible meltthrough. Thus, while the heat flux from the side of thin metallic layer is higher than that of thick metallic

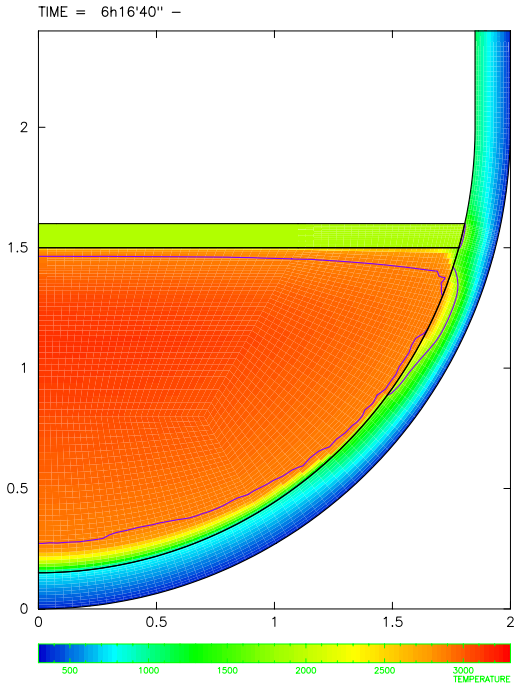

Fig. 6.6: Steady state configuration of in-vessel melt retention (Case ”B”, with thin upper metallic layer).

layer, both thick and thin metallic layers do not reduce the vessel thermal margin against critical heat fluxes; see Fig.6.8.

6.3 Vessel hole ablation and melt discharge

6.3.1 Physical picture

The melt ejection out of the vessel would be governed by the driving forces (vessel over-pressure, hydraulic head of the melt pool) as well as the melt flow and heat transfer-induced ablation of the lower head wall around the initial failure site. The lower head failure location may affect the discharge flow, although eventually, most heat-generating material could be ejected. The melt discharge rate and other characteristics (composition, superheat) are important for determining the consequences of the ex-vessel fuel-coolant interactions (FCIs). Thus, an improved understanding of lower head ablation during melt discharge through a local failure site, is a necessary step towards defining the progression of the ex-vessel FCI process.

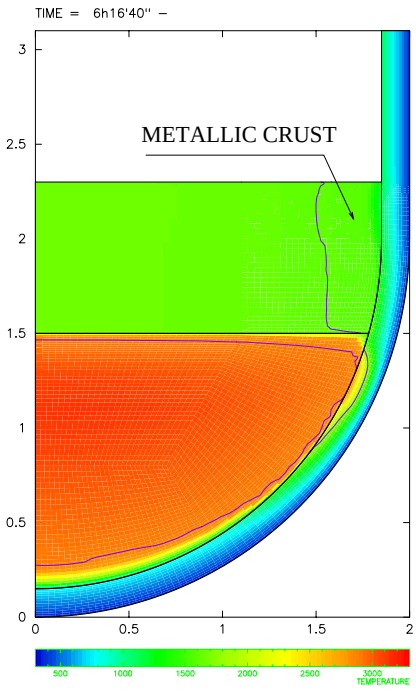

Fig. 6.7: Steady state configuration of in-vessel melt retention (Case ”C”, with thick upper metallic layer).

6.3.2 Assessment of an enveloping reactor scenario

Results of reactor predictions, performed by using the HAMISA code, indicate that most of the melt volume is discharged from the RPV as a coherent jet. The melt volume available in the lower plenum after the gas blowthrough onset is generally less than 10% (for overpressurization of 0.7MPa). The vessel hole enlargement dynamics for the prototypic vessel, with about 70 tonnes of molten core materials in the vessel lower plenum is predicted to be in the range 6-10mm/s, i.e. the time period to have the initial hole of 10cm diameter to grow up to 25-30cm would take 20-25s. Thus, for the ex-vessel FCIs the interaction between coolant pool and quasi-steady jet should be analyzed.

Sensitivity analysis of remaining phenomenological uncertainties indicates that they do not appear to significantly affect the physical picture established from the results of RIT/NPS experiments and analyses. The HAMISA model, validated against experimental data, provides a tool with which to describe the hole ablation process and therefore in defining the ex-vessel melt source for problems involving FCIs. Thus, overriding uncertainties in reactor predictions of vessel melt source for ex-vessel FCIs are the related intangibles of accident scenarios. For instance, knowledge of the configuration of melt pool and frozen crust as well as the fail-

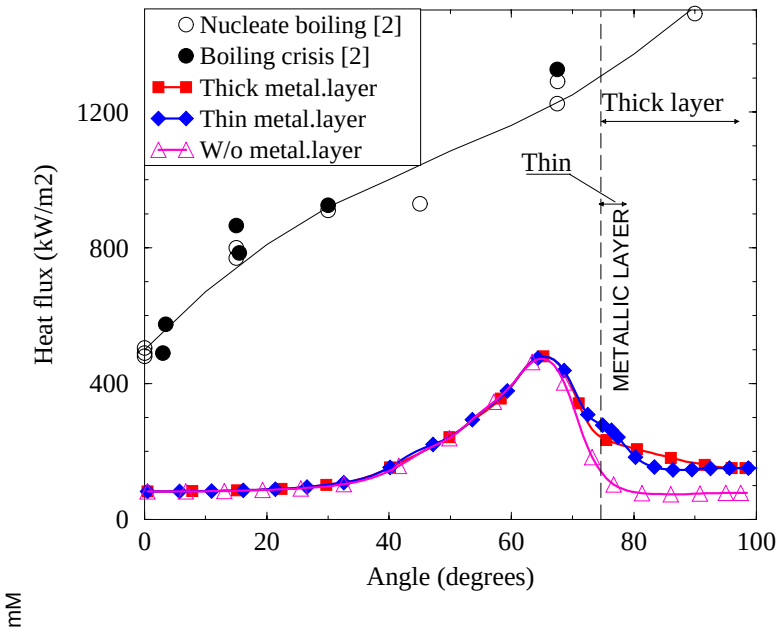

Fig. 6.8: Thermal margins of in-vessel core melt retention by external vessel cooling, with thin and thick upper metallic layers above the oxidic debris (q_v = 0.85 MW/m^3).

ure location are essential for determining the discharge parameters, since the hole ablation dynamics are affected by the presence of the in-vessel (initial) crust layer.

6.3.3 Probabilistic analysis of the hole ablation and melt discharge processes

As mentioned before, the process of melt discharge may be accompanied by hole ablation and enlargement, which feedbacks to the discharge rate and time. Since there still exist many scenario-related and phenomenological uncertainties associated with initial conditions of melt discharge and in-hole ablation process, it deems appropriate to apply probabilistic analysis to investigate the process. In this work, PSA level 2 for the hole ablation and melt discharge processes has been performed. The purpose of this analysis is to investigate the sensitivity of the important process parameters, such as the final failure size and mean discharge rate, to the uncertainties of the scenario-related factors (initial conditions such as melt temperature and vessel pressurization) and phenomenological factors (heat transfer coefficients, crust existence, etc.). The initial and input conditions for the melt

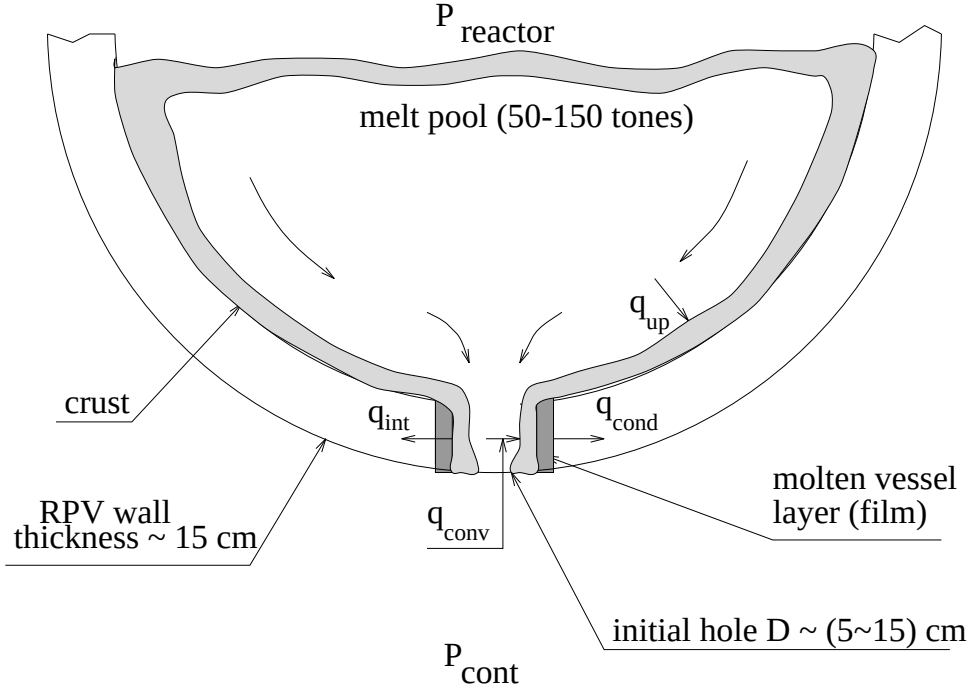

Fig. 6.9: Physical picture of hole ablation phenomenology.

discharge and vessel ablation processes are given in the form of *bounding scenarios*, in which various important factors are sampled from probability distributions (see Table 6.1).

The PSA is based on the simple models of hole ablation and melt discharge processes. The melt discharge regimes can be classified as coherent release and gradual release. The coherent melt release is mainly driven by the pressure difference (between the in- and out-vessel pressures) and the hydraulic head, while the gradual release is controlled by the thermal processes (melting) in the invessel debris bed. The models for coherent and gradual melt releases are defined by

Coherent release

$$\frac{dm_m}{dt} = -\rho_m v_d \cdot \frac{\pi D_d^2}{4} \tag{6.2}$$

$$v_d = C_d \sqrt{\frac{2\Delta p'}{\rho_m}} \tag{6.3}$$

$$\Delta p' = p_{vessel} - p_{cont} + \rho_m g H_m \tag{6.4}$$

Under the coherent release of melt, the discharge coefficient may change in de-

Table 6.1: Initial parameters for the 'bounding' scenarios (Okkonen et al., 1996).

Parameter/Bounding scenario	Scenario 1	Scenario 2	Scenario 3	Scenario 4
ΔP (bar)	2-7	2-7	2-7	4.5
$D_{h,o}$ (cm)	5-15	50-400	5-15	6.5
$m_{m,1}$ (tonnes)	40-160	40-160	20-60	10
$\Delta T_{sup,1}$ (K)	10-190	10-190	10-390	150
Composition	oxidic	oxidic	metallic	metallic
$m_{m,2}$ (tonnes)	20-100	20-100	20-100	40
$\Delta T_{sup,2}$ (K)	10-390	10-390	10-190	100
Composition	metallic	metallic	oxidic	oxidic
$m_{m,3}$ (tonnes)	-	-	160-$m_{m,2}$	120
$\Delta T_{sup,3}$ (K)	-	-	10-190	100
Composition	-	-	oxidic	oxidic
p_{cont} (bar)	2	2	2	2
T_{pool} (K)	323	323	323	323
h_{pool} (m)	4,7,10	4,7,10	4,7,10	4,7,10

Masses $m_{m,1}$ and $m_{m,2}$ are directly correlated.
Melt mass $m_{m,3}$ is released gradually.
"Oxidic" composition refers to mainly oxidic melt.
"Metallic" composition refers to fully metallic melt.

pendence of the hole height. In this work, this coefficient is given by

$$C_d \;=\; \frac{1}{\sqrt{f_e \;+\; f_0}}, \tag{6.5}$$

where $f_e \;=\; 0.45$ and

$$f_0 \;=\; \begin{cases} 0.75 & \text{if } \frac{L}{D} \geq 1 \\ 1.60 & \text{otherwise} \end{cases} \tag{6.6}$$

Gradual release

$$\frac{dm_m}{dt} \;=\; \frac{Q'_{dec}}{\Delta h_m} \tag{6.7}$$

$$Q'_{dec} \;=\; \frac{m_{m,oxid}}{m_{total}} Q_{dec} \tag{6.8}$$

$$\Delta h_m \;=\; c_{p,m,sol}(T_{mp,m} - T_{m,o}) \;+\; \Delta h_{fus} \;+\; c_{p,m,liq}(T_{m,d} - T_{mp,m}) \tag{6.9}$$

Ablation of the lower head of the reactor vessel is governed by many factors. In general the ablation rate is defined by

$$\frac{dD_d}{dt} \;=\; \frac{2h_{m-v}\Delta T_{m-v}}{\rho_v[c_{p,v}(T_{mp,v} \;-\; T_v^0) \;+\; h_{v,fus}]} \tag{6.10}$$

The most important factor here is the temperature difference between the melt and the vessel wall, which defines the heat flux to the wall. If no crust on the wall is assumed, this temperature difference can be as large as

$$\Delta T_{m-v} \;=\; T_m \;-\; T_{mp,w}. \tag{6.11}$$

while with assumption about the existence of the melt crust on the wall, the temperature difference reduces to

$$\Delta T_{m-v} \;=\; T_m \;-\; T_{mp,m}, \qquad T_{mp,w} \approx 2800K. \tag{6.12}$$

Provided a fifty to fifty probability of crust existence, a wide dispersion of the discharge parameters, e.g. final hole diameter and mean discharge rate, was obtained (see figures 6.10-6.12). The series of hole ablation experiments performed at KTH with using a binary melt simulant as well as the analytical results obtained using the HAMISA code indicated that the crust always exists in the hole. Including of this information into the PSA could greatly reduce the uncertainties in the discharge parameters as presented in figures 6.10-6.12.

With the in-hole heat transfer coefficient, h_{m-v}, given in a deterministic manner by

$$h_{m-v} \;=\; Nu_{m-v}\frac{k_m}{D_d} \;=\; (0.0025 \div 0.0030) \cdot Pe, \tag{6.13}$$

uncertainty range of discharge parameters (figure 6.11-6.13) could even be more narrowed.

The effect of the invessel crust to melt discharge was also investigated in this analysis by introducing an even-distributed crust thickness in the range [0..10cm]. The existence of the invessel crust was found to not affect the value of final failure diameter. However, the newly introduced uncertainty could change the probability distribution of the average discharge rate (see 6.13).

Comparing the present results with results of assessments performed in the previous scoping study, it can be shown that improved knowledge of related phenomena, namely, in-hole heat transfer, crust existence, etc., greatly reduce uncertainties about discharge rate and final size of the hole.

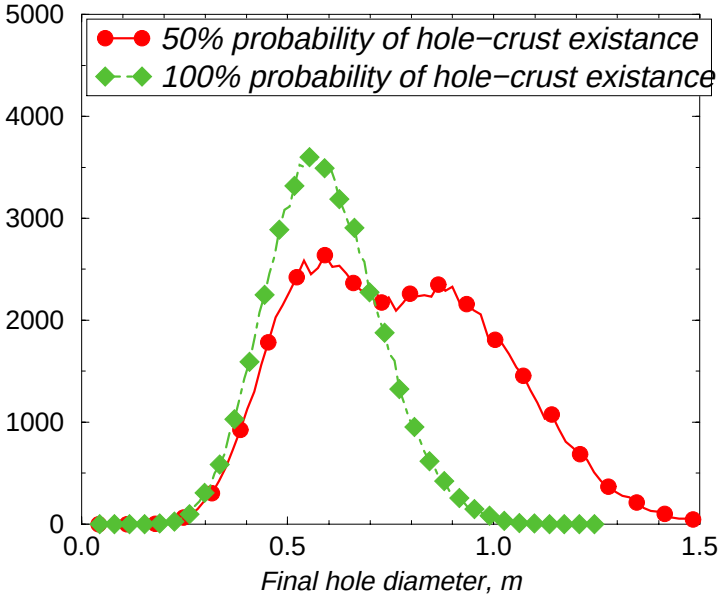

Fig. 6.10: Final hole failure diameter [Scenario 1]

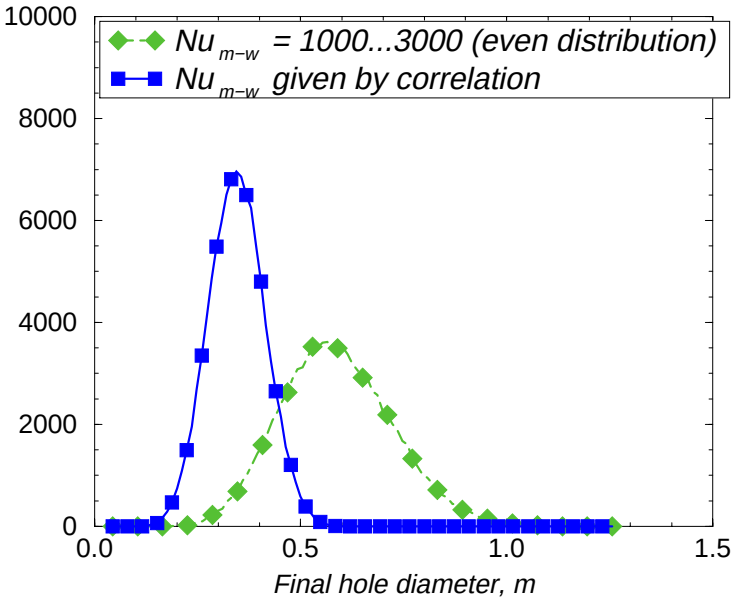

Fig. 6.11: Final hole failure diameter [Scenario 1]

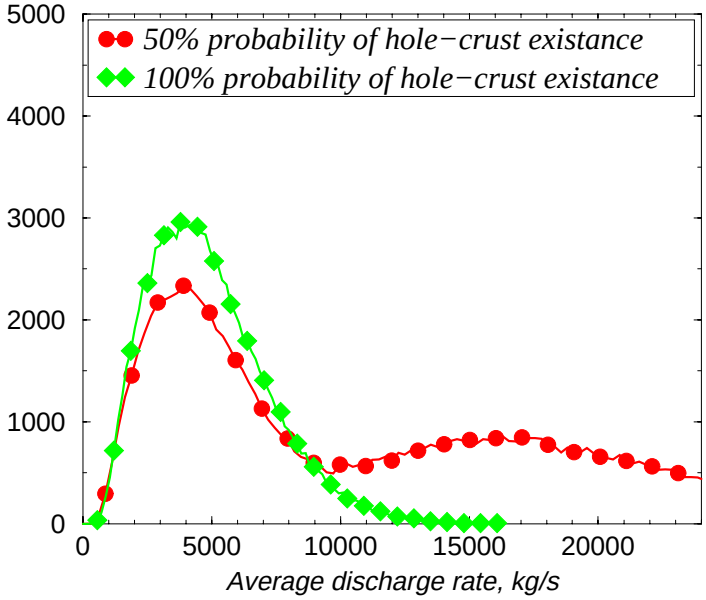

Fig. 6.12: Average discharge rate [Scenario 1]

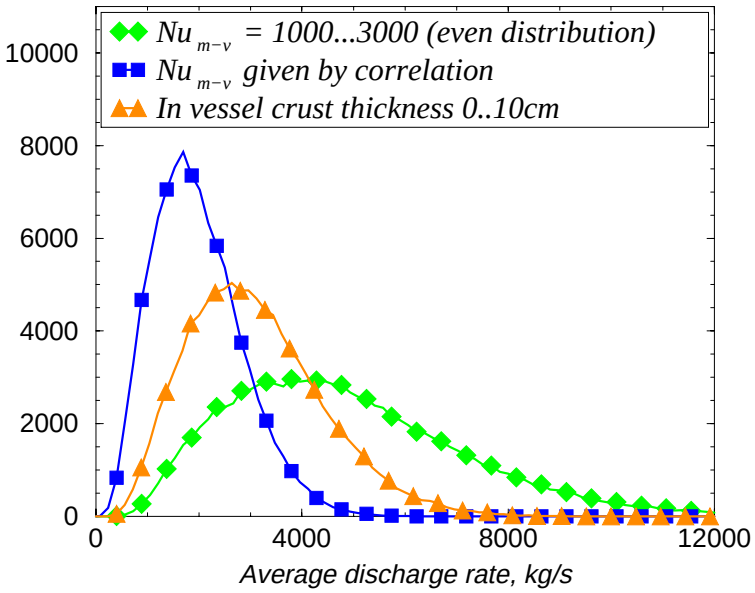

Fig. 6.13: Average discharge rate [Scenario 1]

Bibliography

[1] T.G. Theofanous et.al., ”In-Vessel Coolability and Retention of a Core Melt”, DOE/ID-10460 (July 1995).

[2] M. Epstein et al., ”Simultaneous Melting and Freezing in the Impingement Region of a Liquid Jet”, AIChE J., 26 (5) (1980), p .743.

[3] B.R. Sehgal, W.G. Dong, J.G. Green, and T.N. Dinh, ”Experiments and Analyses of Melt Jet Impingment during Severe Accidents”, Proceedings of the Fifth International Topical Meeting on Nuclear Thermal Hydraulics, Operations, and Safety (NuTHOS-5), Beijing, China, April 1997.

[4] V.A. Bui and T.N. Dinh, ”Modeling of Heat Transfer in Heat-Generating Liquid Pools by an Effective Diffusivity-Convectivity Approach”, *Proc. of 2nd European Thermal-Sciences Conf.*, Rome, Italy, 1996, pp.1365-1372.

Chapter 7

Project Major Findings and Conclusions

The MVI Project has been successfully concluded with the resolution of several MVI issues and several advances of practical significance in risk/consequences analysis and in evaluating existing and proposed SAM measures. Many findings were made, data obtained and methodologies developed. In the following we will describe the most significant findings and conclusions.

The melt jet impingement issue has been resolved. The risk of immediate vessel failure due to melt jet impingement is extremely low. A scaling analysis was developed to demonstrate the applicability of the data to prototypical geometry and the accident conditions.

The hole ablation issue has been resolved. the HAMISA methodology can make predictions for prototypical accidents. the maximum hole size in the vessel will be 15 to 20 cm, rather than 50 cm as estimated earlier, thereby reducing the rate of containment loading by the melt discharged.

Data for melt pool convection were obtained for the Ra numbers at prototypic accident conditions on the COPO and BALI facilities. These data can be used for the validation of computer codes. There appears to be consistency between the data obtained from the COPO and the BALI experiments; however, the data obtained differ from the results obtained earlier from other experiments, in which no crust were formed. The crusted boundaries were found to increase the heat fluxes, however the power split between upward and downward directions fits previous correlations. More importantly, it was found that pool stratification increases downward heat flux. Some issues have to be resolved before a clear statement about the feasibility of in-vessel melt retention, through the accident management scheme of external vessel cooling for a plant of $\leq$1000MWe can be made.

Experiments were performed on the SULTAN facility for critical heat flux

(CHF) on long and wide steel flat plates which were cooled with water at different conditions of pressure, flow rate, etc. The CHF data obtained was fitted to correlations which could be applied for estimating the limit on heat removal by external cooling of the lower head.

The SIMECO facility has provided valuable insight into effect of stratification on natural convection heat transfer. Unique data has been obtained, which could be used for validation of natural convection heat transfer models, in case of stratification of miscible and immiscible fluids.

The FOREVER/C1 test is the first integral experiment, in which a decay-heated oxidic melt pool was maintained in long-term contact with the hemispherical lower head of a pressurized, creeping, steel vessel. The experiment was successful. A sizeable database was obtained on melt pool temperatures, melt pool energy transfer, heat transfer rates, heat flux distribution on the melt (crust)-vessel contact surface, vessel temperatures, and time-dependent multiaxial vessel wall creep deformation. The multiaxial three-dimensional creep deformation data obtained for prototypic reactor vessel steels at high-temperature conditions, could be employed for validation of models for creep deformation, in structural mechanics codes.

The FOREVER experiment did not reveal a gap between the crusted melt and the creep-deformed vessel wall. However this experiment did not have any water. The promise of gap cooling still has to be evaluated for the scenario of most concern, i.e., in which the original water contained in the lower head is evaporated, the core debris remelts and forms a pool, which undergoes natural circulation, and then the water supply is restored. Reliable experiments have to be designed and performed for such a scenario.

The FOREVER data indicated that the location of vessel failure in the prototypic accident will be near the upper corners of the spherical lower head. The mode of failure, the effects of penetrations on the timing and mode of failure have still to be determined. Determination of the timing is important for operator accident management actions e.g. for resumption of water supply to the vessel, for flooding of the containment cavity etc. The mode of failure is important for containment loading analyses.

The model development work also made significant progress. The models HAMISA and MVITA were developed and validated. The LOWHED code was validated and improved. Same can be said about the CORIUM-2D code. Creep and large strain models have been developed in the PASULA code system, which could be coupled with the modeling developed at RIT and at AEA Technology. The models developed, or improved, are candidates for incorporation in a severe accident scenario consequence analysis code e.g. MAAP, MELCORE, and SCDAP/RELAP.

Chapter 8

Remaining issues of melt-vessel interaction

The research in the MVI Project was directed towards resolving[1] some of the key issues (questions) that arise in the prediction of the consequences of the in-vessel progression of a severe accident. The work performed resolved some of the key issues identified at the start of the project e.g., (1) vessel failure due to melt jet attack (2) vessel failure-site ablation rate on melt discharge (3) limitations on in-vessel melt retention by external cooling. Sufficient information however, was not obtained to fully resolve the other issues. In addition, since that time some new issues have been identified by the findings from the RASPLAV Project. In order to deliver the benefits of the research performed in the MVI Project to the end-users, it is also mandatory that the research results and the methodologies developed be applied to practical design and backfit activities for the existing and future LWRs, and in the process examine the applicability of the information to the various designs. We believe that for the late phase of in-vessel accident progression, and for the determination of the feasibility of in-vessel melt retention; the following issues remain to be resolved.

1. Will the lower head, with penetrations, survive a possible steam explosion that could occur during the phase of melt relocation from the original core boundary to the lower head when lower head is full of water and before a melt pool forms, convects and exerts significant thermal loadings on the lower head wall.

2. Can the melt (debris) be cooled e.g. by gap cooling, by the water in the lower head, to preclude vessel failure?

[1]By resolution we mean that sufficient information and validated methodology have been developed to predict the consequences for prototypic accidents scenarios, to the level of acceptable uncertainty.

3. In the absence of cooling inside and/or outside of the lower head, how long will it take to fail the lower head by the melting and creep processes?

4. What is the mode and location of vessel failure with and without penetrations, in particular, when a convecting melt pool resides in the lower head, and what is the total melt discharged to the containment?

5. Does the melt stratification, observed in the RASPLAV Project change the conclusions on the feasibility of in-vessel retention by external cooling?

6. Are the predictions of the maximum heat removal rate (critical heat flux) by external cooling valid for all vessel and lower head geometries (including penetrations) and for the vessel locations along the angle in the lower head?

7. How to apply the information and the methodology developed, thus far, to (1) the design of the accident management procedure for in-vessel retention for some existing or future nuclear power plants, and (2) reduce the uncertainties in the estimation of the loads imposed on the containments of the existing Light Water Reactors (LWRs) in the event of vessel failure?

These issues are believed to be important and must be addressed and resolved in future EU Projects concerned with the later phase of in-vessel melt progression and the assessment of the reactor vessel integrity.

The issue no.1 concerns the lower head failure in the event of a steam explosion during melt relocation, since if the lower head integrity is lost e.g. due to penetration failure caused by a steam explosion in its vicinity, issues (concerns) about in-vessel melt retention become moot. The issue no.2 is about the efficiency of gap cooling, whether it can relied upon to cool the vessel wall from inside, after water delivery to the vessel has been restored, late in the scenario of in-vessel melt progression. The issue no.3 is important for the current generation plants in which no external vessel cooling has been provided. The time to vessel failure is an extremely important parameter for severe accident management (SAM) since this time is of essence in devising SAM measures or correcting reactor system failure e.g. restoring electric power in station black-out scenarios or restoring auxiliary or backup preventive systems which may be temporarily non-operative. Issue no.4 concerns the type and location of failure that may occur in the lower head e.g. it is very probable that the failure will be local (around a penetration) due to the creep and stretching of the lower head, near the upper part of the lower head. This may limit the amount of the melt discharged to the containment. The size, shape and location of the lower head failure are important for the ex-vessel progression of the accident.

Issue no.5 has arisen since the observations made in the first and second RASPLAV-AW-200 experiments, in which the melt pool containing UO_2-ZrO_2-Zr stratified into a lower and heavier pool containing a greater fraction (than input) of UO_2 and an upper lighter layer containing a greater fraction of Zr and ZrO_2. Some preliminary experiments performed in the SIMECO facility during the MVI project simulating the stratified pool convection showed that the power split could change and larger heat could be divided to the lower head which would lower the coolability margins for in-vessel melt retention. Much work has been performed on issue no.6 for clean spherical lower head, however, the influences of the penetrations and different geometries on the values of the CHF, particularly at high angular positions. Finally, the issue (7) concerns the application of research results obtained to current and future plants, both in the design of the accident management scheme, or, in its absence, in the reduction of the uncertainty in the loads imposed on the containment if the vessel fails.

Appendix A

Description of Oxidic Jet Impingement Experiments

A.1 Abstract

This section describes the jet impingement test conducted on May 13, 1997 at the Royal Institute of Technology Division of Nuclear Power Safety (RIT/NPS) laboratory. Fifteen (15) liters of a 1350^{o}C melt of 30-70 w/o $CaO-B_2O_3$ composition was made and directed in a 25mm jet onto a 50mm thick Al disk with embedded thermocouples. No ablation (erosion) of the jet was observed as a result of the highly protective crust layer which was formed.

Results of inverse heat conduction calculations revealed that jet impingement heat fluxes are in a better agreement with RIT/NPS heat transfer correlation $Nu = 0.0027 \cdot Pe$ than with a classical laminar stagnation flow model ($Nu = 0.55 \cdot \sqrt{2}Re^{0.5} \cdot Pr^{0.35}$).

A.2 Experimental Arrangement and Test Conditions

A.2.1 Experimental Arrangement

The purpose of this test was to examine jet impingement heat transfer with phase change for higher temperature conditions than have previously been attempted at RIT/NPS. Approximately 15 liters of a 30-70 w/o $CaO-B_2O_3$ oxide mixture was generated by inductive heating in the Si-C crucible. This melt was heated to nearly 1350^{o}C and then remotely tipped into a heated test section which was connected to a 1 m long tube of 25 mm diameter. Although it was originally intended to heat this tube section by a coil of resistively heated wire, the coil shorted during heating and thus the initial temperature of the tube was very nearly atmospheric

just prior to introducing the melt. A small portion of the melt was tipped into the upper test section and then a plug mechanism was raised to allow the hot melt to flow into the 25 mm tube section.

A.2.2 Test Section

A 50 mm thick Al cylinder was positioned directly below the tube section and aligned such that the center of the 25 mm tube corresponded directly to the center of the Al disk. Eight (8) K-type thermocouples of 1.0mm OD were embedded directly along the centerline of the cylinder which corresponds to the jet stagnation zone. The spacing between these thermocouples is as shown in Figure A.1 and listed in Table A.1. The Al plate was 78 mm in diameter and surrounded by Victor Corund insulating material. The distance from the jet pipe exit to the upper surface of the plate was 174 mm, or $\sim$7 jet diameters. The initial block temperature was 35^oC.

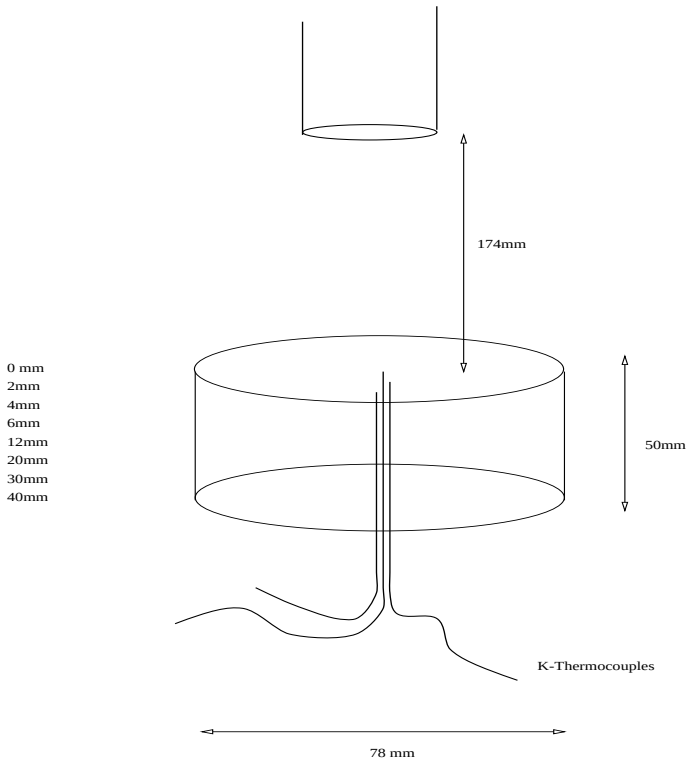

Fig. A.1: Jet Impingement Plate Arrangement

Table A.1: Thermocouple Layout and DAS

Channel	Depth (mm)
ch0	0
ch1	2
ch2	4
ch3	6
ch4	12
ch5	20
ch6	30
ch7	40
ch8	tube
ch9	tube
ch10	tube
ch11	section

A.2.3 Melt Preparation and Characteristics

The melt was prepared by inductively heating a mixture of CaO and H_3BO_3 powder. The amount of powder used was 55 kg however during heating the borsyra (H_3BO_3) loses $\sim$35% of its mass as water. Thus for the 30-70 w/o mixture this means that 12 kg of CaO and 28 kg of B_2O_3 results, or a total mass of melt of 40 kg. If one assume a density of 2500 kg/m^3 this mass provides a volume of 16 liters. The height of melt in the crucible just prior to pouring was measured to be 0.32 m which for the 0.25 m diameter crucible corresponds to 15.7 liters. The difference can easily be attributed to the approximate value of 35% water loss and any powder lost during melt generation.

Although it was planned to employ a B-type thermocouple to measure the melt temperature, difficulty was encountered when this ceramic-protected lead was placed inside the melt and thus inside the magnetic field of the induction coil. Work is necessary on this aspect of the oxide experiments since standard K-type thermocouples have extremely short lifetimes at temperatures above 1200^{o}C. The melt temperature, as measured by an inconel-sheathed K thermocouple, was determined to be 1349^{o}C just prior to pouring out the melt. It is advised that we purchase a single hand-held pyrometer to supplement our thermocouple measurements.

Generation of the melt required close to 5 hours. Some difficulty with the pressure (flow) limit switch of the generator cooling water was encountered but quickly rectified. It was noticed that no more than 40 kW can be delivered to the

coil regardless of the amount of melt in the Si-C crucible. This was found to be a limitation since even at maximum power input, the external temperature of the crucible remained below 1300^{o}C and a fairly long time was required to take the fully molten melt up in temperature. Clearly, heat losses from the surface and sides as well as the degree of magnetic coupling are limitations. The generator readings at full power are 38 kW, 280 VAC and 18 kHz.

The thermal properties shown in Table A.2 are appropriate for Aluminum and the oxide melt employed.

Table A.2: Thermal Properties

Property	30-70 w/o $CaO - B_2O_3$	Al
T_{sol}(^{o}C)	980	660
T_{liq}(^{o}C)	1025	660
ρ (kg/m^3)	2500	2700
$C_{p,l}$ (J/kg.K)	2370	$\sim$530
$C_{p,s}$ (J/kg.K)	1240	$\sim$950
H_{fusion} (kJ/kg)	430	396.3
κ (W/m.K)	$\sim$2.5	220

A.2.4 Test Performance

The melt was remotely poured in less than 10 seconds into the 0.28 m diameter (0.5 m long) upper test section. At approximately 3 seconds into this pouring, the plug rod was removed by the crane to allow the melt to flow into the 1 m long, 25 mm ID flow tube. The reason for raising the plug prior to delivering all of the melt was due to the fact that the resistive heater which was intended to heat the jet tube prior to the test developed a short. This resulted in tube temperatures of near atmospheric ($\sim$30^{o}C) when the melt was delivered.

The twelve (12) thermocouples listed in Table A.1 were scanned by the HP DAS 2000 times at a NPLC value of 0.1. This required 125.4 seconds which implies a between-channel recording speed of 15.9 Hz. The high speed was obtained because millivolts instead of temperature was read and conversion was performed post-test.

A.3 Experimental Results

Essentially all of the melt was delivered into the test section (some small amount in bottom of crucible) and all of the delivered melt was seen to flow through the tube and onto the Al plate. Post-test examination showed that only a thin crust layer remained on the upper test section and that even though the jet tube was not properly heated, that very little of the melt was found to have cooled on the inside of the pipe. This implies that the jet temperature was high enough to prevent any significant solidification prior to exiting the 1m long pipe. In fact, only roughly 3cm at the end of the pipe showed any buildup of oxide crust at all. The remainder of the 1 m length showed nothing more than a very thin glass layer.

An estimate of the contact temperature can be made as

$$T_{contact} = \frac{T_j \kappa_j \sqrt{\alpha}_j + T_w \kappa_w \sqrt{\alpha}_w}{\kappa_j \sqrt{\alpha}_j + \kappa_w \sqrt{\alpha}_w} \tag{A.1}$$

For a 1300^{o}C melt and an initial plate at 35^{o}C, this would predict an initial contact temperature far below the Al melting point and thus a crust should indeed form.

Absolutely no ablation of the Al plate was observed. A crust layer clearly developed and protected the plate from any further attack. The maximum temperature in the plate never exceeded 490^{o}C for the uppermost thermocouple, which is well below the 660^{o}C Al melting point.

Figure A.2 shows the temperature responses of the embedded thermocouples. Notice that the temperature rise begins at $\sim$12 s into the data recording and ends by 30 s implying a jet discharge time of 18 s. Estimate of average jet velocity gives 1.7 m/s. Given that the plug was pulled prior to all the melt being delivered the impingement period of 17 s seems reasonable with the likelihood of a smaller jet velocity (1.5 m/s).

A.4 Analysis and Discussion

The Inverse Heat Conduction Problem (ICHP) is one in which measured temperatures inside a conducting block are used to estimate surface boundary conditions. It is applicable in this jet impingement case. Beck's algorithms are used in a fashion similar to that of his CONTA code [1]. Method of "future time steps" are employed and the entire scheme is based upon the minimization of errors between predicted and measured temperatures. Although the code allows for tabular input of properties with respect to temperature, only constant temperature values for the Al plate were used.

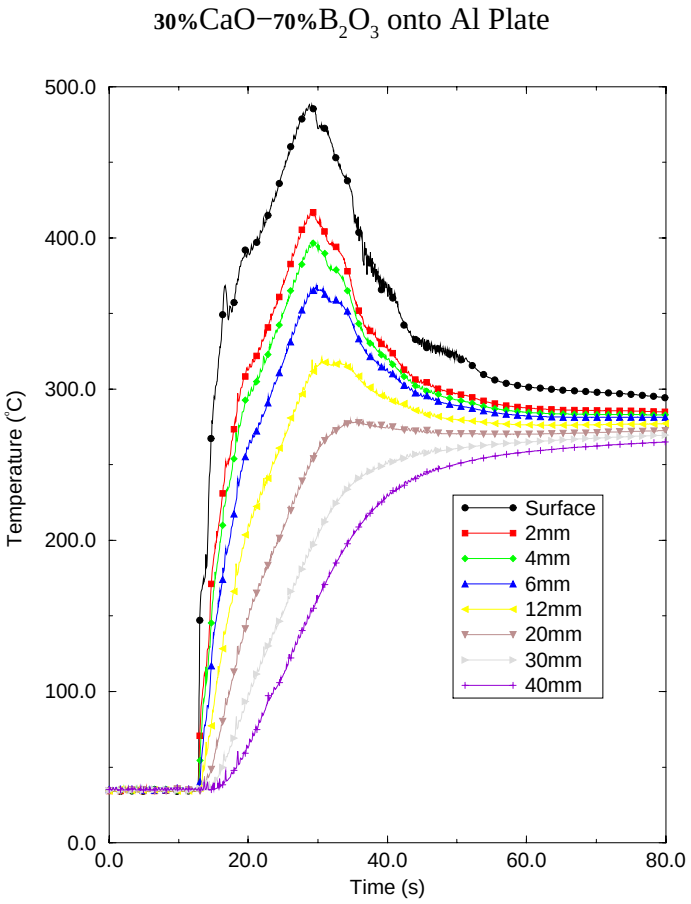

Fig. A.2: Temperatures of Embedded Thermocouples

The variation of temperature inside the plate for the duration of the jet impingement is given in Figure A.3.

Notice that it is likely that the thermocouples at 2mm and 4mm look as if they might actually be located somewhat closer to each other. It is impossible to have a very high degree of precision when placing these thermocouples and then filling them in with molten Al . Next, it is seen by the curvature in these lines that simple conduction alone is not sufficient to explain the heat transfer. That is why the specific heat must be accounted for in the calculation (transient component).

In order to overcome uncertainties associated with temperature measurement and thermocouple locations three thermocouples data were employed in the input file for IHCP solution.

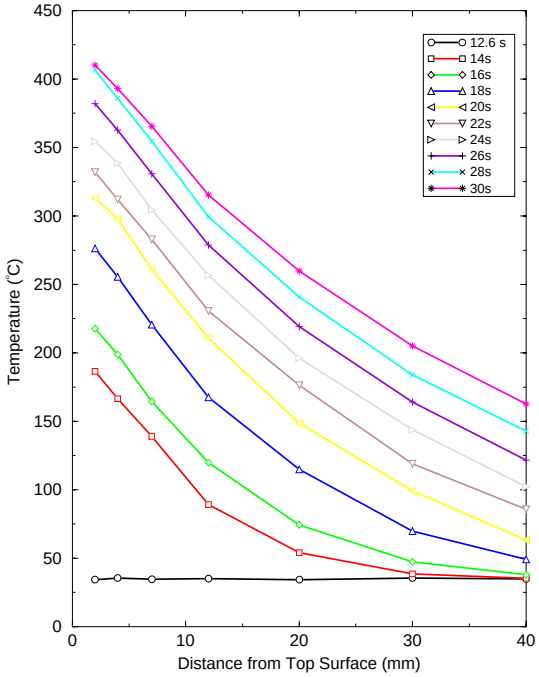

Fig. A.3: Temperature Variation in Al Plate with Depth

The end result is that the calculation predicts a surface temperature which is lower than that for the uppermost thermocouple. Granted, it is more likely that the upper thermocouple reads some intermediate temperature since it is not exactly at the surface. The fact that the predicted surface temperature is less than that measured points to the fact that thermal properties are not entirely certain and also that there is some uncertainty as to the positions of the thermocouples (especially close to the surface). Some residual uncertainty can of course be due to the choice of node sizes and time step for the IHCP but sensitivity to this was found to be quite small. Another difficulty is the choice of boundary condition at the bottom of the plate. In this program an adiabatic assumption was made, however the plate is not adiabatic in reality. In order to overcome this difficulty, the adiabatic boundary condition is given at a distance which is significantly longer than the actual plate thickness.

The surface heat flux resulted from solution of IHCP is shown in Fig. A.5. It can be seen that in the first ten seconds the jet impingement heat fluxes are quite high. The IHCP solution gives values up to 3 MW/m^2. However, it may

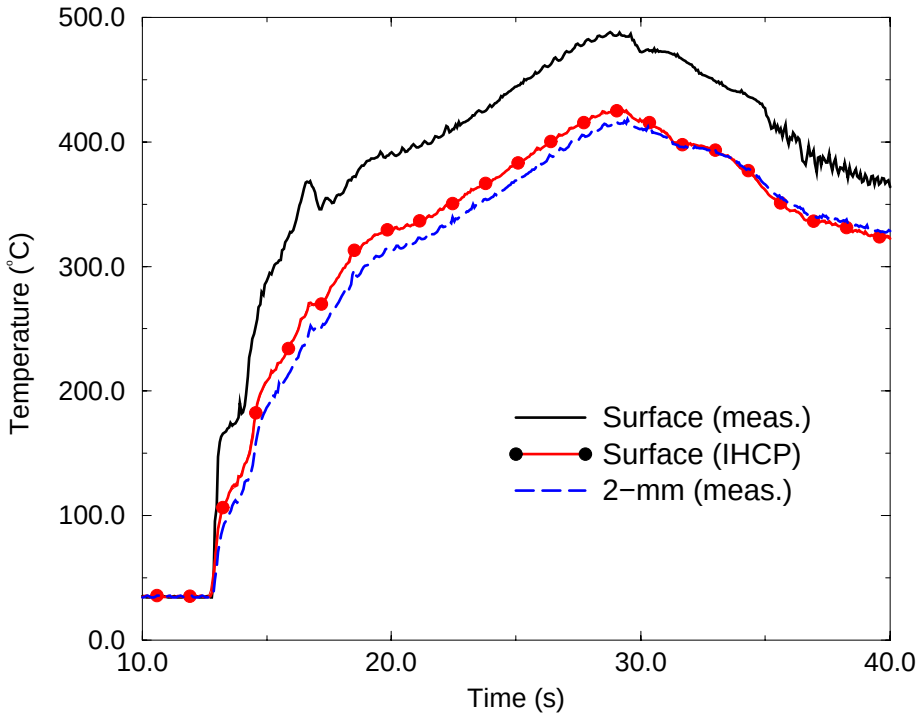

Fig. A.4: Inversely Predicted Surface Temperature.

be expected that the actual heat fluxes are significantly higher. Lower heat fluxes obtained from IHCP solution are related to small temperature differences detected by thermocouples during the first period of fast temperature increase. During the period from 20 to 30 seconds heat-conduction fluxes are estimated to be 1.8 MW/m^2.

Based on the estimated impingement period of 18 s, we assume that the jet velocity is roughly 1.7 m/s and thus the Re for the melt jet flow is $\sim$9200. Since the melt fluid Pr number is $\sim$95, the Peclet number for this test is 874,000, which is quite high. From the thermocouple measurement, it can be assumed that the melt superheat over the liquidus is $\sim$200K.

For the test conditions, the laminar-flow-stagnation model provides $Nu \simeq$ 360 or $h \simeq$ 36,000 W/m^{2}K. As a result, the jet impingement heat fluxes are 0.7 MW/m^2 which are significantly lower than the heat-conduction fluxes determined from thermocouples data by solving IHCP.

The same test conditions would yield a Nu based on the RIT/NPS correlation,

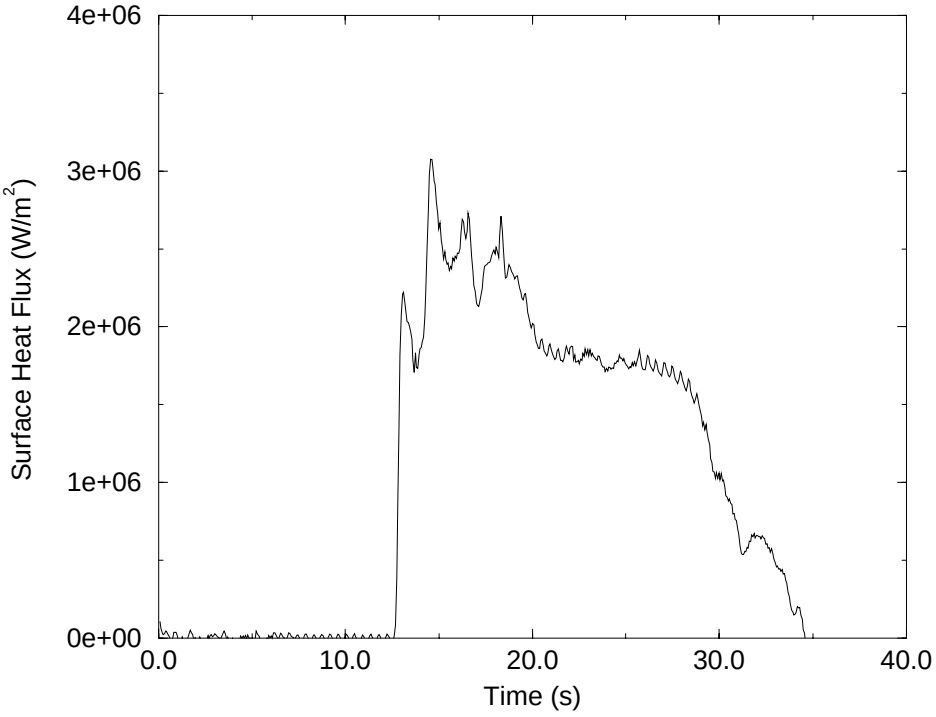

Fig. A.5: Inversely Predicted Surface Heat Flux.

Eq.(A.2), of 2360 or a heat transfer coefficient of 236,000 W/m^{2}K.

$$Nu = 0.0027 \cdot Pe \tag{A.2}$$

As a result, the jet impingement heat flux can be estimated as about 4.5 MW/m^2. It is in a reasonable agreement (factor of 2x) with experiment result, taking into account other uncertainties associated with measurements and solution of IHCP.

Finally, it should be noted that the average jet velocity may be far overestimated as to a significant melt portion was observed to slowly discharge from the jet nozzle in an enlonged period ($t > 30$ s.). Accounting for this fact would further improve the performance of the RIT/NPS model, and increase the disagreement between the measured heat fluxes and the one determined by the laminar stagnation model.

Bibliography

[1] J.V. Beck, B. Blacwell, Ch. Clair, ”Inverse Heat Conduction Ill-Posed Problems”, Walay-Interscience Pub., 1985.

Appendix B

Salt-Salt and Salt-Metal Jet Impingement Experiments

B.1 Abstract

This section presents the results from a series of jet impingement tests conducted in the RIT/NPS laboratory using salt and metal alloy as severe accident simulant materials. The purpose of this experimental research was to determine the jet impingement heat transfer rates in order to compare them to existing correlations and thereby to make predictions regarding the likelihood of reactor pressure vessel failure due to a relocation melt jet during the course of a severe reactor accident. Two types of experiments were conducted; in the first the melt simulant was $NaNO_3$-KNO_3 and the substrate was solidified HITEC salt, while in the second series the impinging jet was either HITEC or the nitrate salt mixture onto a Cerrobend alloy plate. Thermocouples embedded in the jet stagnation zone allowed for a determination of jet impingement heat transfer and ablation rates. Test conditions will be described here along with a presentation of the applicable heat transfer and comparisons.

B.2 Introduction

In the unlikely event that a core melt accident were to occur, a molten melt pool of both oxidic and metallic components could be formed within the core boundaries. Such a melt pool may relocate from its original location in the form of a melt jet. The question of interest here is whether the relocating jet can ablate the lower reactor pressure vessel (RPV) steel and thus provide a release path for fission products to the containment atmosphere. Given the complicated geometry of a nuclear reactor core and pressure vessel and the wide variability in jet composi-

tion, temperature, duration and size, the relocation event will be highly design and scenario dependent. However, the crucial phenomena of interest is that of direct melt contact with the RPV steel and the extent of ablation which could result. The focus must therefore be placed upon melt jets with temperatures greater than the melting point of the impinged-upon metal and which may exhibit a mushy-zone freezing behavior as would corium. Under certain situations the lower plenum could be partially filled with coolant. In that instance, fragmentation of the relocating jet could occur with the potential for in-vessel steam explosions. However, such conditions are not of interest here.

B.3 Description of Tests

Two series of jet impingment tests have been carried out in the RIT/NPS laboratory which will be described here. The first involves a melt jet of salt impinging upon a solidified salt plate. The second series has similar salt melt jets but instead the substrate metal is that of the Cerrobend alloy.

Of high importance to this study is the thermo-physical properties of the melt jet and plate materials. For the salts, the nitrate mixture called HITEC and also the binary salt combination of $NaNO_3$-KNO_3 has been employed. The sodium and potassium nitrate mixture has been described in detail in the report by Green [1] and a phase diagram is included there. Two representative compositions for this salt mixture have been chosen. First is the near-eutectic of 50-50 a/o and the second is the 20-80 $NaNO_3$-KNO_3 mixture which exhibits a roughly 60^oC region between T_{sol} and T_{liq}. The Cerrobend alloy is a mixture of heavy metals with melting point of 70^oC. It is very likely that due to oxidation of the metals that this melting point is higher and that perhaps a mushy region also exists for this simulant.

More about HITEC. The material is not called HITEC here in Sweden but rather by its trade name "Cassell". It is made by CHV Chemie in Cologne, Germany under the name "Heat Transfer Salt 3145" and its use is for the vulcanization of rubber (tires). It should not be used above 550^oC. It is made from a mixture of 53% KNO_3, 40% $NaNO_2$ and 7% $NaNO_3$. The HITEC exhibits a singular melting point of 142^oC (although in practice it has been seen to be nearly 150^oC). T_{mp} = 142^oC. The properties of the melt simulant HITEC are shown in Table B.1. No information for the thermal conductivity of HITEC could be located and thus the value of 0.45 W/(m.K) was assumed since the chemical makeup of this salt is very much similar to that of the binary nitrate mixture.

The experimental arrangement involves a heated C-steel cylinder with a single discharge tube at its bottom. The tube diameter used in all of the experiments here was 25mm. The test section for the melt is 160mm in diameter and 500mm tall

Table B.1: Thermal Physical Properties of Hitec Melt

Property	-	HITEC
T_{mp}	^oC	142...150
ρ_l	kg/m^3	1950 (200^{o}C) ... 1750 (500^{o}C)
$C_{p,l}$	J/(kg.K)	1600 (250^{o}C), 1700 (300^{o}C), 1800 (350^{o}C)
H_{fusion}	kJ/kg	260
κ	W/(m.K)	0.45
μ	Pa.s	3.4x10^{-3} (200^{o}C), 1.4x10^{-3} (300^{o}C), 1x10^{-3} (400^{o}C)

(maximum volume of 10 liters). The discharge of melt from the test section is controlled by a gate valve. The length for melt flow inside the tube is approximately 300mm and the distance from the end of the jet tube and the top of the impinging plate is $\sim$6 tube diameters (thus eliminating any significant impact due to this distance). The melt was generated by electrically heating the test section. Discharge velocities were measured by timing the rate of discharge. It must be strongly noted that the rate of melt discharge, and therefore jet velocity (Re), is *not* constant throughout this process. That is, the gravity driving head is greatest at the the initial impingement time frames and decreases thereafter. Gas blowthrough is unavoidable and thus the last amounts of melt which hits the plate is erratic.

The plates are instrumented with small diameter (1mm) groupings of K-type thermocouples. These thermocouples are spaced a known distance from one another and are soldered into a single bundle. The overall bundle diameter is typically less than 3mm. The plate is made by filling in a form with the thermocouple bundle already in place centrally. The thermocouples are therefore embedded in the solidified plate (be it salt or cerrobend) and the plate is arranged such that the thermocouples are directly under the impinging jet and thus in the stagnation zone of the jet. Typical jet separations are 2 to 2.5mm in the upper region of the plate and more at further depths.

Table B.2: RIT/NPS Salt-Salt Jet Impingement Tests

Test Date	Melt	Plate	D_o (mm)	T_{melt} (^{o}C)	Volume (liters)	δ_p (mm)	P (bar)
1017	50-50 w/o (Na,K)NO_3	HITEC	25	263	7.0	25	n/a
1018	50-50 w/o (Na,K)NO_3	HITEC	25	310	9.2	25	n/a
1118	20-80 w/o (Na,K)NO_3	HITEC	25	400		30	3.0

In some of the tests, the test section was capped and air pressure was supplied at either 2 or 3 bar (gauge). A pressure transducer was employed which was calibrated against a known gauge. The calibration is provided in Figs.B.1-B.2. To test the pressure transducer, the section was filled with water to 400mm and then pressurized to a given pressure and allowed to depressurize by opening the valve. The recorded signal from the transducer is provided as an attached figure. The discharge for these pressurized tests was exceptionally fast, yielding typical velocities on the order of 5 m/s. One of the problems with this arrangement was the fact that the PT cell power supply (10VDC) was introducing noise into the thermocouple readings. In order to read the PT cell, the temperatures must be recorded in millivolts and later converted by post-processing. A second problem with the pressurized tests was the fact that the discharge was initially very high and quickly led to the gas space blowthrough and then a longer period of intermittent melt discharge. In general the current test section design is not proper for conducting pressurized jet impingement tests.

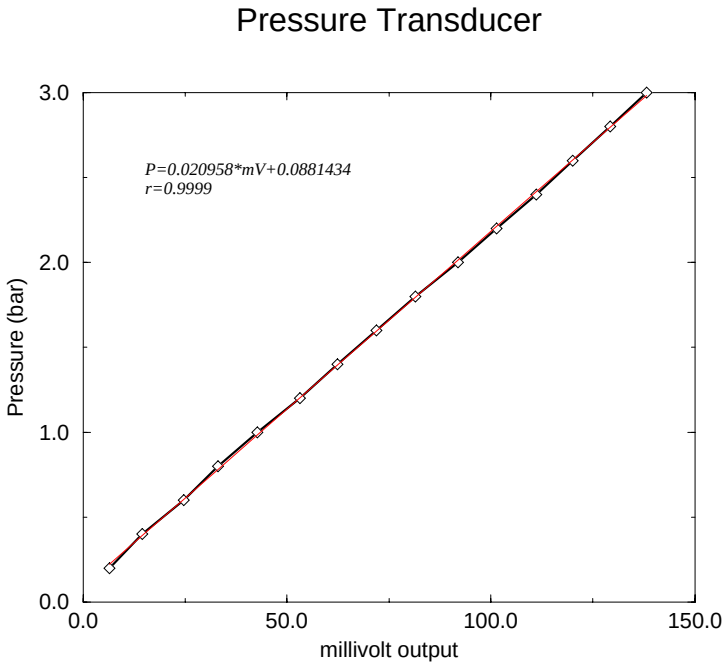

Fig. B.1: Correlation of Pressure Transducer.

All of the applicable jet impingement test data is represented in Tables B.2 and B.3 for the Salt-Salt and Salt-Metal tests, respectively.

In test 1025 (10/25/96) the Cerrobend plate was inclined 30^o to normal. All other tests were conducted with the jet impinging normally to the plate surface.

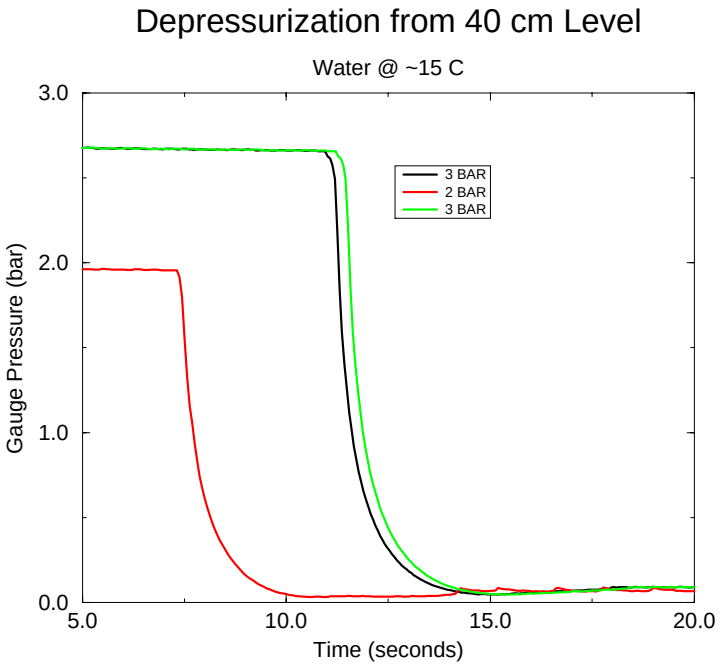

Fig. B.2: Depressurization of test section.

B.4 Experimental Results

Tables B.4 and B.5 provide the determined velocities and any data acquisition system abnormalities for both sets of tests.

All of the recorded thermocouple responses are shown in Figs.B.3-B.5 for the 3 salt-salt tests and Figs.B.6-B.10 the 5 salt-cerrobend tests. One can see that in some cases the impingement resulted in a complete melt-through of the plate, while in others it did not. The timing between when the sequentially embedded thermocouples encountered the jet fluid was taken to provide an ablation velocity. One can see from the figures that in some cases the uppermost (surface) thermocouple was actually above the upper surface of the plate and thus shows an uncharacteristic response. The ablation velocity was then fed into the EES software program with applicable melt and plate thermal properties in order to provide an estimate of the Nusselt number for heat transfer in the stagnation zone. The results from these calculations are provided in Tables B.6 and B.7.

Notice that there are clearly some ”outliers” in the results. Often these points are the from the very last thermocouples just prior to melt-through. These points have been eliminated from the database since they are clearly unreasonable and could likely be due to the fact that at longer times the entire plate has been heated and that these thermocouples embedded at greater distances could perhaps be

Table B.3: RIT/NPS Salt-Cerrobend Jet Impingement Tests

Test Date	Melt	Plate	D_o (mm)	T_{melt} (^oC)	Volume (liters)	δ_p (mm)	P (bar)
1010	HITEC	Cerrobend	25	200	6.2	25	n/a
1014	50-50 w/o (Na,K)NO_3	Cerrobend	25	250	5.1	20	n/a
1025	50-50 w/o (Na,K)NO_3	Cerrobend	25	320	9.1	25	n/a
1112	20-80 w/o (Na,K)NO_3	Cerrobend	25	370		35	2.0
1113	20-80 w/o (Na,K)NO_3	Cerrobend	25	400		30	3.0

Table B.4: RIT/NPS Salt-Salt Data Acquisition

Test Date	$\sim$Velocity (m/s)	# Channels (–)	Scan Time (s)	Comment
1017	1.8	7	53.9	TC5 broken
1018	2.0	7	53.9	TC5 broken
1118	5.0	11	49.3	PT failed, mv read

simply ”falling-out” of the plate and thus recording the higher melt temperatures which are in the collection tray.

In addition there is considerable data scatter. This is attributable to many reasons:

- Experimental error in the distances between sequential thermocouples. This can be a significant aspect since a $\pm$0.5mm change in thermocouple placement will result in a significant change in the determined ablation velocity.
- The aforementioned fact that initially the melt jet velocity is higher and then decreases as either a) the gravity head decreases and/or b) the overpressure decays away.
- Typical errors in measurements (TC uncertainty) and thermal properties.

B.5 Analysis and Discussion

The results of the determined impingement zone heat fluxes (Nu numbers) are presented as attached figures. Figures for the 3 salt-salt tests (Fig.B.11) as well

Table B.5: RIT/NPS Salt-Metal Data Acquisition

Test Date	∼Velocity (m/s)	# Channels (–)	Scan Time (s)	Comment
1010	1.9	8	83.1	Surface TC exposed
1014	1.6	7	54.0	TC5 broken
1025	2.0	10	58.6	TC2 broken, 30^o inclined
1112	4.7	11	50.1	PT noise, mv read
1113	5.4	11	50.1	PT disconnected, mv read

as the 5 salt-cerrobend tests (Fig.B.12) are provided. A combination of both test series is also given in Fig.B.13 . Included in these figures are the comparative lines for the Saito and Epstein correlations. Prandtl numbers typical of the salt jet melts have been provided when considering the laminar correlation of Epstein.

The from all of the heat transfer determinations are shown in the attached plots of Nu versus Pe. The Pe number has been chosen based on the analyses presented in Section 2 of this report.

Results of the salt-metal tests show what would be considered a better agreement with the laminar stagnation zone model of Epstein. Clearly the scatter in the test where the plate was inclined 30^o is very large as it is for the tests conducted under pressurized conditions.

One aspect here is the relatively densities between the melt and plate. For the salt-salt tests the densities are similar but for the case of salt-metal is it ∼2000 to 9670. As a result, the jet flow is likely unable to "sweep out" the melting cerrobend liquid and thus the ablation is probably much more the result of conduction than it is of jet impingement. Compare for example the figures for tests 10/10/96 and 10/14/96 first with that of 10/25/96 where the plate was inclined and then with the later pressurized tests. Clearly the plate is experiencing significant conduction heat transfer from the hot melt jet. Inclination of the plate serves to minimize this and pressurization nearly eliminates it (note time scales). It is evident that proper density differences are necessary to conduct jet impingement heat transfer experiments with relevance to prototypical situations.

Further analysis of this test data is unlikely to yield any more clarification. The fact that the lower density salt could not sweep out the heavier cerrobend is of interest along with the fact that lower heat transfer is realized under those conditions. Also, these experiments pointed to the difficulty in using a small volume test chamber for pressurized tests.

For the salt-salt tests, it can be seen that the Saito correlation does a better job at predicting the heat transfer than the laminar stagnation zone model. Yet

Table B.6: Salt-Salt Plate Erosion Measurements

Test	Temperature Taken (^{o}C)	Depth (mm)	Time (s)	V_{abl} (mm/s)	Nu_{exp} (–)
1017	160	Surface	17.90	–	–
		2.5	20.78	0.87	601
		5.0	23.31	0.99	684
		7.5	26.57	0.77	533
1018	160	Surface	6.90	–	–
		2.5	8.20	1.9	992
		5.0	9.66	1.7	888
		7.5	11.56	1.3	679
		10.0	13.76	1.1	574
1118	200	Surface	4.35	–	–
		2.0	4.83	4.2	1699
		4.0	5.43	3.3	1335
		6.0	5.97	3.7	1497
		9.0	6.62	4.6	1661
		12.0	7.30	4.4	1780
		15.0	7.85	5.4	2185

the agreement is not considered good as Saito correlation predicts somewhat 30% higher than the average heat-transfer data obtained from salt-salt jet impingement experiments. Also the data scatter is relatively high.

Finally, it should be noted that the Nusselt numbers calculated by the RIT/NPS correlation

$$Nu = 0.0027 \cdot Pe$$

are in good agreement with the salt-salt data set; see Fig.B.11.

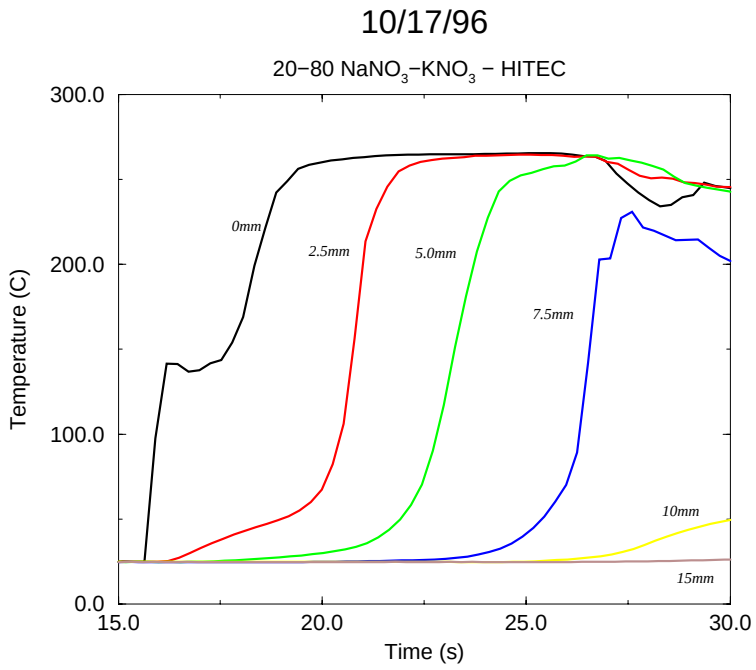

Fig. B.3: Test 10/17/96 - 50-50 a/o $NaNO_3$-KNO_3 onto HITEC.

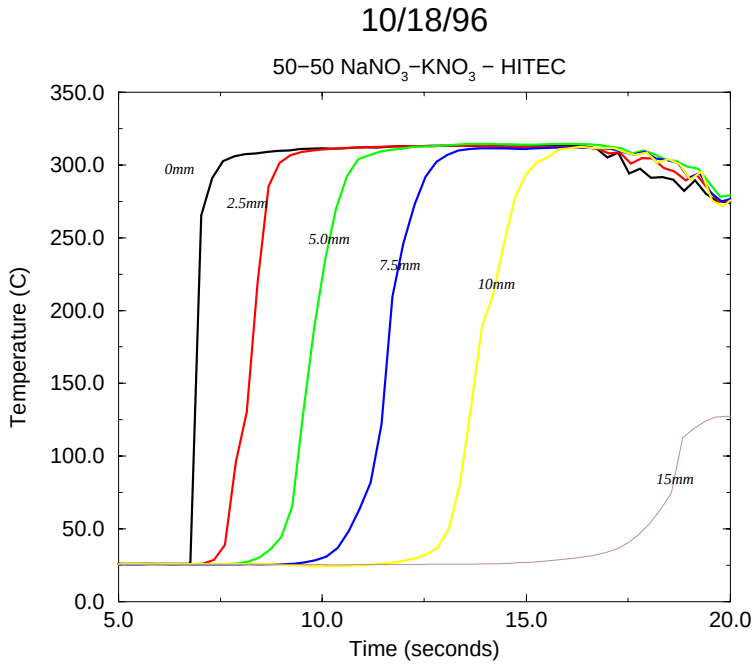

Fig. B.4: Test 10/18/96 - 50-50 a/o $NaNO_3$-KNO_3 onto HITEC.

Table B.7: Salt-Metal Plate Erosion Measurements

Test	Temperature Taken (^{o}C)	Depth (mm)	Time (s)	V_{abl} (mm/s)	Nu_{exp} (–)
1010	100	2.0	19.0	–	–
		4.5	19.9	1.25	402
1014	100	2.5	15.0	–	–
		5.0	16.9	1.33	301
1025	100	1.0	11.28	–	–
		3.0	12.67	1.44	271
		5.0	13.73	1.89	356
		7.0	14.49	2.63	496
		9.0	15.6	1.80	339
		12.0	16.2	5.0	942
		15.0	17.11	3.3	622
1112	100	0.0	5.59	–	–
		2.0	6.12	3.8	650
		4.0	6.67	3.6	616
		6.0	7.18	3.9	667
		9.0	7.69	5.9	1009
		12.0	8.01	9.4	1608
1113	100	0.0	6.71	–	–
		2.0	6.98	7.4	1206
		6.0	7.67	5.8	945
		9.0	8.31	1.9	310
		12.0	8.90	5.1	831
		15.0	9.36	6.5	1059
		19.0	10.15	5.1	831
		23.0	10.69	7.4	1206
		27.0	10.97	14.3	2330

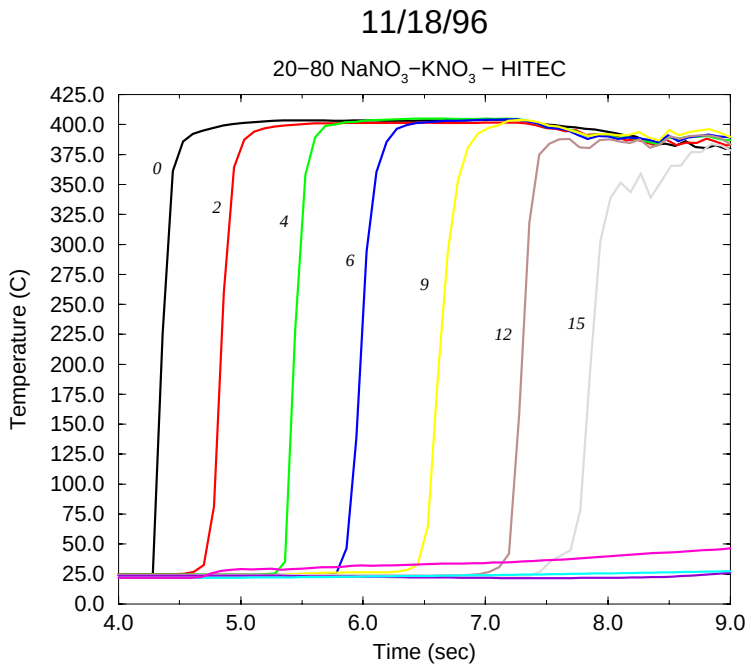

Fig. B.5: Test 11/18/96 - 20-80 a/o $NaNO_3$-KNO_3 onto HITEC.

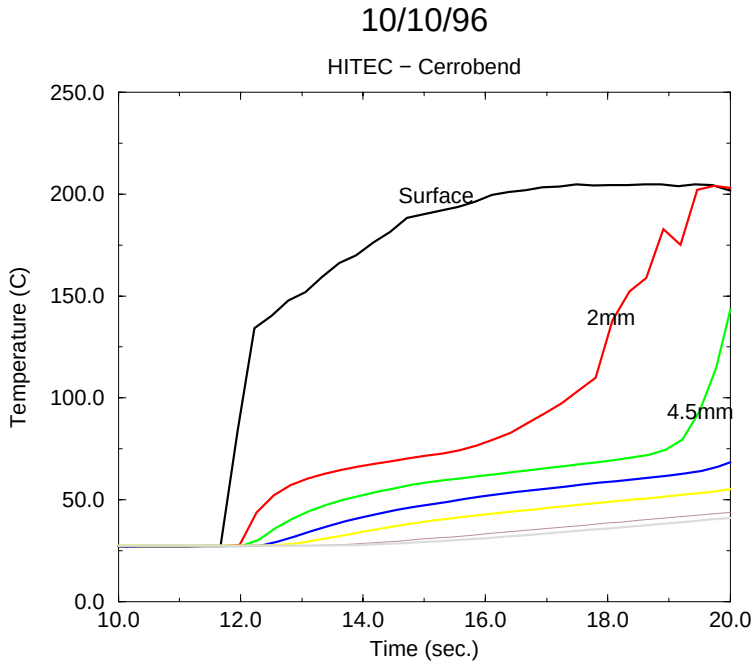

Fig. B.6: Test 10/10/96 - HITEC onto Cerrobend.

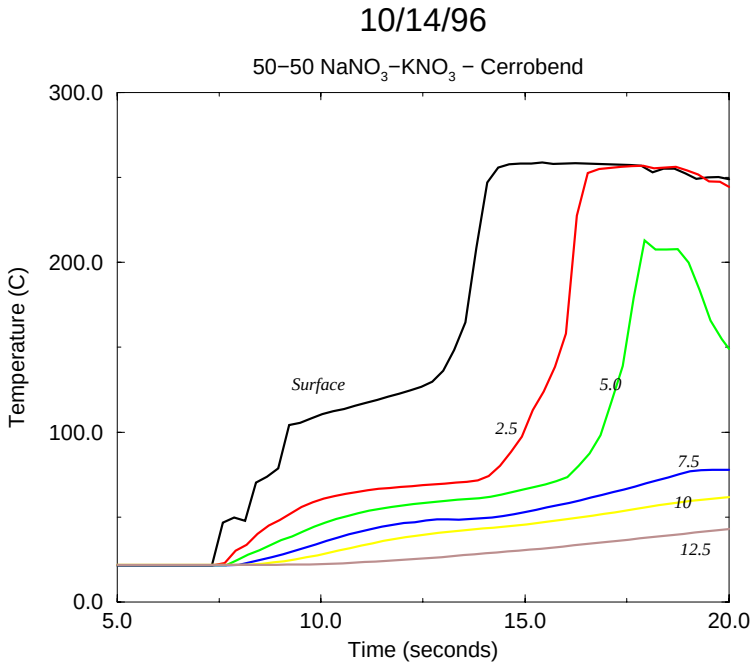

Fig. B.7: Test 10/14/96 - 50-50 a/o $NaNO_3$-KNO_3 onto Cerrobend.

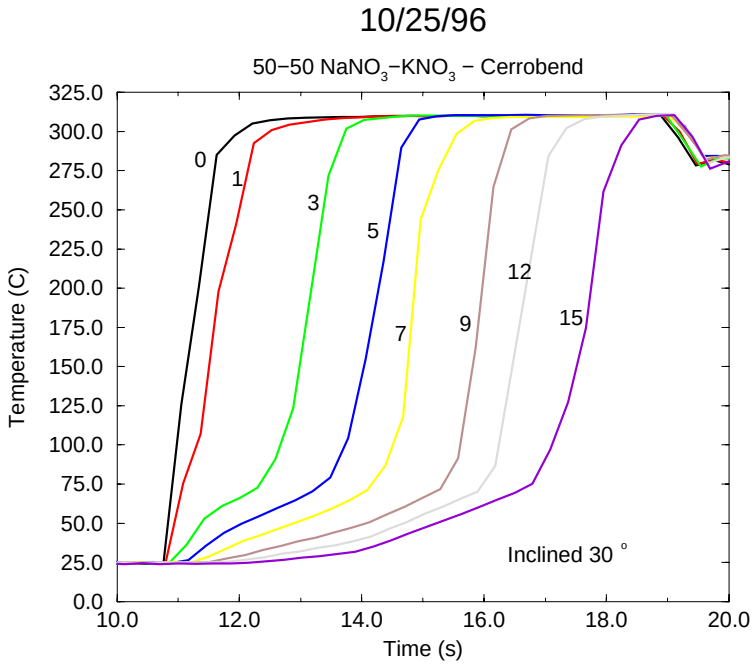

Fig. B.8: Test 10/25/96 - 50-50 a/o $NaNO_3$-KNO_3 onto Cerrobend.

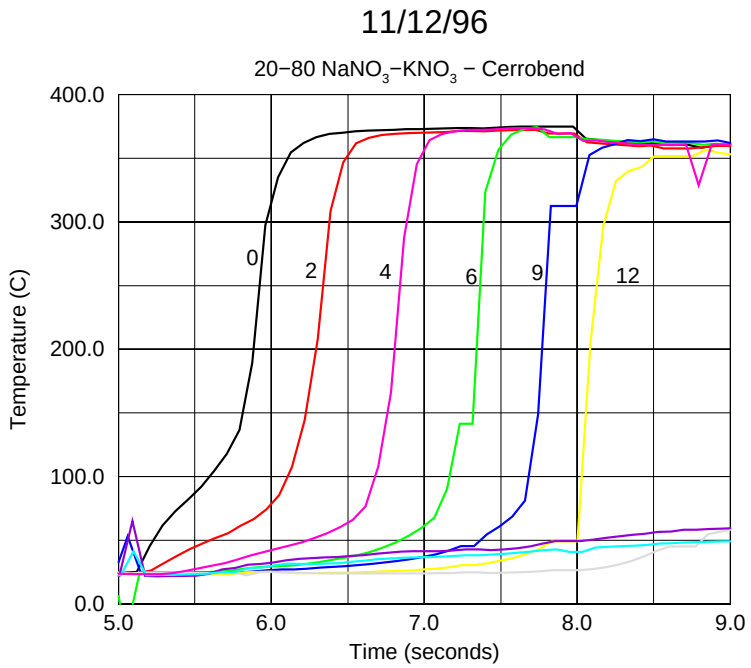

Fig. B.9: Test 11/12/96 - 20-80 a/o $NaNO_3$-KNO_3 onto Cerrobend.

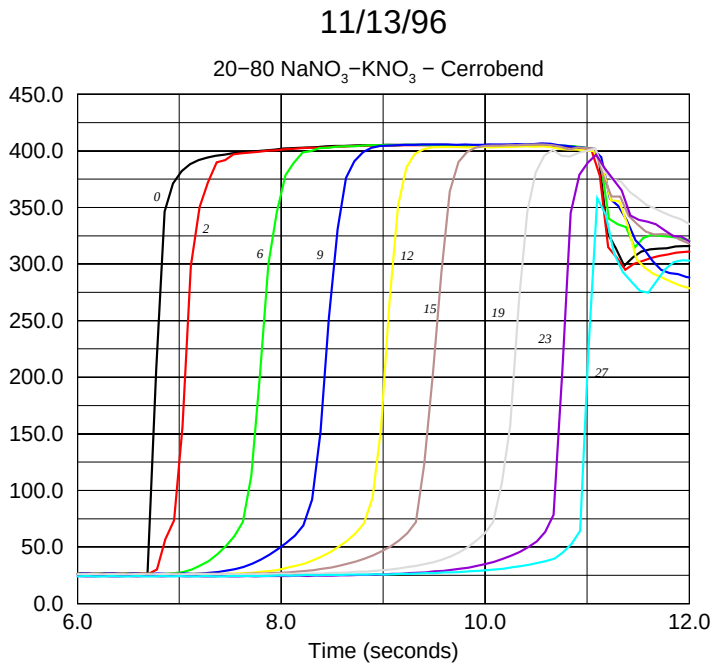

Fig. B.10: Test 11/13/96 - 20-80 a/o $NaNO_3$-KNO_3 onto Cerrobend.

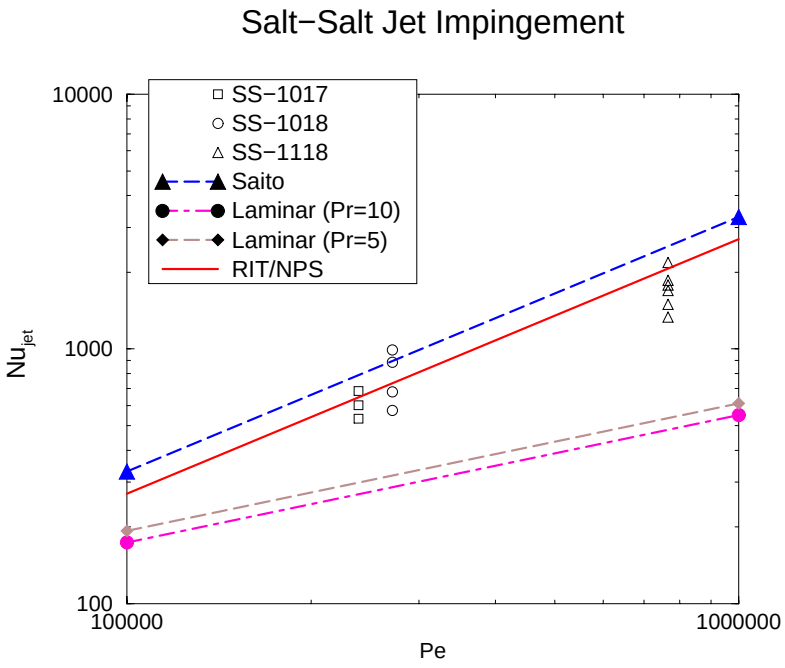

Fig. B.11: Salt-Salt Jet Impingement Heat Transfer.

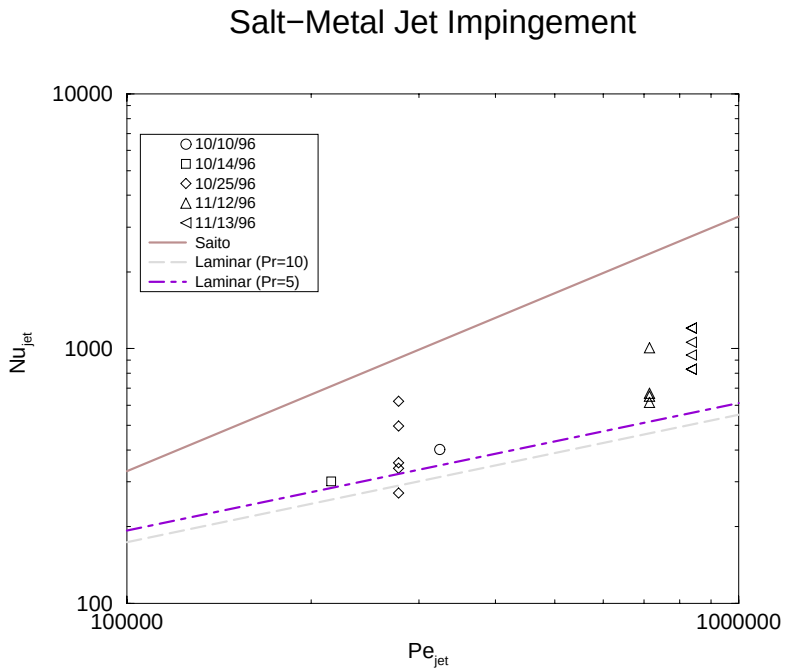

Fig. B.12: Salt-Metal Jet Impingement Heat Transfer.

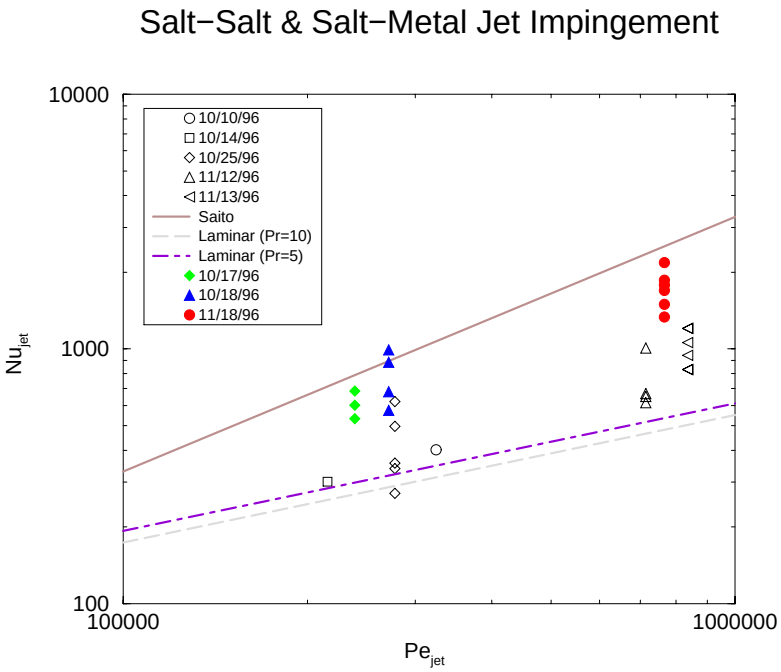

Fig. B.13: Combined Jet Impingement Heat Transfer.

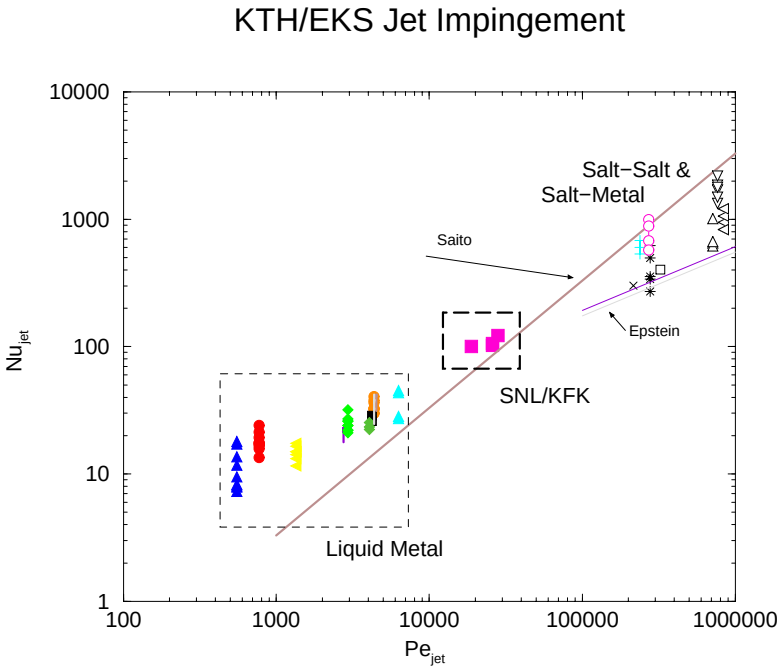

Fig. B.14: RIT/NPS Jet Impingement Heat Transfer.

Bibliography

[1] Green, J.A., ”Thermo-Physical Properties of Cerrobend Alloy and $NaNO_3$-KNO_3 Salt Mixtures,” RIT/NPS Research Report (NPS-LAB-01-97), January, 1997.

Appendix C

Review of Low Temperature Jet Impingement Experiments

C.1 Abstract

An experimental study of jet impingement heat transfer, with phase change, was performed, using water as jet fluid and ice (of tap water and salt water) as test plate. It is shown that the heat transfer law for the stagnation zone (likely to be $Nu_o = a \cdot Re \cdot Pr$) significantly differs from similar correlations, previously obtained for impingement upon flat plate without surface ablation. It is proposed that such a difference is caused by the flow turbulization (in the stagnation zone), associated with phase-change-induced surface ablation processes.

C.2 Introduction

This experimental study is motivated by the need to better understand the physical mechanisms which govern the solid plate ablation processes due to impingement heat transfer from a liquid (melt) jet, which has temperature higher than the melting point of the plate material. Due to application of interest, we consider cases, when the plate size is significantly larger than the jet diameter D_j, and the jet is directed downwards against the plate. Previous works on this subject were very limited; for a review, see e.g. [1]. Most notably, Saito and co-workers performed experiments, using molten salt ($NaCl$) and aluminia (Al_2O_3) as jet fluids, and metallic tin and steel as plate materials [2]. Although, the ranges of governing dimensionless groups (namely, Reynolds number Re and Prandtl number Pr) were limited, the experimental result indicated that the data do not fit heat transfer correlations [e.g, see eq.(C.1)], which were (experimentally, theoretically and/or numerically) obtained for cases of jet impinging upon a surface without any phase

change.

$$Nu_o = 0.55 \cdot \sqrt{2} \cdot Re^{0.5} \cdot Pr^{0.35} \tag{C.1}$$

Another correlation (C.2) was proposed in ref.[2] to generalize the very unique and, unfortunately, limited data bank.

$$Nu_o = 0.0033 \cdot Re \cdot Pr \tag{C.2}$$

As can be seen, this correlation significantly differs from similar correlations of jet impingement heat transfer in stagnation zone *without phase change*. Yet, no attempts were reported in the literature, so far, to explain the physics, which causes such a difference.

This study aims to provide an extended data base for jet impingement heat transfer, with particular emphasis on potential effect of phase change-related processes on heat transfer in stagnation zone.

C.3 Experimental Study

Experiments were conducted at the Laboratory of Nuclear Power Safety at Royal Institute of Technology (Stockholm). Water was chosen as jet fluid, and slabs of ice of tap water and salt water were formed, instrumented, and used as a test section. Ice of salted water (20% weight of $NaCl$) allows to have melting point at -16.5^{o}C.

The experimental facility includes a water tank (of 60 liters), jet-driving tube section, and test plate (impingement) section. The water tank has its heating elements (to provide required water temperature), water mixer, relief valve, and gas pressurizing system. The water temperature varies in the range from 2.5^{o}C to 99.5^{o}C, which provides a large variation in fluid viscosity, and as a result, the jet Reynolds number. The tube section has a valve and connection section, which allows the use of tubes of different diameters. Diameters of the tubes were 6.3mm, 8.9mm, 12.6mm, and 21.7mm. The tube is thermally insulated to minimize heat loss and changes of water temperature during its pass through the tube section. The length of tube section is designed to ensure fully developed turbulent flow at the tube outlet. It is noteworthy that the Reynold numbers in this study correspond to turbulent flow regime ($Re \geq 4000$) in the tube section. Furthermore, distance H_f between the tube outlet and the plate is chosen in a range of distance-to-diameter ratio H_f/D_j, for which jet impingement heat transfer is insensitive to the ratio H_f/D_j ($1.5 < H_f/D_j < 8$).

The test plates (ice slabs) were instrumented with K-type thermocouples. Data acquisition system is based on a Hewlet-Packard system. Accuracy of temperature measurements was evaluated in the operation temperature range to be 0.7^{o}C.

The temperature measurement itself has little influence on test result, compared to effects associated with:
(i)accuracy of determining position of thermocouples and their distances;
(ii) arrangement of thermocouples on the centerline of jet impingement area (symmetry);
(iii) influence of presence of thermocouples on flow pattern in the stagnation zone.

Analysis indicates, however, that the heat flux distribution in the stagnation zone is sufficiently uniform, so only for jets with relatively small diameter, factor (ii) may have some little effect. Since size of thermocouples is less than 1mm, factor (iii) is assumed to be negligibly small for the chosen jet diameters (6.9mm-21.7mm). In addition, care is taken, when analyzing experimental data to exclude error-causing influence of other physical processes [1] in determining heat transfer characteristics.

The ice was formed in freezers, using a metallic form. In case of salted water ice, the solution was well-mixed and gradually filled into the form, as a thin water layer, above the frozen ice. This procedure was required to provide (low air content in ice and) uniform salt concentration in the ice slab. The ice slab (formed in the metallic form) was then taken out off the form, and then kept in the freezer under designed temperature conditions (from -20^{o}C to -60^{o}C) before experiment.

For each jet (tube) diameter, (water) jet velocity was measured at different temperatures (i.e viscosity, density). The jet velocity V_j, used in determining jet-diameter based Reynolds number ($Re = V_j D_j/\nu$), was approximated from these measured data. Properties of water jet are determined for the water temperature, measured in the tank.

C.4 Phase-change experiments (without crust formation)

C.4.1 Experimental conditions

A number of tests were conducted with ice of tap water. The experimental conditions for water-(tap water) ice tests are given in Table C.1.

[1]Most notably, such processes are (i) cracking in the ice, (ii) melting of the uppermost layer of ice slab during the time period between the moment of taking the ice slab from freezing camera and the moment of starting jet impingement.

Table C.1: Test matrix of water-(tap water) ice tests.

#	Test #	Pr –	Re –	# exp. points	D_j mm	T_j ^oC	Δ_p cm	T_p ^oC
1	0403	9.64	17606	1	8.9	10	3	-12
2	0404	8.38	20240	5	8.9	15	6	-20
3	0407	7.23	78519	3	21.7	21	4	-7
4	0408	4.39	132990	6	21.7	45	9	-10
5	0411a	6.13	93378	3	21.7	28	5	-17
6	0411b	4.65	124884	6	21.7	42	9	-15
7	0413	2.35	250925	4	21.7	88	6	-15
8	0414	2.08	284478	5	21.7	98.5	9	-15
9	0415	2.06	288469	5	21.7	99.5	9	-15
10	0417	6.19	46545	5	12.6	27.5	9	-10
11	0422a	9.51	5760	5	6.3	10.5	6	-17.5
12	0426	5.69	9744	6	6.3	32	6	-10.
13	0516a	11.78	4706	5	6.3	3	5	-42
14	0520a	3.42	16179	5	6.3	60	5	-54.
15	0521a	7.4	7367	4	6.3	20	5	-50.

C.4.2 Data processing

In this series, distances of thermocouples were 1cm, beginning from the ice surface. This allows obtaining information about the ablation dynamics.

$$V_{abl,i} = \frac{t_{TC(i)} - t_{TC(i+1)}}{X_{TC(i)} - X_{TC(i+1)}} \tag{C.3}$$

In eq.(C.3), $X_{TC(i)}$ and $X_{TC(i+1)}$ are the location positions of neighbouring thermocouples (TC_i and TC_{i+1}); $t_{TC(i)}$ and $t_{TC(i+1)}$ are the corresponding time moments, when the measurements of these thermocouples show the ice melting point.

Typical temperature measurements for thermocouples, installed in the centerline of jet impingement area, are shown in Fig.C.1-C.2 for test 0411b. As it can be seen, the melting front propagation dynamics is quite the same throughout the plate ablation process. It was observed that, due to heat from the surrounding environment, the uppermost and lowermost layers of ice plate may have an increased temperature before the jet impingement start (for both the layers) and as well as during the impingement process for the lowermost layer. Furthermore, when the ablation reaches the lower layer, the (mechanical) rupture of this layer,

due to impinging flow, may occur. Therefore, such data were excluded from this heat-transfer analysis.

Since the jet fluid and plate material are of the same substance (H_2O), the driving temperature difference is those between the jet temperature and melting point $\Delta T_{ref} = T_j - T_{mp}$. As the melting front progresses relatively fast, the heat conduction in the ice slab should be small. The sensible heat of the ice $[C_{p,p}(T_{mp,p} - T_\infty)]$ is accounted for by modifying the heat of fusion as $H^*_{fusion} = H_{fusion,p} + C_{p,p}(T_{mp,p} - T_\infty)$. Thus, heat flux, which drives the ablation process, can be determined as follows [2].

$$q_{abl} = V_{abl}\rho_p H^*_{fusion,p} \tag{C.4}$$

Since the molten ice is added into the boundary layer between the jet fluid and the melting interface of the solid plate, this relatively cold water layer forms additional thermal resistance for heat transfer process. This effect was investigated in a number of studies [3] [4]. In this experimental study, since the jet and the molten layer are of the same fluid, as it was shown for, so-called, single-component cases [3], the convective heat flux q_{imp} can be calculated from q_{abl}; see eq.(C.5).

$$q_{imp} = q_{abl}\frac{B}{ln(1+B)} \tag{C.5}$$

where $B = \frac{C_{p,j}(T_j - T_{mp}))}{H^*_{fusion,p}}$. Finally, the Nusselt number is determined as

$$Nu_o = \frac{q^*_{imp}}{\Delta T_{ref}}\frac{D_j}{\kappa_j} \tag{C.6}$$

C.4.3 Results and discussion

The experimental data (Nusselt numbers), obtained from this test series, are compared with eqs.(C.1-C.2); see Figs.C.3-C.4. Similar to conclusion by Saito and co-workers (in ref.[2]), we recognize that the experimental data (for Re more than $2{\cdot}10^4$) fit better with eq.(C.2), rather than with eq.(C.1). The Reynolds numbers in the tests covered the range from $5.7{\cdot}10^3$ to about $2.9{\cdot}10^5$. So far, the Prandtl numbers covered the range from 2 to 9.6. It is of interest to note that equation

[2]Exception is test 0516a, which had low water temperature, and relatively slow velocity of ablation front propagation. In such a case, a correction for heat conduction component of heat flux has to be made as described in the next section, since situation with low heat fluxes is generally typical for tests with salt water ice.

(C.2) was used to fit the data obtained in the ranges of $6.8 \cdot 10^4 < Re < 3.5 \cdot 10^5$ and $0.75 < Pr < 1.22$ [3].

It is likely that the physics of fluid flow in the stagnation zone is quite similar in both processes of water jet, impinging upon ice slab (of tap water), and jet of molten salt, impinging upon metallic tin plate. As time scale for ablation process (interface mobilization) is two-three orders of magnitude longer than that for the flow convection (in the stagnation zone), one can suggest that the jet impingement heat transfer, with phase change and surface ablation, is convective heat-transfer dominated. In such a case, the jet-based Reynolds number, the jet-fluid Prandtl number, and the Nusselt number form a sufficient set of scaling groups for the jet impingement heat transfer.

Finally, it is worth noting that good reproducibility of experimental results was obtained in this test series, particularly for higher Reynolds number regimes (compare results of tests 0408 and 0411b, and of tests 0414 and 0415).

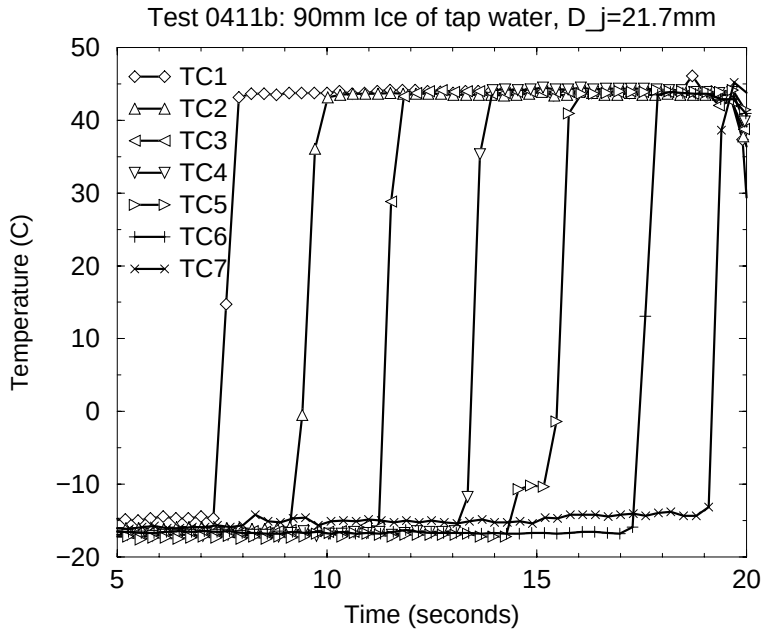

Fig. C.1: Temperature measurements in the jet impingement area (test 0411b, centerline thermocouples).

[3]Beyond the mentioned ranges of Re and Pr numbers, only two data points were obtained in ref.[2] for Re = 1900 and Pr = 5.46. The flow regime in these tests was, however, laminar, and possibly, induced other, unclear, mechanisms on impingement heat transfer.

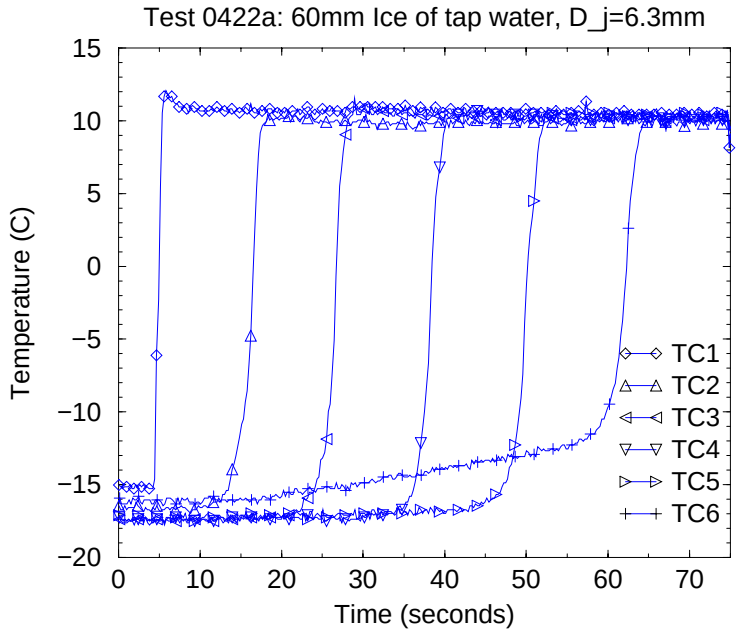

Fig. C.2: Temperature measurements in the jet impingement area (test 0422a, centerline thermocouples).

C.5 Experiments with salted water ice (with crust formation)

In order to explore the jet impingement heat transfer for conditions, in which the freezing point of jet fluid is higher than the melting point of plate material, another series of tests were conducted. Ice of salted water (20% weight of $NaCl$) was employed as a test plate, upon which water jet is impinging.

C.5.1 Experimental conditions and performance

The experimental conditions for water-(salt water) ice tests are given in Table C.2. The distance between the thermocouples, located along the centerline of the jet impingement zone was varied in different tests, namely 2.5mm, 5mm, and 10mm. Also, non-uniform distribution of thermocouples along the centerline was used in order to capture the ablation dynamics, and hence, the heat flux, when the surface ablation is not yet significant. However, in this section, we present and analyze only experimental results, for which the phase-change induced surface ablation is significant (for most cases, ablation cavity has to be deeper than 1/4 of

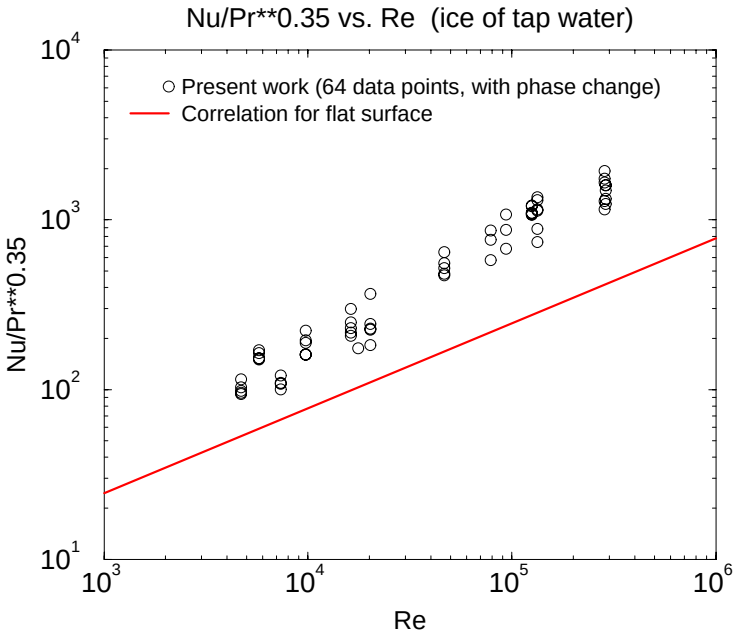

Fig. C.3: Comparison of experimental data with correlation $Nu_o = 0.778 Re^{0.5} Pr^{0.35}$.

the jet diameter). Furthermore, in order to be consistent with the data from [2], measurements from thermocouples, located on distance from plate surface more than four jet diameter, are intentionally excluded from data bank.

C.5.2 Results and discussion

Temperature measurements of a typical test regime are shown on Figs.C.5-C.6. For cases with higher water temperature, and hence impingement heat flux, the ablation front propagates with relatively high velocity (see e.g. Fig.C.5), the heat transfer characteristics can be determined in similar way as described in section C.4.2.

However, for most cases, in order to assure conditions for crust formation and existence, the water temperature was chosen to be low. This resulted in low impingement heat flux and slow ablation processes. When (water) jet temperature is low (e.g., test 0429, Fig.C.6), temperature measurements indicate an increase of temperature in the lower location before it is reached by the ablation front. In such a case, conduction in the ice has to be taken into account, together with phase change, when determining the heat flux. It was calculated, however, that the conduction component of heat flux is still significantly smaller than the fusion-

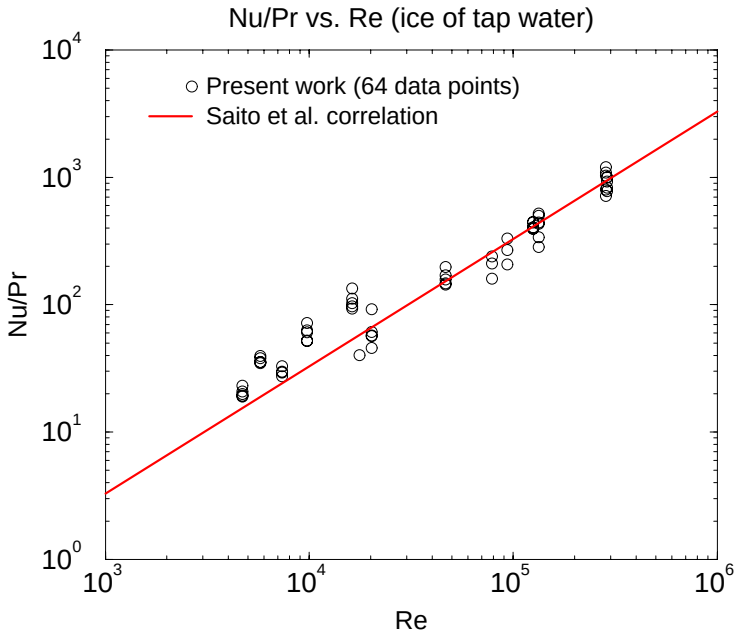

Fig. C.4: Comparison of experimental data with correlation $Nu_o = 0.0033 \cdot Re \cdot Pr$.

related component. The conduction heat flux is, therefore, approximated (the analytical solution of heat conduction equation with moving isothermal boundary) as follows.

$$q_{cond} = \rho_p C_{p,p}(T_{mp,p} - T_{\infty,p})V_{abl} \tag{C.7}$$

In present work, there exist some uncertainties in determining the thermophysical properties of salt water in liquid and solid phases. However, these uncertainties were evaluated to have minor effect on derivation of heat transfer characteristics from the water jet to its physical boundary, namely crust interface [4].

In general, good reproducibility of Nu numbers was obtained, when performing tests with similar Re numbers, but with different tube (jet) diameters and water temperature (viscosity). Again, this demonstrates that the Nu and Re are the most important scaling groups, and hence, proving the convection-dominated character of jet impingement-induced surface ablation.

The experimental results are analyzed as function of $Nu/Pr^{0.35}$ and Nu/Pr versus Re. As it was expected, the experimental heat transfer characteristics agree

[4]Thermal conductivity of salt water is used in calculating the critical temperature of water jet, higher which crust may not be able to form; see e.g. [2] [5]. Thermal conductivity of salt water ice may also affect the conduction heat flux.

Table C.2: Test matrix of water-(salt water) ice tests.

#	Test #	Pr –	Re –	# exp. points	D_j mm	T_j ^oC	Δ_p cm	T_p ^oC
1	0424	11.71	23672	1	12.6	3.2	9	-50
2	0424b	9.64	28761	6	12.6	10.	9	-45
3	0425a	9.39	61207	5	21.7	11.	8	-30
4	0428	8.13	34082	6	12.6	16.	8	-50
5	0429	11.08	25023	3	12.6	5.	5	-50
6	0502a	9.51	59219	4	21.7	10.5	6	-24
7	0503	11.08	50853	6	21.7	5.	6	-24
8	0505	11.78	23924	4	12.6	3.1	5	-48
9	0506a	11.92	4457	5	6.3	2.6	5	-50
10	0507	11.78	14128	4	8.9	3.	5	-46
11	0508	11.71	24067	2	12.6	3.2	5	-50
12	0521	11.75	4524	5	6.3	3.1	5	-47
13	0522	7.4	7492	4	6.3	20	5	-47

better with eq.(C.2), than with eq.(C.1); see Figs.C.7-C.8. In these figures, both data from this study and data by Saito et al. [2] are depicted. In both cases, the driving temperature difference is determined as $\Delta T_{ref} = T_j - T_{mp,j}$, i.e. the crust (of frozen jet fluid) is assumed to exist. It must be noted here that the experimental heat transfer data (Nu numbers) from [2] were obtained, when ablation front already propagated to a distance more than 1/3 D_j, i.e. significant ablation is maintained, as a condition, for the whole data bank.

Such a consistency between results of high-temperature experiments ($T_j = (900 - 1100^oC)$ of Saito et al. and low-temperature experiments ($T_j = (2.5 - 100^oC)$ of present study indicates that the experimental approach used in this study can be used to investigate the phenomena of interest, i.e. jet impingement heat transfer with phase change.

It must be noted here that although eq.(C.2) provides, for the currently existing data bank, better approximation than eq.(C.1), this data bank, with excepting few data points reported in [2] [5], could be generalized by a correlation (C.8); (see Fig.C.3 and Fig.C.7).

$$Nu_o = C \cdot Re^m \cdot Pr^{0.35} \tag{C.8}$$

[5]These include three data points for small jet (10mm) and two data points for laminar Al_2O_3 jet (Re = 1900).

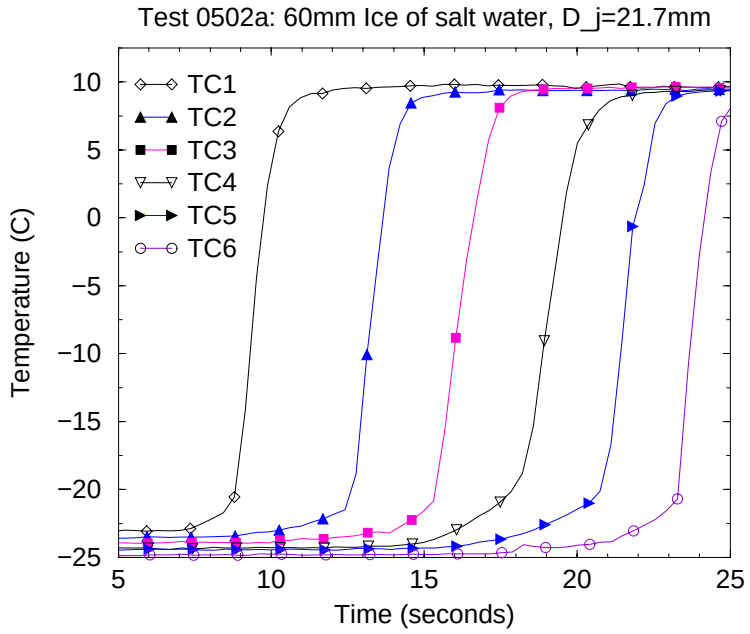

Fig. C.5: Temperature measurements in the jet impingement area (test 0502a, centerline thermocouples).

with $C >> 0.778, m \simeq (0.6 - 0.7)$. Thus, if the power "$n$" of Pr is kept as conventional one ($n = 0.35$), the power for Re number may slightly increase, while the coefficient C should be significantly increased to reflect the remarkably higher (say, 200-300%) Nusselt numbers in cases with phase change.

Since the difference between the data obtained in phase-change experiments and data obtained in no-phase-change experiments is significant, this result has a remarkable effect on application, motivating this work. Therefore, further study is strongly required to explain the physics of fluid flow in the stagnation zone, which appears to govern the jet impingement heat transfer. Higher power "m" of Re number in eq.(C.2), or higher value of coefficient C in eq.(C.8), can probably, be related to turbulence phenomena. Visual observation of the ablation-induced cavity, after completing the jet impingement process, indicated that the cavity surface is rough, rather than smooth [6]. We suggest that turbulization of flow in stagnation zone is the underground physical mechanism, which causes such a behaviour of heat transfer. Particularly, cavity geometry (instead of flat surface) and surface roughness (instead of ideally smooth surface) may contribute to such a turbuliza-

[6] In general, geometry of ice cavity is quite similar to that observed in tin plate by Saito and co-workers [2].

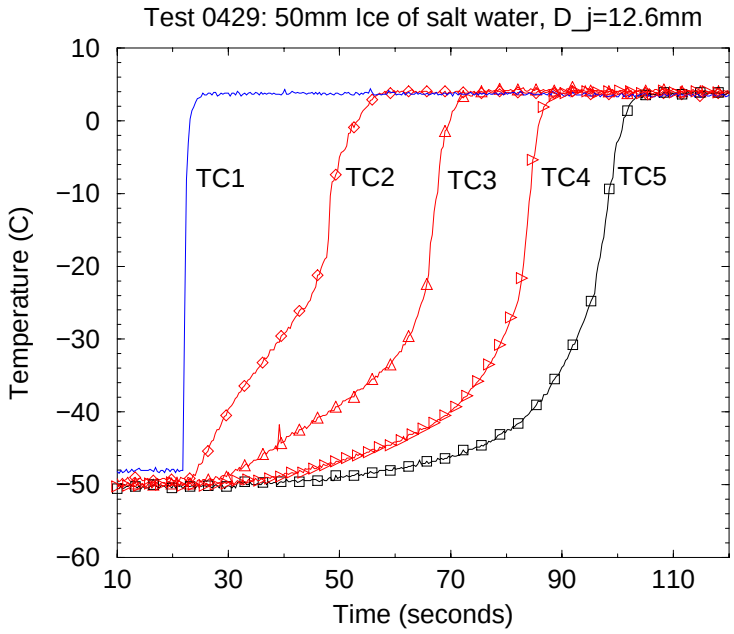

Fig. C.6: Temperature measurements in the jet impingement area (test 0429, centerline thermocouples).

tion. These effects must be investigated by specially designed experiments.

C.6 Summary

Experiments were performed to investigate heat transfer characteristics in the jet impingement stagnation zone, using water as jet fluid and ice of tap water and salt water as test plate. Analysis of the experimental results obtained for regimes, when *significant surface ablation* occurred, showed that the character of dependence $Nu = f(Re, Pr)$ is quite different from the conventional one for no-phase-change jet impingement. It can be concluded that for the currently existing data bank in the range $2 \cdot 10^4 < Re < 3.5 \cdot 10^5$, the correlation (C.2) (by Saito and co-workers) is a better approximation the conventional correlation [eq.(C.8)], developed previously for jet impingement heat transfer on flat smooth surface of a solid plate, without any accompanying phase-change process.

The flow turbulization in the stagnation zone, due to cavity geometry and surface roughness, is proposed as physical explanation for the effect, associated with phase-change-induced surface ablation. It was shown that low-temperature (water-ice) simulant experiments are a very useful and effective approach for

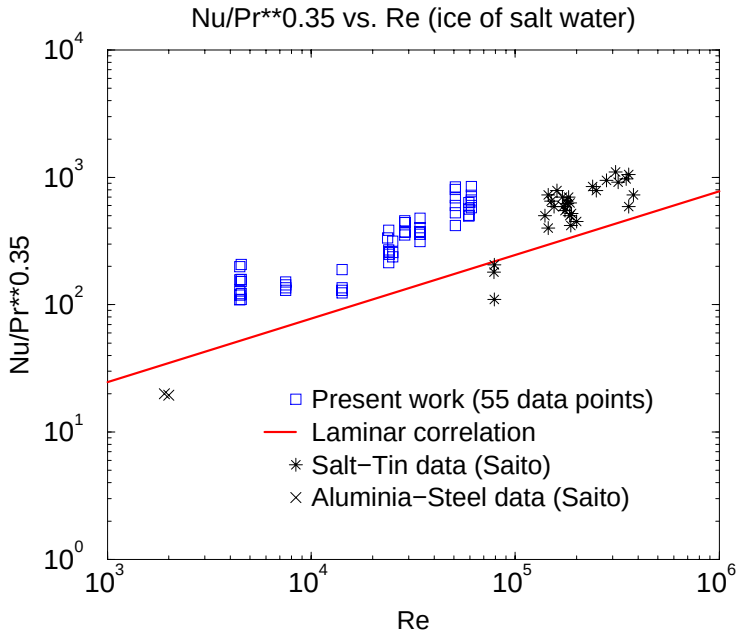

Fig. C.7: Comparison of experimental data (of salt-water ice tests) with correlation $Nu_o = 0.778 Re^{0.5} Pr^{0.35}$.

studying these and other relevant phenomena of jet impingement with phase change.

Nomenclature

Arabic

C_p	Heat capacity coefficient, J/(kg.K)
D_j	Diameter (of jet), m
h	Heat transfer coefficient, W/(m.K)
H_{fusion}	Heat of fusion, J/kg
Nu	Nusselt number, $Nu = hD_j/\kappa$
Pr	Prandtl number, $Pr = \nu/\alpha$
Re	Reynolds number, $Re = \rho_j V_j D_j/\mu_j$
q	Heat flux, W/m^2
T	Temperature, K
V	Velocity, m/s

Greek

α	Thermal diffusivity, m^2/s
κ	Heat conductivity, W/m·K

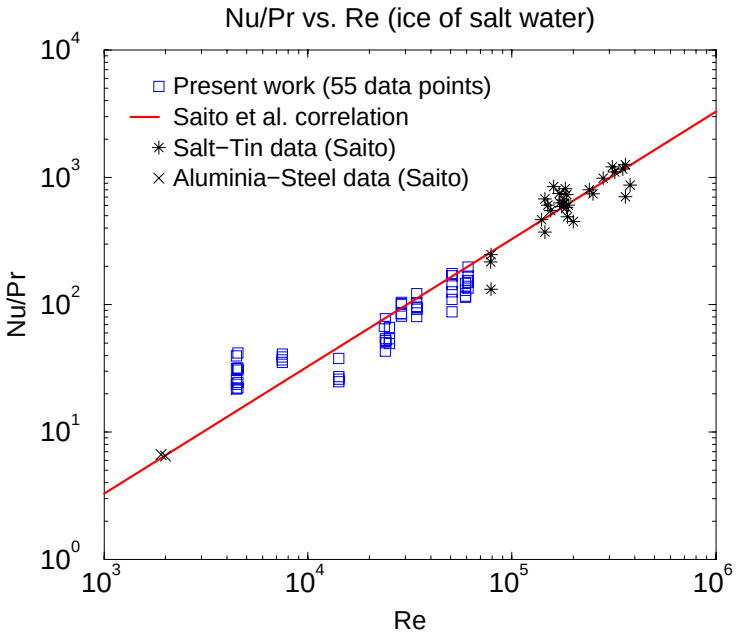

Fig. C.8: Comparison of experimental data (of salt-water ice tests) with correlation $Nu_o = 0.0033 \cdot Re \cdot Pr$.

μ	Dynamic viscosity, Pa.s
ν	Kinematic viscosity, m^2/s
ρ	Density, kg/m^3
ΔT	Temperature difference, K

Subscripts

j	Jet
mp	Melting point
p	Plate

Bibliography

[1] J.L. Rempe et al., ”Light Water Reactor Lower Head Failure Analysis”. NUREG/CR-5642. EGG-2618 (October 1993).

[2] M. Saito et al., ”Melting Attack of Solid Plates by a High Temperature Liquid Jet - Effect of Crust Formation”, J. Nuclear Engineering and Design, 121 (1990), pp.11-23.

[3] M.J. Swedish et al., ”Surface Ablation in the Impingement Region of a Liquid Jet”, AIChE J., 25 (4) (1979), p .630.

[4] A. Furutani et al., ”Erosion Behavior of Solid Plate by a Liquid Jet - Effect of Molten Layer”, ANS Proc. 1989 National Heat Transfer Conf., Philidelphia, PA (August 1989), pp.263-271.

[5] M. Epstein et al., ”Simultaneous Melting and Freezing in the Impingement Region of a Liquid Jet”, AIChE J., 26 (5) (1980), p .743.

Appendix D

Jet Impingement: Study of Flow Turbulization Effect

D.1 Abstract

This study aims to resolute significant difference of heat transfer data, obtained in experiments of jet impingement, accompanied by formation of jet fluid crust and/or melting of plate material. It was found that analysis, taking into account phase-change-induced cavity formation in solid plate, is able to explain large scattering in heat transfer data. The authors suggest that flow turbulization in the stagnation zone is the main physical mechanism, which governs the ablating heat transfer. Specially designed experiments were performed to examine contributions of cavity geometry and surface roughness on heat transfer augmentation. Effects of surface inclination and presence of a fluid layer above the solid plate were also experimentally investigated and analyzed. The experiments show that these phenomena tend to cause earlier flow turbulization in the stagnation zone.

D.2 Introduction

Surface ablation of a solid plate due to heat transfer from an hot impinging jet is of interest to a number of applications in chemical, nuclear and metallurgical industry. However, there exists significant diversification of heat transfer correlations, used to predict ablation dynamics. Furthermore, such a diversification becomes important, when extrapolating these correlations to higher Reynolds number range (say, up to $1.5{\cdot}10^6$, i.e out of the experimental validity range) in modern applications. In fact, bases for applying one or another correlations are equally insufficient, since there is still lacking an appropriate analysis, which would quantify the

utilization of these, yet contradictory, correlations [1].

In this section, no complete review of single-phase jet impingement heat transfer will be made. However, it is worth noting that most of heat transfer data from single phase jet impingement experiments were generalized in the correlation form of $Nu = A \cdot Re^m Pr^n$ for stagnation zone Nusselt number. In most studies, parameters "m" and "n" vary in the range [0.45-0.55] and [0.33-0.4], respectively. Instead, only a limited number of correlations are available for jet impingement heat transfer with phase change (that occurs when $T_{mp,p} < T_j$ and/or $T_{mp,p} < T_{mp,j} < T_j$). Yen and Zehnder (1973) performed water-ice experiments and correlated their integral heat transfer data as $Nu = 0.88 \cdot Re^{0.94} Pr$ [4]. Swedish et al. (1979) [3] and Epstein et al. (1980) [6] performed water-ice, water-octane, water-oil, water-mercury experiments. However, all these experiments employed a upward water jet against meltable surfaces [3] [4], [6]. The situation of interest in the present work is associated with solid substrate ablation due to heat transfer from a downward liquid (melt) jet, vertically impinging upon the solid surface. More recently, Saito et al. performed high-temperature jet impingement experiments and proposed the correlation $Nu = 0.0033 \cdot Re \cdot Pr$ [2]. The data base supporting this correlation is, however, very limited. Most of tests were conducted in the Re range [$7 \cdot 10^4$-$3.5 \cdot 10^5$], with Pr about 1, and two additional laminar tests (Re about 1900) were conducted with Pr = 5.46 [2].

In the previous section, we reported about jet impingement heat transfer experiments, employing water as jet fluid and ice of tap water and salt water as test plate. The experimental results appear to support the use of eq.(D.1), rather than eq.(D.2), for jet impingement regimes, when significant surface-ablation has occurred. It was also concluded that low-temperature simulant experiments are a useful and effective approach for investigating jet impingement heat transfer with phase change and associated with it phenomena.

In present study, jet impingement heat transfer, with phase change, will further be investigated by low-temperature simulant experiments, with particular emphasis on resolving the observed significant difference in behavior of heat transfer

[1] For example, Theofanous (chapter 8, [1]) employed Saito's correlation [2]

$$Nu_o = 0.0033 \cdot Re \cdot Pr \tag{D.1}$$

while Sienicki (Appendix H [1]) made use of correlation from Swedish et al [3]

$$Nu_o = 0.55 \cdot \sqrt{2} \cdot Re^{0.5} \cdot Pr^{0.35} \tag{D.2}$$

[2] Detailed discussion of the past experiments and past experimental results will be provided below in analysis part of this report.

correlations. First, heat transfer from impinging jet to nearly-flat surface is analyzed. Second, solid (ice) plates with specially designed surfaces are used to examine (in a more explicit manner) influence of various flow-turbulizing phenomena. Finally, other aspects of potential importance will be analyzed.

D.3 Experimental Study and Analysis of Experimental Results

General information about the experimental method, test facility, measurement technique, and data acquisition and data processing procedures were described in the previous section, and hence will not be repeated here. Some experimental details, important for examination of particular effects, will be reported in related sections.

D.3.1 Heat transfer characteristics of jet impingement upon a meltable solid plate: Re-discovering the "conventional" laminar heat transfer correlation for flat surface

In the past, single-phase jet impingement experiments were performed with uniformly Joule-heated plates, rendering thus the second type of boundary condition. This is to avoid difficulties, associated with providing the constant-temperature boundary condition and measuring heat fluxes in such experiments. The boundary condition of interest to phase-change related jet impingement is, however, of the first type (i.e. $T_{b.c.}$ = constant). Some theoretical studies (including our numerical analyses) indicate that the jet impingement Nusselt number (for one Re number) are quite the same under different boundary conditions. Most of experimental heat transfer data of single-phase jets, impinging upon a solid flat surface at normal incidence, agree well with the correlation of boundary-layer type, eq.(D.2) [3]. Such a theoretical solution is based on assumption about laminar flow in the stagnation zone.

In present study, tests were performed to obtain heat transfer characteristics of jet impingement of *nearly-flat* solid surface, with constant temperature boundary condition. This means that we consider only data of regimes, when the surface ablation is not yet significant. As a criterion, we use ratio of ablation depth-to-jet diameter $\frac{X_{abl}}{D_j} < 0.2$. Visual observation of the jet impingement process (with phase change) shows that the flow regime in the stagnation zone ($r < R_j =$

[3]Primarily, this is true for cases with sufficiently large jet diameters, i.e. surface tension effect is negligibly small.

$0.5 \cdot D_j$) is laminar during the time period for the ablation front propagates until $X_{abl} = 0.2 \cdot D_j$. In such a case, the experimentally determined Nusselt numbers are much lower than in case, when the significant surface ablation has occurred (compare experimental values Nu_{exp} and values Nu_{tur} determined by eq.(D.1) in Table D.1). More importantly, the experimental Nusselt numbers agree well with prediction Nu_{lam} by the theoretical correlation (D.2) for $\frac{X_{abl}}{D_j} < 0.2$, and Nu_{exp} are much closer to Nu_{lam} than to Nu_{tur} even for $0.2 < \frac{X_{abl}}{D_j} < 0.4$. Thus, this result indicates that phase change (surface melting or crust formation) and isothermal boundary condition are not a reason for heat transfer augmentation under condition of significant surface ablation.

Table D.1: Examination of the laminar stagnation flow model.

	Test #	Pr –	Re –	$\frac{X_{abl}}{D_j}$ -	D_j mm	T_j ^oC	Δ_p (ice)	T_p ^oC	Nu_{lam} eq.(D.2)	Nu_{tur} eq.(D.1)	Nu_{exp} -
1	0511a	11.89	47000	0.12	21.7	2.7	5 (tap)	-50	401	1843	405
2	0503a	11.71	47836	0.12	21.7	3.2	5 (salt)	-52	402	1848	472
3	0504	11.78	47821	0.12	21.7	3	5 (salt)	-45	403	1859	356
4	0505	11.78	23924	0.2	12.6	3	5 (salt)	-48	285	930	384
5	0508	11.71	24067	0.2	12.6	3.2	5 (salt)	-50	285	930	267
6	0429	11.07	25023	0.4	12.6	5	5 (salt)	-50	285	915	421
7	0503a	11.71	47836	0.24	21.7	3.2	5 (salt)	-52	402	1848	520
8	0504	11.78	47821	0.24	21.7	3	5 (salt)	-45	403	1859	543
9	0508	11.71	24067	0.4	12.6	3.2	5 (salt)	-50	285	930	443

To the authors' knowledge, this is the first time when the laminar-stagnation-flow correlation is, explicitly, shown to describe the experimental data from the jet impingement heat transfer, with both crust formation and surface ablation [4].

D.3.2 Heat transfer characteristics during transient ablation processes

The major part of the experimental heat transfer data, presented in the previous section, shows that these data can be approximated by Nu_{tur}, determined

[4]In studies [3] [6], correlations of laminar stagnation flow models were applied. The use of the laminar stagnation flow models can be justified upon features of these experiments. Since the meltable rods were employed as impingement surface, and the heat flux distribution in the laminar stagnation zone is sufficiently uniform, the flatness of melting surface (i.e. no cavity formation in solids) was, probably, maintained over experimental runs. However, experiments of [3] were limited to surface ablation, with no crust formation. No explicit examination of heat transfer correlation was presented in [6], where correlation (D.2) from the laminar stagnation flow model was assumed for calculating convective heat flux from jets to impingement surface.

by eq.(D.1). The data, presented in the previous section, show that they can be best fitted by Nu_{lam}, determined by eq.(D.2). Fig.D.1 depicts behavior of heat transfer rate during some ablation transients. It can be seen that ratio $\frac{Nu-Nu_{lam}}{Nu_{tur}-Nu_{lam}}$ is nearly zero, when the impingement surface is nearly flat, and is increasing with the increasing of ablation depth $\frac{X_{abl}}{D_j}$ (i.e. cavity formation). This trend is clearly observed in the result of tests with both $D_j = 21.7mm$ (runs 0503a and 0504) and $D_j = 12.6mm$ (runs 0505 and 0508), although the transient ablation period of tests 0503a and 0504 was much shorter and, hence, the ablation depth was smaller, due to the given volume of water tank.

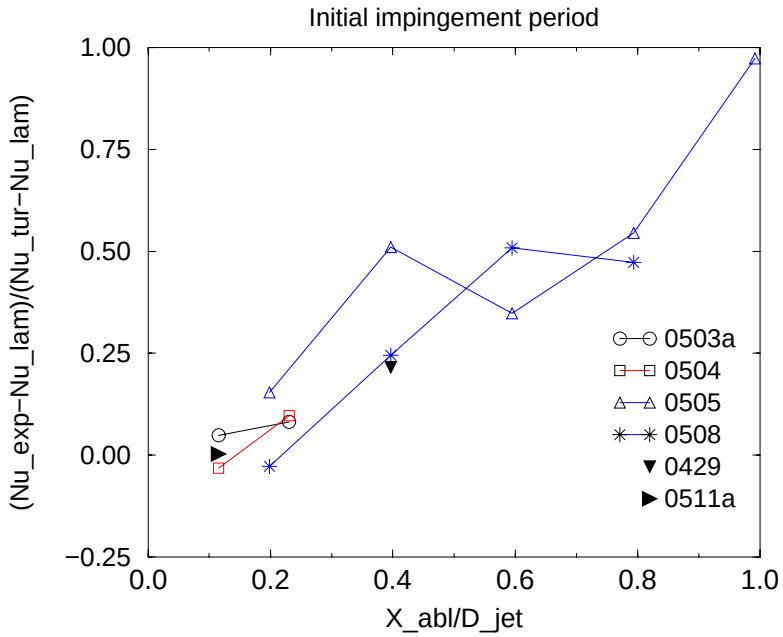

Fig. D.1: Heat transfer rate behavior during the ablation transients.

It must be noted here that experimental data, associated with effect of nearly flat surface, were obtained only in tests (i) with relatively large jet diameters (12.6 and 21.7mm), and (ii) with relatively cold ice plates (the initial ice temperature was maintained as $\simeq$ 30-35K lower than the melting point of salt water ice $T_{mp,p}$). In fact, a number of tests were performed with jet diameters 6.3 and 8.9mm, with measuring heat transfer characteristics for $\frac{X_{abl}}{D_j} < 0.4$ (tests 0506a, 0507, 0516a). However, there exists no indication that the laminar regime or the transition-to-turbulence regime were initially occurred, even though the jet-based Reynolds numbers in these tests are typically smaller than those for cases with larger jet diameters. It is suggested, here, that fluid flow in the stagnation

zone of smaller-diameter jet is more sensitive to phenomena, associated with jet-impingement surface ablation. Similarly, no effect of surface flatness was observed in tests, performed with small values of ice subcooling (tests 0502a and 0503, $\Delta T = T_{mp,p} - T_{\infty,p}$ = 7.5K, D_j = 21.7mm. Primarily, it may be related to a mechanical (rather than thermal) property of the impingement surface. Particularly, the solid-liquid interface of relatively soft ice (near its melting point) can easier be disturbed and disrupted by a high-Reynolds number impinging jet and its shear stress. Perhaps, some solid (ice) pieces could even be eroded and transferred into the liquid flow, rendering thus faster ablation dynamics. In such a case, the surface ablation is governed both by heat and mass transfer processes. The disturbed surface (by mechanical force and mass transfer) may cause to an earlier transition-to-turbulence on the very initial stage of jet impingement and, as a result, provide larger convective heat fluxes, even when the ablation depth is small.

D.3.3 Transition-to-turbulence regime

In order to explain all the observed data, we suggest that the laminar stagnation flow regime is realized during the initial period of jet impingement upon a smooth and flat surface. The flow regime is then changed to the transition-to-turbulence regime and the turbulent regime, as the ablation front propagates into the solid plate and a flow cavity is being formed in the (ice) plate. From theory of boundary layer, it is clear that a boundary layer is developed from the stagnation point along the spreading area in the near-wall flow region. The laminar boundary layer becomes turbulent, when the distance-based Reynolds number $Re_r = \frac{\rho V_r R}{\mu_j}$ reaches a critical value $Re_{r,transition}$ (here V_r is flow velocity in the spreading film and R is the radial distance from the stagnation point). In general, $Re_{r,transition}$ is in the range from 10^5 to $5{\cdot}10^5$ for the boundary layer development over a flat surface or in the tube entry region. In the laminar stagnation flow model of jet impingement heat transfer, the critical $Re_{r,transition}$ number is assumed to be reached somewhere outside the stagnation zone, and hence, having no influence on heat transfer mechanism in the stagnation zone. This assumption has been validated by most of experiments in the past for single-phase jet impingement. Nevertheless, most of these experiments were performed for relatively low Reynolds numbers Re_j, say, up to $2{\cdot}10^5$.

For higher Reynolds numbers, heat transfer characteristics were measured by McMurray and co-workers, who performed two-dimensional jet impingement tests in Reynolds number range from $3{\cdot}10^4$ to $3{\cdot}10^6$ [7]. They reported that experimental data for $Re < 2{\cdot}10^5$ can be approximated as

$$Nu_o = 0.73 \cdot Re^{0.5} \cdot Pr^{1/3} \tag{D.3}$$

while for $Re > 4{\cdot}10^5$

$$Nu_o = 0.037 \cdot Re^{0.8} \cdot Pr^{1/3} \tag{D.4}$$

A transition between correlations (D.3)-(D.4) (and corresponding flow/heat transfer regimes [5]) occurs in the Re range $2 \cdot 10^5 < Re < 4 \cdot 10^5$. Experimental data in this transition range could also be correlated as $Nu = f(Re)$, but with much higher power of Re.

It can be shown, from analytical solutions and measurements, that radial velocity V_r in the spreading film has the same order of the jet velocity V_j. Particularly, $V_r \simeq V_j$ for $R = 0.5D_j$. Since $Re_r = Re_j \frac{R}{D_j}$, values of Re_r (for $R = 0.5D_j$) are close to $Re_{r,transition}$, where the flow regime in the flow stagnation zone changes from the laminar to turbulent, as discussed above. Therefore, we propose that that transition-to-turbulence is the physical mechanism, rendering the change of the heat transfer laws for $Re > 2 \cdot 10^5$. As the Reynolds number increases, the boundary layer may becomes fully turbulent within the stagnation zone, and hence providing "turbulent" heat transfer law (for jet impingement with flat and smooth surface). It is also believed that no transition phenomenon will occur as the Reynolds increases beyond $Re = 3 \cdot 10^5$.

It is worth further employing this idea to explain data of jet impingement with surface ablation. The experimental data, obtained with significant surface ablation, are likely to be of turbulent regime. However, the transition-to-turbulence occurs at much lower Reynolds numbers, after the surface has ablated to a certain degree. Thus, transition-to-turbulence is governed not only by the Reynolds number Re_j, but by other factors and mechanisms, which affect the flow turbulization. The most probable factors are the flow pattern and surface quality. In the next section, experiments are carried out in order to examine contributions of these mechanisms on the flow regime and heat transfer augmentation.

D.3.4 Turbulent flow regime: separate effect studies

Potentially, two mechanisms, namely (i) cavity formation and (ii) surface roughness, may affect the flow pattern in the stagnation zone.

[5] It is noteworthy that theoretical analysis of jet impingement heat transfer under (very) high Reynolds number condition would be desirable. Such an analysis could be based on a potential flow solution (for an outer layer of the spreading liquid film) and a description of turbulent boundary layer development. By doing so, both transition-to-turbulence and heat transfer to turbulent flow could be examined against data by McMurray et al. [7] and present data.

Examining effect of cavity geometry. In order to examine the effect of cavity formation in the solid plate on fluid flow and heat transfer regimes, special experiments were performed. In the test (ice) plate, a pit (of depth H_{pit} and diameter D_{pit}) was initially formed, so that the flow stagnation zone is located within the pit bottom ($D_j < D_{pit}$). Ice plates of the salt water ice, with relatively large subcools to the salt water ice melting point, were used. Jets of relatively large diameters (21.7 and 12.6mm), and low water temperature (3-3.5^{o}C), were used to provide conditions for detecting the laminar flow/heat transfer regime during the initial stage of jet impingement.

Experimental results received from tests with initial cavity in the ice are shown in Fig.D.2. The data depict the same trend of ablation dynamics as in the case with initial flat surface, i.e. lower Nusselt numbers are obtained at the very initial period of jet impingement. The initial "laminar" Nusselt numbers are, however, higher than those obtained with no initially formed pit in the ice, indicating thus the transition-to-turbulence occurs earlier in these tests with initial cavity; see Table D.2 [6]. It is proposed that the initial cavity causes vortex flow motion in the pit, and hence affecting the flow regime in the stagnation zone.

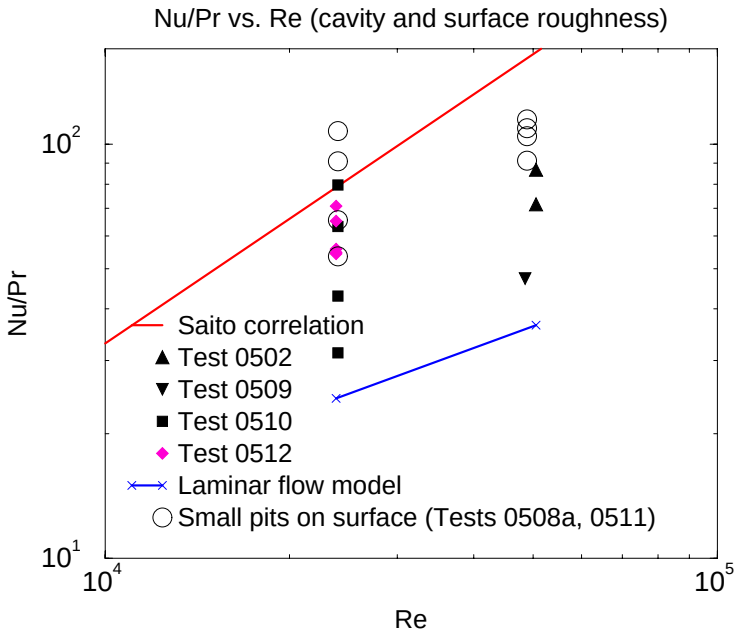

Fig. D.2: Examination of flow turbulization effects.

[6]In addition to the cavity effect on flow turbulization, effect of mass transfer, associated with low subcool in the ice, may present in test 0512.

Table D.2: Conditions and results of tests with an initial cavity in the plate (cases of similar conditions, but without initial cavity, are marked with (*) and given for comparison).

Test #	Pr –	Re –	$\frac{X_{abl}}{D_j}$ –	D_j mm	$\frac{H_{pit}}{D_j}$ $-\ ^oC$	T_j (ice)	Δ_p –	T_p ^oC	Nu_{lam}	Nu_{tur}	Nu_{exp} –
0502	11.08	50566	0.24	21.7	3.5	5 (salt)	2.5	-50	405	1848	793
0503a*											520
0509	11.60	48545	0.12	21.7	3.5	5 (salt)	0.37	-51	404	1859	550
0503a*											472
0511a*						(tap)					405
0504*											356
0510	11.75	23995	0.2	12.6	3.1	5 (salt)	0.24	-51	285	930	368
0508*											267
0512	11.64	23816	0.2	12.6	3.4	5 (salt)	0.4	-30	283	915	632

Since we do not aim at establish a quantitative dependence of heat transfer characteristics on geometrical parameters of the pit, we limit our observation to a conclusion that the preliminarily formed cavity is able to affect the flow pattern in the flow stagnation zone, and hence, affect the heat transfer in the initial impingement period. The effect (about 50%) is, however, not enough to explain the significant difference (as much as 3.5 times for Re = 20000 and 4.5 times for Re = 50000) between the Nusselt numbers, determined by eq.(D.1) and eq.(D.2). Obviously, the initial cavity has no effect on the long-term jet impingement heat transfer, when ablation-induced effects determine the flow and heat transfer regimes in the stagnation zone.

Examining effect of surface roughness. Effect of surface roughness on flow turbulization in the stagnation zone is examined by generating a set of pits (1.5-2 mm in depth and 2-3mm in diameter) on the plate surface, around the symmetry line of the impingement zone. Distances between the pits were about 15mm, so only a limited number of pits were located within the stagnation zone [7]. Nevertheless, experimental results (tests 0508a and 0511) show that the surface roughness has a very significant effect on the fluid flow, and hence, heat transfer characteristics. Already for $\frac{X_{abl}}{D_j} < 0.2$, the Nusselt numbers are much closer to the "turbulent" correlation, than to the "laminar" one; see Fig.D.2.

On one hand, this result means that the surface roughness is able to cause flow turbulization in the stagnation zone, rendering thus much higher Nusselt numbers. On the other hand, the result confirms, indirectly, the validity of the theory, that the flow turbulization is the most probable physical explanation for the significant

[7] $T_j = 3 - 3.7^oC$, $T_p \simeq -52^oC$, D_j = 12.6 and 21.7mm.

difference between well-established experimental data/correlations, obtained for jet impingement upon flat and smooth surfaces, and specific data set, obtained from experiments with phase-change induced surface ablation.

D.3.5 Other aspects

Inclined jets. Impingement heat transfer from an inclined jet is of application interest. A review of currently existing experimental data base indicates that the process of inclined jet impingement heat transfer, with phase change, has not been systematically investigated. Some experimental information is available to inclined jet impingement upon a solid surface (without phase change) shows that effect of inclination on heat transfer characteristics is either not significant [7] or limited to about 20% for 30 degree of inclination, 25% for 45 degree of inclination, and $\simeq$35% for 70 degree of inclination; see e.g. [8]. It needs to say here that such an accuracy level could hardly be captured in jet impingement experiments, with surface ablation. In fact, present experimental data of inclined (30 and 45 degrees) jets upon plate of fresh water ice show no influence of inclination on heat transfer results; see Fig.D.3. Partly, it is because, once the ablation cavity has formed, the jets do not anymore recognize the inclination of the plate as such. Thus, the cavity formation in the solid plate is also found to be the dominant mechanism for inclined jet impingement conditions.

Nevertheless, it is of application interest to evaluate the period, during which the laminar stagnation flow regime governs the jet impingement heat transfer. Special measurements were implemented in tests 0506 and 0509a, 0530 (D_j = 21.7 and 12.6mm, T_j = 2.5 and 3.9^{o}C, T_p = -42 and -52^{o}C) in order to capture the surface flatness effect, which should provide the laminar heat transfer regime. However, it appears that the jet inclination favours the transition-to-turbulence, and hence, enhancing heat transfer in the initial impingement period. Most probably, this phenomenon is associated with the fact that no jet-fluid pool is accumulated in the stagnation zone of a formed, jet-induced cavity.

Submerged jets.

Experiments were performed for jet impingement upon a plate, above which a liquid layer L presents. Ice plates from both fresh (tap) water and salt water were employed; see Table D.3-D.4. Performance of submerged jets experiments encounters difficulties in organizing the liquid layer aprior to the jet impingement starts. During this period, heat is transferred from the liquid layer to the (ice) plate by conduction. However, when temperature of the liquid layer is low (close to its freezing point), good reproducibility of the experimental results was achieved (e.g., tests 0513a and 0520).

Experimental results are depicted on Fig.D.4. In this picture, the correlation by Saito (D.1) is also shown for comparison. It can be seen that the experimental

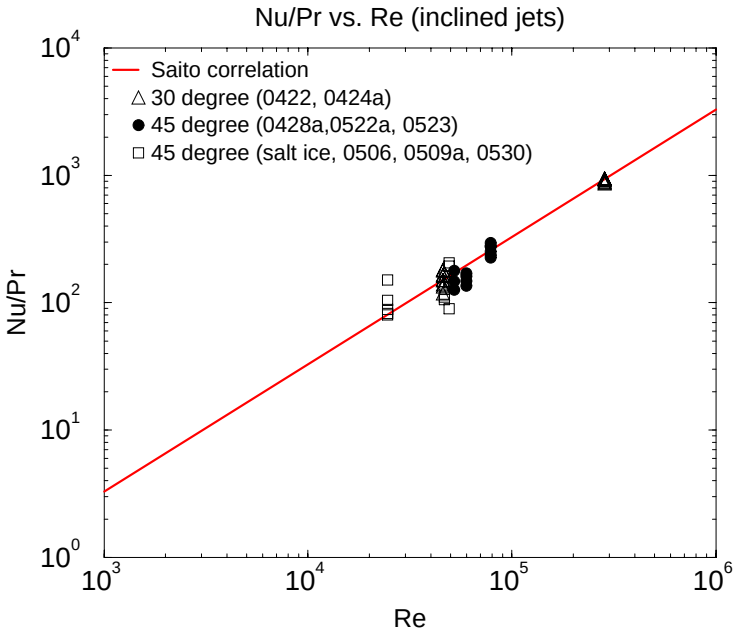

Fig. D.3: Influence of inclination angle on heat transfer.

heat transfer characteristics are close to the "turbulent" correlation, although analysis of data showed that most of the data (Nu numbers), obtained with $\frac{L}{D_j} > 2$, are 25-50% lower than those, obtained for $\frac{L}{D_j}$ in the range from 0 (no liquid layer) to 1.5 (shalow layer). In general, the results are consistent with the major trends of heat transfer behavior, observed in jet impingement experiments without liquid layers. For cases with a relatively cold plate, the "laminarized" heat transfer regime appears to occur at the initial impingement period. More notably, this regime realized even when the jet temperature is relatively high (test 0515, 0515a, 0516; Table D.5). Large scattering of data shown in Fig.D.4 is related with the lower heat transfer rates in the initial impingement period (Fig.D.5) and variation of a pre-installed liquid layer depth L_o (Fig.D.6).

Probably, the presence of liquid layer has a laminarizing effect on the jet flow, and hence, provides condition to delay the transition-to-turbulence. In fact, the shear between the jet and the liquid layer may be able to cause jet erosion and/or deceleration of the jet flow. Speaking in the formal language of dimensionless groups, this would mean that the actual Reynolds number of the jet, while comparing to the case without (significant) liquid layer, is lower than its value, determined from the diameter and velocity of the initial jet, entering the (deep) liquid layer.

Table D.3: Conditions of submerged jet impingement tests (fresh water ice).

#	Test #	Pr –	Re –	# exp. points	D_j mm	T_j ^oC	Δ_p cm	T_p ^oC	L/D_j –
1	0512a	8.48	66397	2	21.7	14.6	7	-10	1.4
2	0513	11.32	49328	1	21.7	4.3	6	-30	2.1
3	0515	8.23	68999	4	21.7	15.6	6	-38	2.1
4	0515a	4.82	118094	6	21.7	40.	9	-40	2.3
5	0516	6.19	91980	7	21.7	27.5	9	-25	2.3
6	0605	4.56	125508	9	21.7	43.	9	-47 (-20)	5.1
7	0605a	2.19	263470	10	21.7	94.	9	-45 (-10)	5.1

D.4 Summary

Experimental study of jet impingement heat transfer, with phase change, was performed, using water as jet fluid and ice (of tap water and salt water) as test plate. It is shown that the experimentally obtained data of heat transfer in the stagnation zone of nearly flat impingement surface can be readily described by the available correlation of the laminar stagnation flow model. Heat transfer rate, however, is shown to increase as the ablation front propagates deeply into the solid plate. Generally, as it was reported in the previous section, heat transfer data for regimes with significant surface ablation are likely to be approximated by the Saito's correlation rather than the laminar stagnation flow model. It is proposed that such a difference is caused by turbulence phenomena (in the stagnation zone), associated with surface ablation processes. Special tests were conducted to explore relevant physical mechanisms. The results indicate that surface ablation-induced roughness (rather than phase-change induced cavity formation) contributes to such a flow turbulization.

In addition, effects of surface inclination and presence of a fluid layer above the solid plate were also experimentally investigated and analyzed. The experiments show that inclination tends to cause earlier flow turbulization in the stagnation zone, while presence of liquid layer above the plate seems to provide stabilizing (laminarization) condition.

Nomenclature

Arabic

D_j Diameter (of jet), m

h Heat transfer coefficient, W/(m.K)

Table D.4: Conditions of submerged jet impingement tests (salt water ice).

#	Test #	Pr –	Re –	# exp. points	D_j mm	T_j ^oC	T_{layer} ^oC	Δ_p cm	T_p ^oC	L_o/D_j –
1	0513a	11.15	50105	5	21.7	4.8	4.8	5	-40	2.5
2	0520	11.71	47564	2	21.7	3.2	3.2	5	-43	2.5
3	0523a	9.84	57257	5	21.7	9.	3.	5	-50 (-25)	3.9
4	0524	11.53	48289	3	21.7	3.7	3.	5	-44 (-17)	4.1
5	0524a	11.14	54923	3	21.7	8.	3.	5	-42	2.8
6	0527	11.67	23981	3	12.6	3.3	3.	5	-45	4.4
7	0527a	10.09	28024	5	12.6	8.2	3.	5	-47 (-21)	7.5
8	0530a	11.78	23767	4	12.6	3.	3.	5	-55	4.8
9	0531	11.64	48809	3	21.7	3.4	3.	5	-43	5.5
10	0531a	11.6	24127	5	12.6	3.5	3.	5	-46 (-23)	7.2
11	0603	10.26	27544	4	12.6	7.5	3.	5	-53 (-23)	2.4
12	0603a	10.14	27885	5	12.6	8.	3.	5	-51 (-24)	7.2
13	0608	10.14	27885	4	12.6	8.	3.	5	-54 (-24)	11.5
14	0608a	10.78	24002	4	12.6	3.	8.	5	-48	11.5

Nu Nusselt number, $Nu = hD_j/\kappa$
Pr Prandtl number, $Pr = \nu/\alpha$
R Radial coordinate, m
Re Reynolds number, $Re = \rho_j V_j D_j/\mu_j$
q Heat flux, W/m^2
T Temperature, K
V Velocity, m/s

Greek

α Thermal diffusivity, m^2/s
κ Heat conductivity, W/m·K
μ Dynamic viscosity, Pa.s
ν Kinematic viscosity, m^2/s
ρ Density, kg/m^3
ΔT Temperature difference, K

Subscripts

abl Ablation
exp Experiment
j Jet
lam Laminar
mp Melting point
p Plate

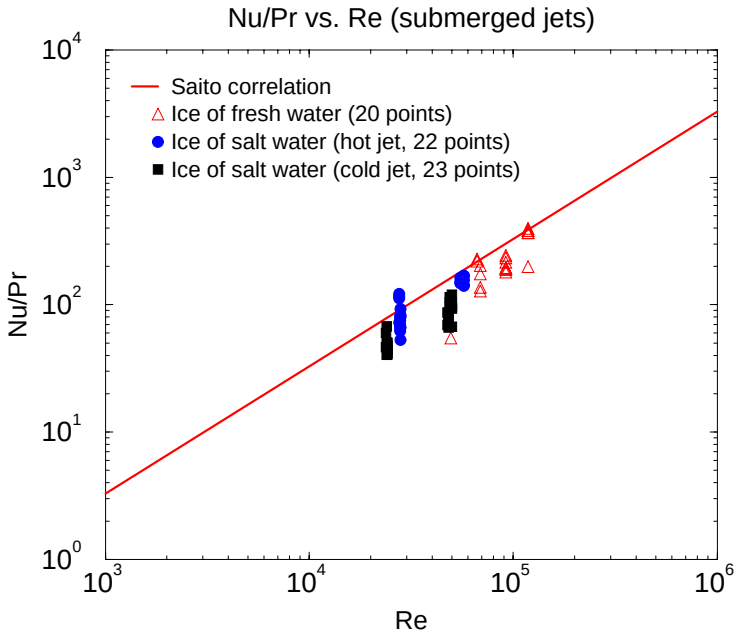

Fig. D.4: Influence of a liquid layer above the impingement surface on heat transfer.

r	Radial
tur	Turbulent

Table D.5: Heat transfer at the initial impingement period.

#	Test	$\frac{X_{abl}}{D_j}$	Nu_{lam}	Nu_{tur}	$Nu_{exp,1}$
1	0513	0.12	404	1843	605
2	0515	0.12	427	1875	977
3	0515a	0.46	463	1880	804
4	0516	0.46	446	1880	974
5	0513a	0.12	405	1843	749
6	0513	0.12	401	1838	813
7	0605	0.12	469	1891	836
8	0605	0.24	469	1891	775
9	0605	0.12	525	1906	739
10	0605	0.24	525	1906	989

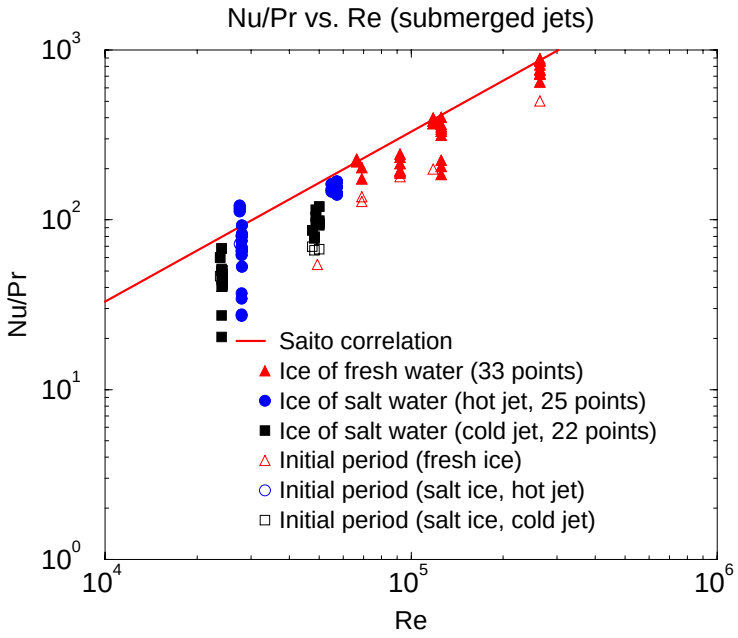

Fig. D.5: Heat transfer during initial and established periods in submerged jet cases.

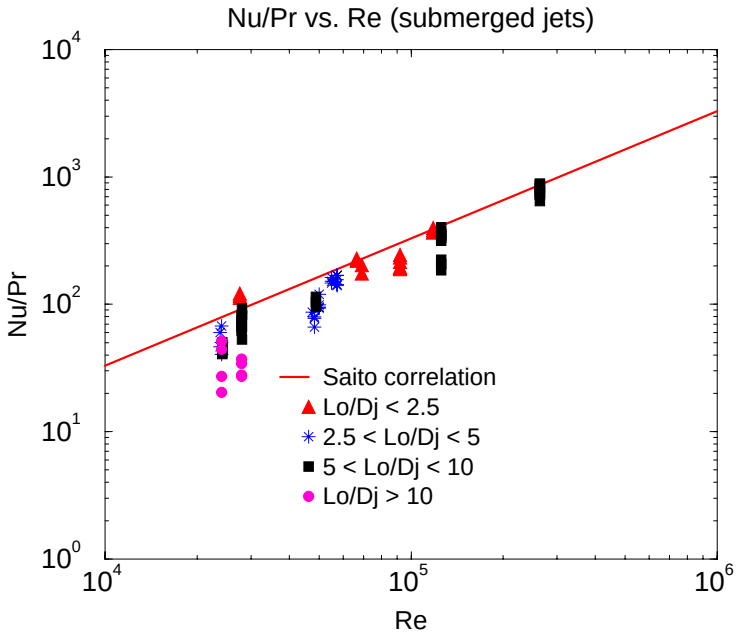

Fig. D.6: Effect of a pre-installed liquid layer depth on heat transfer in submerged jet cases.

Bibliography

[1] T.G. Theofanous et.al., ”In-Vessel Coolability and Retention of a Core Melt”, DOE/ID-10460 (July 1995).

[2] M. Saito et al., ”Melting Attack of Solid Plates by a High Temperature Liquid Jet - Effect of Crust Formation”, J. Nuclear Engineering and Design, 121 (1990), pp.11-23.

[3] M.J. Swedish et al., ”Surface Ablation in the Impingement Region of a Liquid Jet”, AIChE J., 25 (4) (1979), p .630.

[4] Y. Yen and A. Zehnder, ”Melting Heat Transfer with Water Jet”, Int.J. Heat Mass Transfer, 16 (1973), p.219.

[5] A. Furutani et al., ”Erosion Behavior of Solid Plate by a Liquid Jet - Effect of Molten Layer”, ANS Proc. 1989 National Heat Transfer Conf., Philidelphia, PA (August 1989), pp.263-271.

[6] M. Epstein et al., ”Simultaneous Melting and Freezing in the Impingement Region of a Liquid Jet”, AIChE J., 26 (5) (1980), p .743.

[7] D.C. McMurray, P.S. Myers, and O.A. Uyehara, ”Influence of Impinging Jet Variables on Local Heat Transfer Coefficient Along a Flat Surface with Constant Heat Flux”, Proc. 3rd Intern. Heat Transfer Conf. (1966), vol.II, pp.292-299

[8] J.A. Pessanha and M.Z. Podowski, ”Ablation of Solid Walls Subjected to Impinging Inclined Jets”, ANS Proceedings of the 1989 National Heat Transfer Conference, Philadelphia, PA, August 1989.

Appendix E

Review of Salt-Metal Hole Ablation Experiments

E.1 Abstract

This section provides a summary of the four (4) hole ablation tests conducted at RIT/NPS using salt as melt simulant and low melting point metals as vessel steel simulant. These tests were conducted using the larger induction furnace coil and therefore provide for melt volumes of just under 25 liters. As a result, they provide good scaling to prototypical penetration failures. Modeling of these experiments with the HAMISA code is also described.

E.2 Introduction

A severe accident in a nuclear power plant could result in the generation of substantial volumes of high temperature oxidic corium and/or metals. Once generated, this melt can be involved in a variety of phenomena of importance to reactor safety which are highly scenario and design dependent. One such phenomena is the formation of a melt pool in the lower plenum of the reactor pressure vessel (RPV) due to melt relocation, which subsequently results in failure of a lower head vessel penetration (CRDM or drain line in a BWR or instrumentation nozzles in a PWR). Flow of the melt pool fluid through this failure site will in turn result in enlargement of the hole, and thereby increase the rate of melt discharge into the containment.

The ablation of the vessel steel by the discharging melt involves several complex phenomena such as; moving phase change boundaries, multidimensional conduction in the vessel steel and crust formation for an oxidic material which melts over a particular temperature range (T_{liq}-T_{sol}).

A substantial research program has been directed into the understanding of the hole ablation process at RIT/NPS. This report describes a series of tests which were conducted using molten $NaNO_3$-KNO_3 salt mixtures as corium simulant and the low melting point Cerrobend alloy as well as tin (Sn) as RPV plate materials.

Four experiments were conducted in this test series. All four tests were reasonably successful and thereby provide a valid database for the benchmarking of the mechanistic HAMISA code developed by RIT/NPS. This test series also provided valuable experience for future tests which involved higher temperature oxidic melt simulants.

E.3 Description of Tests

A set of four salt-metal hole ablation tests were conducted in the MIRA (Melt Interactions in Reactor Accidents) facility. Table E.1 provides a description of the relevant test conditions.

Table E.1: RIT/NPS Salt Metal Test Parameters

Test Date	Melt	Plate	D_o (mm)	T_{melt} (^oC)	Volume (liters)
1024	20-80 w/o (Na,K)NO_3	Cerrobend	20	350	22
1129	20-80 w/o (Na,K)NO_3	Cerrobend	10	450	23
1205	20-80 w/o (Na,K)NO_3	Tin	10	450	23
1211	50-50 w/o (Na,K)NO_3	Tin	10	440	24

Individual reports regarding the specifics of each test can be found in the applicable directories in the RIT/NPS user4 storage disk. Physical properties for the melt and cerrobend alloy can be found in the report by Green [1]. Tin properties can be found in Incropera [2].

In each of the above tests the induction furnace arrangement, the test section into which the melt was poured, and the plate geometry were identical (Figure E.1). Additionally the embedded thermocouple locations in the metal plates were the same (Figure E.2).

The melt crucible has a 270mm ID with a 17mm thick wall. It is made of common C-steel. The height of the crucible is 480mm which provides for a maximum melt volume of 27.5 liters. The actual melt height is always somewhat lower than this to avoid any spillage. The salt mixture is weighed out in the proper proportions and mixed thoroughly. The melt is generated by induction heating of the steel crucible. As the powder melts, additional salt is added. The generation

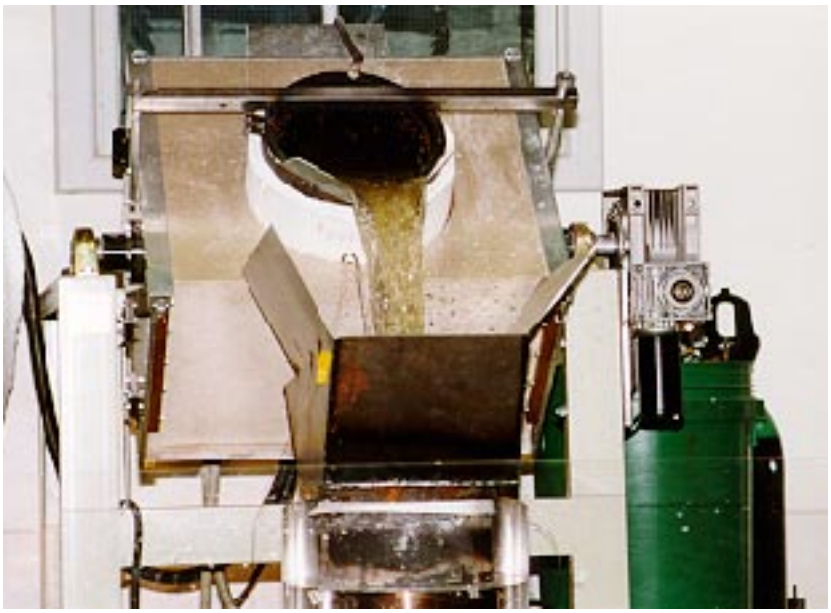

Fig. E.1: Pouring of Salt Mixture into Test Section.

time for just under 25 liters of melt is approximately 2 hours at power levels of 20-30 kW. Note that there is an initial period during which the crucible is heated to its curing point of $\sim 700^o$C. In this period a maximum of only 10-15 kW can be supplied by the generator.

Once the melt has been formed it is remotely tipped into the pre-arranged test section. This test section is 257.5mm ID and 500mm in height. The section is heated using 4 band heaters. The melt is poured into the section via a pour spout and umbrella in order to preclude any direct melt impingement on the plate. Once the melt has been delivered into the test section the pre-installed plug is removed to allow the melt flow to discharge through the instrumented plate. In most tests the scale apparatus was installed to collect the mass discharged from the ablating hole. This was then recorded by the PC data acquisition (DAS) system and manipulated to provide a mass discharge rate in time.

In all cases the plate was 50mm thick. In all tests except that of 1024 the initial hole size was 10mm and a plug mechanism was installed to prevent any melt flow prior to all of the melt being delivered into the test section. For the 1024 test, a 20mm initial hole was used without any plug mechanism (thus melt was being ejected as soon as it was remotely tipped into the test section).

Twelve 1mm OD K-type thermocouples were embedded in the test plates and connected to the HP DAS for scanning. These thermocouples are arranged as shown schematically in Figure E.2 and which can be seen in the photograph of Figures E.3-E.4.

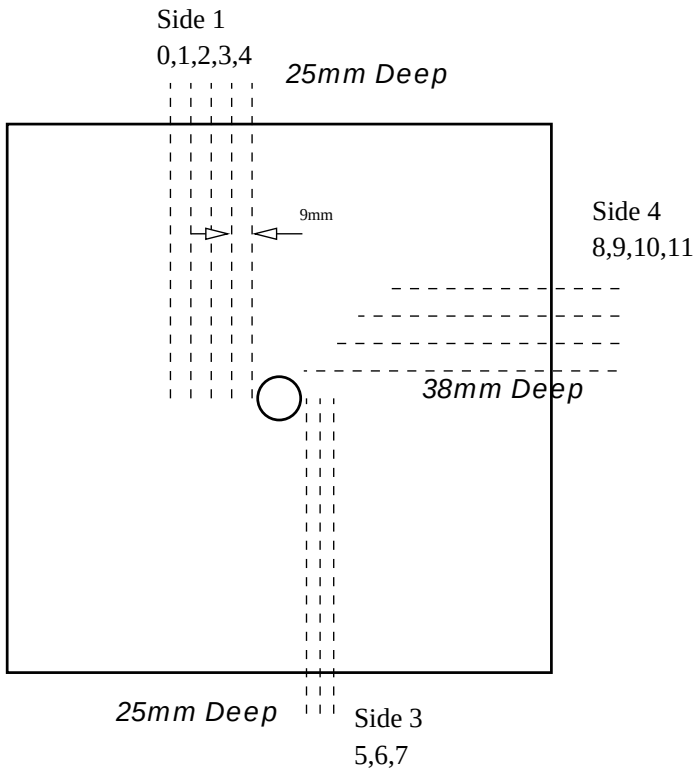

Fig. E.2: Arrangement of Embedded Thermocouples.

E.4 Experimental Results

The information from these tests falls into 2 main categories; (i) integral results such as the final hole size (D_f) and the discharge time (t_d) and (ii) dynamic results such as the ablation front progression (V_{abl}) and rate of melt discharge. All of the tests provided results from the first category. The latter category depends upon the installed instrumentation whose success is not always guaranteed.

The applicable 'integral' type results are presented in Table E.2. Recall that test 1024 is unique in that the plug mechanism was not used there.

Interestingly, the lower surface diameters are in some cases larger than those at the top surface. This is indeed the case although it must be realized that the hole size measurements are slightly subjective (i.e. where to place the ruler) and also that the numbers in Table E.2 represent an average of measurements taken every 45^o around the final hole. The geometry of the ablated holes is not always exactly cylindrical and as a rule the difference in diameter at differing angles never exceeded 6mm.

Another common aspect to these tests is the fact that the diameter of the plate at the center depth is typically the greatest. Indeed, the final hole shapes were

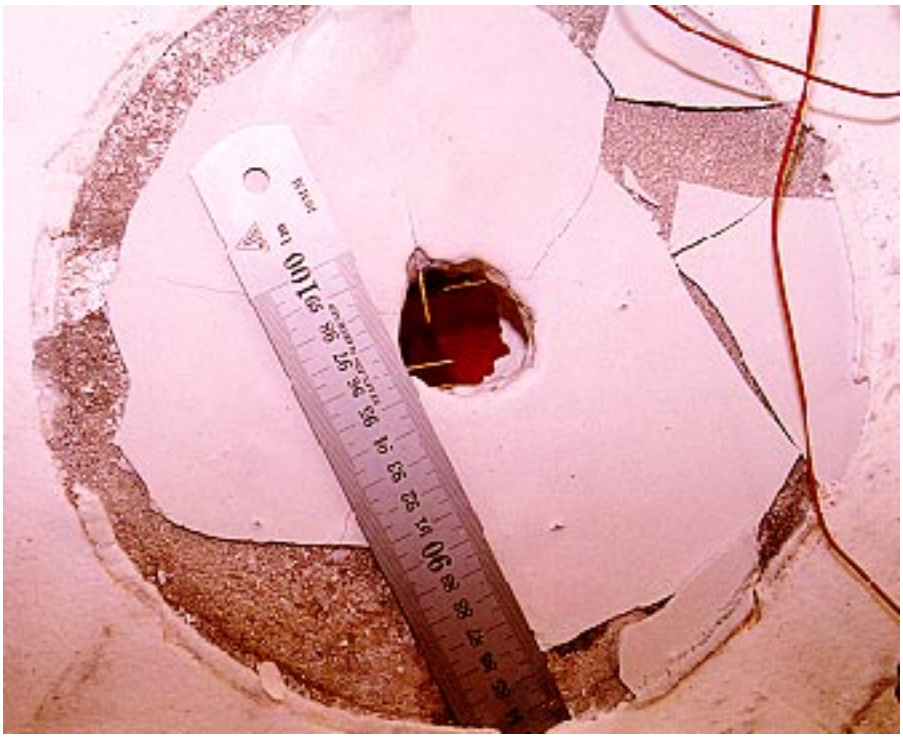

Fig. E.3: Test 1024.

often ”hourglass” shaped. Also of importance is the fact that for the 2 cerrobend plate tests, the plate itself had some ”gaps” which formed during the cooling-off as the plate was formed. It is impossible to ascertain the effect of these gaps on the ablation process. It would not seem to have a major impact however, in one test (1205) it was seen from the video that a path for melt flow developed *away* from the pre-formed initial hole (Figure E.5). Thus, there exists some inherent voiding of the plate materials which is difficult to avoid. The impact of this plate voiding on the overall results is difficult, if not impossible, to quantify. Finally, all measurements are to some extent intrusive on the process to be measured. The embedded plate thermocouples are no exception. They are relatively large at 1mm and certainly have some effect on the flow field in the hole flow. Given other experimental uncertainties however, this is not considered to be a major contributor.

A selection of pictures taken of the ablated plates is presented in Figures E.3 through E.6.

Notice from Table E.2 that the applicable integral scaling parameter of the hole growth to that of the initial hole size ranges from 4.5 to 5.7 for the tests with 10mm initial diameter. This clearly places them into the desired prototypically

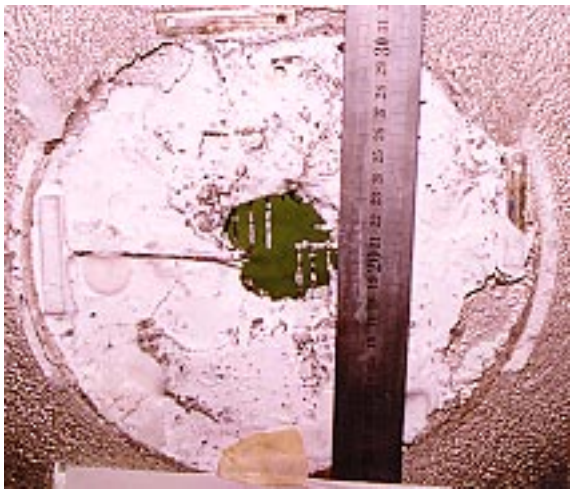

Fig. E.4: Test 1129.

Table E.2: RIT/NPS Salt-Metal Integral Results

Test Date	D_o (mm)	${D_f}^T$ (mm)	${D_f}^B$ (mm)	t_d (s)	t_{pour} (s)
1024	20	49	48	31	10
1129	10	63	70	12	9
1205	10	54	56	12	10
1211	10	68	60	12	9

scaled penetration failure range (see Pilch [3]).

As for *dynamic* measurements, test 1205 was unsuccessful in providing ablation front progression measurements due to the fact that trouble with the tilting mechanism resulted in the DAS "timing out". Also, test 1024 did not reveal sufficient ablation so as to cover several thermocouples (due first to the larger hole size and secondly to the lack of plug).

For each of the 4 tests the collected mass was recorded. This measurement and its time derivative is provided in Figures E.8 to E.11. It can be seen that the discharge times are approximately the same as shown in Table E.2. The differentiation of the mass collected provides a slightly longer discharge period ($\sim$1s) as a result of the fact that some melt continues to drip out after gas blowthrough has taken place.

Results from the embedded thermocouples is provided in Figures E.12 to E.17. From these figures it becomes evident that the actual cerrobend alloy melting point is not 70^{o}C. It would appear that the melting point is much closer to 80^{o}C as was

Fig. E.5: Discharge of Melt from Bottom of Plate (Test 1205).

measured in [1]. Tests 1129 and 1211 provide some indication of the ablation front velocity. These results are summarized in Table E.3.

Fig. E.6: Test 1211.

It must be noted however that even a small deviation in the position of the thermocouples (which is likely given the manner in which the plate was formed) will produce significant changes in the calculated ablation speed. A separation between thermocouples of 9mm is the best estimate however. In addition, there appeared some very hard solid ”lumps” which were caught on the thermocouples in test 1211.

Finally, it was seen for the salt-cerrobend tests that the upper surface of the cerrobend plate was melted over the entire test section geometry. The depth of

Table E.3: Ablation Velocities

Between TC's	V_{abl} 1129 (mm/s)	V_{abl} 1211 (mm/s)
0 - 1	2.4	2.7
1 - 2	2.8	1.8
5 - 6	n/a	3.5
6 - 7	1.6	3.8
8 - 9	2.8	1.8
9 - 10	2.5	2.8

this melting was as much as 10mm. A non-uniform mix of the alloy and salt was realized on the top surface of the plate. This was not true of the subsequent tests using the higher melting point Sn.

E.5 Modeling with HAMISA Code

These tests were employed for validation of the HAMISA code. Although an initial attempt at modeling of the 1024 test was made, it proved to be unsuccessful due to the fact that mass was discharged as soon as it was delivered. The subroutines were modified to allow for this (and also to prevent the code from stopping due to gas blowthrough) however the rate at which the mass is added to the test section is very difficult to include since it changes in time at an unknown rate. The remaining 3 tests were modeled using HAMISA using the property database provided in [1]. The greatest uncertainty in properties appears to be that of the melting temperature and mushy behavior of Cerrobend. In these simulations a melting temperature of 75^oC was used with a 5^oC freezing zone. It appears likely that as the Cerrobend is repeatedly used, it oxidizes to some extent and therefore the melting point increases and also a larger mushy zone results.

The results are quite good as can be seen. This has been achieved with a minimum of "tuning" of the input parameters for these tests. It is likely that the remaining discrepancies between experimental and predicted parameters are due to remaining uncertainties in the thermophysical parameters. In addition, it is very difficult to know the exact volume of melt which is available for ablation. That is due to the fact that some material remains on the induction crucible, some on the pouring spout and umbrella and some on the test section walls. Differences in melt volume input to the code can have significant effects upon the predicted results. Note also that although Table E.4 provides sizes of 68/60 mm for the

Table E.4: HAMISA Validation on Salt-Metal Tests

Test	HAMISA Options	Experiment D_f (mm)	HAMISA D_f (mm)	Experiment t_d (s)	HAMISA t_d (s)
1129	*f*=0.0055, MODS=0	63/70	64/74	11	9
1129	*f*=0.0055, MODS=1	63/70	64/68	11	9
1205	*f*=0.0055, MODS=0	54/56	50/53	12	12
1205	*f*=0.0055, MODS=1	54/56	50/51	12	12
1211	*f*=0.0055, MODS=0	68/60	55/58	12	12
1211	*f*=0.0055, MODS=1	68/60	55/56	12	12

bottom and top dimensions in test 1211, these are in reality averages of different measurements. At 45^o angles the actual upper surface yielded dimensions of 62, 71, 70 and 68 mm and the bottom of 63, 62, 57, and 58mm. (i.e. the holes were not entirely cylindrical). The HAMISA predictions are well within this uncertainty.

Extensive sensitivity calculations were performed. It is found that the driving temperature difference governing the hole ablation process is that between the melt and its liquidus point (T_{melt}-T_{liq}) rather than the solidus point. This is tested in the HAMISA model by artificially changing the salt mixture liquidus point to values closer to the solidus point with the results being that large differences in predicted hole sizes and discharge times were realized. Changes in solidus temperature, while maintaining the proper liquidus temperature yielded no changes in results.

E.6 Summary

This report has presented an overview of 4 hole ablation experiments conducted in the RIT/NPS laboratory using $NaNO_3$-KNO_3 salt as melt and either cerrobend alloy or tin as plate material. The experiments performed have provided well-scaled data points for reactor penetration-type failures. Additionally, the HAMISA code was validated using these tests with reasonable results.

Some conclusions can be made from these experiments;

- The experiments provide the only known database of hole ablation tests for prototypically scaled penetration-type failures.
- The final hole sizes and discharge times are well predicted by the HAMISA code.

- The final hole geometry was primarily cylindrical, thus indicating minor multidimensional effects. This can be attributed to the phase-change surface roughness which minimizes any entrance region effects.

- There appears to be little impact due to the composition of the binary salt mixture. The test conditions between 1205 and 1211 were approximately similar except for the melt composition. Yet the final hole size is not significantly changed. In fact, the slightly larger final hole in test 1211 is more likely due to a slightly larger volume and 10 additional degrees of melt temperature.

- From these tests it is found that the driving temperature difference governing the hole ablation process is that between the melt and its liquidus point (T_{melt}-T_{liq}) rather than the solidus point.

Fig. E.7: Test 1205.

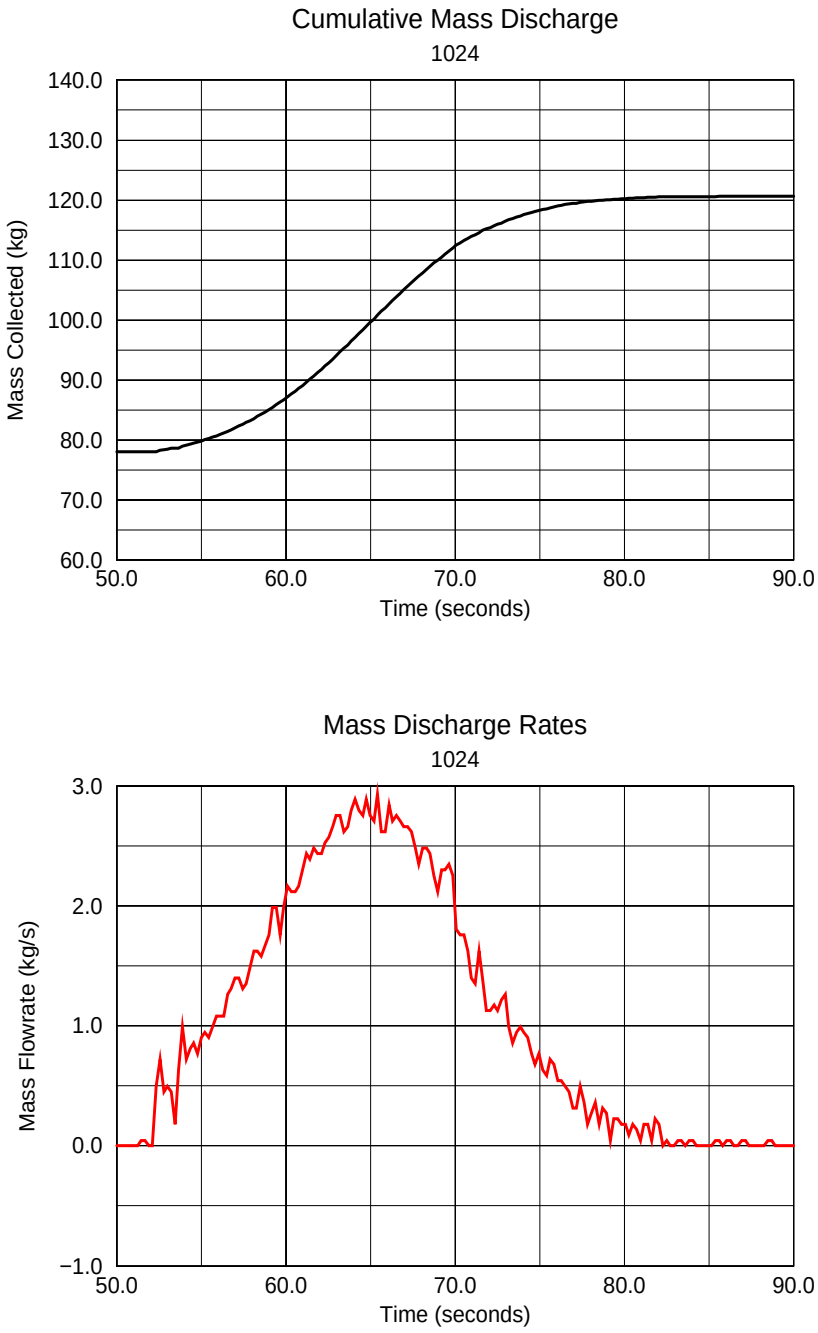

Fig. E.8: Mass Discharge Data for Test 1024.

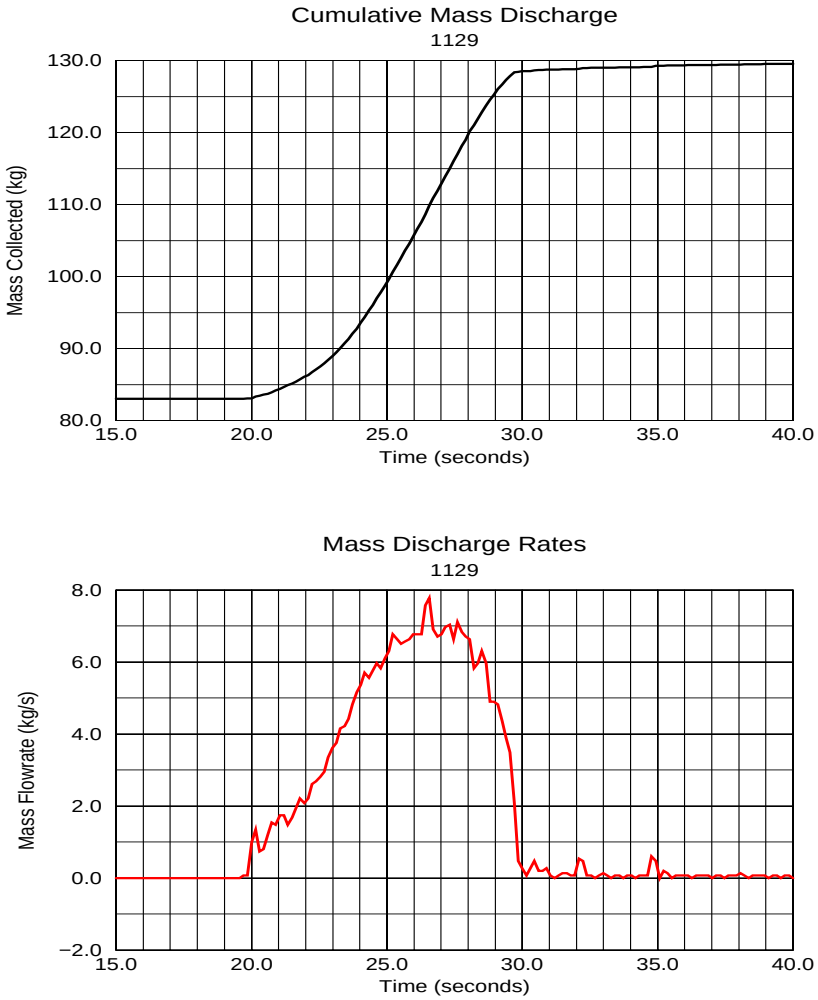

Fig. E.9: Mass Discharge Data for Test 1129.

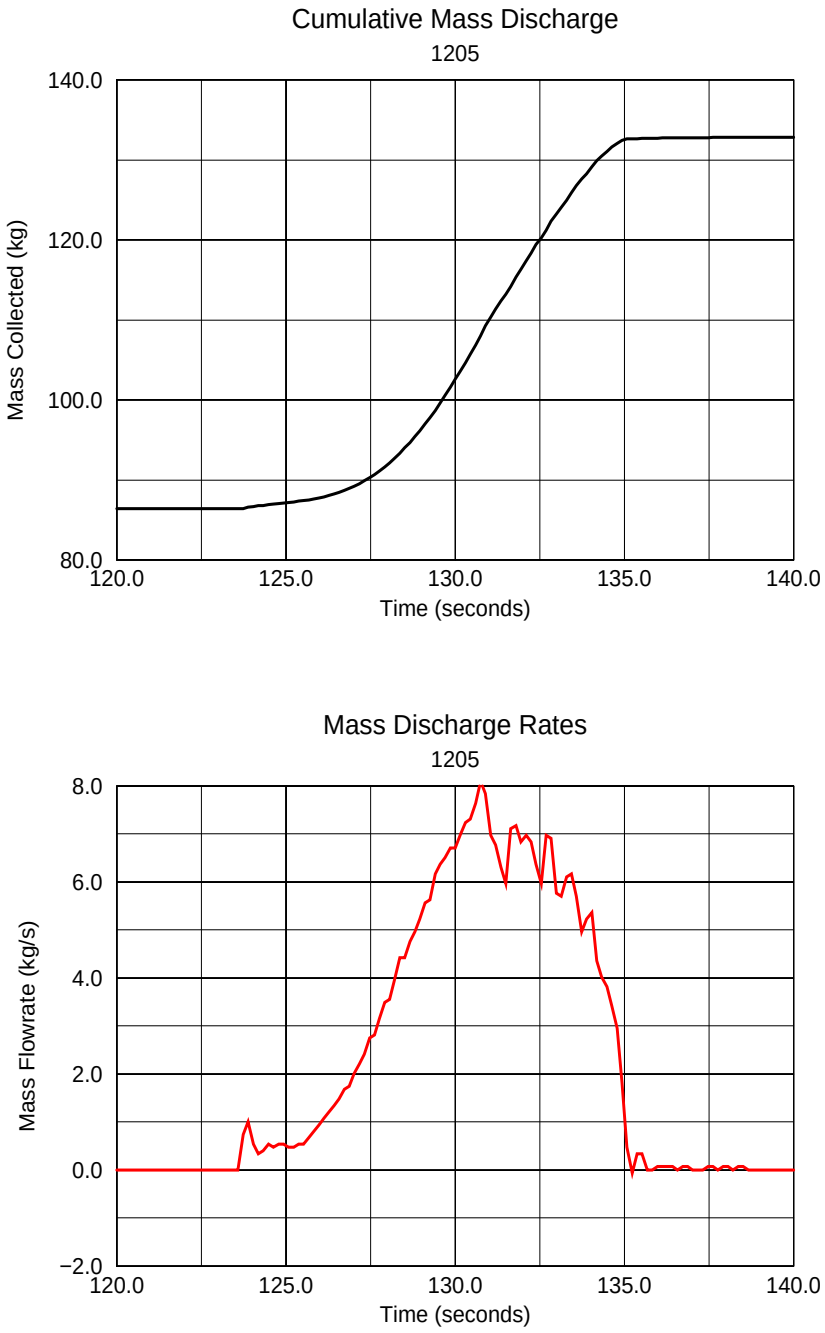

Fig. E.10: Mass Discharge Data for Test 1205.

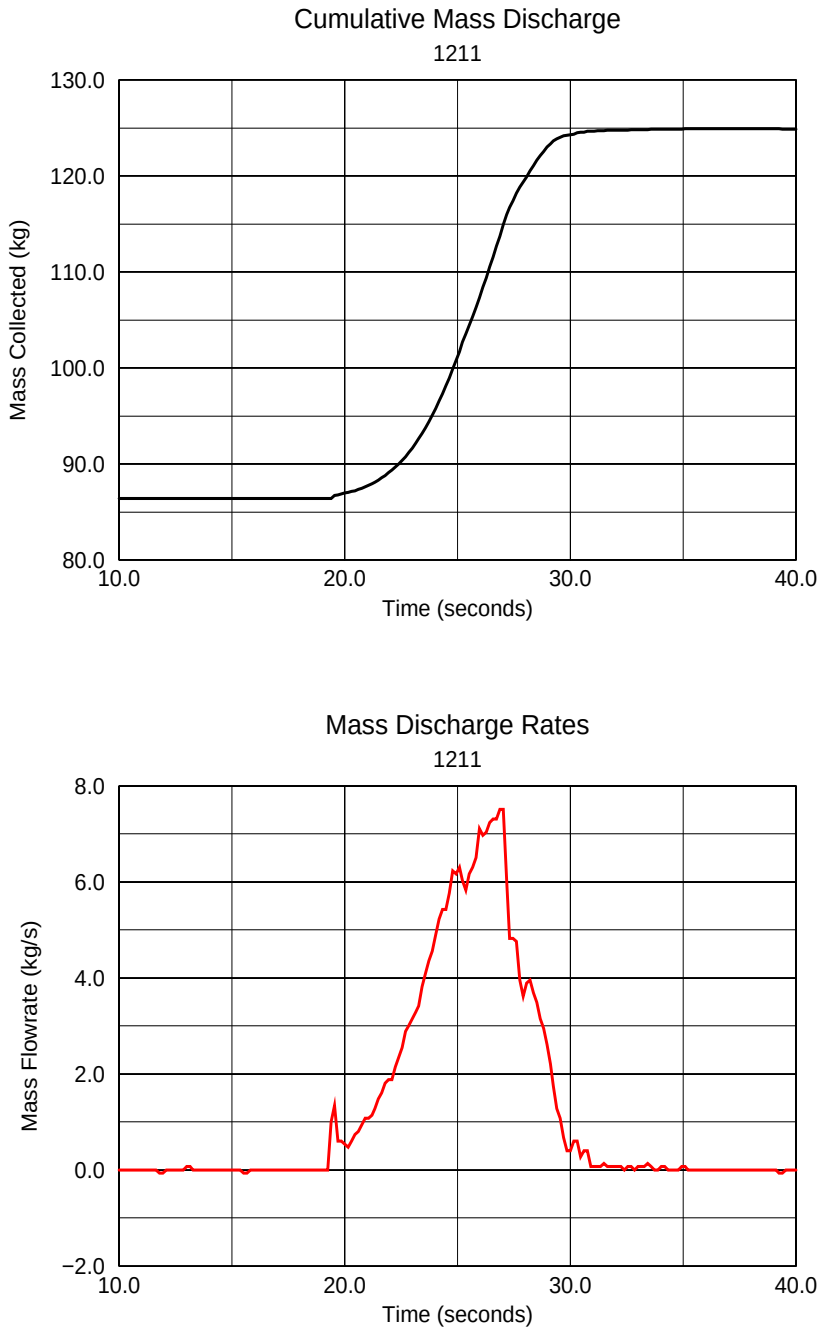

Fig. E.11: Mass Discharge Data for Test 1211.

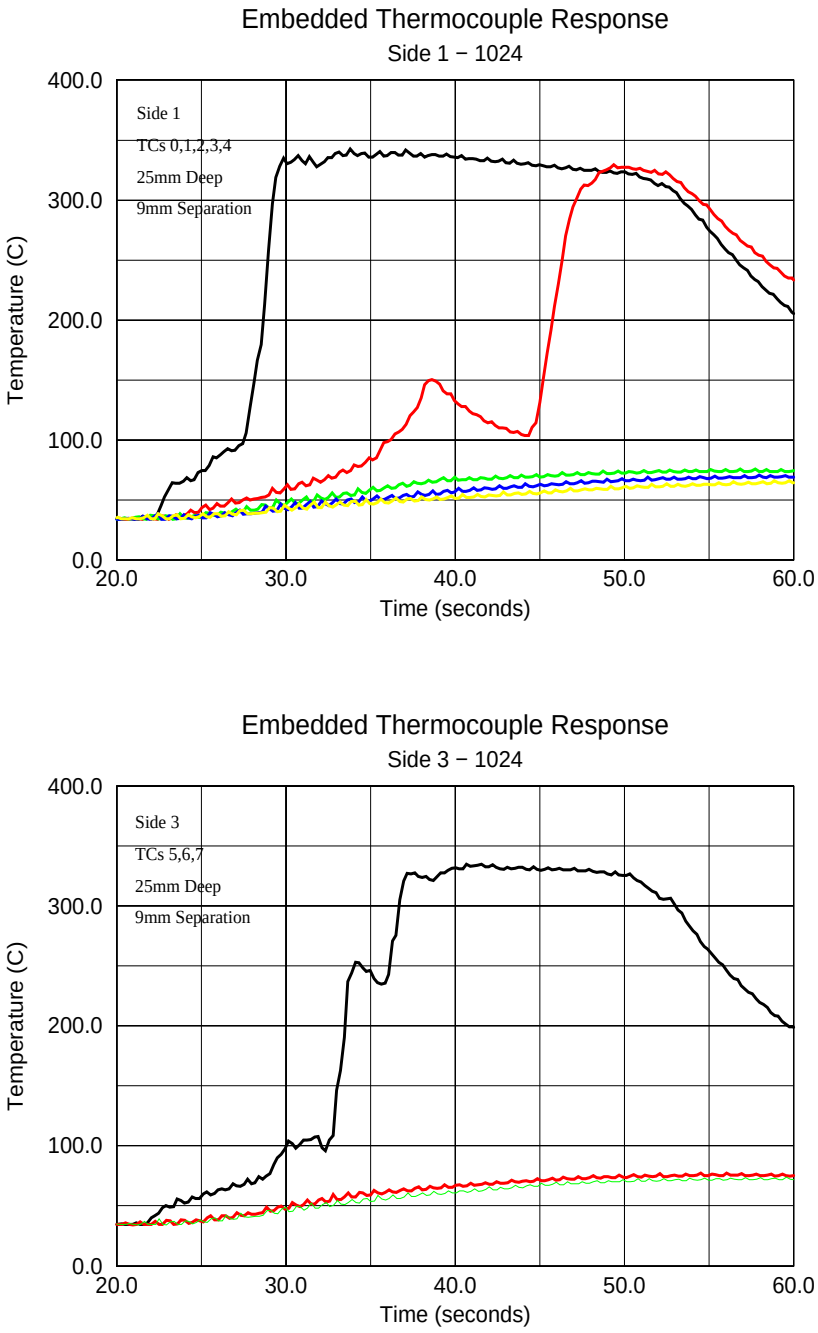

Fig. E.12: Temperatures - Salt-Cerrobend Hole Ablation Test 1024.

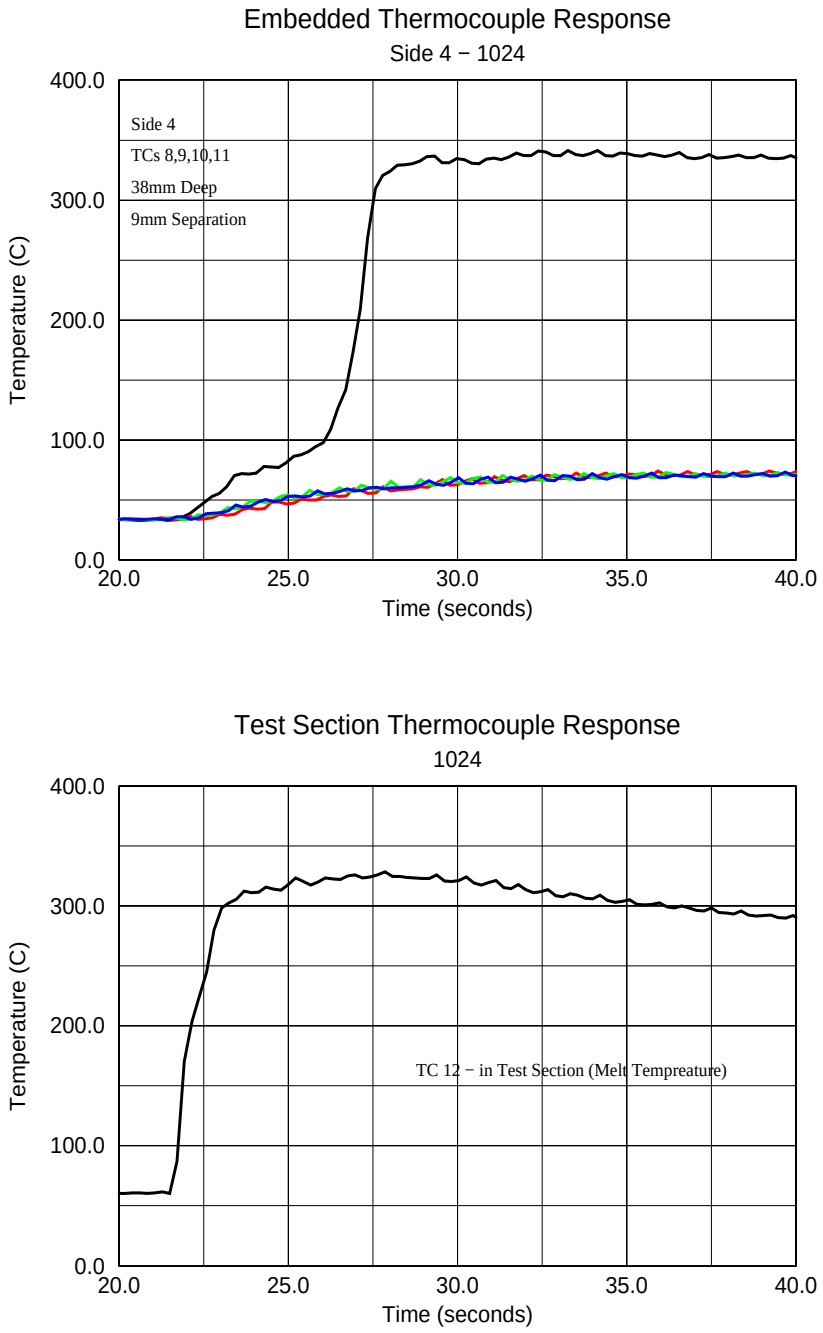

Fig. E.13: Temperatures - Salt-Cerrobend Hole Ablation Test 1024.

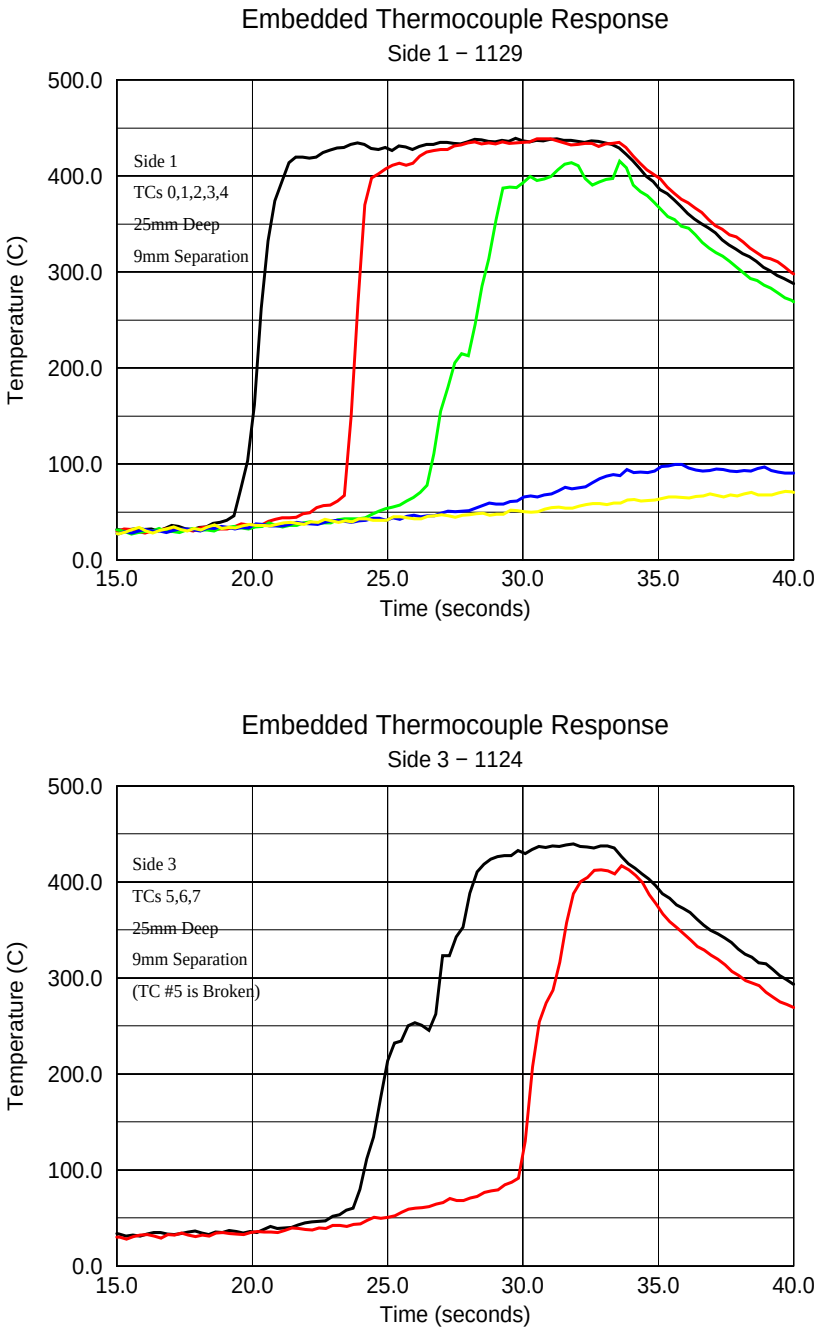

Fig. E.14: Temperatures - Salt-Cerrobend Hole Ablation Test 1129.

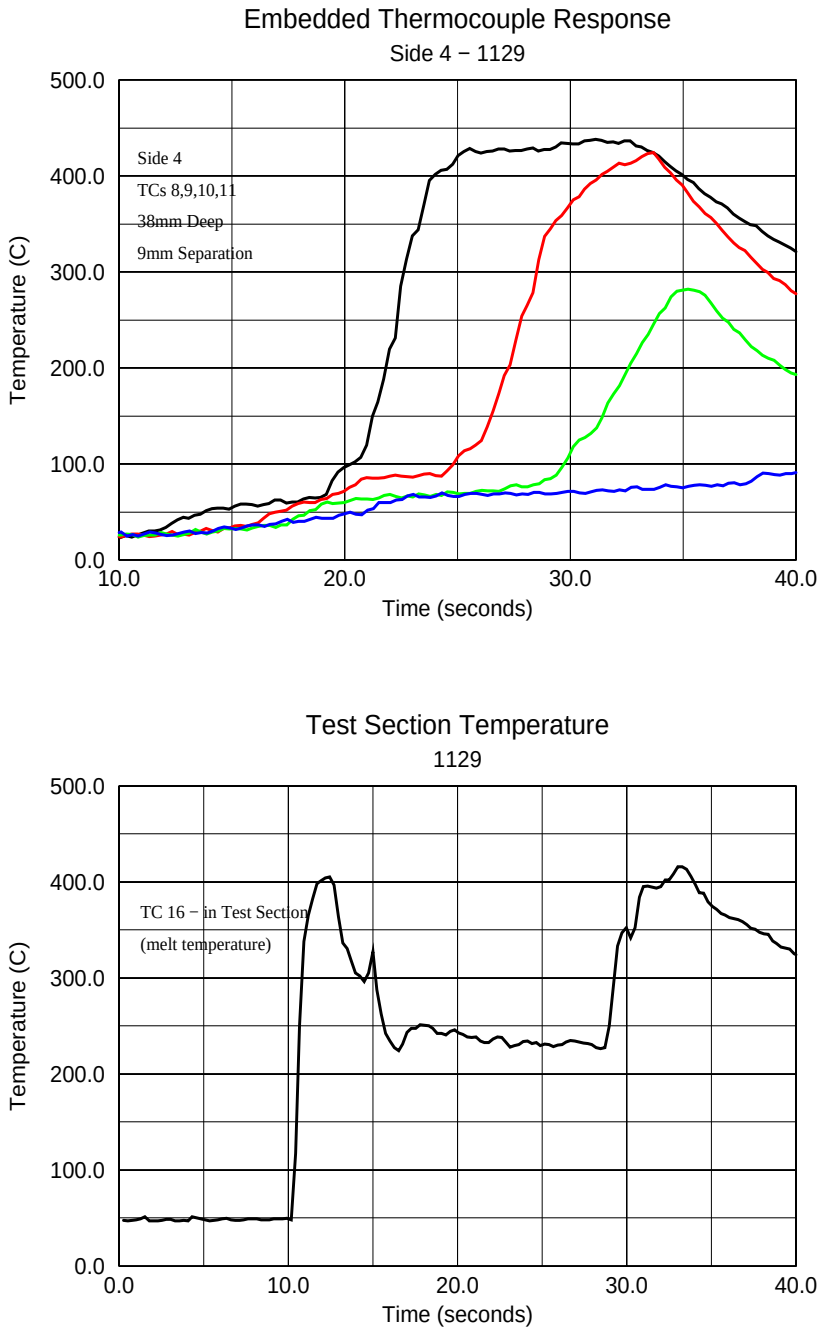

Fig. E.15: Temperatures - Salt-Cerrobend Hole Ablation Test 1129.

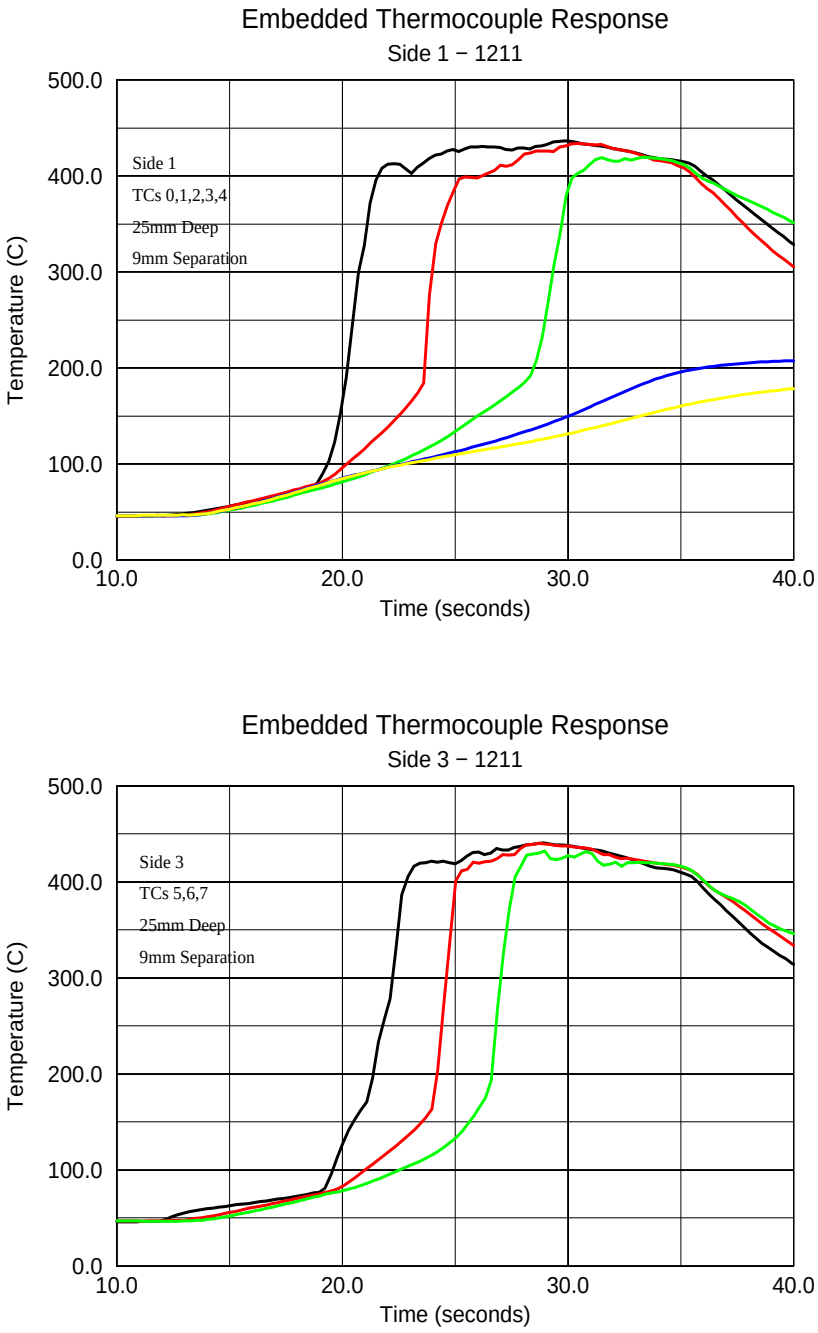

Fig. E.16: Temperatures - Salt-Tin Hole Ablation Test 1211.

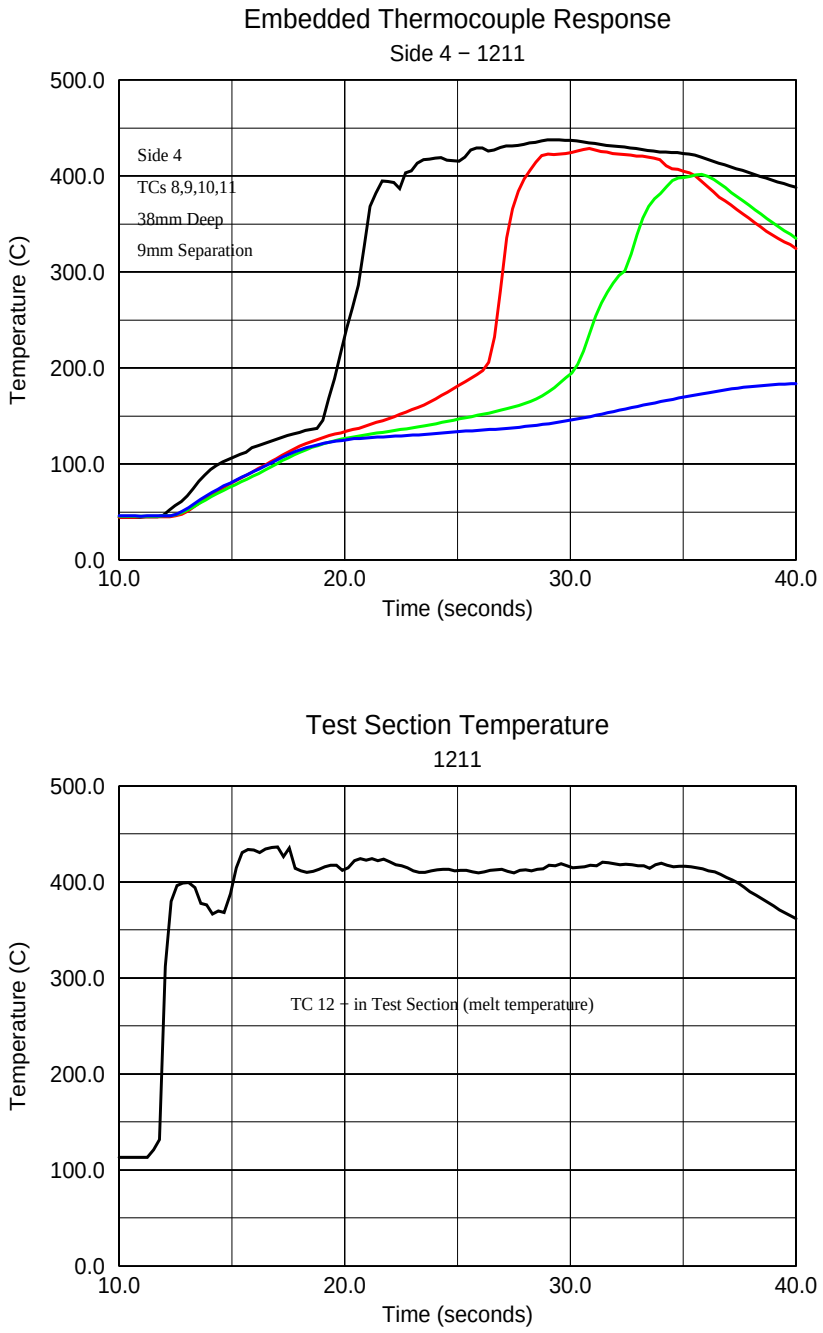

Fig. E.17: Temperatures - Salt-Tin Hole Ablation Test 1211.

Bibliography

[1] Green, J.A., ”Thermo-Physical Properties of Cerrobend Alloy and $NaNO_3$-KNO_3 Salt Mixtures,” Research RIT/NPS Report (NPS-LAB-01-97), January, 1997.

[2] Incropera, F.P., and Dewitt, D.P., ”Fundamentals of Heat and Mass Transfer”, John Wiley and Sons, New York, 1990.

[3] Pilch, M.M. ”Continued Enlargement of the Initial Failure Site in the Reactor Pressure Vessel”, J. Nucl. Eng. Des., Vol. 164, pp.137-146 (1996).

Appendix F

A 20-liters Oxide Melt-Lead Plate Hole Ablation Experiment

F.1 Abstract

This section summarizes the results from a hole ablation experiment conducted on April 28, 1997 at the RIT/NPS laboratory. Approximately twenty (20) liters of 30-70 w/o CaO-B_2O_3 was inductively melted and poured into the pre-heated test section. The plate was 55mm thick Pb with 12 embedded thermocouples and an initial central hole of 15mm in diameter. This test showed a minimal ablation after pouring of the melt which was followed by a heatup of the Pb plate to its melting point which then resulted in an overall plate melting. Although there was not significant ablation evident, the results confirm the predictions of the pre-test HAMISA calculations.

F.2 Experimental Conditions and Melt Preparation

The following amounts of powders were mixed to make the melt:
20.7 kg CaO
74.3 kg H_3BO_3

If one assumes the typical loss of 35% of the boric acid mass due to the loss of water, then the resulting mass of B_2O_3 is 48.3 kg which yields a weight ratio of CaO to B_2O_3 30-70. The solidus and liquidus temperatures for this concentration are 980 and 1025^{o}C respectively.

The test began at 9:30 am and the 18 liters was available after roughly 5 hrs at maximum power of the induction furnace. Note that 40kw was the maximum power possible for the coil configuration employed. However, that is acceptable since it corresponds to an outside crucible temperature of nearly 1250^{o}C. The cru-

cible was made of Si-C and this particular crucible had been used twice before. It was noticed that some of the graphite from the crucible had entered into the melt and floated on the top of the melt as a slag. From post-test examination of the crucible, it does not appear to be significantly degraded and can be employed in another experiment. One of the major difficulties during the test is the exceptional amount of steam which is driven off and which typically overpowers the ventilation system. As in previous tests, the filters had to be removed in order to ensure enough suction. The ventilation system suffers from the difficulty that the fan decreases in speed now that the absolute filters have been removed. Satchwell is still working on this aspect.

There were 12 K-type thermocouples of 1mm OD embedded in the plate at varying depths and distances from the initial hole. The layout of the 12 TCs can be seen in Figure F.1.

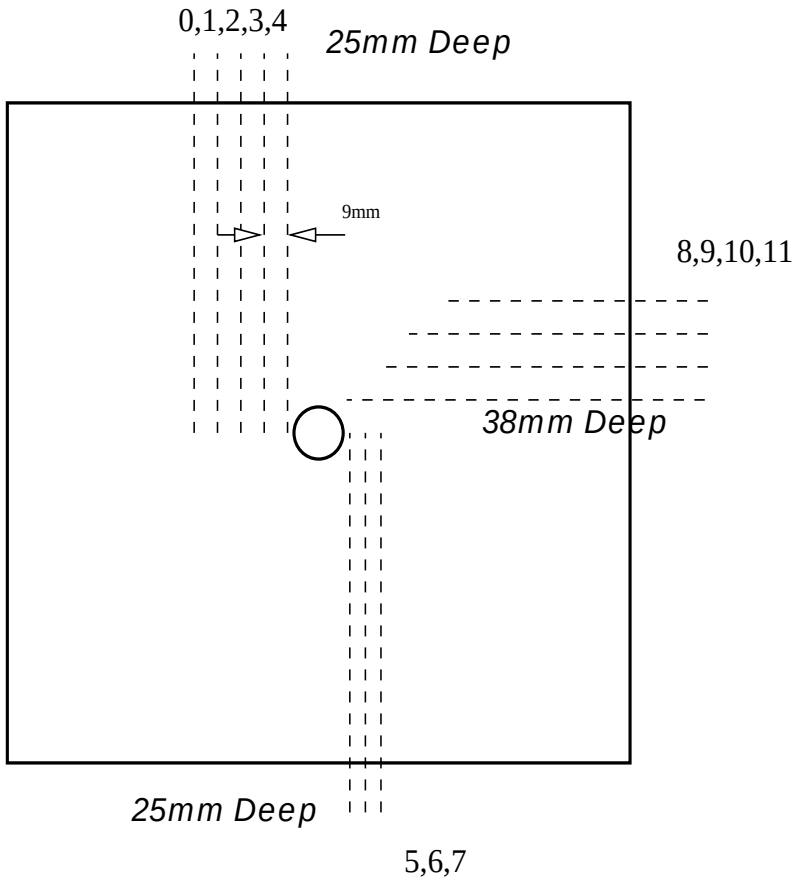

Fig. F.1: Thermocouple Layout.

The melt was approximately 18 liters at 1350^{o}C just before pouring from the furnace into the test section. The B-type thermocouple was used and for certain

periods it worked properly. However, there is evidently a loose connection in this TC and measurements were highly dependent upon any slight movement of the thermocouple wire leads. The only use of this higher temperature thermocouple is for the measurement of temperatures in excess of 1200^oC, since K-type TC's often fail at such temperatures.

The test section is 280mm ID and 500mm high. It was preheated to over 400^oC by an arrangement of gas burners. Only a minimal crust layer was formed on the test section walls as realized by post-test examinations.

The melt of 18 liters would fill the test section to roughly 29 cm. An assumed C_d value of 1.0 would equate to a roughly 2.4 m/s discharge velocity without hole ablation.

F.3 Test Conduct

The melt was remotely tipped into the section and then the plate plug was pulled out. The tilting was accomplished quite quickly, estimated at less than 5 s, and the plug was removed immediately thereafter.

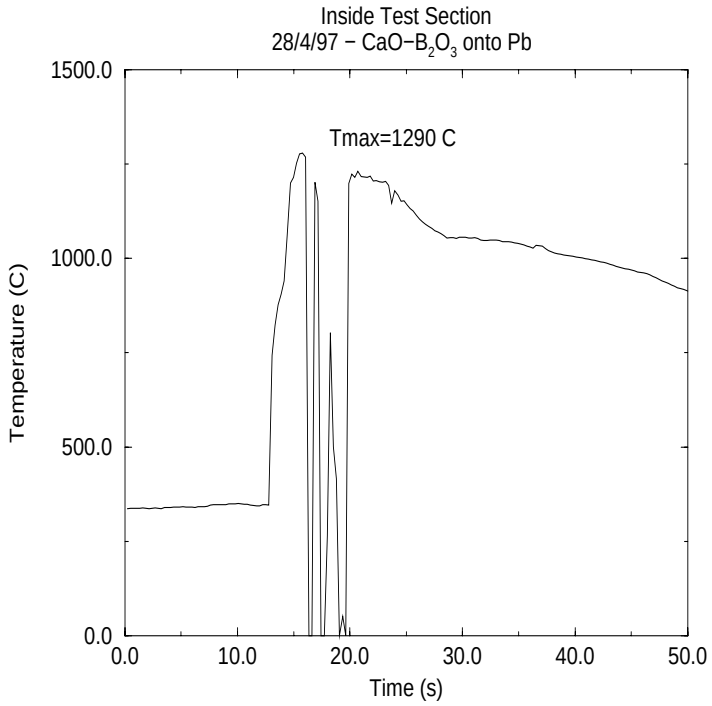

Fig. F.2: Test Section Melt Temperature

The Hewlett-Packard Data Acquisition System (DAS) functions well. 400 scans of 15 channels were conducted with NPLC=0.01 and the time required was 109.2 seconds. (3.7 Hz). In addition, the mass discharged from the section was collected and recorded in time using the terminal application of the DAS PC (6.7 Hz).

The temperature of the thermocouple inside the test section wall is given in Figure F.2 while the readings from the embedded thermocouples are presented in Figures F.3 - F.5 and the mass collected from the discharge hole is shown in Figure F.6. The maximum temperature recorded in the section was 1290^{o}C however the scanning was not done for a long enough period to capture the final rupture of the melt through the Pb plate. However, subsequent readings of these temperatures showed readings as high as 1300^{o}C by some of the embedded thermocouples. At these temperatures the K-type TCs are not useful and typically give erratic readings (if not absolute failure). During the period of recording, the melt discharged as a relatively small jet and essentially little plate ablation was realized. By the time the DAS scanning had finished, the plate temperatures were well above the melting point of 330^{o}C and shortly thereafter the entire Pb plate simply discharged away and the remaining melt was discharged with it. This is seen at 125s of Figure F.6 where the mass collected increases rapidly.

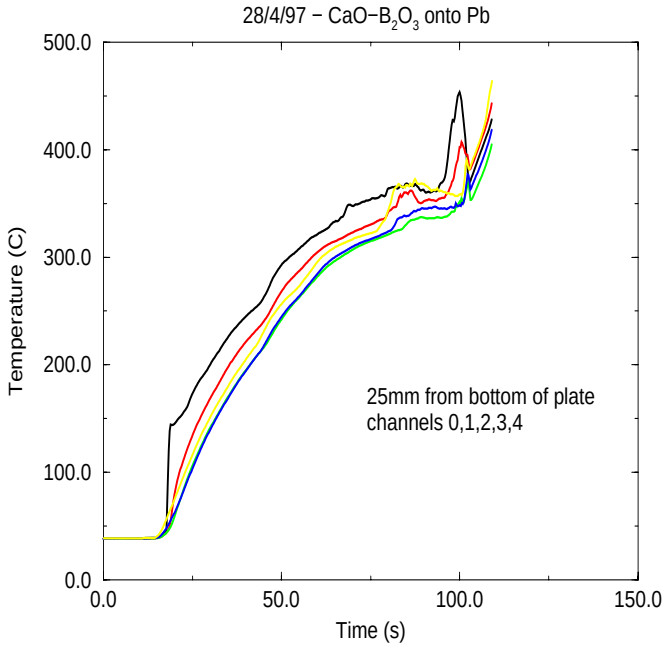

Fig. F.3: Temperatures inside Pb Plate.

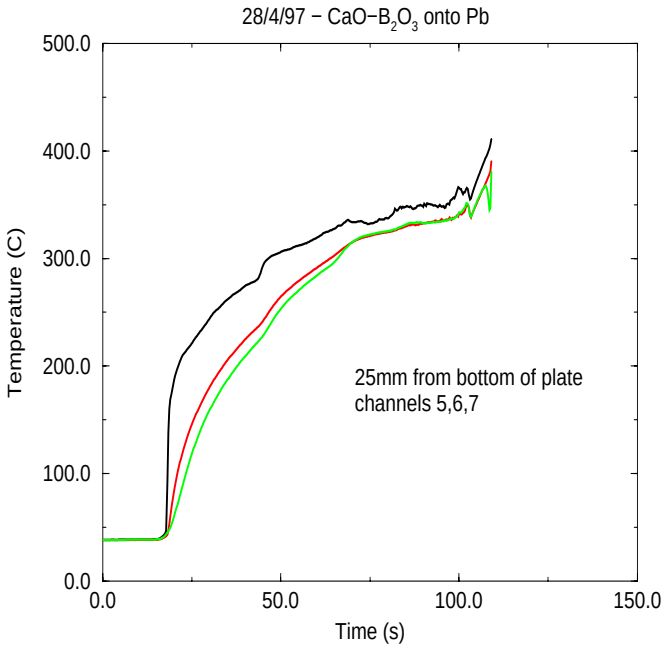

Fig. F.4: Temperatures inside Pb Plate.

F.4 Analysis and Discussion

Since the final hole size is not available, the test results can only be analyzed in qualitative manner. The readings from the embedded thermocouples also do not reveal any useful information in term of hole enlargement dynamics, since the crust formation eventually plugged the melt discharge and thereafter the entire plate reached its melting point and discharged rapidly with the remainder of the melt in the test section.

However the test is useful for validation of the crust-formation model in the HAMISA code since the HAMISA pre-test calculation for these particular conditions showed that the crust would be developed to plug the initial hole. This is not the first time when the HAMISA crust formation model forecasts the choke-off the melt discharge flow in oxide-melt hole ablation experiments.

The reason for this plugging of the discharge flowpath is attributable directly to the kinematic viscosity of the melt simulant; $\mu = 0.1$ Pa-s and $\rho = 2400 kg/m^3$. This results in laminar flow conditions and thus minimal heat transfer from the flowing melt to the ablating Pb plate. The crust which forms then grows and eventually prevents any further melt discharge. In this case however, the conductive

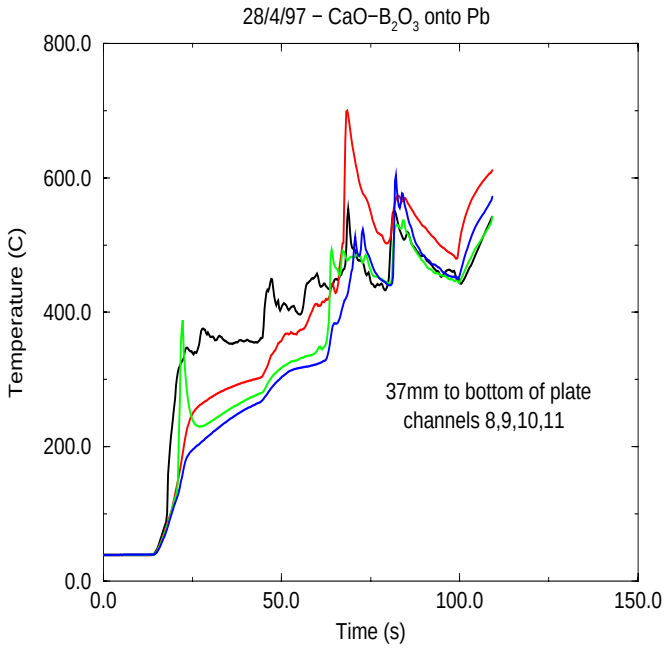

Fig. F.5: Temperatures inside Pb Plate.

heat transfer from the overlying pool of melt resulted in the majority of the Pb plate attaining temperatures greater than the melting point, which simply led to a massive failure of the plate. The current version of the HAMISA code does not predict the mechanical failure of the plate due to the attainment of liquid conditions.

Technically, the test demonstrated that:

(i) the B-type thermocouples can be used at the higher temperatures involved in these tests;

(ii) the Si-C crucibles are quite useful and result in only a slight contamination of the melt with C;

(iii) roughly 20 liters of the oxide melt can be generated repeatedly now in the MIRA facility at the RIT/NPS laboratory;

(iv) the HAMISA code properly predicted the choking-off of the melt discharge due to in-hole crust formation.

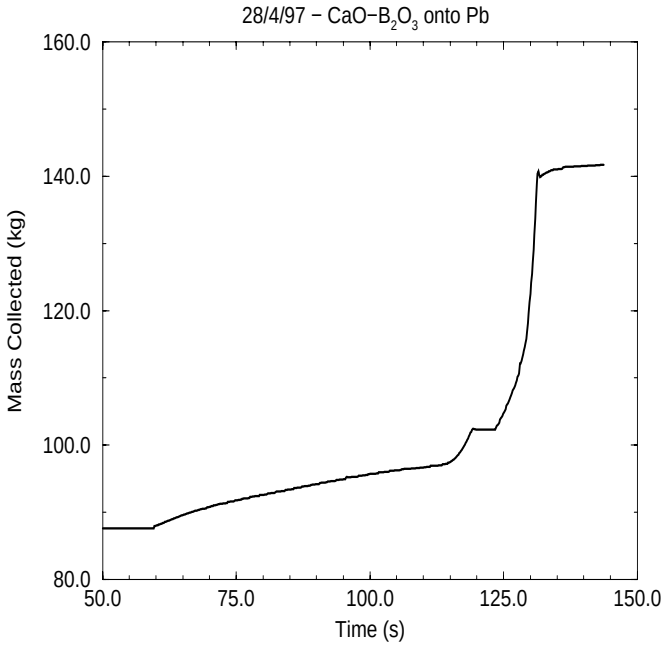

Fig. F.6: Mass Discharged from Section.

Appendix G

Review of Low Temperature Hole Ablation Experiments

G.1 Abstract

A large number of hole ablation tests were conducted at RIT/NPS using water or paraffin oil as melt simulant and ice of salted water as vessel steel simulant. Employing large volumes (up to 80 liters) of low-viscosity and high-viscosity fluids, these tests provide good scaling to prototypical penetration failures. The test results were extensively used to validate the HAMISA model. This section presents original experimental results (temperature data) for some selected hole ablation tests.

G.2 Thermocouple Arrangement and Data Processing

Standard 1mm OD K-type thermocouples (TCs) are used with a typical accuracy of $\pm 0.7\%$. The data from the thermocouples is read using a high speed Hewlett Packard data acquisition system connected to a 486PC. Typical recording frequencies are 2 Hz or more for over 38 channels.

Thermocouples are arranged such that timing of the ablation front can be obtained (see Figure G.1).

The ablation front speed can be determined from the known distance of separation between individual thermocouples positioned on the same elevations.

$$V_{ablation} = \frac{R_{TC(i)} - R_{TC(i+1)}}{t_{TC(i)} - t_{TC(i+1}} \tag{G.1}$$

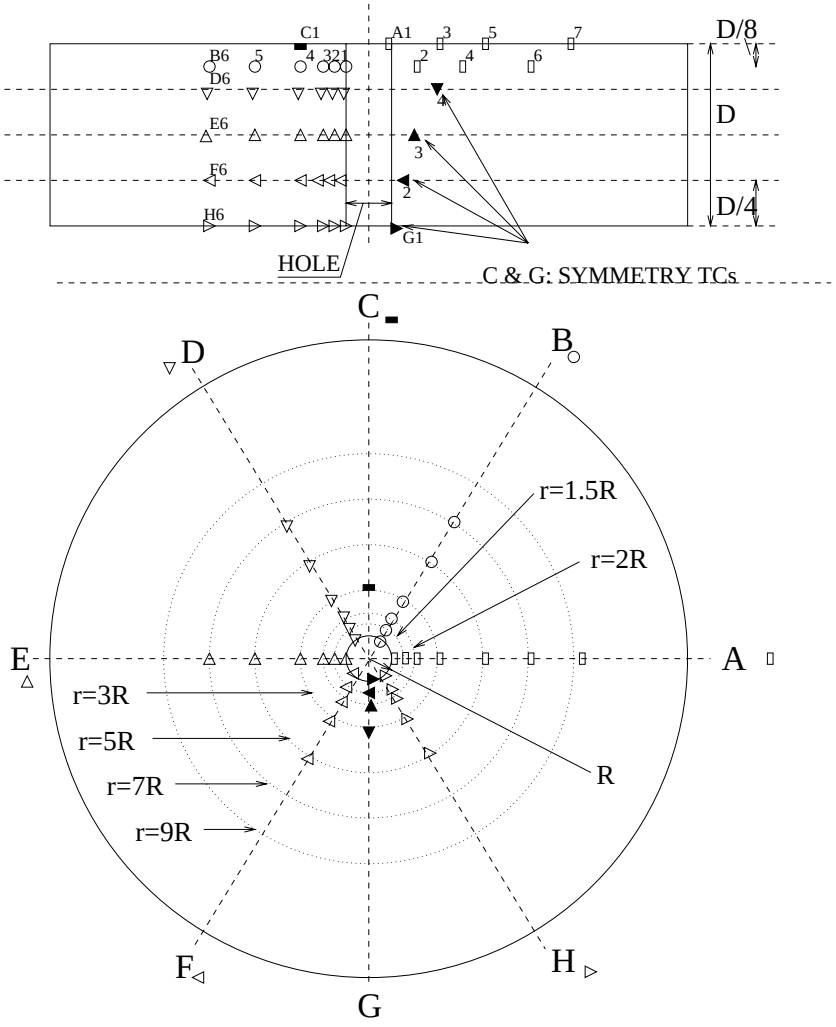

Fig. G.1: Thermocouple Arrangement for Hole Ablation Experiments

The reference temperature difference is that between the melt jet and its corresponding melting point ($\Delta T_{ref} = T_j - T_{mp}$). Since the progression of the melt front is rapid, conduction in the plate material can be assumed to be small and the sensible heat of the plate is incorporated into the heat of fusion;

$$h^*_{fus} = h_{fus,p} + C_{p,p}(T_{mp,p} - T_\infty) \tag{G.2}$$

One can then determine the heat flux as;

$$q_{abl} = V_{abl}\rho_p h^*_{fus,p} \tag{G.3}$$

For these single-component tests, it was shown by Swedish [1], that the con-

vective heat flux can be accounted for as;

$$q^*_{imp} = q_{abl}\frac{B}{ln(1+B)} \tag{G.4}$$

where

$$B = \frac{C_{p,j}(T_m - T_{mp}))}{h^*_{fus,p}} \tag{G.5}$$

Finally, the Nusselt number is determined as

$$Nu_o = \frac{q^*_{imp}}{\Delta T_{ref}}\frac{D_h}{\kappa_j} \tag{G.6}$$

$$q_{cond} = \rho_p C_{p,p}(T_{mp,p} - T_{\infty,p})V_{abl} \tag{G.7}$$

The data from the thermocouples is read using a high speed Hewlett Packard data acquisition system connected to a 486PC. Typical recording frequencies are 2...10 Hz for over 38 channels. Temperatures of the induction crucible, test section wall and test section melt are also recorded along with the time variation of the melt mass collected below the ablation hole.

G.3 Water-Ice Hole Ablation Tests

G.3.1 Test 0925

Figure G.2 shows temperature data of Test ICE0925. The test conditions are given in Section 2 of the present report.

G.3.2 Test 1015

Test was conducted October 15, 1996 on a 80mm plate of pure ice, with initial temperature of -24 ^{o}C. Initial hole diameter is 10mm. 78 liters of water at 44 ^{o}C was used as melt simulant.

10 temperature measurement channels were scanned, with 2 rows of 5 thermocouples at 2 depths: (i) #0-#4 TCs of first row at 45 mm from top surface, and (ii) #5-#9 TCs of second row at 60 mm from top surface (Figure G.3).

Final hole size was irregular, with 92-100mm at top surface and 93-96mm at bottom surface.

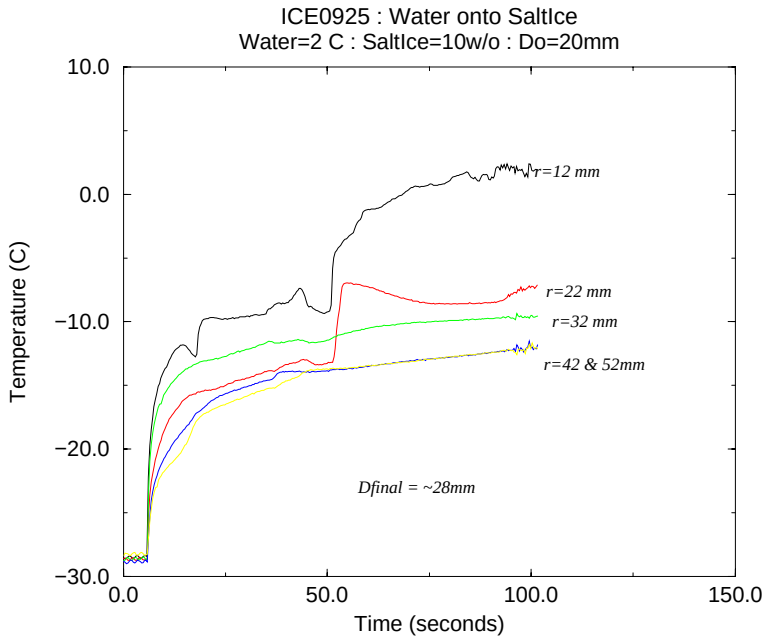

Fig. G.2: Temperatures - Water-Salt-ice Hole Ablation Test 0925.

G.3.3 Test 1016

Test was conducted October 16, 1996, using a 78mm thick plate of salt ice (10w/o NaCl). Initial diameter hole is 20mm and initial plate temperature is -30 ^{o}C. 78 liters of 90 ^{o}C water is used as melt simulant.

2 rows of embedded thermocouples. At 0^o angle 6 thermocouples are installed 5mm apart at 45mm depth from the plate top surface (Figure G.4). At 180^o angle other 6 thermocouples are installed 5mm apart at 60mm depth from the plate top surface (Figure G.5).

A scale build underneath of the test section is used to measure water discharge rate (Figure G.6).

Final hole sizes are 105/102 mm at top surface and 104/107 mm at bottom surface.

G.4 Paraffin-oil-Salt-ice Hole Ablation Tests

The test conditions of these tests (Test 1023 and Test 1024) were shown in the Section 2 of the present report. It was observed that, in both tests, little melting of the hole occurs. In Test 1023, the hole ablation was not detected by the embedded

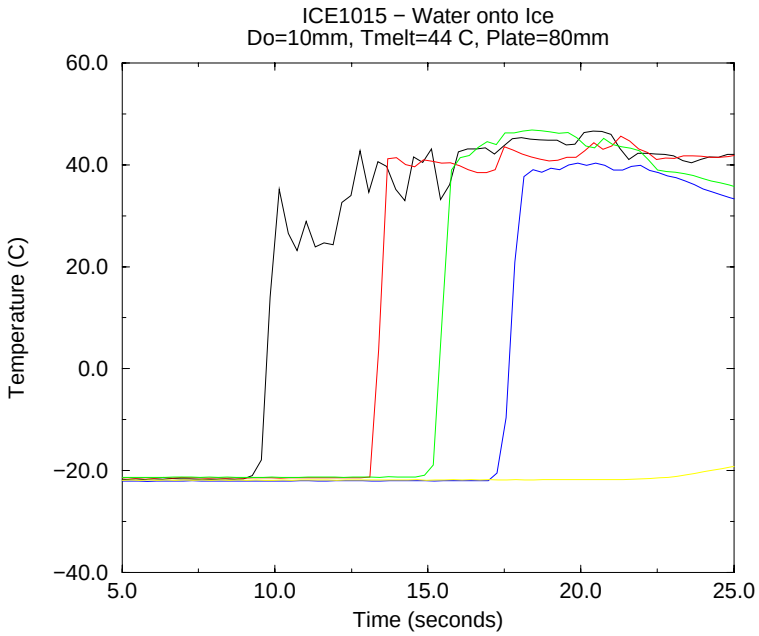

Fig. G.3: Temperatures - Water-Ice Test 1015 (thermocouples #5-#9).

thermocouples. Temperature data (Figure G.7), however, can be used to determine the heat fluxes, utilizing, e.g. an inverse heat conduction problem. In Test 1024, the final size was 30mm at top and 22 mm at bottom. In this case, thermocouples closest to hole indicated ice melting (Figure G.8).

In both tests, the top surface was found curved in but the hole is perfectly cylindrical through most the length. The observation agrees with calculations by the HAMISA code, when utilizing two-dimensional model of heat conduction in the ice plate and taking into account the in-hole friction due to high viscosity of the paraffin oil.

Nomenclature

Arabic

C_p	Heat capacity coefficient, J/(kg.K)
D_h	Diameter (of hole), m
h	Heat transfer coefficient, W/(m.K)
h_{fus}	Heat of fusion, J/kg
Nu	Nusselt number, $Nu = hD_j/\kappa$
q	Heat flux, W/m^2
T	Temperature, K

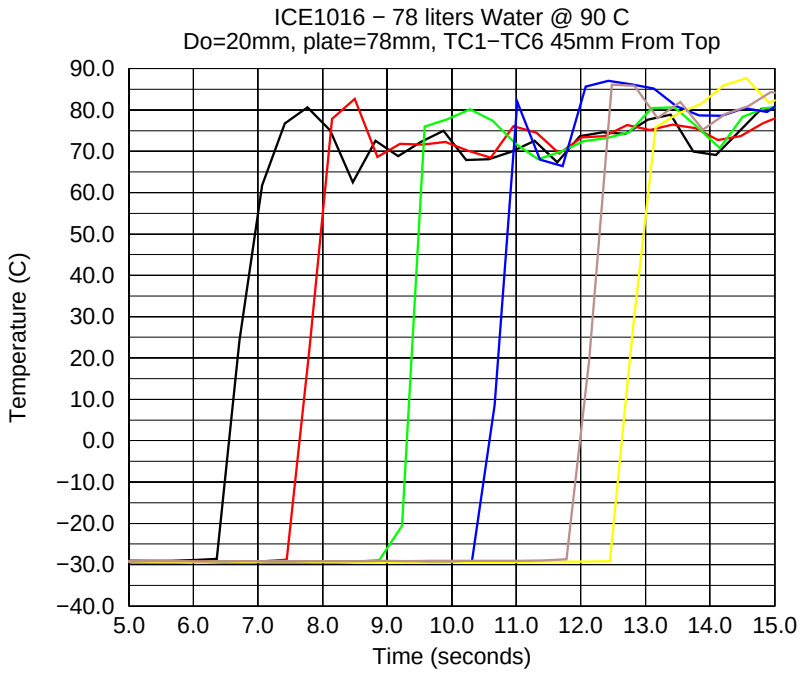

Fig. G.4: Temperatures - Water-Salt-ice Test 1016 (thermocouples #0-#5).

V_{abl} Ablation Velocity, m/s

Greek

κ Heat conductivity, W/m·K

ρ Density, kg/m^3

ΔT Temperature difference, K

Subscripts

m Melt (flow)

mp Melting point

p Plate

l liquid

s solid

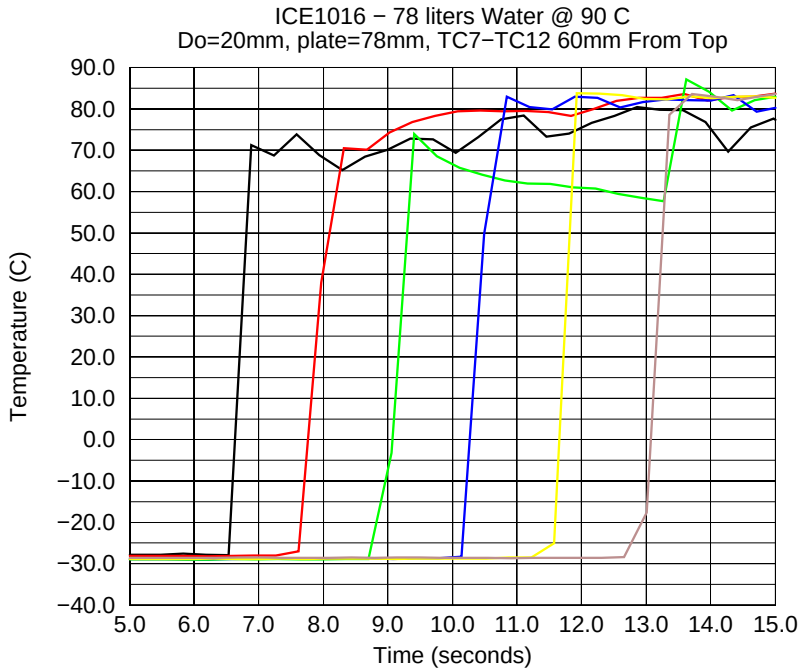

Fig. G.5: Temperatures - Water-Salt-ice Test 1016 (thermocouples #6-#11).

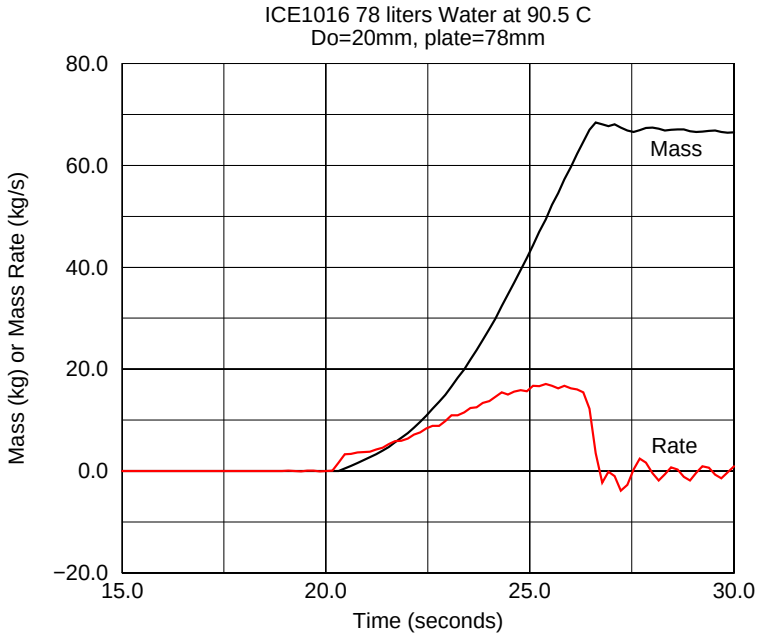

Fig. G.6: Mass Discharge Rate - Water-Salt-ice Hole Ablation Test 1016.

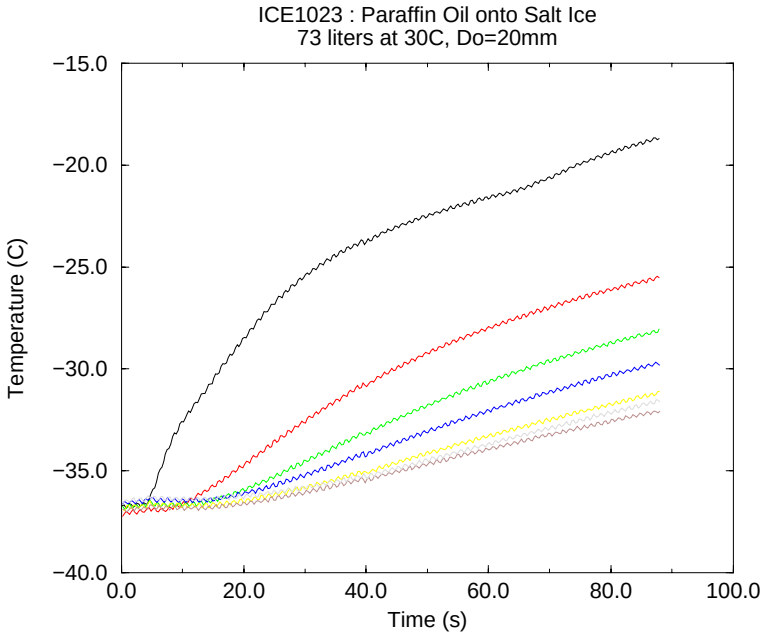

Fig. G.7: Temperatures - Paraffin-oil-Salt-ice Hole Ablation Test 1023.

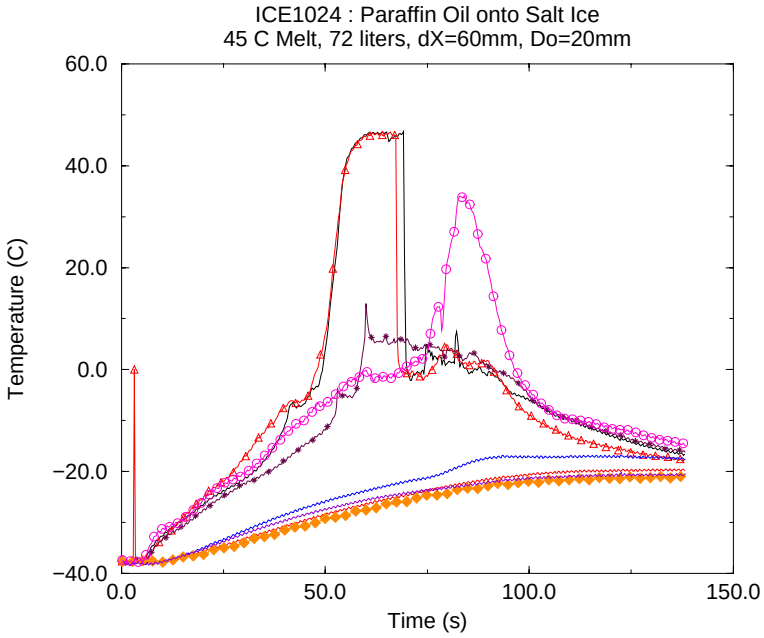

Fig. G.8: Temperatures - Paraffin-oil-Salt-ice Hole Ablation Test 1024.

Bibliography

[1] Swedish, M.J., et al., ”Surface Ablation in the Impingement Region of a Liquid Jet, AIChE Journal, Vol.25 (4), (1979), pp. 630.

Appendix H

Study of Discharge Coefficients in Hole Ablation Process

H.1 Abstract

Experiments were conducted in the Division of Nuclear Power Safety (NPS) of the Royal Institute of Technology (RIT) to determine the discharge coefficients for flow exiting a geometry similar to that employed for vessel hole ablation experiments. The discharge coefficients obtained in these experiments cover a range of nozzle diameters and lengths. It was found that the commonly employed discharge coefficient of 0.6 is improper for typical reactor and experimental situations. The entrance, in-hole, and exit pressure losses for flow exiting the nozzle strongly influence the flow velocity which in turn plays an important role in the heat transfer and thus ablation of the plate structure when phase change is considered. Dependence of these coefficients upon fluid (melt) properties and geometry are discussed. A model is proposed for prediction of the overall nozzle discharge coefficient.

H.2 Introduction

Discharge coefficients, C_d, are used extensively in a variety of industrial engineering applications usually for the express purpose of determining the pressure loss-velocity relationship for fluid flow past an area change of known dimension. Values of C_d are empirically measured for particular geometries and flow conditions. These conditions are typically the ratio of upstream to orifice area, β, and the flow Reynolds number, respectively. For the case when fluid flows past an infinitely short orifice (sharp edged), the discharge coefficient has been shown to be 0.6 at high Reynolds numbers for most area ratios. The situation changes for

the laminar and transition flow regimes in pipe flow, where the resulting C_d values for sharp orifii show considerable variation with Re [1]. However, for situations with longer lengths of the reduced area (L), such as nozzles, the discharge coefficient is seen to be dependent upon both the length-to-diameter ratio (L/D) as well as the Reynolds number of the discharging flow. Lichtarowicz [2] and Kiljanski [3] show pipeline discharge coefficients for a variety of L/D ratios and Re. Additionally, the work by Lichtarowicz provides a comprehensive overview of the experimental data obtained from a variety of other investigators.

Knowledge of C_d values is also necessary when examining the mass discharge from a vessel, under both atmospheric and pressurized conditions. In this respect, a sharp-edged orifice is unlikely to be employed and instead a finite L/D ratio (with L being typically the vessel wall thickness) will be a characteristic of the discharging flow.

A very specific example, related to severe accidents in nuclear power plants, is the discharge of an in-vessel melt pool through a failure location in the lower reactor pressure vessel (RPV). For a given driving pressure difference between the in-vessel and ex-vessel atmosphere, a higher value of C_d will yield greater velocities, and thereby greater mass discharge rates.

$$U_{disc} = C_d \sqrt{2(P_{in-vessel} - P_{atmosphere})/\rho} \tag{H.1}$$

In the case of gravity driven flow (for example the experimental case where $P_{in-vessel} \approx P_{atmosphere}$) then the melt velocity is driven simply by the height of fluid, h, over the overlying melt pool and discharge hole and the discharge coefficient, C_d, accounts for losses at the discharge point.

The rate of mass discharge from the pressure vessel to the containment atmosphere is a crucial parameter in determining the subsequent loadings placed on the containment during a severe accident. Unlike the case of orifii or nozzles in pipe flow, this involves the discharge of fluid into a different density medium, such as air or perhaps water. In the case of a nuclear reactor however, the situation is substantially complicated by the fact that the discharging flow is at a temperature higher than the melting point of the vessel melting point, and thus the discharge hole is increasing in diameter (ablating) in time. More detailed discussions of the hole ablation process can be found in the references by Dinh [4],[5] and Pilch [6].

The objective of the present study is to obtain experimental data for the discharge coefficient when fluid is ejected from the vessel through a nozzle of finite length into an air atmosphere. Application of these results to the situation of corium melt discharge from a RPV is then discussed.

H.3 Calculation Methods for C_d

Lichtarowicz et al. [2] examination of the substantial body of experimental work in the area of discharge coefficients including their dependence upon the geometry (L/D) and flow (Re) resulted in the following empirically-fitted correlation;

$$\frac{1}{C_d} = \frac{1}{C_{du}} + \frac{20}{Re}(1 + 2.25\frac{L}{D}) - \frac{0.005\frac{L}{D}}{1 + 7.5(log(0.00015 \cdot Re)^2)} \tag{H.2}$$

where the *ultimate* discharge coefficient, C_{du} is that at fully turbulent flow conditions as determined by;

$$C_{du} = 0.827 - 0.0085\frac{L}{D} \tag{H.3}$$

Although this empirical approach provides good indication of C_d values for a range of L/D and Re, it is nonetheless based upon conditions of pipe flow where both the upstream and downstream fluids are the same.

A model with more physical underpinnings is proposed by the present authors here for the case of short nozzles with discharge into air. The velocity of the discharged flow can be determined from

$$U_d = C_d\sqrt{\frac{\Delta P}{\rho}} = \frac{1}{\sqrt{\sum F\rho}}(\sqrt{2(P_{vessel} - P_{atmosphere} + \rho g H)} \tag{H.4}$$

where F represents the sum of the entrance, in-hole and exit form losses as the fluid passes the nozzle/orifice. Expansion of the form losses in these terms provides;

$$C_d = \frac{1}{\sqrt{F_c + F_{in-hole} + F_{ex}}} \tag{H.5}$$

The value of $F_{in-hole}$ is obtained from the frictional losses for common pipe flow and a variety of correlations exist for the laminar, transition and turbulent flow regimes. The term can of course be included or excluded with ease depending upon the situation at hand and indeed, for consideration of melt flow and discharge through over a rather long length, as envisioned for bottom penetrations of the RPV, inclusion of this term is necessary. Likewise, at low Re values the in-hole frictional term increases which in turn decreases the value of C_d.

The contraction form loss coefficient for a sharp contraction falls between 0.44 and 0.5 [7] whereas the expansion form loss coefficient varies depending upon the length of the orifice/nozzle. For extremely short nozzles, a value of F_{ex} of 2.25 allows for agreement with the classical orifice discharge coefficient of 0.6 for fully turbulent flows regardless of the mediums. Agreement with the data of Lichtarowicz implies a value of F_{ex} of 1.0.

H.4 Experimental Study

In order to better quantify the values of C_d for short nozzles with expansion into a lower density fluid, a simple tank apparatus was arranged. This involved a rectangular glass tank of dimension 0.3 x 0.3 m with a 1.0 m height, thus providing for a maximum discharge volume of 90 liters. At the bottom of the tank, plastic plates of various thicknesses with centrally located holes of known diameter formed the container boundary. The ratio of hole-to-tank diameter is kept small to prevent any non-uniformity in the approach to the hole. Straight bore holes were made in the plastic with high precision.

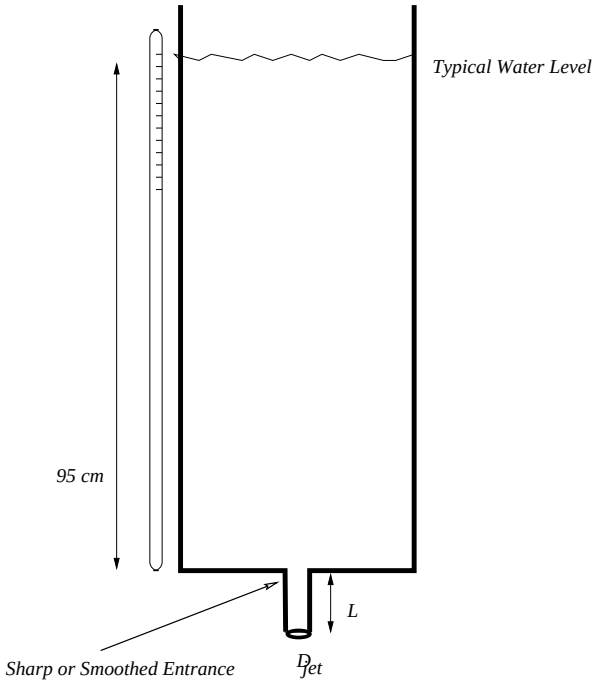

Fig. H.1: Experimental Arrangement

Water over a range of temperatures ($3 < Pr < 12$) was employed in the majority of testing but in some cases higher viscosity (μ=35cSt) paraffin oil was used. The level of the tank was measured in time along with the mass discharge in time via an electronic scale. In this manner the experimentally determined discharge coefficient could be obtained as;

$$C_d = \frac{U_{meas}}{\sqrt{2 \cdot g \cdot H}} \tag{H.6}$$

where H is the tank level and U_{meas} is determined from the derivative of the collected mass in time. The only pressure driving force is that due to the gravity

head since the test section is open to the atmosphere. It must be emphasized that the discharge coefficients determined in this fashion are transient in nature since the driving force decreases in time. Under these circumstances however, the deceleration of the fluid is negligibly small [8]. Also, data obtained when the tank was nearly drained was excluded since it is substantially influenced by the swirling gas vortex which is formed [9].

Table H.1 lists all the hydraulic water tests and their corresponding geometry and flow conditions.

Table H.1: Hydraulic Tests - Water

Tests #	D_{jet} (mm)	L (mm)	Avg. T ^{o}C	Range T ^{o}C	L/D_{jet} (–)	Pr (m^2/s)	Re (–)	C_d (–)
4	15	400	19.9	16.5-22.8	26.7	7.03	38,000-57,800	0.76-0.81
4	15	62	16	$\sim$16	4.13	7.85	25,600-51,500	0.88-1.06
3	15	43	16.4	16-17	2.87	7.85	25,300-53,500	0.91-1.10
3	15	32.5	15.5	15-16	2.17	7.85	24,200-51,200	0.89-1.12
2	15	32.5	51.9	51-52	2.17	3.43	51,100-99,400	0.94-1.13
1	15	32.5	3	3	2.17	12.0	16,900-33,300	0.89-1.13
1	15	32.5	11.7	11.7	2.17	8.94	22,400-48,300	0.93-1.14
2	15	32.5	65.3	63-67	2.17	2.74	61,000-133,900	0.92-1.17
3	15	16	20.8	18-23	1.07	7.0	25,700-71,900	0.93-1.13
1	15	16	48.5	48.5	1.07	3.66	45,500-109,600	0.94-1.14
5	25	50	42.6	38-45	2.0	4.10	72,200-162,100	0.91-1.07
4	25	50	16.8	15-18	2.0	7.85	41,100-87,900	0.88-1.04
2	25	50	68.6	67-70	2.0	2.61	107,700-254,900	0.91-1.06
4	25	30	16.6	15-18	1.2	7.85	39,400-84,500	0.89-1.07
5	25	16	15.3	14-15	0.64	7.85	29,600-63,800	0.67-0.87
3	25	8	21.1	18-23	0.32	7.0	38,600-68,700	0.69-0.72
3	25	4	20.0	19-21	0.16	7.0	33,800-70,400	0.69-0.72
2	25	2	16.2	16-20	0.08	7.85	34,000-70,800	0.69-0.72

The experimental velocity, U_{exp}, was determined simply from the volumetric discharge rate divided by the tube area. The actual head of water for use in determining the discharge coefficients is that of the water in the measured section plus the length of the tube.

Typical results for the experimental velocity as a function of the water head are shown in Figure H.2 for different tube lengths and diameters ambient temperatures. One can see from Figure H.2 that both the 15 and 25 mm diameter tubes at $\approx$30mm length yield similar velocity discharge curves. However, when the same 25mm diameter tube is reduced by roughly 1/2 in length (16mm) that the discharge velocity as a function of water level is significantly reduced. For comparison, a very long tube (400mm), was examined since this provides a situation where the in-hole friction pressure loss is substantial in comparison to the entrance/exit effects.

From known thermo-physical parameters at the water temperature the Reynolds

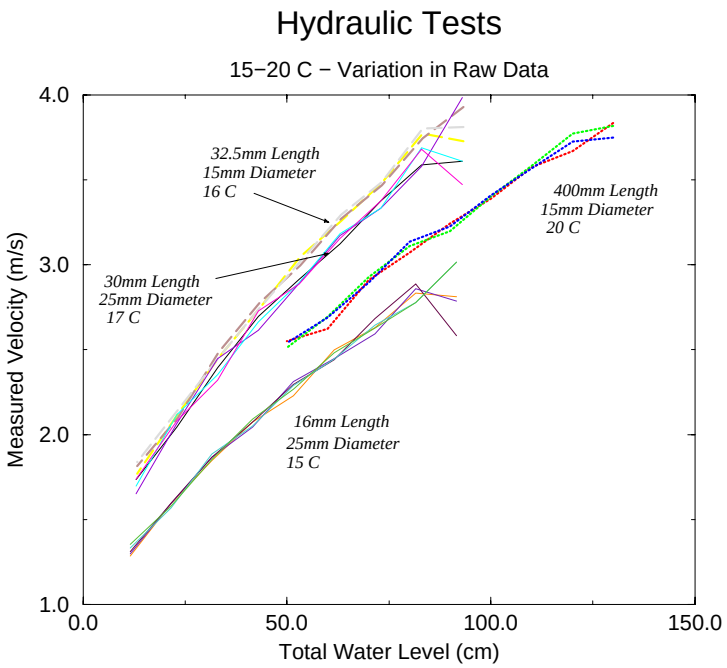

Fig. H.2: Discharge Velocity as a Function of Gravity Head

number can be determined. An indication of the uncertainty in the data is given in Figure H.3 which shows the results of 4 individual tests for a given flow diameter of 15mm and tube length of 32.5mm. Water temperature is kept nearly constant for the four runs shown. The greatest variance is found to always occur at the highest water levels due to the rapid rate of fluid discharge at that point in time. Figure H.4 shows data for the same geometry tube but over a range of temperatures. The figure shows that variation in temperature, from 3 to 67 ^{o}C, and thereby a substantial change in viscosity and thus Pr (2 to 10), plays little role in the discharge velocity from the tube. The implication being that viscous shear forces are *not* a dominant feature of this process.

The experimentally determined discharge coefficients have been plotted against water height and measured velocity for all of the data (except the first test which employed a 400mm long tube) in Figures H.5 and H.6, respectively. The data for L/D greater than 1 covers diameters of 15 and 25mm and a range of tube lengths and fluid temperatures. Yet, all the data is seen to be closely clustered. The data for L/D below $\approx$1 is for a 25mm diameter tube at ambient fluid temperatures. All of the data plotted in these figures are *averaged* values for similar conditions. Each test set shows a characteristic rise in discharge coefficient at low water height (which is equivalent to low discharge velocity). This agrees with data found in Perry [1] which shows C_d as a function of Re and the ratio of upstream

to constriction area, β.

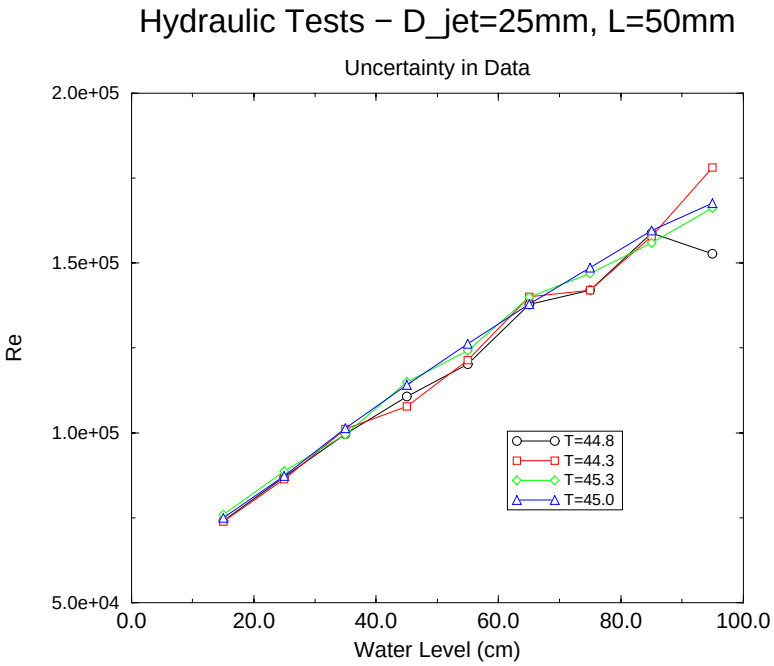

Fig. H.3: Variability in Test Data

For Re number above ∼30,000 the values of C_d are essentially constant between 0.595 and 0.620 regardless of β. At lower Re number, the value of C_d is found to increase with increasing Re. However, care must be taken in employing data obtained from orifii in pipe flow to the case of interest here [1].

Temperature effects are manifested in the calculated Re number primarily as a result of viscosity changes. This is clearly seen in Figures H.7 and H.8 for L/D ratios of approximately 2 for the 15 and 25mm diameter tubes. Recall, there is little if any discernable difference in measured velocity as a function of the water temperature (Figure H.4). Thus in Figures H.7 and H.8, the shift in the curves is simply a result of the variation in the kinematic viscosity as a function of temperature. The experimental C_d is seen to increase with decreasing Re which

[1]There are two fundamental differences:
(i) The fluid (water in this case but corium in the reactor case) is being discharge into a different (much lower density) fluid. Orifice related C_d are for pipe flow with the system 'full' of the same type fluid.
(ii) Flow orifii are very thin (along the flow path) and thus there is little to no length in which the flow can develop. For application to hole ablation, the length for flow is much longer (even 150mm in reactor cases.

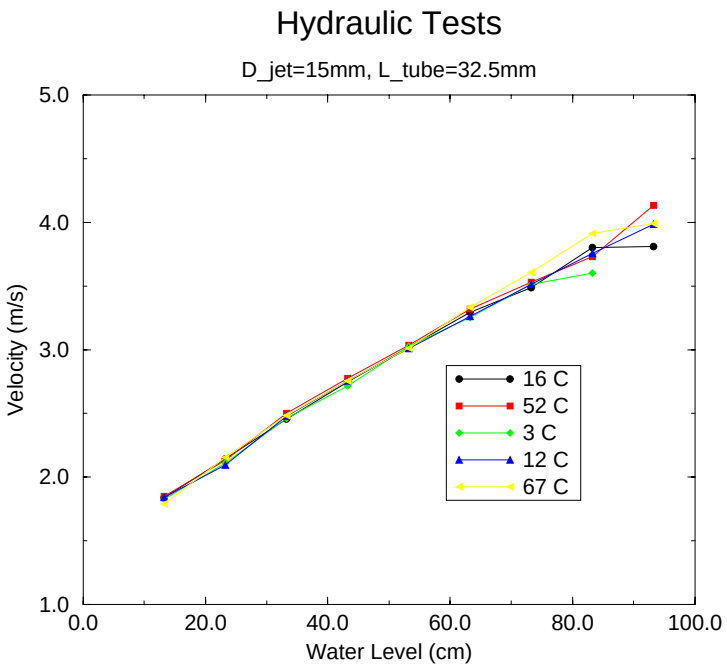

Fig. H.4: Impact of Temperature Variation upon Discharge Velocity

of course is the result of the decrease in velocity as the tank empties. In addition, one should note the y-axis, and realize that the change is not significantly large.

The effect of diameter change is given in Figure H.9 where the fluid temperature and tube length have been maintained the same.

As was seen previously, the shorter L/D ratios (below ~ 1) result in substantially lower velocity discharge rates and thus experimentally determined discharge coefficients (see Figures H.4 & H.5). Such results are more clearly seen in Figure H.10 where the velocity-water level data are plotted for a given diameter tube of varying lengths at roughly the same temperature. Such data reflects a *step* behavior relationship upon the L/D ratio rather than a functional relationship. That is to say, after reaching a *critical* value of L/D, somewhere less than 1.0, that the measured discharge coefficient becomes significantly reduced.

Clearly there exists a *transition point* which depends strongly upon the geometric L/D ratio. However, the transition does not appear to be solely due to the geometry but rather a combination of the geometry and gravity head (driving force). This is evident from tests conducted with a 15mm flow diameter at varying lengths the results of which are shown in Figure H.11. At a length of 16mm (L/D = 1.07) the discharge coefficients fell into the 0.9 to 1.1 range. Shortening of the tube length to 10mm revealed a transition from the higher values of discharge coefficient (in reality discharge velocity) *during* the discharge process.

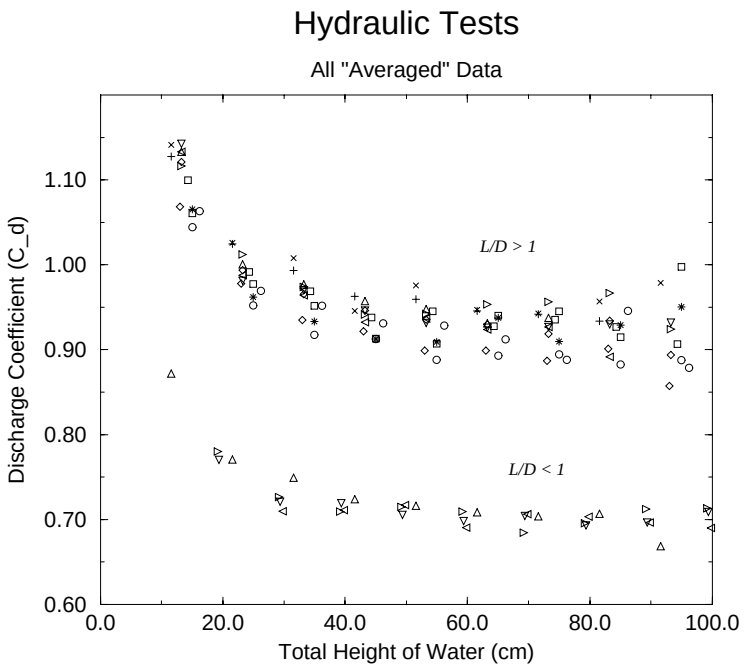

Fig. H.5: Discharge Coefficient as a Function of Gravity Head and Geometry

That is to say, the rate of fluid discharge from the nozzle dropped (or transitioned) as the gravity head fell. The complication with this particular L/D value was the fact that this transition was not reproduceable (even though water temperature was held very nearly constant). Thus in some instances the transition to lower discharge velocities occurred quite early, in others the tank level was seen to decrease by over 40cm before the transition was observed. Furthermore, the transition was not only realized from the data calculation, but rather it could be clearly noted from visual and audio observation during the tests. When the nozzle length was reduced to 7 and subsequently 3.5 mm (L/D of 0.47 and 0.23 respectively) the lower discharge velocities (C_d) were always realized.

In general, it was found that the method proposed in section H.3, Eq.(H.5), can adequately describe the experimental results obtained (e.g. Figures H.12-H.13).

H.5 Smoothed Entrance Effect

From past experiments using PbO-B_2O_3 and CaO-B_2O_3 melts onto Pb plates [11], [12], the geometry of the hole ablation location has been shown to be multi-dimensional with a typically ”funnel-like” shape. Fundamental fluid flow experi-

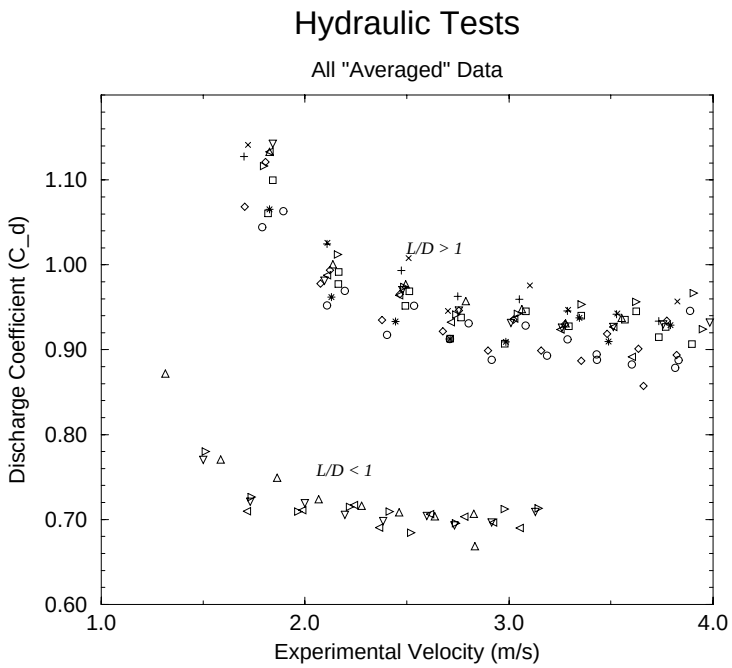

Fig. H.6: Discharge Coefficient as a Function of Velocity and Geometry

ments have shown that a smoothed entrance exhibits a higher equivalent discharge factor as shown in Table H.1. Measurements similar to that of the nozzle were completed with a plate of dimensions shown in Figure H.14. A comparison with the sharp-edged nozzle of similar L/D is provided in Figure H.15. The difference is small yet noticeable. The smoothed entrance provides for higher discharge velocities at equivalent gravity driving forces. This is as would be expected due to the lesser entrance pressure loss.

H.6 Viscosity Effect

Experiments were also conducted using paraffin oil as working fluid. It was found that the fluid viscosity affects, primarily, the in-hole friction. Once the pressure loss in the hole is properly accounted for, the discharge coefficient can be predicted by Eq.(H.5).

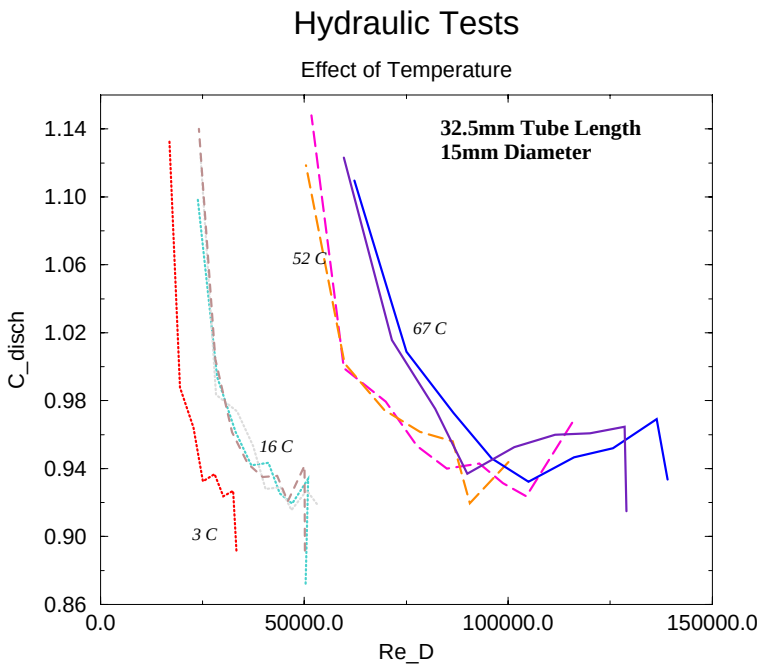

Fig. H.7: Discharge Coefficient as a Function of Re

H.7 Discussion

In the above, values of the discharge coefficient, C_d, for water and paraffin oil draining from an open tank through a lower flat plate with a centrally located opening are obtained and analyzed. Of particular interest is the fact that the discharge considered here is for a more dense fluid into air, whereas most previous studies have dealt with orifii/nozzles in pipe flow where upstream and downstream fluids are identical.

It was found that for cases with $L/D \geq 1$, the discharge coefficient approaches 1, while for cases with $L/D < 1$ a transition to $C_d \simeq 0.7$ was observed. Thus, when the discharge nozzle has a certain finite length the fluid is ejected from the pressure vessel easier than when the nozzle is very short or being an orifice. The expansion pressure loss is found to be responsible for such a behavior. Dependence of the discharge coefficient on fluid viscosity and surface tension was also experimentally examined for selected fluids. It is suggested that for fluids with high surface tension coefficient the discharge flow is generally coherent and the discharge coefficient is in the range 0.9-1.1.

The measured discharge coefficient values are well predicted by a combination of entrance, in-hole and exit form loss pressure drops; Eq.(H.5).

Application of these results is made for the situation of melt discharge from

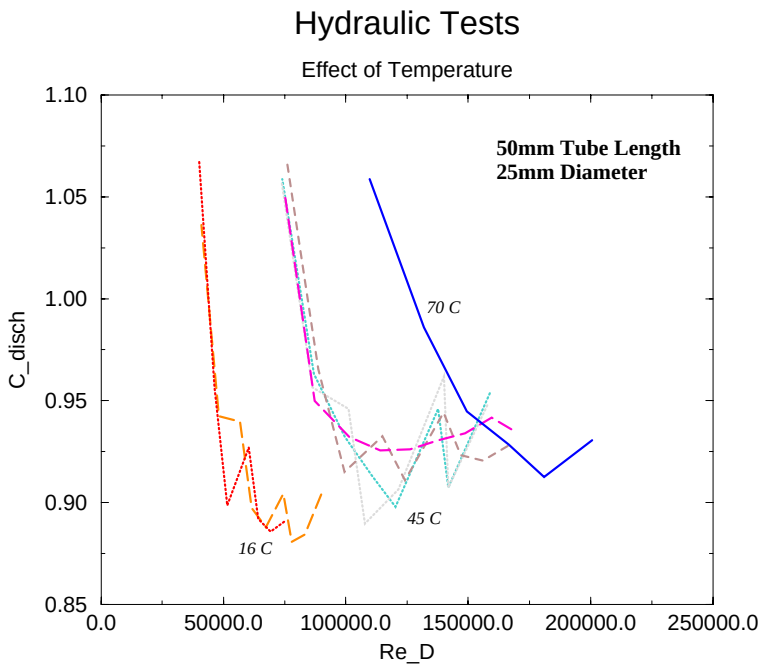

Fig. H.8: Discharge Coefficient as a Function of Re

a nuclear plant pressure vessel during a postulated severe accident in which a melt pool has formed in the reactor pressure vessel lower head. Longer discharge path-lengths are also considered here since the possibility exists for the melt to discharge via a longer nozzle or through a combined length of melt pool crust layer and vessel metal.

For conditions of interest to melt discharge during a severe reactor accident due to a penetration failure, the sensitivity to the hole ablation process may not be significant. This is the result of competing mechanisms. As shown above, increased values of C_d are associated with increased fluid discharge velocities which then decreases the time required to discharge a given volume under equivalent pressure driving conditions. Yet, the increased flow velocity will also produce increased convective heat transfer to the ablating structure (vessel wall) and thus a faster rate of hole growth. Combined, the overall sensitivity of this process to the value of C_d may not appear large but since the the source terms for melt discharge to the containment may be significantly altered, a more mechanistic manner of determining discharge coefficients is desirable.

When applying the above model to determine the discharge coefficient C_d, the flow discharge periods measured in hole ablation experiments were well predicted by the HAMISA code. This result confirms that the discharge coefficient, being a form parameter, is insensitive to transient (hole enlargement) process and to

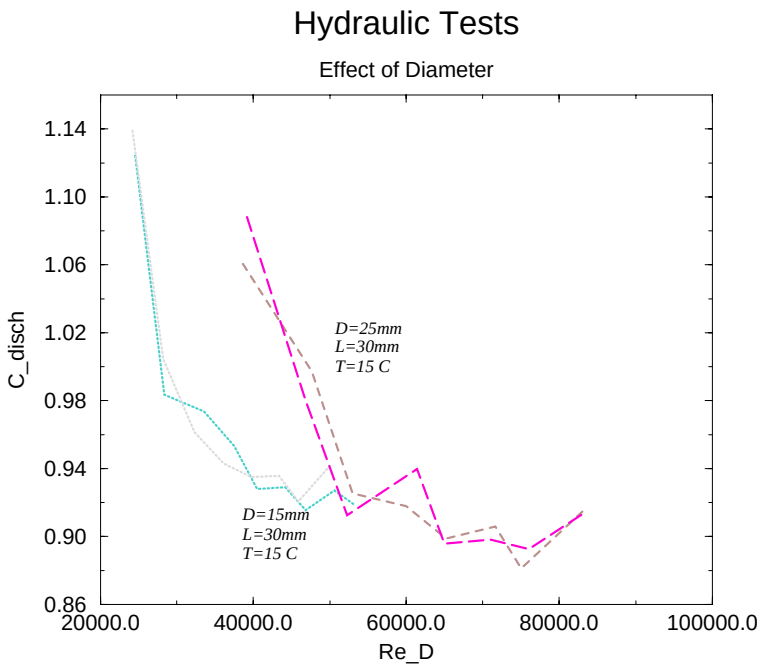

Fig. H.9: Effect of Diameter Change upon C_d

surface roughness, induced by phase change process within the discharge hole (crust formation and/or wall melting). The later is associated with a minor role of the in-hole friction in comparison to the expansion and contraction pressure losses.

H.8 Summary

A series of experiments were performed in the RIT/NPS Laboratory to investigate the discharge coefficient for flow exiting an overlying pool through a known geometry nozzle. The data was collected in order to reduce the uncertainty associated with melt pool flow through the bottom of a RPV lower head during a severe reactor accident. Several past scaling analysis which were directed at vessel hole ablation had employed an empirical discharge coefficient that is not directly applicable for a reactor situation. This is due to the fact that the common L/D ratio in the reactor case is not small enough to warrant a discharge coefficient typically employed for orifii.

The conclusions from this experimental study can be summarized as follows:

- Discharge coefficients were measured for 15 and 25 mm diameter holes with L/D ratios ranging from 0.08 to 4;

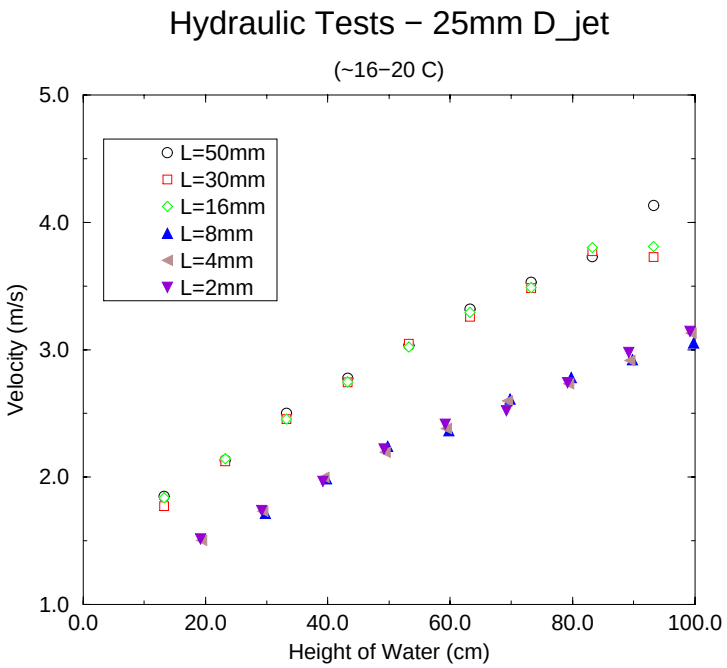

Fig. H.10: Effect of L/D Ratio on Discharge Velocity

- A range of water temperatures were employed in order to significantly vary the Pr ($3 < Pr < 12$) and Re (15, 000 $< Re <$ 300,000) of the fluid;
- Results were consistently reproducible;
- Measured discharge coefficients vary by a factor of 2x to that of the value of 0.6 used in previous scaling work;
- At lower nozzle lengths a *step* transfer into lower C_d values was observed;
- A method of employing contraction, in-hole and expansion loss coefficients to determine the discharge coefficient is proposed and shown to adequately represent the test data.

Nomenclature

Arabic

C_d	Discharge Coefficient
D	Diameter (of hole), m
F	Pressure Loss Factor
g	Gravitational Acceleration Coefficient, m/s^2

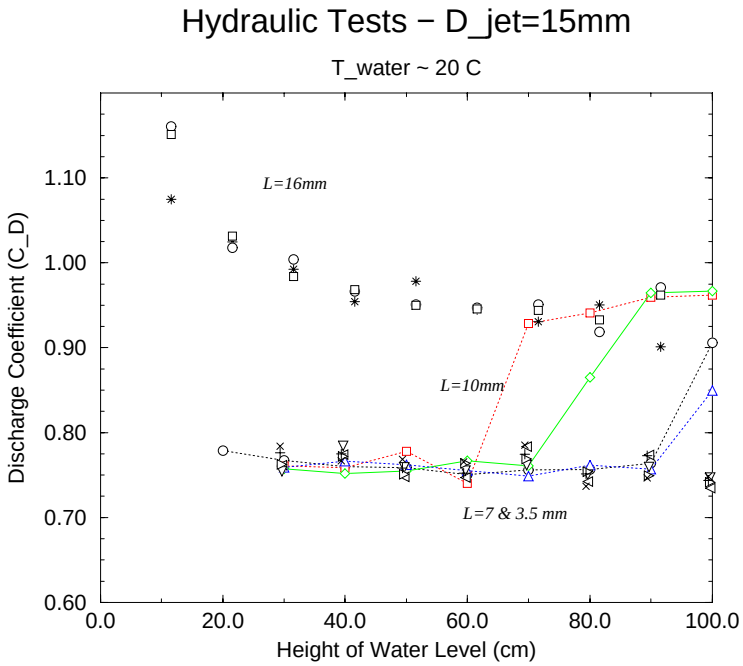

Fig. H.11: Transition Point

H	Height, m
P	Pressure, Pa
Pr	Prandtl number, $Pr = \nu/\alpha$
Re	Reynolds number, $Re = UD/\nu$
U	Discharge velocity, m/s
Greek	
α	Thermal diffusivity, m^2/s
β	Ratio of flow areas, $\beta = \frac{A_{downstream}}{A_{upstream}}$
ν	Kinematic viscosity, m^2/s
ρ	Density, kg/m^3

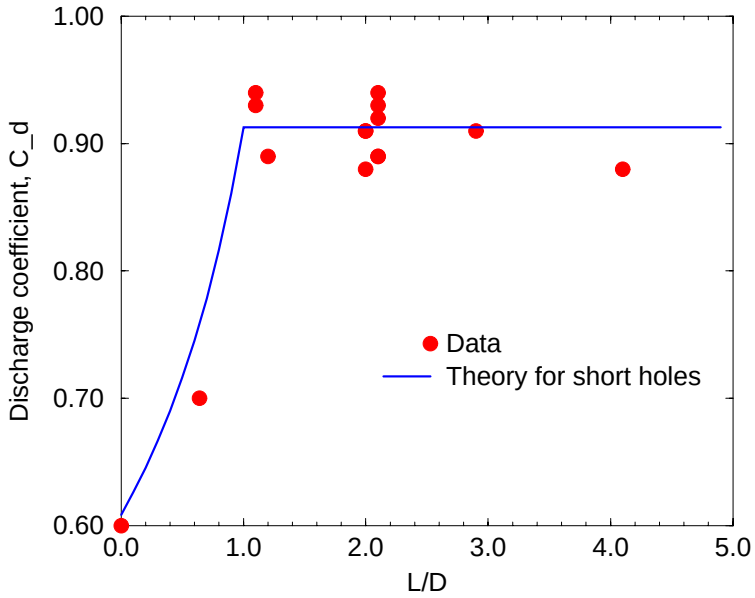

Fig. H.12: Comparison and prediction for different hole lengths and Re numbers.

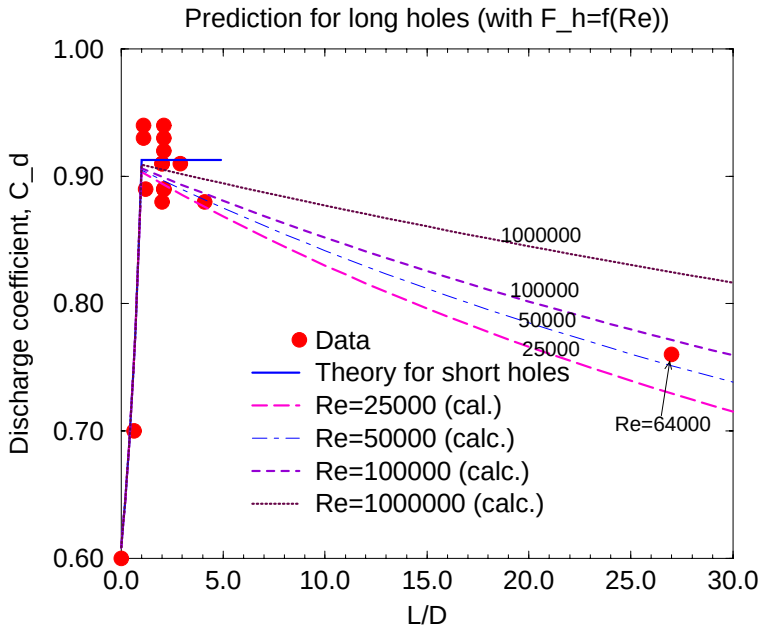

Fig. H.13: Comparison and prediction for different hole lengths and Re numbers.

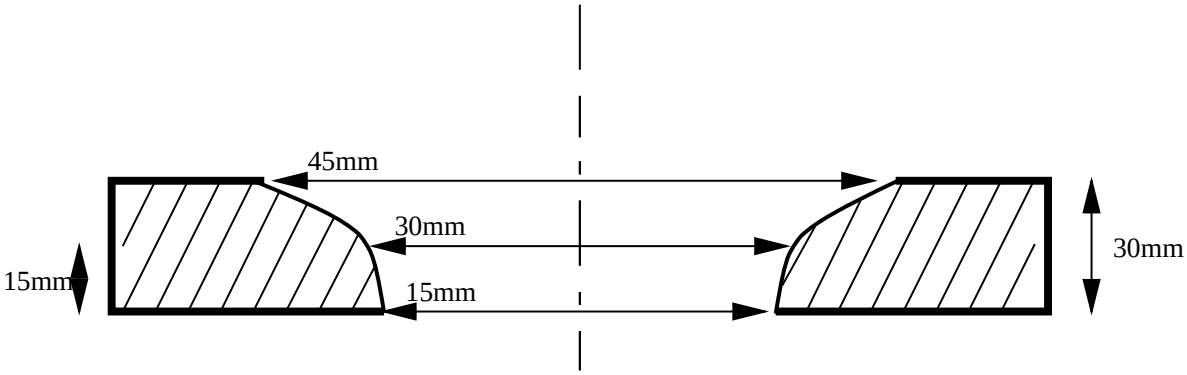

Fig. H.14: Smoothed Entrance Geometry

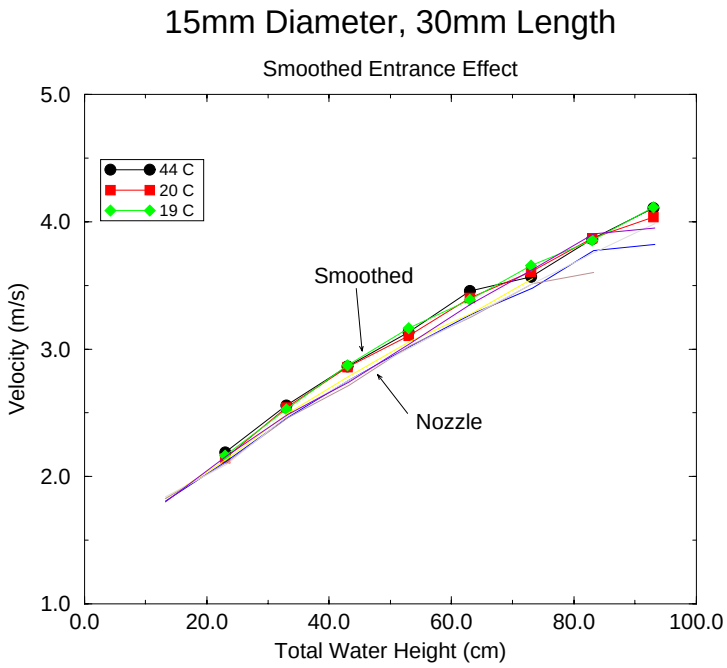

Fig. H.15: Comparison of Smoothed and Sharp Entrance Geometry

Bibliography

[1] R.H. Perry and C.H. Chilton, Chemical Engineer's Handbook, McGraw-Hill Book Company, New York, 1973.

[2] A. Lichtarowicz, R.K. Duggins and E. Markland, "Discharge Coefficients for Incompressible Non-Cavitating Flow Through Long Orifices," Journal of Mechanical Engineering Science, Vol. 7, No. 2, 1965, pp. 210-219.

[3] Kiljanski, T., "Discharge Coefficient for Free Jets from Orifices at Low Reynolds Number," Journal of Fluids Engineering, Vol. 115, pp. 778-781, 1993.

[4] T.N. Dinh, V.A. Bui, R.R. Nourgaliev, T. Okkonen, and B.R. Sehgal, "Modeling of Heat and Mass Transfer Processes During Core Melt Discharge From A Reactor Pressure Vessel", J. Nuclear Engineering and Design, Vol. 163, pp.191-206 (1996).

[5] T.N. Dinh, J.A. Green and B.R. Sehgal, "On Mechanisms That Govern the Vessel Melt Source for Ex-Vessel FCIs," Proceedings of ICONE-5, May, 1996.

[6] M.M. Pilch, "Continued Enlargement of the Initial Failure Site in the Reactor Pressure Vessel," J. Nuclear Engineering and Design, Vol. 164, pp. 137-146, (1996).

[7] B.R. Bird, W.E. Stewart and E.N. Lightfoot, "Transport Phenomena," Wiley International, New York, 1960.

[8] L.V. Boronina, N.V. Tarasova and V.P. Kovrizhnykh, "Experimental Study of the Effect of Transiency of Water Flow on Orifice Measurements of Flowrate," Fluid Mechanics-Soviet Research, Vol. 18, No. 1, January-February, 1989, pp. 95-99.

[9] A.S. Dudko, "Conditions for Entry of the Air Core of a Vortex Funnel into an Orifice on the Bottom," Fluid Mechanics-Soviet Research, Vol. 18, No. 1, January-February, 1989, pp. 35-41.

[10] Morton, D., ”Process Fluid Mechanics”, Prentice Hill, Englewood Cliffs, N.J., 1980.

[11] Sehgal, B. R., et al., ”Experiments on Vessel Hole Ablation During Severe Accidents”, Proceedings of the International Seminar on Heat and Mass Transfer in Severe Reactor Accidents, Izmir, Turkey, 1995.

[12] Green, J., et al., ”Experiments on Melt Jet Impingement and Vessel Hole Ablation Phenomena,” International Topical Meeting on Probabilistic Safety Analysis, Park City Utah, (October 1996).

Appendix I

Technical specification and data from the FOREVER/C1 test

I.1 Vessel

The FOREVER pressure vessel is a scaled version of the lower half of a typical LWR reactor pressure vessel, fig.I.1. It consists of 4 parts, tab.I.1. The Vessel-Lid is made of German steel 16Mo3, while the V-Flange, Cylindrical part and Hemispherical part were made of German steel 15Mo3, with the composition given in tables I.3-I.2.

Table I.1: *Vessel main parts*

%	*Vessel part*	*Dimention*	*Grade*
1	Vessel-Lid.	DN400, T=55	16Mo3
2	V-Flange.	DN400	15Mo3
3	Cylindrical part	$\phi 406.4 * 16.00$	15Mo3
4	Hemispherical part	$\phi 380 * 15.00$	15Mo3

The following mechanical properties of the vessel steel are provided by manufacturer:

- Yield point.....$\geq 270\ N/mm^2$
- Tensile Strength.....$450 * 600\ N/mm^2$

- Elongation..... 20 %
- Brinell Hardness..... 150-160
- Test temperature..... 20°C

Table I.2: *Composition of the steel 16Mo3.*

C	*Si*	*Mn*	*P*	*S*	*N*	*Al*	*Cu*	*Cr*	*Mo*	*Ni*
%	%	%	%	%	%	%	%	%	%	%
$0.12 - 0.20$	≤ 0.35	$0.4 - 0.9$	≤ 0.03	≤ 0.025	-	-	≤ 0.3	≤ 0.35	$0.25 - 0.35$	≤ 0.3
0.18	0.26	0.76	0.013	0.001	0.005	0.028	0.03	0.04	0.31	0.05

Table I.3: *Composititon of the Steel 15Mo3.*

C	*Si*	*Mn*	*P*	*S*	*N*	*Al*	*V*	*Cr*	*Mo*	*Ni*
%	%	%	%	%	%	%	%	%	%	%
$0.12 - 0.20$	≤ 0.35	$0.4 - 0.9$	≤ 0.03	≤ 0.025	-	-	-	≤ 0.35	$0.25 - 0.35$	≤ 0.3
0.16	0.17	0.62	0.009	0.011	-	0.021	-	-	0.28	-

The Yield Stress as function of temperature for different pressure vessel steel is shown in fig.I.2.

I.2 Melt

The high-temperature (up to $1300^{\circ}C$) CaO-B_2O_3 oxide melt is prepared in a SiC-crucible placed in a 50kW induction furnace and is, then, poured into the test section. Thermophysical properties of CaO-B_2O_3 are presented in table I.4.

I.3 Internal Heater

A $MoSi_2$ 50kW electric heater is employed in the melt pool to heat and keep its temperature in the range up to $1500^{\circ}C$. Thus, the vessel wall temperature can be maintained, in steady state, in the range up to $1100^{\circ}C$. The heater was specially designed to fit the internal space of the vessel lower head, figs.I.4 and I.5. The temperature limit of the $MoSi_2$ heat element is 1700°C. Fig.I.3 presents the resistance of the heater as a function of temperature.

Table I.4: *Thermophysical properties of the CaO-B_2O_3 20-80 a/o mixture*

%	*Property*	*Value*	*Dimensions*
1	Liquidus temperature, T_l	1027	$^\circ$ C
2	Solidus temperature, T_s	977	$^\circ$ C
3	Latent heat, Δh_{fus}	0.46	MJ/kg
4	Thermal conductivity, κ_l	3	W/(m·K)
5	Thermal conductivity, κ_s	2	W/(m·K)
6	Density, ρ	2500	kg/m^3
7	Specific heat, $C_{p,l}$	2.2	kJ/kg
8	Specific heat, $C_{p,s}$	1.53	kJ/kg
9	Dynamic viscosity, μ	0.1-0.3 (0.1 used)	Pa·s
10	Kinematic viscosity, ν	$4 \cdot 10^{-5}$	m^2/s
11	Thermal diffusivity, α_l	$5.5 \cdot 10^{-7}$	m^2/s
12	Prandtl number, Pr	73	-
10	Thermal expansion, β	$0.904 \cdot 10^{-4}$	1/K

I.4 Instrumentation

I.4.1 Temperature measurments

A number of B- and K-type thermocouples are used to measure temperature of the melt (debris) at different locations in the hemispherical pool and to measure the temperatures along the vessel wall.

Positions of internal wall thermocouples are shown in fig.I.7 and table I.5. External wall thermocouples are located on the outer surface of the wall, at the same position as corresponding internal thermocouple, fig.I.7. Thermocouples are fixed on the wall surface as shown in fig.I.8.

In the centerline of the melt pool, there are three thermocouples, installed in the $MoSi_2$ tube, at three axial positions (1cm, 8cm and 16cm measured from the wall).

I.4.2 Wall deformation measurements

The creep deformations of the wall are monitored by linear displacement transducers, LDTs, which are mounted at five latitude locations of the hemispherical lower head. Typically, at each level, four LDTs are deployed, in order to measure local vertical and horizontal displacements in two local positions, shifted in latitude on 180° (%Lh, %Lv, %Rh, %Rv, see fig.I.9 and table I.6).

Table I.5: *Position of thermocouples in the hemispherical and cylindricalparts of the vessel*

%	*Z, cm*	ϕ	θ	%	*Z, cm*	θ
TC_1	-20	$0°$	$0°$	TC_7	5	$36°$
TC_2	-18	$26°$	$36°$	TC_8	15	$108°$
TC_3	-14	$46°$	$108°$	TC_9	25	$180°$
TC_4	-10	$60°$	$180°$	TC_{10}	35	$252°$
TC_5	-6	$73°$	$252°$	TC_{11}	45	$324°$
TC_6	-2	$84°$	$324°$			

Table I.6: *Positions of displacement measurement point*

% Point	ϕ	θ
4L	$-72°$	$0°$
4R	$+72°$	$180°$
3L	$-57°$	$0°$
3R	$+59°$	$180°$
2L	$-43°$	$0°$
2R	$+45°$	$180°$
1L	$-24°$	$0°$
1R	$+22°$	$180°$
0	$0°$	$0°$

I.4.3 Pressure measurements

Three pressure gauges were used to control the pressure, fig.I.10, in different parts of the test section. One Pressure-Transducer was connected to the DAS to record the pressure during the test. All pressure gauges and the pressure transducers were calibrated before the test.

I.5 Chronology of the test

History of the FOREVER-C1 test is summarized in table I.7. Events marked by * are unplanned. These are the temporal failure of the induction furnace (which was successfully fixed in a few minutes), and change of balloon with Ar, caused by small leakage through the vessel lid. During the test, the DAS was temporally stopped three times, in order to process experimental results and update quanti-

tative information about the vessel thermal and mechanical conditions. Together with visual information from two video cameras, these data provided information about the vessel thermo-elastic-plastic deformations and creep.

Table I.7: *Chronology of the FOREVER-C1 test.*

%	*Procedure/(Event)*	*Time, hrs:min*
1	Start melt generation in the induction furnace	-09:00
2	Start pre-heat of the vessel	-01:00
3*	Temporal failure of the induction furnace	-00:50
4*	Induction furnace is fixed	-00:44
5	Shout down the heaters, the vessel is pre-heated up to 600°C	-00:15
6	Pour the melt into the vessel, initial temperature of the melt is about 1300°C	00:00
7	Close the system	00:01-00:05
8	Start pressurization	00:20
9	Pressure achieved steady-state	01:00
10	Vessel wall temperature achieved quasi-steady-state	03:00
11	Stop DAS in order to process experimental data	05:00-05:19
12	Stop DAS in order to process experimental data	13:00-13:18
13*	Change Balloon with Ar	14:05-14:15
14	Stop DAS in order to process experimental data	20:30-20:52
15	Start de-pressurization	24:20
16	Shout down the heaters	26:00
17	Stop DAS	28:00

I.6 Experimental data from FOREVER/C1 test

I.6.1 Pressure

Figs.I.19-I.21 present the history of internal pressure as a function of time. During the test, the average pressure inside the vessel was kept about 25 bar. Due to small gas leakage through the vessel lid and thermocouple fittings, the system was feeded from outside Ar ballon system. The upper limit of internal pressure was kept by regulator valve.

I.6.2 Deformations

Total vessel wall displacements as functions of time, are shown in figs.I.22-I.24, for five different measurement points, on the right side of the pressure vessel (see

fig.I.9 and table I.6). It is instructive to note, that the radial displacements presented are calculated as $\Delta r = r(t) - r(T = 20^{\circ})$.

Radial and angular creep displacements are depicted in figs.I.25-I.37 and figs.I.40-I.44, respectively. Note, the radial displacements shown are calculated as $\Delta r_c = r(t) - r(t = t_{pressurization})$. Thus, deformation due to thermal expansion is substructed. It is assumed, the variations of thermal expansions after pressurization were negligible, since the system was close to the steady-state condition.

I.6.3 Temperature distributions in the vessel and melt.

Temperature in the melt pool was measured by three centerline thermocouples, figs.I.45-I.47. As can be seen, the temperature inside liquid melt pool achieved nearly steady state in 0.5 hr, and stayed at the level of 1050-1100°C until the depressurization. This corresponds to the melt superheat above the liquidus point up to 50°C. The lowest thermocouple was located 3 cm above the vessel wall, in the crust. Due to the crust growth during the first 3-4 hrs, this thermocouple registered slow temperature drop from about 850°C in the begining of the test to about 700°C at the steady-state stage, fig.I.46.

Temperature of the vessel wall was registered by 21 internal and external thermocouples, see figs.I.48-I.77. During the test, five thermocouples were destroyed (TC1i, TC2i, TC3i, TC4i and TC3E). Internal thermocouples were down during the melt pouring, in the very begining of the test.

Steady-state conditions for upper ($\phi > 60^{\circ}$) lower head thermocouples were achieved in 1 hr after the beginning of the test. The lower thermocouples ($\phi < 60^{\circ}$) reached approximately steady-state conditions after 3-4 hrs of the test, when the bottom crust was fully established and achieved steady-state thickness, see figs.I.48-I.55.

Estimate of thermal loadings on the vessel wall. As seen from the measured thermocouple data, the temperature difference between the internal and external thermocouples is rather high, in the range of 150°C. It seems, that there was additional resistance in between thermocouples and the vessel surface, caused by the method of installation of the thermocouples, fig.I.8. Thus, the actual temperature of the measured point was about 50°C above (for external TCs) or below (for internal TCs), than what was measured. Fig.I.78 presents the angular local distribution of temperature measured by external thermocouples, in the hemispherical part of the vessel, at different moments of experiment. In fig.I.79, the local distribution of temperature is presented for hemispherical and cylindrical part of the

vessel. External wall temperature is evaluated as

$$\begin{array}{ll} T_{\text{ext, eval}} = T_{\text{ext, meas}} + 50°C & \text{for hemispherical part, and} \\ T_{\text{w, eval}} = \frac{T_{\text{ext, meas}} + T_{\text{int, meas}}}{2} & \text{for cylindrical part} \end{array} \tag{I.1}$$

Next, from the evaluated wall temperature, the heat flux at the wall is calculated as

$$q_w = q_{rad} + q_{conv} = \varepsilon\sigma\left(T^4_{w,eval} - T^4_{cont}\right) + h_{conv}\left(T_{w,eval} - T_{cont}\right) \tag{I.2}$$

where the vessel wall emmissivity is taken as $\varepsilon = 0.9$, the temperature in the containment is $T = 320K$ (measured during the test), and the convective heat transfer coefficient is estimated as $h_{conv} = 10$ W/(m^{2}K). The evaluated heat flux distribution is plotted as functions of angle (in the hemispherical part) and axial coordinate (in the cylindrical part) in fig.I.80. As can be seen, the maximal wall heat flux is located in the hemispherical part, $\phi \simeq 75°$, exactly where the maxamal wall temperature is registered. The local distribution is typical for natural convection in the hemispherical melt pool, with minimum heat flux at the very bottom.

From the evaluated wall heat flux, the through the wall temperature difference can be estimated, see fig.I.81, assuming the 1D heat conduction in the vessel:

$$\Delta T_w = \frac{q_w \delta_w}{\kappa} \tag{I.3}$$

where $\kappa = 30$ W/(m·K) and $\delta_w = 15$ mm. The maximal "thru the wall" temperature difference is about 45°C[1].

Fig.I.82 presents the evaluated total heat removal, integrated begining from the very bottom of the hemispherical part, and finishing at the top of the cylidrical part. It can be seen, the the heat balance is within 90%[2].

[1]It is believed, that 2D effect should reduce this value.

[2]The rest 10% are due to uncertainties in the evaluation of the wall temperature, wall heat flux, and, in addition, canbe attributted to the heat losses through the lid and by convection of the Ar.

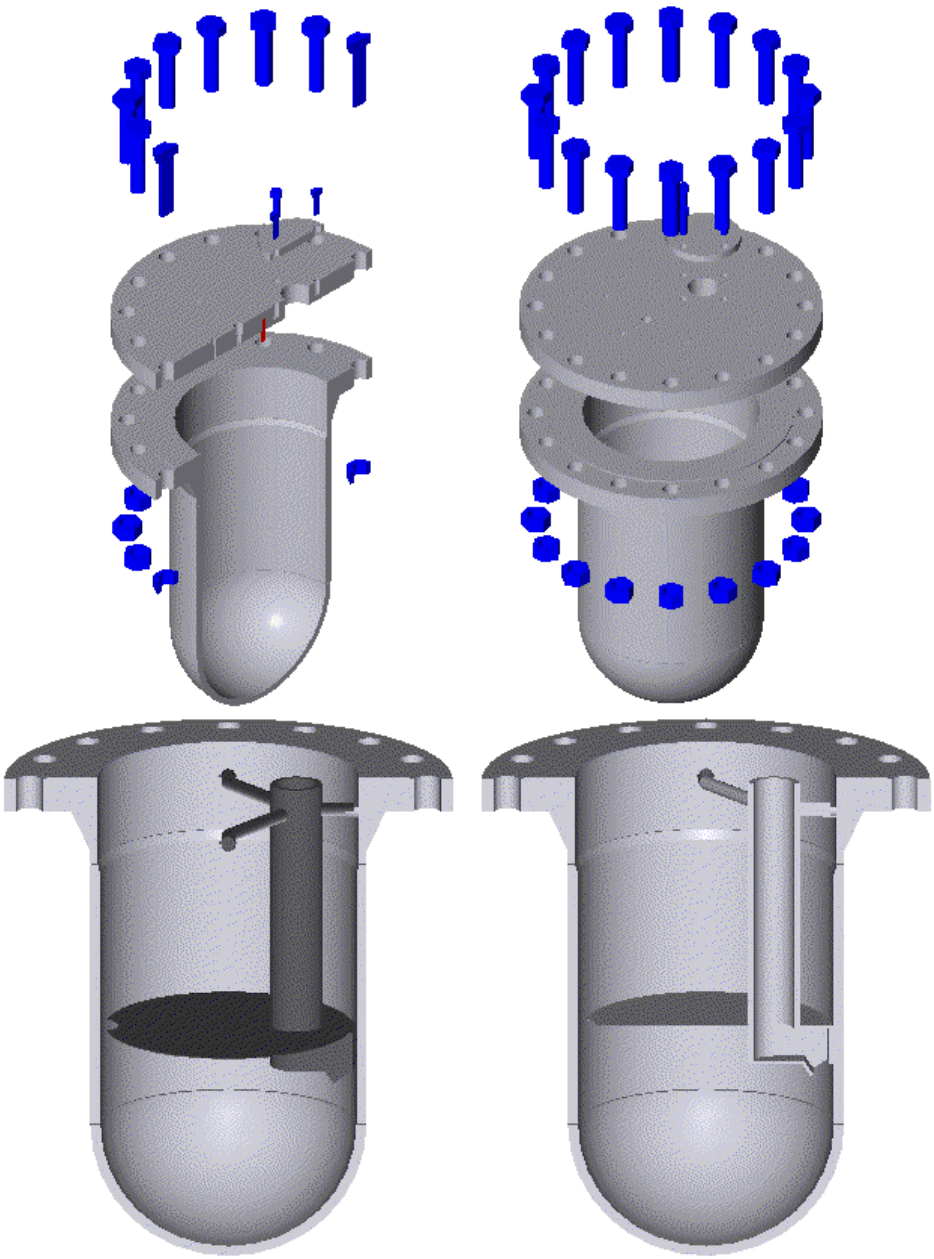

Fig. I.1: *Design of the pressure vessel for FOREVER facility.*

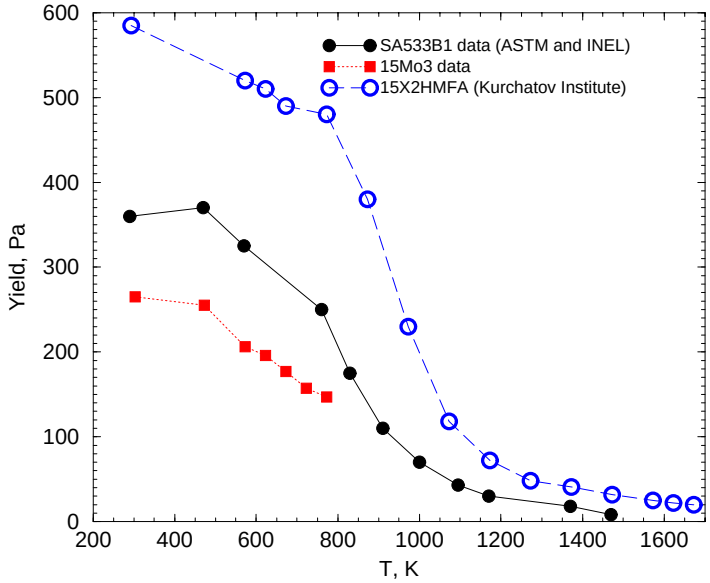

Fig. I.2: *Yield stress as function of temperature for different pressure vessel steels.*

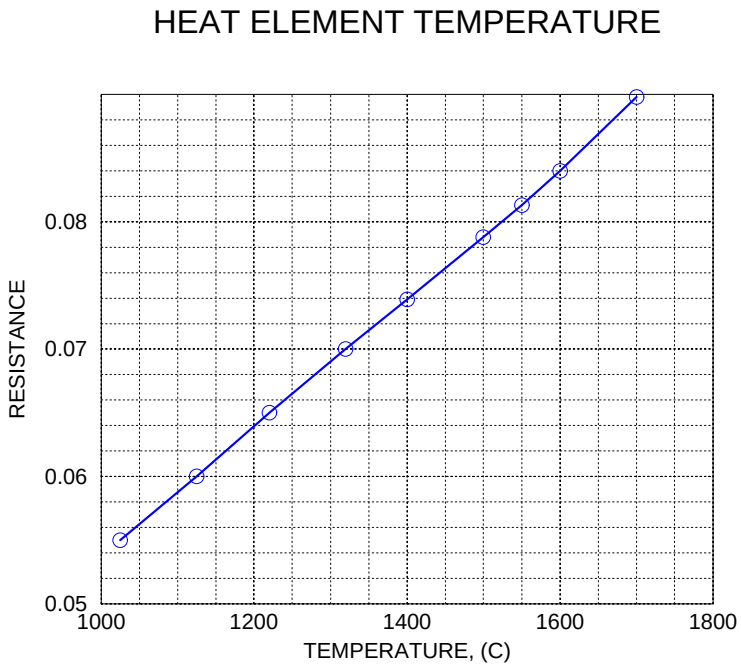

Fig. I.3: *Dependence of resistance of the heat element on temperature.*

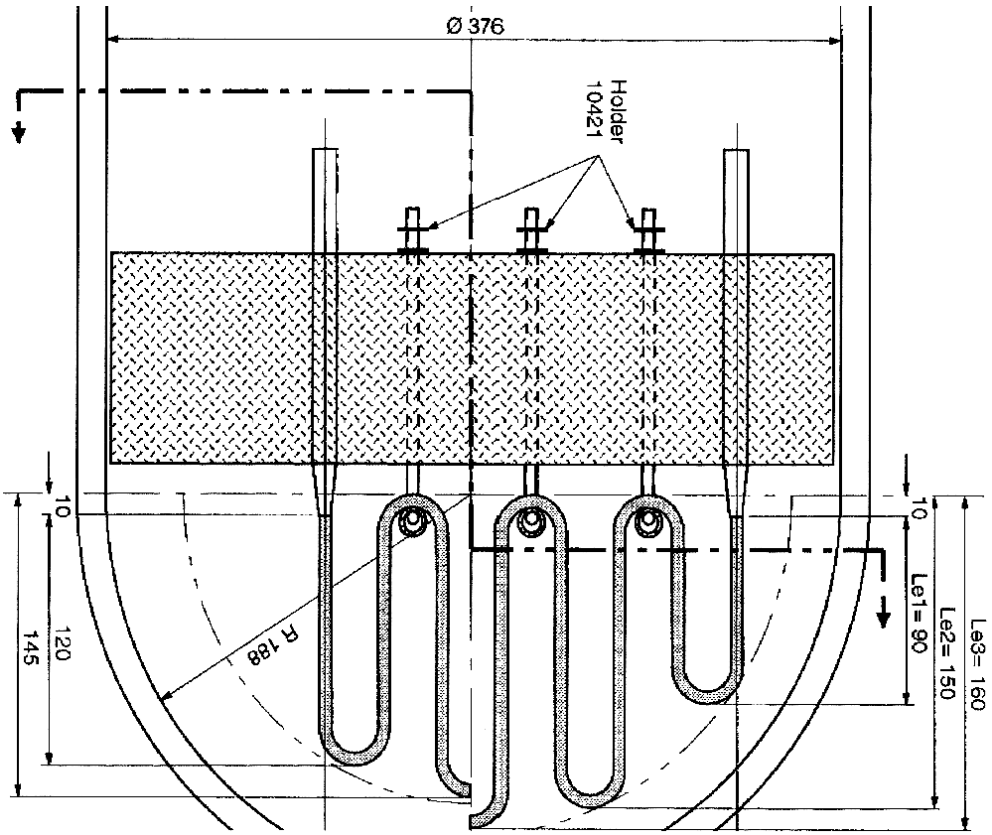

Fig. I.4: *View of internal heater.*

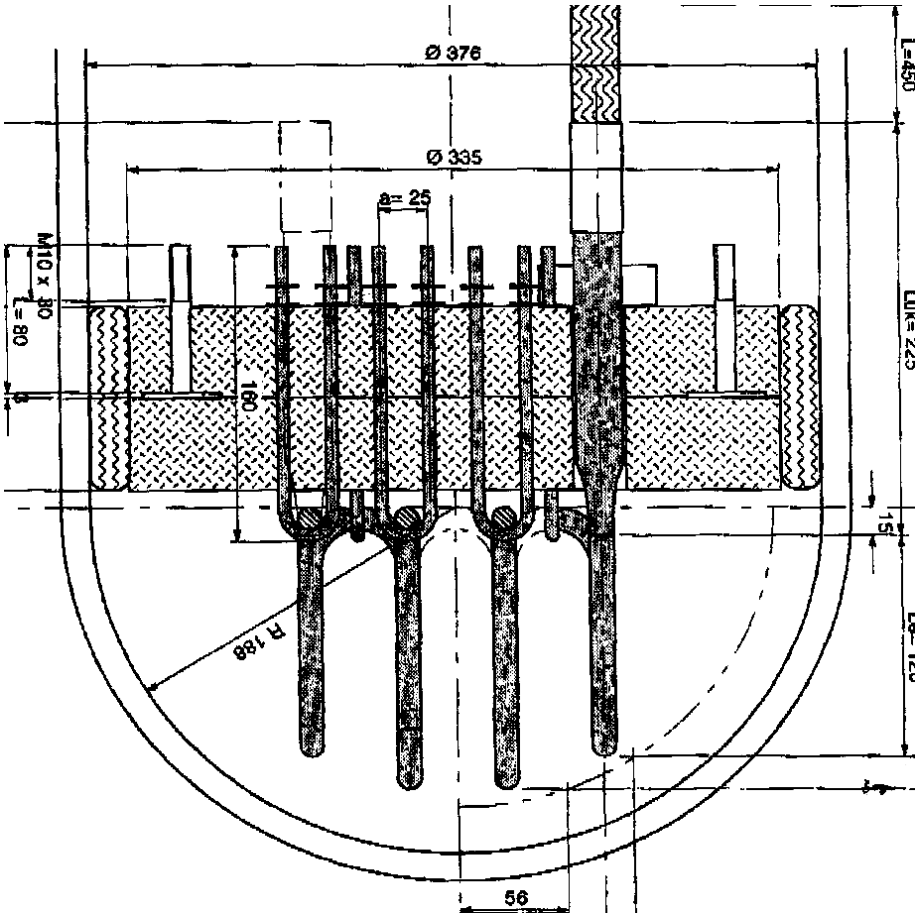

Fig. I.5: *View of internal heater.*

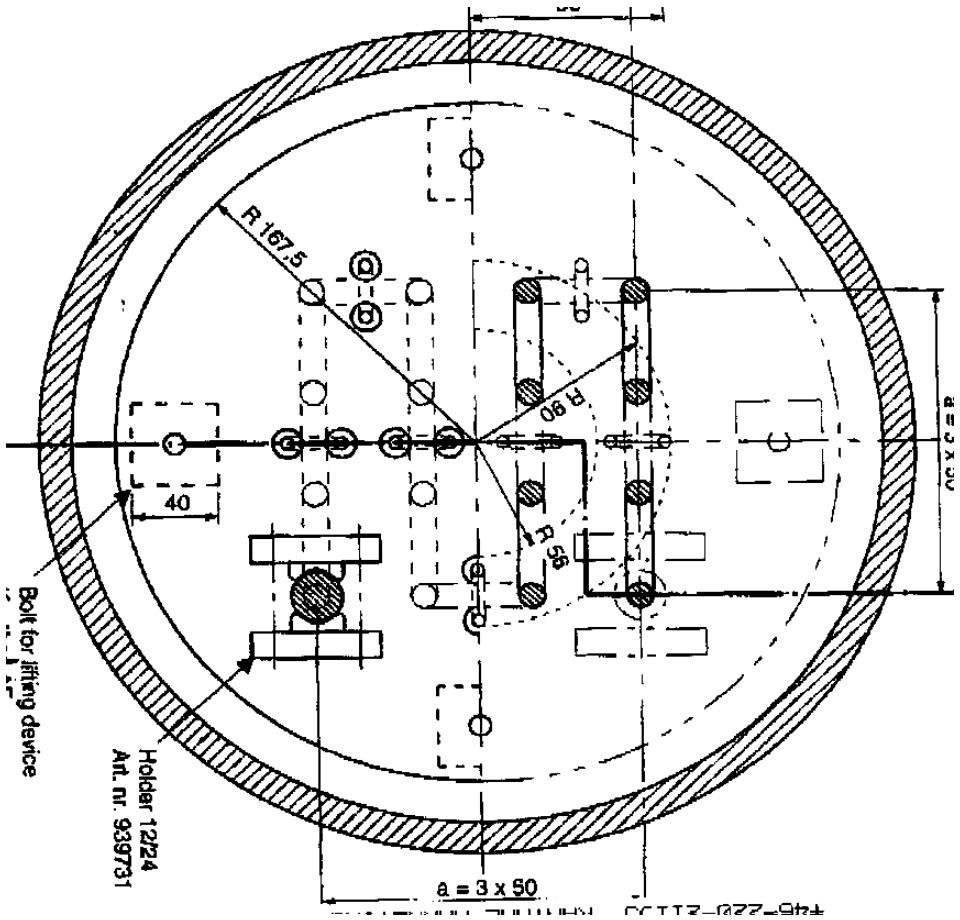

Fig. I.6: *View of internal heater.*

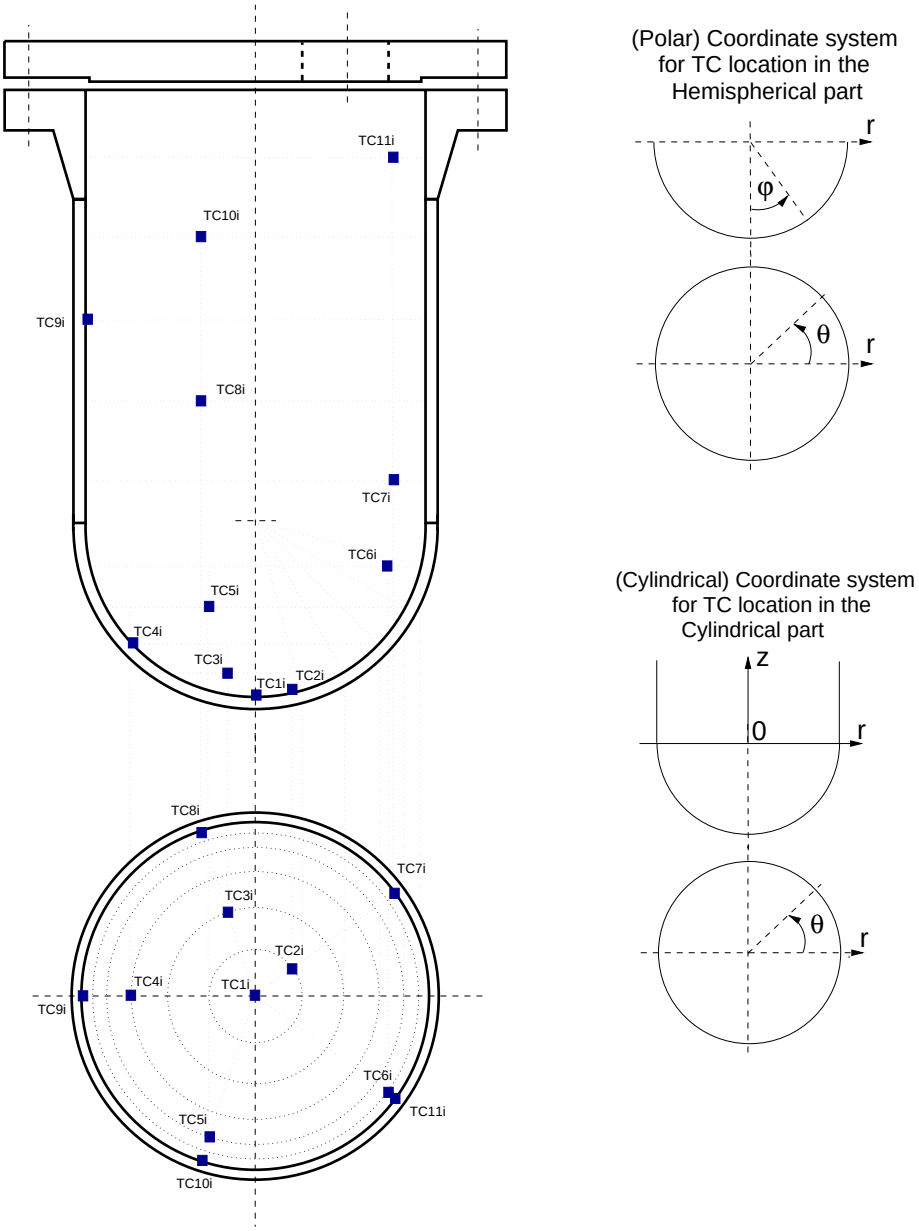

Fig. I.7: *Location of internal wall thermocouples.*

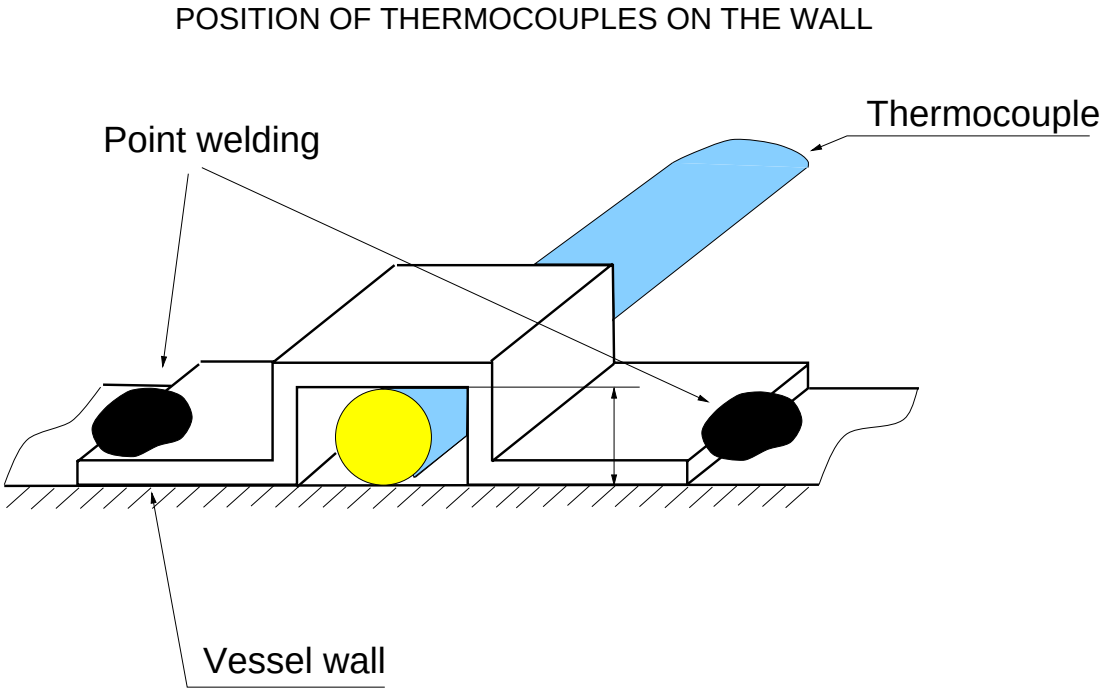

Fig. I.8: *Position of thermocouples at the vessel wall.*

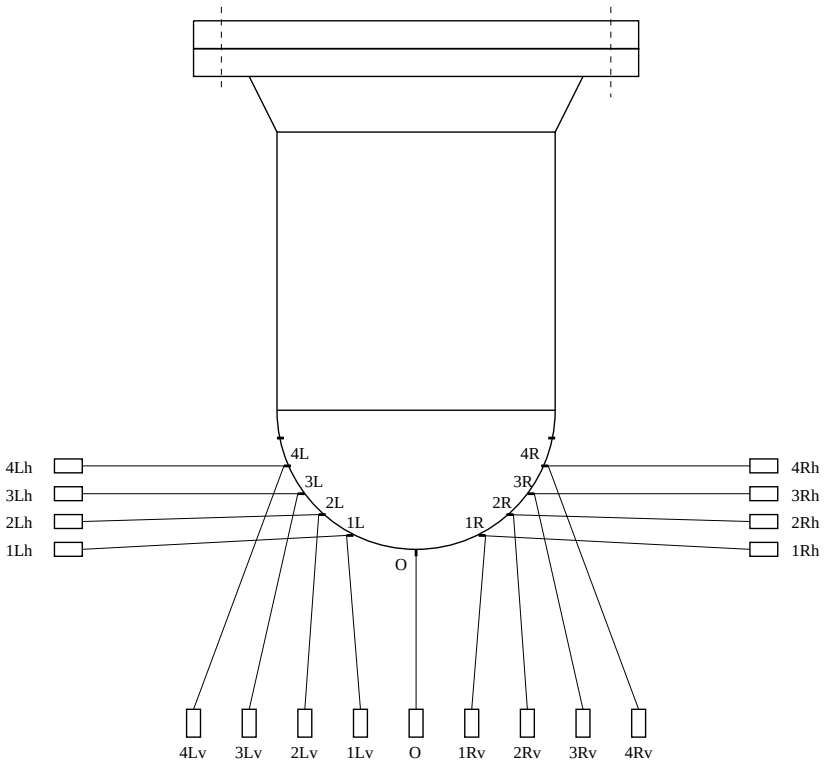

Fig. I.9: *Location of linear displacement transducers (LDTs).*

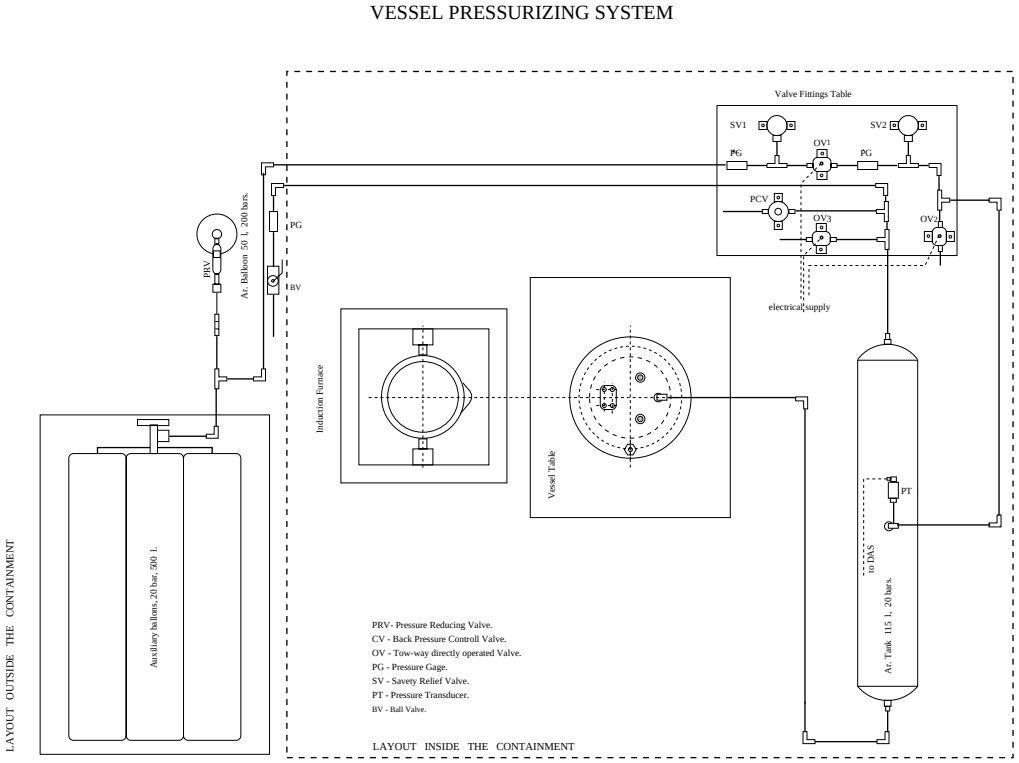

Fig. I.10: *FOREVER-C1 pressurization system.*

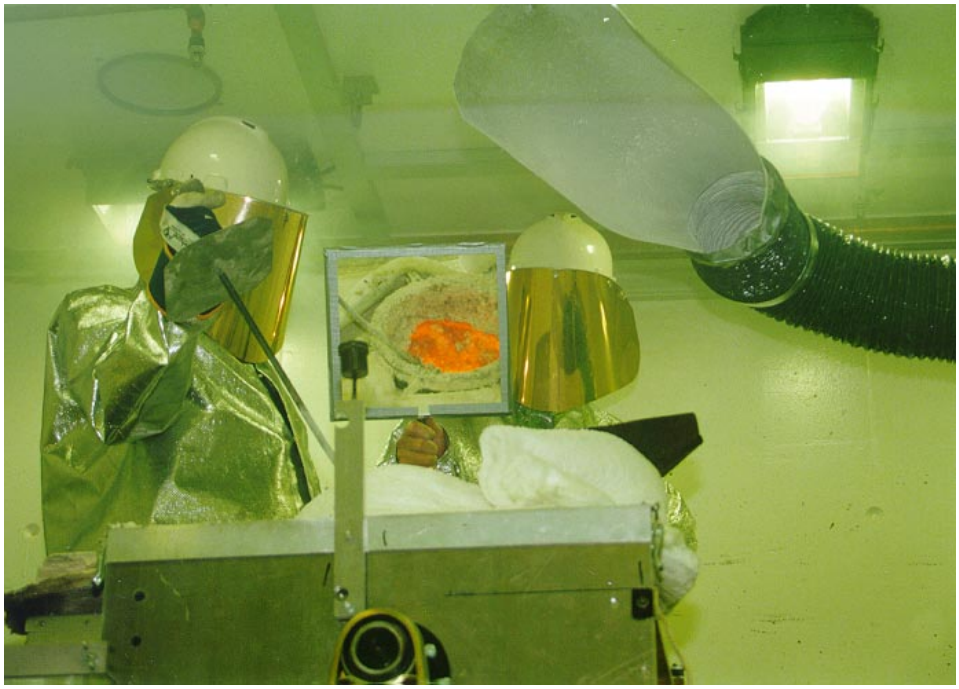

Fig. I.11: *Preparation of melt in the induction furnace.*

Fig. I.12: *Melt Pouring during the FOREVER-C1. Experiment.*

Fig. I.13: *End of the melt pouring.*

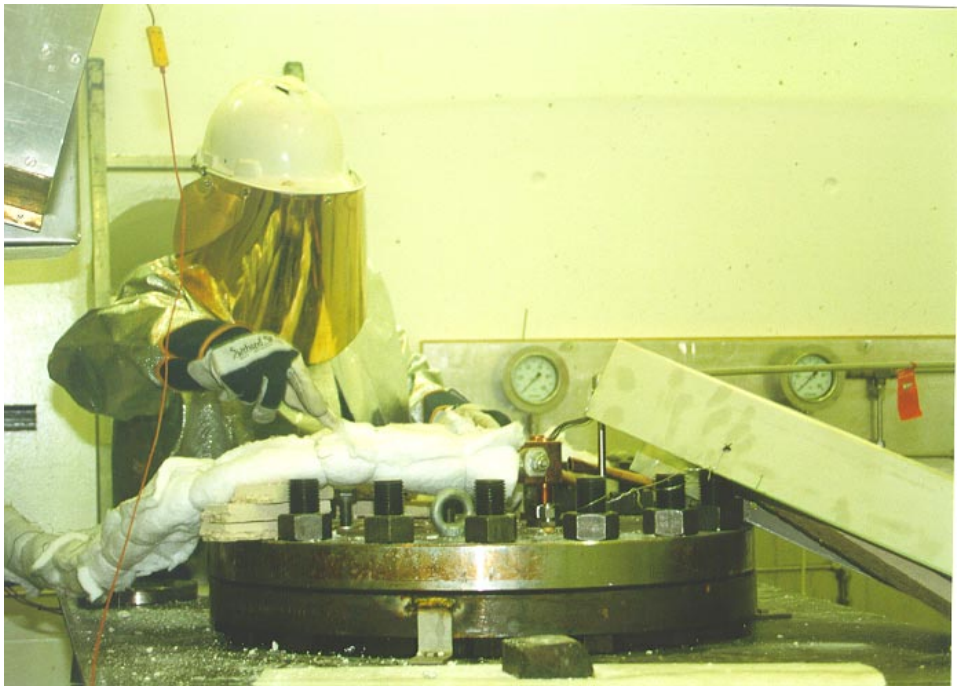

Fig. I.14: *Sealing of the vessel, before pressurization.*

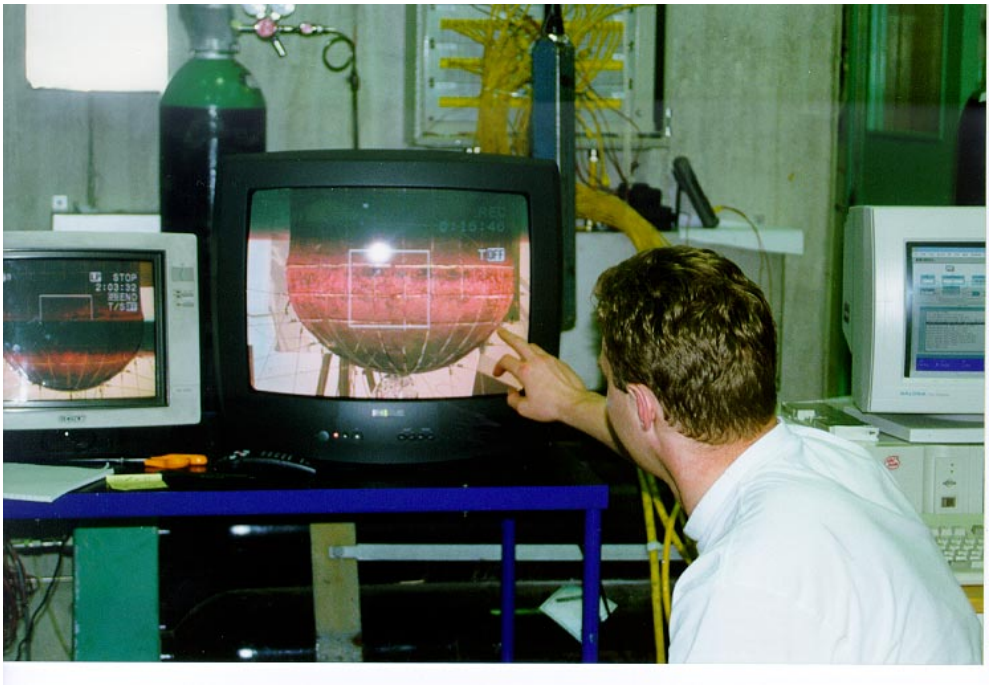

Fig. I.15: *Visualization of the vessel during FOREVER-C1. Experiment.*

Fig. I.16: *Visualization of the vessel during FOREVER-C1. Experiment.*

Fig. I.17: *Vessel inside. After the experiment.*

Fig. I.18: *Vessel inside. After the experiment.*

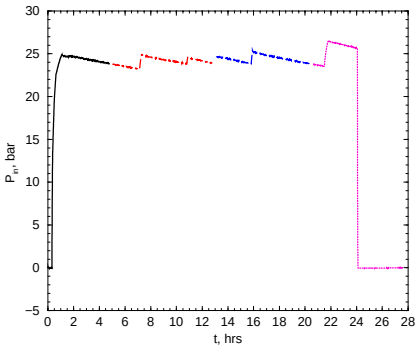

Fig. I.19: *Internal pressure as a function of time.*

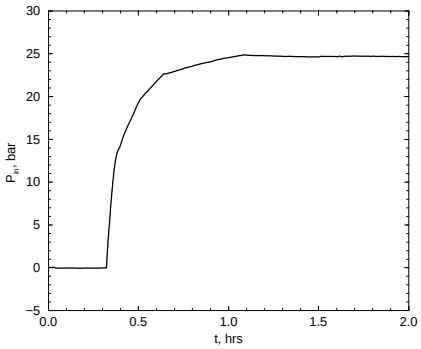

Fig. I.20: *Internal pressure as a function of time in the beginning of the test.*

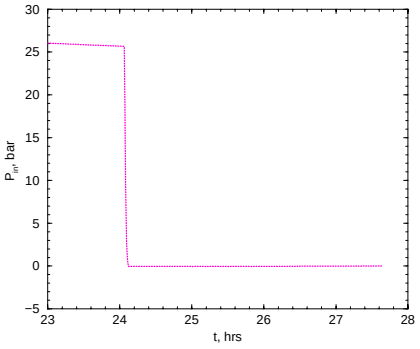

Fig. I.21: *Internal pressure as a function of time in the end of the test.*

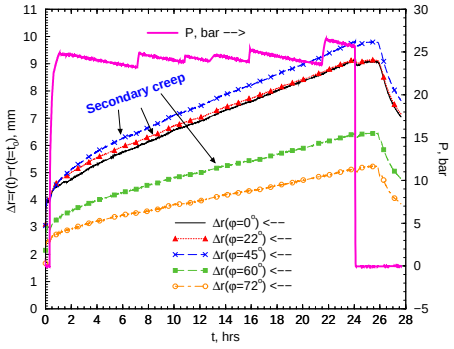

Fig. I.22: *History of the vessel wall displacements, at the right side ($\phi > 0°$) of the vessel, together with pressure history.*

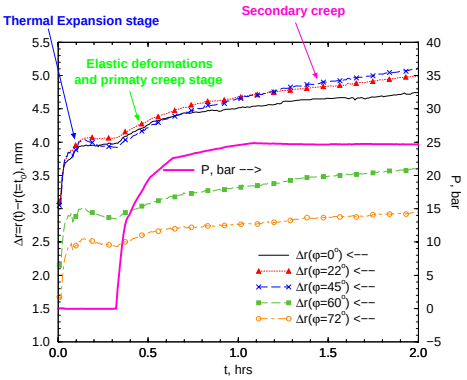

Fig. I.23: *Total displacements of the vessel wall at the begining of the test (t from 0 to 2 hrs).*

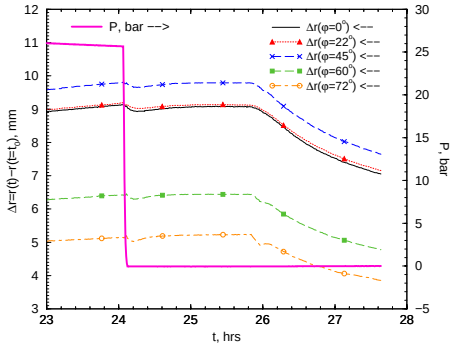

Fig. I.24: *Total displacements of the vessel wall in the end of the test (t from 23 to 28 hrs).*

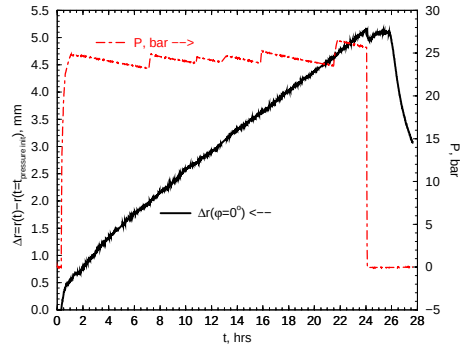

Fig. I.25: *Creep displacement at the very bottom ($\phi = 0°$) of the vessel and internal pressure as function of time.*

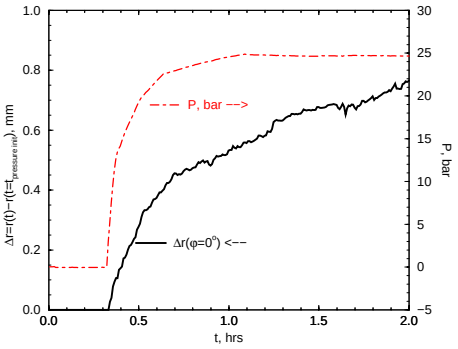

Fig. I.26: *Creep displacement at the very bottom ($\phi = 0°$) of the vessel and internal pressure as function of time, at the begining of the test (t from 0 to 2 hrs).*

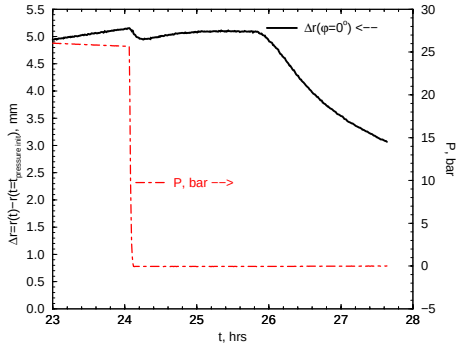

Fig. I.27: *Creep displacement at the very bottom ($\phi = 0°$) of the vessel and internal pressure as function of time, in the end of the test (t from 23 to 28 hrs).*

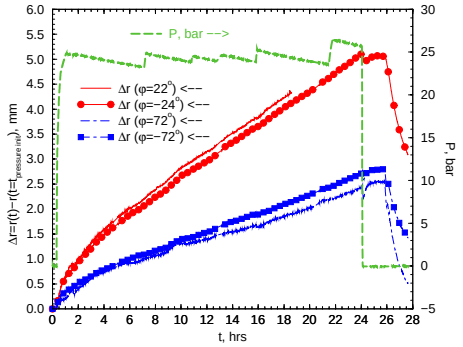

Fig. I.28: *Creep displacement at the position ($\phi \simeq \pm 24°$) and ($\phi = \pm 72°$) of the vessel, and internal pressure as function of time.*

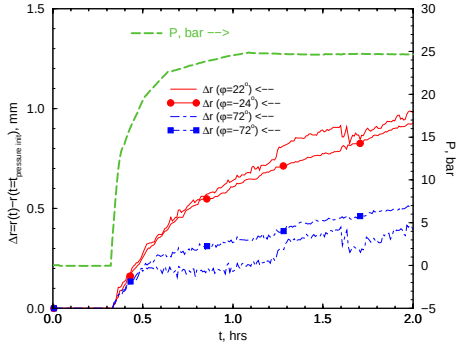

Fig. I.29: *Creep displacement at the position ($\phi \simeq \pm 24°$) and ($\phi = \pm 72°$) of the vessel, and internal pressure as function of time, at the begining of the test (t from 0 to 2 hrs).*

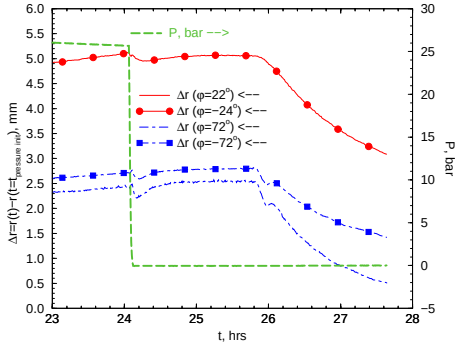

Fig. I.30: *Creep displacement at the position ($\phi \simeq \pm 24°$) and ($\phi = \pm 72°$) of the vessel, and internal pressure as function of time, in the end of the test (t from 23 to 28 hrs).*

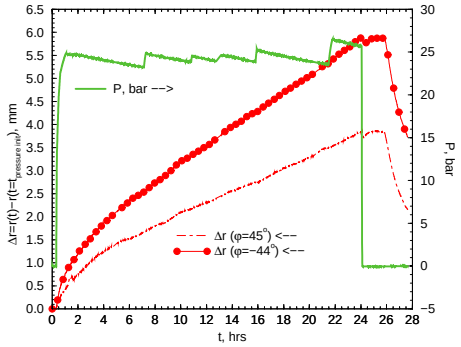

Fig. I.31: *Creep displacement at the position ($\phi \simeq \pm 45°$) of the vessel, and internal pressure as function of time.*

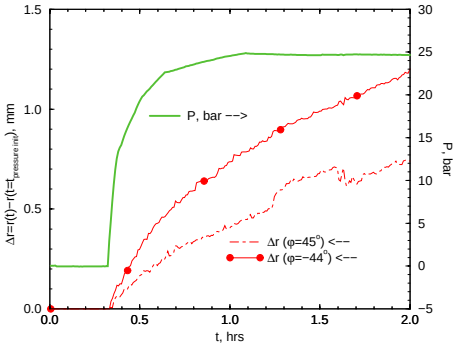

Fig. I.32: *Creep displacement at the position ($\phi \simeq \pm 45°$) of the vessel, and internal pressure as function of time, at the begining of the test (t from 0 to 2 hrs).*

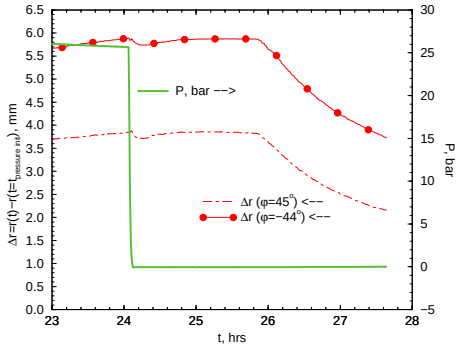

Fig. I.33: *Creep displacement at the position ($\phi \simeq \pm 45°$) of the vessel, and internal pressure as function of time, in the end of the test (t from 23 to 28 hrs).*

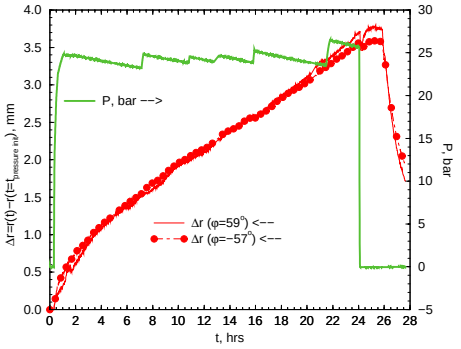

Fig. I.34: *Creep displacement at the position ($\phi \simeq \pm 60°$) of the vessel, and internal pressure as function of time.*

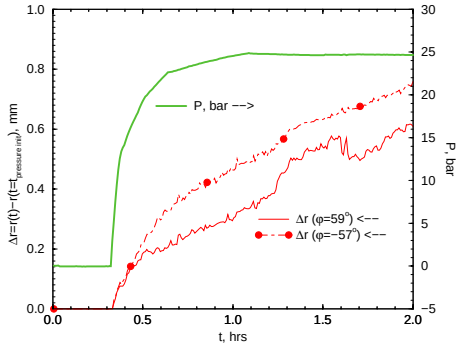

Fig. I.35: *Creep displacement at the position ($\phi \simeq \pm 60°$) of the vessel, and internal pressure as function of time, at the begining of the test (t from 0 to 2 hrs).*

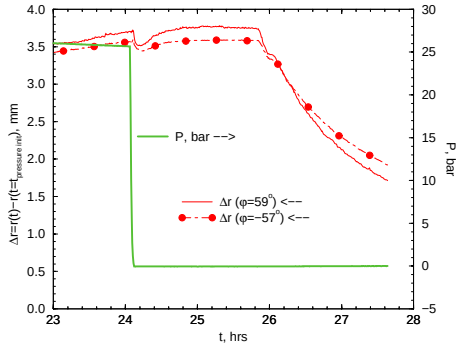

Fig. I.36: *Creep displacement at the position ($\phi \simeq \pm 60°$) of the vessel, and internal pressure as function of time, in the end of the test (t from 23 to 28 hrs).*

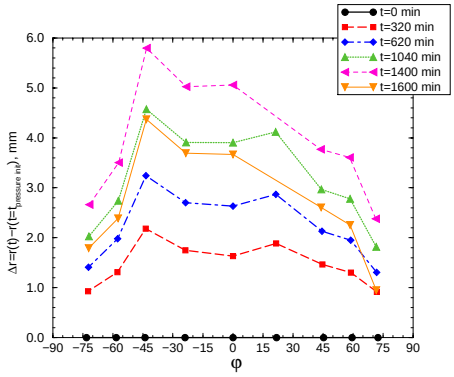

Fig. I.37: *Angular distribution of the radial creep displacements, deducted from the LDT data.*

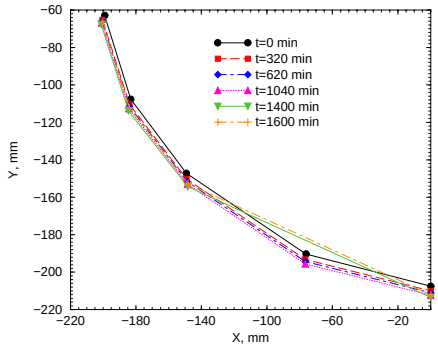

Fig. I.38: *History of wall shape at the left ($\phi < 0°$) part of the vessel. Note: in the end of the test, the LDT, located at ϕ about $-24°$, was broken.*

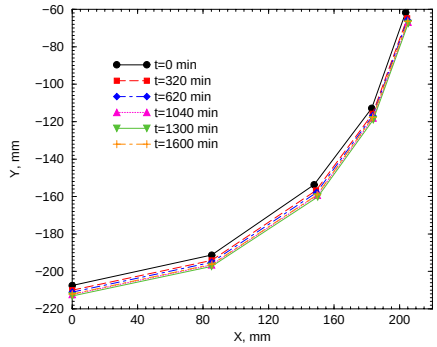

Fig. I.39: *History of wall shape at the right ($\phi > 0°$) part of the vessel.*

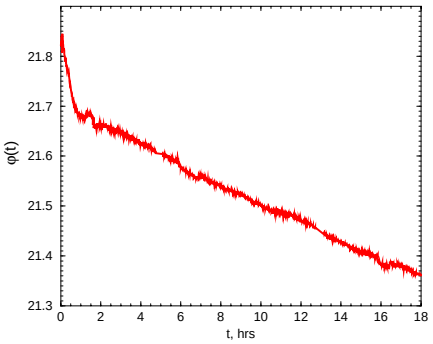

Fig. I.40: *History of the angular displacement, measured at the angular position $\phi \simeq +22$.*

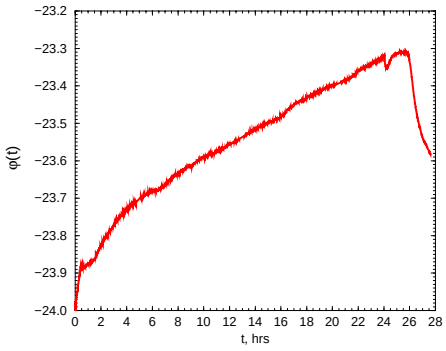

Fig. I.41: *History of the angular displacement, measured at the angular position $\phi \simeq -24$.*

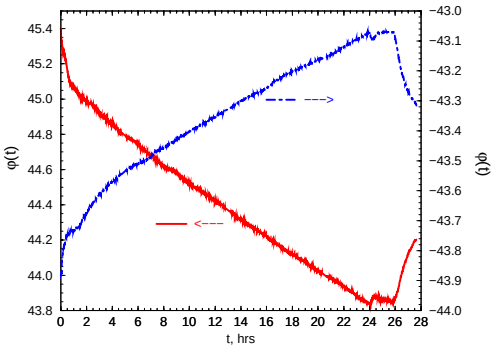

Fig. I.42: *History of the angular displacement, measured at the angular position $\phi \simeq \pm 45$.*

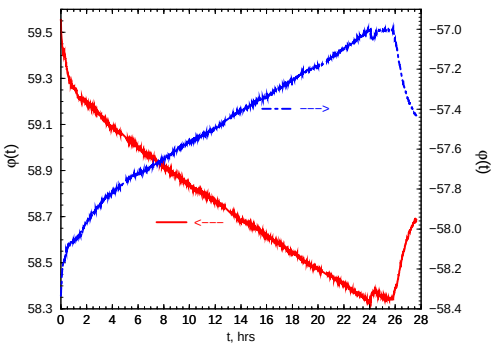

Fig. I.43: *History of the angular displacement, measured at the angular position* $\phi \simeq \pm 60$.

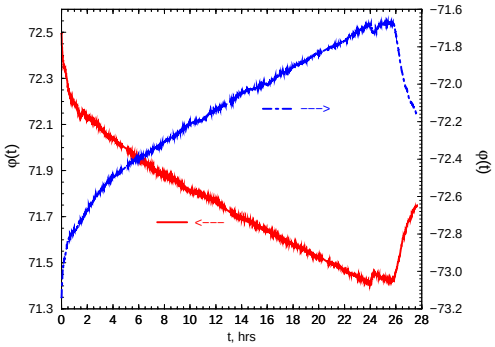

Fig. I.44: *History of the angular displacement, measured at the angular position* $\phi \simeq \pm 72$.

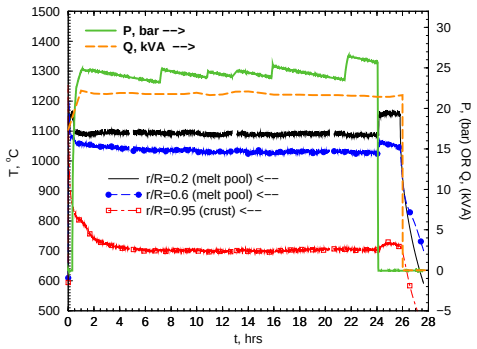

Fig. I.45: *Temperature of the melt as a function of time, measured at the centerline, at different radial locations. History of the pressure and power supply.*

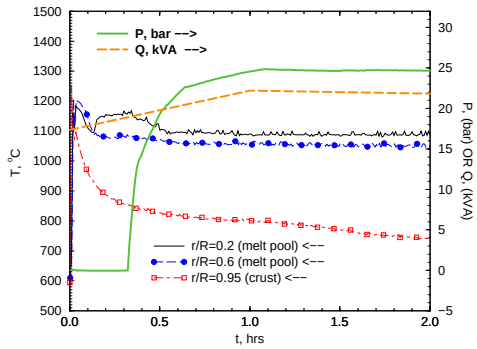

Fig. I.46: *Temperature of the melt as a function of time, measured at the centerline, at different radial locations. History of the pressure and power supply. Beginning of the test (t from 0 to 2 hrs).*

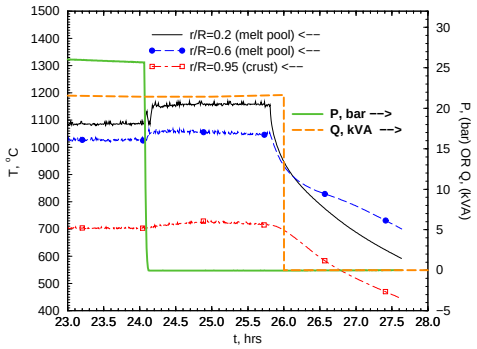

Fig. I.47: *Temperature of the melt as a function of time, measured at the centerline, at different radial locations. History of the pressure and power supply. End of the test (t from 23 to 28 hrs).*

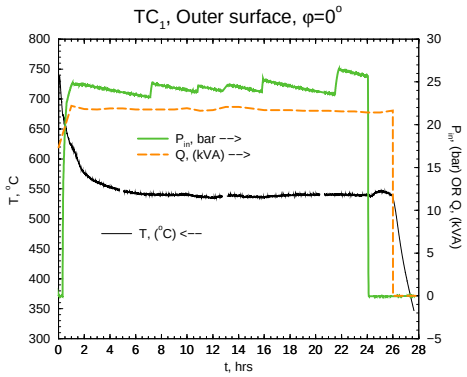

Fig. I.48: *Temperature of the vessel as a function of time, measured at the angular position $\phi = 0°$, in the hemispherical part of the vessel. History of the pressure and power supply.*

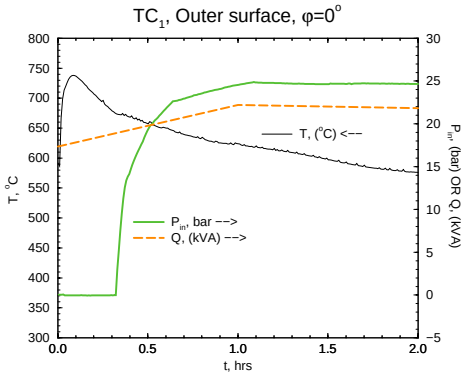

Fig. I.49: *Temperature of the vessel as a function of time, measured at the angular position $\phi = 0°$, in the hemispherical part of the vessel. History of the pressure and power supply. Begining of the test (t from 0 to 2 hrs).*

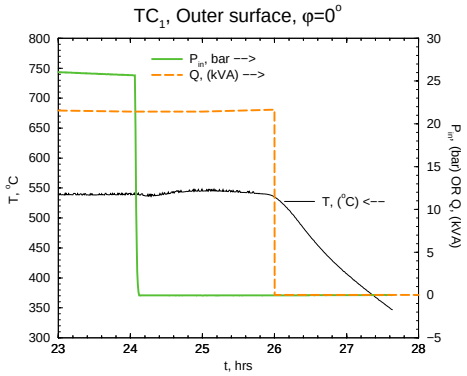

Fig. I.50: *Temperature of the vessel as a function of time, measured at the angular position $\phi = 0°$, in the hemispherical part of the vessel. History of the pressure and power supply. End of the test (t from 23 to 28 hrs).*

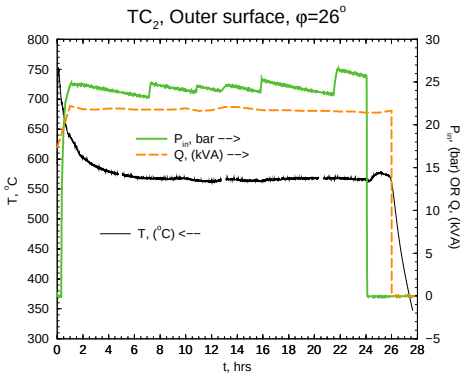

Fig. I.51: *Temperature of the vessel as a function of time, measured at the angular position $\phi = 26°$, in the hemispherical part of the vessel. History of the pressure and power supply.*

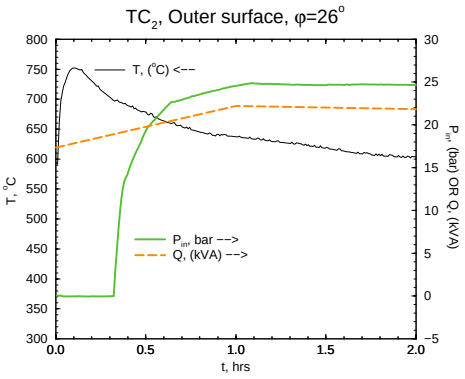

Fig. I.52: *Temperature of the vessel as a function of time, measured at the angular position $\phi = 26°$, in the hemispherical part of the vessel. History of the pressure and power supply. Begining of the test (t from 0 to 2 hrs).*

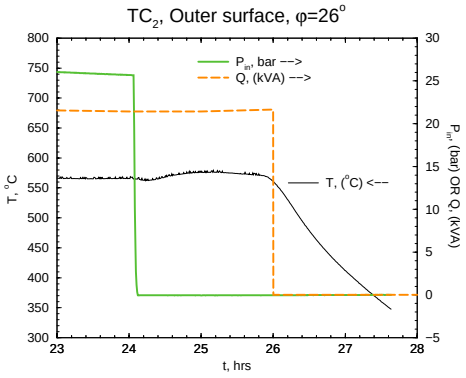

Fig. I.53: *Temperature of the vessel as a function of time, measured at the angular position $\phi = 26°$, in the hemispherical part of the vessel. History of the pressure and power supply. End of the test (t from 23 to 28 hrs).*

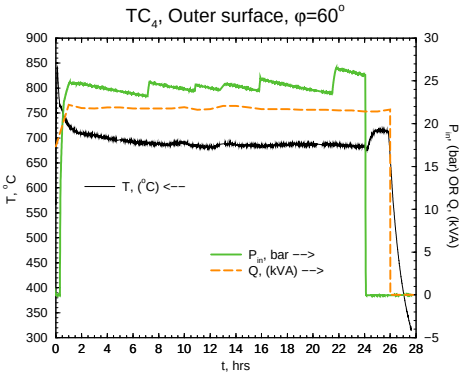

Fig. I.54: *Temperature of the vessel as a function of time, measured at the angular position $\phi = 60°$, in the hemispherical part of the vessel. History of the pressure and power supply.*

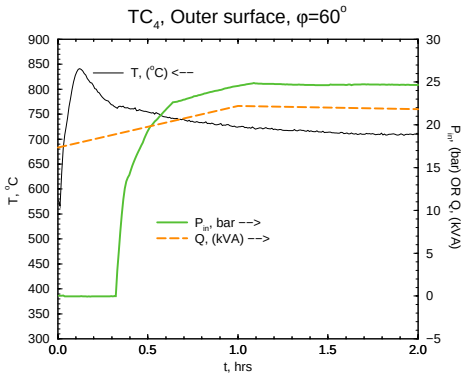

Fig. I.55: *Temperature of the vessel as a function of time, measured at the angular position $\phi = 60°$, in the hemispherical part of the vessel. History of the pressure and power supply. Begining of the test (t from 0 to 2 hrs).*

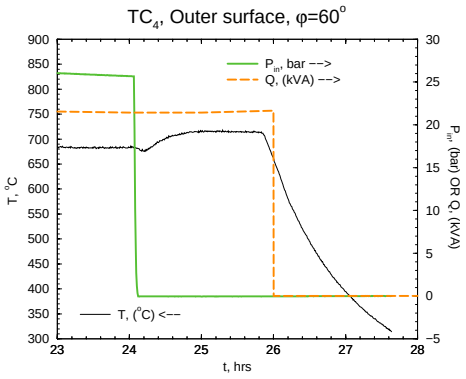

Fig. I.56: *Temperature of the vessel as a function of time, measured at the angular position $\phi = 60°$, in the hemispherical part of the vessel. History of the pressure and power supply. End of the test (t from 23 to 28 hrs).*

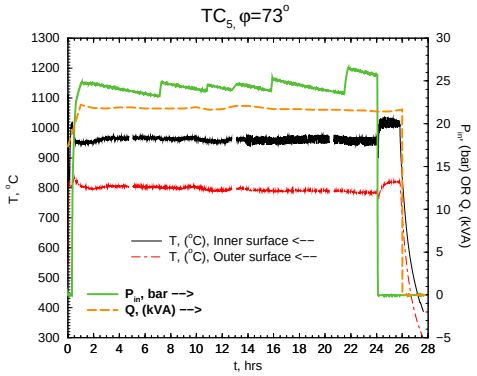

Fig. I.57: *Temperature of the vessel as a function of time, measured at the angular position $\phi = 73°$, in the hemispherical part of the vessel. History of the pressure and power supply.*

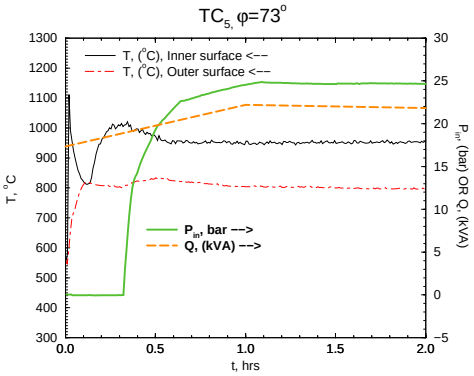

Fig. I.58: *Temperature of the vessel as a function of time, measured at the angular position $\phi = 73°$, in the hemispherical part of the vessel. History of the pressure and power supply. Begining of the test (t from 0 to 2 hrs).*

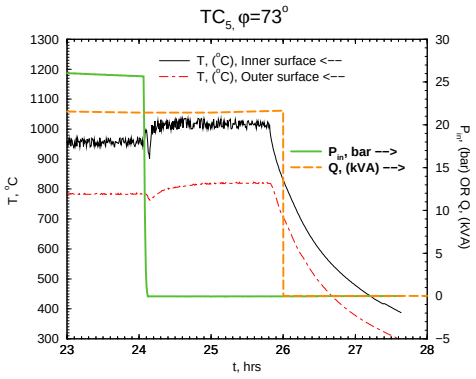

Fig. I.59: *Temperature of the vessel as a function of time, measured at the angular position $\phi = 73°$, in the hemispherical part of the vessel. History of the pressure and power supply. End of the test (t from 23 to 28 hrs).*

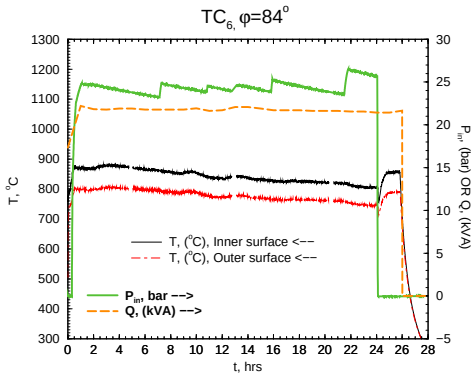

Fig. I.60: *Temperature of the vessel as a function of time, measured at the angular position $\phi = 84°$, in the hemispherical part of the vessel. History of the pressure and power supply.*

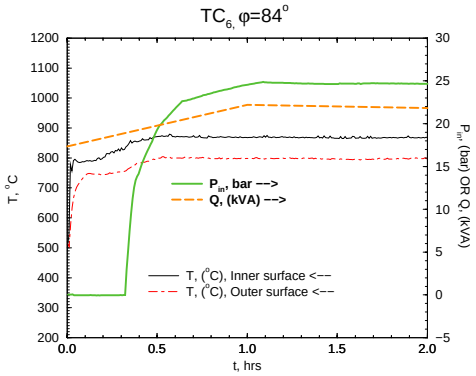

Fig. I.61: *Temperature of the vessel as a function of time, measured at the angular position $\phi = 84°$, in the hemispherical part of the vessel. History of the pressure and power supply. Begining of the test (t from 0 to 2 hrs).*

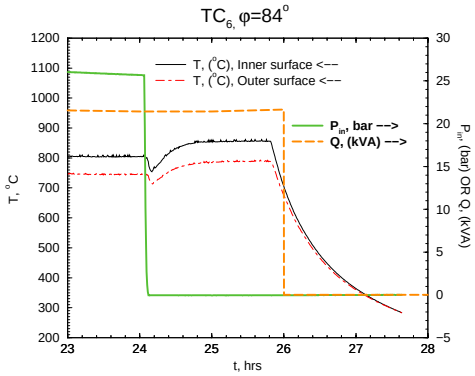

Fig. I.62: *Temperature of the vessel as a function of time, measured at the angular position $\phi = 84°$, in the hemispherical part of the vessel. History of the pressure and power supply. End of the test (t from 23 to 28 hrs).*

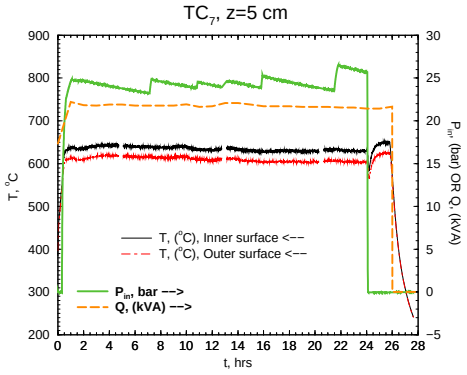

Fig. I.63: *Temperature of the vessel as a function of time, measured at the axial position $z = 5cm$, in the cylindrical part of the vessel. History of the pressure and power supply.*

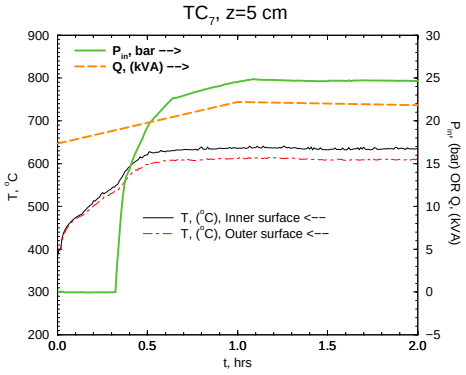

Fig. I.64: *Temperature of the vessel as a function of time, measured at the axial position $z = 5cm$, in the cylindrical part of the vessel. History of the pressure and power supply. Begining of the test (t from 0 to 2 hrs).*

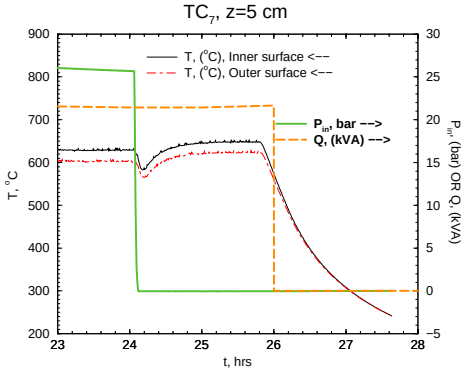

Fig. I.65: *Temperature of the vessel as a function of time, measured at the axial position $z = 5cm$, in the cylindrical part of the vessel. History of the pressure and power supply. End of the test (t from 23 to 28 hrs).*

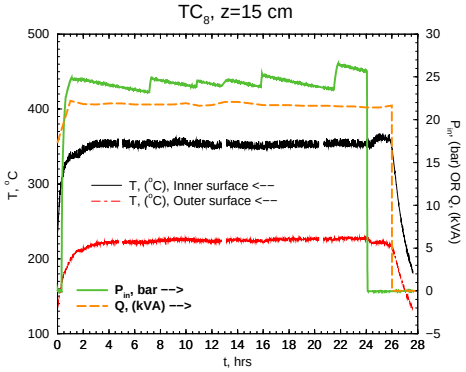

Fig. I.66: *Temperature of the vessel as a function of time, measured at the axial position $z = 15cm$, in the cylindrical part of the vessel. History of the pressure and power supply.*

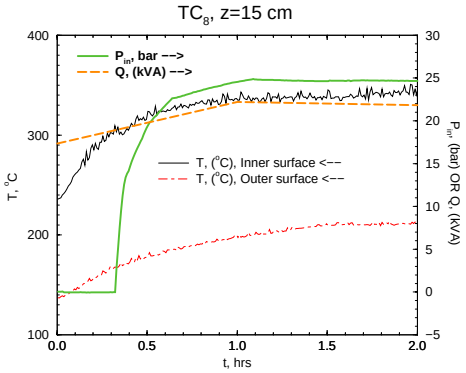

Fig. I.67: *Temperature of the vessel as a function of time, measured at the axial position $z = 15cm$, in the cylindrical part of the vessel. History of the pressure and power supply. Begining of the test (t from 0 to 2 hrs).*

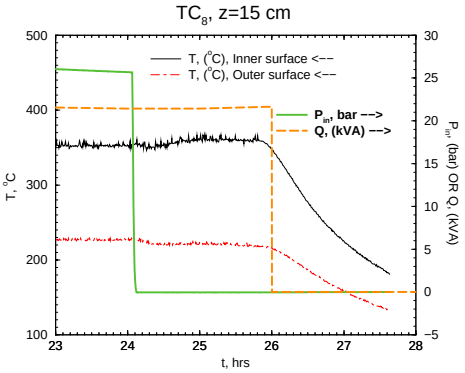

Fig. I.68: *Temperature of the vessel as a function of time, measured at the axial position $z = 15cm$, in the cylindrical part of the vessel. History of the pressure and power supply. End of the test (t from 23 to 28 hrs).*

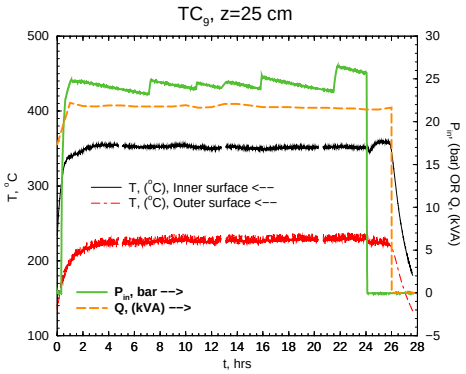

Fig. I.69: *Temperature of the vessel as a function of time, measured at the axial position $z = 25cm$, in the cylindrical part of the vessel. History of the pressure and power supply.*

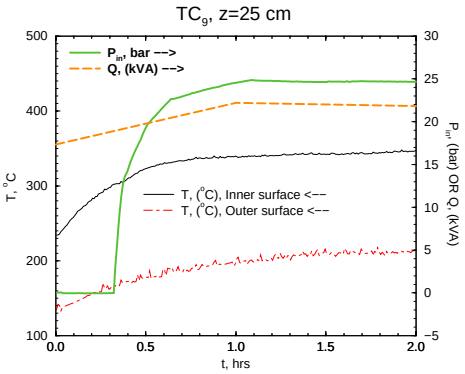

Fig. I.70: *Temperature of the vessel as a function of time, measured at the axial position $z = 25cm$, in the cylindrical part of the vessel. History of the pressure and power supply. Begining of the test (t from 0 to 2 hrs).*

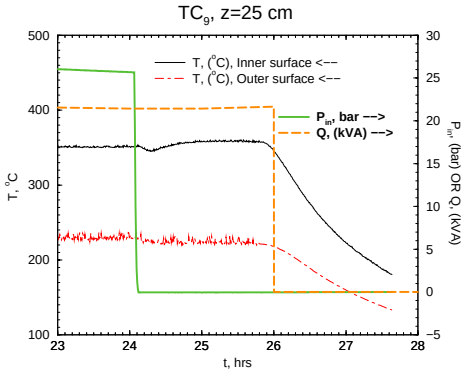

Fig. I.71: *Temperature of the vessel as a function of time, measured at the axial position $z = 25cm$, in the cylindrical part of the vessel. History of the pressure and power supply. End of the test (t from 23 to 28 hrs).*

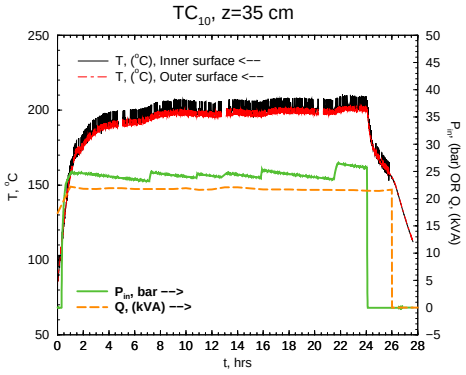

Fig. I.72: *Temperature of the vessel as a function of time, measured at the axial position $z = 35cm$, in the cylindrical part of the vessel. History of the pressure and power supply.*

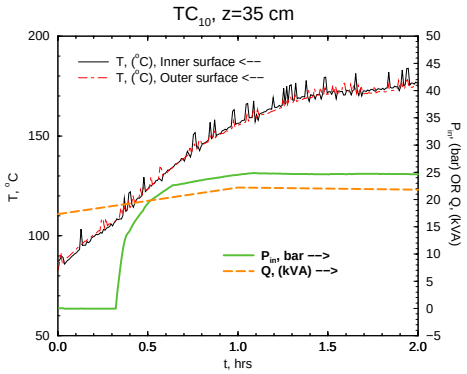

Fig. I.73: *Temperature of the vessel as a function of time, measured at the axial position $z = 35cm$, in the cylindrical part of the vessel. History of the pressure and power supply. Begining of the test (t from 0 to 2 hrs).*

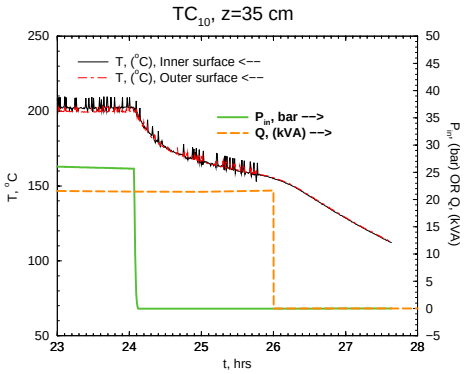

Fig. I.74: *Temperature of the vessel as a function of time, measured at the axial position $z = 35cm$, in the cylindrical part of the vessel. History of the pressure and power supply. End of the test (t from 23 to 28 hrs).*

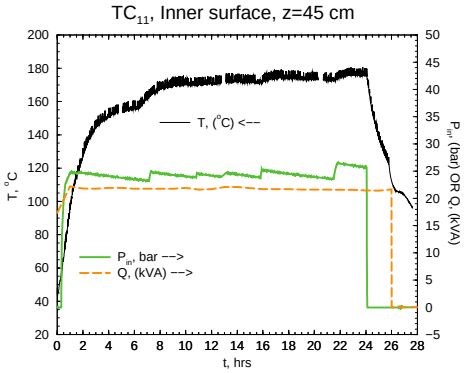

Fig. I.75: *Temperature of the vessel as a function of time, measured at the inner surface of the vessel lid. History of the pressure and power supply.*

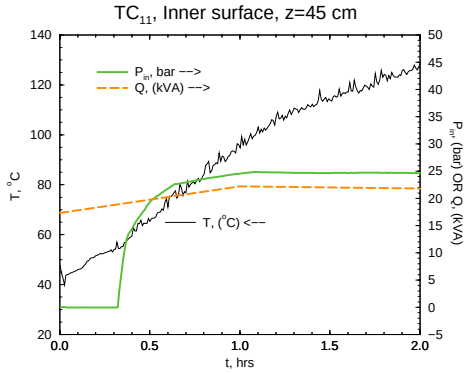

Fig. I.76: *Temperature of the vessel as a function of time, measured at the inner surface of the vessel lid. History of the pressure and power supply. Begining of the test (t from 0 to 2 hrs).*

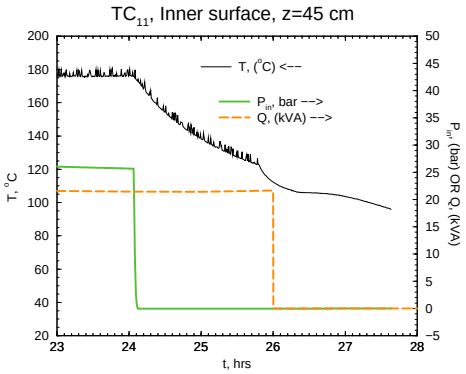

Fig. I.77: *Temperature of the vessel as a function of time, measured at the inner surface of the vessel lid. History of the pressure and power supply. End of the test (t from 23 to 28 hrs).*

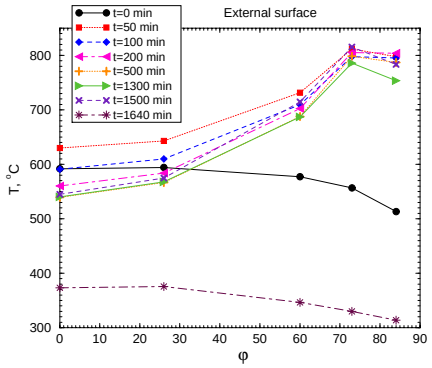

Fig. I.78: *Measured local (angular) distribution of the external surface temperature, as a function of time.*

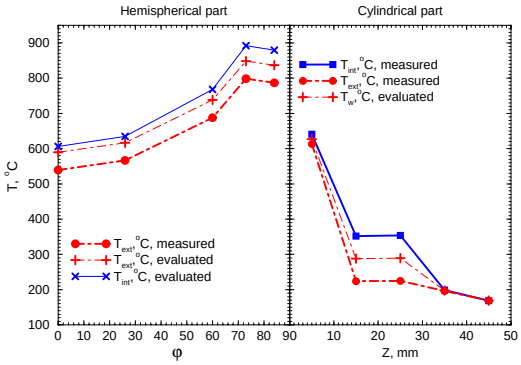

Fig. I.79: *Local temperature distribution on the inner and outer surface of the vessel wall, at the steady-state stage of experiment (t=8 hrs).*

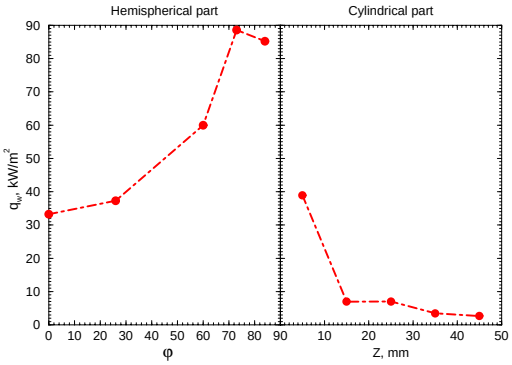

Fig. I.80: *Evaluation of the local heat flux distribution on the vessel wall, at the steady-state stage of experiment (t=8 hrs).*

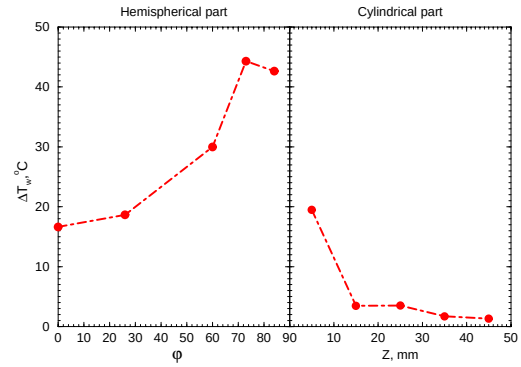

Fig. I.81: *Evaluation of the local distribution of the temperature difference through the wall, at the steady-state stage of experiment (t=8 hrs).*

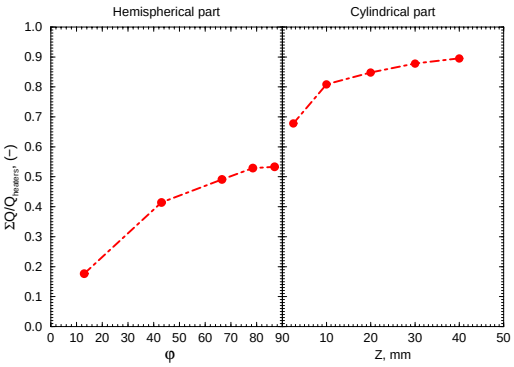

Fig. I.82: *Evaluation of the local distribution of the heat losses through the wall, at the steady-state stage of experiment (t=8 hrs).*

Appendix J

Crust Effect in the COPO-II experiments

Nuclear Power / Maria Helle 9 December 1998 YDIN-GT1-50

1. INTRODUCTION

COPO II experiments are carried out for studying heat transfer behavior in a molten corium pool on the lower head of the reactor pressure vessel (RPV). COPO II experiments are continuation of the COPO I experiments [1], which were a crucial part of the demonstration of In-Vessel Retention (IVR) concept for IVO's Loviisa NPP. In order to apply IVR for reactors with higher power densities, further refinement of the existing data base was deemed necessary. Specific questions addressed in the COPO II experiments are the detailed heat flux distribution on the upper boundary, effect of bottom geometry, effect of non-constant fluid properties, effect of crust boundary, and heat transfer phenomena in stratified pools.

The test matrix of the COPO II-experiments is shown in Table 1. The tests which focus on the effect of ice layer on the heat transfer coefficient are presented in this report. The COPO II-Lo and COPO II-AP base case tests (homogenous pool, all boundaries cooled till freezing) are presented in [2] and [3], respectively. Experiments with stratified pool will be presented in a separate report.

Table 1: Test matrix of COPO II -experiments

Objective	Facility	Number of Runs	Schedule	Ref.
Shape effect, scale effect (homogenous pool)	COPO II-AP	2[1)]	completed before MVI project (12/95)	[3]
Base case test, shape effect (homogenous pool)	COPO II-Lo	5	part of MVI-project completed 9/97	[2]
Adiabatic upper surface (homogenous pool)	COPO II-Lo	1	part of MVI-project completed 9/97	[2]
Stratified pool	COPO II-Lo	2[2)]	part of MVI-project completed 11/96	-
Shape effect, scale effect (homogenous pool)	COPO II-AP	1	part of MVI-project completed 2/98	this report
Stratified pool	COPO II-AP	2	part of MVI-project completed 5/98	-
Crust effect (homogenous pool, only upper boundary cooled)	COPO II-AP	6[3)]	part of MVI-project completed 10/98	this report

[1)] four power levels
[2)] three power levels
[3)] 13 power levels

2. FACILITIES

In COPO II experiments a molten corium pool on the lower head of a RPV is simulated by a two-dimensional slice of it in linear scale 1:2. The thickness of the slice is 94 mm. The pool is bounded at its periphery and at the top by aluminum walls which are divided into cooling units to prevent longitudinal heat conduction. At the lateral sides, pool is bounded by insulated, parallel plywood walls. The corium is simulated by water-zincsulfate solution with volumetric Joule heating. The temperature distribution in the pool and the heat flux distribution on the boundaries are measured, local heat fluxes are obtained by measuring temperature gradients in the cooling units. A distinctive feature in COPO II is the cooling arrangement which is based on circulation of liquid nitrogen on the outside of the pool boundaries. The use of liquid nitrogen leads to formation of ice on the inside of boundaries.

Two geometrically different versions of the COPO II facility have been constructed: one with a torispherical bottom shape (called COPO II-Lo), simulating the RPV of a VVER-440 reactor as COPO I, and another one (COPO II-AP) with semicircular bottom simulating a western PWR such as AP600. The modified Rayleigh number in the COPO II experiments corresponds to the one in a prototypic corium pool (~10^{15}). More detailed description of the COPO II-Lo and COPO II-AP facilities is given in [2] and [3], respectively. Experiments described in this report have been carried out using COPO II-AP facility (Figure 1).

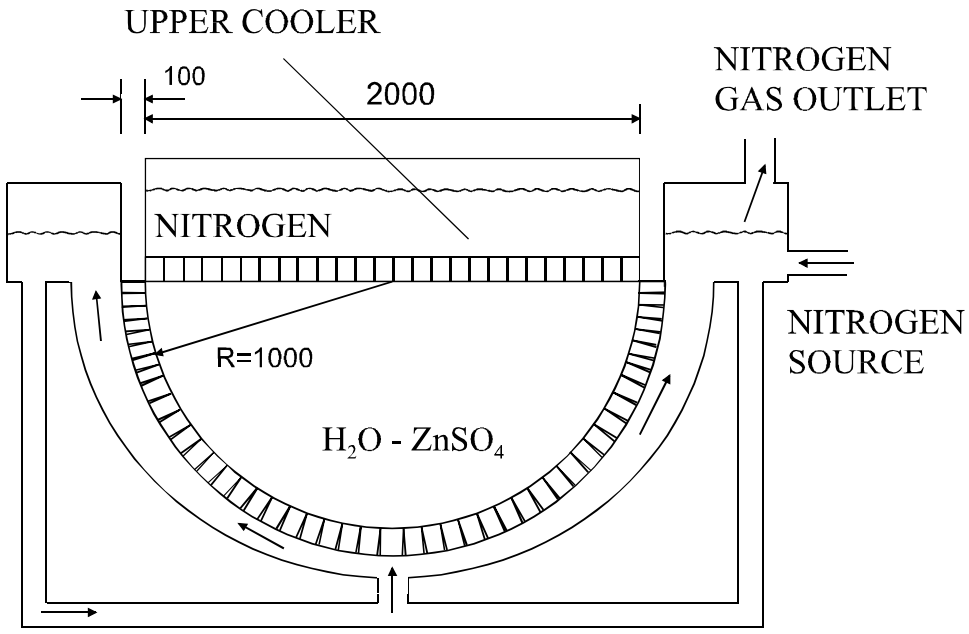

Figure 1: Schematic of the COPO II-AP facility

3. HEAT TRANSFER CORRELATIONS

One of the main questions regarding RPV integrity applying IVR is the average upward heat transfer coefficient from the heat generating pool. In the earlier COPO II experiments [2,3], the measured upward heat transfer coefficients were found to be rather consistent with the COPO I [1] and the French BALI [4] results. However, they were higher than predicted by the widely used correlation by Steinberner and Reineke [5]:

$$\mathrm{Nu}_{up} = 0.345 \cdot \mathrm{Ra}'^{0.233}, \quad \textbf{(1)}$$

and also higher than measured in the ACOPO experiments [6]:

$$\mathrm{Nu}_{up} = 1.95 \cdot \mathrm{Ra}'^{0.18}. \quad \textbf{(2)}$$

The dimensionless parameters Ra' and Nu are calculated at the film temperature (average between the fluid maximum and the boundary temperatures) and taking into account the concentration of $ZnSO_4$. The modified Rayleigh number Ra' is calculated based on the measured cooling power, not the used heating power.

To study the possible reasons for the discrepancy between COPO II and ACOPO results, some experiments were carried out cooling only the upper boundary of the pool similarly to one special ACOPO experiment [7]. According to [7], both externally- and internally-driven natural convection problems are analogous at high enough Rayleigh numbers, and the upward heat transfer coefficient can be calculated as:

$$\mathrm{Nu}_{up} = 0.206 \cdot \mathrm{Ra}^{0.303} \cdot \mathrm{Pr}^{0.084}, \quad \textbf{(3)}$$

where the fluid properties for Ra and Pr are evaluated at the bulk temperature and the length scale is selected as discussed in Appendix A.

The measured average heat transfer coefficients to the curved boundary in COPO II experiments are compared to a correlation by Jahn and Mayinger [8]:

$$\mathrm{Nu}_{dn} = 0.54 \cdot \mathrm{Ra}' \cdot \left(\frac{H}{R}\right)^{0.26}, \quad \textbf{(4)}$$

which is based on experiments in a 2D-slice geometry with $10^7 < \mathrm{Ra}' < 10^{11}$. It is emphasized that the correlation is now extended beyond its original data base. According to 3D numerical calculations by Mayinger et al., the average downward heat transfer coefficient can be calculated as:

$$\mathrm{Nu}_{dn} = 0.55 \cdot \mathrm{Ra}'^{0.2}. \quad \textbf{(5)}$$

Slightly higher average downward heat transfer coefficients were measured in the ACOPO experiments [6]:

$$\mathrm{Nu}_{\mathrm{dn}} = 0.3 \cdot \mathrm{Ra}'^{0.22}. \quad \textbf{(6)}$$

Based on mini-ACOPO experiments [9], the local heat transfer coefficient distribution in the lower boundary is:

$$\frac{\mathrm{Nu}_{\mathrm{dn}}(\theta)}{\mathrm{Nu}_{\mathrm{dn}}} = 0.1 + 1.08\left(\frac{\theta}{\phi}\right) - 4.5\left(\frac{\theta}{\phi}\right)^2 + 8.6\left(\frac{\theta}{\phi}\right)^3, \quad (0.1 \le \frac{\theta}{\phi} \le 0.6) \quad \textbf{(7a)}$$

$$\frac{\mathrm{Nu}_{\mathrm{dn}}(\theta)}{\mathrm{Nu}_{\mathrm{dn}}} = 0.41 + 0.35\left(\frac{\theta}{\phi}\right) + \left(\frac{\theta}{\phi}\right)^2, \quad (0.6 < \frac{\theta}{\phi} \le 1). \quad \textbf{(7b)}$$

4. CHECK OF REPEATABILITY, RUN P7

Before the experiments described in this report, the COPO II-AP facility was modified (comparing to the tests described in [3]) based on experiences of the COPO II-Lo experiments and the first COPO II-AP experiments in 1995:

- Number of windows in the lateral walls was increased to improve visualization.
- Accurate contact between the aluminum and thermocouples was ensured with copper paste.
- Holes were drilled to lateral walls at the location of air space to vent out any nitrogen gas and to prevent gas leakage into the test section.
- The copper electrodes were modified to prevent thermal conduction through them past the intermediate plate during stratified pool tests (Figure 2).
- Thermal insulation of the lateral walls and the clamps were modified to facilitate test procedure (Figure 3).

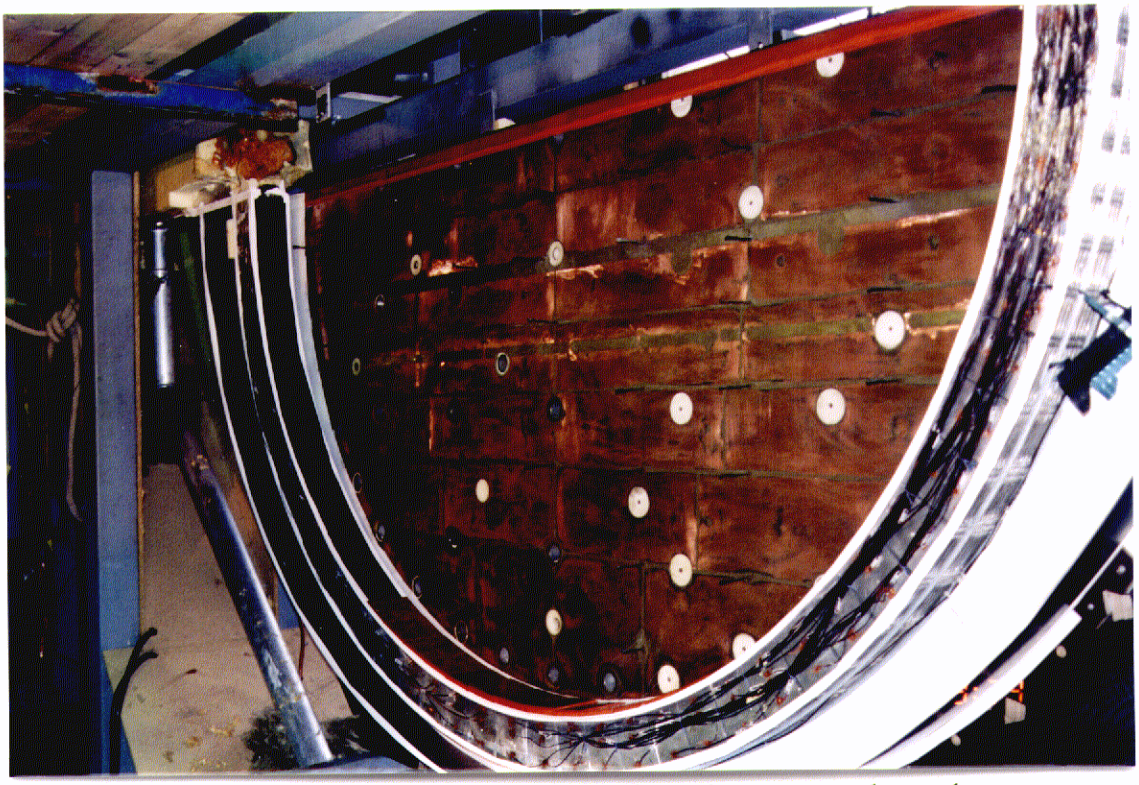

Figure 2: Two horizontal cuts were sawn into the copper electrodes to prevent thermal conduction through them past the intermediate plate during stratified pool tests. Additional thermal resistance can been seen at the bottom of the test section. PTFE tape gives to the PTFE-lead assembly the brown color

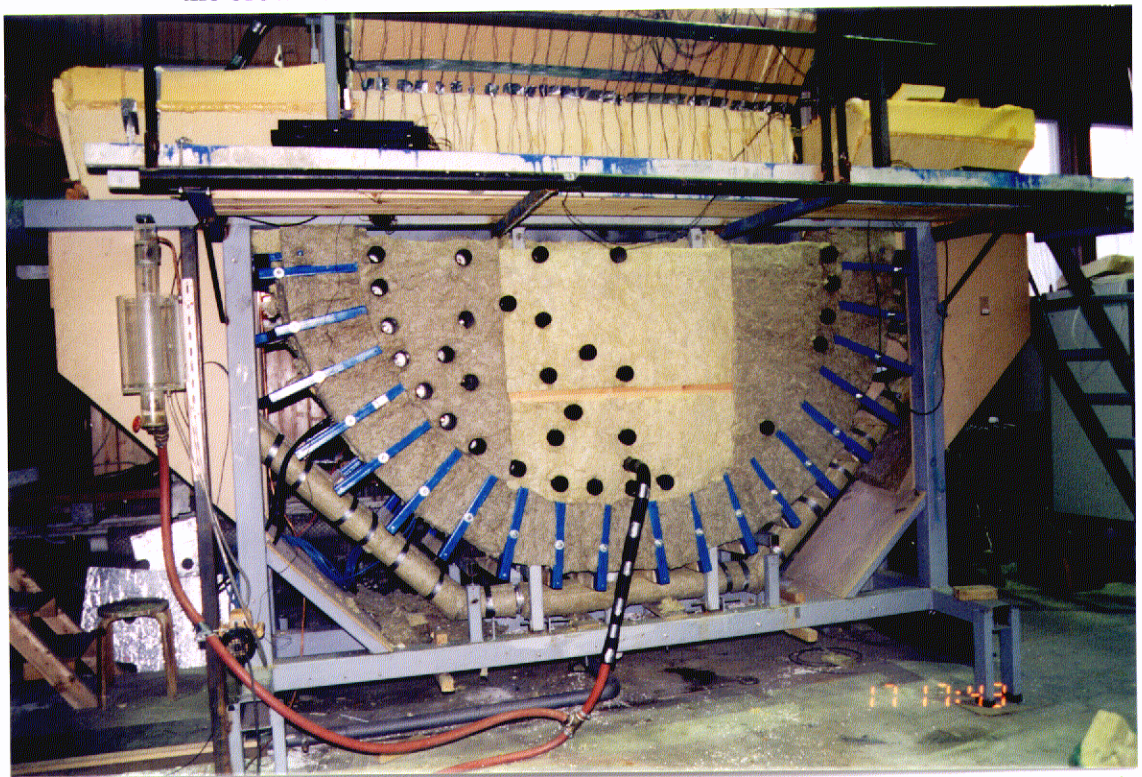

Figure 3: Lateral walls are insulated with a 200 mm thick layer of mineral wool. Clamps are accessible and can be tightened during the whole test period

Therefore, to check repeatability with earlier tests, one base case test with all boundaries cooled till freezing was carried out on February 18, 1998. The sequence number of the test was P7. The power input during the test is shown in Figure 4 and the temperature of the center of the pool in Figure 5. The water was pumped into the test section at 3800 s and the upper cooler was lowered in its place at 5900 s.

The power consumption as well as the upper cooler temperature in places starts to decrease at 9000 s. This is due to fact that the valve in the expansion tank line was accidentally closed. The water level starts slowly decrease due to some leakages from the windows, and the upper cooler loses gradually the contact to the water. The decrease of the water level was observed about at 13 000 s, and the valve was opened.

In addition to the actual P7, an attempt was made to measure the upward heat transfer coefficient in case of non-frozen upper boundary in the end of test P7. Non-frozen boundaries were attempted by creating film boiling conditions at the upper surface of the upper cooler. In order to establish film boiling at the aluminum nitrogen boundary, nitrogen was allowed to temporarily boil off. Despite the attempts to direct the nitrogen feed not to gush to the right side of the upper cooler, the boiling mode persist changing to nucleate boiling, and ice boundary was formed below cooling units 12 - 26.

The analysed data corresponds to the time interval 8400 s - 9000 s. Based on video observations, reasonably steady state was reached (ice was no longer evolving) and the height of the molten pool was 955 mm. The maximum temperature of the pool was 61.5°C and the electrical power input 21.5 kW. The time averaged steady state heat fluxes at the upper boundary are shown in Figure 6 and at the curved boundary in Figure 7. Data labels show the thickness (mm) of the additional thermal resistance[1]. The corresponding Nusselt numbers are shown in Figure 8 and Figure 9. The temperatures in the upper cooler are shown in Figure 10 and the temperatures in the lower cooler in Figure 11.

As expected, the heat flux profile at the upper boundary is very flat, the deviation from the average value is about 10%. Due to geometry of the cooling units[2], the outermost cooling units in the upper cooler are slightly warmer than the others.

A step is seen in the heat flux profile at the edge of the additional thermal resistance region (Figure 7). However, similar "elbow" is seen in the previous experiments in the same elevation (Figure 18, Figure 19) although the additional thermal resistance regions were different. A small "elbow" can also be seen at ~60°, where is the interface between well mixed part and stratified part of the pool (Figure 12). No peaking is observed at the upper edge of the curved boundary.

---

1 Additional thermal resistance was used at the very bottom to reduce the thickness of the ice: necessary number of PTFE layers and a 3 mm thick weight made of lead were wrapped inside a 0.1 mm thick PTFE tape (see Figure 2). Outermost additional thermal resistance was just a lead weight wrapped inside PTFE tape to smooth down the profile.

2 Water facing area vs. nitrogen facing area is 1.5 for outermost cooling units, and 1.3 for the other cooling units.

The summary of the main results is shown in Table 2. The average Nusselt number at upper boundary (Figure 13) is consistent with earlier COPO II-AP and COPO II-Lo results, but higher than in ACOPO experiment and also higher than predicted by the well-known correlation by Steinberner and Reineke. The dependence of the average downward Nusselt numbers on the modified Rayleigh number seems to be very weak (Figure 14). Averages calculated using 3D weighting (Figure 15) are quite consistent with ACOPO results for high Ra' numbers. The up-to-down energy split is shown in Figure 16 and in Figure 17.

An estimated uncertainty range for the results is also presented in Figure 13 and Figure 14. A uncertainty range for the measured heat flux (up- and downwards) is due to the finite accuracy of the temperature measurements in the cooling units (ΔT = 0.1°C), of the location of the thermocouple (Δx = 0.85 mm) and of thermal conductivity of aluminum ($\Delta\lambda_{upper\ cooler}$ = 7 W/(m·K), $\Delta\lambda_{lower\ cooler}$ = 12 W/(m·K)):

$$q'' = q''_{be} \pm \Delta q'' \text{ ,} \qquad \textbf{(12)}$$

where

$$\Delta q'' = \left|\frac{\partial q''}{\partial T}\right| \cdot \Delta T + \left|\frac{\partial q''}{\partial x}\right| \cdot \Delta x + \left|\frac{\partial q''}{\partial \lambda}\right| \cdot \Delta\lambda \text{ .} \qquad \textbf{(13)}$$

The uncertainty bands for the average Nusselt numbers include the above uncertainty ranges for q'' and the estimated uncertainties in pool height (ΔH = 1 cm) and in the temperature difference between the boundary and the pool maximum (ΔT_{pool} = 0.5°C). The uncertainty range for the Ra' is constructed based on the estimated uncertainties in the cooling power and pool height. The uncertainty of the cooling power, in turn, is based on the uncertainty range of heat fluxes assuming that the uncertainty in the surface areas is negligible. The dominating contribution to the uncertainty of Nu and Ra' is given by the uncertainty in the heat flux. The heat flux uncertainty in turn is dominated by the uncertainty in thermal conductivity.

Table 2: Summary of main results

	P7
Electric power input (kW)	21.5
Upper surf. cooling power (kW)	13.0
Lower boundary cooling power (kW)	7.6
Total cooling power (kW)	20.6
Heat capacity effects (kW)	0.0
Heat balance (kW) [1)]	0.9
Power to upper surface (%)	62.9
Heat flux upwards (kW/m^2)	70.3
Heat flux downwards (kW/m^2)	25.9
Height of the pool (mm)	955
Maximum temperature of the pool (°C)	61.5
Ra'	$4.8 \cdot 10^{15}$
Pr	5.5
Nu_{up}	1769.8
Nu_{dn}	651.5
$Nu_{dn,3D}$ [2)]	809.0

1) Heating power - measured cooling power - water pool heat capacity effects

2) Average Nusselt number with each cooling unit weighted assuming a hemispherical (3D) geometry

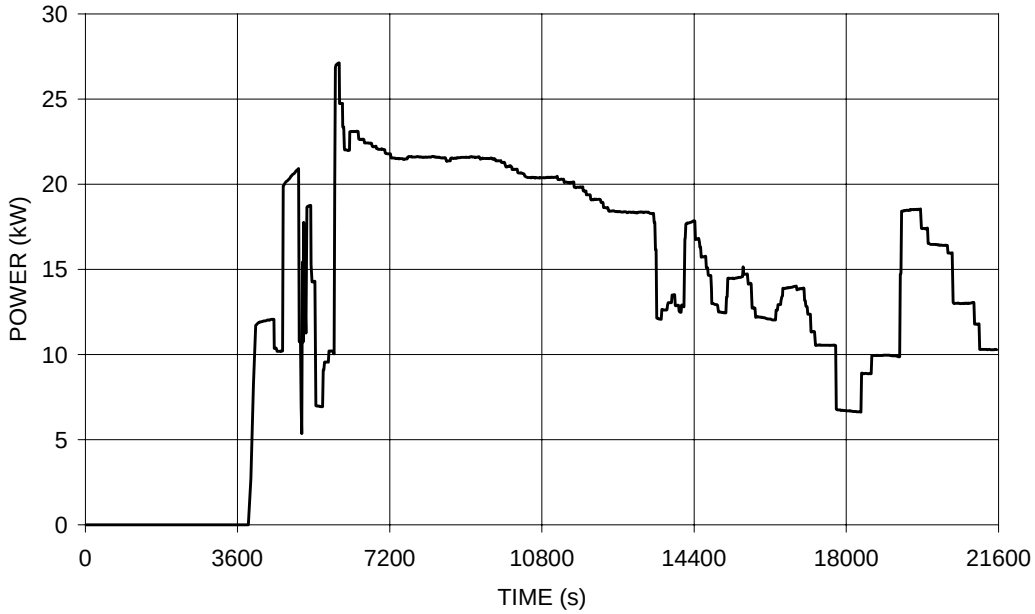

Figure 4: Electric power input during run P7

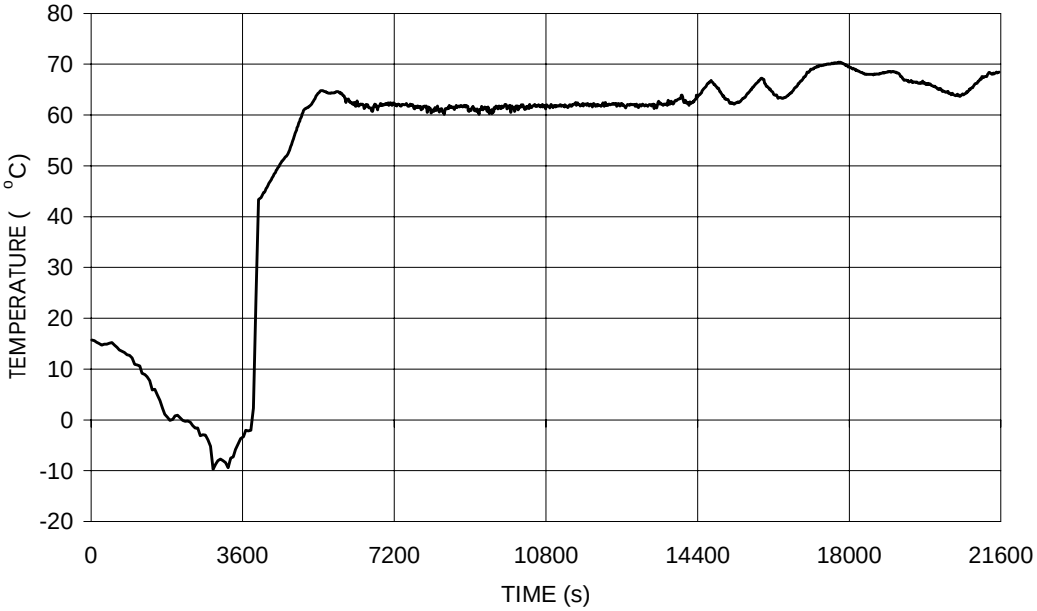

Figure 5: Temperature in the center of the pool during run P7

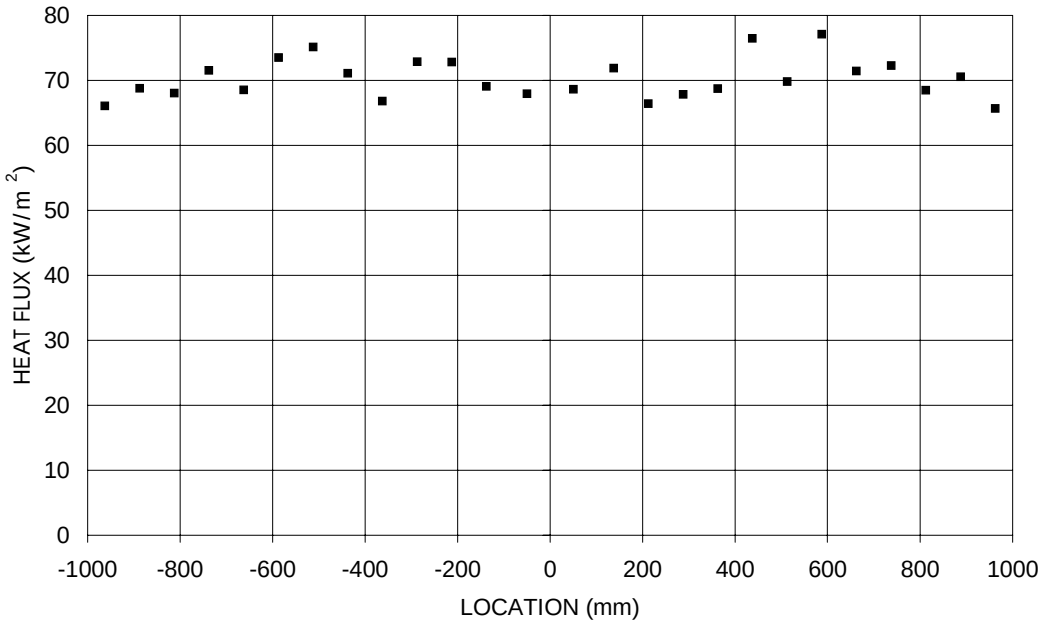

Figure 6: Local heat fluxes at the upper surface in run P7

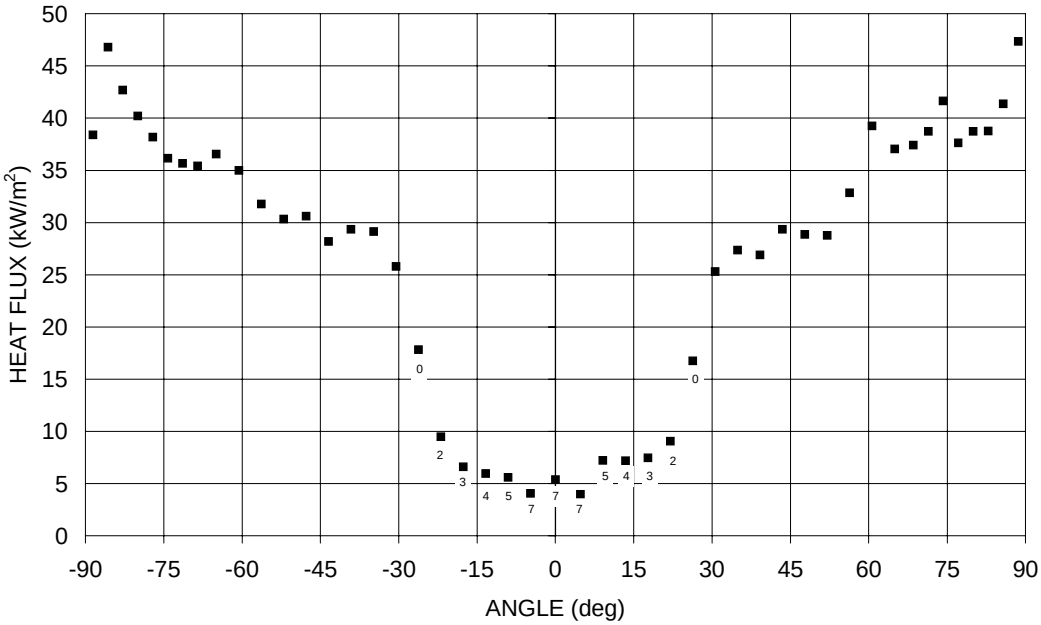

Figure 7: Local heat fluxes at the curved surface in run P7. Data labels show the thickness of the additional thermal resistance at the bottom of the pool

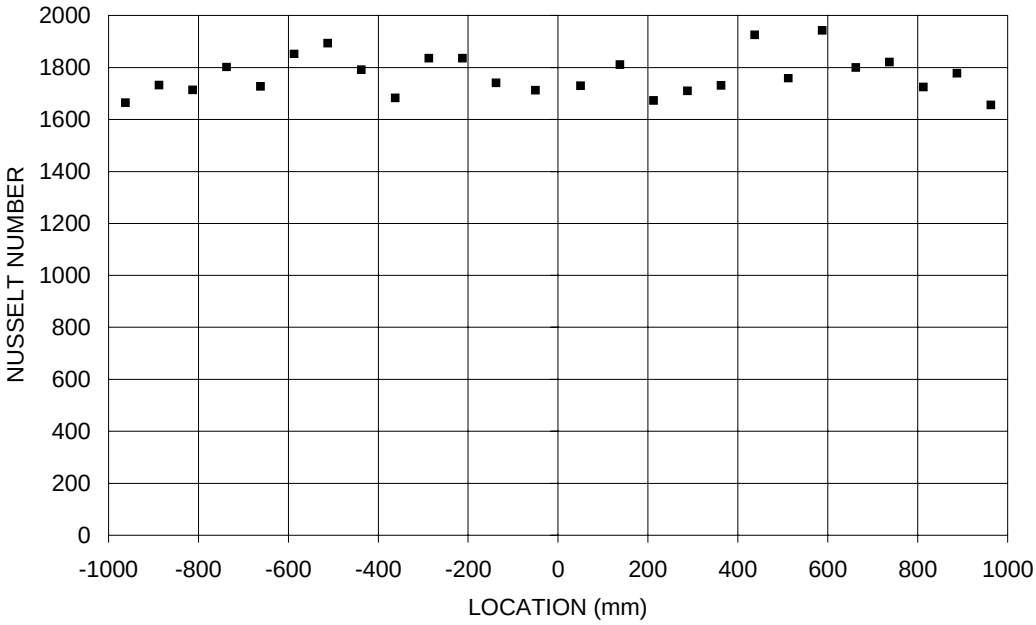

Figure 8: Local Nusselt numbers at the upper surface in run P7

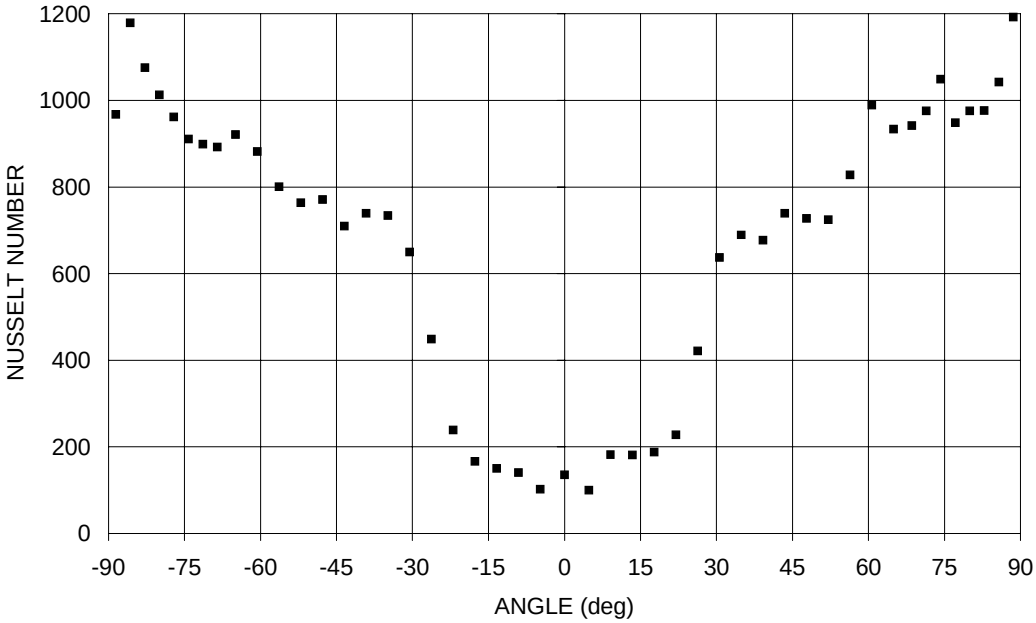

Figure 9: Local Nusselt numbers at the curved surface in run P7

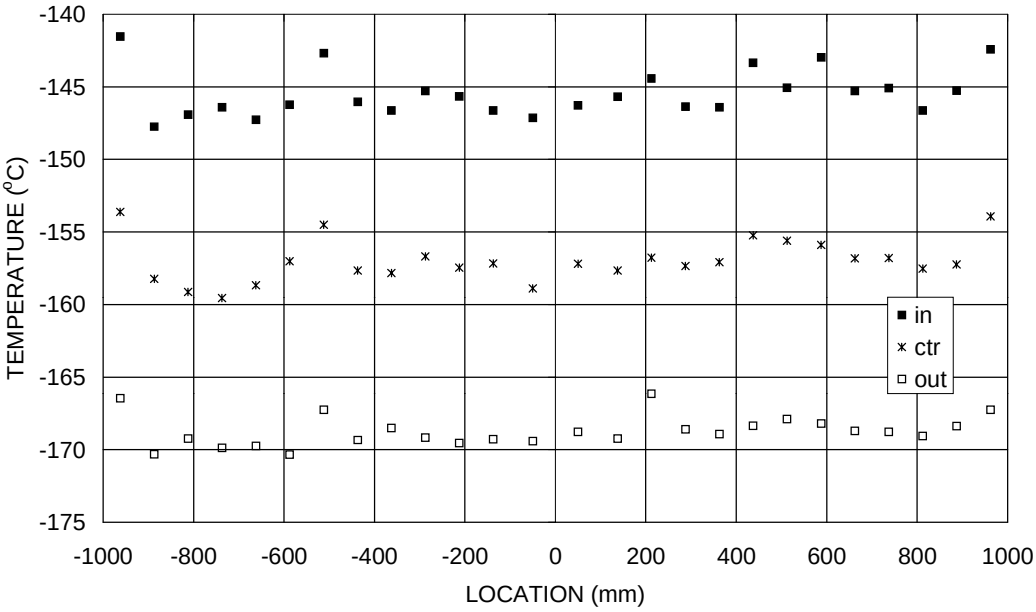

Figure 10: Upper cooler temperatures in run P7

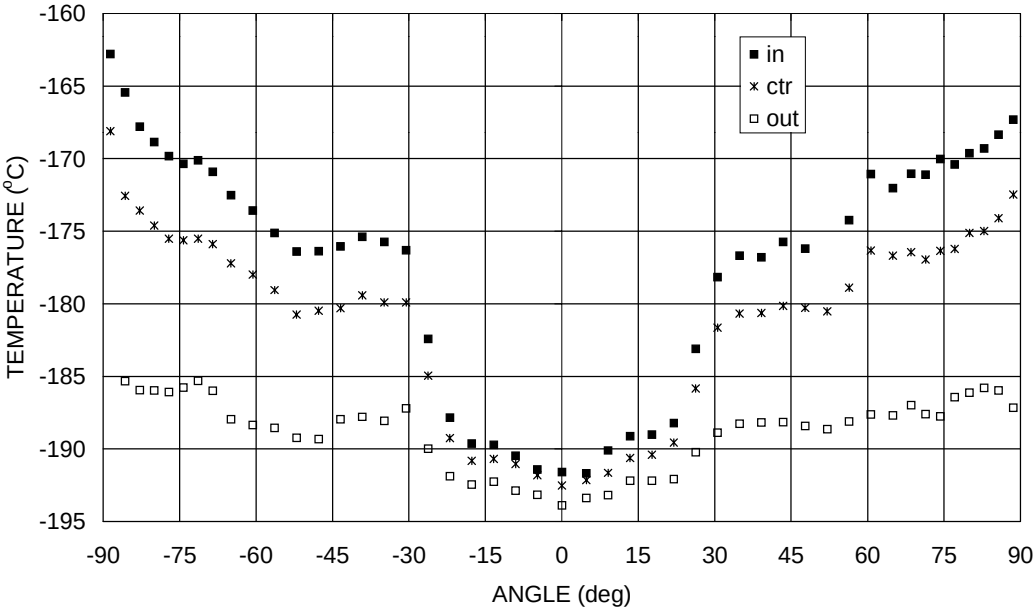

Figure 11: Lower cooler temperatures in run P7

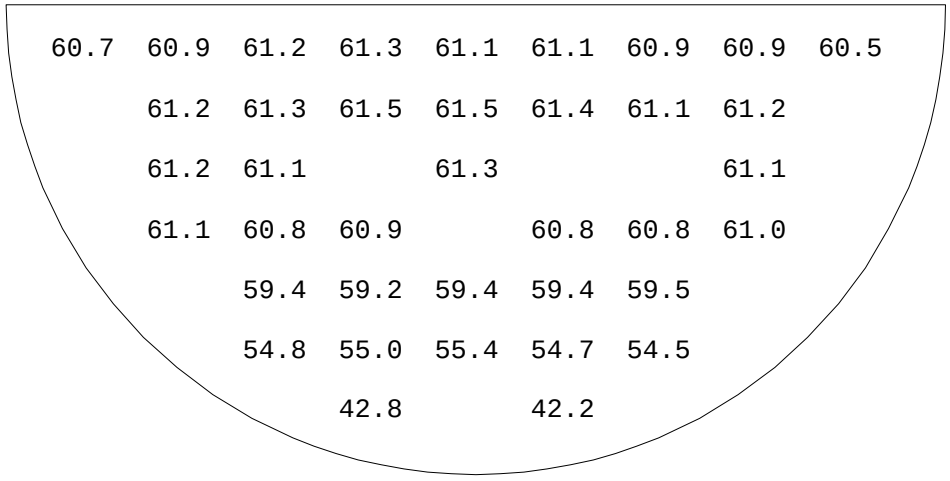

Figure 12: Measured temperature field in the pool in run P7

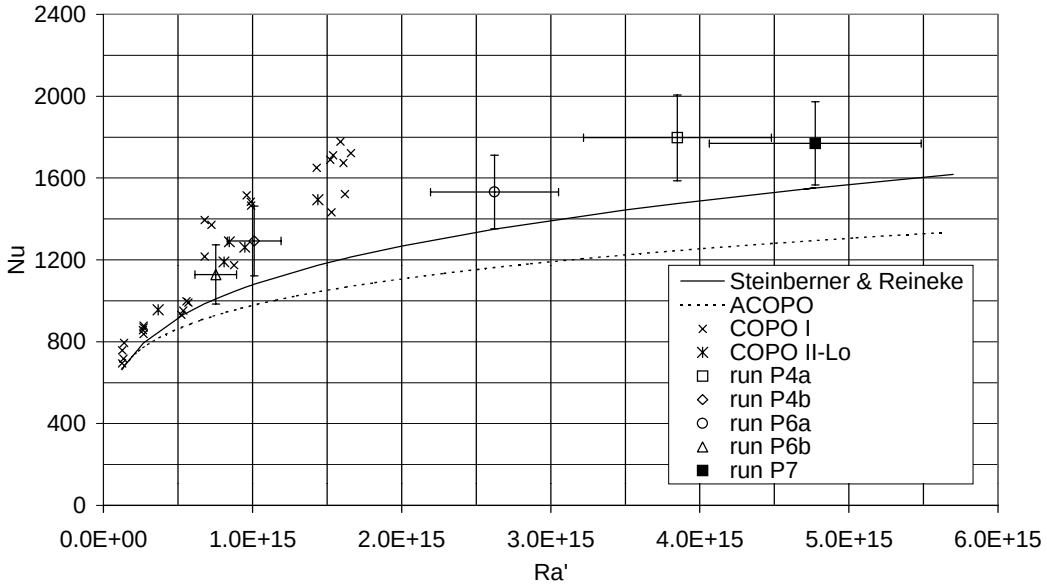

Figure 13: Measured average upward Nusselt number in run P7

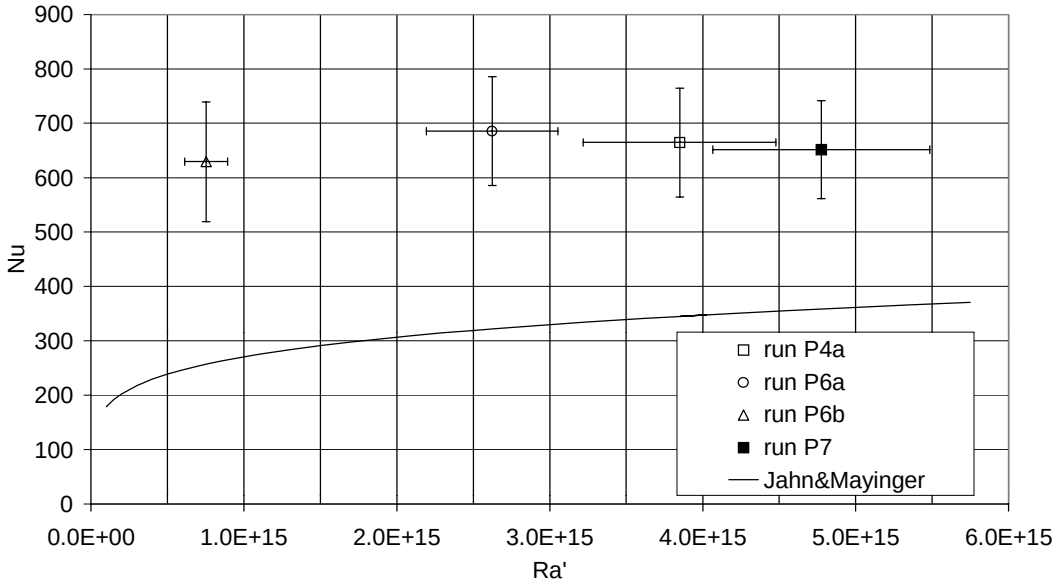

Figure 14: Measured average downward Nusselt number in run P7

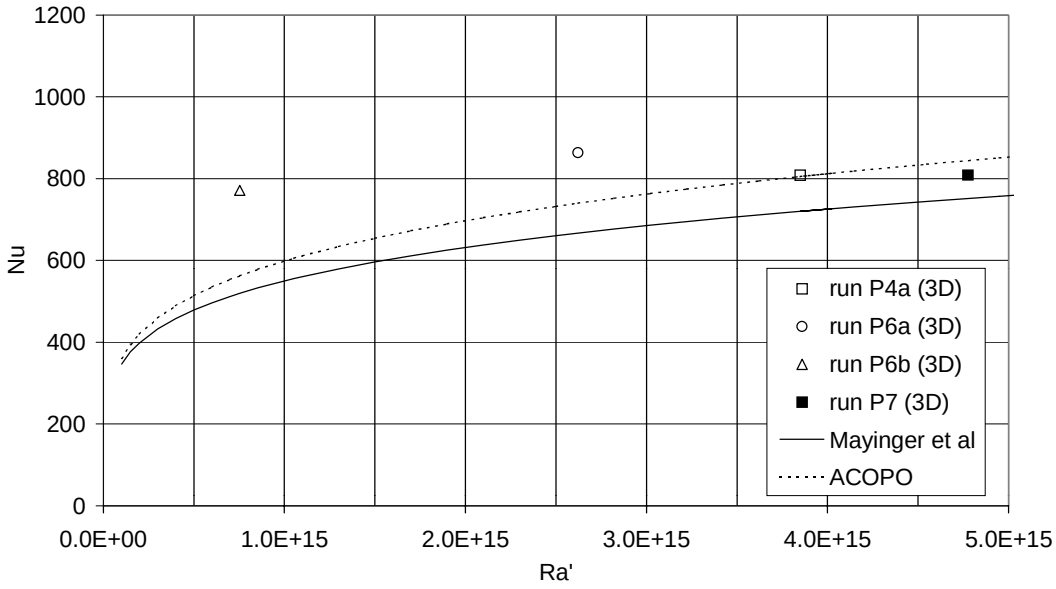

Figure 15: Measured downward Nusselt number in run P7. Averages calculated using weighting according to an assumed hemispherical (3D) geometry

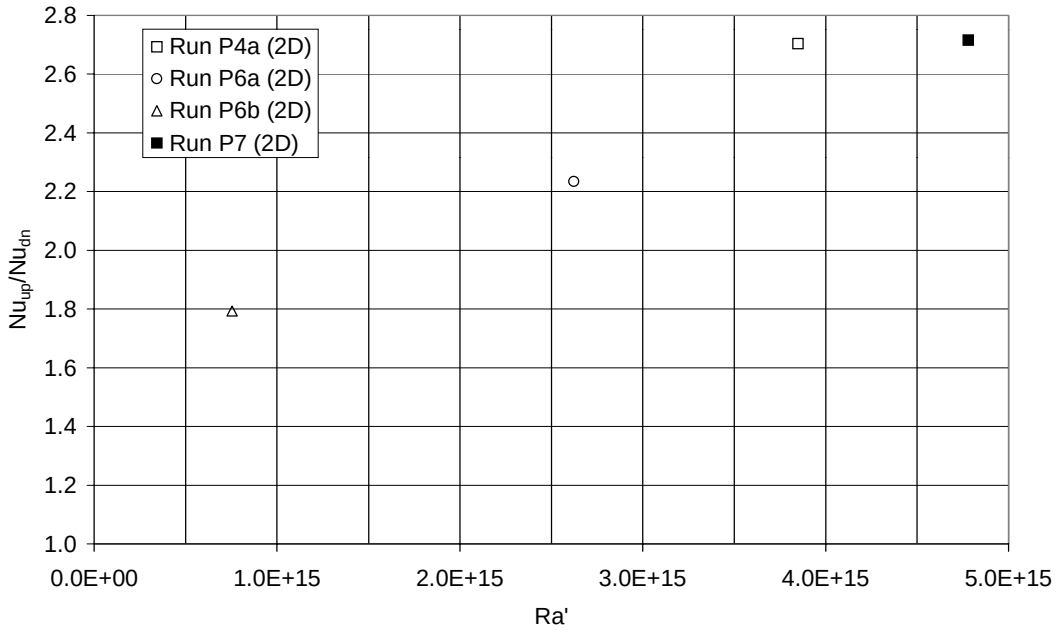

Figure 16: Up-to-down energy split

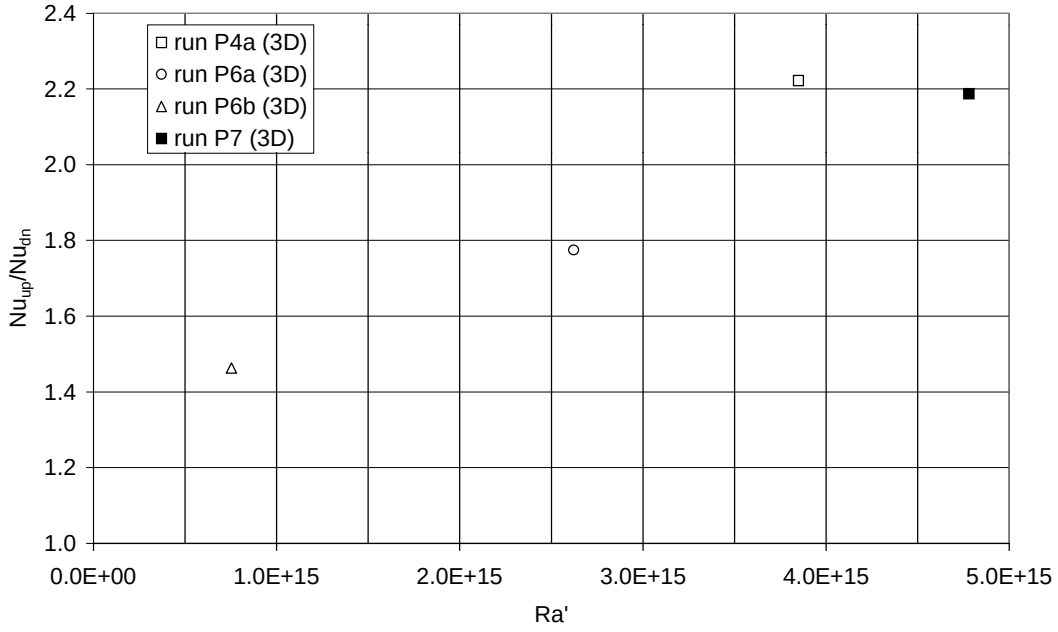

Figure 17: Up-to-down energy split. Average downward Nusselt number calculated by weighing the local values assuming a hemispherical (3D) geometry

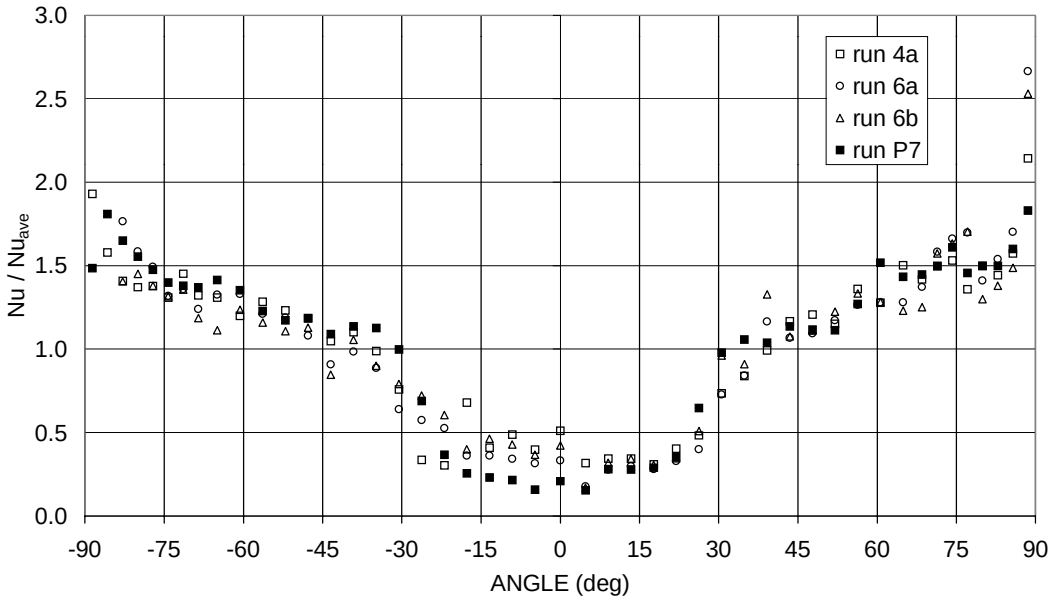

Figure 18: Normalized, local Nusselt numbers at the curved boundary

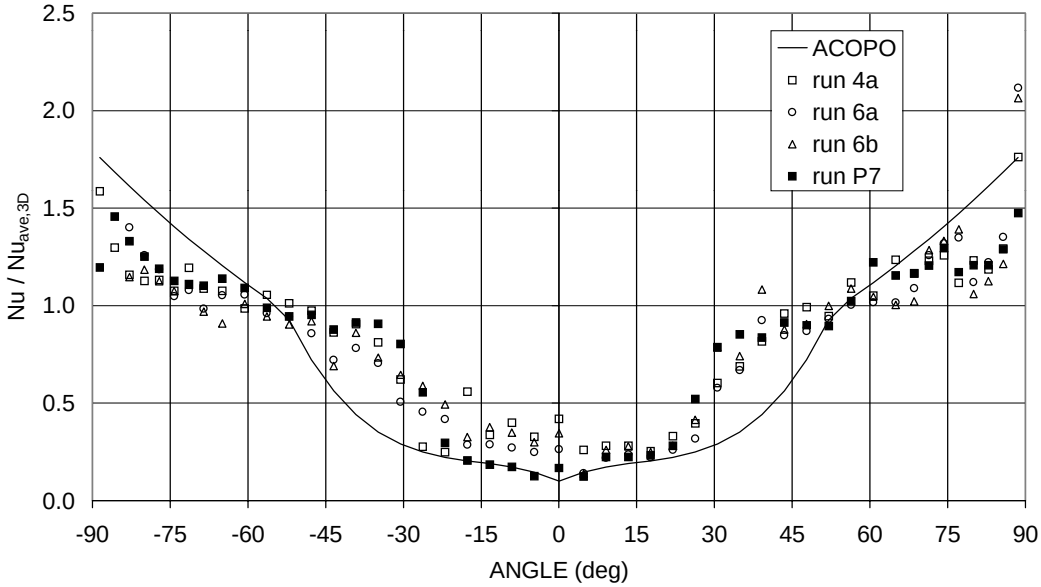

Figure 19: Normalized, local Nusselt numbers at the curved boundary. The average Nu is calculated by weighing the local values assuming a hemispherical (3D) geometry

5. EXPERIMENTS WITH ONLY UPPER BOUNDARY COOLED

5.1 Run P8

In test P8, carried out on March 25, 1998, only the upper surface of the pool was cooled. The objective was to get data directly comparable to externally driven experiments and to one special ACOPO experiment with only top boundary cooled [7]. The backside of the aluminum arc was insulated with loose Styrofoam particles, which were poured into the nitrogen space (lateral walls were not opened after test P7). Due to additional thermal resistance at the bottom of the pool, the height of the pool was 985 mm (measured before the test). Test P8 was done at two power levels (Figure 20) without interrupting the experiment between the measurement of the two levels. Run 8a corresponds to the time interval 9180 s - 9780 s and run P8b to the time interval 13 700 s - 14 300 s. The temperature of the pool was 71.1°C in test P8a and 43.3°C in test P8b (Figure 21).

Since the sidewalls were not cooled with liquid nitrogen, the water was not preheated in the separate container but pumped into the test section and allowed to heat up there to the selected temperature. Because the sidewalls were warm, water in the pool was not circulating before lowering the upper cooler in its place. Therefore, care was taken to remove air bubbles within test section before lowering the upper cooler: water was stirred to allow the dissolved gases to escape and the lateral walls were swept to remove small gas bubbles formed in the electrolysis.

The heat flux profile at the upper boundary is very flat (Figure 22). At the curved boundary the measured heat fluxes (heat losses) are very small (Figure 23). The heat flux exceeds 1 kW/m^2 only in the uppermost cooling units, just below the upper surface of the pool. During run P8b, the local heat fluxes at the curved boundary are negative, i.e., the aluminum boundary is actually warmer than the pool and it is slowly cooling down.

The asymmetrical temperature profile at the curved boundary (Figure 27) indicates that the additional thermal insulation may have been shifted. The possible effect to the height of the pool is very small and is neglected. No correction terms based on nitrogen calibration were used for the temperatures measured in the curved boundary cooling units.

The pool is well mixed (Figure 28 and Figure 29). Unlike in experiments with all boundaries cooled, no temperature stratification is seen at the bottom of the pool.

An attempt was made to measure the upward heat transfer coefficient in case of non-frozen boundary in the end of test P8. After test P7, the nitrogen feeding line was modified to ensure uniform and surgeless nitrogen feed. The temperature level of the pool was risen to 84.3°C and the film boiling was established at the aluminum nitrogen boundary by letting the nitrogen temporarily boil off. The results indicate that the upward heat transfer coefficient might be somewhat lower when the upper boundary is non-frozen. However, this result should be interpreted very cautiously,

since the heat transfer may have been disturbed by a large amount of small bubbles below the upper cooler. Gas was generated at the electrodes because of the high heating power needed to maintain film boiling. Furthermore, the results may have been affected by uncertainties in estimating the upper boundary temperature. Extrapolated (see Appendix B) boundary temperature varied from -12.6°C to 20.6°C (average value 6.5°C) though no ice formation was seen through windows.

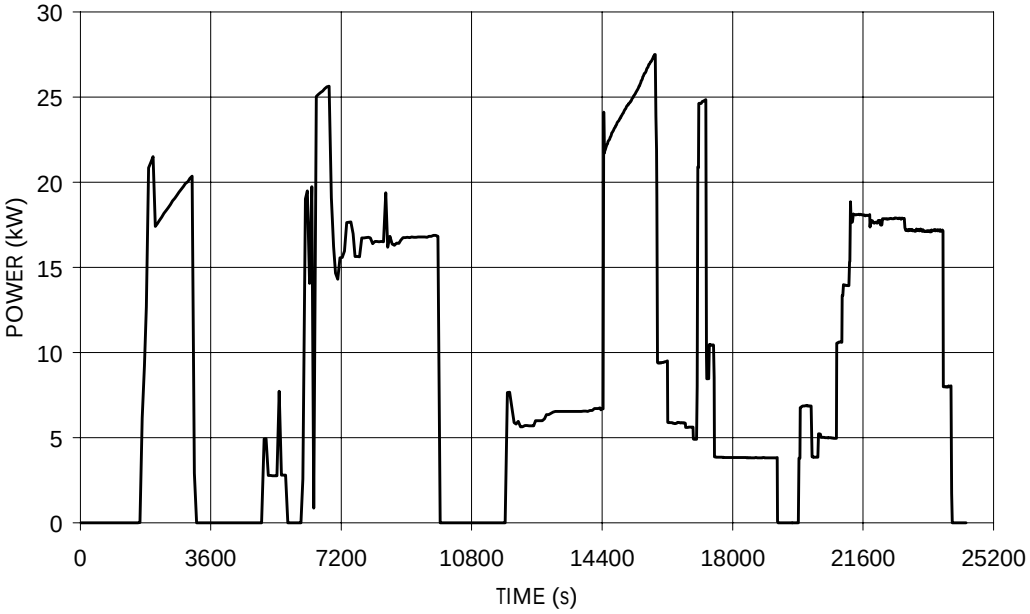

Figure 20: Electric power input during run P8

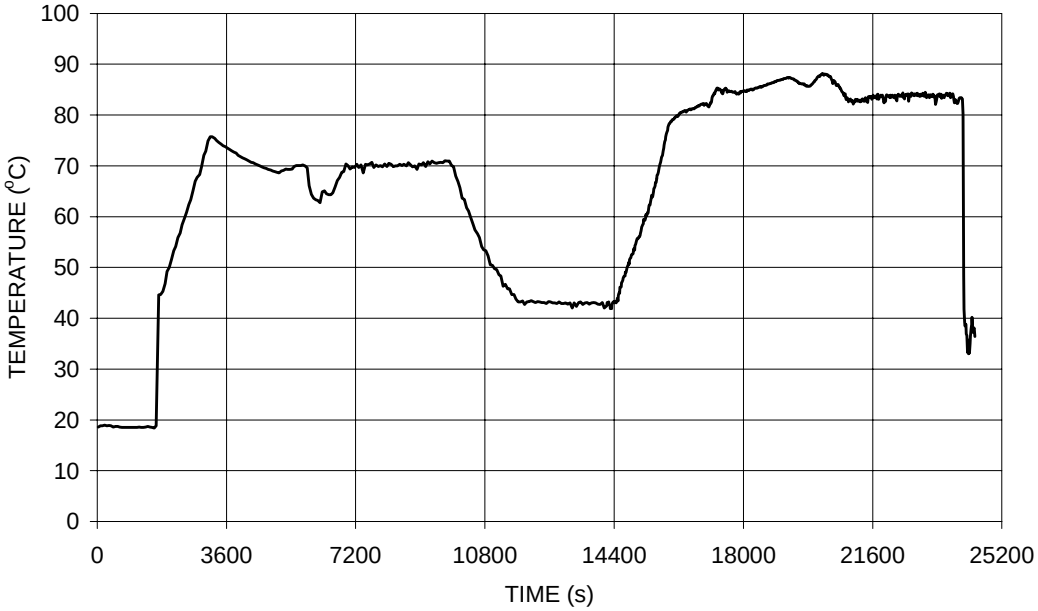

Figure 21: Temperature in the center of the pool during run P8

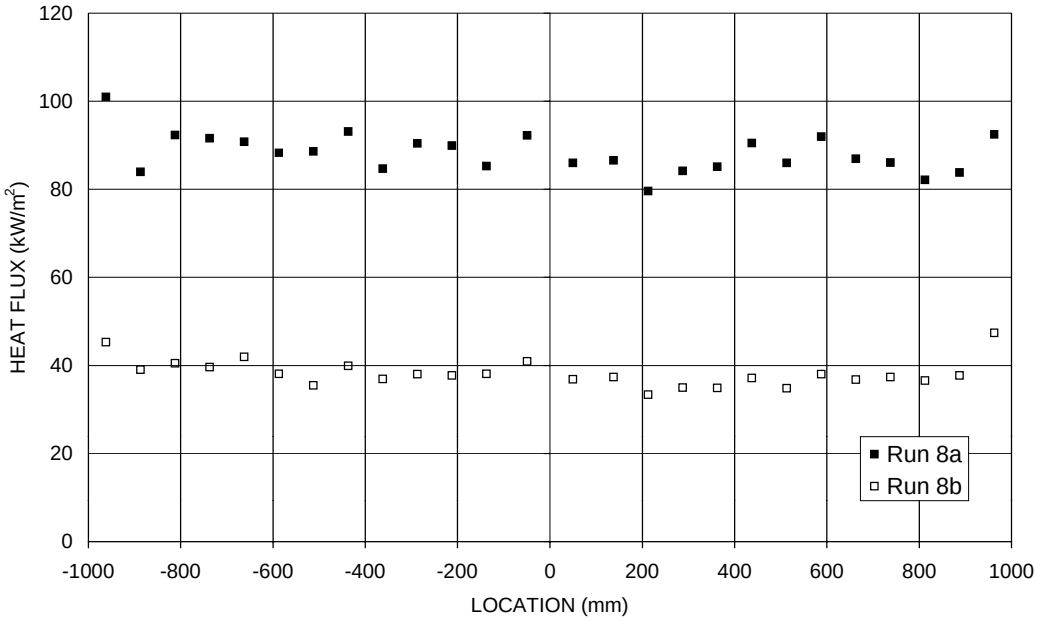

Figure 22: Local heat fluxes at the upper surface in run P8

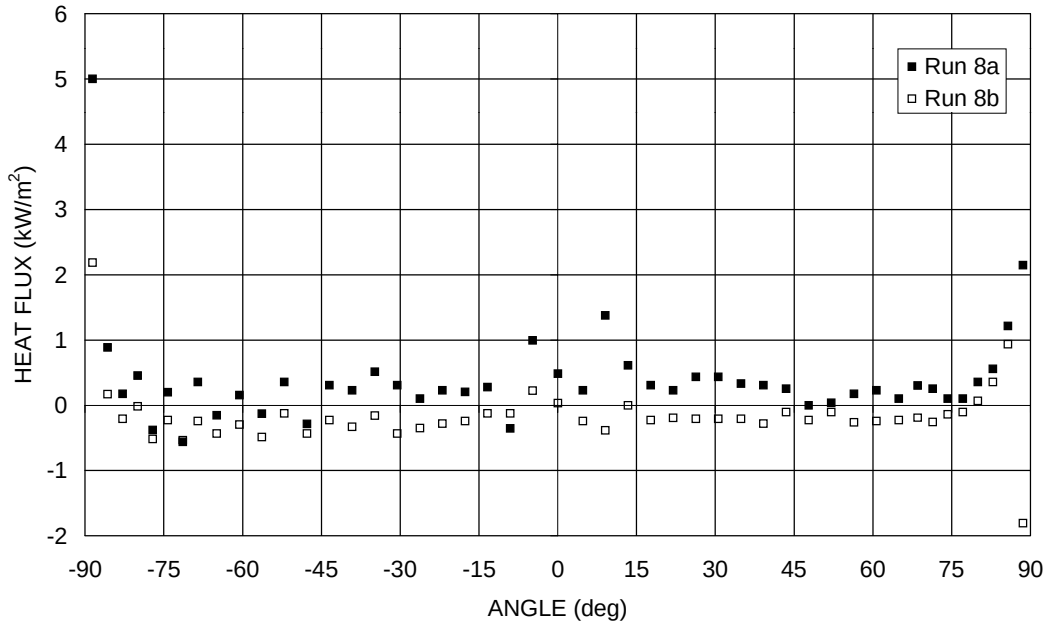

Figure 23: Local heat fluxes at the curved surface in run P8

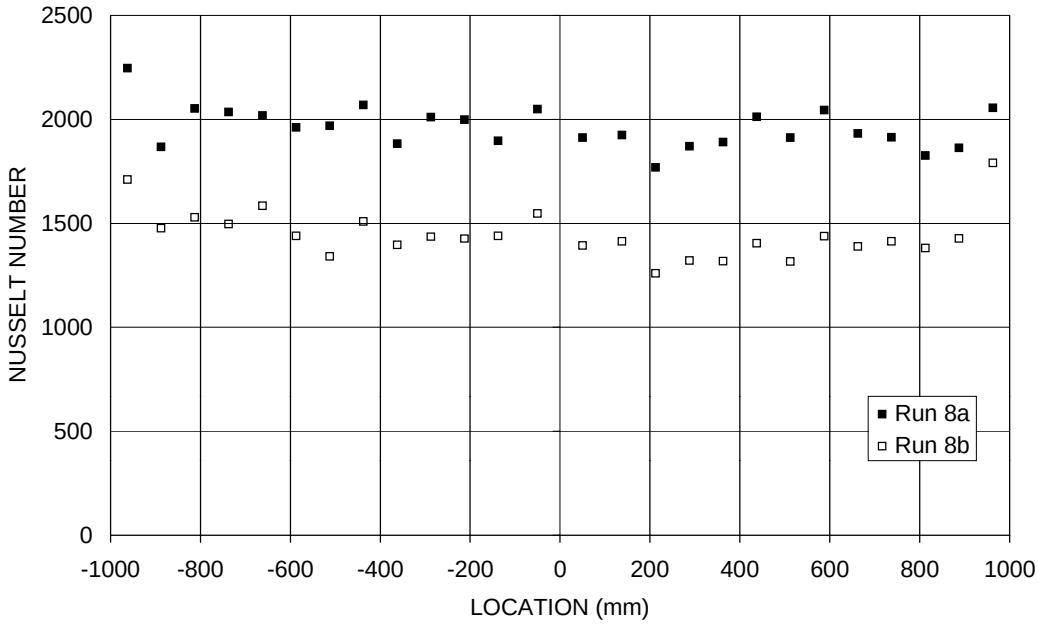

Figure 24: Local Nusselt numbers at the upper surface in run P8

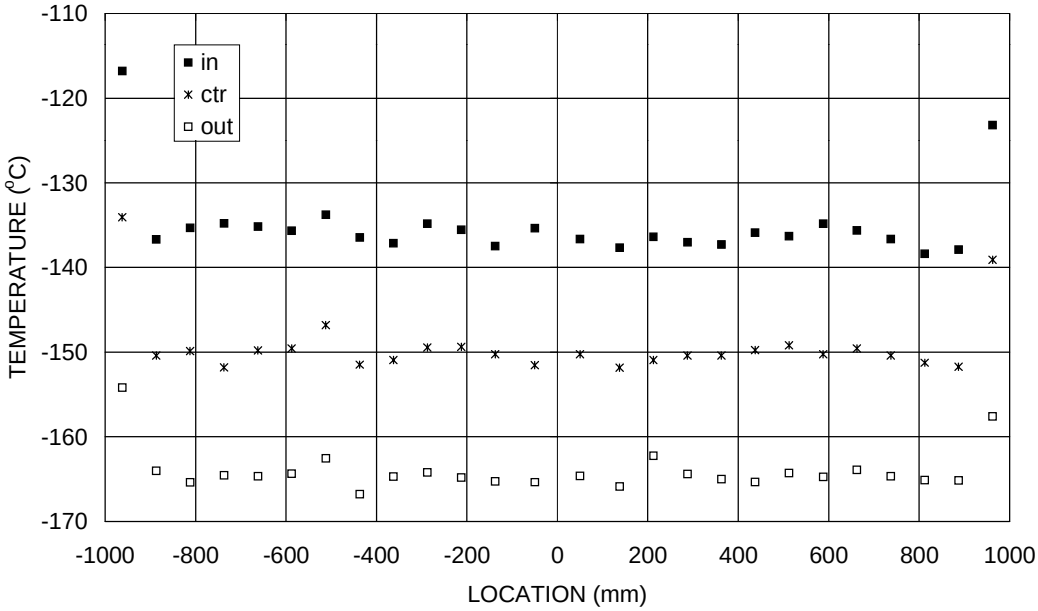

Figure 25: Upper cooler temperatures in run P8a

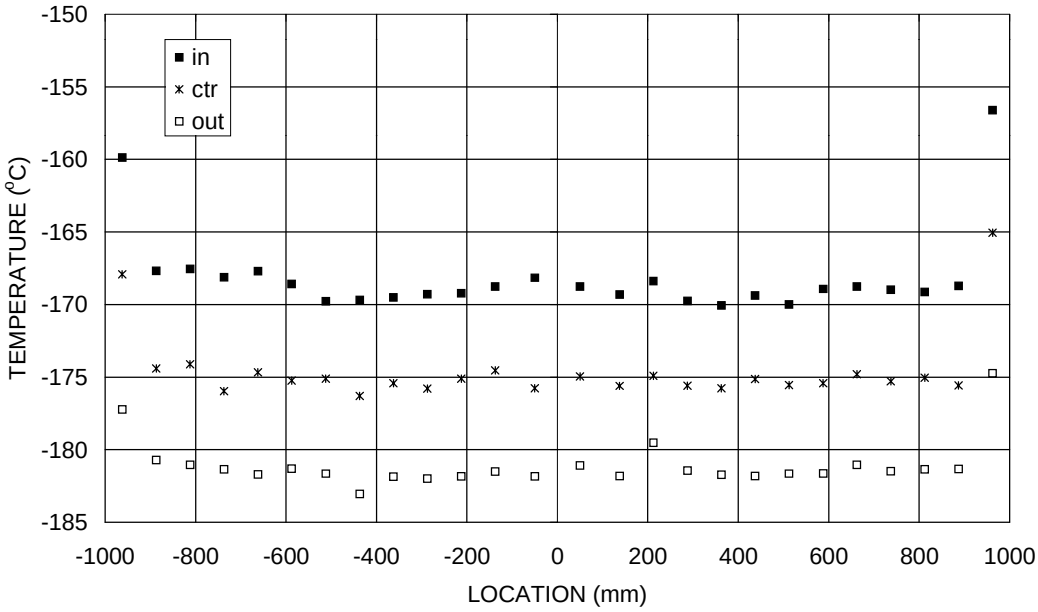

Figure 26: Upper cooler temperatures in run P8b

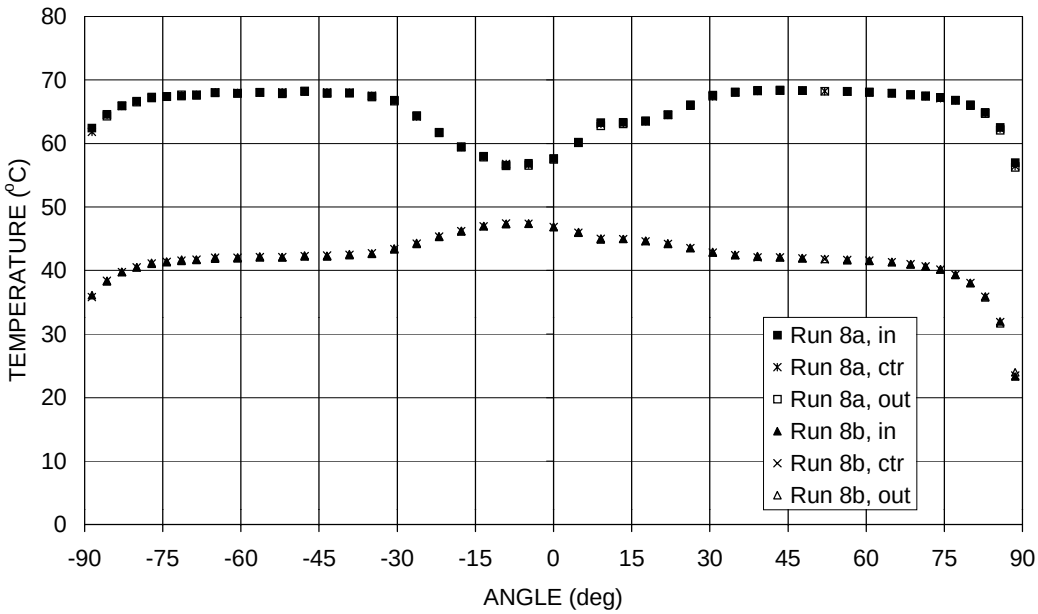

Figure 27: Side/bottom cooler temperatures in run P8

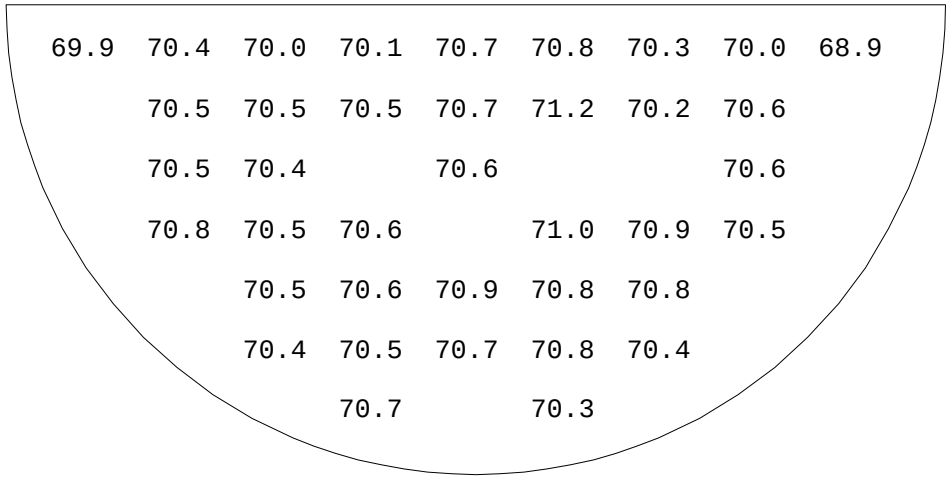

Figure 28: Pool temperatures in run P8a

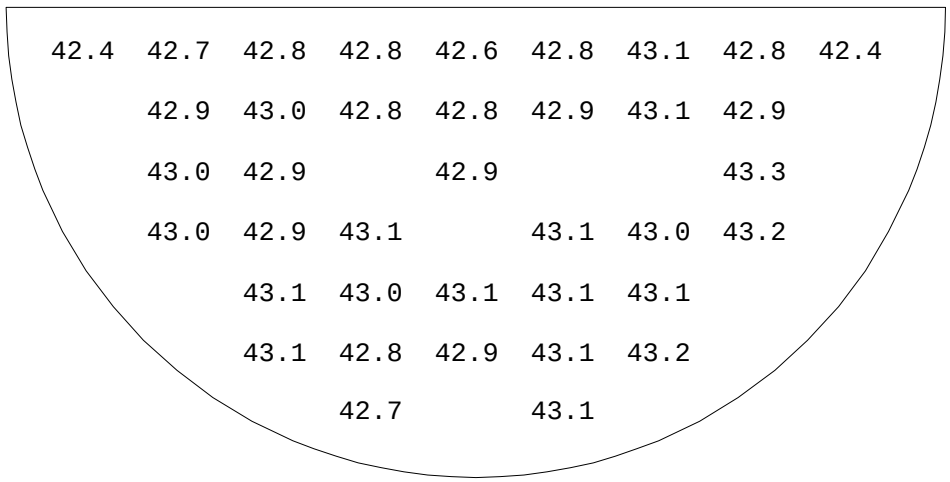

Figure 29: Pool temperatures in run P8b

5.2 Run P11

Test P11, carried out on June 12, 1998, was a rerun of test P8. The backside of the aluminum arc was insulated with mineral wool and the additional thermal resistance removed from the bottom of the test section. The power input and the temperature of the center of the pool are shown in Figure 30 and Figure 31, respectively. The steady state data corresponds to the time interval 7380 s - 7980 s. The temperature level of the pool was 61.2°C.

The results (Figure 32 - Figure 37) are consistent with test P8. The heat flux measured in the cooling unit #16 of the upper boundary is lower than in the other units (Figure 32), and was neglected when calculating the average heat flux and Nusselt number. There were no windows in the facility at that location, but its plausible that the heat transfer below cooling unit #16 was disturbed by an air bubble trapped under the upper cooler.

The film boiling was attempted also in the end of test P11, but problems were faced with accomplishing film boiling, and thus nitrogen ran out before a reasonable steady state was reached.

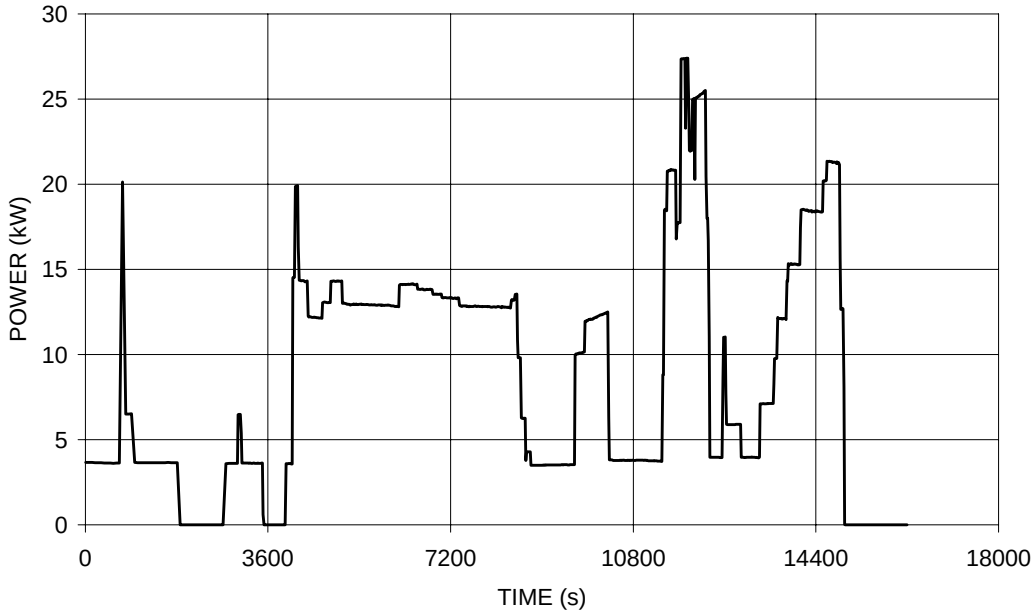

Figure 30: Electric power input during run P11

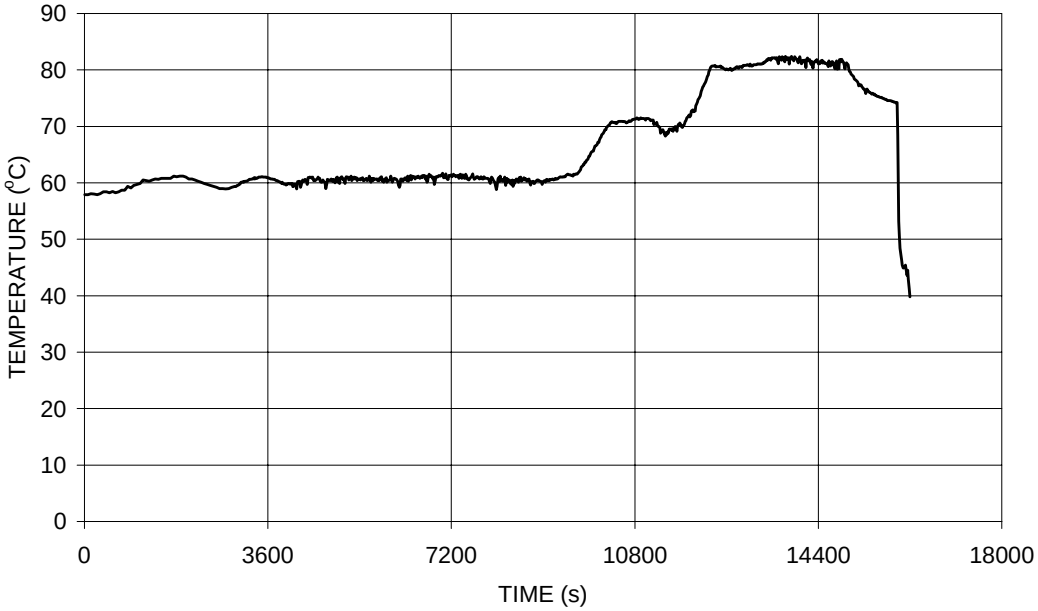

Figure 31: Temperature in the center of the pool during run P11

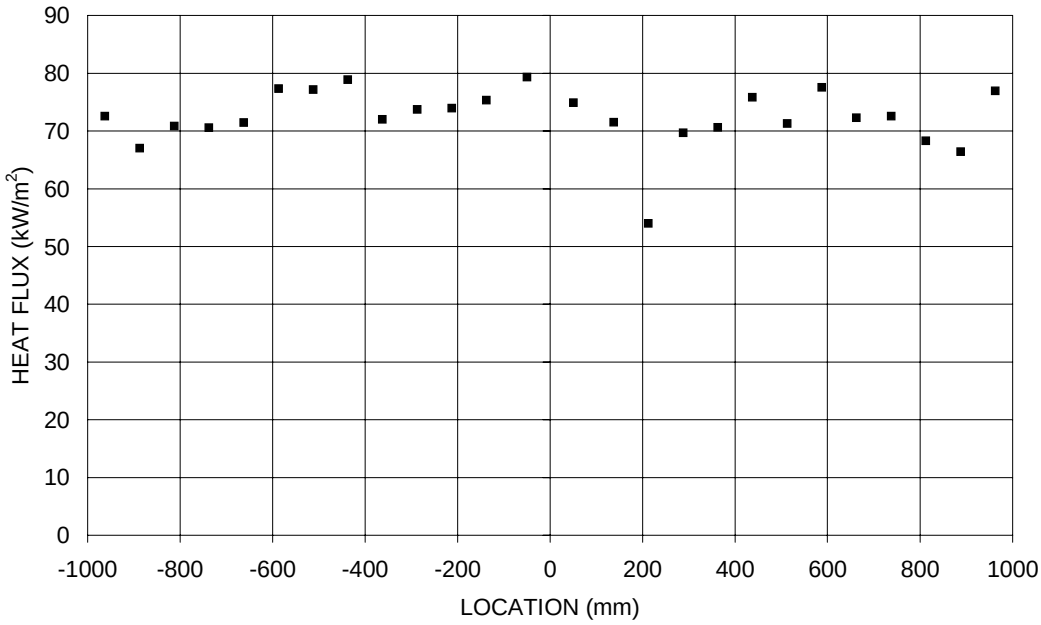

Figure 32: Local heat fluxes at the upper surface in run P11

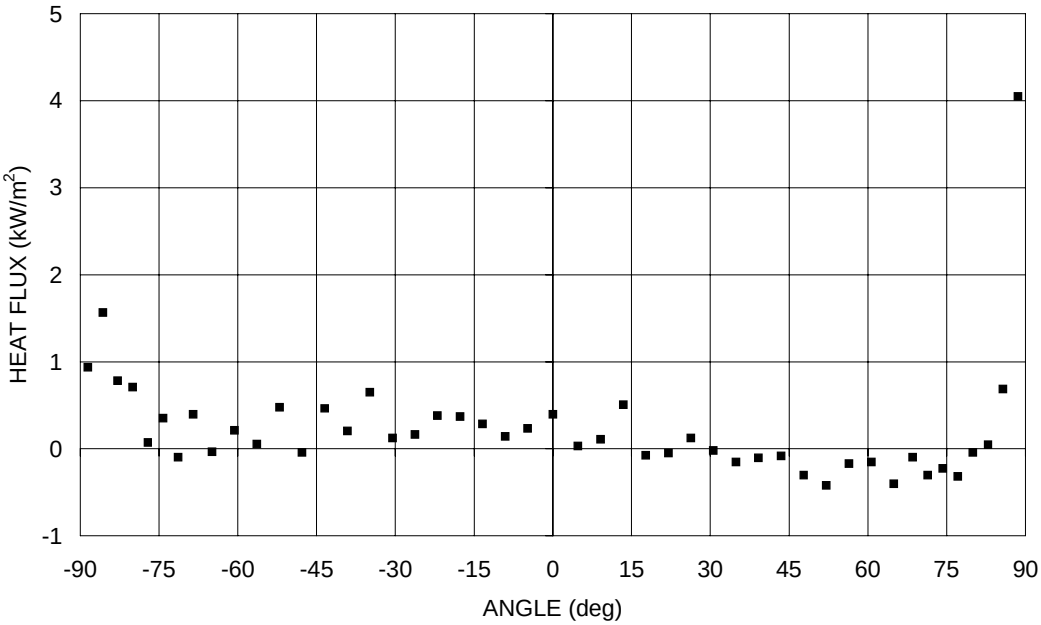

Figure 33: Local heat fluxes at the curved surface in run P11

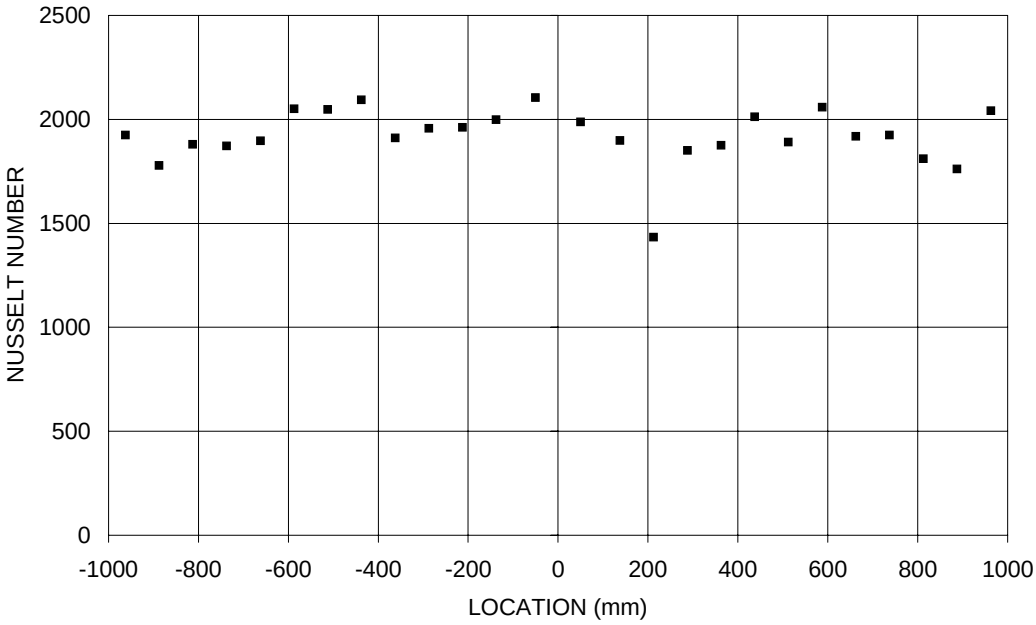

Figure 34: Local Nusselt numbers at the upper surface in run P11

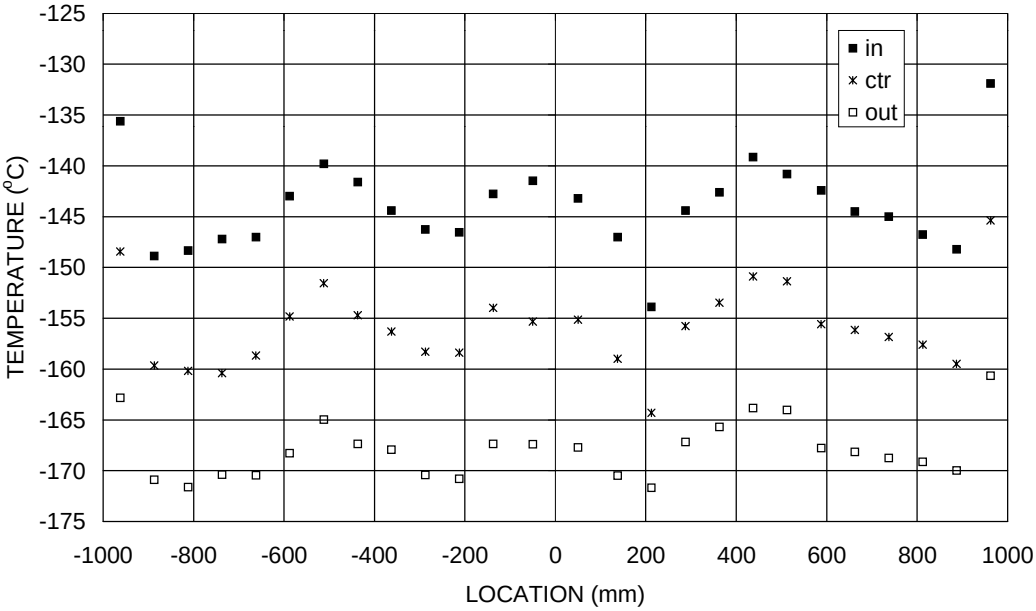

Figure 35: Upper cooler temperatures in run P11

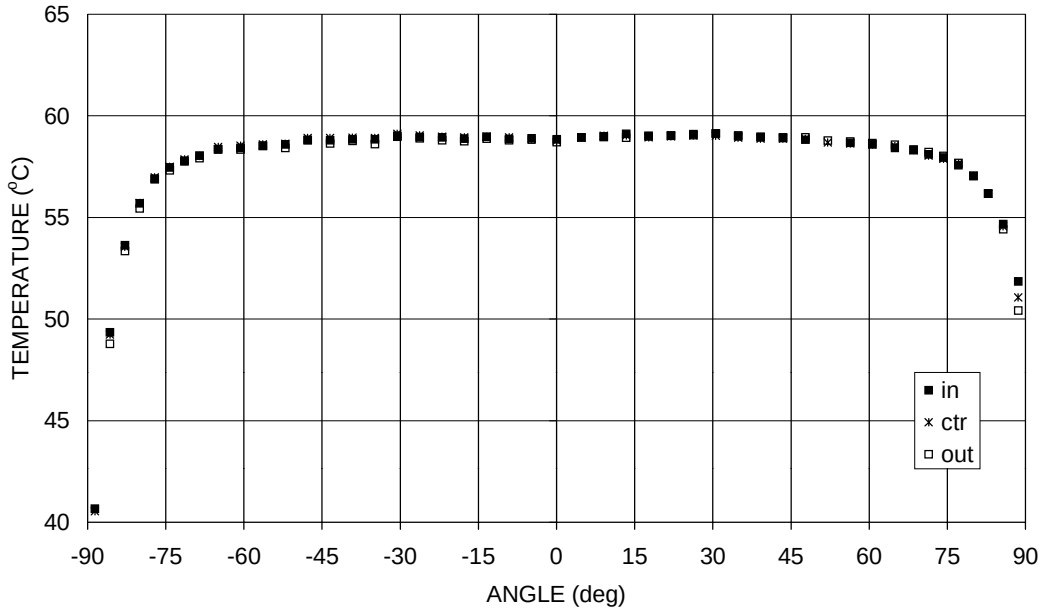

Figure 36: Side/bottom cooler temperatures in run P11

60.1	60.5	60.6	60.6	60.7	60.4	60.4	59.8	59.0
	60.7	60.9	61.1	60.9	60.9	60.6	60.5	
	60.7	60.9		60.7			60.5	
	61.0	61.2	61.1	60.9	60.7	60.9	60.2	
		61.1	61.0	60.7	60.7	60.8		
		60.9	60.9	60.6	60.9	60.5		
			61.1		60.5			

Figure 37: Pool temperatures in run P11

5.3 Run P12

Because of the problems in accomplishing and maintaining film boiling at the aluminum nitrogen boundary, new cooling mechanism was introduced in run P12 in order to measure upward heat transfer coefficient in case of non-frozen boundary. In the new setup (Figure 38), dry ice pellets were used as a coolant and about 50 dm^3 of ethanol was used as a heat carrier. In order to ensure uniform boundary condition, a dense grid was set 10 cm above the upper surface of the cooling units. Three thermocouples were installed in the ethanol-layer to control the uniformity of the coolant temperature. The backside of the aluminum arc was insulated with mineral wool as in run P11.

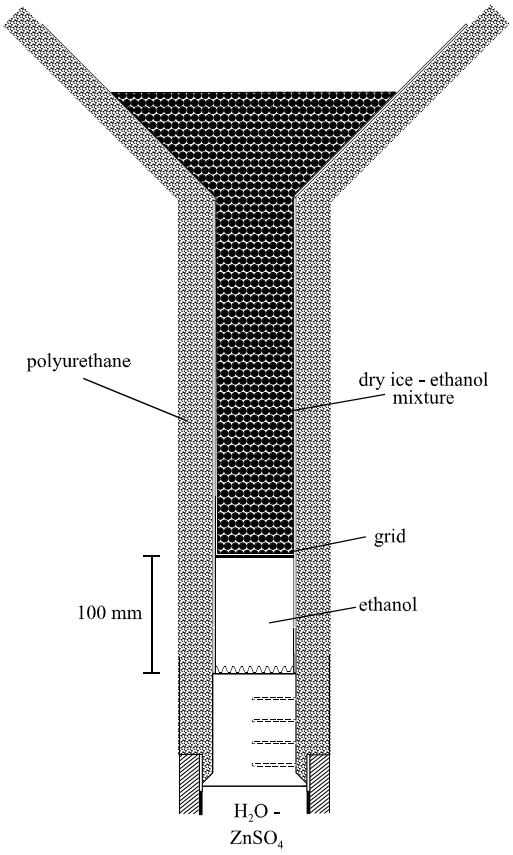

Figure 38: New cooling arrangement

Run P12, carried out on August 25, 1998, was done at three power levels (Figure 39) without interrupting the experiment between the measurement of the three levels. Run P12a corresponds to time interval 14 100 s - 14 700 s, run P12b to time interval 19 680 s - 20 280 s, and run P12c to time interval 25 800 s - 26 400 s. The temperature of the pool was 70.5°C in test P12a, 55.5°C in test P12b, and 30.3°C in test P12c (Figure 40). Before lowering the upper cooler in its place, the temperature of the water was risen to 90°C and the water was stirred in order to degas the water.

The heat flux profiles (Figure 41 and Figure 42) are qualitatively similar to tests P8 and P11. The extrapolated surface temperature in test P12a was 16.2°C and in test P12b 1.4°C (see Appendix B). During test P12c, the upper boundary was frozen. All the thermocouple readings are without correction terms based on nitrogen calibration.

The lateral walls were not opened after test P11, and consequently, the pool was not totally leaktight. Some water was draining from the lower ventilation holes in the lateral walls (at the location of air space). Because the upper boundary was non-frozen in test P12a and P12b, the right width of the test section is important. If the water can access the lateral faces of the cooling units, the temperature field in the cooling unit may be distorted. The measured uniform heat flux profiles do not support this assumption. However, the width of the test section was not checked before test P12, and therefore, this possible error in test setup cannot be excluded[1].

[1] The lateral walls were opened after test P12. At the beginning of test P13, the width of the pool in the middle was oberved to be ~12 cm, and the lateral walls were straightened.

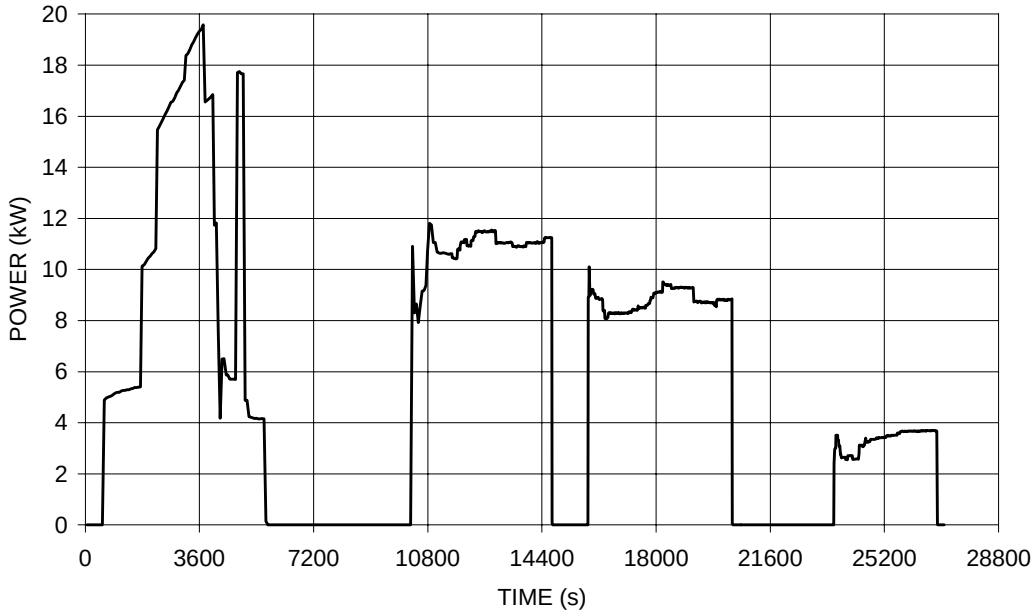

Figure 39: Electric power input during run P12

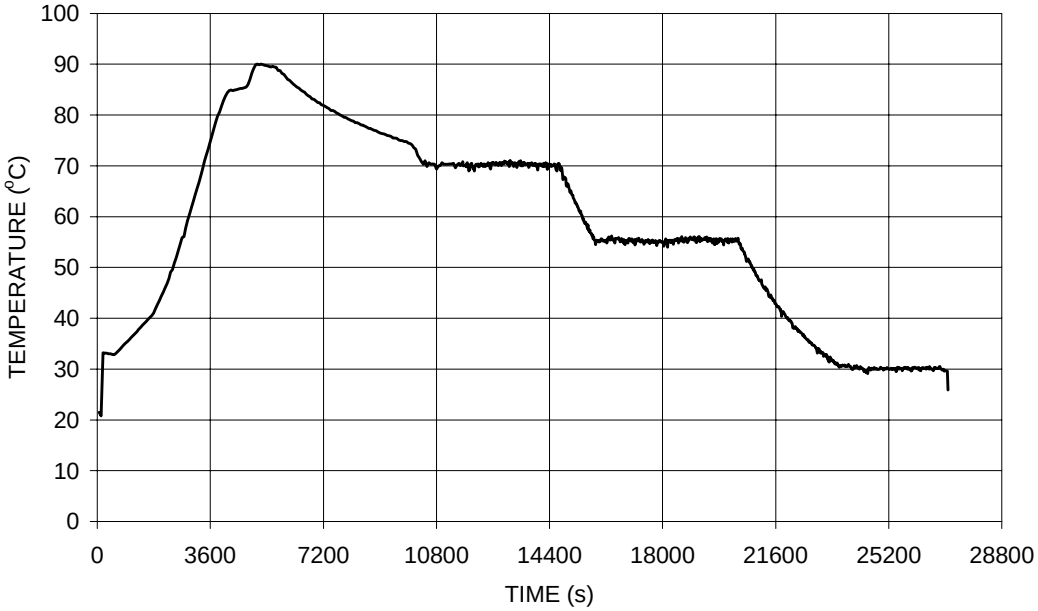

Figure 40: Temperature in the center of the pool during run P12

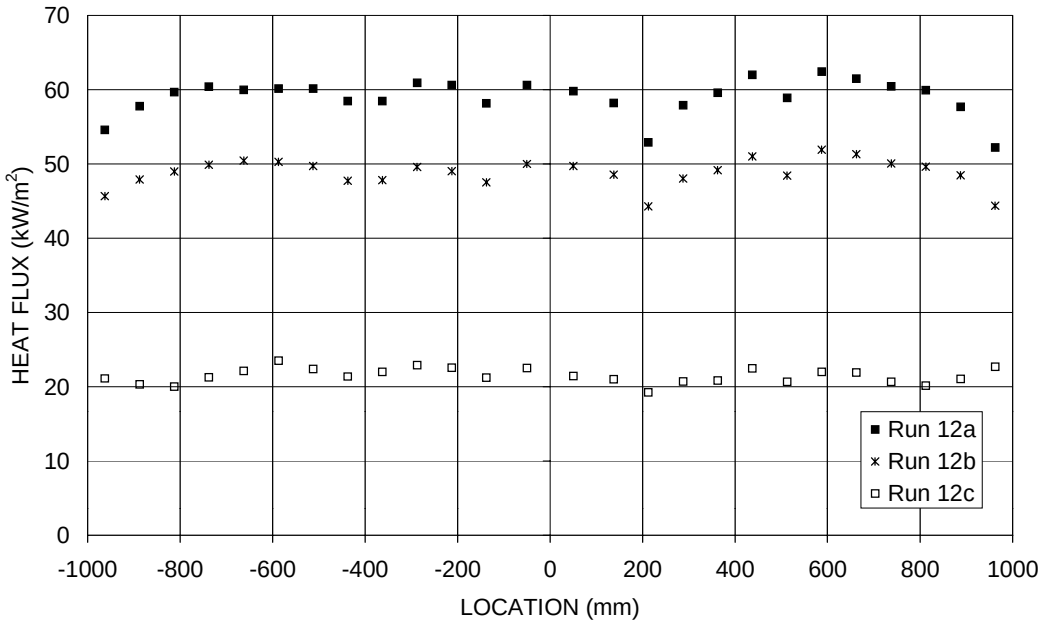

Figure 41: Local heat fluxes at the upper surface in run P12

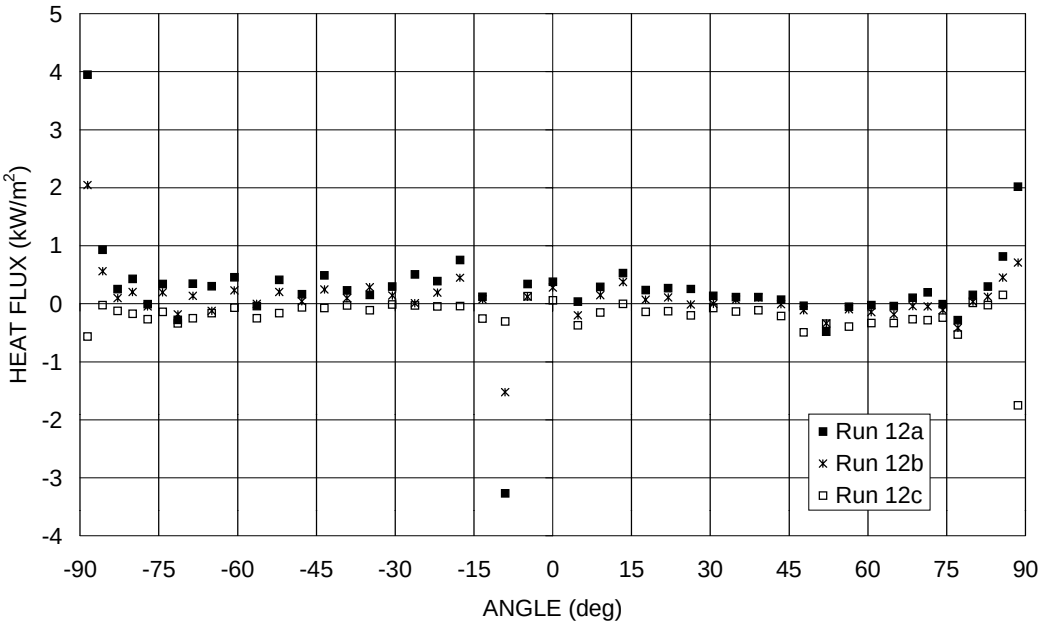

Figure 42: Local heat fluxes at the curved surface in run P12

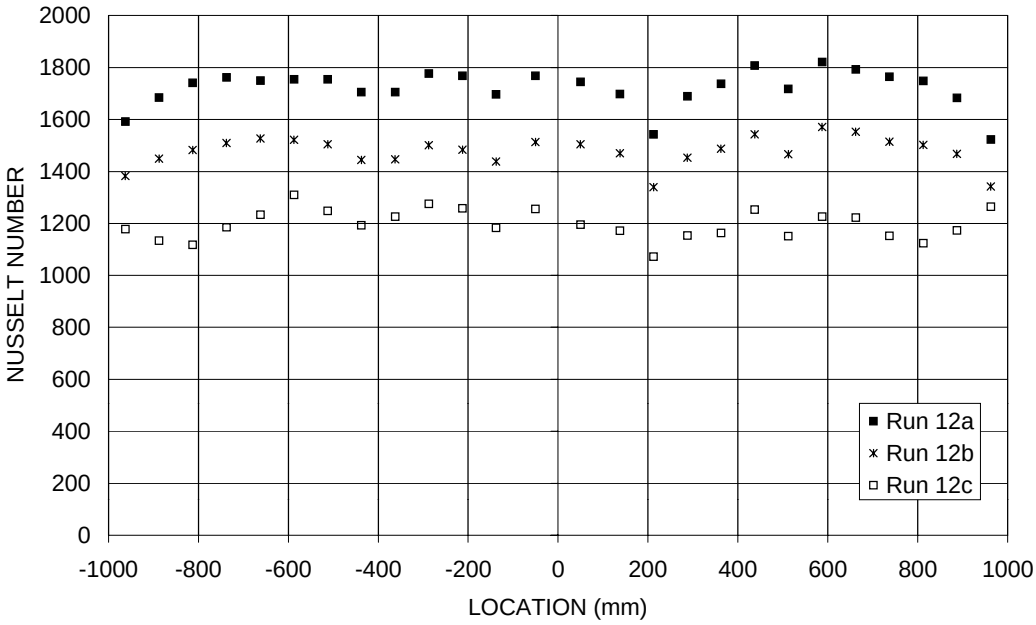

Figure 43: Local Nusselt numbers at the upper surface in run P12

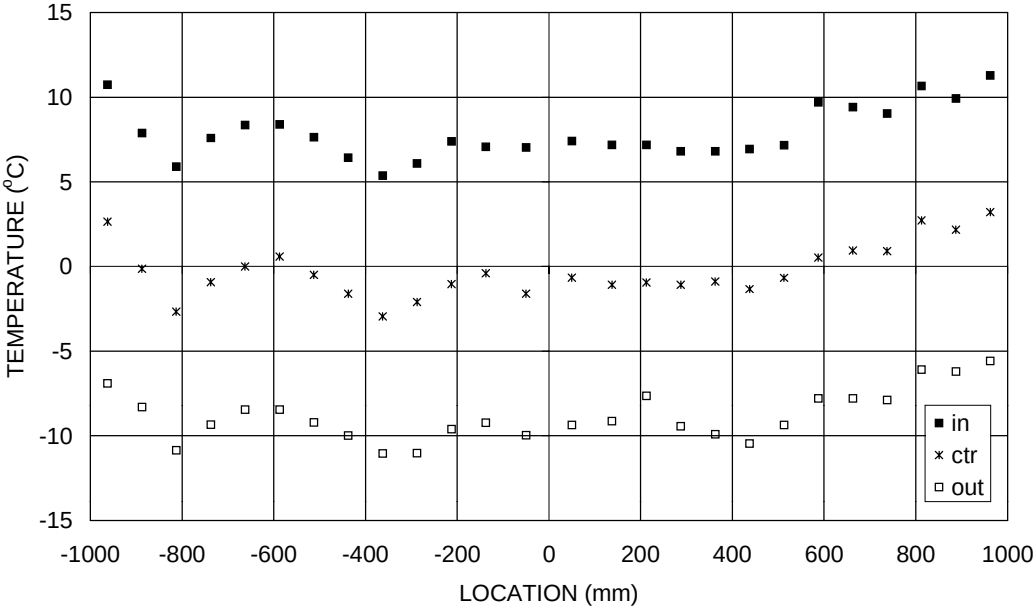

Figure 44: Upper cooler temperatures in run P12a

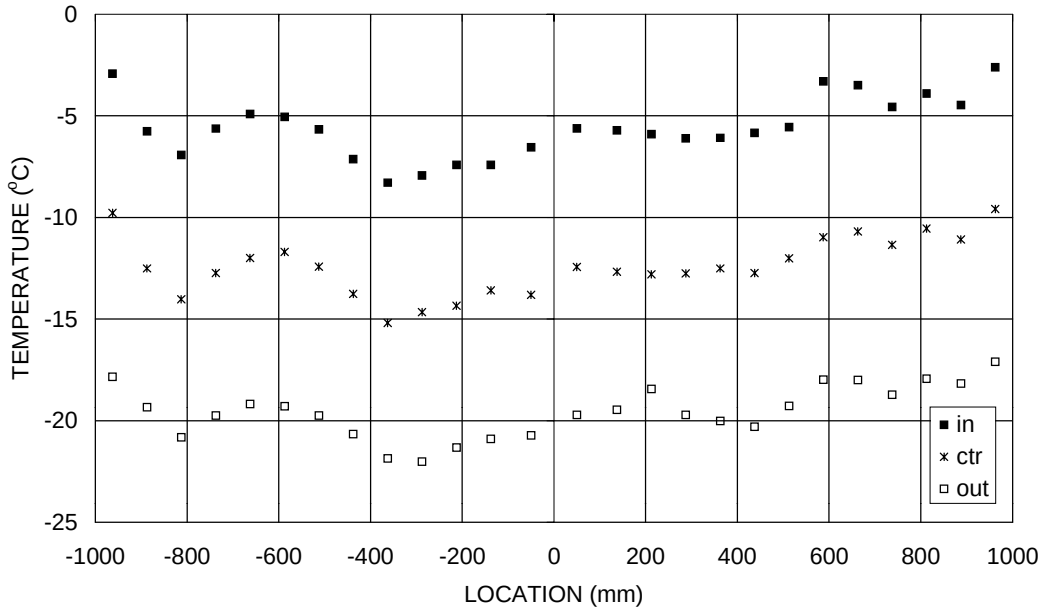

Figure 45: Upper cooler temperatures in run P12b

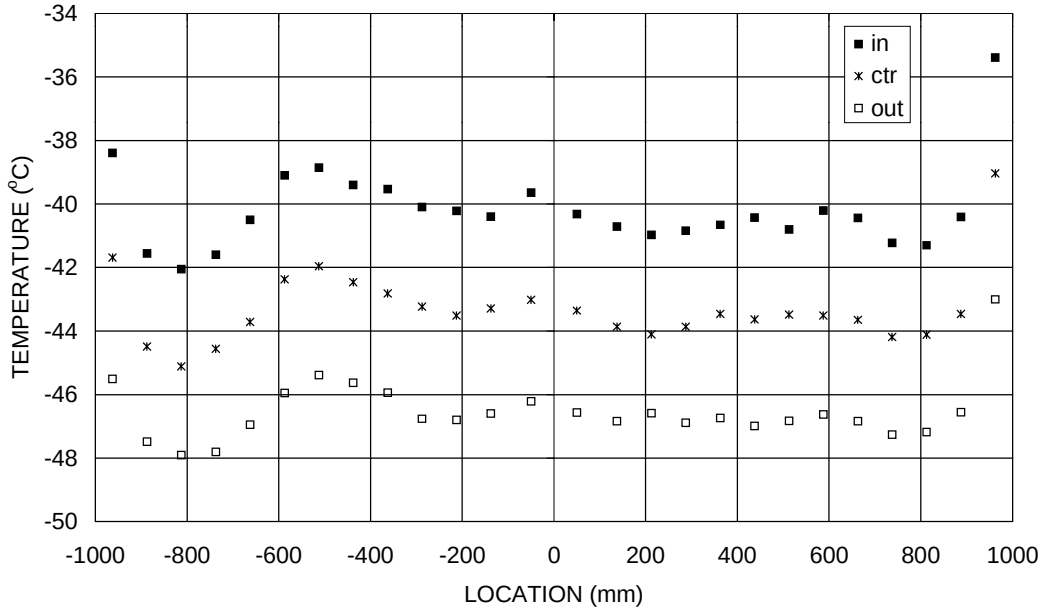

Figure 46: Upper cooler temperatures in run P12c

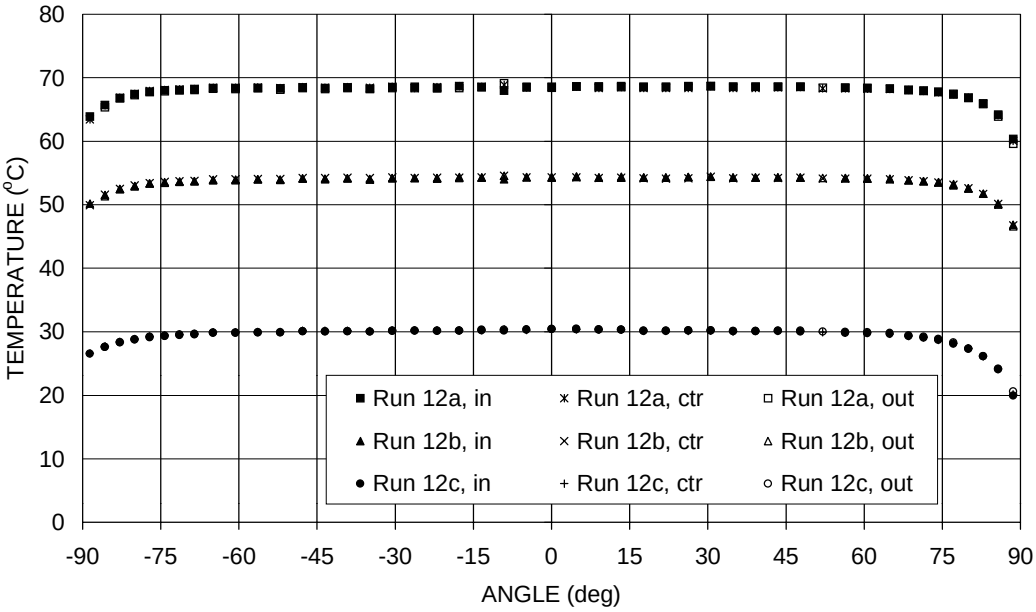

Figure 47: Side/bottom cooler temperatures in run P12

69.6	70.0	70.1	70.1	69.8	69.7	69.5	69.6	68.9
	70.2	70.4	70.2	70.1	70.0	69.7	69.7	
	70.2	70.3		70.1			69.8	
	70.3	70.5	70.2	70.2	70.2	70.0	69.7	
		70.5	70.2	70.1	70.0	69.9		
		70.3	70.2	70.1	70.0	69.9		
			70.1		69.9			

Figure 48: Pool temperatures in run P12a

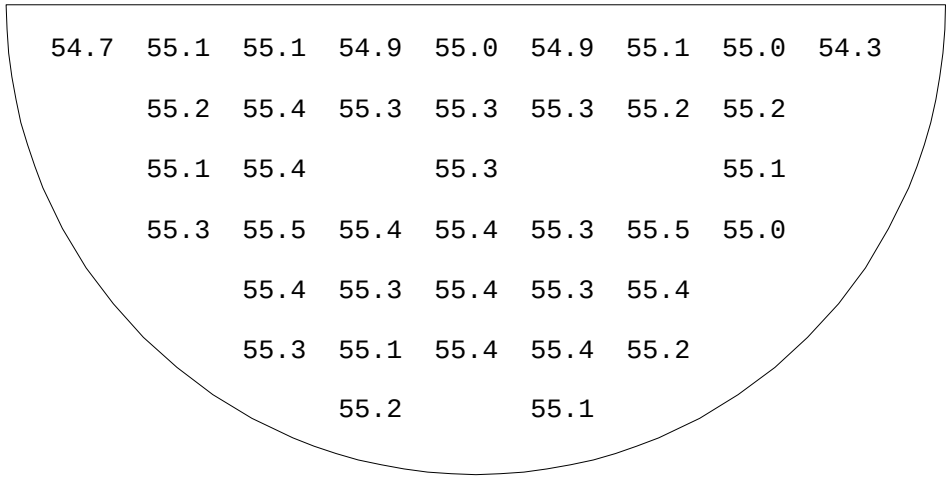

Figure 49: Pool temperatures in run P12b

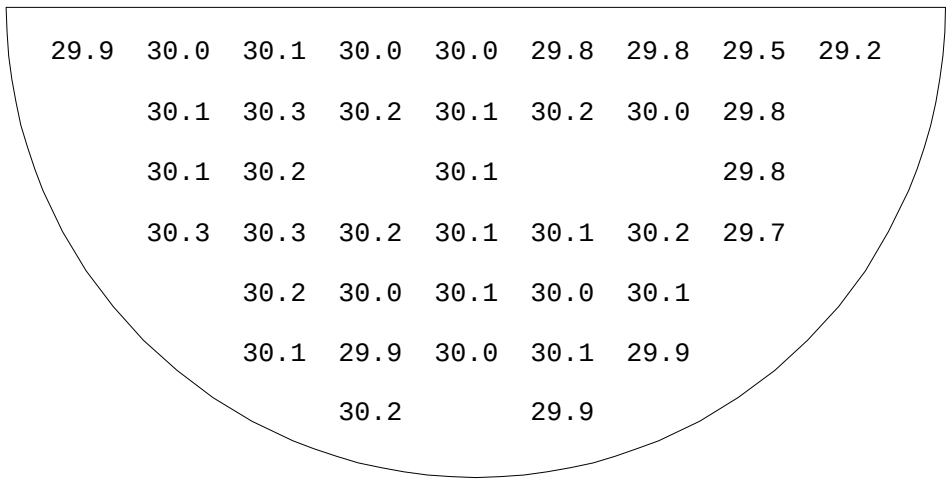

Figure 50: Pool temperatures in run P12c

5.4 Run P13

In COPO II-AP facility, the elevation of the upper cooler cannot be varied. Therefore, to change the height of the pool (and Ra'), a segment of insulant material was installed on the bottom of the test section as shown in Figure 51. The height of the segment was 250 mm. The upper surface of the segment was between cooling units #14 and #15 (#34 and #33 on the right side of the arc), and between electrodes 6 and 7 (i.e., the lowest electrode was not in use). The backside of the curved boundary was insulated with mineral wool and the upper boundary of the pool cooled with dry ice-ethanol -mixture.

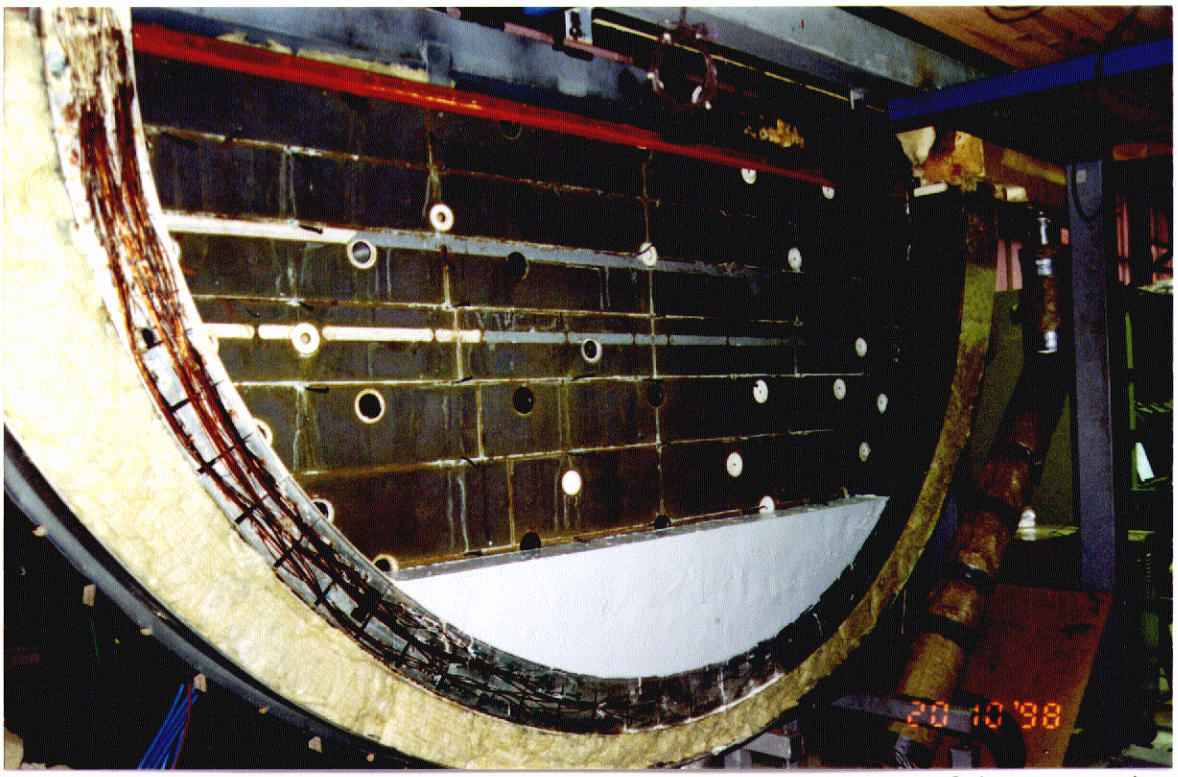

Figure 51: 250 mm height polyurethane segment on the bottom of the test section before run P13

Run P13, carried out on October 22, 1998, was done at four power levels (Figure 52). Run P13a corresponds to time interval 10 080 s - 10 380 s, run P13b to time interval 15 900 s - 16 200 s, run P13c to time interval 22 800 s - 24 900 s, and run P13d to time interval 27 600 s - 27 900 s. The temperature of the pool (Figure 53) was 70.2°C, 55.4°C, 30.3°C and 80.7°C, respectively.

The results are shown in Figure 54 - Figure 65. Except for run P13d, all the cooling units were taken into account when calculating the average heat fluxes and Nusselt numbers. In run P13d, the heat flux measured from the upper boundary cooling unit #26 was neglected, because a small air bubble was trapped under it disturbing the heat transfer.

The extrapolated surface temperature in test P13a is 14.3°C, in test P13b -0.2°C[1], and in test P13d 22.0°C (see Appendix B). During test P13c, the upper boundary was frozen. All the thermocouple readings are without nitrogen calibration based correction terms.

The temperature profile at the curved boundary (Figure 61) is not symmetrical. There is no clear explanation for this. One possible reason is the fact, that the pool-segment joint was not totally leaktight. The water in the gap between the polyurethane segment and the lateral walls of the pool may have warmed the aluminum arc unevenly. However, the measured temperature fields (Figure 62 - Figure 65) don't seem to support this assumption. The two lowermost thermocouples were located at the level of polyurethane segment, and they were bent between the segment and the lateral wall. The readings from these two thermocouples don't significantly differ from each other.

The gasket between the lateral walls and the aluminum arc was modified after test P12. Since the aluminum arc was not cooled, the former PTFE sheets were replaced with a rubber sheet. No leakages from the pool into the air space were observed during test P13.

[1] Extrapolated surface temperature is -0.3°C. However, since no ice was seen at the upper boundary, the best estimate value for the upper boundary temperature was selected to be the freezing temperature -0.2°C.

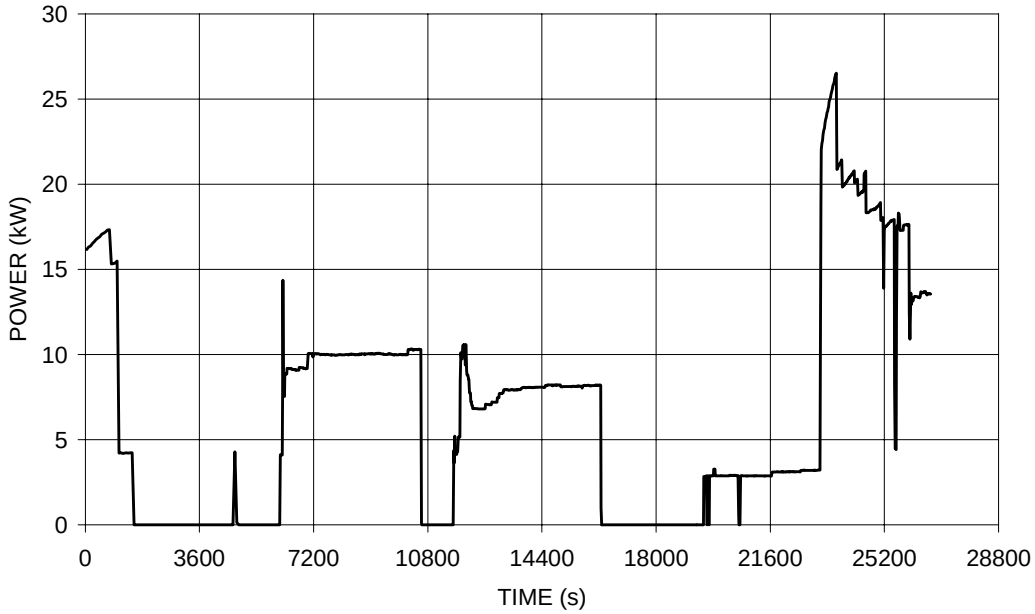

Figure 52: Electric power input during run P13

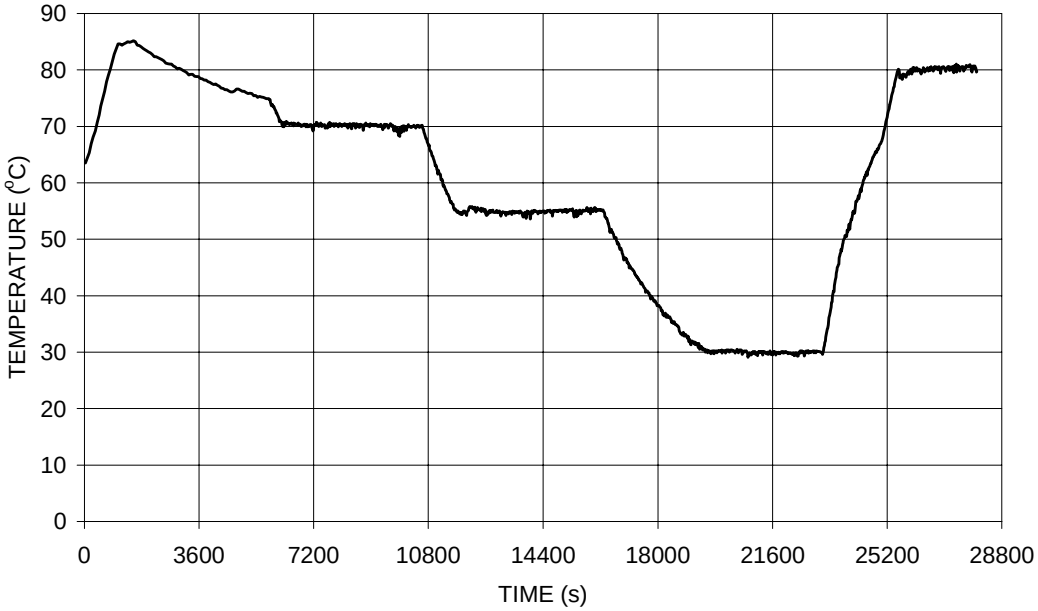

Figure 53: Temperature in the center of the pool during run P13

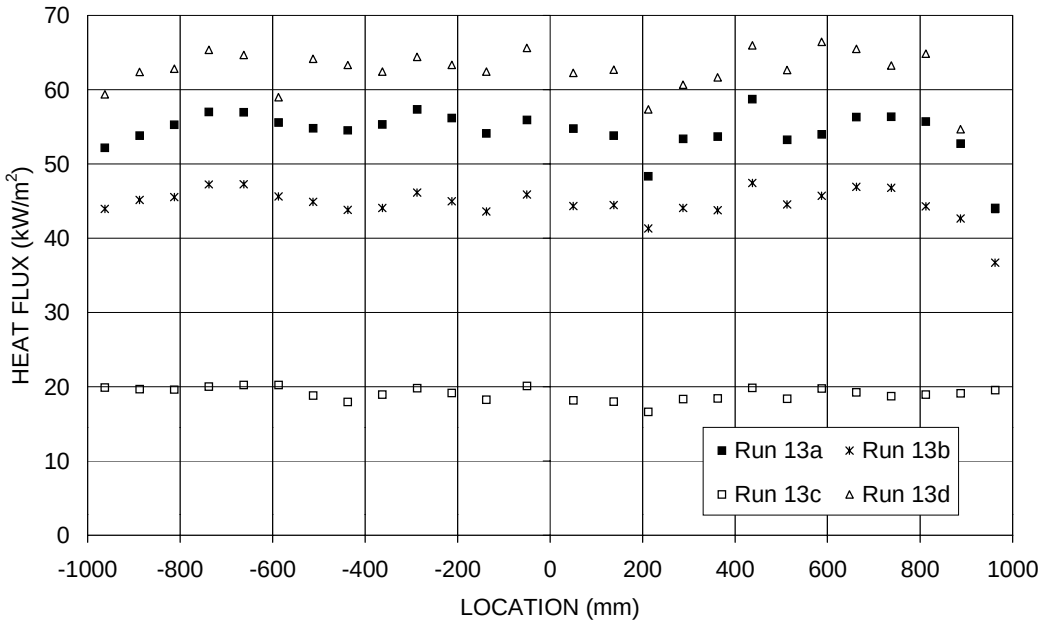

Figure 54: Local heat fluxes at the upper surface in run P13

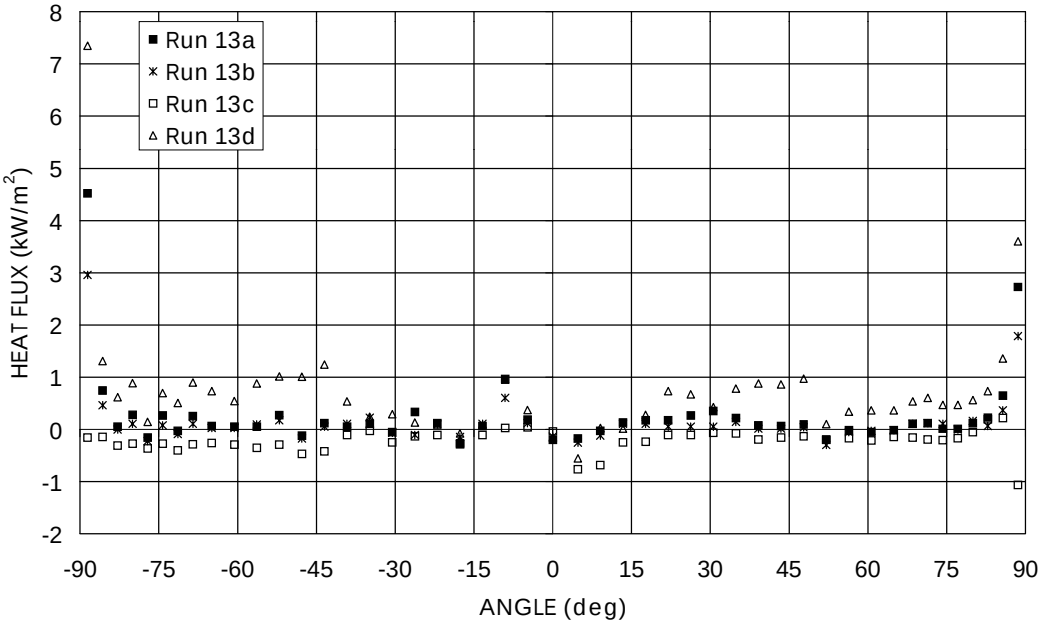

Figure 55: Local heat fluxes at the curved surface in run P13

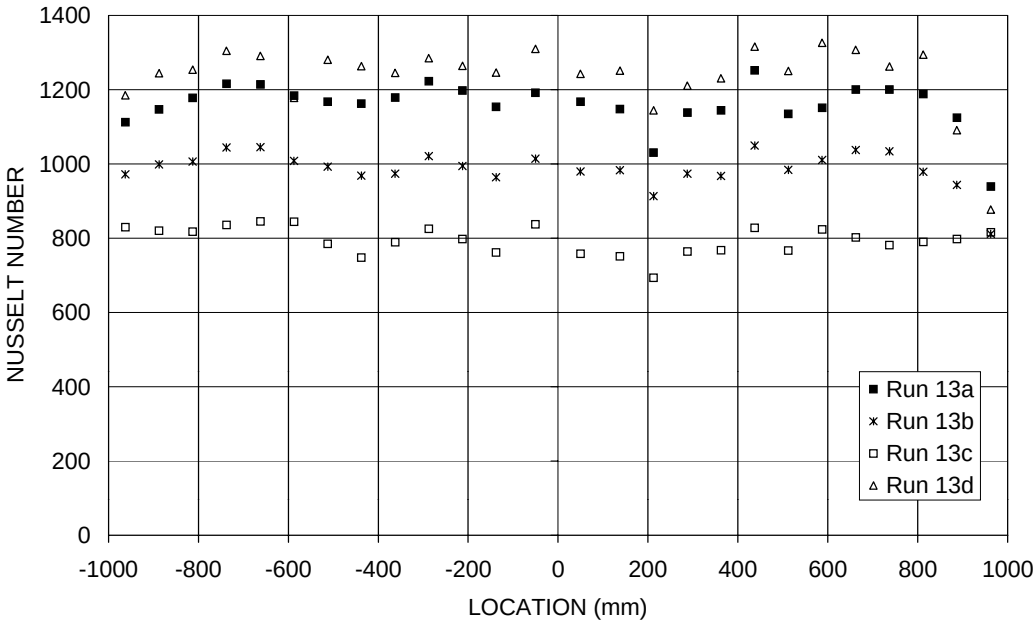

Figure 56: Local Nusselt numbers at the upper surface in run P13

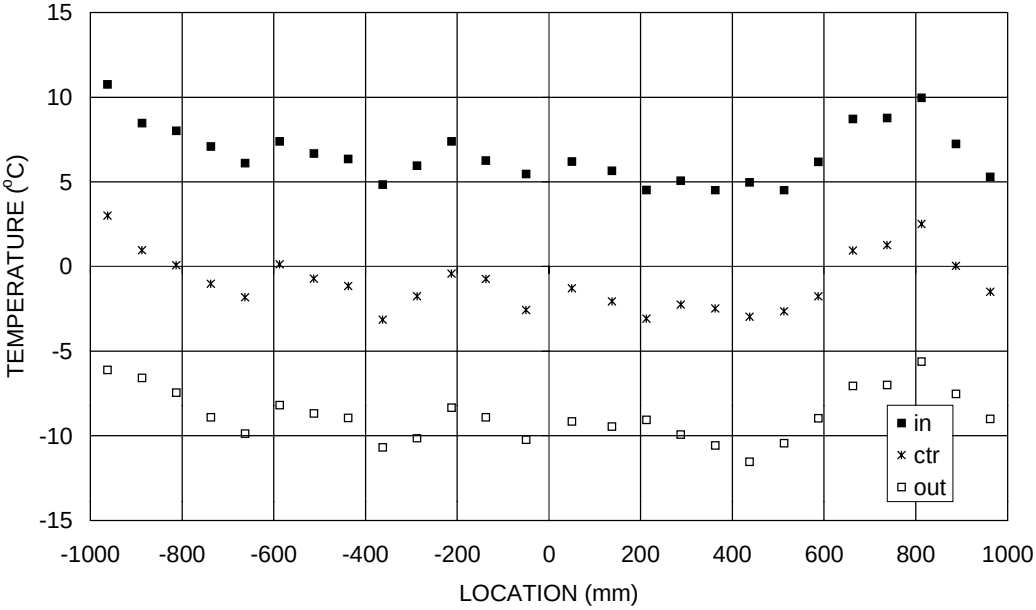

Figure 57: Upper cooler temperatures in run P13a

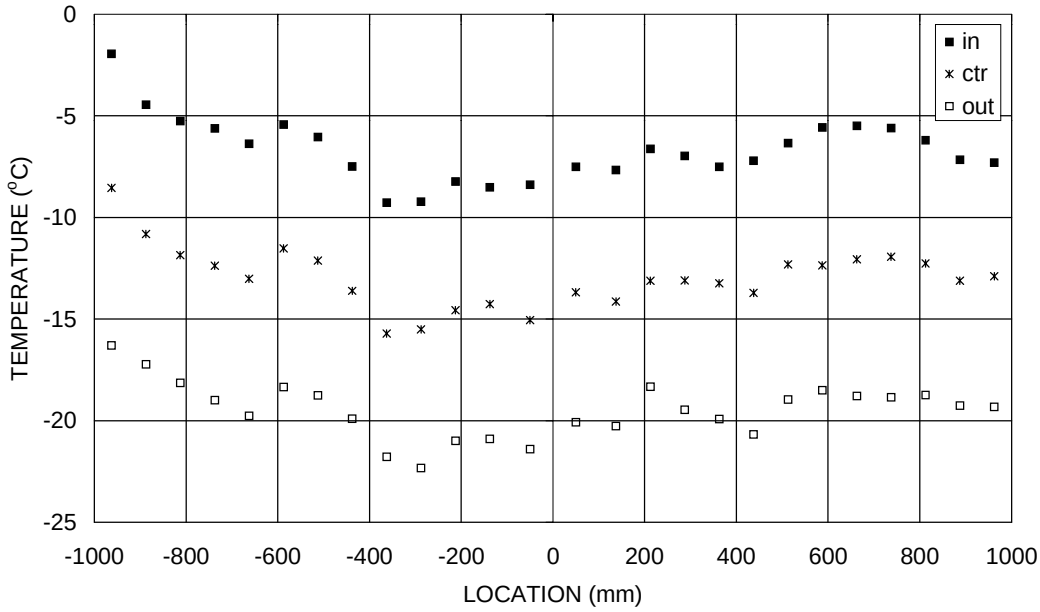

Figure 58: Upper cooler temperatures in run P13b

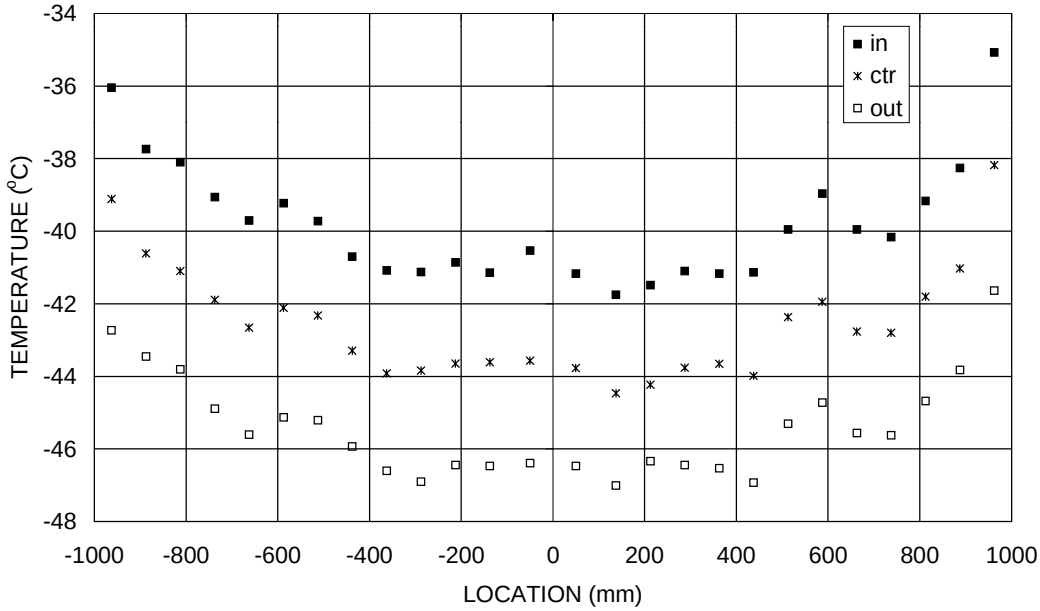

Figure 59: Upper cooler temperatures in run P13c

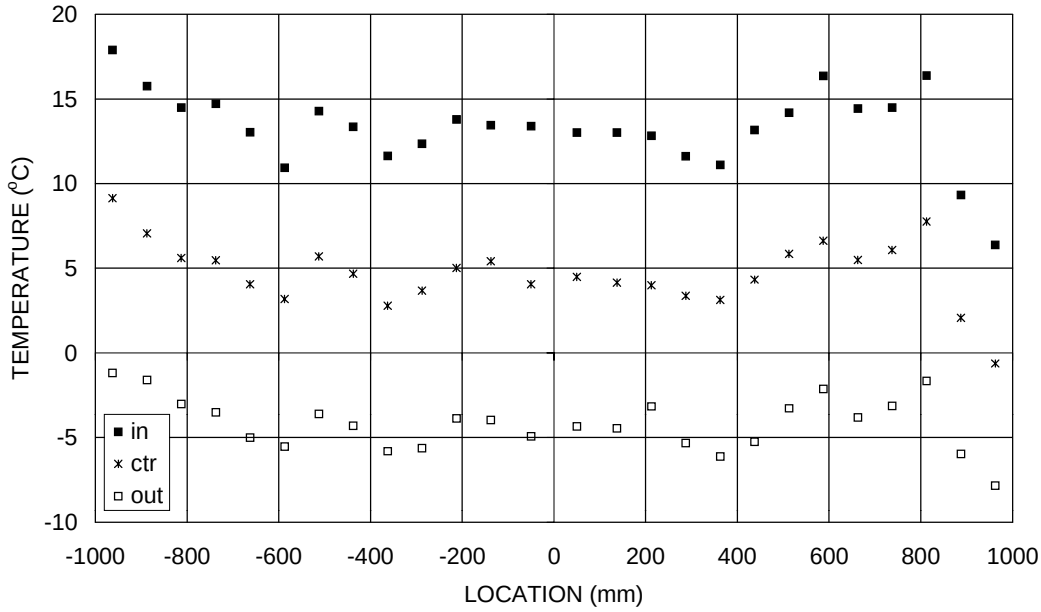

Figure 60: Upper cooler temperatures in run P13d

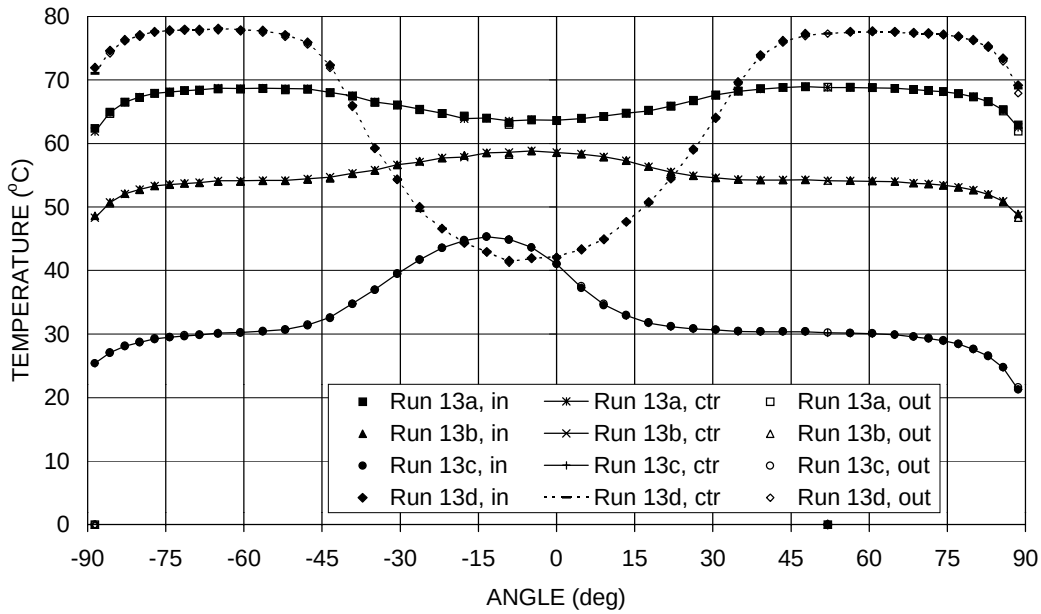

Figure 61: Side/bottom cooler temperatures in run P13

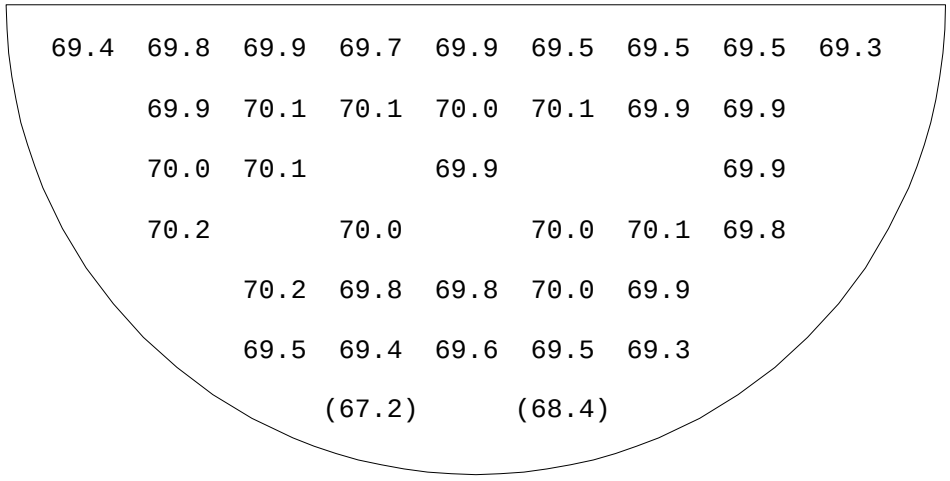

Figure 62: Pool temperatures in run P13a. Two lowermost thermocouples are located at the level of polyurethane segment

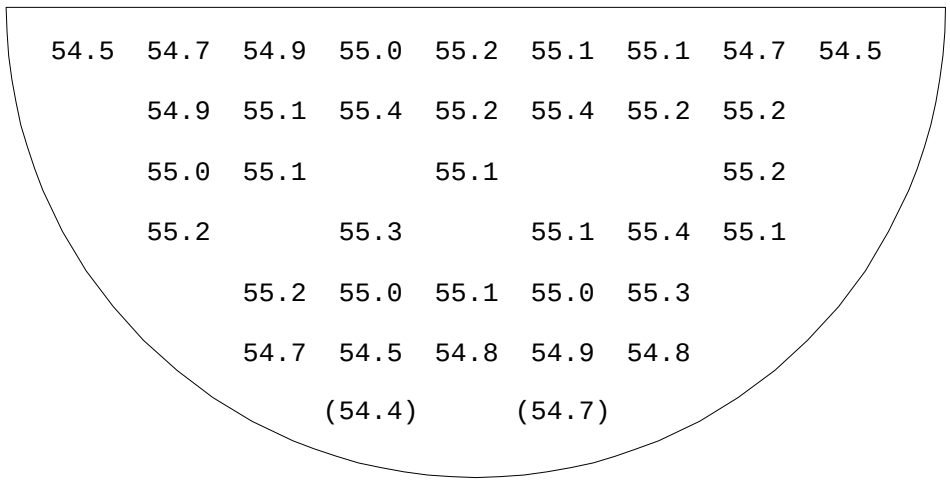

Figure 63: Pool temperatures in run P13b. Two lowermost thermocouples are located at the level of polyurethane segment

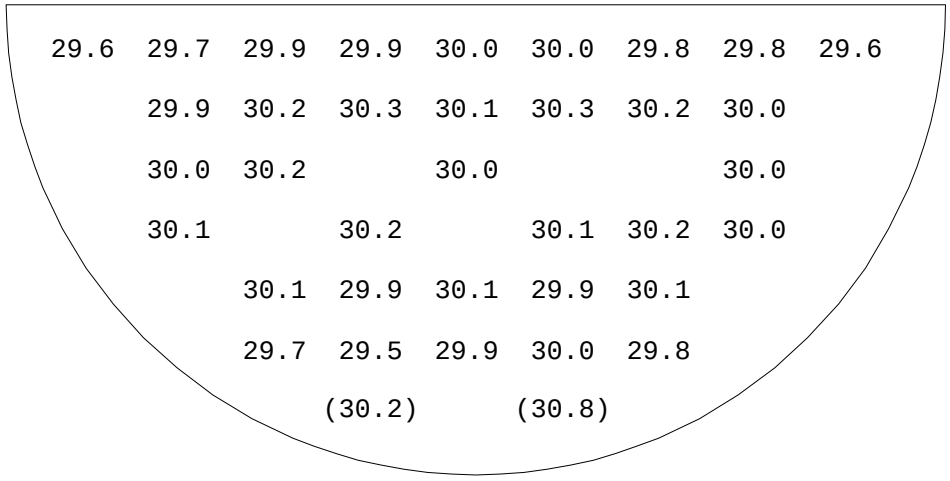

Figure 64: Pool temperatures in run P13c. Two lowermost thermocouples are located at the level of polyurethane segment

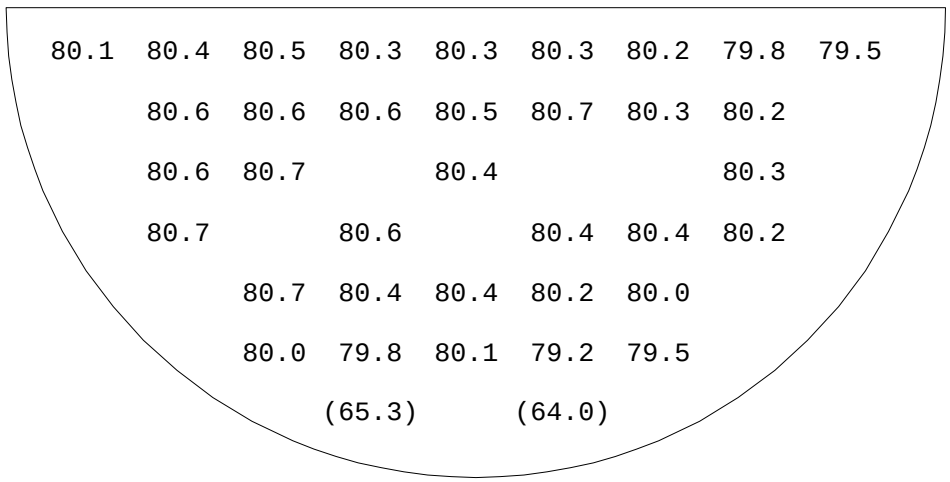

Figure 65: Pool temperatures in run P13d. Two lowermost thermocouples are located at the level of polyurethane segment

5.5 Run P14

As discussed in Section 5.3, the tests section may have been too wide during experiment P12 disturbing[1] the heat transfer results. Therefore, a rerun of test P12 was carried out on November 3, 1998. Before the experiment, the polyurethane segment was removed from the bottom of the test section. Care was taken to ensure right width of the test section, as well as with other preparations.

The power input during the test is shown in Figure 66 and the temperature of the center of the pool in Figure 67. The steady state data corresponds to time interval 14 400 s - 15 000 s. The temperature level of the pool was 70.5°C and the extrapolated upper surface temperature 19.9°C. Qualitatively, the results (Figure 68 - Figure 73) are similar to the test P12. Difference between the average values is discussed in Section 5.7 below.

During the experiment, a question was raised of the effect of the 1.5 mm width cuts between the cooling units. Because the lower boundary of the cooling units is non-frozen, water may access these gaps[2] disturbing the heat transfer. Therefore, after measurement of one power level, the experiment was stopped and the gaps between the cooling units were blocked with plastic paste.

[1] Because the upper boundary was non-frozen in test P12a and P12b, the right width of the test section is important. If the water can access the lateral faces of the cooling units, the temperature field in the cooling units may be distorted.

[2] Most of these gaps were, at least partly, blocked with polyurethane.

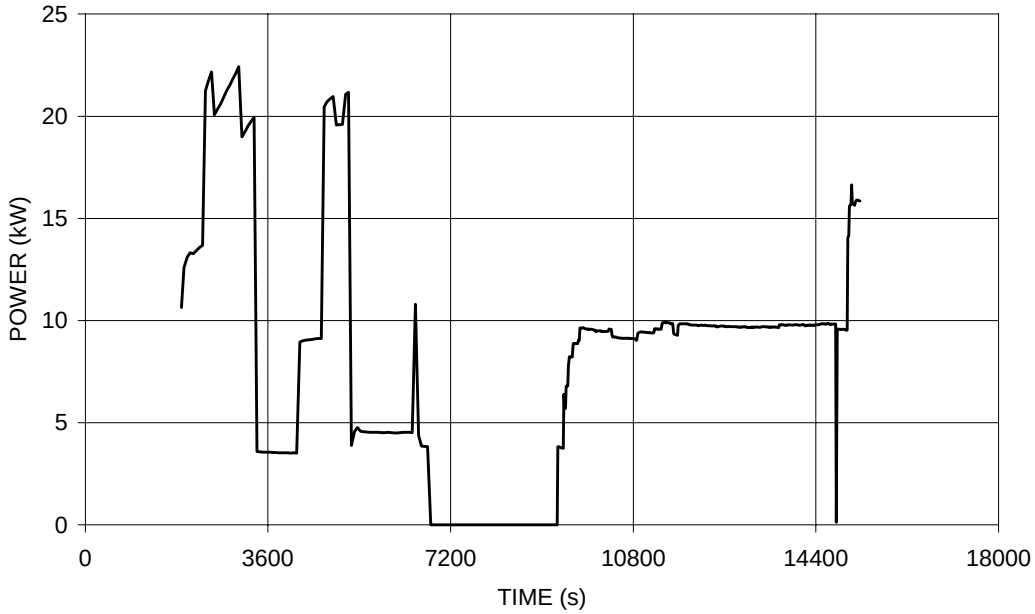

Figure 66: Electric power input during run P14

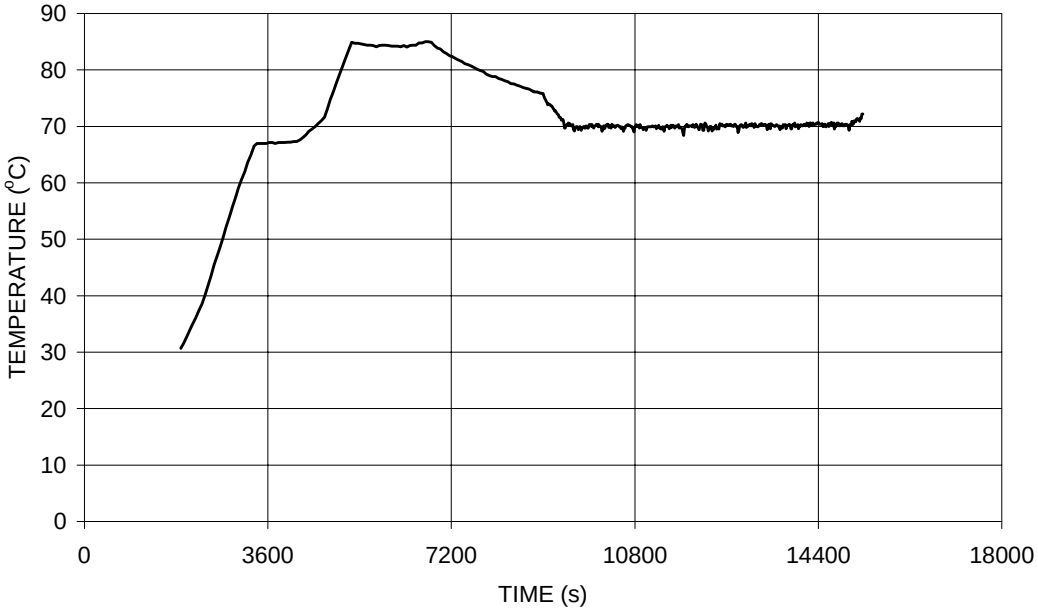

Figure 67: Temperature in the center of the pool during run P14

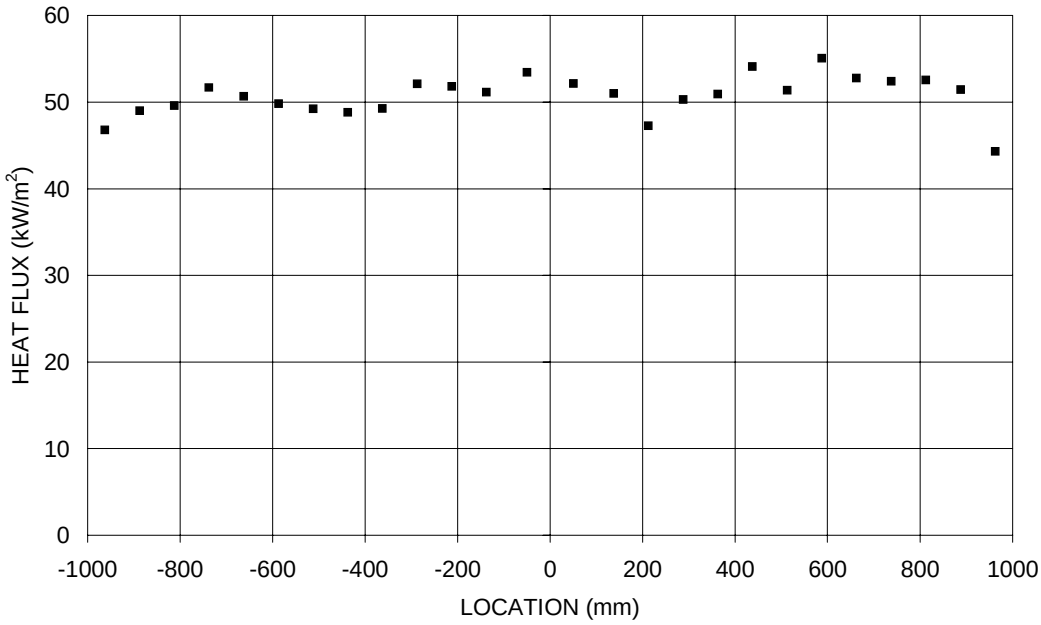

Figure 68: Local heat fluxes at the upper surface in run P14

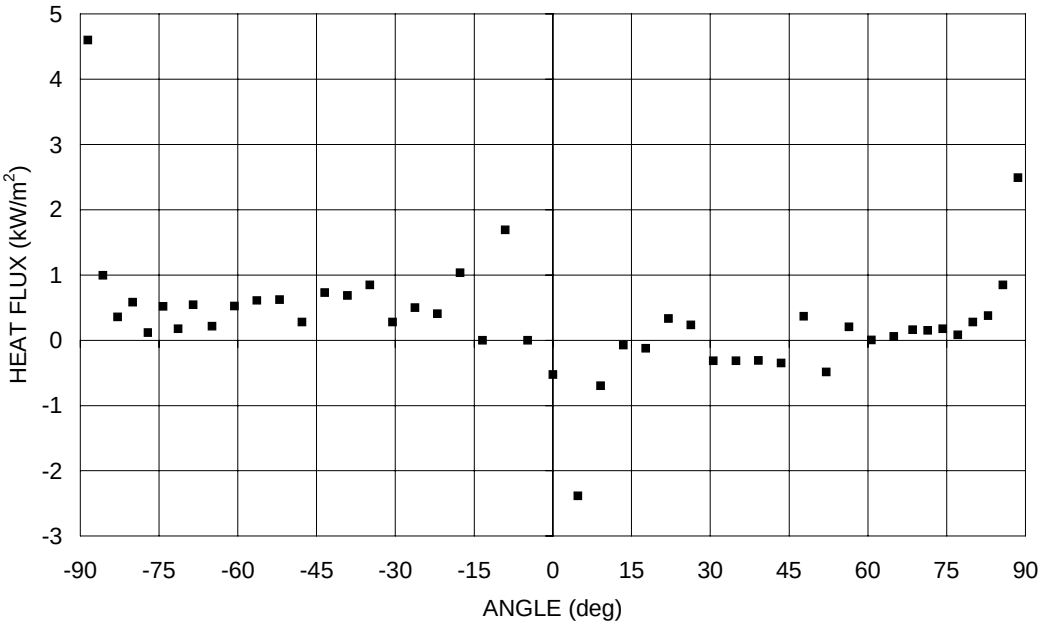

Figure 69: Local heat fluxes at the curved surface in run P14

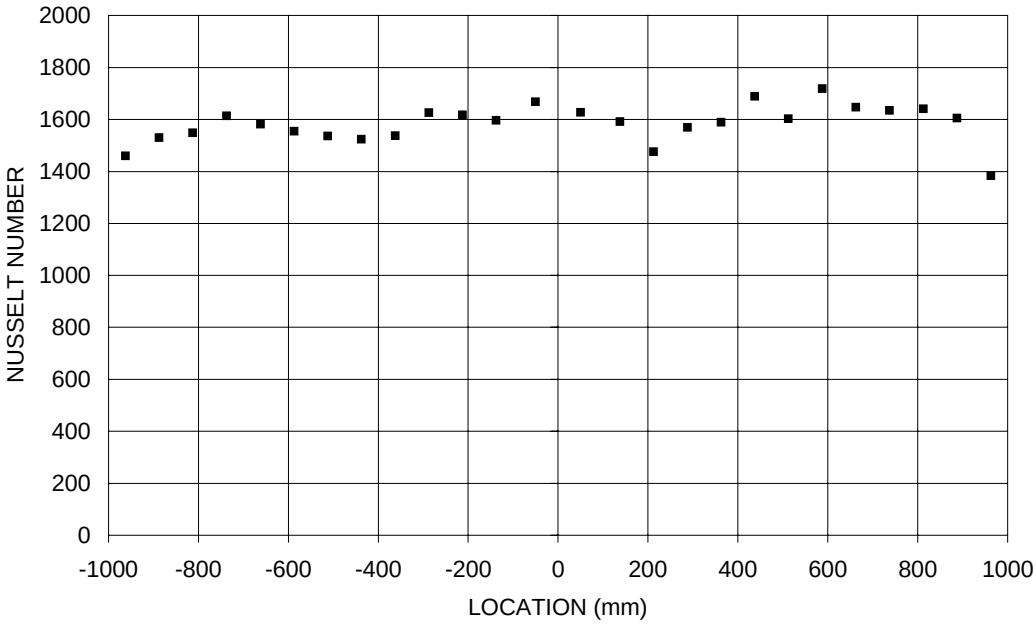

Figure 70: Local Nusselt numbers at the upper surface in run P14

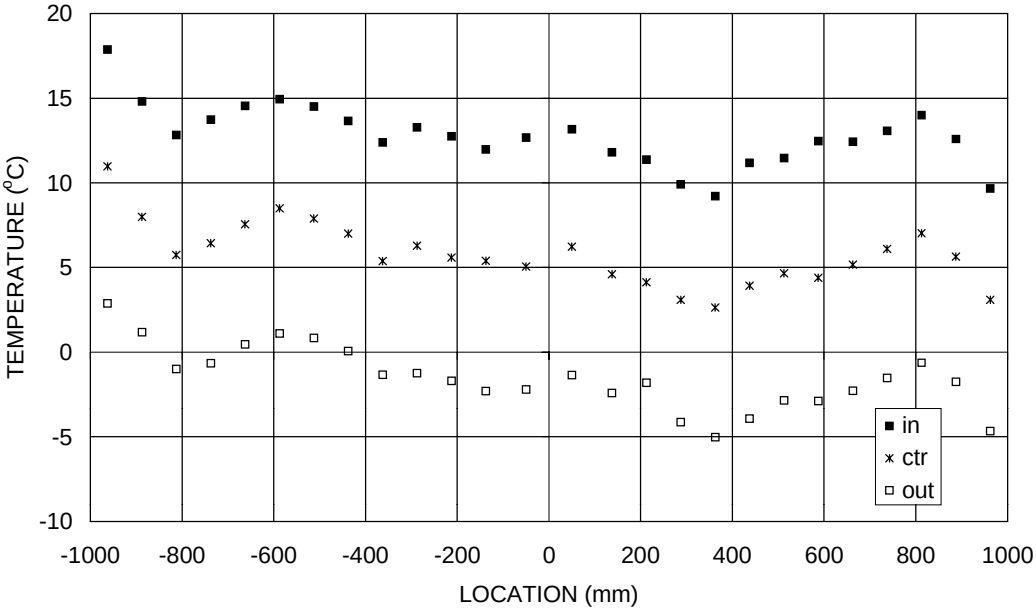

Figure 71: Upper cooler temperatures in run P14

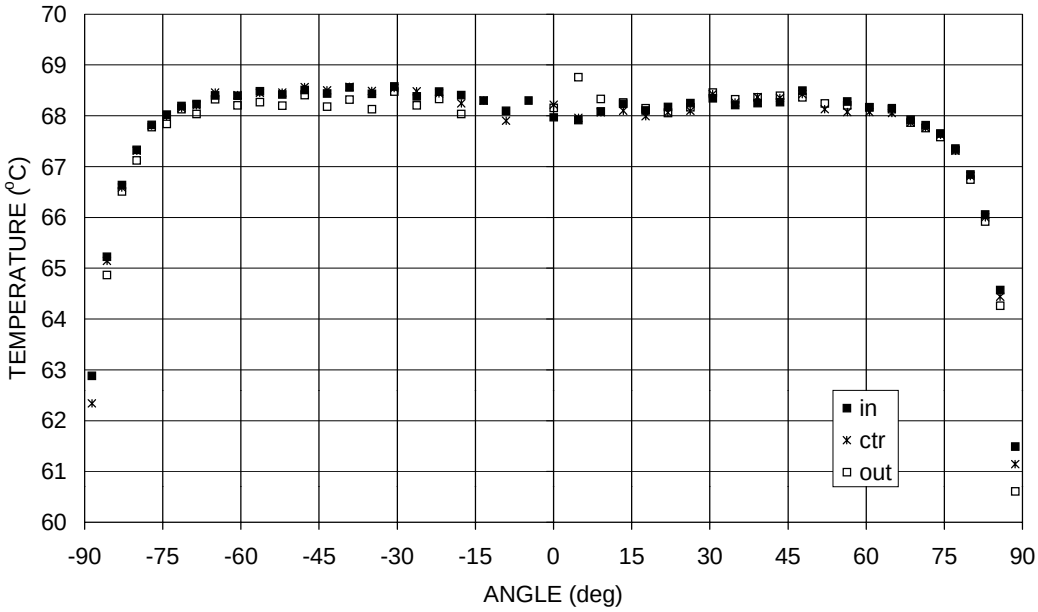

Figure 72: Side/bottom cooler temperatures in run P14

69.8	70.0	70.1	70.1	70.1	70.0	69.9	69.7	69.4
	70.2	70.5	70.4	70.3	70.3	70.2	69.9	
	70.2	70.4		70.2			70.1	
	70.4		70.4		70.5	70.4	70.0	
		70.4	70.3	70.4	70.4	70.4		
		70.2	70.1	70.4	70.4	70.2		
			70.3		70.2			

Figure 73: Pool temperatures in run P14

5.6 Run P15

Test P15 was carried out on November 4, 1998, after blocking the gaps between the upper cooler cooling units. The power input during the test is shown in Figure 74. The temperature level in test P15a (14 040 s - 14 340 s) was 70.6°C, in test P15b (18 540 s - 18 840 s) 54.0°C, and in test P15c (24 960 s - 25 260 s) 32.3°C (Figure 75). The extrapolated surface temperature in test P15a was18.1°C and in test P15b 2.4°C (see Appendix B). During test P15c, the upper boundary was frozen.

The results (Figure 76 - Figure 85) are in good agreement with results of test P14, and thus the open gaps do not seem to affect the heat transfer phenomenon. Instead, blocking of the gaps did hamper the test procedure. Several attempts were needed to lower down the upper cooler in such a way that no air was trapped below it, since the air could not escape through the gaps. Finally, at 9500 s, the situation was deemed to be satisfactory and the measurement of the first power level was started.

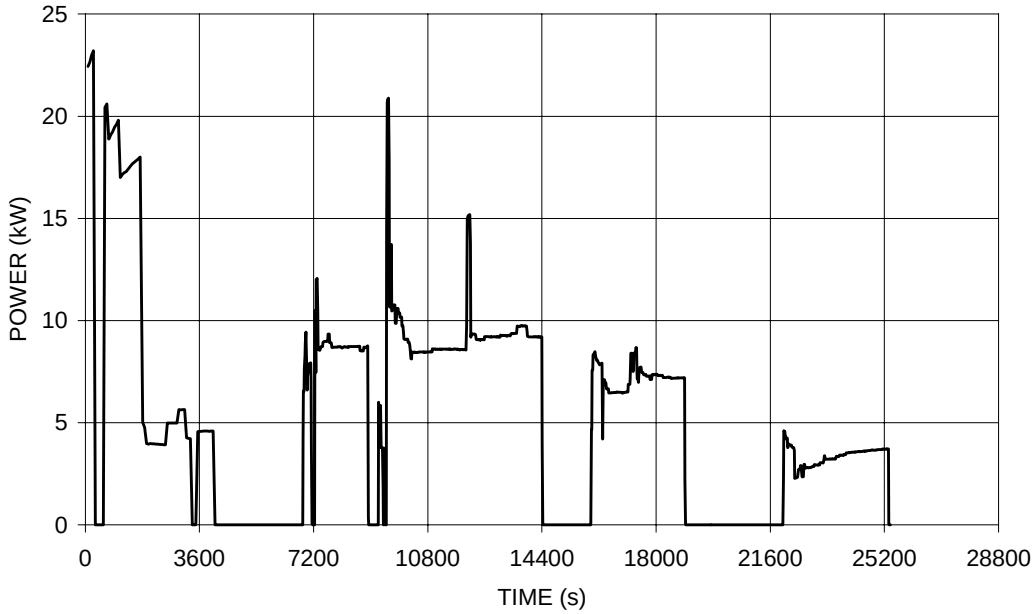

Figure 74: Electric power input during run P15

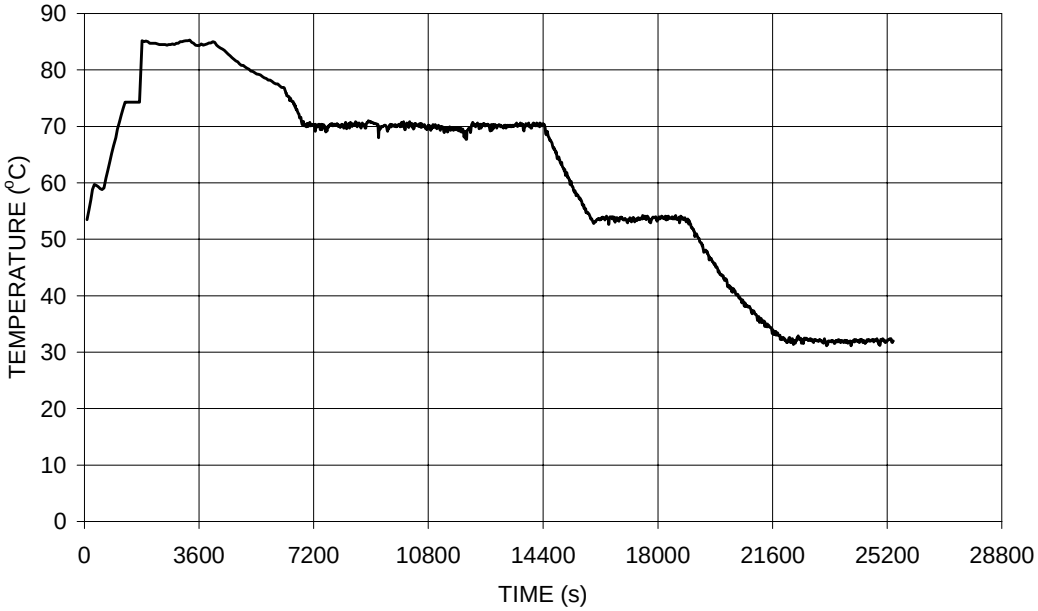

Figure 75: Temperature in the center of the pool during run P15

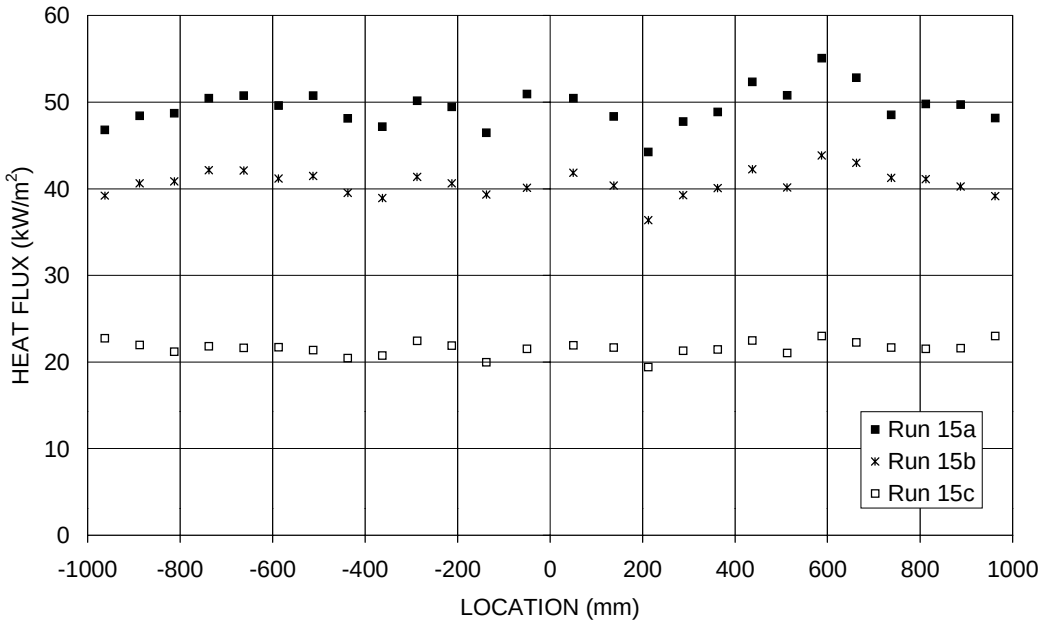

Figure 76: Local heat fluxes at the upper surface in run P15

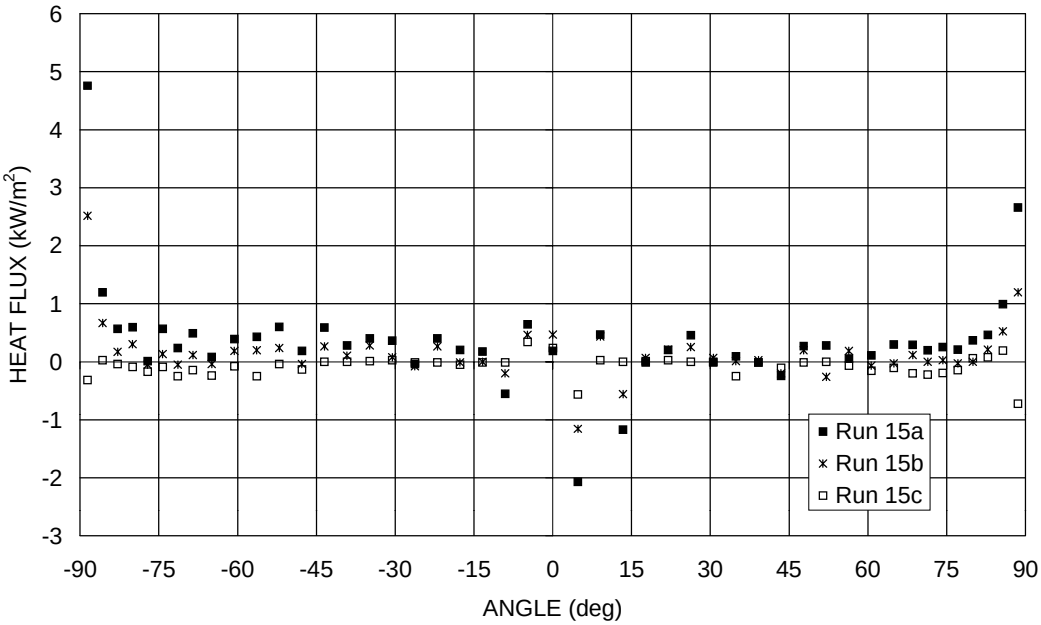

Figure 77: Local heat fluxes at the curved surface in run P15

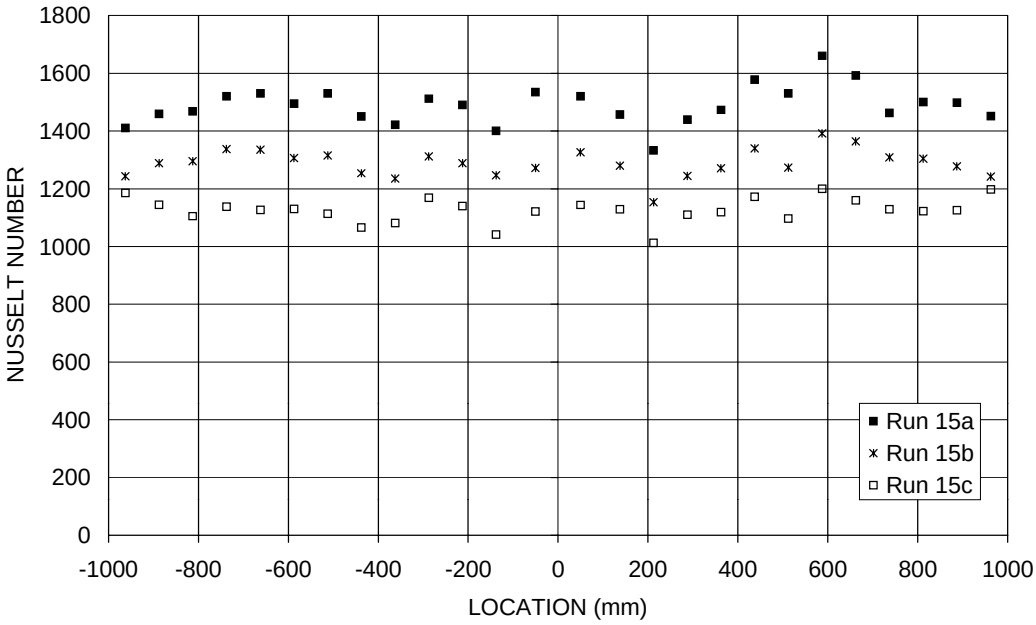

Figure 78: Local Nusselt numbers at the upper surface in run P15

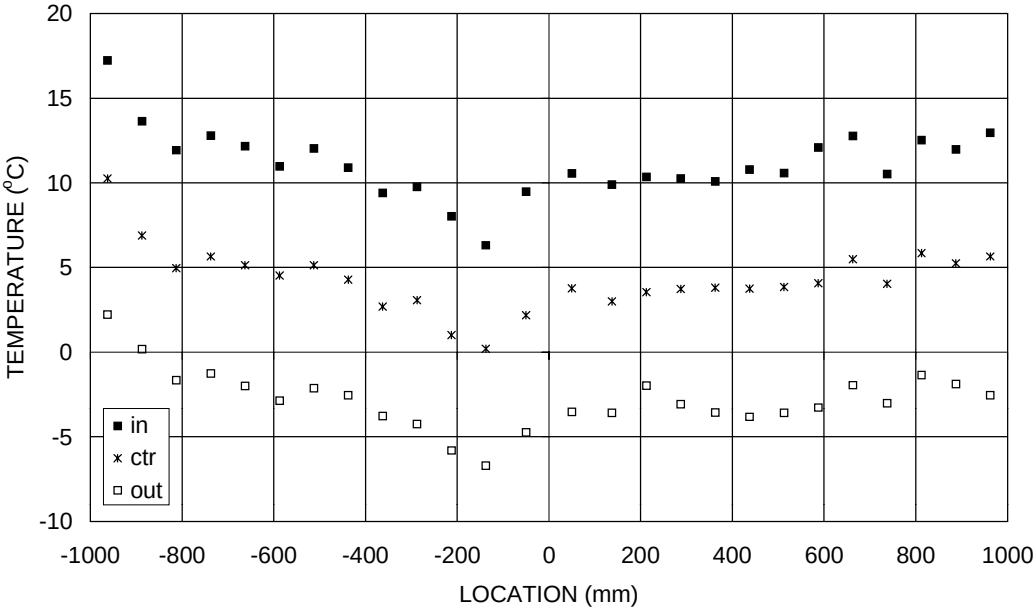

Figure 79: Upper cooler temperatures in run P15a

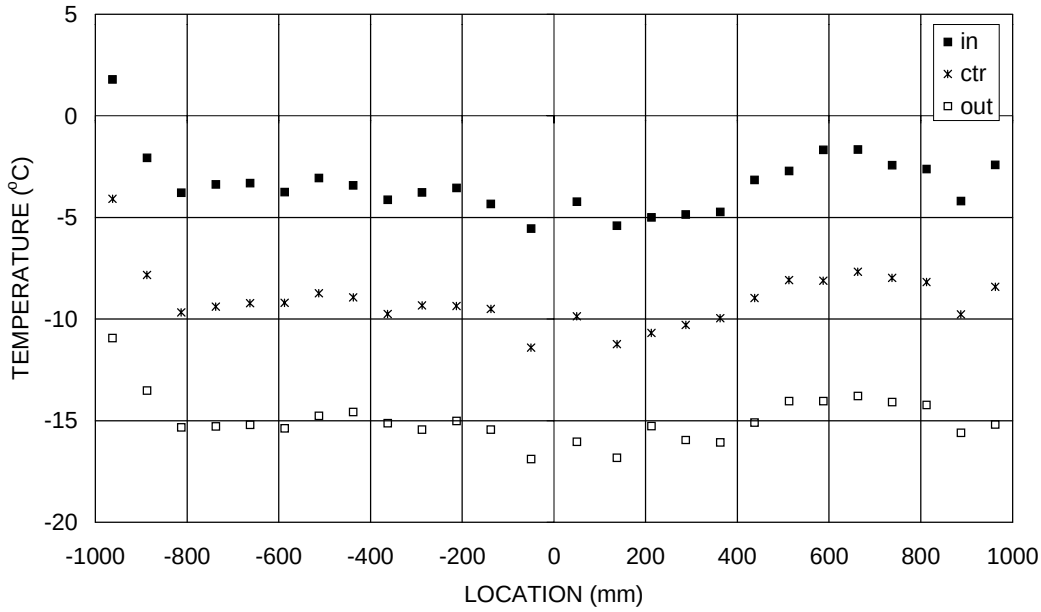

Figure 80: Upper cooler temperatures in run P15b

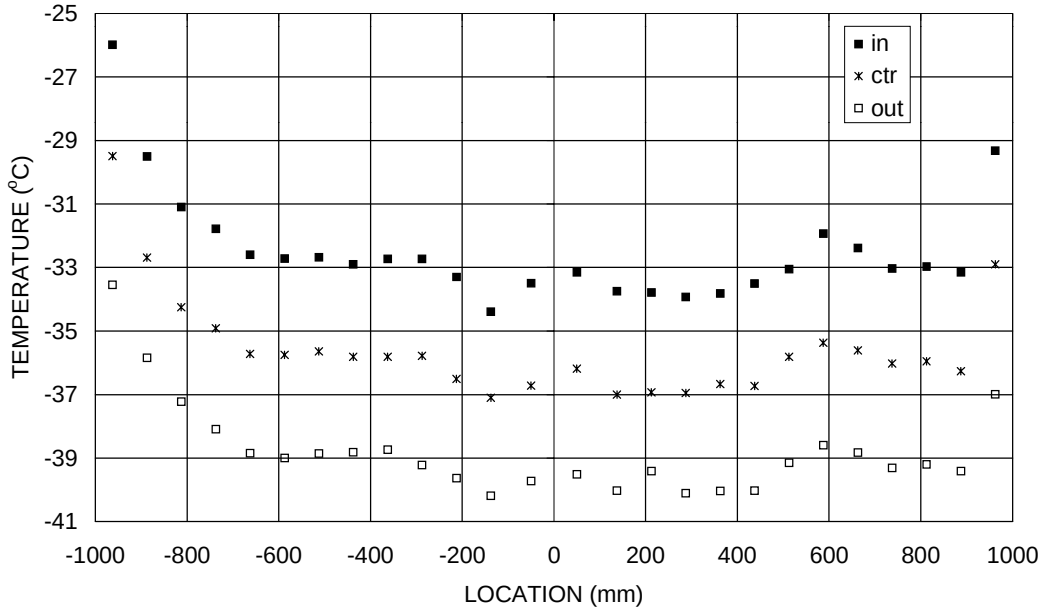

Figure 81: Upper cooler temperatures in run P15c

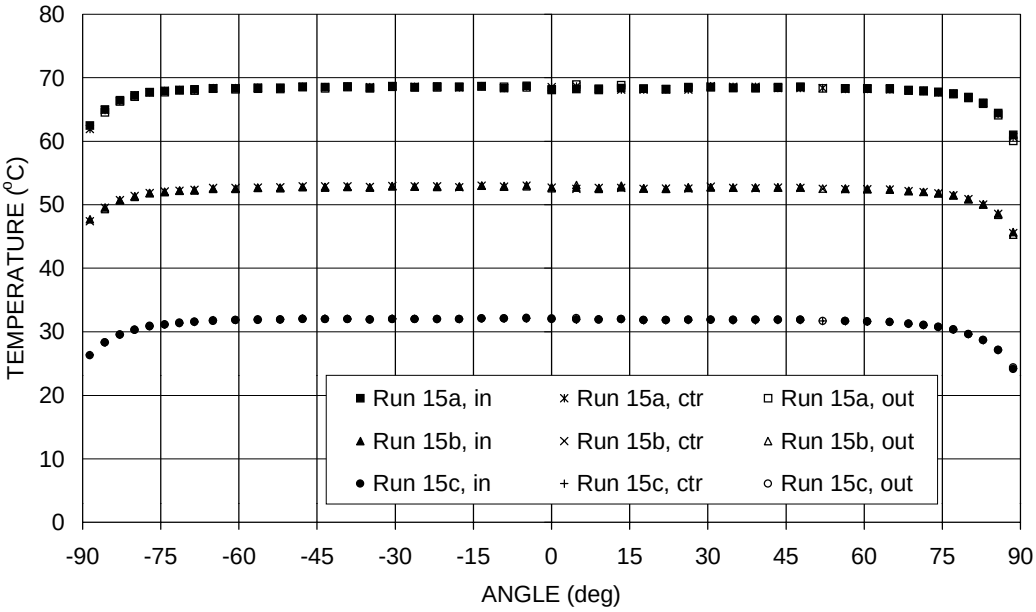

Figure 82: Side/bottom cooler temperatures in run P15

69.8	70.1	70.2	70.1	70.1	70.2	70.1	69.9	69.6
	70.4	70.4	70.3	70.3	70.5	70.3	70.3	
	70.4	70.3		70.3			70.3	
	70.3	70.4	70.5		70.4	70.4	70.3	
		70.4	70.5	70.6	70.3	70.3		
		70.3	70.4	70.5	70.4	70.2		
			70.3		70.3			

Figure 83: Pool temperatures in run P15a

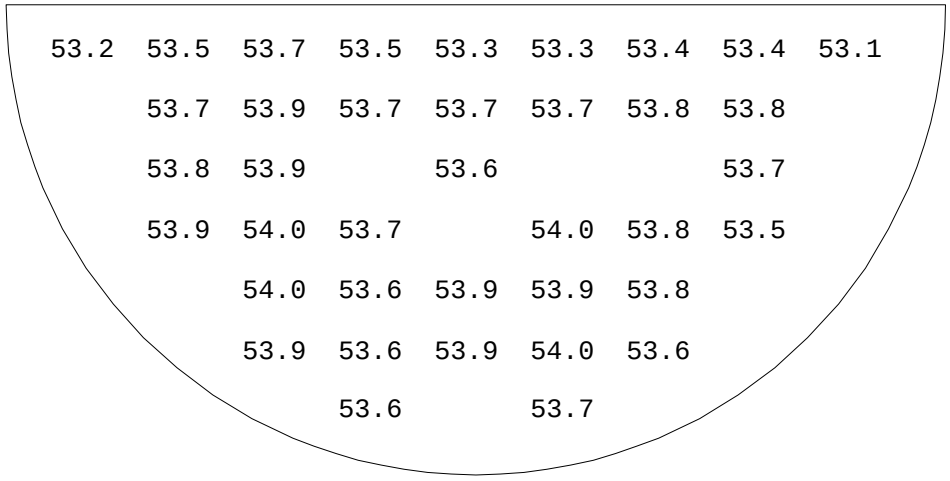

Figure 84: Pool temperatures in run P15b

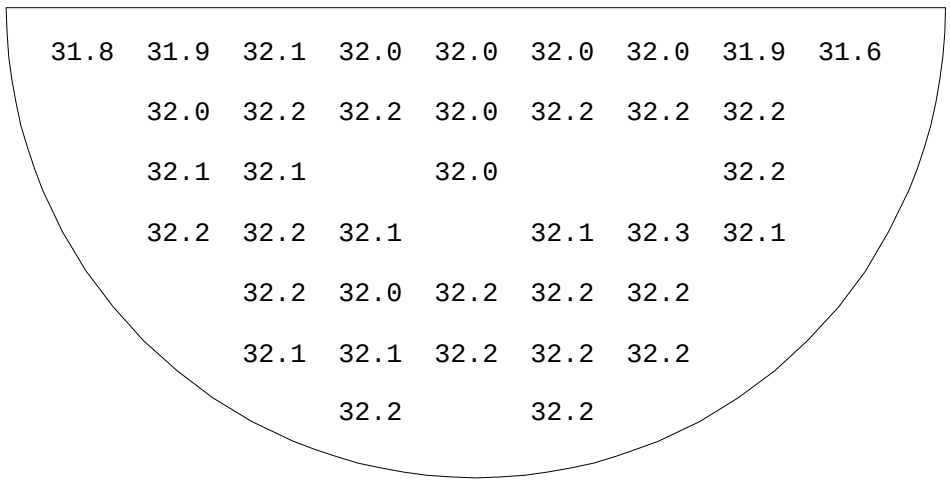

Figure 85: Pool temperatures in run P15c

5.7 Summary of experiments with only upper boundary cooled

The main parameters of the COPO II-AP experiments with only upper boundary cooled are summarized in Table 3. Ra' is calculated based on measured total cooling power. The measured average upward Nusselt numbers are shown in Figure 86. For the sake of clarity, the same results are shown without error bars in Figure 87. The error bars are estimated as discussed in Section 4. However, if the upper boundary was ice-free, the error in the temperature difference between the boundary and the pool maximum temperatures was assumed to be 1°C (not 0.5°C) and the uncertainty in the pool height was assumed to be negligible. The dominating contribution to the uncertainty of Nu and Ra' is due to uncertainty in thermal conductivity of aluminum.

In experiments P8 and P11, liquid nitrogen was used as a coolant and the upper boundary was frozen. The measured Nusselt numbers are equal (or maybe even slightly higher) than in the experiments with all boundaries cooled till freezing. Except experiment P12[1], measured Nusselt numbers are remarkably lower in the experiments with ice-free upper surface (i.e., in experiments P13a, P13b, P13d, P14, P15a and P15b). In fact, the measured Nusselt numbers are in good agreement with correlation by Steinberner and Reineke.

In the dry ice cooled experiments in which the temperature level of the pool was set low enough to create crust (tests P13c and P15c), the Nusselt numbers are higher than in the ice-free experiments. This supports our theory that the crust enhances the heat transfer. However, due to low heating power in tests P13c and P15c, the heat losses are quite large (about 10% of the measured cooling power) decreasing the reliability of these results[2]. One possible explanation for the heat losses is the heat capacity effect of the insulated lateral walls. The "hysteresis" of the heat losses seems to support this assumption: heat losses are negative if the previous temperature level of the pool was higher, and positive if the temperature level was lower.

The thermal conductivity of aluminum (needed to calculate heat fluxes) was estimated based on calibration measurements in which $T \leq -150$°C [2, 3]. In the dry ice cooled experiments, the temperature of the cooling units was in the range of -50°C to 20°C. Since the overall energy balance is well satisfied, for example, in the experiments P13a and P15a, the used thermal conductivity of the aluminum is believed to be appropriate.

Similar crust effect can also be seen when viewing the measured Nusselt numbers as a function of external Rayleigh number Ra (Figure 88 and Figure 89). Possible explanations for the crust effect are given in Section 6.

---

1 Experiment P12 was first experiment with the new dry ice based cooling system, and as discussed in Section 5.3, its results must be interpreted with caution due to possible error in test setup.

2 The heat losses are, however, smaller than the estimated uncertainty in the cooling power, and thus the error bars are representative

Table 3: COPO II-AP experiments with only upper boundary cooled, summary of main results. Note: results from tests P12a and P12b must be interpreted with caution due to possible error in test setup

	P8a	**P8b**	**P11**	**P12a**
Electric power input (kW)	16.8	6.6	12.8	11.1
Upper surf. cooling power (kW)	16.3	7.1	13.4	10.9
Lower boundary cooling power (kW)	0.1	-0.1	0.1	0.1
Total cooling power (kW)	16.4	7.0	13.4	11.0
Heat capacity effects (kW)	0.1	-0.1	-0.5	-0.1
Heat balance (kW) [1)]	0.3	-0.2	-0.1	0.3
Power to upper surface (%)	99.3	100.7	99.6	99.4
Heat flux upwards (kW/m^2)	88.3	38.3	73.2	59.0
Heat flux downwards (kW/m^2)	0.4	-0.2	0.2	0.2
Height of the pool (mm)	985	985	1000	1000
Maximum temperature of the pool (°C)	71.2	43.3	61.2	70.5
Temperature of the upper surf. of the pool (^oC)	-0.1	-0.1	-0.1	16.2
Ra'	$5.2 \cdot 10^{15}$	$1.1 \cdot 10^{15}$	$3.7 \cdot 10^{15}$	$4.9 \cdot 10^{15}$
Ra [2)]	$1.2 \cdot 10^{13}$	$3.5 \cdot 10^{12}$	$8.4 \cdot 10^{12}$	$9.3 \cdot 10^{12}$
Pr	4.9	6.9	5.5	4.2
Pr [2)]	2.6	4.2	3.0	2.6
Nu_{up}	1962.5	1447.7	1944.0	1721.2

	P12b	**P12c**	**P13a**	**P13b**
Electric power input (kW)	8.8	3.7	10.2	8.2
Upper surf. cooling power (kW)	9.0	4.0	10.0	8.2
Lower boundary cooling power (kW)	0.0	-0.1	0.1	0.0
Total cooling power (kW)	9.0	3.9	10.1	8.3
Heat capacity effects (kW)	-0.2	0.0	0.1	-0.1
Heat balance (kW) [1)]	-0.1	-0.2	0.1	0.0
Power to upper surface (%)	99.8	101.4	99.4	99.6
Heat flux upwards (kW/m^2)	48.9	21.5	54.4	44.7
Heat flux downwards (kW/m^2)	0.1	-0.2	0.2	0.1
Height of the pool (mm)	1000	1000	750	750
Maximum temperature of the pool (°C)	55.5	30.3	70.2	55.4
Temperature of the upper surf. of the pool (^oC)	1.4	-0.2	14.3	-0.2
Ra'	$2.3 \cdot 10^{15}$	$4.0 \cdot 10^{14}$	$1.2 \cdot 10^{15}$	$5.5 \cdot 10^{14}$
Ra [2)]	$6.4 \cdot 10^{12}$	$1.5 \cdot 10^{12}$	$7.4 \cdot 10^{12}$	$5.1 \cdot 10^{12}$
Pr	5.8	8.4	4.3	6.0
Pr [2)]	3.3	5.5	2.7	3.4
Nu_{up}	1478.2	1197.6	1160.1	987.7

[1)] Heating power - measured cooling power - water pool heat capacity effects

[2)] Fluid properties evaluated at bulk temperature, length scale selected as shown in Appendix A

Table 3: COPO II-AP experiments with only upper boundary cooled, summary of main results (continued)

	P13c	P13d	P14	P15a
Electric power input (kW)	3.2	12.8	9.4	9.2
Upper surf. cooling power (kW)	3.5	11.4	9.4	9.1
Lower boundary cooling power (kW)	-0.2	0.2	0.1	0.1
Total cooling power (kW)	3.5	11.6	9.5	9.2
Heat capacity effects (kW)	0.0	0.3	-0.2	0.0
Heat balance (kW) [1)]	-0.3	0.9	0.2	0.0
Power to upper surface (%)	101.8	98.3	99.1	99.1
Heat flux upwards (kW/m^2)	19.1	62.7	50.8	49.4
Heat flux downwards (kW/m^2)	-0.2	0.7	0.3	0.3
Height of the pool (mm)	750	750	1000	1000
Maximum temperature of the pool (°C)	30.3	80.7	70.5	70.6
Temperature of the upper surf. of the pool (^oC)	-0.2	22.0	19.9	18.1
Ra'	$9.8 \cdot 10^{13}$	$1.8 \cdot 10^{15}$	$4.5 \cdot 10^{15}$	$4.2 \cdot 10^{15}$
Ra [2)]	$1.2 \cdot 10^{12}$	$9.7 \cdot 10^{12}$	$8.6 \cdot 10^{12}$	$9.0 \cdot 10^{12}$
Pr	8.5	3.6	4.0	4.1
Pr [2)]	5.6	2.3	2.6	2.6
Nu_{up}	795.49	1252.0	1585.4	1490.3

	P15b	P15c
Electric power input (kW)	7.2	3.7
Upper surf. cooling power (kW)	7.5	4.0
Lower boundary cooling power (kW)	0.0	0.0
Total cooling power (kW)	7.5	4.0
Heat capacity effects (kW)	0.0	0.1
Heat balance (kW) [1)]	-0.4	-0.4
Power to upper surface (%)	99.5	100.5
Heat flux upwards (kW/m^2)	40.6	21.6
Heat flux downwards (kW/m^2)	0.1	-0.1
Height of the pool (mm)	1000	1000
Maximum temperature of the pool (°C)	54.0	32.3
Temperature of the upper surf. of the pool (^oC)	2.4	-0.1
Ra'	$1.9 \cdot 10^{15}$	$4.5 \cdot 10^{14}$
Ra [2)]	$5.8 \cdot 10^{12}$	$1.7 \cdot 10^{12}$
Pr	5.8	8.1
Pr [2)]	3.4	5.3
Nu_{up}	1289.0	1126.5

[1)] Heating power - measured cooling power - water pool heat capacity effects

[2)] Fluid properties evaluated at bulk temperature, length scale selected as shown in Appendix A

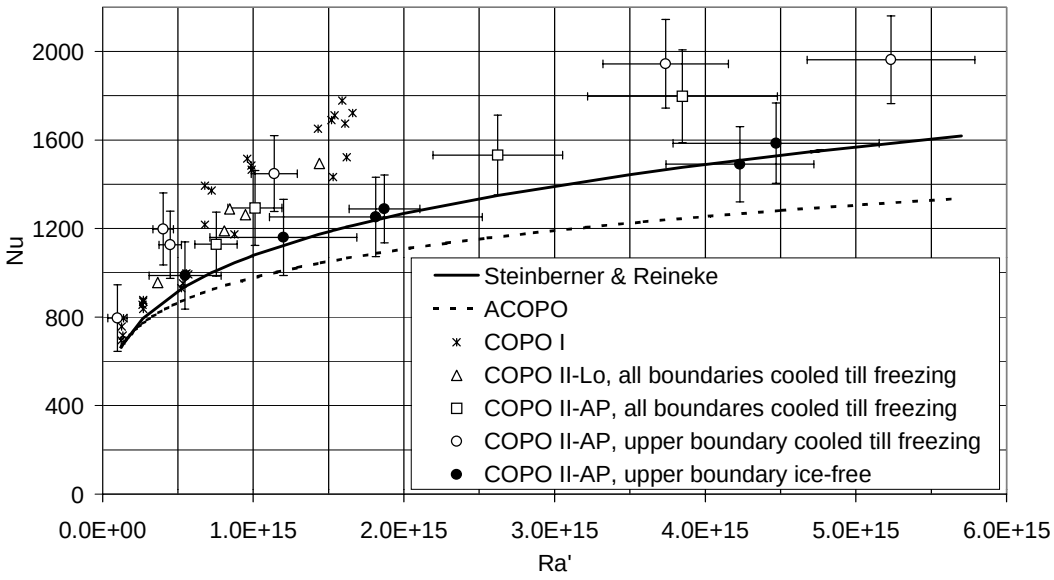

Figure 86: Average upward Nusselt numbers

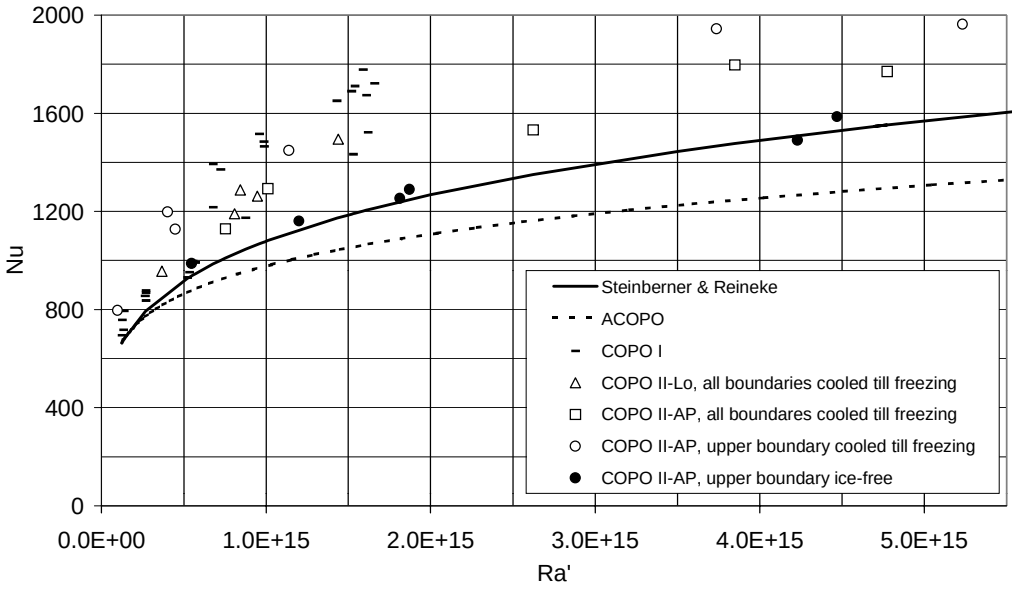

Figure 87: Average upward Nusselt numbers

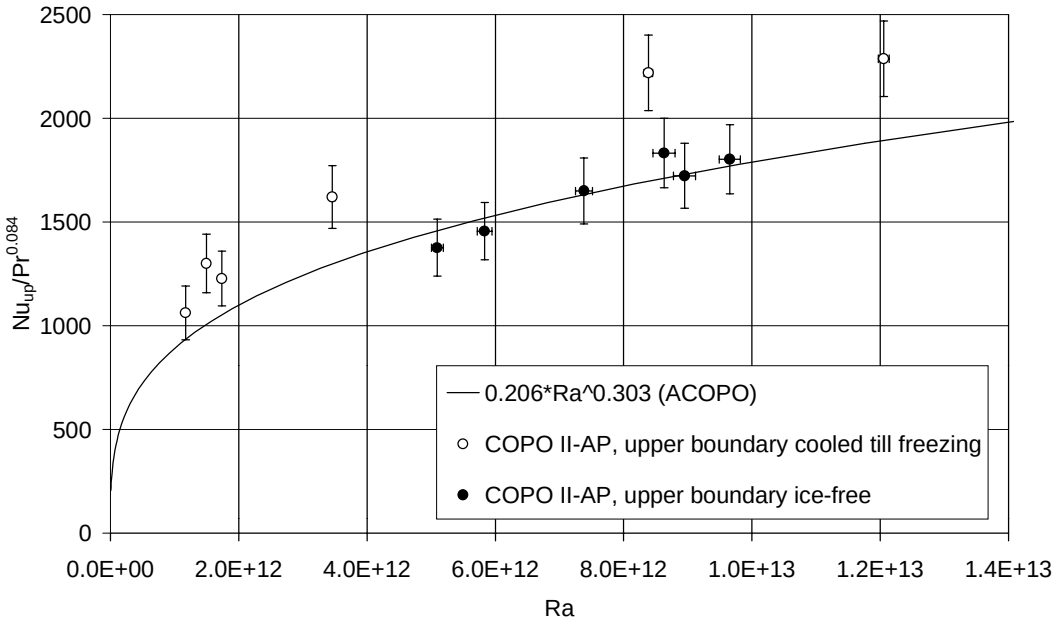

Figure 88: Nusselt number dependence on external Rayleigh number

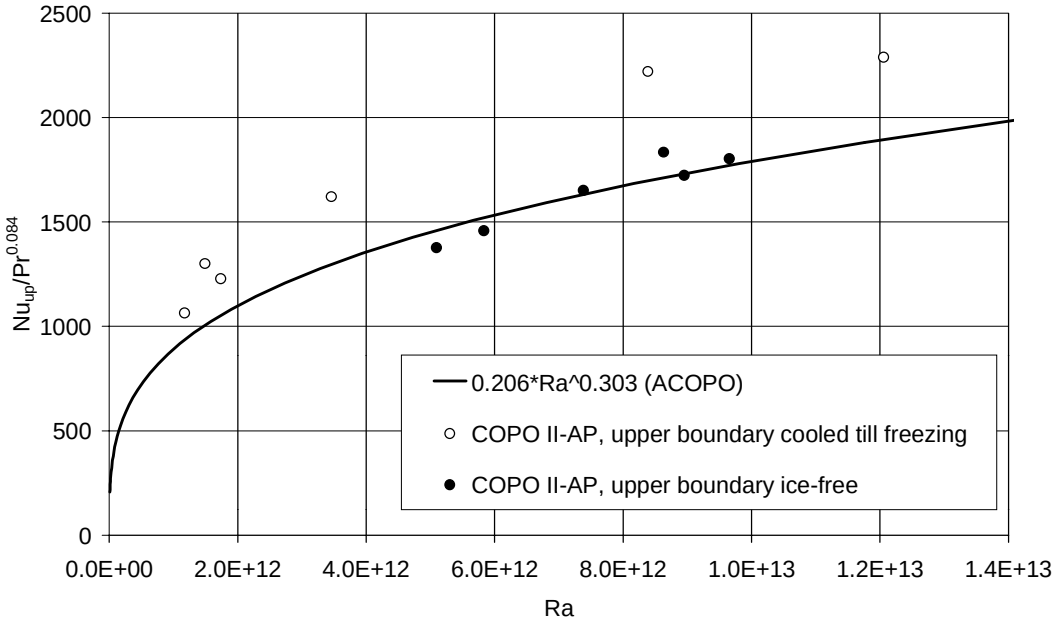

Figure 89: Nusselt number dependence on external Rayleigh number

6. DISCUSSION AND CONCLUSIONS

The average heat transfer coefficients measured in the COPO II tests seem to deviate somewhat from what might have been expected based on earlier experiments such as Steinberner and Reineke, COPO I and ACOPO. In this report, the reason for the discrepancy between the results from different facilities has been studied cooling only the upper surface of the test section. The new results indicate that the heat transfer is enhanced if the upper boundary is frozen. Obviously, there are at least two thinkable phenomena that can cause this "crust effect":

1 It is well known that the density of the pure water is maximum at 4°C. According to [10], the density extremum also occurs in saline water up to a salinity level of about 26 p.p.t. The temperature at maximum density decreases with increasing salinity (as does also the ice-melting temperature). Density gradient inversion in the boundary layer may affect the heat transfer (in fact, because the density depends on temperature and salinity, and the extremum temperature depends on salinity, several extrema may occur across a boundary layer). In test P13b, with no ice boundary, the upper surface temperature was at the freezing point of water or possibly even slightly lower (subcooled water). However, the measured average heat transfer coefficients were consistent with the tests in which the temperature of the upper surface was clearly higher than the extremum temperature. Therefore, the density gradient inversion is not expected to be the reason of the discrepancy between the results from experiments with and without crust formation.

2 The ice surface was "rippled" (irregular waves, which at the upper boundary had height of typically several millimeters or even close to one centimeter). It is plausible that the heat transfer behavior may be affected by the structure of the ice surface. However, even the increase of the ice - water interface area may be sufficient of explaining the higher heat transfer coefficients. The effect of the irregular ice-water interface to forced convection heat transfer has been studied experimentally e.g. in [11], in which 30 to 60 per cent larger heat transfer rates were measured for the rippled surface than for the undisturbed surface.

Earlier, it was speculated that the non-constant fluid properties could be one reason for the unexpectedly high heat transfer coefficients measured in COPO II experiments. Since the temperature difference between the pool boundary and the bulk of the fluid was high (~50°C) also in the new non-crust experiments, non-constant fluid properties is not expected to be the reason for the higher heat transfer coefficients. Furthermore, this explanation was not supported by ACOPO experiments, in which the temperature difference is similar or even larger than in COPO II.

As a conclusion, the reason for the high heat transfer coefficients measured in the COPO II experiments seems to be, at the moment, the roughness of the ice surface. However, this does not explain why the upward heat transfer coefficients in the COPO I experiments (non-frozen boundaries) were higher (being consistent with COPO II results) than predicted by the well-known correlation by Steinberner and Reineke.

7. REFERENCES

[1] O.Kymäläinen, H.Tuomisto, O.Hongisto and T.G.Theofanous, "Heat Flux Distribution from a Volumetrically Heated Pool with High Rayleigh Number," Nuclear Engineering and Design, **149** (1994) pp. 401-408.

[2] M.Helle, O.Kymäläinen and E.Pessa, "COPO II-Lo Experiments," IVO Power Engineering, YDIN-GT1-43, October 1997.

[3] O.Kymäläinen, M.Helle and E.Pessa, "COPO II-AP Experiments," IVO Power Engineering, YDIN-GT1-28M1, August 1997.

[4] B.R.Sehgal, J.Artnik, J.M.Bonnet, M.Caira, K.Ikonen, O.Kymäläinen, F.Parozzi, A.Siccama and B.Turland, "Core Melt Pressure Vessel Interactions During a Light Water Reactor Severe Accident (MVI Project)," FISA-97 Symposium, Luxembourg, November, 1997.

[5] U.Steinberner and H.H.Reineke, "Turbulent Buoyancy Convection Heat Transfer with Internal Heat Sources," Proc. 6th Int. Heat Transfer Conf., Toronto, Canada, August, 1978.

[6] T.G.Theofanous, M.Maguire, S.Angelini and T.Salmassi, "The First Results from the ACOPO Experiments," Nuclear Engineering and Design, **169** (1997) pp. 49-57.

[7] T.G.Theofanous and S.Angelini "Natural Convection for In-Vessel Retention at Prototypic Rayleigh Numbers," Eighth International Topical Meeting on Nuclear Reactor Thermal-Hydraulics, Kyoto, Japan, September 30 - October 4, 1997.

[8] M.Jahn and F.Mayinger, "Holographische Untersuchung der freien Konvektion in einer Kernschmelze," BMFT-Forschungsvorhaben RS 48/1, Institut für Verfahrenstechnik der T.U.Hannover, 1975.

[9] T.G.Theofanous, C.Liu, J.Scott, D.Williams and T.Salmassi, "Natural Convection in Hemispherical Enclosures at Internal Rayleigh Numbers up to $7 \cdot 10^{14}$," Appendix D in: T.G.Theofanous, C.Liu, S.Additon, S.Angelin, O.Kymäläinen and T.Salmassi (1995) "In-Vessel Coolability and Retention of a Core Melt," DOE/ID-10460, U.S.Department of Energy, Advanced Reactor Severe Accident Program (ARSAP), July 1995.

[10] B.Gebhart and J.C.Mollendorf "Buoyancy-Induced Flows in Water under Conditions in which Density Extrema May Arise," J. Fluid Mech., **89** (1978) pp. 673-707.

[11] R.R.Gilpin, T.Hirata and C.Cheng "Wave Formation and Heat Transfer at an Ice-Water Interface in the Presence of a Turbulent Flow," J. Fluid Mech., **99** (1980) pp. 619-640.

Nuclear Power / Maria Helle 9 December 1998 YDIN-GT1-50

APPENDIX A

LENGTH SCALE IN THE COPO II-AP EXPERIMENTS WITH ONLY UPPER BOUNDARY COOLED

For rectangular pools with cooled upper surface and adiabatic other surfaces, the Nusselt number is exactly equal to Dammköhler number:

$$\mathrm{Nu}_{up} = \frac{q_{up} \cdot H}{\Delta T \cdot \lambda} = \frac{\frac{P}{A_{up}} \cdot H}{\Delta T \cdot \lambda} = \frac{\frac{P}{V_{pool}} \cdot H^2}{\Delta T \cdot \lambda} = \frac{Q \cdot H^2}{\Delta T \cdot \lambda} = \mathrm{Da}\,, \qquad \textbf{(A-1)}$$

and thus any Nu-Ra' number relation can be converted to a Nu-Ra relation. In ACOPO experiments (hemispherical geometry) $\mathrm{Nu} = 2/3 \cdot \mathrm{Da}$, and in COPO II-AP experiments $\mathrm{Nu} = \pi/4 \cdot \mathrm{Da}$. Therefore, to satisfy Eq. (A-1), the length scale for ACOPO experiment with only upper boundary cooled was taken as an equivalent depth that preserves the volume of the hemisphere [A-1]. Similarly, the length scale L in COPO II-AP experiments with only top boundary cooled was assumed to be:

$$L = \sqrt{\frac{\pi}{2}} \cdot H\,, \ (\mathrm{H} = \mathrm{R}) \qquad \textbf{(A-2a)}$$

$$L = \sqrt{\frac{V_{pool}}{d}}\,, \ (\mathrm{H} < \mathrm{R}). \qquad \textbf{(A-2b)}$$

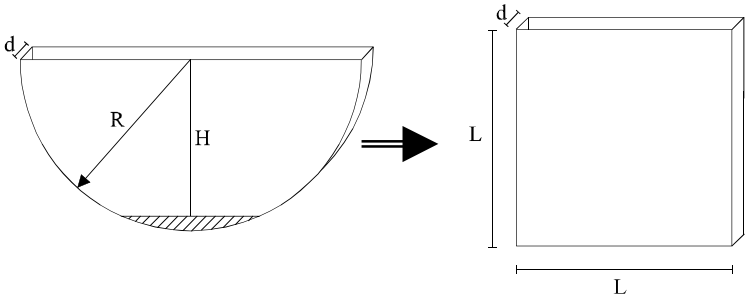

It can be seen, however, that the choice of the length scale is rather unimportant when L is close to 1 m:

$$\mathrm{Nu}_{up} \propto L \qquad \textbf{(A-3a)}$$

$$0.206\mathrm{Ra}^{0.303}\,\mathrm{Pr}^{0.084} \propto L^{0.91}. \qquad \textbf{(A-3b)}$$

REFERENCES

[A-1] T.G.Theofanous and S.Angelini "Natural Convection for In-Vessel Retention at Prototypic Rayleigh Numbers," Eighth International Topical Meeting on Nuclear Reactor Thermal-Hydraulics, Kyoto, Japan, September 30 - October 4, 1997.

Nuclear Power / Maria Helle 9 December 1998 YDIN-GT1-50

APPENDIX B

SELECTION OF BOUNDARY TEMPERATURE IN EXPERIMENTS WITH NON-FROZEN UPPER BOUNDARY

B-1. INTRODUCTION

Some COPO II-AP experiments have been carried out with non-frozen upper boundary. For these experiments, the upper boundary temperature has to be estimated using measured temperatures inside the cooling units (see Figure B-1). Correct selection of the boundary temperature is important, since dimensionless Nusselt number is directly proportional to the temperature difference between the bulk maximum and boundary temperatures. Moreover, the fluid properties are evaluated at the film temperature, which is the average temperature between the fluid maximum and the boundary temperatures.

In this appendix, heat conduction in the upper cooler is studied numerically with Fluent/Uns 4.2 to support the boundary temperature selection.

B-2. MODEL

The calculations were made in 2D. One upper boundary cooling unit was modelled as shown in Figure B-3. Boundary conditions were selected according to run P13a. The heat flux to the lower surface of the cooling unit was assumed to be 54.36 kW/m^2. The coolant temperature (T_{amb}) was set to 200 K, which was roughly the ethanol temperature just above the aluminum wall in run P13a. The convective heat transfer coefficient was assumed to be 1.4 kW/(m^2·K), because it gave the best match to the measured temperatures[1] (Figure B-2). All the other surfaces were assumed to be adiabatic. The thermal conductivity of aluminum was assumed to be[2]

$$\lambda_{upper\ cooler} = 0.1677 \cdot T + 135.69 \ \text{(W/(m·K))}, \quad [T] = \text{K}. \qquad \textbf{(B-1)}$$

B-3. RESULTS

The calculated temperature distribution is shown in Figure B-4. Due to cooling unit geometry, the temperature contours are curved near the lower surface. The extrapolated surface temperature[3] (14.3°C, Figure B-5) is higher than the calculated temperature in the middle of the cooling unit (13.0°C). However, because of the

1 Unlike in nitrogen cooled experiments, no correction terms were used.

2 Same as used for COPO II data processing. Based on calibration measurements in which T ≤ -150°C.

3 Calculated using innermost and outermost ones of the three thermocouples.

convex shape of the temperature profile at the lower surface (Figure B-6), calculated area weighted surface temperature (14.5°C) is same as the extrapolated one. The result is, of course, not very surprising considering the boundary conditions and conservation of energy. The small difference is due to uncertainty in selection of convective heat transfer coefficient used in the calculation.

Because the temperature of the upper cooler is now relatively close to the ambient temperature, and because the polyurethane is a good insulation material ($\lambda \sim 0.03$ W/(m·K)), the heat losses are very small and the used adiabatic boundary condition is believed to be appropriate. Therefore, the best estimate for the upper boundary temperature is obtained by extrapolating from the innermost and outermost thermocouples.

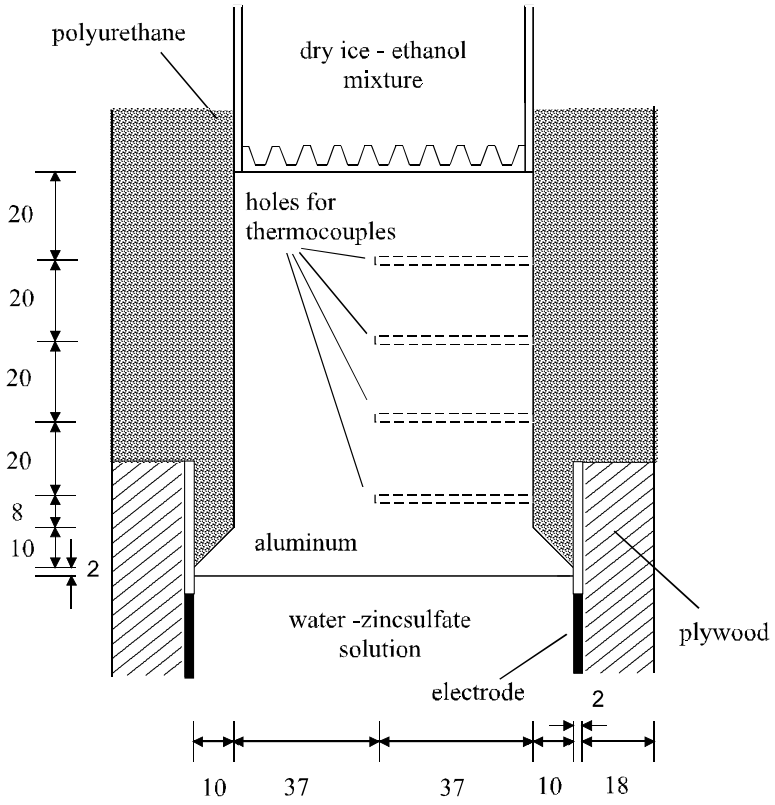

Figure B-1: Cross-section of an upper cooler cooling unit. The three thermocouples are placed into the first, second and third hole from inside (bottom)

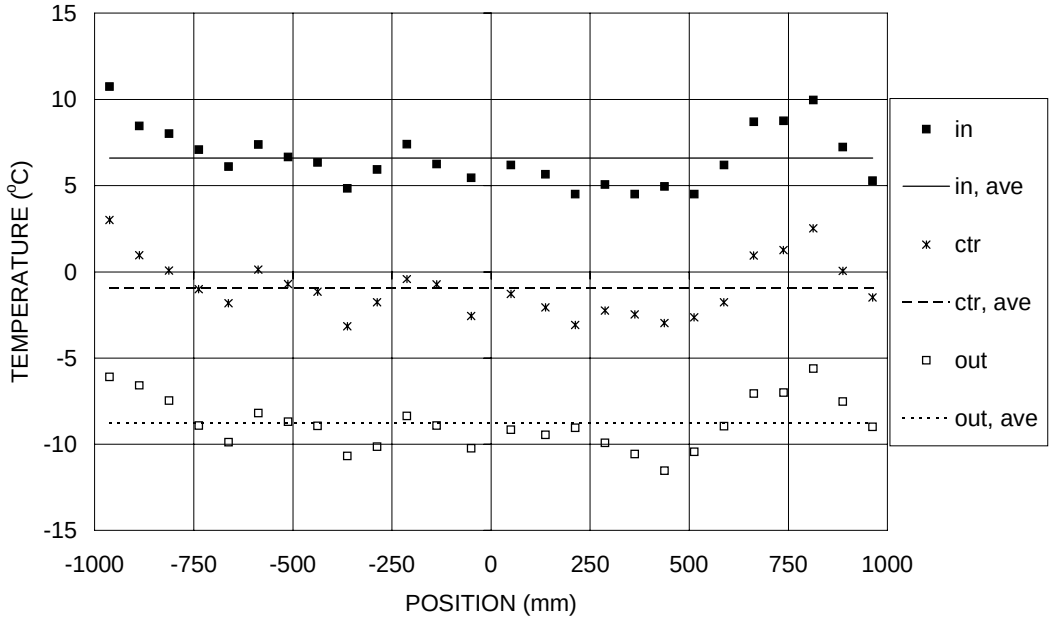

Figure B-2: Measured temperature profile at the upper boundary in run P13a

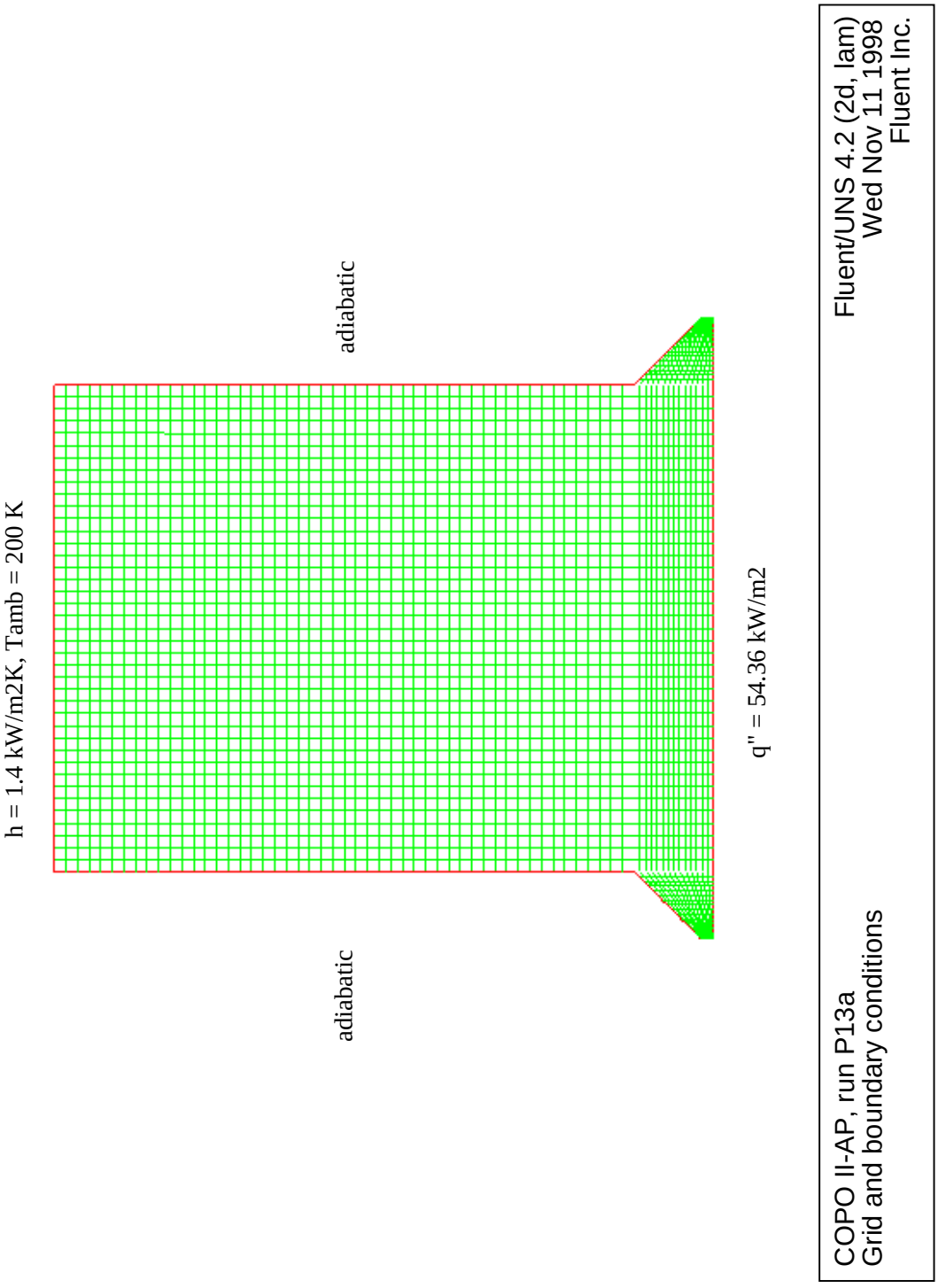

Figure B-3: Grid and boundary conditions

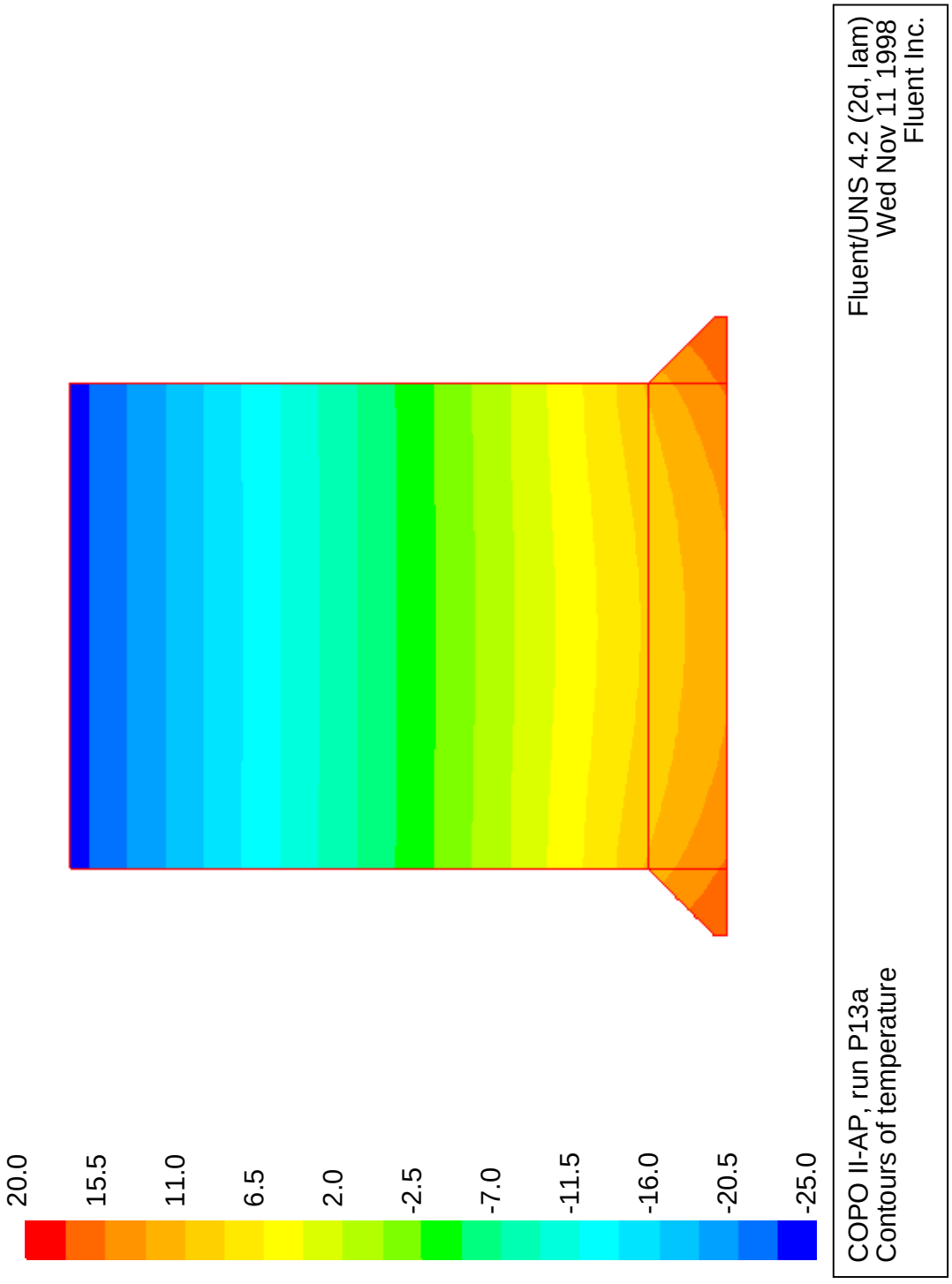

Figure B-4: Calculated temperature field

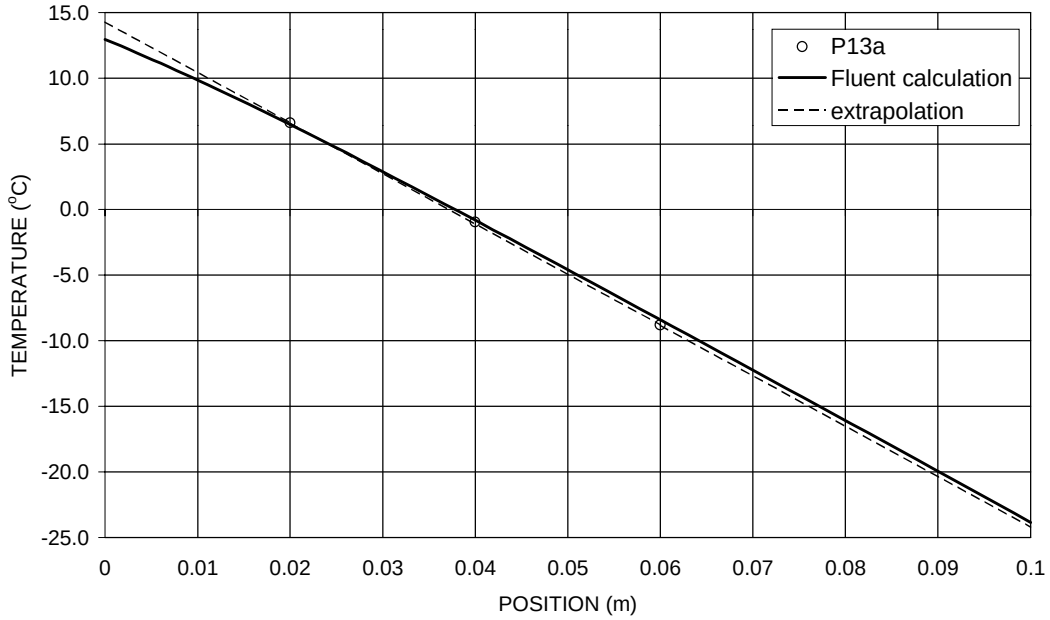

Figure B-5: Calculated vertical temperature profile in the middle of the cooling unit compared to the measured average values (0 cm = lower surface)

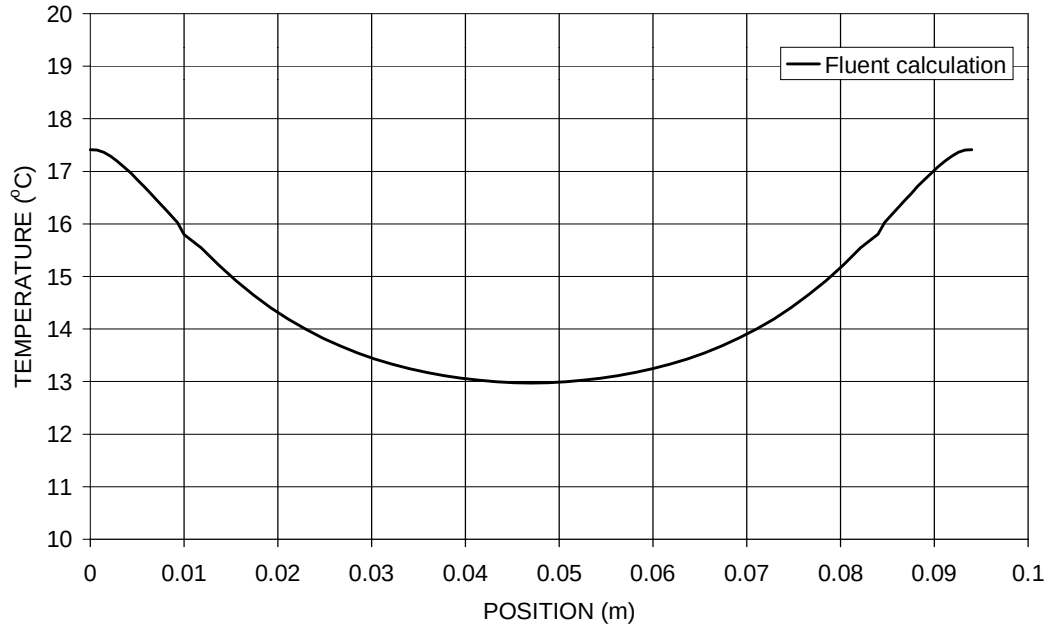

Figure B-6: Calculated cross-sectional temperature profile at the lower surface of the cooling unit

Appendix K

BALI test reports for in-vessel configurations

1 Introduction

In the framework of severe accident studies performed at DRN/DTP under CEA, EDF and FRAMATOME agreement, the BALI experiment has been designed in 1993 to create a data base about heat transfer distribution at boundaries of corium pools for in-vessel or ex-vessel configurations. During the last European 4th PCRD, the in-vessel part of the BALI program has been included in the MVI project co-ordinated by Professor Sehgal.

The knowledge of heat transfer distribution in corium pools is one of the important issues for corium retention; with CHF limits, it defines the safety margin for vessel integrity and provides the necessary inputs for core catcher design. Of course, for reactor applications the assessment of heat transfer laws is not sufficient. It has to be completed by an appropriate description of corium physical properties and by thermo-mechanical calculation. The severe accident scenarios and the physico-chemical effects are various and complex. Thus, different pool configurations such as homogeneous pool, stratified pool or porous pool have to be studied.

For reasons of safety but also for technological and cost reasons, the BALI program makes use of simulant fluid. It is the only way to obtain reasonably prototypic values of dimensionless parameters in order to respect high turbulent natural convection regime of reactor cases.

After a synthesis of the results obtained for in-vessel situations, local or average heat transfer correlations derived from BALI results are presented and compare with other experimental data. Depending on the kind of code used for severe accident simulation, the need will not be the same. The validation on the basic data base could be done by Direct Numerical Simulation code in the future or by code having their own sub-grid model. For other codes such as TOLBIAC (9), (developed also at DTP and specific to severe accident simulation) local heat transfer laws have to be used. For safety code, considering corium pools as only one mesh, heat flux distribution laws can be used in addition to average heat transfer correlation to obtain more realistic spatial pool evolution or thermal loads on the vessel.

2 Description of the facility

As the facility has been already described in reference [10], this description will be reduced to the main characteristics of the facility.

The use of simulant fluid requires particular cares to reproduce the same physical behavior. The dimensionless parameters and the boundary conditions have to be respected.

In the case of heat transfer by natural convection in a cavity with volumetric heating, we have to respect three dimensionless parameters :

- the Prandtl number,
- the aspect ratio of the cavity
- the internal Rayleigh number (built on the volumetric power density Q).

$$\mathrm{Pr} = \frac{u}{a} \qquad e = \frac{H}{R} \qquad Ra_i = \frac{gbQH^5}{lua}$$

By using water as simulant fluid for corium, the same order of magnitude for Prandtl number is maintained as for oxidic corium. Nevertheless, to check the effect of viscosity on heat transfer the pool viscosity could be increased by adding cellulose compound in water.

To respect the internal Rayleigh number, which depends on the length scale at the power 5, the test sections used to reproduce lower head or core catcher shapes are full scale. In this way, the aspect ratio of the cavity is also maintained.

Concerning the boundary conditions we have to reproduce : uniform volumetric power, uniform temperature at pool boundaries and uniform gas superficial velocity at downward or lateral pool boundaries for configuration such as MCCI.

Volumetric heating is obtained by direct current heating in a 2D full scale hemi-cylindrical (fig. 1) or rectangular geometry (15cm thick) by using the slice of water itself as electrical resistance. The power dissipated from two electrodes in water by Joule effect could vary up to 50 kW. The use of electrode grids allows direct qualitative and quantitative flow motion observations.

The condition of uniform temperature at the boundaries of the pool is obtained by change of state. Ice crust formation is obtained and controlled by heat exchanger cooled at low temperature (-50° to –80°C) with organic liquid cooled itself by liquid nitrogen. To take into account different conditions of cooling at the upper surface, tests have been run for extreme configurations : with or without top cooling.

The lateral or downward heat exchanger walls are externally covered by multi layer porous medium which allows both gas injection and heat transfer by conduction. In this way, the gas can be injected uniformly through the ice crust. This feature will be used for MCCI applications or to simulate a partial vaporisation of metal for in-vessel situation.

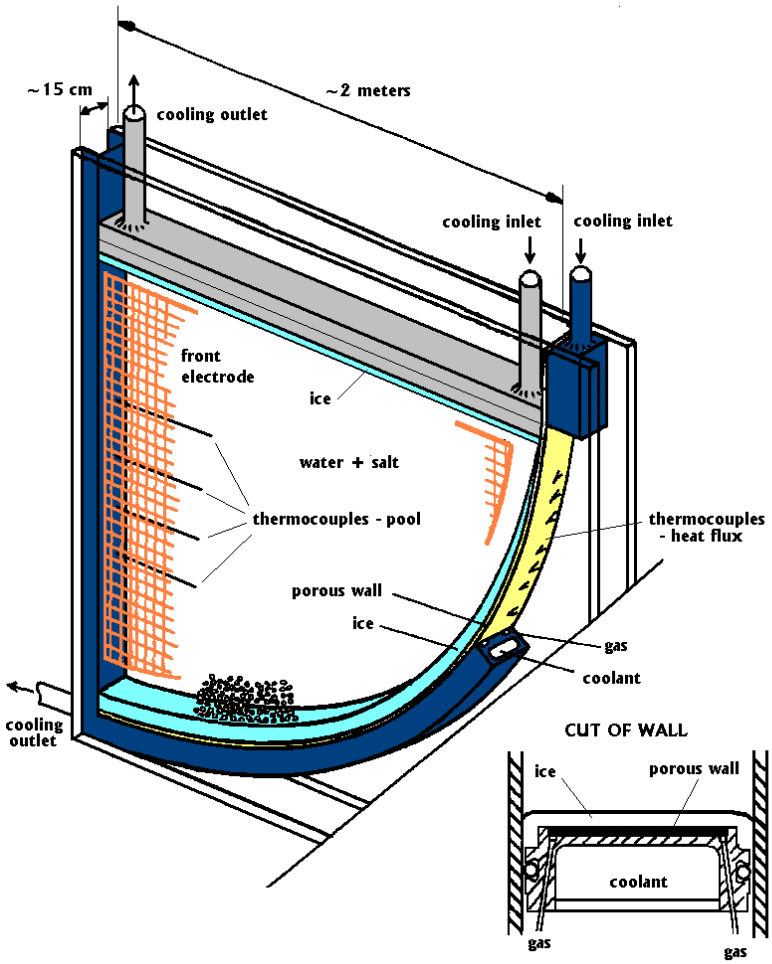

Figure 1 : In-vessel test section

For all the tests the thermal balances on upper and curvilinear or lateral heat exchanger, temperature profiles in the fluid and heat flux distributions are measured. For some tests, specific measurements such as Particle Imaging Velocimetry for velocity field, Laser Induced Fluorescence for temperature field, and gamma absorption for void fraction measurement have been done. The thermal balances are usually better than 10%.

3 Synthesis of results

3.1 Tests matrix

The purpose of the first campaign was to study the effect of internal Rayleigh number in the range 10^{15} to 10^{17}. To vary this parameter, tests have been carried out for different pool heights (1.0, 1.5, and 2.0 m) and different volumetric power densities.

The second campaign was dedicated to study the effect of Prandtl number on heat transfer. The viscosity of pool has been increased by adding cellulose compound in water to obtain Pr number from 10 to 1000.

The third campaign was dedicated to the study of heat transfer by natural convection in a porous medium. In that case, we simulate a metallic pool with solid oxidic debris by a water pool filled with 1cm diameter solid glass balls. From reactor point of view, the main difference is that in our case the power is dissipated directly in the fluid phase and not in the debris. Nevertheless, because the convection effects are more important than the conduction in debris this difference has a limited influence.

A specific test, with gas injection has been performed to simulate a partial vaporisation of steel for in-vessel geometry. The description of this very specific test is discussed only in the individual test report

All the individual test reports available in the frame of MVI project are appended at the end of this document.

3.2 General observations

For all tests with uniform cooling, three different zones as shown in figure 2 have been observed, an upper unstable layer (H_{up}) at uniform temperature, a lower zone stratified in temperature where the fluid rises in the centre with low velocity (~ few mm/s) and a boundary layer where the fluid in contact with the ice is cooled and comes back with high velocity to the bottom of the pool.

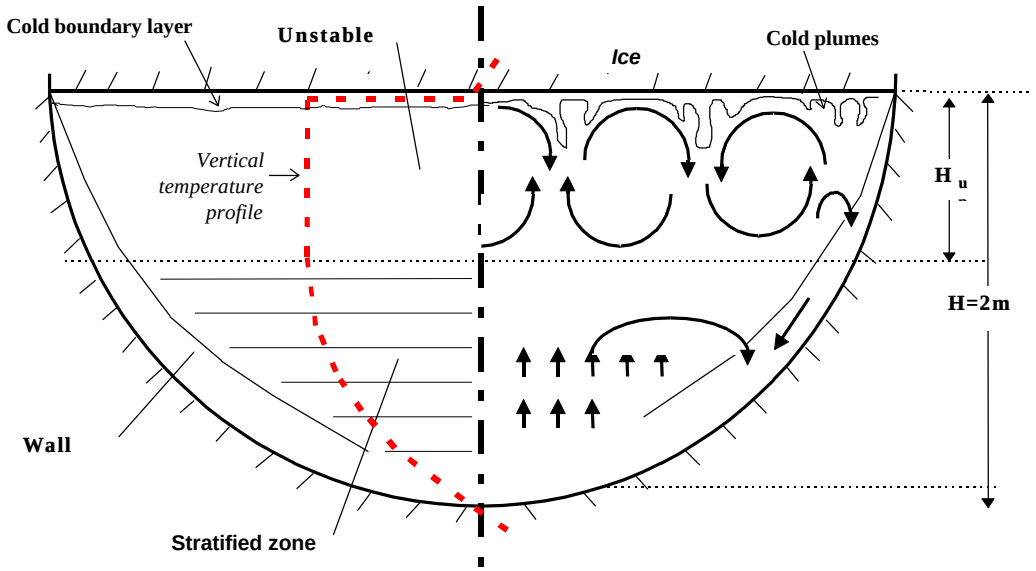

Figure 2 : General flow observations

The upper layer is a consequence of the instability induced by the presence of a cold layer at the top. This tiny denser layer (~ 0.1mm at high Rayleigh number) is periodically released as cold plumes in the hot fluid (configuration of Rayleigh Bénard convection). This mechanism is responsible for the heat transfer in the upper part of the pool and has been studied in detail in the frame of a thesis (7) to develop a phenomenological model of heat transfer. At high Rayleigh number in the cavity, large

scale convection cells appears and disturb the basic mechanism introducing some deviation in heat transfer correlation which is also called the transition between soft and hard turbulence. Among other measurements, wavelength between thermoconvective plumes have been measured from visualisation of temperature field by Laser Induced Fluorescence technology. Wavelengths around 1 cm have been measured. As these plumes control the upward heat transfer, it is concluded that a 15 cm thickness of test section is large enough to have representative heat transfer mechanism.

3.3 Temperature profiles

The temperature profiles have been measured on the vertical axis of the pool with thermocouples inserted in the mid-plane of the test section 10 cm from the adiabatic side which simulates the axis.

For the comparison of different tests, the temperature and the depth are reduced to the following dimensionless values: T/T_{max} and $Depth/H_{max}$.

The main difference on the shapes of the profiles appears between tests with or without top cooling (fig.3). For test without top cooling, the profile has an inclined S shape with a very small upper layer at uniform temperature which is only due to the thermal losses from the top surface. For all the tests with top cooling, even for viscous and porous tests, the height of upper layer H_{up} is about 40% of the total height.

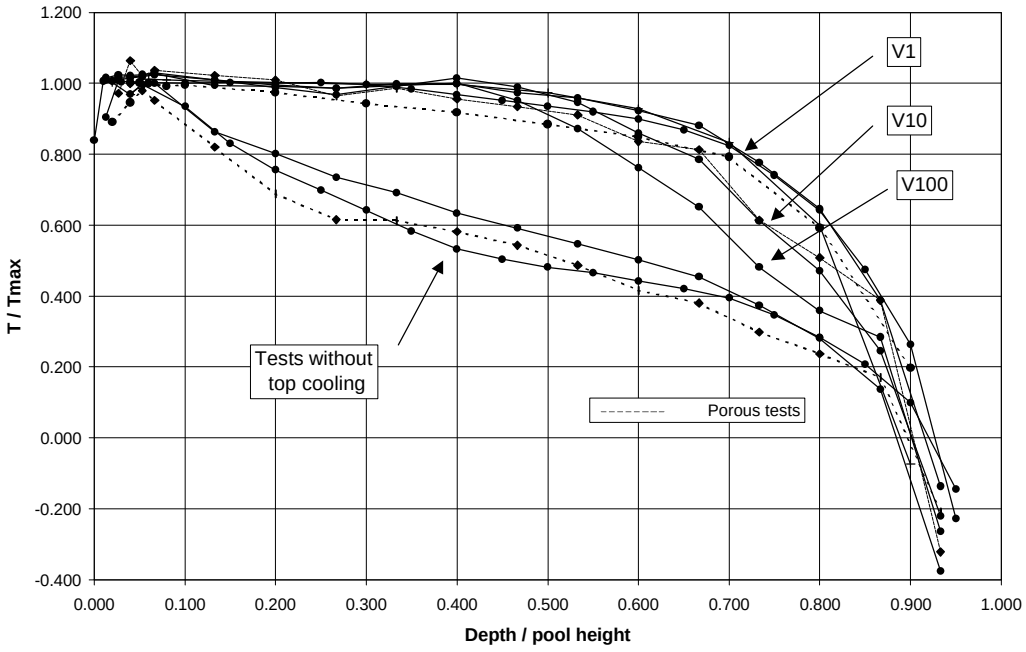

Figure 3 : Temperature profiles

Nevertheless, for viscous tests V10 and V100 (~10 and ~100 times the viscosity of water) differences are observed in the lower part of the profile. For porous medium the profiles are quite similar to those obtained for non porous medium even if the temperature profiles show a small linear increase in the upper part of the pool for test with top cooling.

For cases with top cooling, the ratio between maximum and average volume weighed pool temperature is quite constant, it ranges from 1.10-1.13 for 1.0m and 1.5m height tests to 1.12-1.14 for 2.0m height tests. For tests with viscous fluid, this ratio is a little bit higher : 1.16 and 1.21 respectively for V10 and V100. Of course for tests without top cooling the ratio is higher with a value around 1.7.

3.4 Curvilinear heat flux profiles

The heat flux profiles on curvilinear wall have been calculated from local temperature difference measurements obtained from thermocouple pairs inserted in the porous layer used for gas injection. The main source of uncertainty is the local thermal resistance between each pair of thermocouple. An average value for thermal resistance has been used. It is calculated from a comparison between average thermal balance and local heat flux integration on the surface of curvilinear heat exchanger.

To compare different tests, the heat flux and the depth are reduced to the following dimensionless values: ϕ/ϕ_{max} and Depth/H_{max}. For tests with uniform cooling, the maximum heat flux is defined as the average sideward heat flux in the upper unstable layer.

For the first test campaign (fig. 4), the shapes of the heat flux profile are similar to the shape of temperature profile. For tests with top cooling, the heat flux is quite uniform over the top height (60% Hmax). This is connected with the temperature profile shape and with the turbulent regime of the boundary layer flow (in that case heat transfer coefficient do not depend on curvilinear abscissa). The ratio between maximum value and average value is constant (about 1.75) for different aspect ratio. For tests without top cooling this ratio is equal to about 3.7. The heat flux profiles have been satisfactorily compared to profiles calculated from measured temperature profiles and local Chawla or Churchill heat transfer correlations (5-6) in turbulent regime.

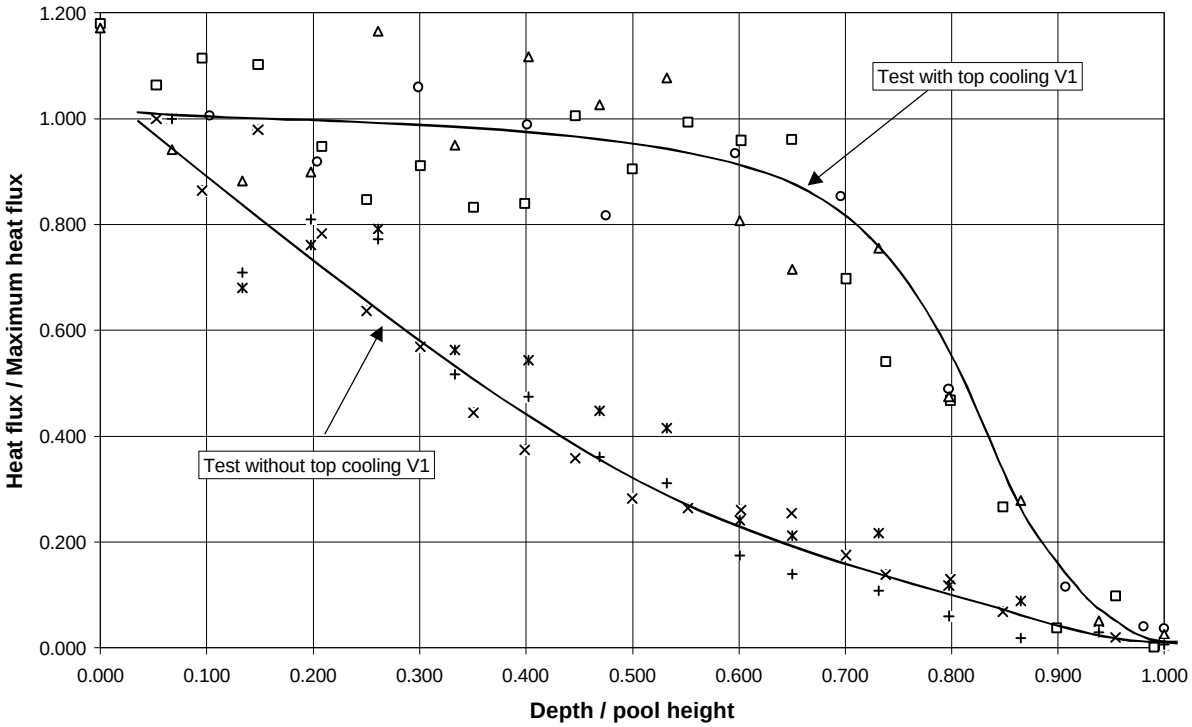

Figure 4 : Heat flux profiles (Turbulent regime)

For viscous or porous tests with top cooling, the shapes of heat flux and temperature profiles are different (fig. 5). Despite the fact that the temperature is uniform in the upper part, the heat flux increases at the upper corner of the pool. This is because the boundary layer flow regime is laminar. For viscous tests, the comparison with local Chawla or Churchill heat transfer correlations (5-6) in laminar regime gives also good results. For porous test the shape of the heat flux profile is well reproduced but when we compare the absolute values, the experimental ones are lower.

The ratio between maximum and average heat flux values is equal to 3.6 and 5.7 respectively for V10 and V100 viscous tests. For porous tests, this ratio ranges from 4 to 6.6.

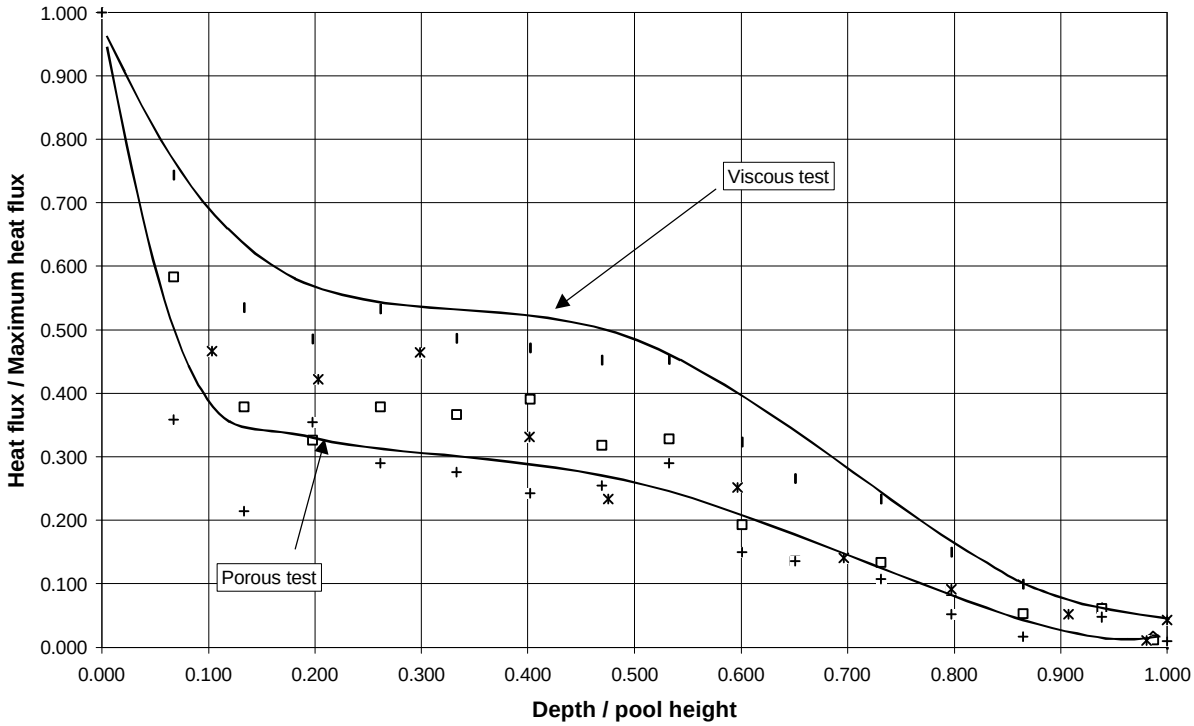

Figure 5 : Heat flux profiles (Laminar regime)

For laminar profile shape with heat flux peak at the top of the pool, the maximum heat fluxes are not accurate values because the measurements are performed only every 10 cm. It can explain the dispersion on concentration factor.

4 Average heat transfer comparison with other experiments

The BALI results are compared with two complementary experimental programs: COPO at IVO in Finland (1-2) and ACOPO at UCSB in USA (3). In order to compare our different results, it is important to define the same references in particular for the temperature used to calculated the physical properties in dimensionless numbers. For our comparison the temperature used for the calculation of physical properties is the film temperature between the wall and the bulk temperature. For test with top cooling, the bulk temperature is defined as the average volume weighted temperature in the upper unstable layer (it is also the maximum pool temperature). For test without top cooling, the bulk temperature is defined as the average volume weighted temperature in the pool.

The average Nusselt numbers for upward and downward heat transfer are calculated from bulk pool difference. This definition is used for 0D model consistency, where only one temperature is defined.

The pool heights used to calculated dimensionless numbers do not take into account the ice crust thickness in the bottom of the pool (about 10cm).

4.1 Average upward heat transfer

The COPO I experiments have been conducted on a 2D half scale test section designed for LOVIISA geometry. Before BALI results have been obtained, a transition with a significant increase for upper heat transfer was assumed for Ra_i greater than 6 10^{14} on the basis of COPO I results. The new COPO II experiments were carried out with crust formation for LOVIISA and PWR geometry. A good agreement is observed between results from COPO II and BALI. The transition assumed previously is not confirmed and the correlation derived from COPO II and BALI is only 10% higher than the extrapolation of Steinberner correlation (4).

$$Steinberner: \ \overline{Nu_{up}} = 0.345 Ra_i^{0.233}$$

$$COPO - BALI: \overline{Nu_{up}} = 0.383 Ra_i^{0.233}$$

In ACOPO experiment the tests are conducted in a 3D half scale hemispherical geometry using a different approach for simulating volumetric heating. As uniform heating by joule effect is not possible for 3D geometry, a transient cooling of the pool is used. From their experimental results two correlations are derived for upward and downward heat transfer : $\overline{Nu_{up}} = 1.95\, Ra_i^{0.18}$ and $\overline{Nu_{dn}} = 0.3\, Ra_i^{0.22}$

Because the geometry are different, the comparison between ACOPO and BALI requires particular cares. For upward heat transfer, as the distribution of heat flux is uniform, the local or average heat transfer coefficient values are the same. The small wavelength of thermoconvective instabilities and the small effect of large scale convection motion observed in hard turbulent Rayleigh Bénard regimes assess the direct transposition between 2D and 3D geometry for upward heat transfer.

For upward heat transfer, the ACOPO Nusselt numbers are 20 to 30% lower than those obtained on BALI or COPO for Rayleigh numbers greater than 10^{15}. Up to now, the different hypothesis formulated to explained this difference have not been fully successful (effect of geometry, system effect, roughness of ice crust…).

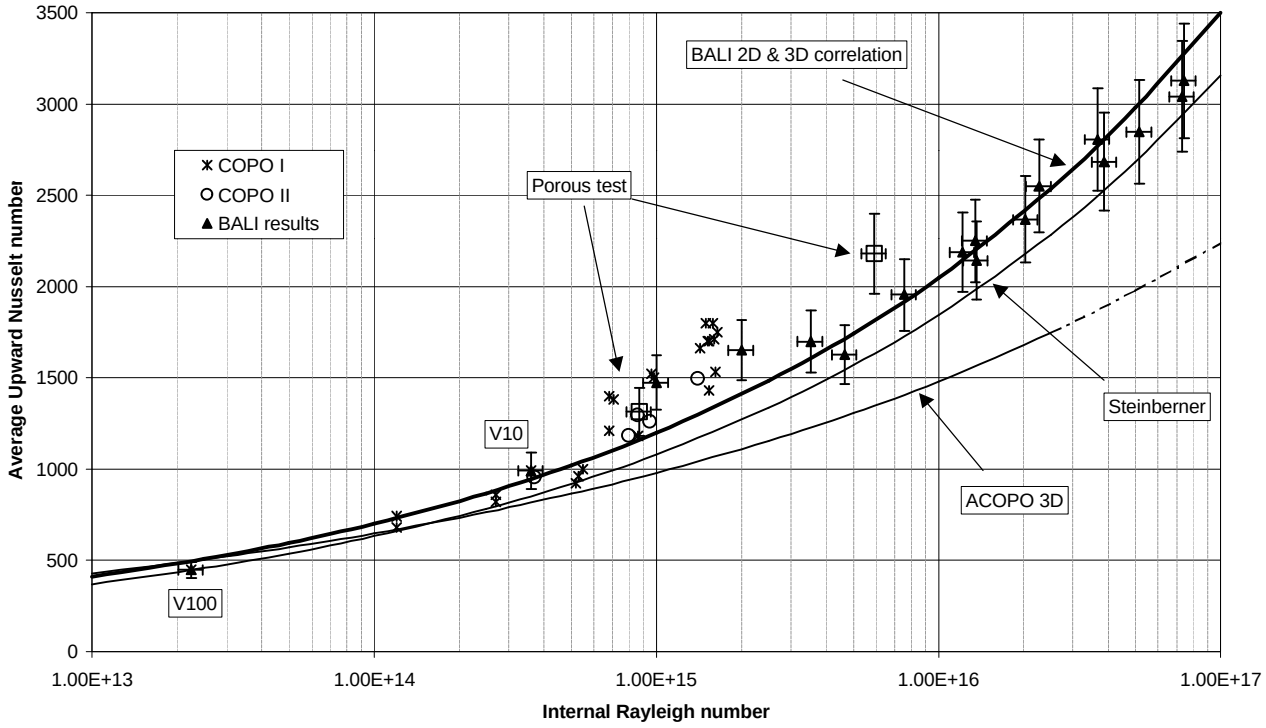

Figure 6 : Average Upward heat transfer

4.2 Average Downward heat transfer, transposition 2D-3D

For downward heat transfer, it is not possible to compare directly the results from BALI and those from ACOPO. To take into account the effect of geometry, a simplified model is used to transpose 2D results in 3D average heat transfer correlation.

From the BALI results, average 3D downward heat transfer correlation is derived by integration of local heat transfer correlation on hemispherical geometry. In this approach we consider that the local heat transfer correlation checked on BALI results is valid for both 2D or 3D geometries.

For the needs of the model, the temperature profile is simplified (uniform maximum temperature on the height H_{up} and linear decrease in the bottom part). H_{up} and T_{max} are determined by the calculation.

In a first step, the calculation has been performed for 2D geometry to check the model on BALI results. Correlation obtained for 2D geometry :

$$\overline{Nu_{dn}} = 0.116\left(\frac{H}{R_V}\right)^{0.32} Ra_i^{\,0.25} \quad \text{for } 10^{13} < Ra_i < 10^{17} \text{ with } R_v = \left(\frac{4V_{pool}}{p\ l}\right)^{1/2}$$

The aspect ratio of the pool has a small effect which is taken into account here by the term H/R_v. R_v is the radius of an equivalent hemicylindrical geometry with same volume as pool geometry.

The correlation obtained is plotted for $H/R_v=1$ and compared with experimental data on figure n°7.

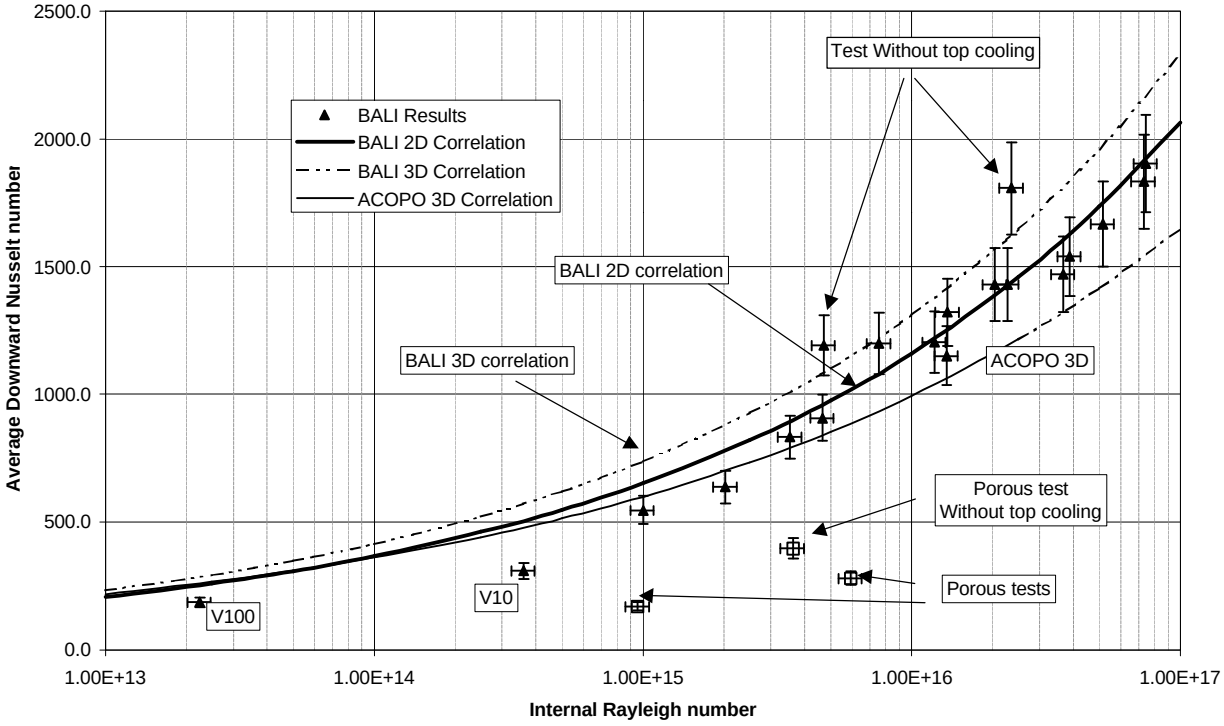

Figure 7 : Average downward heat transfer

The ratio between H_{up}/H calculated for 2D geometry ranges from 0.45 to 0.38 respectively for 1.0m and 2.0 m height pool tests. These results are consistent with experimental temperature profiles where upper layer is defined for 40% of the full pool height.

In a second step, the calculation has been performed for 3D geometry. The correlation obtained is plotted also on figure 7 for $H/R_v=1$ and compared with results from

ACOPO. So doing, it is also possible to observe on this figure the differences between 2D and 3D geometry. Correlation obtained for 3D geometry :

$$\overline{Nu_{dn}} = 0.131\left(\frac{H}{R_V}\right)^{0.19} Ra_i^{0.25} \quad \text{for} \, 10^{13} < Ra_i < 10^{17} \text{ with } R_v = \left(\frac{3V_{pool}}{2p}\right)^{1/3}$$

Here R_v is defined as the radius of equivalent hemispherical geometry.

The ratio between H_{up}/H calculated for 3D geometry is lower and ranges from 0.36 to 0.30 respectively for 1.0m and 2.0 m height pool tests.

For downward heat transfer, the ACOPO Nusselt numbers are 10 to 25% lower than the correlation derived for 3D geometry. Nevertheless for reactor applications, when we calculate from 3D correlations the ratio between power extracted from the top of oxidic pool and the total dissipated power we obtained similar values to those obtained with ACOPO correlations.

H/R	0.25	0.50	0.75	1.0
P_{up}/P_{tot}	~64%	~56%	~51%	~44%

Results obtained from 3D BALI correlations

For ACOPO experiments and Ra_i around 10^{16} this ratio is about 43% (H/R=1 for ACOPO). So, even if the results are not exactly the same for absolute heat exchange coefficients, the power splits to top and bottom are the same for the oxidic pool. For the oxidic pools different absolute values of heat transfer coefficients lead only to different pool temperatures.

For viscous tests, there is no significant difference for upward heat transfer but a 40% decrease due to laminar boundary layer regime is observed for downward heat transfer.

For tests in porous medium, the differences for downward Nusselt numbers are very important whereas for upward heat transfer we have been surprised to observe similar values to those obtained in non-porous tests. Complementary tests with different glass ball diameters (2mm, 6mm and 10mm) have been performed in a small Rayleigh-Bénard mock-up. The result for 10 mm diameter is confirmed, but an important reduction of heat transfer coefficient is observed for 2 mm diameter (values are 10 times lower). We assume that this effect might be due to an interference between the diameter of particles and the wavelength of thermoconvective instabilities. Similar results have been also observed in the work of David, Lauriat and Cheng (8).

4.3 Analogy with Rayleigh-Bénard convection

Specific tests have been performed at ACOPO (11) and COPO (12) facilities without downward cooling in order to be directly compared to Rayleigh-Bénard convection tests.

This comparison is based on an heat transfer mechanism analogy between volumetric heated test cooled from the top and Rayleigh-Bénard convection tests, i.e. tests performed in a cavity heated from the bottom and cooled from the top.

To express the BALI results in Rayleigh Bénard coordinate system, Nu=f(Ra), the following dimensionless numbers are calculated with the same definition as ACOPO (11). Because the BALI tests were also cooled from the bottom, the length scale used in dimensionless number is the height of the upper unstable layer. The definition of this length scale due to the Rayleigh exponent in heat transfer correlation is not very important.

- $Nu_{up} = \dfrac{hH_{up}}{l}$ with λ calculated at $(T_{max}+T_{wall})/2$

- $Ra = \frac{gb\Delta T_{\max} H_{up}^{\ 3}}{n^2}\Pr$ with physical properties calculated at T_{max}

So doing, the BALI results can be compared with ACOPO external Rayleigh number correlation described in (11).

$$Nu_{up} = 0.206 Ra^{0.303} \Pr^{0.084} \qquad \text{ACOPO (11)}$$

The influence of Prandtl number has not been checked in ACOPO tests. So, the Prandtl dependence has been chosen by analogy with Globe and Dropkin definition (13).

In order to compared BALI and ACOPO results, the BALI experimental values of $Nu_{up}/Pr^{0.084}$ are plotted as a function of Ra and compared with the following expression : $0.206Ra^{0.303}$.

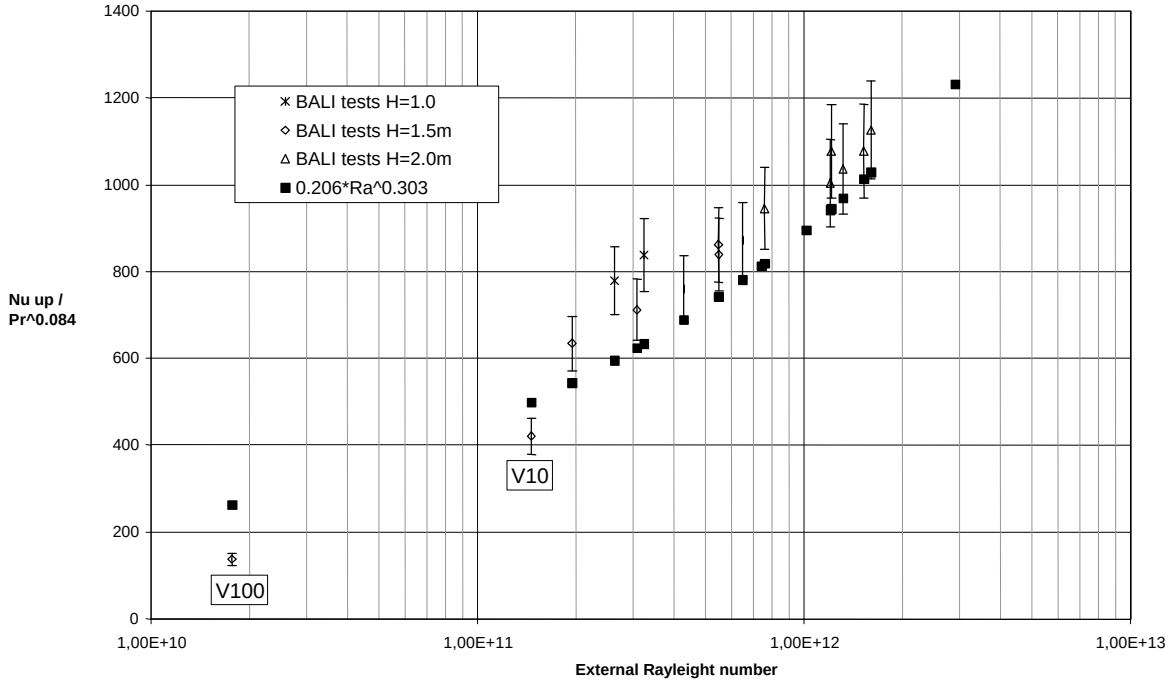

Figure 8 : BALI-ACOPO comparison in Rayleigh Bénard coordinate system

For the first test campaign, differences are reduced to about 10% for 1.5m and 2.0m height tests. For 1 m height tests the differences are about 20% (fig. 8).

For viscous tests, the dependence on Prantdl number is too important. Different exponents for Prandtl number have been checked. The results are summarised in the following chart :

Difference	Pr^0.084	Pr^0.04	Pr^0.02	Pr^0
V10	-18%	0%	8%	14%
V100	-92%	-48%	-32%	-17%

From V10 and V100 BALI tests, we conclude that the upward heat transfer is quasi independent from Prantdl number.

This tendency is confirmed by MINIBALI tests performed in the frame of Bernaz thesis (7). The exponent obtained for Prantdl number was about 0.04 for experimental results whereas for phenomenological model approach the exponent is 0.

The COPO tests performed without bottom cooling (12) give results that are similar to those of ACOPO for an external Rayleigh number coordinate system. Nevertheless, the results confirm the results obtained for uniform cooling and they are still different when

they are expressed as a function of internal Rayleigh number and compared to the first ACOPO correlation (3).

These results are puzzling as far as simple transposition expressions exist between volumetrically heated cavity and Rayleigh-Bénard's cavity. If there is an agreement in one coordinate system, there would be an agreement in the other coordinate system.

In the frame of Bernaz thesis (7), these transposition relations have been developed and BALI results have been satisfactory compared with expressions transposed from different Rayleigh-Bénard experiments.

The transposition can be defined with the followings elements :

- The same mechanism of heat transfer has been identified for both configurations
- For uniformly cooled tests, the upper unstable layer H_{up} can be transposed in a Rayleigh-Bénard cavity of same height.
- For a same upward heat flux : $\Delta T_{RB} = 2\ \Delta T_{max}$.

Volumetrically heated cavity

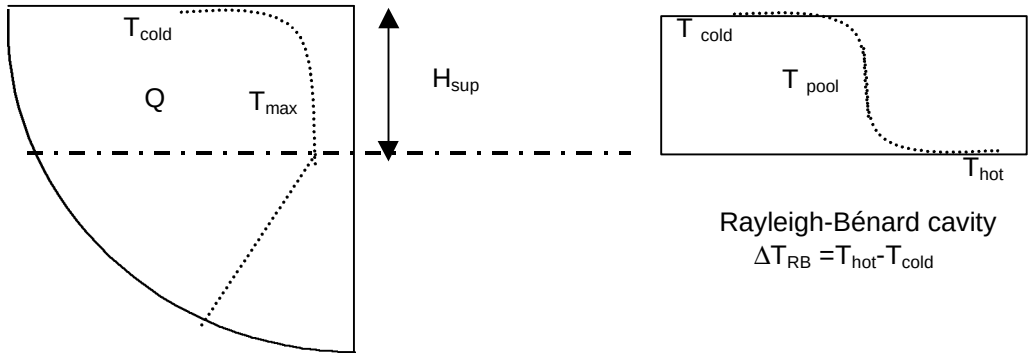

$$Nu_{\sup}^{H_{\sup}} = 2A^{\frac{1}{b+1}}\left(Ra_i^{H_{\sup}}\right)^{\frac{b}{b+1}} \quad \Leftrightarrow \quad Nu_{R.B} = ARa^b$$

The Theofanous expression in (11) is compared with correlation transposed for an half Rayleigh Bénard cavity.

In that case, classical Rayleigh bénard correlation, $Nu_{R.B} = ARa^b$, becomes for an half cavity if we consider symmetrical heat transfer $Nu_{R.B_{1/2}} = 16^b\, ARa_{1/2}^b$.

According to this two transposition relations, the ACOPO correlation expressed as a function of external Rayleigh number $Nu_{up} = 0.206Ra^{0.303}\,\mathrm{Pr}^{0.084}$ can be transposed and becomes :

$Nu_{up} = 0.312Ra_i^{0.233}\,\mathrm{Pr}^{0.064}$ or for a Prandtl number about 5

$Nu_{up} = 0.346Ra_i^{0.233}$ ACOPO (11) transposed as a function of Ra_i.

This expression is similar to the Steinberner and Reinecke expression but it is different than the initial ACOPO correlation presented in the first publication for tests uniformly cooled (3) : $Nu_{up} = 1.95Ra_i^{0.18}$.

In that case, same differences are observed between BALI and ACOPO. The 10% differences observe in figure 8 are similar to those observed in figure 6 between BALI and Steinberner correlation (similar to ACOPO (11) expression transposed as a function of Ra_i).

As a conclusion, the two correlations presented by Theofanous in (3) and (11) are judged not consistent. The correlation expressed in external Rayleigh number depend only on pool temperature and upward thermal balance measurement whereas the initial correlation depends on upward thermal balance and equivalent volumetric power density calculated from global thermal balance. An overestimation of this volumetric power density could explain the difference observed both in figure 6 and 7 for upward and downward heat transfer correlation.

Nevertheless, from the available information on ACOPO experiment we can not conclude anything else in particular about the evolution of power split

Some COPO tests cooled only by the top (12) have been performed without ice crust formation. The results of these tests show a reduction of upward heat transfer coefficient about 10%, and consequently a good agreement with Steinberner correlation. For Hele et al. (12), highest value of heat transfer coefficient for test with ice crust formation would be due to the roughness of the crust.

5 Conclusion

From this experimental program, the data base on heat transfer in corium pool has been enlarged. For the first time, prototypic values of dimensionless parameters have been obtained ($Ra_i \sim 10^{17}$).

A good agreement is observed with COPO II results. The comparison with ACOPO shows 20 to 30% differences for absolute heat exchange coefficients, but the power split is the same. Recent comparison with Rayleigh-bénard convection shows a better agreement for upward heat transfer between ACOPO, BALI and COPO experiments. From this observation we conclude that there is inconsistency between the different upward heat transfer correlations presented in ACOPO publications.

Chawla or Churchill heat transfer correlations in turbulent regime has been satisfactory checked with first test campaign results.

From experimental results and simplified transposition model, 3D correlations are derived for reactor applications. As a complement for global heat transfer correlations, simplified shapes of temperature and heat flux profiles can be used.

From viscous test results, we can conclude that the effect of viscosity on upward heat transfer is small. For downward heat transfer, a change in the flow regime is observed, the turbulent boundary layer flow regime becomes laminar. The heat flux profiles are well calculated by Chawla or Churchill heat transfer correlations in laminar regime.

From test results in porous medium, we observe that the upward heat transfer is not affected. This surprising result may be related to the same order of magnitude between the diameter of glass balls (1cm) and the wavelength of thermoconvective instabilities at high Rayleigh number. This result has been confirmed in a Rayleigh-Bénard mock-up for 1cm diameter glass balls, but for small diameter (2 mm), the heat transfer is reduced by a factor about 10. For downward heat transfer, the boundary layer flow is affected by the porous medium. The shape of the profile looks like a laminar profile shape but the absolute heat flux values are lower.

6 References

1- KYMALAINEN, O., HONGISTO, O., PESSA, E., 1993, COPO Experiments on Heat Transfer From a Volumetrically Heated Pool, Imatran Voima Oy Process Laboratory, DLV1-G380-0377.

2- HELLE, M., KYMALAINEN, O., PESSA, E., 1997, COPO II-Lo Experiments, IVO POWER ENGINEERING LTD, YDIN-GT1-43. Transmitted in the frame of the MVI Project, 4th PCRD of the European Community.

3- THEOFANOUS, T.G., MAGUIRE, M., ANGELINI, S., SALMASSI, T., 1997, The First Results from the ACOPO Experiment, Nucl. Eng. Des., 169, 49-57.

4- STEINBERNER, U. , REINEKE H.-H., 1978, "Turbulent Buoyancy Convection Heat Transfer with Internal Heat Sources" Proceedings of Sixth International Heat Transfer Conference. Toronto Canada August 7-11,1978

5- CHAWLA, T.C., CHAN, S.H., 1977, " Heat Transfer from Vertical/Inclined Boundaries of Heat Generating Boiling Pools ", In. J. Heat Mass Trans., 20 (5), pp 499-506.

6- CHURCHILL, S. W., CHU, H. H. S., 1975, "Correlating Equations for Laminar and Turbulent Free Convection From a Vertical Plate", International Journal of Heat and Mass Transfer, Vol. 18, 1975, pp. 1323-1329

7- BERNAZ, L. Thesis, 1998, "Etude du Transfer de Chaleur à la Frontière Supérieure d'un Bain Fluide avec Dissipation Volumique de Puissance", University Joseph Fourier Grenoble

8- DAVID, E., LAURIAT, G., CHENG P., 1991, "A Numerical Solution of Variable Porosity Effects on Natural Convection in a Packed-Sphere Cavity", Journal of Heat Transfer, May 1991, Vol.113 pp. 391-399

9- BERNAZ, L., BONNET, J.-M., SPINDLER, B., VILLERMAUX, C., 1998 "Thermalhydraulic Phenomena in Corium Pools : Numerical Simulation with TOLBIAC and Experimental Validation with BALI." Workshop on in-vessel core debris retention and coolability, Garching 3-6 March 1998

10- BONNET, J.-M., 1997 "BALI project - Description of the facility" note SETEX/LTEM/97-21

11- THEOFANOUS, T.G., ANGELINI, S., 1997, ''Natural Convection for In-Vessel Retention at Prototypic Rayleigh Numbers'' Eight International Topical Meeting on Nuclear Reactor Thermal-Hydraulics, Kyoto, Japan, September 30 – October 4,1997

12- HELLE, M., KYMALAINEN, O., 1998, ''Crust effect in the COPO II Experiments'', IVO POWER ENGINEERING LTD, YDIN-GT1-50.

13- GLOBE, S., DROPKIN, D., 1959, ''Natural-Convection Heat Transfer in Liquids Confined by Two Horizontal Plates and Heated from Below'', J. Heat Transfer, 81, pp24-28

APPENDICES: TEST REPORTS

BALI FACILITY
IN-VESSEL TEST SECTION

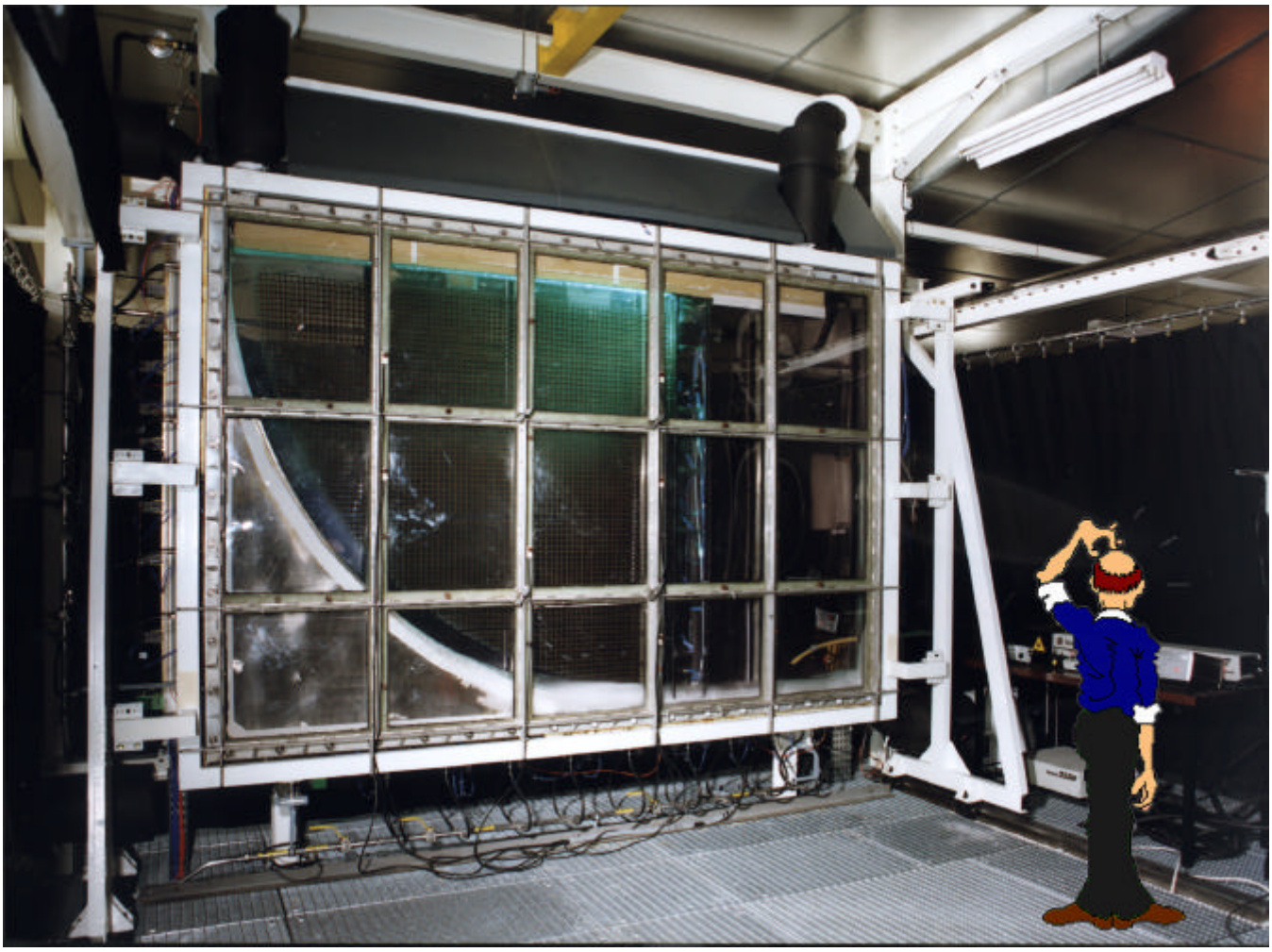

APPENDIX A : FIRST TEST CAMPAIGN RESULTS

APPENDIX B : SECOND TEST CAMPAIGN RESULTS

APPENDIX C : THIRD TEST CAMPAIGN RESULTS

APPENDIX D : TEST WITH GAS INJECTION

APPENDIX A : First test campaign results

The purpose of the first campaign was to study the effect of internal Rayleigh number in the range 10^{15} to 10^{17}. To vary this parameter, tests have been carried out for different pool heights (1.0, 1.5, and 2.0 m) and different volumetric power densities.

Summary of the test matrix

Run n°	Height	Power	Cooling conditions	Comments	Report Reference
1-0	1.5 m	15 / 20 kW	Uniform cooling		BALI_1.5_20kW_031096
1-1	1.5 m	10 kW	Uniform cooling		BALI_1.5_10kW_051196
1-2	1.5 m	30 kW	Uniform cooling		BALI_1.5_30kW_121196
1-3	1.5 m	20 kW	Uniform cooling	Not enough LN_2	No record
1-4	1.5 m	20 kW	Uniform cooling		BALI_1.5_20kW_211196
1-5	1.5 m	15 kW	Uniform cooling		BALI_1.5_15kW_261196
1-6	1.5 m	10 kW	Without top cooling		BALI_1.5_10kW_281196

Run n°	Height	Power	Cooling conditions	Comments	Report Reference
1-7	2.0 m	15 kW	Uniform cooling		BALI_2.0_15kW_171296
1-8	2.0 m	30 kW	Uniform cooling	Video	BALI_2.0_30kW_290197
1-9	2.0 m	20 kW	Uniform cooling		BALI_2.0_20kW_110297
1-10	2.0 m	25 kW	Uniform cooling		BALI_2.0_25kW_180297
1-11	2.0 m	15 kW	Without top cooling		BALI_2.0_15kW_200297
1-12	2.0 m	15 kW	Uniform cooling	F.I.L.	No record
1-13	2.0 m	20 kW	Uniform cooling	Video	BALI_2.0_20kW_180397
1-14	2.0 m	30 kW	Uniform cooling	P.I.V.	BALI_2.0_30kW_210397

Run n°	Height	Power	Cooling conditions	Comments	Report Reference
1-15	1.0 m	9 kW	Uniform cooling	P.I.V.	BALI_1.0_9kW_280498
1-16	1.0 m	15 kW	Uniform cooling		BALI_1.0_15kW_280498

Summary of the results

General remarks :

- For dimensionless number calculation, physical properties have been calculated at film temperature $(T_{bulk}+T_{wall})/2$.
- For test with top cooling T_{bulk} is the average temperature in the upper unstable layer and T_{max} is equal to T_{bulk}. Nusselt numbers are calculated from thermal balances and temperature difference between bulk and wall.
- For test without top cooling T_{bulk} is the average temperature of the pool. Downward Nusselt number is calculated from downward thermal balance and temperature difference between bulk and wall.

Run n°	P kW	T_{max} °C	T_{max}/T_{mean}	ϕ_{max} W/cm²	ϕ_{max}/ϕ_{mean}	Ra	Ra_i	Pr	Nu_{dn}	Nu_{up}
1-0	20.4	45.2	1.10	3.7	1.78	2.58E+12	1.35E+16	6.6	1151	2250
1-1	9.8	29.5	1.12	1.6	1.71	8.93E+11	3.52E+15	8.2	833	1699
1-2	25.9	51.5	1.11	5.3	1.77	3.53E+12	2.04E+16	6.0	1429	2367
1-4	20.8	44.9	1.12	4.2	1.77	2.53E+12	1.36E+16	6.6	1321	2142
1-5	15.0	37.3	1.13	3.1	1.73	1.61E+12	7.58E+15	7.3	1200	1954
1-6	9.3	60.5	1.62	5.8	3.55	1.61E+12	4.72E+15	7.3	1191	-

Run n°	P kW	T_{max} °C	T_{max}/T_{mean}	ϕ_{max} W/cm²	ϕ_{max}/ϕ_{mean}	Ra	Ra_i	Pr	Nu_{dn}	Nu_{up}
1-7	15.7	37.1	1.14	2.8	1.85	3.75E+12	2.27E+16	7.3	1430	2550
1-8	30.0	54.1	1.13	5.3	1.81	9.42E+12	7.31E+16	5.8	1832	3040
1-9	20.1	43.8	1.12	3.2	1.72	5.64E+12	3.67E+16	6.7	1470	2805
1-10	24.3	48.8	1.12	4.1	1.71	7.35E+12	5.15E+16	6.3	1666	2847
1-11	15.0	79.0	1.74	8.4	3.77	5.48E+13	2.36E+16	6.5	1807	-
1-13	20.4	45.1	1.12	3.5	1.75	6.07E+12	3.88E+16	6.6	1539	2683
1-14	30.5	54.2	1.13	5.3	1.78	9.46E+12	7.43E+16	5.8	1903	3127

Run n°	P kW	T_{max} °C	T_{max}/T_{mean}	ϕ_{max} W/cm²	ϕ_{max}/ϕ_{mean}	Ra	Ra_i	Pr	Nu_{dn}	Nu_{up}
1-15	9.0	36.2	1.11	2.0	1.74	4.42E+11	1.00E+15	7.4	547	1474
1-16	14.5	42.4	1.12	2.9	1.78	6.53E+11	2.03E+15	6.8	949 637*	1651

* See individual test report

APPENDIX B : Second test campaign results

The second campaign was dedicated to study the effect of Prandtl number on heat transfer. The viscosity of pool has been increased by adding cellulose compound in water to obtain Pr number from 10 to 1000.

All the tests have been performed for 1.5m height pool and uniform cooling conditions

Summary of the test matrix

Run	Power	Viscosity	Comments	Report Reference
2-0	10 kW	V1 Water + 0.6g/l $ZnSO_4$ Pr~10	Not enough LN_2 Tc fluctuations	no record
2-1	10 kW	V1 Water + 0.6g/l $ZnSO_4$ Pr~10		BALI_V1_10kW_030298
2-2	30 kW	V10 Water+2%QP3L Pr~100	Tc fluctuations	BALI_V10_10kW_060298
2-3	20 kW	V100 Water+3%QP40 Pr~1000	Tc fluctuations	BALI_V100_5kW_250398
2-4	20 kW	V1 Water + 0.6g/l $ZnSO_4$ Pr~10	Tc fluctuations	BALI_V1_20kW_310398

"Tc fluctuations" means that temperature fluctuations have been measured in this test from thermocouples located just below the upper ice crust. These measurements provide information about thermoconvective instabilities. Experimental files are available on request.

Summary of the test results

General remarks :

- For dimensionless number calculation, physical properties have been calculated at film temperature $(T_{bulk}+T_{wall})/2$.
- For tests with top cooling, T_{bulk} is the average temperature in the upper unstable layer and T_{max} is equal to T_{bulk}. Nusselt numbers are calculated from thermal balances and temperature difference between bulk and wall.

Run n°	P kW	T_{max} °C	T_{max}/T_{mean}	ϕ_{max} W/cm²	ϕ_{max}/ϕ_{mean}	Ra	Ra_i	Pr	Nu_{dn}	Nu_{up}
2-1	10.1	34.9	1.11	2.1	1.71	1.37E+12	4.66E+15	7.5	908	1808
2-2	7.8	53.4	1.16	2.6	3.61	2.14E+11	3.60E+14	106	309	991
2-3	5.2	65.5	1.21	2.5	5.69	2.51E+10	2.24E+13	1284	186	446
2-4	19.0	44.1	1.11	3.6	1.68	2.43E+12	1.22E+16	6.6	1204	2431

APPENDIX C : Third test campaign results

The third campaign was dedicated to the study of heat transfer by convection in a porous medium. In that case, we simulate a metallic pool with solid oxidic debris by a water pool filled with 1cm diameter solid glass balls. From reactor point of view, the main difference is that in our case the power is dissipated directly in the fluid phase and not in the debris.

Summary of the test matrix

Run	Height	Power	Cooling conditions	Comments	Report Reference
3-0	1.5 m	10 kW	Uniform cooling	Tc fluctuations	BALI_Porous_1.5_10kW_070498
3-1	1.5 m	10 kW	Without top cooling		BALI_Porous_1.5_10kW_090498
3-2	1.0 m	5 kW	Uniform cooling		BALI_Porous_1.0_5kW_050598

Summary of the test results

General remarks :

- For dimensionless number calculation, physical properties have been calculated at film temperature $(T_{bulk}+T_{wall})/2$.
- For test with top cooling T_{bulk} is the average temperature in the upper unstable layer and T_{max} is equal to T_{bulk}. Nusselt numbers are calculated from thermal balances and temperature difference between bulk and wall.
- For test without top cooling T_{bulk} is the average temperature of the pool. Downward Nusselt number is calculated from downward thermal balance and temperature difference between bulk and wall.

Run n°	P kW	T_{max} °C	T_{max}/T_{mean}	ϕ_{max} W/cm²	ϕ_{max}/ϕ_{mean}	Ra	Ra_i	Pr	Nu_{dn}	Nu_{up}
3-0	10.4	40.7	1.17	3.0	6.58	2.00E+12	5.93E+15	7.0	281	2421
3-1	6.1	74.7	1.79	2.7	4.13	2.11E+12	3.62E+15	6.9	860 397*	-
3-2	6.8	42.5	1.20	1.4	4.8	6.55E+11	9.58E+14	6.8	170	1220

* See individual test report

APPENDIX D : test with gas injection

A specific test, with gas injection has been performed to simulate a partial vaporisation of steel for in-vessel geometry.

Summary of the test matrix

Run n°	Height	Power	Cooling conditions	Comments	Report Ref.
G-0	2.0 m	15 kW	Uniform cooling	Gas injection	BALI_2.0_15kW_120397

Summary of the test results

See individual test report Reference : BALI_2.0_15kW_120397

Appendix L

SULTAN Experimental Program

Workshop on in-vessel core debris retention and coolability
Garching, Germany, 3rd - 6th March, 1998

Reactor Vessel External Cooling for Corium Retention SULTAN Experimental Program and Modelling with CATHARE Code

S. Rougé, I. Dor, G. Geffraye
CEA/Grenoble, DRN/ DTP, 17, rue des Martyrs, 38054 GRENOBLE CEDEX 9, France

INTRODUCTION

In case of severe accident, a molten pool may form at the bottom of the lower head, and some pessimistic scenarios estimate that heat fluxes up to 1.5 MW/m^2 should be transferred through the vessel wall. An efficient, though completely passive, removal of heat flux during a long time is necessary to prevent total wall ablation, and a possible solution is to flood the cavity with water and establish boiling in natural convection. High heat exchanges are expected, especially if the system design (deflector along the vessel, riser ...) emphasize water natural circulation, but are unfortunately limited by the critical heat flux phenomena(CHF).

CHF Data are very scarce in the adequate range of hydraulic and geometric parameters and are clearly dependent of the system effect in natural convection. The system effect can both modify flow velocity and two phase flow regimes, counter-current phenomena and flow static or dynamic instabilities.

SULTAN purpose was of two kinds, increasing CHF Data for realistic situations, and improving the modeling of large 3D two phase flow circuits in natural convection.

The CATHARE thermalhydraulic code is used for interpreting the data and for extrapolation to real geometry. As a first step, a one-dimensional model is used. It is shown that some closure laws have to be improved. Reasonable predictions may be obtained but, for some test conditions, multi-dimensional effects such as recirculation appear to be dominant. Therefore the 3-dimensional module of CATHARE is also used to investigate these effects. This model well predicts qualitatively the existence and the development of a 2-phase layer along the heated wall as well as the existence of a recirculation zone. But modelling problems still require further development as part of a long term program for a better prediction of multi-dimensional two-phase flows.

SULTAN TEST FACILITY

SULTAN Program is supported by CEA, EdF and FRAMATOME. The SULTAN facility (figure 1) was designed as a full scale analytical forced convection experiment, on a wide range of parameters covering most of the situations involved in a slow transitory situation after a severe accident (mass velocity : 10 => 5000 kg/s/m^2, pressure : 0.1 => .5 MPa, inlet subcooling : 50 => 0 °C, heat flux : 0.1 => 1 MW/m^2 (with some data up to 2 MW/m^2)). Fluid is demineralized and degassed water.

The Test section itself (figure 2) is simplified regarding reality, the purpose being to validate codes and calculate as many different realistic situations as desired. It is a flat plate, 1.5 mm thick, 4 m long and 15 cm wide, uniformly electrically heated, in a rectangular channel. Channel width (gap) can be enlarged from 3 to 15 cm, and the test section can be inclined from vertical to horizontal position. It is highly instrumented : mass velocity, electric power, absolute and differential pressures, wall temperatures, fluid temperatures, local void fraction, large windows for video films and high speed films. Precision of measurement is between 1 and 3 % of the measures.

TEST PROCEDURES

Eight campaigns of tests have been performed, each campaign involving one inclination and one gap of the test section, with the following range of parameters :

Campaign N° :	1	2	3	4	5	6	7	8
Inclination (°) :	90°	10°	90°	45°	45°	10°	10°	90°
Gap (cm) :	3	15	15	15	3	3	6	15
Heated length (m) :	4	4	4	4	4	4	4	2
Cover pressure (MPa) :	0.1-0.5	0.1-0.5	0.1-0.5	0.1-0.5	0.1	0.1	0.1	0.1-0.5
Inlet subcooling (°C)	0-50	0-50	0-50	0-50	0-50	0-50	0-50	0-50
Heat fluxes (kW/m^2)	←----------100 to 1000 step 100----------→							200 to 2000
Mass velocity ($kg/s/m^2$)	20 to 5000	10 to 2000	10 to 2000	10 to 2000	20 to 5000	20 to 5000	10 to 4000	10 to 2000

Two kind of tests were performed :

Pressure drops and CHF limits tests : for a constant cover pressure, inlet subcooling and uniform heat flux, mass velocity is slowly reduced with a relative ratio of 2% per minute, pressure drops and fluid temperatures are measured every 10 s. Limit of boiling crisis may be obtained before minimal flow rate, and is determined by a sharp increase of one or more of the thermocouples welded on the heated plate above a level set at Saturation temperature + 150°C.

Spacial local characteristics of two phase flow : for constant cover pressure, inlet subcooling, heat flux and mass velocity, void fraction and water temperature are measured at 25 positions in the test section gap and for 4 elevations along the test section. Temporal convergence of measures is assured with 30 to 600 s of integration for one position.

EXPERIMENTAL RESULTS

Two phase flow in SULTAN channel was thoroughly observed and measured, in order to better predict and calculate the behavior of a complete natural convecting system, with an emphasis on the evaluation of the recirculating mass flow rate and the static stability of the system based on the Internal and External Characteristics method [1],[2].

Experimental results : flow behavior

A general description of the flow in the test section will first try to sum up all the information provided by local measurements and films (figure 3).

First, a thermal layer develops near the heated plate, but never reaches the opposite side in large gaps or inclined positions of the test section. Thermal stratification is observed for inclined positions. Due to the low inlet flow velocities, mixed convection regimes are common in the test section, inducing internal recirculation cells which tend to homogenize temperatures, profiles of temperature become flatter, a secondary maximum can be observed on the cold wall opposite to the heated wall.

A two phase layer starts to develop in subcooled conditions. Subcooling is dependent of heat flux, flow velocity and test section inclination and can be up to 50 °C. Bubbles are first separate, with a oblong shape, about 3 or 4 cm long and 1 cm thick, which coalesce when they become numerous.

Generation of vapor is poorly predicted by correlations like Saha-Zuber's [3], it is probably partly due to the fact that this correlation was established for smaller and uniformally heated channels A new correlation will be optimized but is not yet available.

The two phase layer thickens in a more or less wavy manner, its development is highly non linear and increases much faster when saturation is imminent. In subcooled conditions, it never invades the whole channel and the maximum void fraction, up to 40% is always located on the heated plate.

When saturation is reached , the vapor invades the whole channel, even for large gaps and low inclinations. Stratification is important : for inclined positions of test section, the maximum of void fraction remains on or very near the heated plate whereas, for vertical positions, it moves toward the center of the channel, and can reach 90%.

Two different regimes may be observed : the first one corresponds to a rather steady two phase flow, with the particularity of heterogeneous vapor inclusions in size, from a few mm to about 1 m.

The second regime is pulsated flow with a period of 1 to 3 seconds, big pockets of vapor develop and are washed away periodically, count current water follows. CHF is avoided by a persisting thin film of liquid on the heated plate. Such a regime was described by Theofanous [4] and Chu [5] on the bottom of their hemispherical test sections. It was observed on SULTAN facility for inclinations of 10°, up to 1MW/m^2 for gap 3 cm, but only up to 500 kW/m^2 for gap 15 cm. Though its erratic aspect, this regime does not modify the average pressure drops in the test section, nor the limits of CHF.

A phenomena of reversal flow , with water flowing back from the pipe between the end of the test section and the condenser, was observed when outlet mean velocity was low enough, that is to say for any configurations at low heat fluxes, but only for vertical position, gap 15 cm and pressure 0.5 MPa at 1 MW/m^2. This phenomena improves considerably the limit of CHF, but is not easily predicted by the existing correlations of flow reversal, like Wallis' or Puskina and Solokin [6].

Experimental results : Pressure drops

The Internal Characteristics (IC) of the test section, i.e. the variation of pressure drop versus the mass velocity for constant thermohydraulic conditions of pressure, heat flux and inlet subcooling, were systematically investigated.

For vertical position (figure 4), the IC shape is the same for any gap, pressure, inlet subcooling and heat flux : the slope of the IC is quite flat at high mass flow velocity and tend to gravity head value, then becomes steeper after average saturation is reached. CHF always occurs rather low on the steep slope, for saturation conditions.

For that kind of IC curves, natural circulation should be efficient up to 1 MW/m^2 and even more, provided that the rest of the circuit is designed for little friction pressure drops. A two phase adiabatic riser above the heated length could improve significantly the performance of the circuit. No static instabilities are expected as the IC curve is strictly monotonous. Dynamic instabilities should be of small amplitude thanks to the steeples of the slope.

For inclined position of 10°, the behavior is more complex and of three kind : at low heat fluxes (< 400 kW/m^2), there is no difference with the vertical position. For large gap of 15 cm and high heat fluxes, CHF occur on the flat part of the IC, before average saturation is reached, there is no opportunity that steady natural convection should be established. For small gaps (figure 5) of 3 and 6 cm and high heat fluxes, boiling start at high mass velocity and the IC curves tend to the 'S' shape measured in small channels. Static instability is there expected in natural convection, with a rapid reduction of flow rate and destruction of the heated plate.

Experimental results : CHF Limits

191 CHF Data have been obtained on SULTAN facility. Dry patches are generally rather small (2-6 cm^2) and cannot expend much due to the thinness of the heated plate. Though CHF location is expected at the end of a uniformly heated test section, many dry patches have occurred at lower elevation, within the last meter and even the last two meters for inclined positions. In term of local quality, it still represent little difference, but was taken into account in the SULTAN CHF Correlation giving Heat Flux (F) in MW/m^2, in term of Cover Pressure (P) in

MPa, mass velocity (G) in kg/s/m^2, local thermodynamic quality (X), gap (E) in m and inclination (Θ = sin (I), I inclination above horizontal) :

$F = A0(E,P,G) + A1(E,G)*X + A2(E)* X^2 + A3(E,P,G,X)*\Theta + A4(E,P,G,X)*\Theta^2$

Standard deviation : 9.7%

with G' = LN(G)

$A0 = b0 + b1* E*G' + b2 /P^2 + b3*G + b4*E/P + b5*E/P^2 + b6*P*G'^2$

A1 = b7*G'2 + b8*E*G'

A2 = b9*E

$A3 = b10*G'^2 + b11*E*P + b12*X*G'$

A4 = b13*P + b14*G' + b15*X + b16*E

b0 = .65444	b4 = 1.36899	b8 = -4.49425	b12 = .855759	b16 = 2.2636
b1 = -1.2018	b5 = -.077415	b9 = 9.28489	b13 = -1.74177	
b2 = -.008388	b6 = .024967	b10 = -.0066169	b14 = .182895	
b3 = .000179	b7 = -.086511	b11 = 11.62546	b15 = -1.8898	

The term A0 + A1*X represents the general behavior of CHF phenomena, extensively studied for PWR conditions [7], [8], [9] : heat flux decreases almost linearly with X, with a positive influence of G at low quality and a negative one at high quality.

The term A2*X2 expresses the fact that, for high quality, the curves F versus X tend toward an asymptotic flat line : due to flooding phenomena, the heated plate is wetted by counter current water and boiling crisis is suppressed. In that particular case, boiling crisis does not depend any more of the conditions at the outlet of the test section, but of the amount of water stored above it and of the delay before uncovering. Flooding phenomena is correlated to low outlet velocities, it was then more or less observed on SULTAN for all campaigns at low heat fluxes, but only restricted to vertical position, gap 15 cm and pressure 0.5 MPa for heat fluxes up to 1 MW/m^2 (campaign 3) and even 2 MW/m^2 (campaign 8). This configuration was then maintained for more than 2 hours, until uncovering.

The influence of inclination is expressed through the terms A3*Θ + A4*Θ2. As expected [10], [11],heat flux decreases when inclination increases. The expression is very similar to the correlation obtained on the ULPU experiment, though it is difficult to compare as ULPU correlation does not take into account the effect of gap, pressure, velocity and local subcooling or quality, this last parameter being predominant.

The other parameters have a limited influence : F increases slightly when the pressure P increases. Gap seems to have no effect when CHF is reached for saturated conditions (generally in vertical position) and a limited positive effect in subcooled conditions (corresponding to inclined positions of test section).

OBJECTIVES OF THE CATHARE STUDY - 2 APPROACHES

The CATHARE thermalhydraulic code is used for interpreting the data and for extrapolating to the real geometry. Two approaches are proposed :

- ***1-D approach*** based on the 1-D modelling of the test section. The objective is then to handle a tool as simple and as fast as possible, assessed against the SULTAN experimental data. The objective is therefore to be able to recalculate the SULTAN experiment in order to predict, on one hand, the $\Delta P'$s which control the natural circulation, and on the other hand, the heat transfer coefficient and the CHF limits. It will allow to extrapolate the SULTAN experimental results to predict the system efficiency in real geometry (figure 6).

Anyhow this modelling has some limits which should be kept in mind, due to the characteristics of the test section (geometrical and range of parameters) and to the features of the flow :

- ✠ *assessment and improvment* of certain correlations due to the SULTAN domain: low pressure (1 bar to 5 bar), large hydraulic diameter, small mass inlet velocity, inclined heated surface of large dimension. This will lead to improve the Net Vapor Generation Point, the CHF, the interfacial and the wall friction and the condensation in case of subcooling. At present, considering the modification of the NVG point correlation proposed by H. Nehme [12], the 1-D approach gives satisfactory results (good qualitative description of the main phenomena occuring in the test section) as far as the flow is mainly one-dimensional [13].
- ✠ certain SULTAN observations have pointed out the presence of *multi-dimensional effects,* i.e. recirculation area as well as the simultaneous presence of 2 layers, a subcooled single-phase layer and a saturated 2-phase layer.The slip between the two layers can be taken into account by introducing a corrective factor in the interfacial friction correlation, whereas the presence of a stagnation zone and a recirculation area will be drastic limits to the 1-D approach.

- ***The 3-D approach*** is based on the 3-D modelling of the test section. The objectives is to handle a tool "as simple as possible", able to take into account the multi-dimensional effects of the flow. It will be used to confirm the 1-D results or the presumptions questioning the presence of multi-dimensional effects.
  - ✠ the *main phenomena* to describe are the followings :
    - ♦ *wall transfers*, i.e. wall friction and heat flux correlations
    - ♦ *void fraction profile predictions*, i.e. the interfacial forces, the dispersion due to turbulence, the recondensation of saturated vapour in subcooled liquid
    - ♦ the *turbulence transfer*, of energy and of momentum type. They are modelled by means of a turbulent diffusivity, derived from a (k,ε) model type (monophasic model which can be applied on both phases)
    - ♦ *prediction of the recirculation area*
  - ✠ nevertheless *some limits* have to be considered :
    - ♦ the state of the art of turbulence modelling, taking into account the fact that the domain is 2-phase flow, 3-dimensional and that the whole range of void fraction must be covered (all types of flow). Therefore, at present, the *(k,e) turbulence model* is implemented, which can be activated for any phase.
    - ♦ a certain "industrial constraint" has to be taken into account, i.e. considering the CPU time constraints, the complex physical phenomena and the lack of very fine measurements in the test section (especially concerning the phase velocity), the calculations are carried out with a rather coarse meshing for the test section.

PRESENTATION OF A SULTAN 3-D CALCULATION

Test section modelling

The 3-D calculation is carried out with the CATHARE 2 code version 1.4^{E} revision 5.

As the flow is assumed to be mainly 2-dimensional, the test section meshing is limited to a 2-D meshing, with only one mesh in the width. Taking into account the limits of the 3-D approach, it yields a 10 x 1 x 42 meshes, in cartesian coordinates (see fig.7), the mesh cell being very small close to both walls (heated and adiabatic) and expanding towards the centre-line of the test section.

The (k,ε) model is activated for the liquid phase. The imposed inlet turbulence level represents a slightly turbulent flow in a tube ($\nu = 9.10^{-4}$) where the turbulence level and the flow profiles are still not totally established. Indeed numerical tests have shown that the results of the simulation are only slightly dependant on the inlet imposed turbulence level.

CATHARE 3-D module

The CATHARE 3-D module [14] is based on a 2-fluid 6-equation model.

The discretization is based on a finite-volume method, structured mesh. It is of first order in space and time. It is based on the donor cell principle and staggered mesh grid. The numerical method is semi-implicit.

The physical relationships are extrapolated from those of the CATHARE 1-D module and extended in the three directions.

Test conditions

The selected test is a complex one which combines recirculation area, pre-heating of injected water to saturation and resulting evaporation process.

The test condition are the followings

- vertical configuration
- gap width = 0.15 m
- outlet pressure P_{out} = 5 bar
- cooling inlet temperature $T_{liq,in}$ = 100°C (ΔT_{sat} = 50°C)
- heat flux φ_{wall} = 470 kW/m^2
- inlet mass flowrate $G_{liq,in}$ = 42 kg/m^{2}s

CATHARE results

All the CATHARE results, analysed and compared to experimental data, are steady-state data. The analysis is based on velocity fields (gas and liquid), void fraction and temperature fields and radial profiles, as well as axial profiles for the temperature.

- ***liquid velocity field***
  - The results are drawn on figure 8.
  - The flow is accelerated in the vicinity of the heated wall, whereas the liquid velocity is nearly null close to the adiabatic wall.
  - In the lower part of the test section, the natural convection is the driving force. In the upper part of the test section, the water is even more accelerated which results in a recirculation region close to the upper part of the adiabatic wall.
- ***gas velocity field***
  - The results are drawn on figure 9.
  - As soon as the evaporation starts, the gas velocity is accelerated, mainly due to buoyancy forces
  - Because of bubble diffusion by turbulence, an effective horizontal mixing is observed. Due to the convection process, vapour at saturation is transported into subcooled liquid region. This leads to vapour recondensation.
  - It can be observed that the gas recirculation zone is less extended than the liquid one.
- ***Void fraction field and radial profile***
  - The results are drawn on figures 10, 11.
  - As subcooled liquid is injected, evaporation starts within a considerable margin from the heated wall leading edge. As soon as the onset of evaporation occurs, the void fraction increases strongly with a significant vertical gradient then tends to be homogeneous vertically as well as horizontally.
  - The horizontal transport of gas bubble is mainly due to diffusion and recirculation.

- Comparing the experimental and calculated radial profiles, it is observed that CATHARE does not perfectly predict the profiles but the main trends are correct. Indeed, at 2 meters high, a thin 2-phase layer is predicted as observed experimentally. At 4 meters high, the spreading of α with an asymmetrical profile is predicted but the average value is overestimated by CATHARE.

- ***Liquid temperature field and profiles***
  - The results are drawn on figures 12, 13.
  - The liquid temperature increases almost nearly till saturation is reached.
  - The CATHARE and experimental radial profiles show a very good agreement. In the liquid zone (at 1 and 2 meters high), the temperature profiles are well predicted. In the upper part (3 and 4 meters high), the liquid is nearly-saturated due to recirculation.

CONCLUSIONS AND PERSPECTIVES

SULTAN program supported by CEA, EdF and FRAMATOME, has provided a great amount of data concerning CHF, pressure drops and local measurements of 2-D two-phase flow on a large scale experiment. The main phenomena of flow have been analyzed, together with the influence of thermohydraulic and geometric parameters. A more complete interpretation is still under progress.

Some SULTAN experiments have been calculated then analysed with the thermalhydraulic system code CATHARE. Two approaches have been followed simultaneously : a 1-D and a 3-D approach.

The 1-D approach provides a simple and efficient tool. It can be improved by adjusting the interfacial friction and the condensation. Nevertheless it will remain limited when multi-dimensional effects as recirculation are dominant.

The 3-D modelling is already capable of revealing such multi-D effects. Nevertheless its application has to be extended to inclined and nearly-horizontal tests. The accuracy of its prediction might be improved by further modelling developments, as an improved formulation for the bubble diffusion based on the interfacial forces (drag, buoyancy, lift …). Also the addition of an interfacial area transport equation is discussed.

The experimental results indicate favourable possibilities of the coolability of a reactor vessel under natural convection. But it will have to be confirmed by validated CATHARE code calculation applied on realistic geometrical configuration and boundary conditions.

BIBLIOGRAPHY

[1] G.F. Hewitt, J.M. Delhaye, N. Zuber, *Multiphase Science and Technology*, Hemisphere Publishing Corporation, vol.4, chapter 3, 1989.

[2] S. Rougé*, SULTAN test facility for large-scale vessel coolability in natural convection at low pressure*, Nuclear Engineering and Design, 1996.

[3] P.N. Saha, N. Zuber, *Point of net vapor generation void fraction in subcooled boiling*, Proc. 5th Int. Heat Transfer Conf., Volume IV, pp. 175-179, 1974.

[4] S. Angelini, T.G. Theofanous*, The mechanism and prediction of a critical heat flux in inverted geometrics*, Department of Chemical and Mechanical Engineering Center for Risk Studies and Safety, University of California, Santa Barbara, CA 93106.

[5] T.Y. Chu, S.E.E. Slezaci, J.H. Bentz, W.F. Padedag*, Large scale boiling experiments of the flooded concept for In-Vessel retention*, OECD/CSNI/NEA Workshop on Large Molten Pool Heat Transfer, Nuclear Center Grenoble, France, March 9-11, 1994.

[6] J.M. Delhaye, M. Giot, M.L. Riethmuller*, Thermohydraulics of Two-Phase Systems for Industrial Design and Nuclear Engineering*, Hemisphere Publishing Corporation, McGraw-Hill Book Company, chapter 4, , pp. 61-68, 1981.

[7] R.W. Bowring, A *simple but accurate round tube uniform heat flux, dryout correlation over the pressure range 0.7 - 17 MN/m^2 (100 - 2500 psia)*, AEEW-R-789, 1972.

[8] G.F. Hewitt, J.M. Delhaye, N. Zuber, *Multiphase Science and Technology*, Hemisphere Publishing Corporation, vol.2, chapter 4, 1986.

[9] D.C. Groeneveld, *A general CHF prediction for water suitable for reactor accident analysis*, Rapport interne CEA, 1982.

[10] T.G. Theofanous, S. Syri, *The coolability limit of a pressure vessel lower head*, NUREG/CP-0142, Volume I, pp. 627-647, , NURETH-7, Saratoga Springs, NY, September 10-15, 1995.

[11] F.B. Cheung, K.H. Haddadn Y.C. Liu, *Critical Heat Flux (CHF) phenomenon on a downward facing curve surface*, NUREG/CR-6507, PSU-ME-97-7321, June 1997.

[12] H. Nehmé, *Etude de l'ébullition dans un canal rectangulaire, inclinable, de grand diamètre hydraulique*, Thesis Report, Institut National Polytechnique de Grenoble, France, February 1997.

[13] I. Dor, G. Geffraye*, Modelling of SULTAN experiment about reactor vessel cooling in case of corium retention*, 35th European Two-Phase Flow Group Meeting, Brussels (Belgium), June 6-7, 1997.

[14] F. Barré, I. Dor, C. Sun, *The multi-dimensional module of CATHARE 2, description and application*, NURETH-7 Conference, Saratoga Springs, NY (USA), September 10-15, 1995.

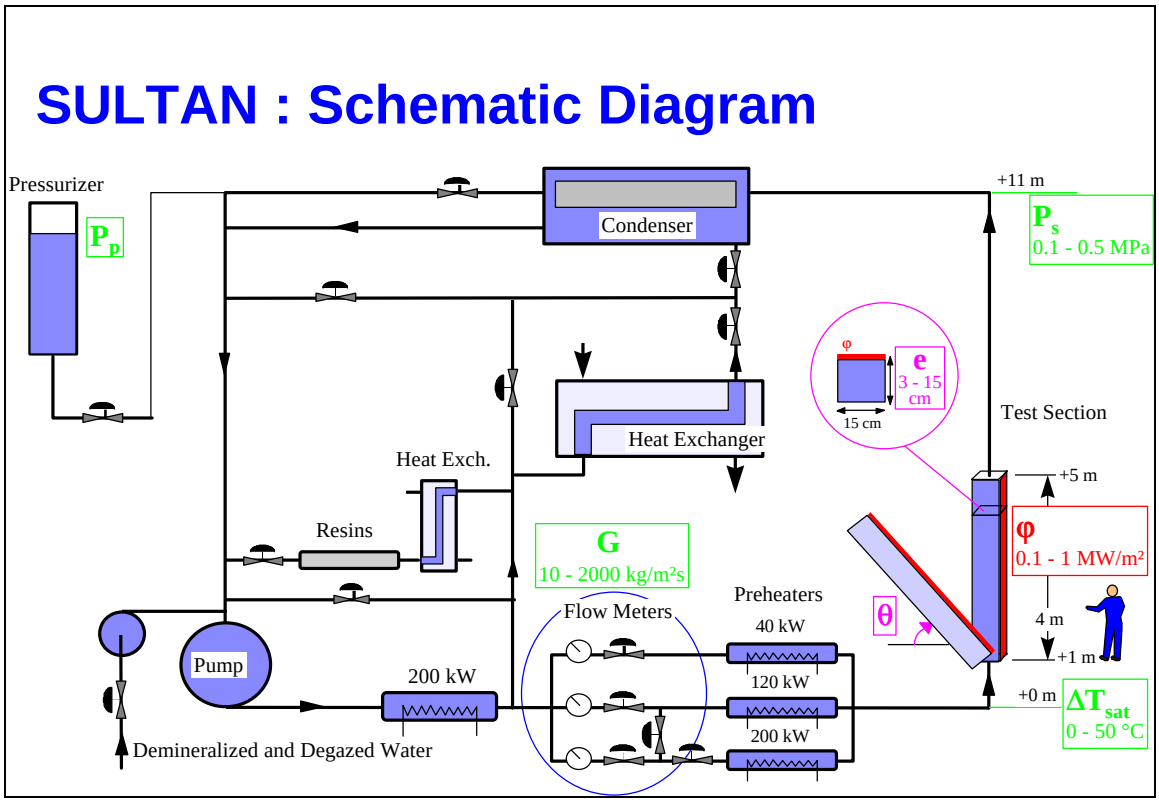

FIGURE 1

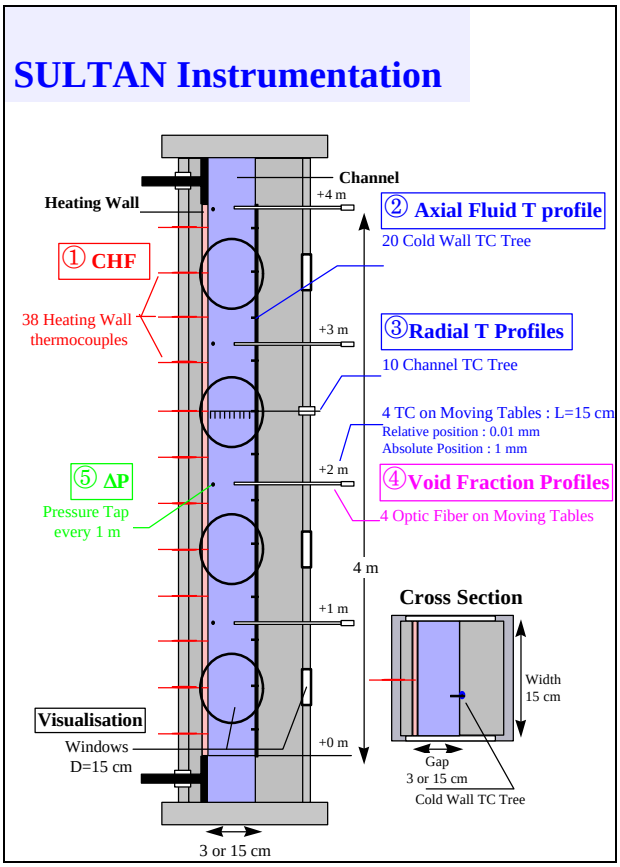

FIGURE 2

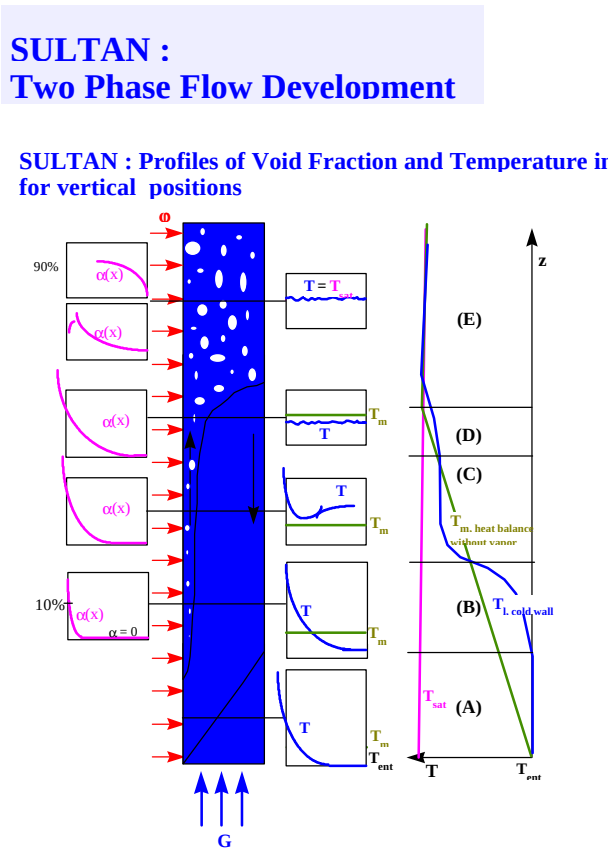

FIGURE 3

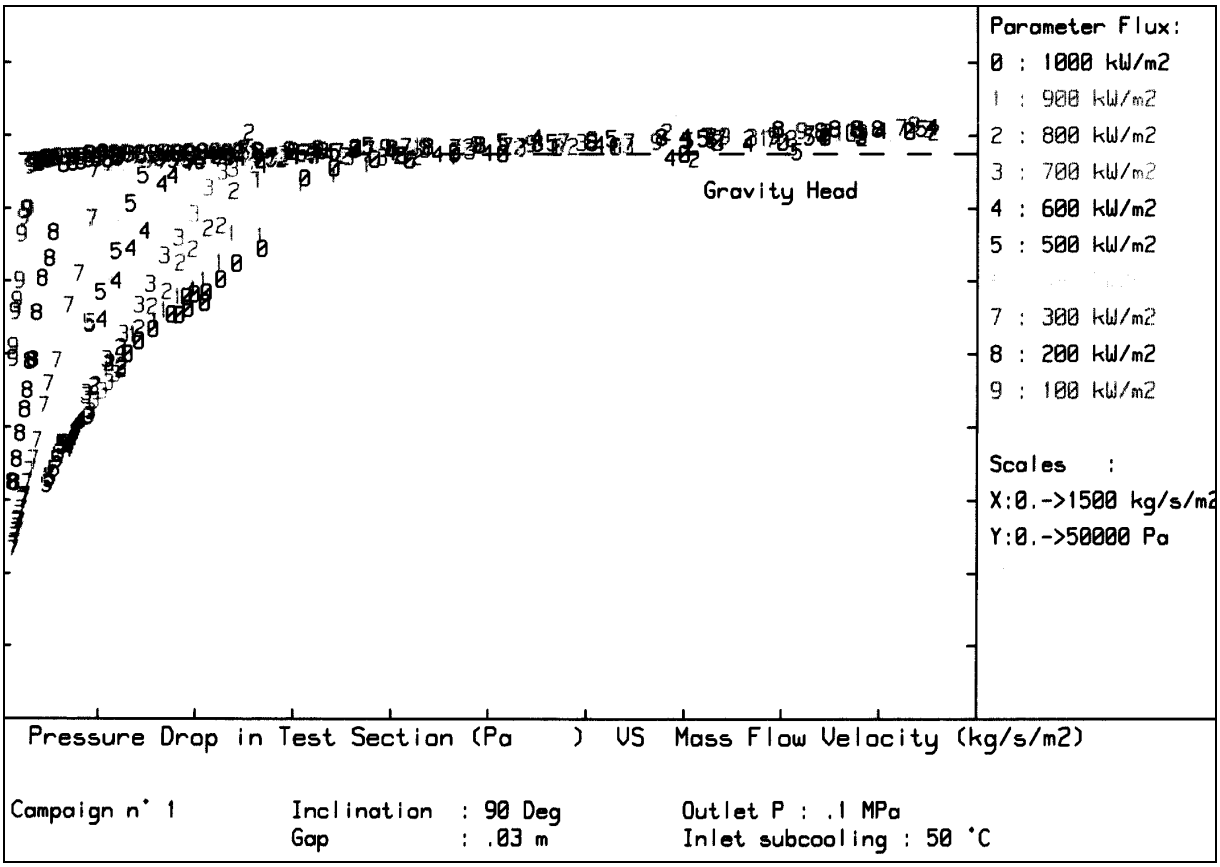

FIGURE 4

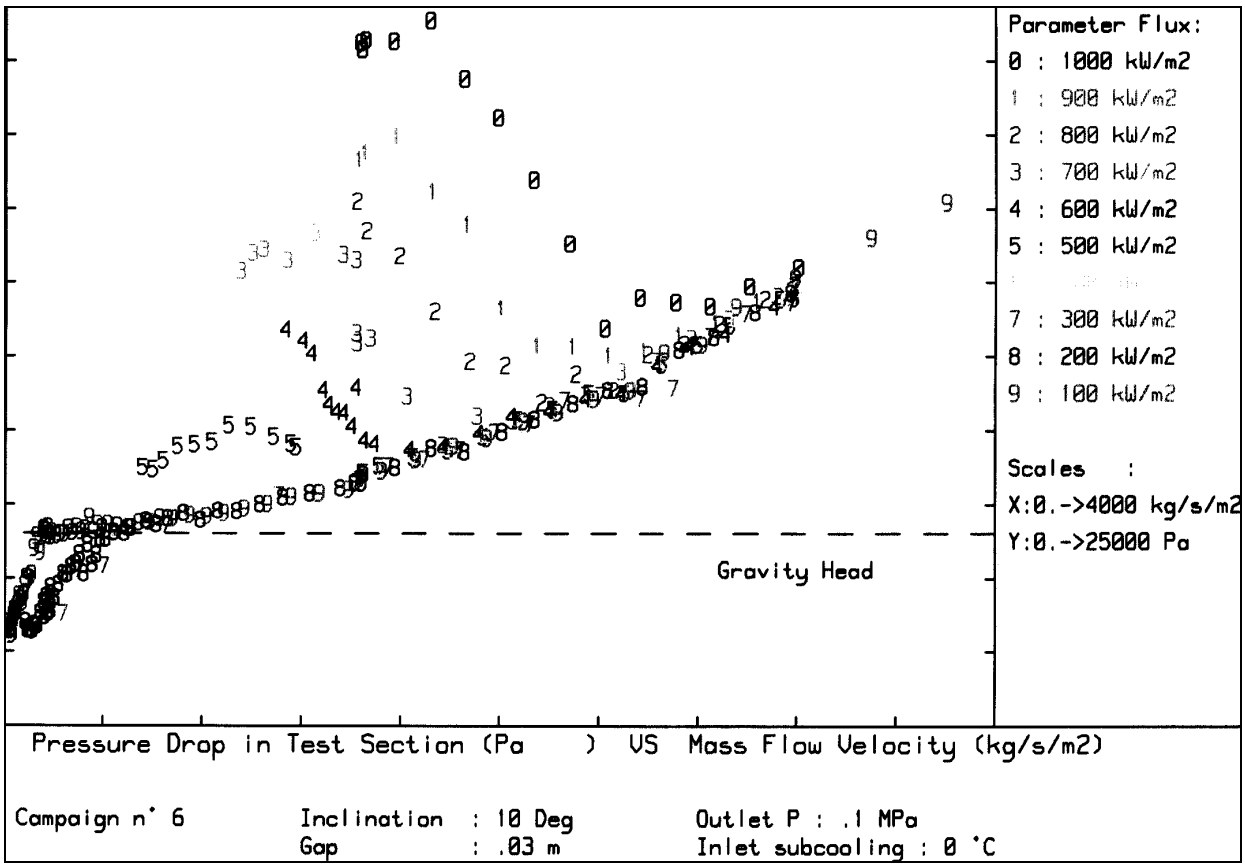

FIGURE 5

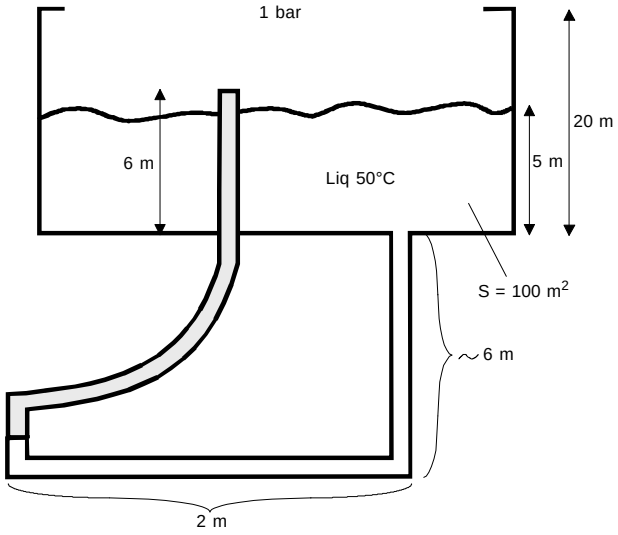

Circuit modelling

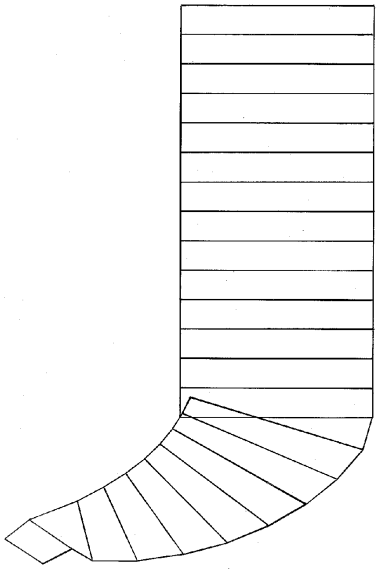

Meshing of the test section

FIGURE 6 : 1-D extension to real geometry

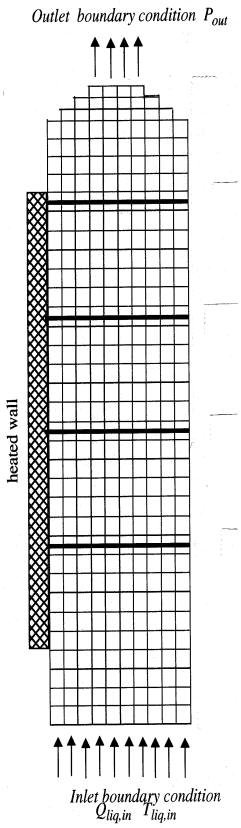

FIGURE 7 : SULTAN test section 3-D modelling

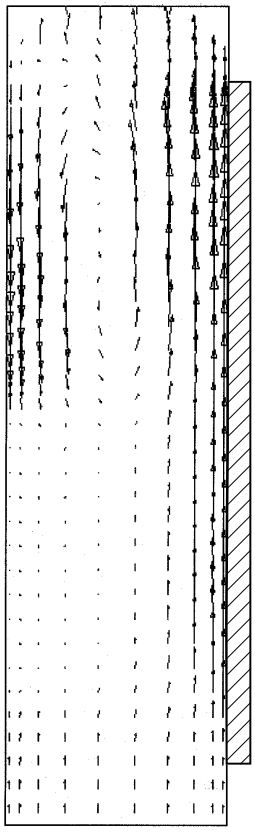

FIGURE 8 : Velocity field liquid phase

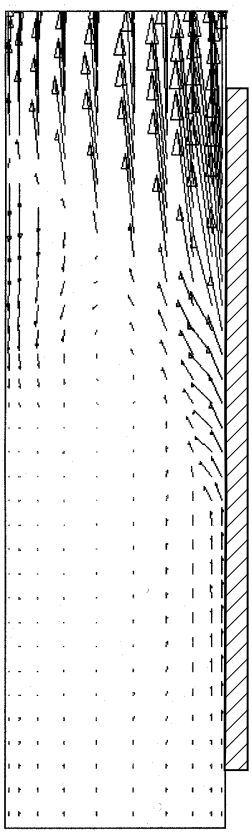

FIGURE 9 : Velocity field gas phase

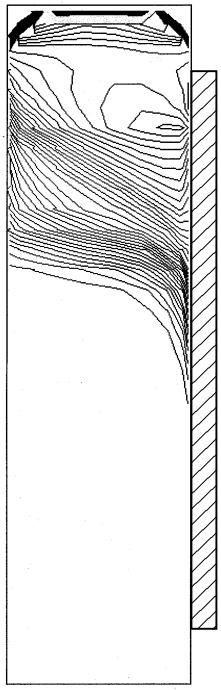

FIGURE 10 : Void-fraction distribution

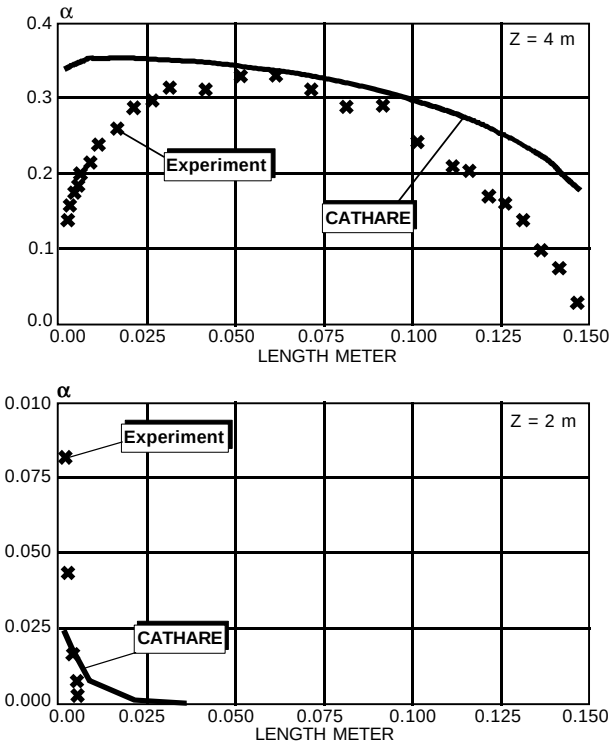

FIGURE 11 : Void fraction horizontal profiles, 2 m and 4 m

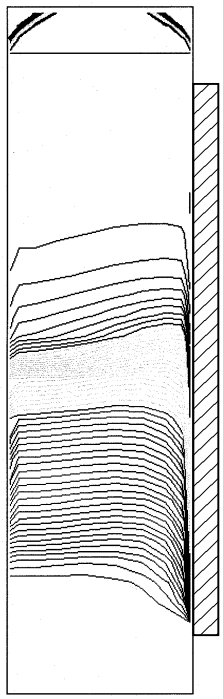

FIGURE 12 : Liquid temperature distribution

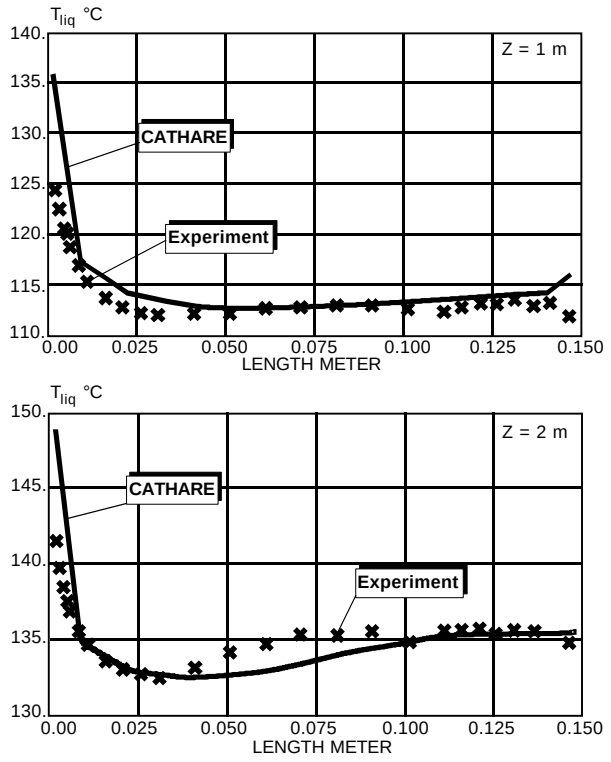

FIGURE 13 : Liquid temperature horizontal profiles, 1 m and 2 m

Appendix M

Experimental results from the SIMECO experiment

M.1 Introduction

A hypothetical core melt accident in a light water reactor (LWR) may result in accumulation of core debris in the lower head of the reactor pressure vessel (RPV). The core debris, if unquenched, may heat up and commence natural circulation. The core melt pool formed, likely, will consist of a decay-heated oxidic region at the bottom and a metal layer on the top. The thermal loads exerted on the vessel wall by the natural circulation pool have been a subject of study for the last several years [1]. The primary interest has been the determination of the feasibility of an accident management scheme of retaining the melt within the lower head by cooling the vessel outside wall with water.

The SIMECO (**S**imulation of **I**n-vessel **ME**lt **CO**olability) experimental facility was developed originally in order to investigate the effects of (i) boundary crust and mushy layer on natural convection heat transfer; (ii) melt stratification on natural circulation; (iii) turbulent flow on the possible amelioration of melt stratification; (iv) integral and multidimensional heat transfer between and in, the melt pool, the top metallic layer and the vessel.

The RASPLAV Program [4], conducted in Russia, employs prototypic (UO_2-ZrO_2) melt materials in a 200 kg slice facility, in which the thermal loads imposed by the prototypic melt on a cooled vessel wall are measured. The RASPLAV experiments, conducted at $Ra' \leq 10^{11} - 10^{12}$, have shown corium melt stratification for prototypic compositions and temperatures. Following these results, it was also decided to use the SIMECO facility to study the heat transfer at the boundaries of an internally heated stratified pool during mixing and separation process. The objectives are to determine the effect of, the miscibility or immiscibility of the

layers, the density difference between the layers, the layers thicknesses and the heat generation in one or both layers, on heat transfer.

M.2 SIMECO Facility and Experimental Program

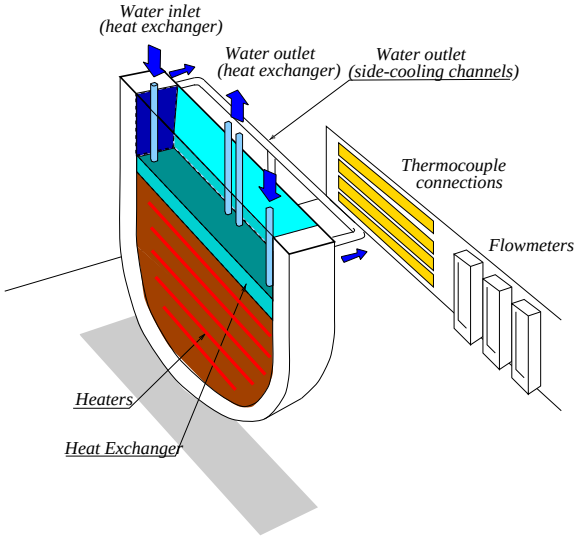

Fig. M.1: SIMECO experimental facility - Overview.

The experiment facility consists of a slice-type geometry including a semi circular section and a vertical section (Fig. M.1). The diameter, height and width of the test section are 530x620x90mm (Fig. M.2). The slice walls are made of brass, except for the front wall which is made of a special glass allowing flow and crust visualisation.The vessel wall is cooled by controlled flow rate water loops (Fig. M.2). On the top of the pool a controlled flow rate water heat exchanger is used to provide the top boundary condition.

Internal heating in the pool is provided by thin cable-type heaters. Two heaters, 3-mm cable diameter and 4-m long are uniformly distributed in the semi-circular section. They can supply a maximum of 4 kW power to the pool.

For uniform pool, water and binary salt mixtures are employed as melt simulants. Both eutectic mixture (50%-50%) and non-eutectic mixture (20%-80%) of $NaNO_3$-KNO_3 are used in the SIMECO experiments. The binary-mixture phase diagram is quite similar to that of the binary-oxide core melt UO_2-ZrO_2. For the 20%-80% mixture the temperature difference between the liquidus and solidus is about 60K. The liquidus temperature of the binary mixtures are 220^{o}C and 280^{o}C, respectively, for the 50%-50% and 20%-80% compositions. Previously, these salt mixtures were extensively, and successfully, employed as core melt simulants in

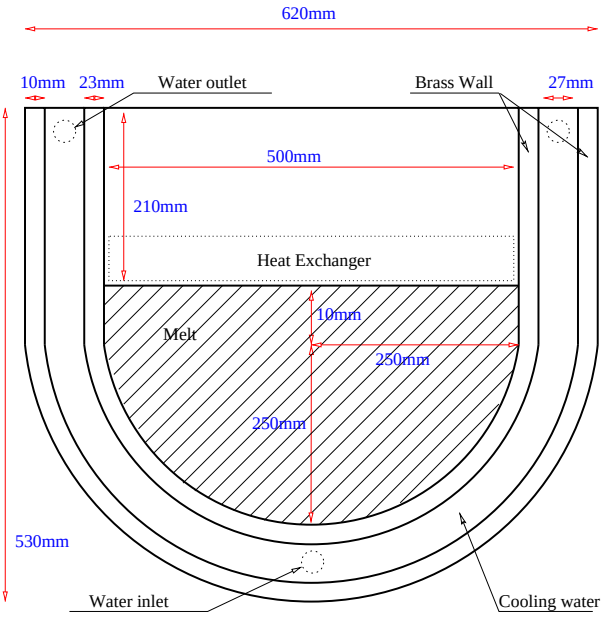

Fig. M.2: SIMECO experimental facility - Main dimensions.

melt-vessel interaction experiments performed at RIT/NPS [3]. The heat of fusion, heat capacity, density, viscosity, heat conductivity of these mixtures were measured to enable pre-test and post-test analyses of the experiments. For stratified pool, water and salt water (with different salt concentrations), as well as, parafin oil and water are pairs employed respectively, as simulant for stratification of miscible and immiscible fluids.

The water loop temperatures are used to obtain the average heat flux on the side wall and on the top of the pool. A total of 36 K-type thermocouples are kept inside the brass vessel wall at different angular locations in order to derive local heat fluxes . Inside the pool, 34 K-type thermocouples are installed to measure the local temperature variation, with emphasis on the near wall region and the interface between the two stratified layers (Fig. M.3).Video recording of the test section is used to track, for the uniform salt pool the crust behavior, and for the stratified pool the interface behavior and mixing process.

For the uniform pool, the SIMECO test matrix is designed to cover:
(i) different pool compositions;
(ii) different top and sidewall cooling conditions;
(iii) different heat generation rates.

In a scoping test series, water was employed as melt simulant, while in the main test series, binary salt mixtures are employed. The SIMECO facility enables experiments with Rayleigh numbers up to $1.9 \cdot 10^{13}$ (with salt) or $5.5 \cdot 10^{13}$ (with water) for the pool natural convection. The flow fields are expected to be turbulent

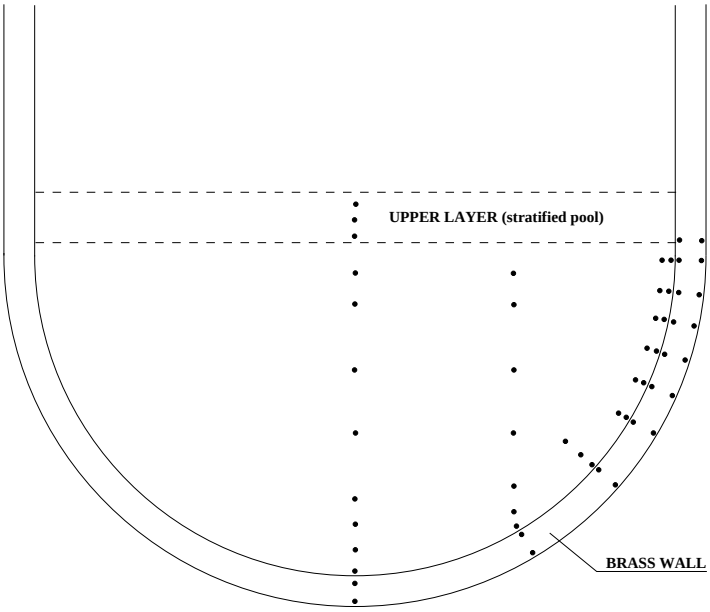

Fig. M.3: SIMECO experimental facility - Thermocouples location.

for these values of the Ra'.

For the stratified pool, the SIMECO test matrix is designed to cover:
(i) immiscible and miscible fluids;
(ii) different upper layer thicknesses;
(iii) different heat generation rates;
(iv) one or both layers heated;
(v) different density difference.

During these experiments the Rayleigh number (Ra'), based on the lower pool, vary from $3.8{\cdot}10^{11}$ to $5.5{\cdot}10^{13}$.

All the tests done so far are listed in appendix A.

M.3 Experimental Results

The SIMECO data are presented in two different sections on:

- The study of uniform pool where water and salt mixtures are used as simulants.

- The study of stratified pool where water, salt water and parafin oil are used as simulants.

M.3.1 Uniform Pool Test Series

Mini SIMECO Test Series

The mini-SIMECO test series was performed in a test facility similar to that described in the previous section, but smaller and much simpler. The main purpose of the mini-SIMECO program was to examine the technical problems for building the SIMECO facility with internal heaters. Nonetheless, the mini-SIMECO test series provided useful data on melt pool formation and heat transfer. In particular, visualization of the melt pool formation dynamics was obtained. The crust was found thickest at the lowermost region of the pool, while the top crust and the crust at the pool's corner was very thin. More importantly, analysis of the mini-SIMECO test results revealed, about, the longer-term transients of melt pool formation and heat transfer; the heating method used (i.e. internal heaters) provides good simulation of the volumetric heat source. This is valid because the time scale of convective heat transfer from the heater's surface to a given control volume is much smaller than the time scales of either melt pool formation or transient heat up. Additionally, while the energy transfer rate is important, heat transfer processes in a particular control volume in the pool are indifferent to the way in which the heat was generated in other parts of the pool.

Water Test

The SIMECO water test series was conducted to test the performance of the water cooling circuit, heaters, thermocouples and DAS.

In this test series, truly isothermal boundary conditions were not provided on the pool boundaries. The vessel semi-circular wall adapted itself to the heat fluxes. A non dimensionalized temperature, proposed previously [2], is used to put together all water tests. The upper part of the pool (y/H$>$0.6) is essentially at a uniform temperature (T_{max}), and the lower part is characterized by a well defined temperature gradient (Fig.M.6). It is clear that the uniform temperature layer on the upper part of the pool is directly related to the agitation created by top cooling. Figure M.7 shows the nondimensionnal downward local heat flux along the vessel, where an angle of 0 degree corresponds to the bottom of the pool. Two distinct regions are identified, for $\theta<50$ the heat flux increases almost linearly, it reaches a maximum at $\theta\sim50$ and when $\theta>50$ it fluctuates around a value of 1.3. It appears that these two regions corresponds exactly to the two regions of the stratification pattern described by the temperature.

Salt Mixture ($NaNO_3$-KNO_3) Test

Fourteen experiments were conducted in this series (Thirteen with an eutectic mixture and one with a non-eutectic mixture). This section focuses on comparison between the eutectic and non-eutectic cases. All data presented are measured during the steady state. This steady state is defined based on two criteria: a global thermal balance greater than 90% and a thermal evolution lower than 1^o/h (slope of linear data interpolation). As an exemple, the global heat balance and the centerline temperature of the test SSEu-4 are presented on figures M.8 and M.9. It is clear that above 6500 seconds the two steady state criteria are respected.

The visual observations of the pool every twenty minutes, allows us to delimitate clearly the liquid pool during the steady state. A crust is formed at the bottom of the pool. The thickness of the crust start from 1.9 cm (+/- 2mm) at the bottom and dicreases as the angle along the vessel wall increases until a value around 45 degrees. These observations are reproductibles both for eutectic and non-eutectic experiments. Figure M.10 presents the nondimensionnal centerline temperature for both eutectic and non-eutectic tests. Two regions can be distinguished in the liquid pool (y/H$>$0.08). For 0.08$<$y/H$<$0.75 a region caracterizes by a temperature gradient, and for y/H$>$0.75 a region where the temperature is almost constant at T_{max}, due to the top cooling of the pool. The data present on figure M.11 shows three distinct regions along the vessel wall. The region where the crust is present is characterized by a constant heat flux ($0<\theta<40$). In the intermediate zone ($40<\theta<76$), the heat flux increases until an average peaking value of 1.73, and stays almost constant above an angle of 76 degrees. With reference to figure M.10, it can be seen that the constant heat flux region corresponds exactly to the constant temperature zone. In order to compare the heat fluxes obtained in eutectic case and non-eutectic case, some of eutectic experiments are plotted together on figure M.12. No major differences are observed between eutectic and non-eutectic cases. The three same heat fluxes region can still be observed. The transient heat flux splitting between the upward and downward heat flux is presented on figure M.13 for both eutectic and non-eutectic cases. The steady state regime (above 8000 s) is characterized by an almost constant splitting heat flux where both average splitting heat flux are of same order (1.15 for the eutectic experiment, 1.01 for the non-eutecic experiment).

M.3.2 Stratified Pool Test Series

All the test are done with two stratified fluid layers. Several parameters vary during this study, like, the power supply, the fluid layer composition, and the height of the upper layer. The other parameter possible is to have one or both layers heated (Figs. M.4 and M.5).

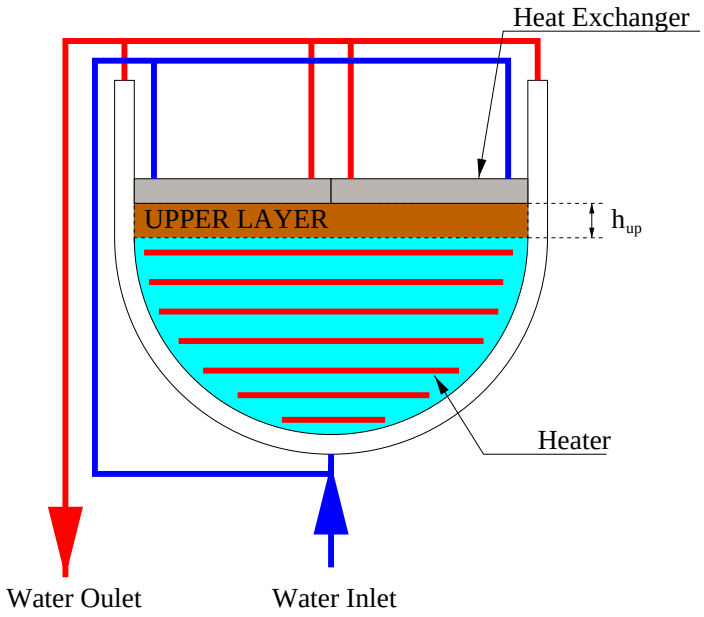

Fig. M.4: One Layer Heated.

With one layer heated (Fig. M.4) the downward pool, 26 cm in height, is filled up with the first fluid and the second layer is placed on top of it without heat generation. The thickness of the top layer h_{up} can vary between 1 cm up to 6 cm.

When two layer are heated, the total height of the pool (lower plus upper layers) is 26 cm and both layers received heat generation (Fig. M.5). In this case, the thickness of the upward layer vary from 4 cm to 12 cm. As the heater is uniformly distributed in the semicircular section, the mean internal heat flux (based on the power supply and the volume of each layer) is always the same in both layers.

Immiscible Fluids Test

In all these experiments the lower fluid layer is water and the upper fluid layer is parafin oil, which gives a density difference of 12%. The same two criteria are used to defined the steady state regime.

- One Layer Heated

  The transient centerline temperature obtained during the test SE-W-20 is presented on figure M.14. It is clear that after 2000 s that the upper part of the heated pool (0.1105m <y< 0.26 m)is boiling. The same behavior is observed for all high power supply (around 3600 W) experiments, whereas

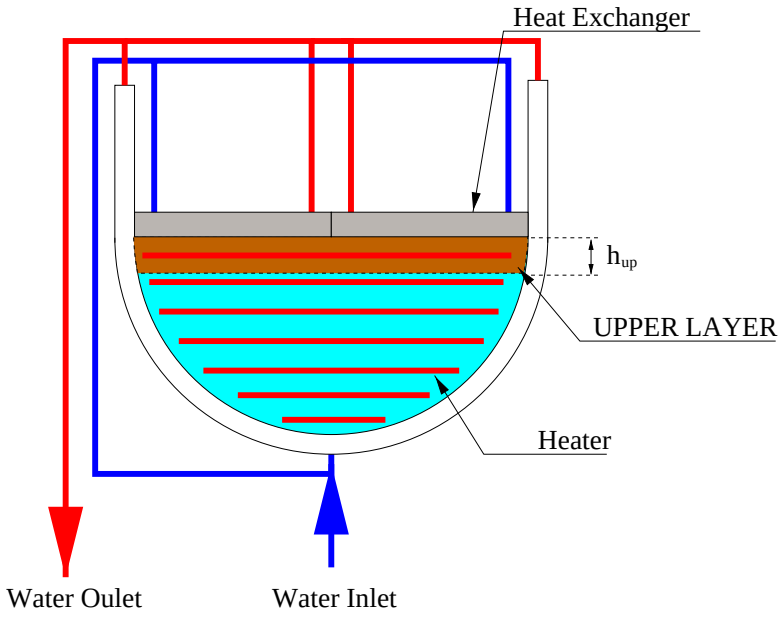

Fig. M.5: Two Layers Heated.

there is no boiling of the downward pool when it is heated with low power supply (around 1200 W).

Figure M.15 shows the splitting heat flux for different upper layer thicknesses and different power supplies. No major effect of the upper layer thickness on the heat transfer can be seen since the splitting heat flux stays almost constant at 0.33 during the steady state for all upper layer thickness studied. But the splitting heat flux is double when the power supply increases by a factor 3. If we consider the ratio between the splitting heat flux for high and low power supply $(q_{up,high}/q_{dn,high})/(q_{up,low}/q_{dn,low})$, it can be rewrite in the form $(q_{up,high}/q_{up,low})/(q_{dn,high}/q_{dn,low})$. The ratio $(q_{dn,high}/q_{dn,low})$ is around 2.3 whereas the ratio $(q_{up,high}/q_{up,low})$ is around 4.7. The increase of the downward heat flux is principaly due to the increase of the power supply, but in case of upward heat flux it is due to the fact that for high power supply boiling was observed in the upper part of the pool. So the increase of the splitting heat flux when the power supply is tripled is essentially due to the boiling of the upper part of the heated pool.

In the downard layer, the local nondimensional heat flux along the wall has a similar shape to the one obtained in a uniform water pool, i.e. a linear increase from an angle of 0 to 50 degrees, and a constant value above 50 degrees (Fig. M.16). The interface between the upper and lower layer located at 91 degrees is characterized by a steep decrease of the heat flux

(from 1.45 to 0.8). The shape of heat flux curve is not affected neither by the thickness of the upper layer or the power supply (Fig. M.16).

- Two Layers Heated

  The transient splitting heat flux is presented for different upper layer thicknesses and power supplies (Fig. M.17). During the steady state, the splitting heat flux is almost constant at a value, which increases as the upper thickness increases. In fact, this increase is directly due to the rise of the power supply when the upper layer thickness increases, since the power supply delivered into each layer is proportionnal to the layer volume. An increase is observed, between the lower and higher power supply case, from 0.33 to 0.73. Similar to the one layer cases, when power supply is high , boiling of the upper part of the lower pool is established, which enhances the upward heat tranfer by a factor 2.2 (in this case).

  The location of the interface between the two layers can be easily tracked from the local nondimensional downward heat fluxes plot (Fig. M.18). In fact, the heat flux is peaking to its maximum value just below the interface. The lower pool is characterized by a constant increase of the heat flux along the vessel until its maximum value (located at the interface), while, the upwper pool is characterized by a decrease in heat flux until it reaches a constant value (more obvious for h_{up}=12 cm). Changing the power supply does not affect the shape heat flux curve.

The splitting heat flux of the one layer and two layers cases are compared, respectively, for low and high power supply on figures M.19 and M.20. In both graphs the splitting heat flux of a two layers case is at least the twice of the one layer case. It appears that the ratio of the downward heat flux between the two and one layer cases stays constant around the unity. The ratio of the upward heat flux between the two and one layer cases increase at least by a factor 2. So the fact that in the two layer heated case the upper layer is heated enhance the upward heat flux and then increases dramatically the splitting heat flux.

Miscible Fluids Test

- Effect of the Density Difference

  Two kinds of interface behavior have been identified. Unstable interface is characterized by for low density differences ($<$5%) and blurred boundaries, while stable interface is defined by distinct boundaries and higher density differences ($>$5%). Images of the interface evolution between the two layers are recorded by a video camera. Movement of the upper layer is extracted

from the processing of these images . Figures M.21 and M.23 present the upper layer thickness evolution for unstable and stable interfaces, respectively. The upward/downward heat flux splitting is presented for unstable and stable interfaces on figures M.22 and M.24, respectively.

For unstable interface, the mixing process is faster than that for a stable interface. A sudden disappearance of the interface is observed for all unstable interfaces (Fig. M.21) corresponding to the complete mixing of the upper layer with the lower pool. As the mixing is complete, the upward/downward heat flux splitting rise to a steady state value of 1.5 in steps (Fig. M.22). During the mixing process of the upper layer with stable interface, the heat flux split is constant around a value of 0.5 (Fig. M.24). As soon as the mixing is complete it increase steadily to a steady state value of 1.6 (Fig. M.24).

Here after a classification has been established as a function of the density difference. We will always consider layers with 5% density difference as a representative of an unstable interface, and layers with 30% density difference as a representative of a stable interface.

- One Layer Heated

  Like immiscible fluids, a boiling upper layer is established in the upper part of the lower pool when the interface is still present and power supply is high (Fig. M.25). But this phenomena occurs only during the mixing process, as soon as the upper and lower layers are mixed (after 2000 s in this test), all temperatures of the pool drop to below 100^{o}C (Fig. M.25).

  The upward/downward heat flux splitting is presented for low and high power supply, respectively, for unstable and stable interface in figures M.26 and M.27. The upward/downward mixing time scale is similar for stable and unstable interfaces when high power is supplied to the pool, and the splitting heat flux rise around a value of 1.55 for both interfaces during the steady state (Fig. M.26 and M.27). When power supplied to the pool is low, the upward/downward mixing time scale is multiplied by 3 for unstable interfaces and by 15 for stable interfaces (Fig. M.26 and M.27). The stable interfaces are sharper and imposes a greater resistance for the upward heat transport which results in an higher mixing time scale. The major difference in mixing time scale observed between high and low power supply comes from the boiling, present in high power supply case, that enhances the upward heat transfer and create an additionnal mixing motion when the bubbles rises. During the steady state (after mixing), both stable and unstable interfaces have almost a constant upward/downward heat flux splitting around 1.8.

The effect of the upper layer thickness is shown in figure M.28 for unstable interfaces. Similar results were found for stable interfaces. No major influence of the upper layer thickness on upward/downward heat flux splitting can be found. The same observations are reproductibles for the local nondimensional downward heat flux along the vessel (Fig. M.29). The heat flux shape is similar to the one observed for uniform water pool (i.e rising below an angle of 50 degrees and constant value above this angle).

- Two Layers Heated

  Similar mixing process was observed for all cases studied (both unstable and stable interfaces), only the mixing time scale change as a function of the power supply and the interface sharpness. To illustrate this mixing process, the test SE-W-27 is examined in detail. The transient centerline temperature is presented in figure M.30, and the centerline temperature profile during the mixing process in figures M.31 and M.33. Figures M.32 and M.34 shows the local heat flux profiles along the vessel wall during the mixing process.

  Three stages can be distinguished. The first one, representative of the zone (a) in figure M.30, is characterized by the mixing of the upper layer with an intermediate lower layer (0.12 $<$y$<$ y_i, where y_i is the elevation, from the pool bottom, corresponding to the interface). During the first stage the lower layer is characterized by an increasing temperature, from the bottom of the pool until the interface, whereas the temperature decreases, from the interface to the top of the pool, in the upper layer (Fig. M.31). Then the temperature in the upper layer increases and becomes constant above an height of 12 cm representativing the final mixing between the upper layer and the intermediate lower layer. From the beginning, a similar behavior is observed for the heat flux along the vessel (Fig. M.32). Then the heat fluxes increases in the upper layer and decreases in the lower layer, the final intermediate upper layer mixing is characterized by a constant heat flux above an angle of 60 degrees, which correspond to the region above an height of 12 cm (Fig. M.32). At the end of the first stage a new upper layer is created above a pool elevation of 12 cm, it is expressed by a switching of the temperature and heat flux peaking value to respectively 11 cm and 60 degrees (Figs.M.33 and M.34).

  Zone (b) in figure M.30 is characteristic of the second mixing stage where the new upper layer finally mixes with the lower layer. In general, the second stage is much more longer than the first one, except when the initial upper thickness is equal to 4 cm. In this case, the second stage is really short and so the final mixing occurs rapidly. During the second stage the peaking temperature decreases to the constant temperature representative of

the upper layer (Figs. M.30 and M.33). The peaking heat flux in the vessel is switched to an angle of 49 degrees and decreases as the heat flux in the upper layer increases to finally have a constant heat flux above the angle of 49 degrees (Fig. M.34).

After the complete mixing of the two layers, the new uniform pool reaches a steady state regime (zone (c) in figure M.30). Then, the centerline temperature and heat fluxes in the vessel are similar to those of a uniform pool (steady state curves on Figs. M.33 and M.34).

The next part will focus on the transient upward/downward heat flux splitting which is presented for unstable interface, respectively, in figure M.37 for low power supply and in figure M.35 for high power supply. For stable interfaces, it is presented in figure M.38 for low power supply and in figure M.36 for high power supply. For unstable interfaces and high power supply the transient splitting heat flux first decreases to a minimum value around 1 and then increases smoothly to the steady state value around 1.9. The three mixing stage can be distinguished, the first one is characterized by the decrease to the minimum value, then the second stage by the increase to the steady state value, and the steady state regime is described by the constant splitting heat flux (Fig. M.35). The main difference between each curves representating different initial upper layers thickness is the time scale during each stage of the mixing process. The time scale of each stage increases when the initial upper layer thickness increases. The same observations can be extracted from figure M.36 for stable interface and high power supply. But in this case there is a major difference for the initial upper layer thickness of 12 cm. In this case we never reach the third mixing stage even after 22 hours of experiment. In fact we stayed in the second mixing stage and reached a steady state with two stratified layers of miscibles fluids. For stable interfaces and low power supply none of the experiments reach the third mixing stage, all experiments reaches a steady state of two stratified layers of miscible fluids (Fig. M.38). All the data presented in figure M.38 remained constant for 22 hours. For the unstable interfaces all experiment finally mixed but the time scale to reach the third mixing stage is 2h45 for h_{up}=4 cm, 5h30 for h_{up}=8 cm, more than 7h for h_{up}=12 cm (Fig. M.37). Despite the different time scale the general splitting heat flux shape is similar for low and high power supply (Figs. M.37 and M.35).

M.3.3 Conclusions

Uniform Pool Test Series

The steady state regime is characterized by two disctinct zone in the water and liquid salt mixture pool. First a downward zone where the temperature and the heat fluxes along the vessel is rising below a nondimensionnal height in the range 0.6 to 075, correponding to an angle along the vessel of 50 to 76 degrees. Then, above there is an upper zone characterized by a constant temperature and heat fluxes along the vessel, where both the temperature and the heat fluxes reaches their maximum value.

No major differences are found between the eutectic and non euctectic salt mixture, the upward/downward splitting heat fluxes are for both cases constant around the unity for the steady state.

Stratified Pool Test Series

A classification in miscible fluids stratification is established, as, stratification with unstable interface for low density difference ($<5\%$) between the two layers, and stratification with stable interfaces for high density difference ($>5\%$). Boiling of the lower layer enhances dramatically the upward heat transfer and then increases, at least by a factor 2, the upward/downward splitting heat flux. The upward/downward splitting heat flux is affected by the stratification, more heat is transfered downwards when stratification is present. Miscibility of the two layers has to be taken into account since immiscibility of the two layers makes more heat to flow downward compared to miscibles fluids. The upward heat transport increases when both layers have heat generation. For larger density differences ($>5\%$) between the two layers, the interface is sharper and imposes a greater resistance for the upward heat transport.The mixing time scale is directly dependant on the power supplied in the pool, it increases when the power supply decreases and, also, when both layers have heat generation. The lower layer of a stratified pool is characterized by an increasing temperature and heat flux along the vessel wall until both reaches their maximum value just below the interface. In the upper layer, both the temperature and the heat flux decreases from the maximum value at the interface. A mixing process of both layers heated is pointed out. First the upper layer mixes with an intermediate layer in the lower layer. Then it creates a new thicker upper layer which mixes with the remaining lower layer. When both layers are heated, and for stable interface, the stratification is a stable configuration since no complete mixing is observed as a steady state is reached slowly.

Bibliography

[1] ”In-Vessel Melt Retention and Coolability”, Special Volume, Intern. J. Nuclear Engineering and Design, Vol. 169, 1997.

[2] T.G. Theofanous et.al., ”In-Vessel Coolability and Retention of a Core Melt”, DOE/ID-10460 Volume 1 (October 1996).

[3] B.R. Sehgal et al., ”Core Melt - Pressure Vessel Interactions During a LWR Severe Accident (MVI)”, FISA-97 Symposium on EU Research on Severe Accidents, November 17-19, 1997, Luxembourg.

[4] V.V. Asmolov, Personal communications, 1997.

M.4 APPENDIX A

M.4.1 Uniform Pool Test Series

Water Test

Table M.1: List of SIMECO experiments with water as simulant

Experiment	Power Supply (W)	Remarks
SW-1	3330	No heat exchanger.
SW-2	3668	No heat exchanger.
SW-3	1063	No heat exchanger.
SW-4	3668	With heat exchanger, medium cooling flow rate.
SW-5	3420	High cooling flow rate.
SW-6	3410	High cooling flow rate, hot water for cooling (55^oC).
SW-7	3408	High cooling flow rate.
SW-8	2019	High cooling flow rate.
SW-9	3731	High cooling flow rate.
SW-10	3586	High cooling flow rate, adding of pipe on back wall.
SW-11	4018	High cooling flow rate, modification of the back wall.
SW-12	3625	High cooling flow rate.

Salt Mixture ($NaNO_3$-KNO_3) Test

Table M.2: List of SIMECO experiments with salt mixture as simulant

Experiment	Power Supply (W)	Remarks
SSEu-1	3430	Transient cool down.
SSEu-2	3570	Transient heat up and cool down.
SSEu-3	3704	Steady state pool.
SSEu-4	3786	Steady state pool, adding of pipe on back wall.
SSEu-5	3820	Steady state pool.
SSEu-6	2022	Steady state pool.
SSEu-7	3961	Steady state pool, modification of the back wall.
SSEu-8	3734	Steady state pool.
SSEu-9	3793	Steady state pool, hot water for cooling (55^oC).
SSEu-10	3721	Steady state pool, hot water for cooling (55^oC).
SSEu-11	3674	Steady state pool, without heat exchanger on top.
SSEu-12	3751	Steady state pool.
SSEu-13	2114	Steady state pool.
SNEu-1	3625	Steady state pool, non-eutectic salt mixture.

M.4.2 Stratified Pool Test Series

For each experiment, the density difference, the upper layer tickness and the experiment name is presented in the following tables.

Immiscible Fluids

Table M.3: List of SIMECO experiments with parafin oil/water stratification

	Low Power Supply ($\sim 1200W$)	**High Power supply ($\sim 3600W$)**
1 Layer Heated	h_{up}=0.04 m : **SE-W-24**	h_{up}=0.01 m : **SE-W-19** h_{up}=0.04 m : **SE-W-07** h_{up}=0.06 m : **SE-W-20**
2 Layer Heated	h_{up}=0.04 m : **SE-W-23** h_{up}=0.08 m : **SE-W-21** h_{up}=0.12 m : **SE-W-22**	h_{up}=0.04 m : **SE-W-18**

Miscible Fluids

M.5 APPENDIX B

M.5.1 Uniform Pool Test Series

Water Test

Table M.4: List of SIMECO experiments with salt water/water stratification

	Low Power Supply ($\sim 1200W$)	**High Power supply ($\sim 3600W$)**
1 Layer Heated	$\Delta\rho$=5% - h_{up}=0.04 m : **SE-W-30**	$\Delta\rho$=2% - h_{up}=0.04 m : **SE-W-10** $\Delta\rho$=5% - h_{up}=0.01 m : **SE-W-33** $\Delta\rho$=5% - h_{up}=0.04 m : **SE-W-11** $\Delta\rho$=5% - h_{up}=0.06 m : **SE-W-34** $\Delta\rho$=10% - h_{up}=0.04 m : **SE-W-04** $\Delta\rho$=20% - h_{up}=0.04 m : **SE-W-06** $\Delta\rho$=30% - h_{up}=0.04 m : **SE-W-09**
2 Layer Heated	$\Delta\rho$=5% - h_{up}=0.04 m : **SE-W-32** $\Delta\rho$=5% - h_{up}=0.08 m : **SE-W-38** $\Delta\rho$=5% - h_{up}=0.12 m : **SE-W-39** $\Delta\rho$=30% - h_{up}=0.04 m : **SE-W-26** $\Delta\rho$=30% - h_{up}=0.08 m : **SE-W-37** $\Delta\rho$=30% - h_{up}=0.12 m : **SE-W-36**	$\Delta\rho$=5% - h_{up}=0.04 m : **SE-W-28** $\Delta\rho$=5% - h_{up}=0.08 m : **SE-W-29** $\Delta\rho$=5% - h_{up}=0.12 m : **SE-W-31** $\Delta\rho$=30% - h_{up}=0.04 m : **SE-W-17** $\Delta\rho$=30% - h_{up}=0.08 m : **SE-W-27** $\Delta\rho$=30% - h_{up}=0.12 m : **SE-W-35**

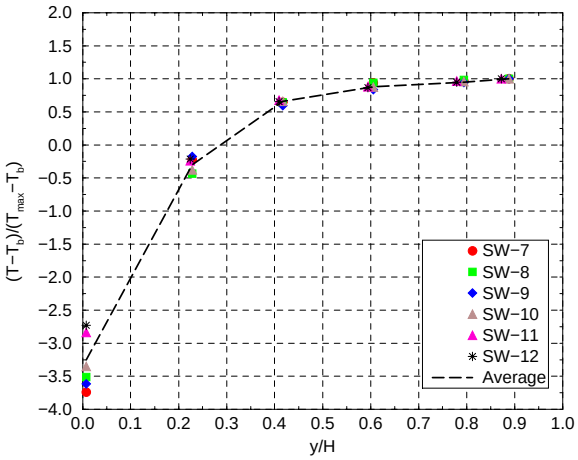

Fig. M.6: Centerline temperature in the pool for several water test.

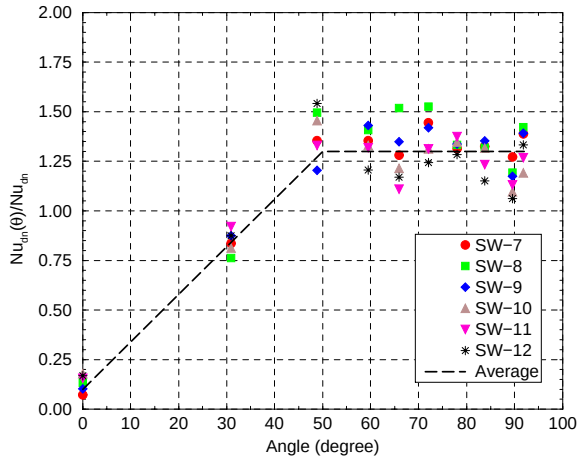

Fig. M.7: Heat fluxes in the vessel wall (determined from thermocouple readings).

Salt Mixture ($NaNO_3$-KNO_3) Test

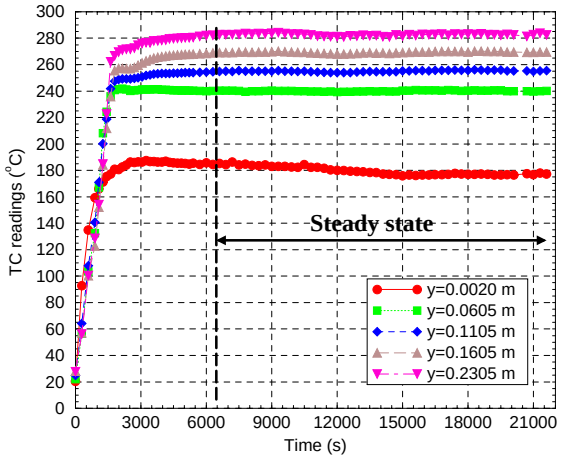

Fig. M.8: SSEu-4 test: transient centerline temperature inside the pool.

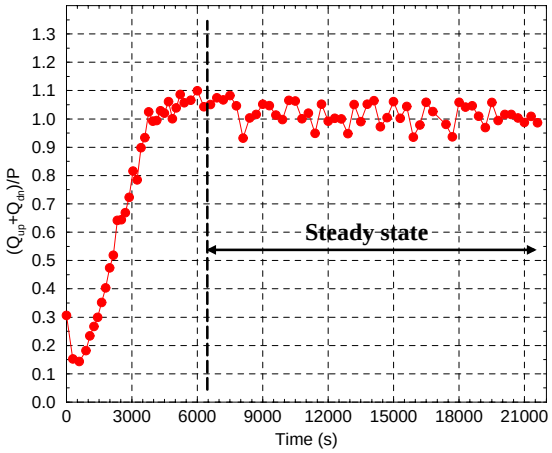

Fig. M.9: SSEu-4 test: transient global heat balance.

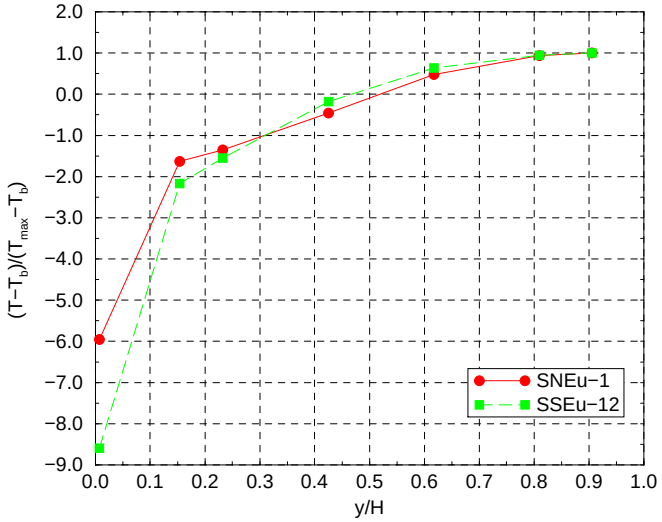

Fig. M.10: Nondimensional centerline temperature for an eutectic and non-eutectic experiment.

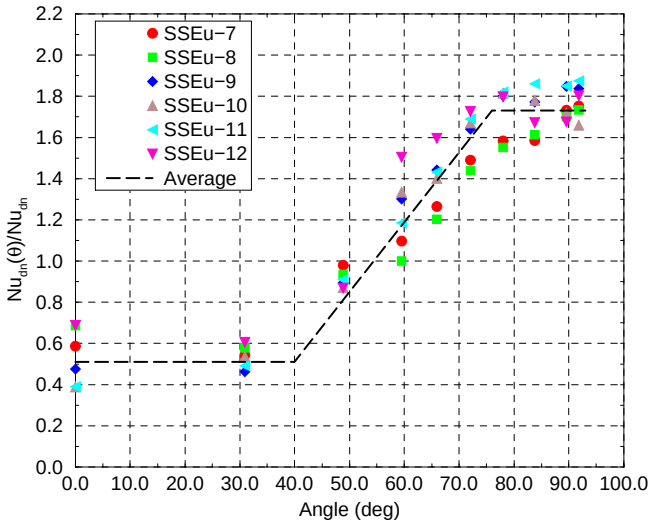

Fig. M.11: Heat fluxes in the vessel wall for different eutectic experiment.

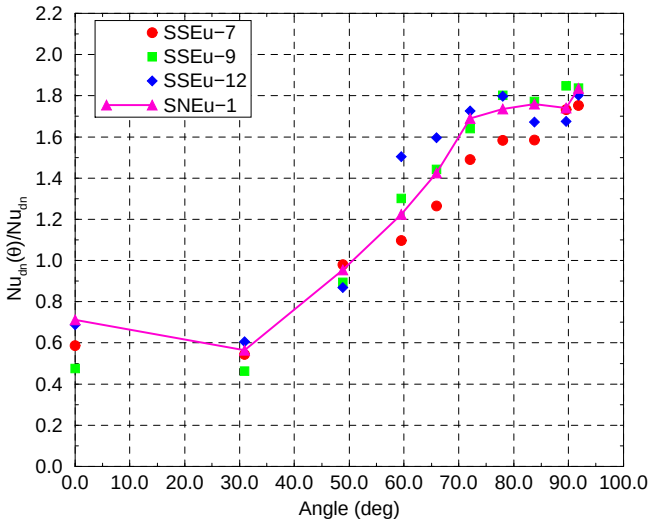

Fig. M.12: Heat fluxes in the vessel wall for both eutectic and non-eutectic cases.

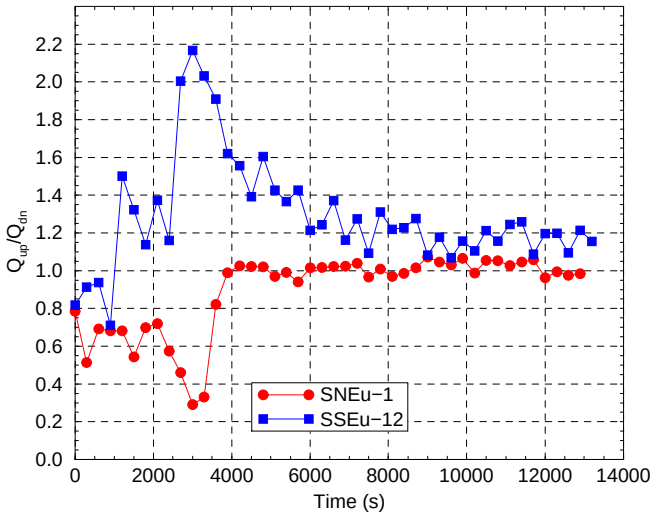

Fig. M.13: Transient upward/downward splitting heat fluxes for both eutectic and non-eutectic cases.

M.5.2 Stratified Pool Test Series

Immiscible Fluids Test

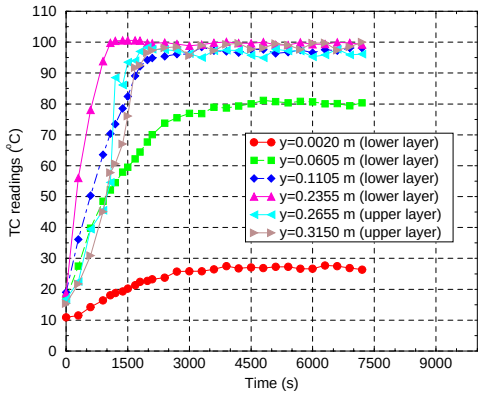

Fig. M.14: SE-W-20 test: transient centerline temperature inside the pool.

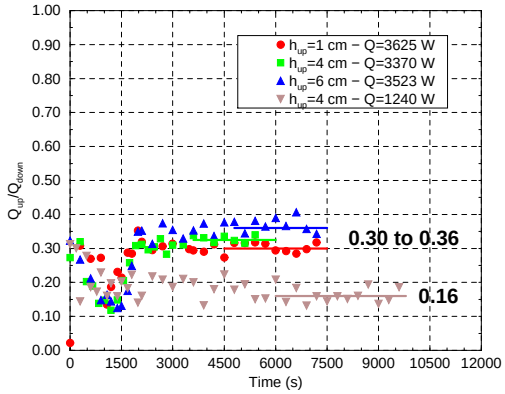

Fig. M.15: Splitting upward/downward heat fluxes for different upper layer thickness.

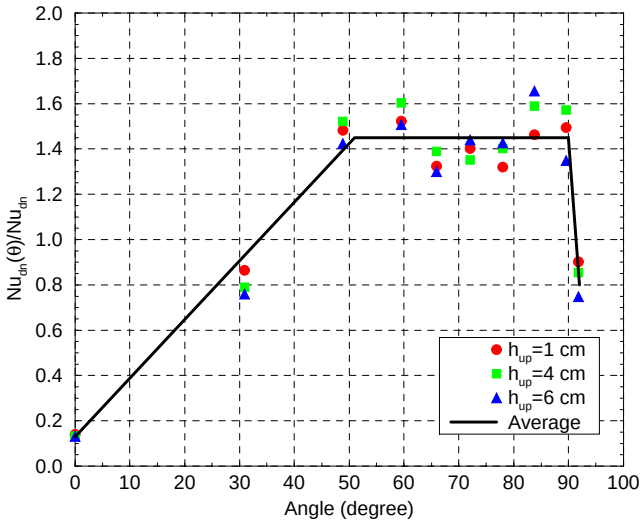

Fig. M.16: Heat fluxes in the vessel wall for different upper layer thickness.

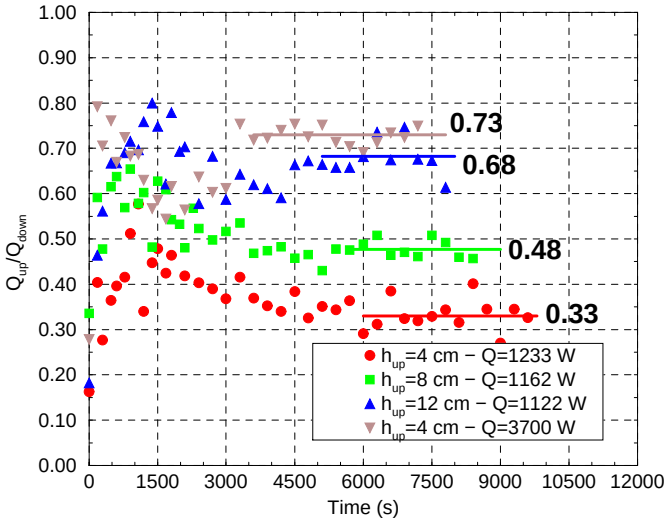

Fig. M.17: Splitting upward/downward heat fluxes for different upper layer thickness.

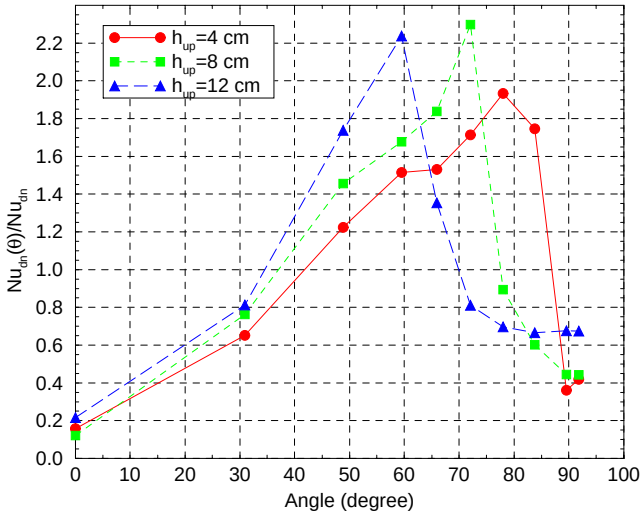

Fig. M.18: Heat fluxes in the vessel wall for different upper layer thickness (Q∼1200 W).

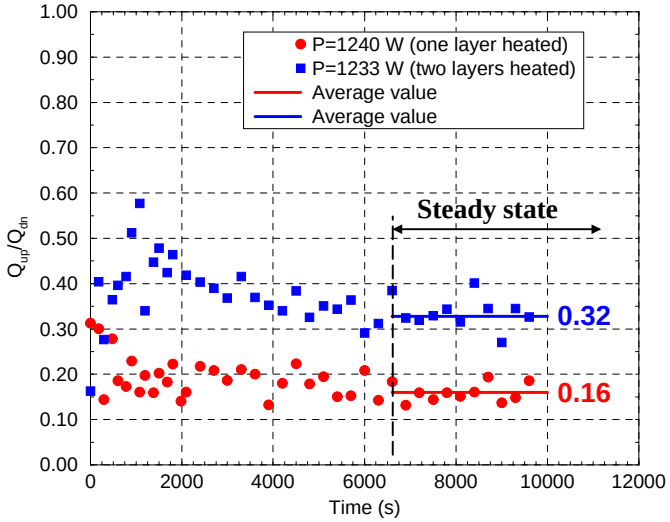

Fig. M.19: Splitting upward/downward heat fluxes for low power supply (Q∼1200 W), h_{up}=4 cm.

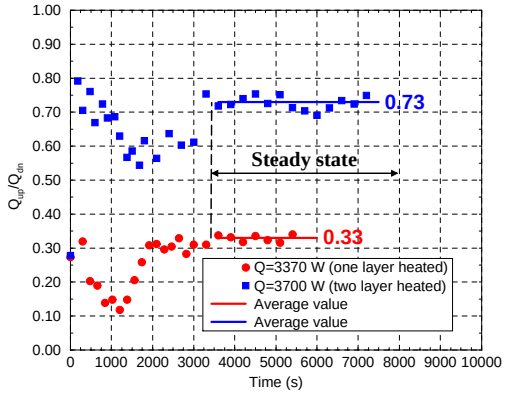

Fig. M.20: Splitting upward/downward heat fluxes for high power supply (Q∼3600 W), h_{up}=4 cm.

Miscible Fluids Test: Effect of the Density Difference

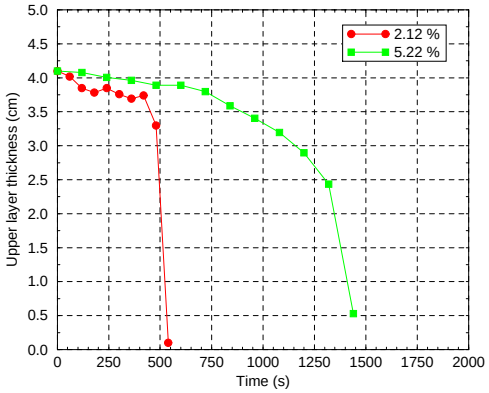

Fig. M.21: Upward layer thickness for unstable interfaces.

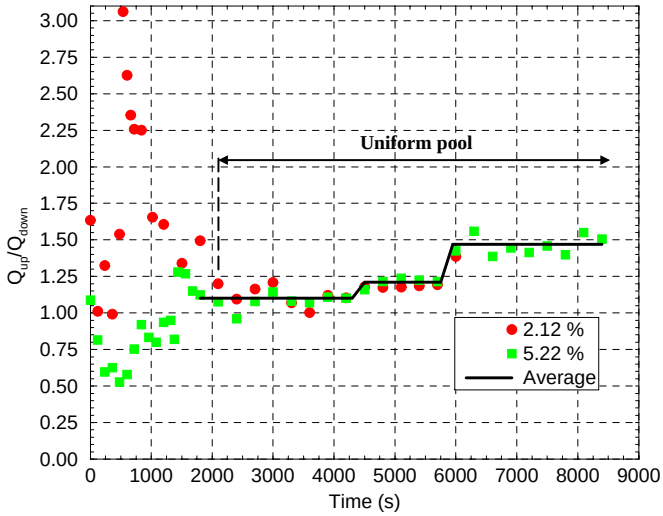

Fig. M.22: Splitting upward/downward heat fluxes for unstable interfaces.

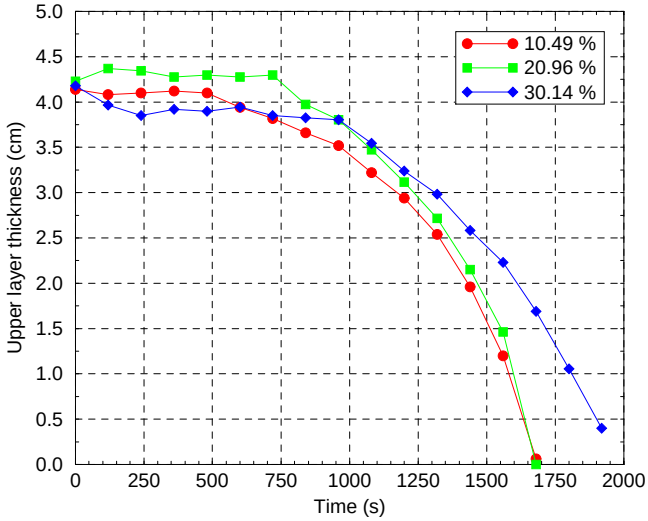

Fig. M.23: Upward layer thickness for stable interfaces.

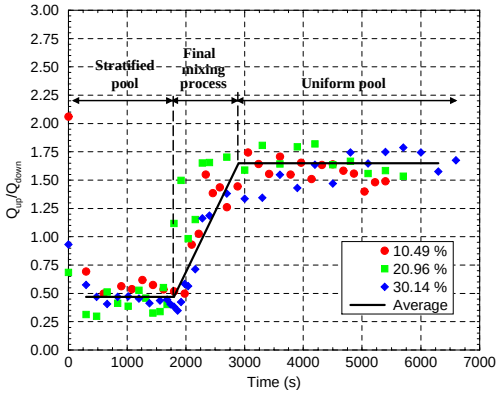

Fig. M.24: Splitting upward/downward heat fluxes for stable interfaces.

Miscible Fluids Test: One Layer Heated

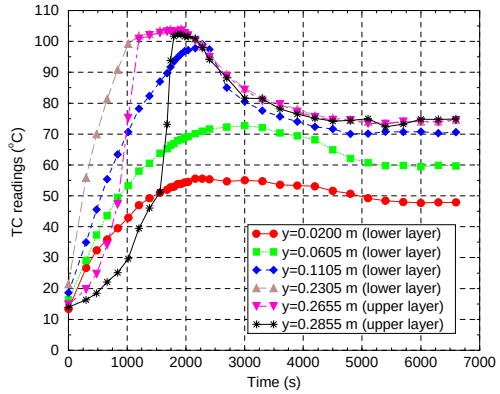

Fig. M.25: SE-W-9 test: transient centerline temperature inside the pool.

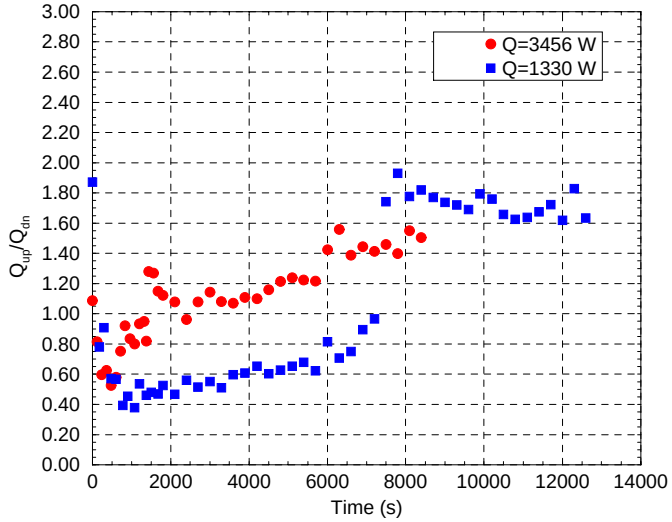

Fig. M.26: Splitting upward/downward heat fluxes for unstable interfaces ($\Delta\rho$=5%), h_{up}=4 cm.

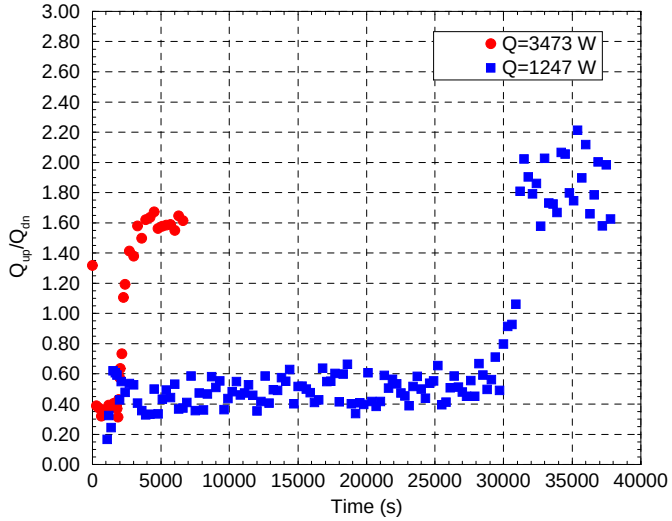

Fig. M.27: Splitting upward/downward heat fluxes for stable interfaces ($\Delta\rho$=30%), h_{up}=4 cm.

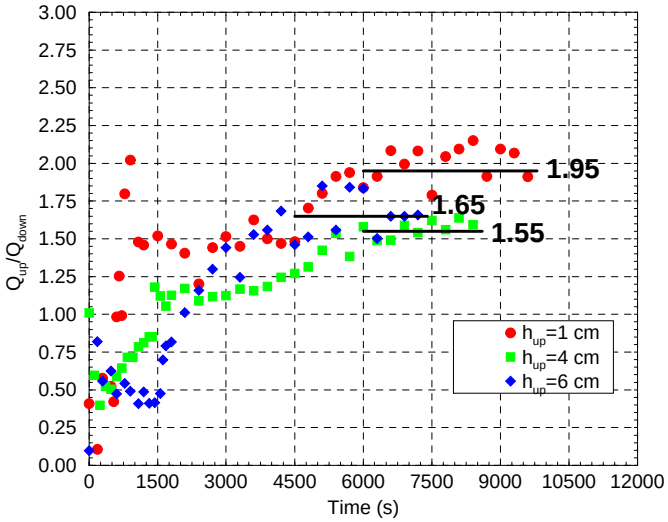

Fig. M.28: Splitting upward/downward heat fluxes for different upper layer thickness ($\Delta\rho$=5%).

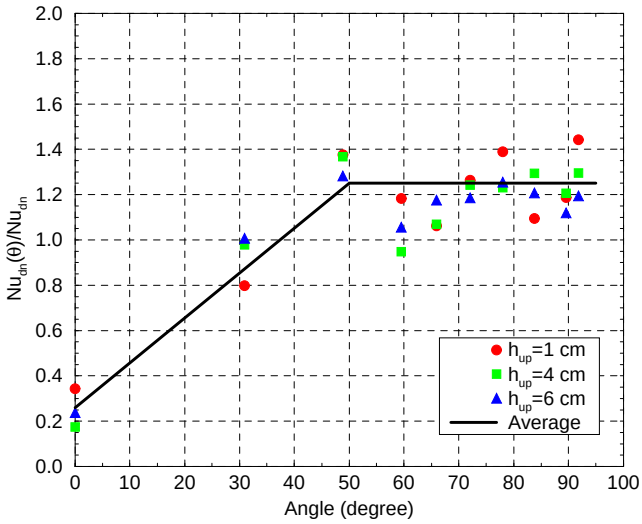

Fig. M.29: Heat fluxes in the vessel wall for different upper layer thickness ($\Delta\rho$=30%).

Miscible Fluids Test: Two Layers Heated

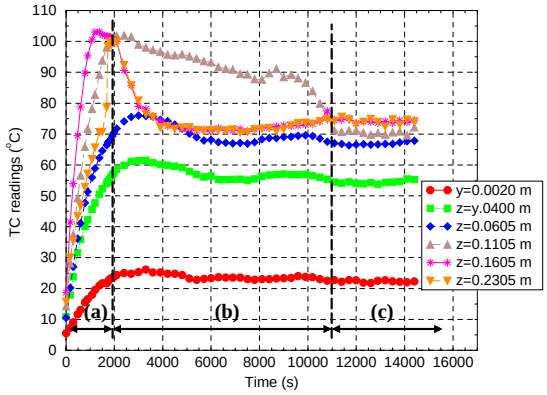

Fig. M.30: SE-W-27 test: transient centerline temperature inside the pool.

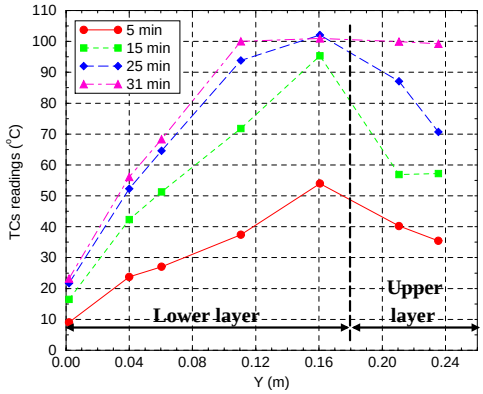

Fig. M.31: SE-W-27 test: Evolution with time of the centerline temperature profile.

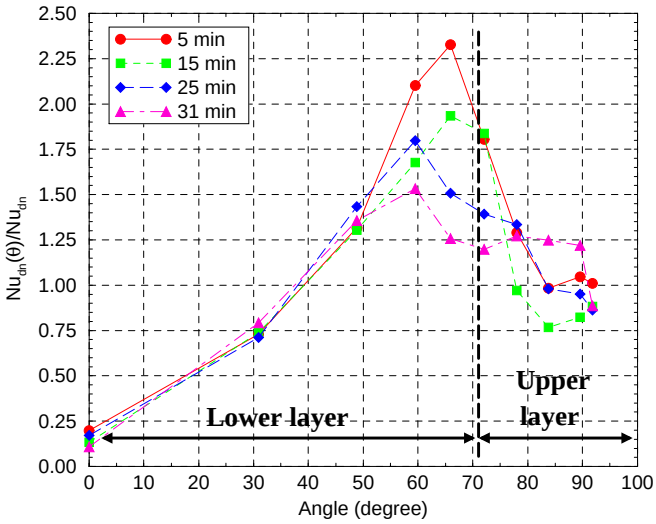

Fig. M.32: SE-W-27 test: Evolution with time of the heat fluxes in the vessel wall.

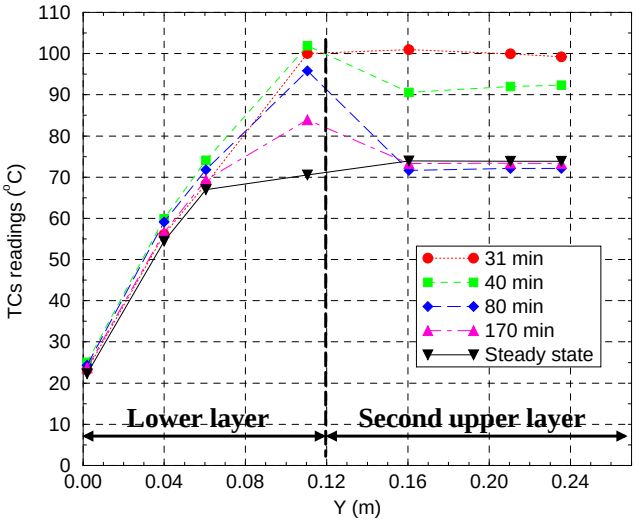

Fig. M.33: SE-W-27 test: Evolution with time of the centerline temperature profile.

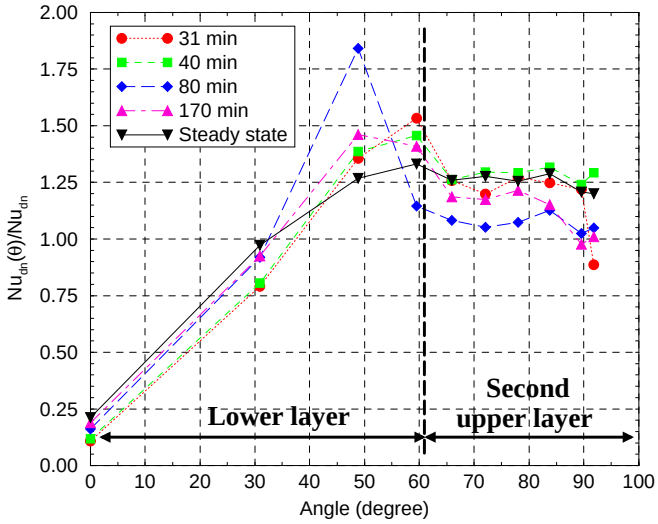

Fig. M.34: SE-W-27 test: Evolution with time of the heat fluxes in the vessel wall.

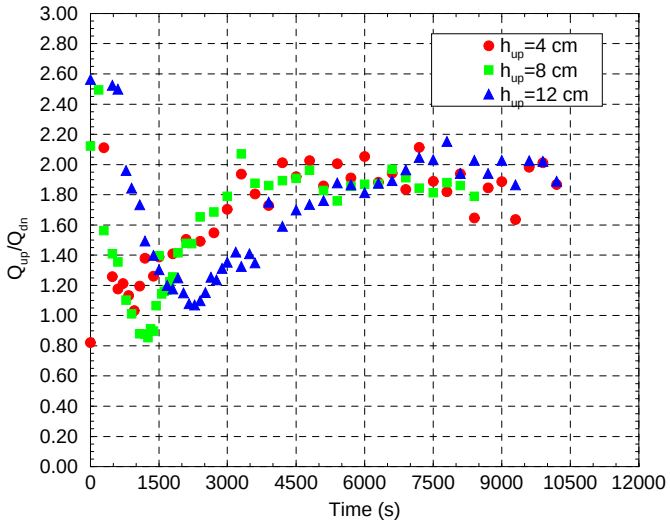

Fig. M.35: Splitting upward/downward heat fluxes for high power supply (Q∼3600 W $\Delta\rho$=5%).

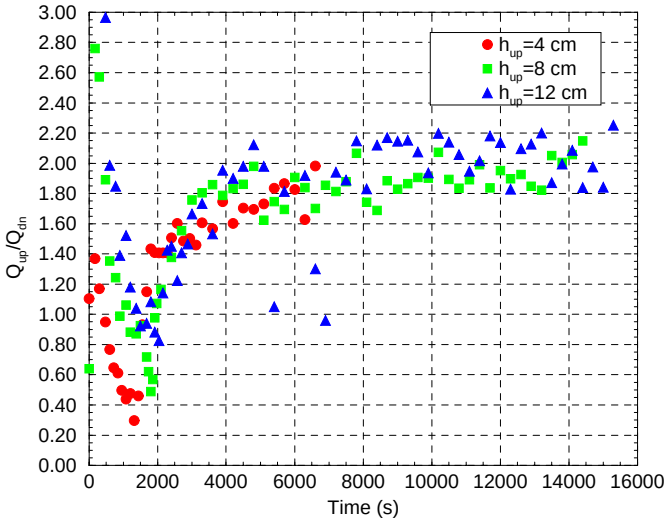

Fig. M.36: Splitting upward/downward heat fluxes for high power supply (Q∼3600 W $\Delta\rho$=30%).

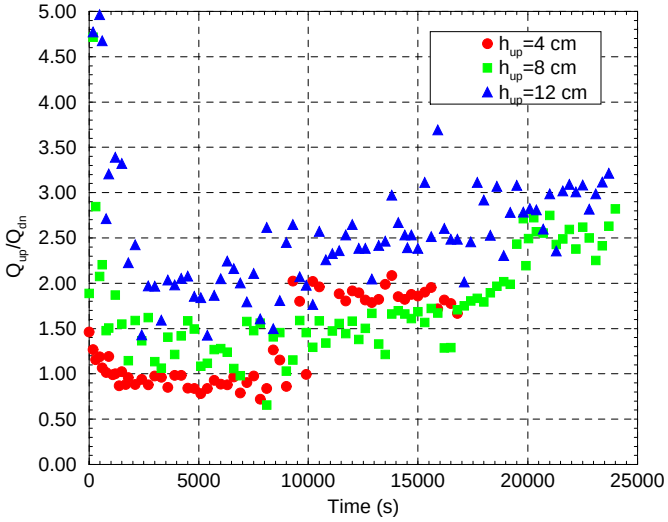

Fig. M.37: Splitting upward/downward heat fluxes for low power supply (Q∼1200 W $\Delta\rho$=5%).

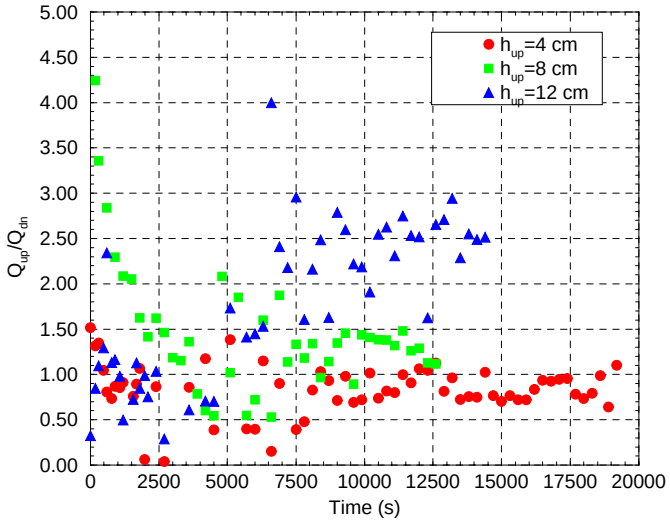

Fig. M.38: Splitting upward/downward heat fluxes for low power supply (Q∼1200 W $\Delta\rho$=30%).

Appendix N

Publications of the MVI project

EU MVI project publications has two numbers, the first one is given according to the EU conventions and the other number was given localy in RIT. The local number is based on the followingfollowing conventions:

$$C_n\text{-EU-MVI(}Y_n\text{)-}Org\text{-}N_n$$

where

- C_n is the confidentiality Level:
  - Level 1 = restriction within the 'inner circle' of the contractants of the project.
  - Level 2 = diffusion extended towards the 'outer ring' of the other projects of the current Nuclear Fission Safety Programme 1994-1999.
  - Level 3 = open communication.
- Y_n is the year of the report publication.
- Org is the abbreviation of organization (e.g., RIT, CEA, AEA etc.)
- N_n is the number of the report.

Bibliography

[INV-MVI(97)-D000] B.R. Sehgal, O. Kymaläinen, J.M. Bonnet, B.D. Turland, et al., ”Core Melt - Pressure Vessel Interactions During a LWR Severe Accident (MVI)”, FISA-97 Symposium on EU Research on Severe Accidents, November 17-19, 1997, Luxembourg. And FISA-99, Luxembury, November 29 - December 1, 1999.

[INV-MVI(97)-M001] B.R. Sehgal, Minutes of the Yearly Progress Review meeting, Rome University, ”La Sapienza”, January 9, 1997. Mars 1997.

[INV-MVI(97)-M002] B.R. Sehgal, Minutes of the 2nd Yearly Progress Meeting, 12 December 1997, Ispra.

[INV-MVI(96)-M003] B.R. Sehgal, First half-yearly project meeting, RIT Stockholm, June 1996.

[INV-MVI(97)-M004] B.R. Sehgal, Minuts of the third semi-annual meeting, 1-2 July 1997, London. July 1997.

[INV-MVI(96)-EC001] G. VAN GOETHEM, First half-yearly MVI project meeting: RIT Stockholm, July 1996

[INV-MVI(96)-EC002] EC and partners of the project, Contract and technical Annex for the Project, January 1996.

[INV-MVI(96)-EC003] B.R. Sehgal, Cost statments 1996, Mars 1997.

[INV-MVI(97)-P001] B.R. Sehgal, Annual Programme Report 1997. Mars 1998.

[INV-MVI(97)-P002] B.R. Sehgal, Yearly Programme Report: 01/01/97 - 31/12/97. Fabruary 1998.

[INV-MVI(96)-P003] B.R. Sehgal, First half-yearly Progress Report: 01/01/96 - 30/06/96, December 1996.

[INV-MVI(96)-P004] B.R. Sehgal, Yearly Progress Report: 01/01/96 - 31/12/96, Mars 1997.

[INV-MVI(96)-P005] B.R. Sehgal, Annual Programme Report 1996, Mars 1997.

[INV-MVI(96)-P006] B.R. Sehgal, Third Half-Yearly Progress Report: 01/01/97 - 30/06/97, July 1997.

[RIT JET IMPINGEMENT EXPERIMENTAL PROGRAM:]

[INV-MVI(97)-D001] (2-EU-MVI(97)-RIT-1), B.R. Sehgal, T.N. Dinh, J.A. Green, M. Kolovalikhin, W.G. Dong, R.R. Nourgaliev, "Experimental Investigation of Melt Jet Impingement During Severe Accidents". RIT/NPS Research Report for European Union: EU-MVI-JI1-97, 95p. (November, 1997)

[INV-MVI(96)-D002] (3-EU-MVI(97)-RIT-2), B.R. Sehgal, Studies on melt-water-structure interaction duringsevere accidents, January 1997.

[INV-MVI(97)-D003] (3-EU-MVI(97)-RIT-3), B.R. Sehgal, J.A. Green and T.N. Dinh, "Experimental and Analytical Investigations of Vessel-Hole Ablation during Severe Accidents", Proceedings of the Fifth International Topical Meeting on Nuclear Thermal Hydraulics, Operations, and Safety (NuTHOS-5), Beijing, China, April 1997.

[INV-MVI(97)-D004] (3-EU-MVI(97)-RIT-4), B.R. Sehgal, J.A. Green, T.N. Dinh and W.G. Dong, "Experiments and Analyses of Melt Jet Impingment during Severe Accidents", Proceedings of the Fifth International Topical Meeting on Nuclear Thermal Hydraulics, Operations, and Safety (NuTHOS-5), Beijing, China, April 1997.

[INV-MVI(97)-D005] (3-EU-MVI(97)-RIT-5), T.N. Dinh, W.G. Dong, J.A. Green, R.R. Nourgaliev, and B.R. Sehgal, "Melt Jet Attack of Reactor Vessel Lower Plenum: Phenomena and Prediction Method", Proceedings of the Eighth International Topical Meeting on Nuclear Reactor Thermal Hydraulics (NuReTH-8), Kyoto, Japan, September 1997.

[INV-MVI(97)-D006] (3-EU-MVI(97)-RIT-6), J.A. Green, T.N. Dinh and B.R. Sehgal, "Molten Metal Jet Impingement: Insights from Experiments and Analyses", 5th International Conference on Nuclear Engineering, Nice, France, May 26-30, 1997.

[INV-MVI(96)-D007] (3-EU-MVI(96)-RIT-7), J. A. Green, W. Dong, T.N. Dinh, and B.R. Sehgal, "Experiments on Melt Jet Impingement and Vessel Hole Ablation", Proceedings of International Topical Meeting on Probabilistic Safety Assessment PSA-4, September 29 - October 3, 1996, Park City, Utah, 1996.

[**RIT HOLE ABLATION EXPERIMENTAL PROGRAM:]**

[INV-MVI(97)-D008] (2-EU-MVI(97)-RIT-8), B.R. Sehgal, T.N. Dinh, J.A. Green, D. Paladino, "Experimental Investigation of Vessel-Hole Ablation During Severe Accidents", SKI Research Report 97:44, 91p. (December, 1997)

[INV-MVI(95)-D009] (3-EU-MVI(95)-RIT-9), B.R. Sehgal, J. Andersson, V.A. Bui, T.N. Dinh and T. Okkonen, "Experiments on Vessel Hole Ablation During Severe Accidents", Proceeding of the Intern. Seminar on Heat and Mass Transfer in Severe Reactor Accidents, Izmir, Turkey, 1995, Begel House Publ., 1996.

[INV-MVI(94)-D010] (3-EU-MVI(94)-RIT-10), B.R. Sehgal, J. Andersson, T.N. Dinh and T. Okkonen, "Scoping Experiments on Vessel Hole Ablation During Severe Accidents", Proceedings of the Workshop on Severe Accident Research in Japan, SARJ-4, Japan, pp.230-236, 1994.

[INV-MVI(97)-D011] (3-EU-MVI(97)-RIT-11), T.N. Dinh, J.A. Green, and B.R. Sehgal, "On Mechanisms that Govern the Vessel Melt Source for Ex-Vessel FCIs", 5th International Conference on Nuclear Engineering, Nice, France, May 26-30, 1997.

[INV-MVI(98)-D012] (3-EU-MVI(98)-RIT-12), T.N. Dinh, J.A. Green, and B.R. Sehgal, "Investigation And Modeling Of Mechanisms That Govern The Vessel-Hole Ablation And Core Melt Discharge", Submitted to Intern. J. Nuclear Engineering and Design (1998).

[INV-MVI(98)-D013] (3-EU-MVI(98)-RIT-13), T.N. Dinh, W.G. Dong, J.A. Green, R.R. Nourgaliev, and B.R. Sehgal, "The Mechanisms of Melt Jet Attack of the Reactor Vessel Wall", Submitted to Intern. J. Nuclear Engineering and Design (1998).

[INV-MVI(96)-D014] (3-EU-MVI(96)-RIT-14), T.N. Dinh, V.A. Bui, R.R. Nourgaliev, T. Okkonen, and B.R. Sehgal, "Modeling of Heat and Mass Transfer Processes During Core Melt Discharge From A Reactor Pressure Vessel", Intern. J. Nuclear Engineering and Design, Vol. 163, pp.191-206 (1996) (also [INV-MVI(95)-D015]).

[INV-MVI(95)-D015] (3-EU-MVI(95)-RIT-15), T.N. Dinh, V.A. Bui, R.R. Nourgaliev, T. Okkonen and B.R. Sehgal, "Modeling of Heat and Mass Transfer Processes During Core Melt Discharge From A Reactor Pressure Vessel", Proceedings of the Seventh International Topical Meeting on Nuclear Reactor Thermal Hydraulics NURETH-7, New York, USA, 1995, NUREG/CP-0142, Vol.3, pp.1809-1829.

[**RIT FOREVER EXPERIMENTAL PROGRAM:]**

[INV-MVI(98)-D016] (3-EU-MVI(98)-RIT-16), Sehgal, B. R., Nourgaliev, R. R., Dinh, T. N., Bui, V. A., Green, J. A. and Karbojian, A., FOREVER Experiment on Thermal and Mechanical Behavior of a Reactor Vessel during a Severe Accident, *Proceedings the OECD/CSNI Workshop on 'In-Vessel Core Debris Retention and Coolability'*, Garching, Germany, 3-6 March, 1998.

[INV-MVI(98)-D017] (3-EU-MVI(98)-RIT-17), Sehgal, B. R., Nourgaliev, R. R., Dinh, and Karbojian, A., Integral Experiments on In-Vessel Coolability and Vessel Creep: Results and Analysis of the FOREVER-C1 test, *Proceedings the SARJ-98, Workshop on Severe Accident Research held in Japan*, Tokyo, Japan, 4-6 November, 1998.

[INV-MVI(99)-D018] (3-EU-MVI(99)-RIT-18), Sehgal, B. R., Nourgaliev, R. R., Dinh, and Karbojian, A., FOREVER Experimental Program on Reactor Pressure Vessel Creep Behavior and Core Debris Retention, *Proceedings the SMiRT-15, 15^th International Conference on Structural Mechanics in Reactor Technology*, Seoul, Korea, 15-20 August, 1999.

[INV-MVI(99)-D019] (3-EU-MVI(99)-RIT-19), Sehgal, B. R., Nourgaliev, R. R., Dinh, and Karbojian, A., Characterization of Heat Transfer Processes in an Integral Coolability and Vessel-Creep FOREVER Experiment, *Proceedings the NURETH-9, Ninth International Topical Meeting on Nuclear Reactor Thermal Hydraulics* San Francisco, California, October 3-8, 1999.

[**RIT SIMECO EXPERIMENTAL PROGRAM:]**

[INV-MVI(98)-D020] (3-EU-MVI(98)-RIT-20), B.R. Sehgal, T.N. Dinh, V.A. Bui, J.A. Green, G. Kolb, "SIMECO Experiments on In-Vessel Melt Pool Formation and Heat Transfer with and without a Metallic Layer", OECD/CSNI Workshop on "In-Vessel Core Debris Retention and Coolability", Garching, Germany, 3-6 March 1998.

[**RIT MELT POOL CONVECTION ANALYSIS:]**

[INV-MVI(97)-D021] (3-EU-MVI(97)-RIT-21), B.R. Sehgal, V.A. Bui, T.N. Dinh and R.R. Nourgaliev, "Heat Transfer Processes in Reactor Vessel Lower Plenum during Late Phase of In-Vessel Core Melt Progression", J. "Advances in Nuclear Science and Technology", Plenum Publ. Corp, Vol.26, 1998.

[INV-MVI(96)-D022] (2-EU-MVI(96)-RIT-22), B.R. Sehgal, T.N. Dinh, and R.R. Nourgaliev, "Analysis of Natural Convection in Volumetrically-Heated

Melt Pools", Research Report published by Swedish Nuclear Power Inspectorate (SKI). Work jointly funded by SKI and US Nuclear Regulatory Commission (NRC), December 1996, 130p.

[INV-MVI(98)-D023] (3-EU-MVI(98)-RIT-23), V.A. Bui, R.R. Nourgaliev, Z.L. Yang, T.N. Dinh, and B.R. Sehgal, "Advances in MVITA Modeling of Thermal Processes in the Reactor Pressure Vessel Lower Plenum with a Core Melt Pool", CD-ROM Proceedings of International Conference on Nuclear Engineering, ICONE-6, San Diego, CA, USA, May, 1998.

[INV-MVI(96)-D024] (3-EU-MVI(96)-RIT-24), V.A. Bui, T.N. Dinh, and B.R. Sehgal, "In-Vessel Core Melt Pool Formation during Severe Accidents", Proceedings of the 1996 National Heat Transfer Conference, in the session "Fundamental Phenomena in Severe Accidents", Houston, Texas, August 3-6, 1996, HTC-Vol.9, pp.86-94.

[INV-MVI(96)-D025] (3-EU-MVI(96)-RIT-25), V.A. Bui, T.N. Dinh and B.R. Sehgal, "Numerical Modeling of Heating and Melting Processes in Internally-Heated Debris Beds in a Reactor Vessel Lower Plenum", Proceedings of the Fourth International Conference "Heat Transfer-96", in the session "Advanced Computational Methods in Heat Transfer", 8-10 July 1996, Udine, Italy.

[INV-MVI(97)-D026] (3-EU-MVI(97)-RIT-26), T.N. Dinh, V.A. Bui, R.R. Nourgaliev, and B.R. Sehgal, "Modeling of Heat Transfer Processes in Reactor Vessel Lower Plenum during a Late Phase of In-Vessel Core Melt Progression", Proceedings of the Eight International Topical Meeting on Nuclear Reactor Thermal Hydraulics (NuReTH-8), Kyoto, Japan, September 1997.

[INV-MVI(96)-D027] (3-EU-MVI(96)-RIT-27), T.N. Dinh, V.A. Bui, R.R. Nourgaliev, and B.R. Sehgal, "Crust Dynamics under PWR In-Vessel Melt Retention Conditions", Proceedings of the 1996 National Heat Transfer Conference, in the session "Scaling and Simulation", Houston, Texas, August 3-6, 1996, HTC-Vol.9, pp.368-375.

[INV-MVI(95)-D028] (3-EU-MVI(95)-RIT-28), T.N. Dinh, R.R. Nourgaliev and B.R. Sehgal, "On Heat Transfer Characteristics of Real and Simulant Melt Pool Experiments", Proceedings of the Seventh International Topical Meeting on Nuclear Reactor Thermal Hydraulics NURETH-7, New York, USA, 1995, NUREG/CP-0142, Vol.2, pp.827-845; also [INV-MVI(97)-D029].

[INV-MVI(97)-D029] (3-EU-MVI(97)-RIT-29), T.N. Dinh, R.R. Nourgaliev and B.R. Sehgal, "On Heat Transfer Characteristics of Real and Simulant Melt Pool

Experiments", Intern. J. Nuclear Engineering and Design, Special Volume on "In-Vessel Melt Retention and Coolability", Vol. 169, pp.151-164, 1997.

[INV-MVI(99)-D030] (3-EU-MVI(99)-RIT-30), A.A. Gubaidulline, Jr, T.N. Dinh and B.R. Sehgal "Simulation and Analysis of Natural Convection Heat Transfer and Flows in Internally-Heated Superimposed Liquid Pools", Proceedings of US National Heat Transfer Conference Albuquerque, New Mexico, August 1999 (submitted).

[INV-MVI(99)-D031] (3-EU-MVI(99)-RIT-31), A.A. Gubaidullin, T.N. Dinh and B.R. Sehgal, 'Analysis of natural convection hear transfer and flows in internally heated stratified liquid pools', Proceedings of 33rd National Heat Transfer Conference, Albuquergue, New Mexico, Aug. 15-17, 1999.

[INV-MVI(98)-D032] (3-EU-MVI(98)-RIT-32), R.R. Nourgaliev, A.T. Dinh, T.N. Dinh, B.R. Sehgal, "Numerical Investigation of Turbulent Natural Convection Heat Transfer in an Internally-Heated Melt Pool and Metallic Layer", OECD/CSNI Workshop on "In-Vessel Core Debris Retention and Coolability", Garching, Germany, 3-6 March 1998.

[INV-MVI(97)-D033] (3-EU-MVI(97)-RIT-33), R.R. Nourgaliev and T.N. Dinh, "The Investigation of Turbulence Characteristics in an Internally Heated Unstably Stratified Fluid Layers", Intern. J. Nuclear Engineering and Design, 1997 (accepted).

[INV-MVI(96)-D034] (3-EU-MVI(96)-RIT-34), R.R. Nourgaliev, T.N. Dinh, and B.R. Sehgal, "Simulation and Analysis of Transient Cooldown Natural Convection Experiments", Proceedings of the 1996 National Heat Transfer Conference, in the session "Fundamental Phenomena in Severe Accidents", Houston, Texas, August 3-6, 1996, HTC-Vol.9, pp.72-85; also [INV-MVI(97)-D035].

[INV-MVI(97)-D035] (3-EU-MVI(97)-RIT-35), R.R. Nourgaliev, T.N. Dinh, and B.R. Sehgal, "Simulation and Analysis of Transient Cooldown Natural Convection Experiments", Intern. J. Nuclear Engineering and Design, 1997 (accepted).

[IVN-MVI(97)-D036] (3-EU-MVI(97)-RIT-36), R.R. Nourgaliev, T.N. Dinh, and B.R. Sehgal "Effect of Fluid Prandtl Number on Heat Transfer Characteristics in Internally Heated Liquid Pools with Rayleigh Numbers up to 10^{12}", Intern. J. Nuclear Engineering and Design, Special Volume on "In-Vessel Melt Retention and Coolability", Vol. 169, pp.165-184, 1997.

[IVN-MVI(95)-D037] (3-EU-MVI(95)-RIT-37), R.R. Nourgaliev, T.N. Dinh, and B.R. Sehgal, "Natural Convection in Volumetrically Heated and Sidewall

Heated Melt Pools: Three-Dimensional Effects", Proceedings of the IMACS-COST Conference on Computational Fluid Dynamics "3D Complex Flows", Lausanne, Switzerland, 1995. Also published in "J. Notes on Numerical Fluid Mechanics", Vol.53, pp.202-209, (ed. M. Deville, S. Gavrilakis and I.L. Ryhming) Viewed, Braunschweig 1996.

[**CEA BALI EXPERIMENTAL PROGRAM:]**

[INV-MVI(97)-D038] (2-EU-MVI(97)-CEA-1), J.M.Bonnet, BALI project - Description of the facility, SETEX/LTEM/97-21, CEA, Grenoble, 17 rue des Martyrs, 38054 GRENOBLE CEDEX 9 - France, MVI Project, Contract FI4S-CT95-0007, Task 3-1.

[INV-MVI(98)-D039] (2-EU-MVI(98)-CEA-2), J.M.Bonnet, BALI test reports for in-vessel configurations, SETEX/LTEM/98-114, CEA, Grenoble, 17 rue des Martyrs, 38054 GRENOBLE CEDEX 9 - France, MVI Project, Contract FI4S-CT95-0007, Task 3-1.

[INV-MVI(98)-D040] (3-EU-MVI(98)-CEA-3), L. Bernaz, J.-M. Bonnet, B. Spindler, C. Villermaux, Thermalhydraulic Phenomena in Corium Pools: Numerical Simulation with TOLBIAC and Experimental Validation with BALI, *Proceedings ot the OECD/CSNI Workshop on 'In-Vessel Core Debris Retention and Coolability'*, pp. 185-193, Garching, Germany, 3-6 March, 1998.

[INV-MVI(99)-D041] (3-EU-MVI(99)-CEA-4), J.M.Bonnet and J. M. Seiler, Thermal Hydraulic Phenomena in Corium Pools: The BALI Experiment, CD-ROM Proceedings of the *7th International Conference on Nuclear Engineering*, Tokyo, Japan, April 19-23, 1999, ICONE-7057.

[**CEA SULTAN EXPERIMENTAL PROGRAM:]**

[INV-MVI(96)-D042] (2-EU-MVI(96)-CEA-5), S. Rouge, M. Marcoux, A. Liegeois, SULTAN test report - First campaign - Vertical position - Fluid depth: 3cm. STR/LTEM/96-28, CEA-CEE MVI #FI4S-CT95-0007, CEA, Grenoble, 17 rue des Martyrs, 38054 GRENOBLE CEDEX 9 - France, May 1996, MVI Project, Contract FI4S-CT95-0007, Task 3-2.

[INV-MVI(96)-D043] (2-EU-MVI(96)-CEA-6), S. Rouge, M. Marcoux, A. Liegeois, SULTAN test report - Second campaign - Inclination: 10° from horizontal - Fluid depth: 15cm. STR/LTEM/96-29, CEA-CEE MVI #FI4S-CT95-0007, CEA, Grenoble, 17 rue des Martyrs, 38054 GRENOBLE CEDEX 9 - France, May 1996, MVI Project, Contract FI4S-CT95-0007, Task 3-2.

[INV-MVI(96)-D044] (2-EU-MVI(96)-CEA-7), S. Rouge, M. Marcoux, A. Liegeois, SULTAN test report - Third campaign - Vertical position - Fluid depth: 15cm. STR/LTEM/96-28, CEA-CEE MVI #FI4S-CT95-0007, CEA, Grenoble, 17 rue des Martyrs, 38054 GRENOBLE CEDEX 9 - France, May 1996, MVI Project, Contract FI4S-CT95-0007, Task 3-2.

[INV-MVI(96)-D045] (2-EU-MVI(96)-CEA-8), S. Rouge, M. Marcoux, A. Liegeois, SULTAN test report - Third campaign - Vertical position - Fluid depth: 3cm. STR/LTEM/96-28, CEA-CEE MVI #FI4S-CT95-0007, CEA, Grenoble, 17 rue des Martyrs, 38054 GRENOBLE CEDEX 9 - France, August 1996, MVI Project, Contract FI4S-CT95-0007, Task 3-2.

[INV-MVI(97)-D046] (2-EU-MVI(97)-CEA-9), S. Rouge, and A.Carenza, SULTAN test report - Fourth campaign - Inclination: 45° - Fluid depth: 15cm. STR/LTEM/98-97, CEA, Grenoble, 17 rue des Martyrs, 38054 GRENOBLE CEDEX 9 - France, September 1998, MVI Project, Contract FI4S-CT95-0007, Task 3-2.

[INV-MVI(98)-D047] (2-EU-MVI(98)-CEA-10), S. Rouge, and A. Carenza, SULTAN test report - Fourth campaign - Inclination: 45° - Fluid depth: 3cm. STR/LTEM/98-98, CEA, Grenoble, 17 rue des Martyrs, 38054 GRENOBLE CEDEX 9 - France, September 1998, MVI Project, Contract FI4S-CT95-0007, Task 3-2.

[INV-MVI(96)-D048] (2-EU-MVI(96)-CEA-11), S. Rouge, and M. Marcoux, SULTAN facility - Description of the test loop and a test campaign. STR/LTEM/96-26, CEA-CEE MVI #FI4S-CT95-0007, CEA, Grenoble, 17 rue des Martyrs, 38054 GRENOBLE CEDEX 9 - France, May 1996, MVI Project, Contract FI4S-CT95-0007, Task 3-2.

[INV-MVI(98)-D049] (3-EU-MVI(98)-CEA-12), S. Rouge, I. Dor, G. Geffraye, Reactor Vessel External Cooling for Corium Retention SULTAN Experimental Program and Modeling with CATHARE Code, *Proceedings ot the OECD/CSNI Workshop on 'In-Vessel Core Debris Retention and Coolability'*, pp. 351-363, Garching, Germany, 3-6 March, 1998.

[INV-MVI(98)-D050] (2-EU-MVI(98)-CEA-13), S. Rouge, Reactor Vessel External Cooling for Corium Retention. Application of the SULTAN Experimental Results and Code Validation to the ULPU and EPR Cases *MVI Project, Contract FI4S-CT95-0007, Task 3-2*.

[INV-MVI(96)-D051] (3-EU-MVI(96)-CEA-14), S. Rouge, , SULTAN Test Facility for Large-Scale Vessel Coolability in Natural Convection at Low Pressure, *Nuclear Engineering and Design*, 1996.

[**FORTUM COPO EXPERIMENTAL PROGRAM:]**

[INV-MVI(97)-D052] (2-EU-MVI(97)-FORTUM-1), M.Helle, O.Kymlinen and E.Pessa, "COPO II-Lo Experiments," IVO Power Engineering, YDIN-GT1-43, October 1997.

[INV-MVI(98)-D053] (2-EU-MVI(98)-FORTUM-2), M.Helle and O.Kymlinen, "Crust Effect in the COPO II Experiments," IVO Power Engineering, YDIN-GT1-50, December 1998.

[INV-MVI(99)-D054] (2-EU-MVI(99)-FORTUM-3), M.Helle, "COPO II Experiments with a Stratified Pool," IVO Power Engineering, YDIN-GT1-52, January 1999.

[**AEA Technology:]**

[INV-MVI(98)-D055] (2-EU-MVI(98)-AEAT-1), G.P. Dobson and B.D. Turland, Interim Report - Models for Melt Coolability by Water Ingress. AEA Technology report AEAT - 2903 (Issue 1), January 1998.

[INV-MVI(97)-D056] (2-EU-MVI(97)-AEAT-2), G.P. Dobson and B.D. Turland, Review of the CORVIS experiments,Feb 1998.

[IVN-MVI(98)-D057] (2-EU-MVI(98)-AEAT-3), E.J. Allen, B.D. Turland and G.P. Dobson, Interim Report - Models for Melt Vessel Interactions: Molten Pool Natural Convection Heat Transfer. AEA Technology report AEAT - 3853 Issue 1, July 1998.

[IVN-MVI(98)-D058] (2-EU-MVI(98)-AEAT-4), B.D. Turland and G.P. Dobson, Models for Lower Head Failure in a LWR Severe Accident. AEA Technology report AEAT - 4197 (September 1998)

[INV-MVI(96)-D059] (2-EU-MVI(96)-AEAT-5), B.D. Turland, Strategy for Model Development, October 1996.

[INV-MVI(97)-D060] (2-EU-MVI(98)-AEAT-6), G.P. Dobson and B.D. Turland, The Modelling of Jet Impingement Ablation. AEA Technology report AEAT - 1034, December 1996.

[INV-MVI(97)-D061] (2-EU-MVI(98)-AEAT-7), G.P. Dobson and B.D. Turland, The Modelling of Hole Ablation. AEA Technology report AEAT - 1033, December 1996.

[INV-MVI(96)-D062] (2-EU-MVI(96)-AEAT-8), B.D. Turland, Corium relocation scenarios for melt-vessel interaction studies(draft), September 1996.

[INV-MVI(96)-D063] (2-EU-MVI(96)-AEAT-9), B.D. Turland, Corium Properties for Melt-Vessel Interaction Studies, July 1996.

[INV-MVI(96)-D064] (2-EU-MVI(96)-AEAT-10), G.P. Dobson and B.D. Turland, Retention of debris of the lower head by in- and ex-vessel flooding. Final Report, June 1996.

[**ENEL:]**

[INV-MVI(98)-D065] (2-EU-MVI(98)-ENEL-1), F. Parozzi, R. Fontana, and E. Salina, Radiative Heat Removal Processes Affecting In-Vessel Corium Retention. *Proceedings ot the OECD/CSNI Workshop on 'In-Vessel Core Debris Retention and Coolability'*, pp. 351-363, Garching, Germany, 3-6 March, 1998.

[INV-MVI(98)-D066] (2-EU-MVI(98)-ENEL-2), F. Parozzi and R. Fontana, CORIUM-2D Advanced Code, ENEL report, PAM 98-006, 1998.

[**ECN:]**

[INV-MVI(98)-D067] (2-EU-MVI(98)-ECN-1), J.A. Lycklama and A. Nijeholt, Heat Transfer Chararcteristics of an Internally Heated Pool of Water in a Quarter of a Circular Slice, ECN-CX–98-115, April 1998.

[INV-MVI(98)-D068] (2-EU-MVI(98)-ECN-2), N.B.Siccama, M.Houkema, and E.M.J.Komen, Computational Fluid Dynamivs Calculations on the BALI Experiment, 21042/99.23726/C PPT/AS/MH, NRG, 15 March 1999.

[**VTT:]**

[INV-MVI(96)-D069] (2-EU-MVI(96)-VTT-1), Ikonen K., Creep in thermo-elastic-plastic deformation and stress analysis. VTT Energy. Technical Report, VAHTI-6/96. 48 p.

[INV-MVI(96)-D070] (2-EU-MVI(96)-VTT-2), Ikonen K., Lindholm I., A Numerical analysis for determination of the effective thermal conductivity of granular core debris. VTT Energy. Technical Report, VAHTI-11/96. 16 p.

[INV-MVI(97)-D071] (2-EU-MVI(97)-VTT-3), Ikonen K., Heating of reactor pressure vessel bottom head and penetrations in a severe reactor accident. Espoo: Technical Research Centre of Finland, 1997. 120 p. + app. 12 p.

[INV-MVI(97)-D072] (2-EU-MVI(97)-VTT-4), Ikonen K., Kelppe S., Ranta-Puska K., Mechanical analysis of a nuclear fuel rod in a fast thermal transient. VTT Energy. Technical Report, PATRA-3/97 & ROIMA-6/97. 44 p.

[INV-MVI(97)-D073] (2-EU-MVI(97)-VTT-5), Ikonen K., Lindholm I., Melting Analysis of Penetrations in BWR Pressure Vessel lower Head in severe Accidents. VTT Energy. Technical Report, ROIMA-10/97. 35 p.

[INV-MVI(97)-D074] (2-EU-MVI(97)-VTT-6), Lindholm I., Hedberg K., Thomsen K., Ikonen K., On debris behaviour in a pressure vessel lower head of Nordic boiling water reactors. Final Technical Report NKS/RAK-2(97) TR-A4. October 1997. 84 s.

[INV-MVI(97)-D075] (2-EU-MVI(97)-VTT-7), Lindholm I., Ikonen K., Hedberg K., Studies on core melting behaviour in a pressure vessel lower heads. OECD meeting in Garching 3-5.3. 1997. 8p.

[INV-MVI(99)-D076] (2-EU-MVI(99)-VTT-8), Ikonen K., REVISA RUPTHER #14 Post-test analysis. VTT Energy. Technical Report, x/99., 20 p.

[INV-MVI(99)-D077] (2-EU-MVI(99)-VTT-9), Ikonen K., FOREVER Post-test analysis. VTT Energy. Technical Report, x/99. 20 p.

[INV-MVI(99)-D078] (2-EU-MVI(99)-VTT-10), Ikonen K., Dinh N., Green J., Mechanical analyses of AP-600 RPV bottom in core melting accident. VTT Energy. Technical Report, x/99. 20 p.

[INV-MVI(99)-D079] (2-EU-MVI(99)-VTT-11), Ikonen K., Fittings for REVISA creep measurement data. VTT Energy. Technical Report, x/99. 20 p.

[**SIEMENS:]**

[INV-MVI(96)-D080] (3-EU-MVI(97)-SIEMENS-1), J.ARTNIK, Outside cooling of RPV of a PWR KONVOI size with modeling of two-phase molten pool by ADINA-F,August 1996.

[INV-MVI(99)-D081] (3-EU-MVI(99)-SIEMENS-2), N. I. Kolev, I. Roloff-Bock, Potential for external cooling of Boiling Water Reactors during postulated sever accidents with melt relocation, december 1999.

[**UNIVERSITA' DI ROMA "LA SAPIENZA":]**

[INV-MVI(99)-D082] (3-EU-MVI(99)-UNIVERSITA' DI ROMA "LA SAPIENZA"-1), M. Caira, G. Caruso, U. Pasquali, CHF Prediction for Downward-Facing Inclined Surfaces, March 1999.